

2009

# New Liquid Crystalline [2]Rotaxanes

Natalie Suhan  
*University of Windsor*

Follow this and additional works at: <http://scholar.uwindsor.ca/etd>

---

## Recommended Citation

Suhan, Natalie, "New Liquid Crystalline [2]Rotaxanes" (2009). *Electronic Theses and Dissertations*. Paper 399.

This online database contains the full-text of PhD dissertations and Masters' theses of University of Windsor students from 1954 forward. These documents are made available for personal study and research purposes only, in accordance with the Canadian Copyright Act and the Creative Commons license—CC BY-NC-ND (Attribution, Non-Commercial, No Derivative Works). Under this license, works must always be attributed to the copyright holder (original author), cannot be used for any commercial purposes, and may not be altered. Any other use would require the permission of the copyright holder. Students may inquire about withdrawing their dissertation and/or thesis from this database. For additional inquiries, please contact the repository administrator via email ([scholarship@uwindsor.ca](mailto:scholarship@uwindsor.ca)) or by telephone at 519-253-3000ext. 3208.

# *New Liquid Crystalline [2]Rotaxanes*

By

Natalie D. Suhan

A Dissertation

Submitted to the Faculty of Graduate Studies  
through the Department of Chemistry and Biochemistry  
in Partial Fulfillment of the Requirements for  
the Degree of Doctor of Philosophy at the  
University of Windsor

Windsor, Ontario, Canada

2009

© Natalie D. Suhan

All Rights Reserved

---

**AUTHOR'S DECLARATION OF ORIGINALITY**

I hereby certify that I am the sole author of this thesis and that no part of this thesis has been published or submitted for publication.

I certify that, to the best of my knowledge, my thesis does not infringe upon anyone's copyright nor violate any proprietary rights and that any ideas, techniques, quotations, or any other material from the work of other people included in my thesis, published or otherwise, are fully acknowledged in accordance with the standard referencing practices. Furthermore, to the extent that I have included copyrighted material that surpasses the bounds of fair dealing within the meaning of the Canada Copyright Act, I certify that I have obtained a written permission from the copyright owner(s) to include such material(s) in my thesis and have included copies of such copyright clearances to my appendix.

I declare that this is a true copy of my thesis, including any final revisions, as approved by my thesis committee and the Graduate Studies office, and that this thesis has not been submitted for a higher degree to any other University or Institution.

---

**ABSTRACT**

This thesis presents design, synthesis and characterization of a range of new liquid crystalline interlocked molecules and to study structure-property relationships between rotaxane design and mesomorphism. Chapter 1 introduces concepts of supramolecular chemistry and liquid crystals and cooperative effect between [2]rotaxane and liquid crystals towards functional molecular machines.

In Chapter 2, a systematic approach to introduce liquid crystallinity into the 1,2-bis(pyridinium)ethane/**DB24C8** motif is described. The chapter begins with synthesis and purification of dumbbells (without macrocycle) and [2]rotaxanes (with macrocycle) substituted with purely aliphatic extended 3,5-disubstituted stoppers with increasing alkyl chain length. Chapter continues with phase characterization and structure-property relationships between dumbbells and rotaxanes. The dodecane chain was sufficiently fluid to induce smectic mesomorphism in both the dumbbell and [2]rotaxane, with [2]rotaxane forming SmA phase by POM and XRD analysis.

Chapter 3 presents an extension to Chapter 2 with the addition of longer straight chain and branching aliphatic chains to our 1,2-bis(pyridinium)ethane/**DB24C8** rotaxane motif to study structure-property relationships and phase characteristics. The ability of the side-chain to self-organized showed large differences in phase behaviour. The pentadecane straight chain extended [2]rotaxane exhibited a unidentified mesophase, the hexadecane straight chain [2]rotaxane showed SmA mesomorphism, the branched hexadecane and the hyperbranched [2]rotaxanes both showed lamellar soft crystal phases.

Chapter 4 describes the effect of applying groups typical for low molecular weight LCs (siloxanes) to our 1,2-bis(pyridinium)ethane/**DB24C8** motif and a modified

---

rotaxane design based on a bis(oxymethylbenzylpyridinium)ethane/**DB24C8** motif. The structure-property relations between both systems, and in comparison with the dodecane chain substituted systems, are presented. The new design revealed SmC mesophases for both the dodecane and siloxane substituted [2]rotaxanes.

Chapter 5 focuses on the introduction of chirality into the siloxane substituted [2]rotaxane with SmC mesomorphism presented in Chapter 4. Chirality was introduced via a chiral anion as well as incorporation of a chiral crown. Observations to changes in the superstructure from the incorporation of chirality is addressed. The chiral anion exchanged [2]rotaxane showed SmC\* mesomorphism and the chiral crown [2]rotaxane showed SmX\* mesomorphism.

Chapter 6 presents the design and synthesis of a molecular shuttle based upon the structure-property relations determined from the previous chapters.

*This work is dedicated to my mother, father, Tina and to my best friend Sarah.  
Thank you for always believing in me.*

---

**ACKNOWLEDGEMENTS**

First and foremost, I would like to thank my advisor, Steve Loeb, for his guidance and support throughout the years, and for patience with me for I do not possess that virtue. I can only imagine how difficult I was to deal with at times, though I think I've gotten better with age...like a fine 'non-eucalyptus' red wine. I would also like to thank you for all the wonderful toys that you've purchased over the years, partially due to my unstoppable whining. Without the automated chromatography system and microwave nearly half of the thesis would not have been complete. Thank you for all of your support, encouragement and great times.

I would also like to thank my second advisor, Holger Eichhorn, for giving me the opportunity to work with him. Thanks for the training on all of the instrumentation and again for your patience with me and my clumsy fat fingers, for I cannot and do not want to have to draw fibres ever again. I have learned so much from both of my advisors and I truly appreciate all of their efforts to help make this thesis a success.

A special thank you to Steve, Holger and Elizabeth Viljoen for proof reading my thesis. I still can't believe how many mistakes I made that you caught, "potassium tribromide"!

To my friends and co-workers in the Loeb group, past and present, thanks for all the great times and laughs we shared, even if most were at my expense.

Lastly, I would like to thank my family, which of course includes you Sarah, for standing by me through all these years of school. They have always been a source of encouragement.



---

**TABLE OF CONTENTS**

AUTHOR'S DECLARATION OF ORIGINALITY .....	iv
ABSTRACT .....	v
DEDICATION .....	vii
ACKNOWLEDGMENTS .....	viii
LIST OF FIGURES .....	xvii
LIST OF TABLES .....	xxvii
LIST OF SCHEMES .....	xxxiv
LIST OF ABBREVIATIONS .....	xxxv
CHAPTER 1 – <i>Introduction</i> .....	1
1.1 SUPRAMOLECULAR CHEMISTRY .....	1
1.2 SUPRAMOLECULAR INTERACTIONS .....	2
1.3 INTERPENETRATED AND INTERLOCKED MOLECULES .....	3
1.3.1 Threading and Dethreading of Pseudorotaxanes .....	4
1.3.2 Rotaxanes .....	6
1.3.3 Molecular Machines .....	6
1.4 LIQUID CRYSTALS .....	12
1.4.1 General Introduction .....	12
1.4.2 Calamitic Liquid Crystals .....	14
1.4.2.1 Nematic Liquid Crystals .....	16
1.4.2.1 Smectic Liquid Crystals .....	17
1.4.3 Chirality in Liquid Crystals .....	20
1.4.4 Liquid Crystal Phase Characterization .....	22

---

1.4.4.1 Differential Scanning Calorimetry.....	23
1.4.4.2 Polarizing Optical Microscopy .....	24
1.4.4.3 X-Ray Diffraction .....	27
1.5 THE COOPERATIVE EFFECT.....	28
1.6 THE <i>LOEB</i> MOTIF .....	33
1.7 SCOPE OF THESIS .....	35
CHAPTER 2 – <i>Discovery of a Liquid Crystal [2]Rotaxane</i> .....	37
2.1 INTRODUCTION .....	37
2.2 SYNTHESIS AND CHARACTERIZATION .....	40
2.2.1 Synthesis .....	40
2.2.2 <sup>1</sup> H NMR Spectroscopy.....	44
2.2.3 Single Crystal Structure .....	46
2.3 LIQUID CRYSTAL PHASE CHARACTERIZATION .....	48
2.3.1 Thermal Gravimetric Analysis (TGA).....	48
2.3.2 Defect Textures Observed by Polarized Optical Microscopy (POM) .....	50
2.3.3 Differential Scanning Calorimetry (DSC) .....	54
2.3.4 Variable Temperature X-Ray Diffraction (XRD).....	57
2.3.5 Processing and Alignment of LC Materials.....	59
2.3.6 Calculated Packing Volumes Ratios and Molecular Lengths.....	63
2.3.7 Liquid Crystal Phase Determination.....	64
2.4 SUMMARY AND CONCLUSIONS .....	66
2.5 EXPERIMENTAL.....	67
2.5.1 General Comments.....	67

---

2.5.2 Synthesis of Compound [2-1][OTf] .....	69
2.5.3 Synthesis of Compound [2-2][OTf] <sub>2</sub> .....	70
2.5.4 Synthesis of Compound 2-3.....	72
2.5.5 Synthesis of Compound 2-4.....	73
2.5.6 Synthesis of Compound 2-5.....	74
2.5.7 Synthesis of Compound 2-6.....	75
2.5.8 Synthesis of Compound 2-7.....	76
2.5.9 Synthesis of Compound 2-8.....	78
2.5.10 Synthesis of Compound 2-9.....	80
2.5.11 Synthesis of Compound [2-10][OTf] <sub>4</sub> .....	82
2.5.12 Synthesis of Compound [2-11][OTf] <sub>4</sub> .....	85
2.5.13 Synthesis of Compound [2-12][OTf] <sub>4</sub> .....	86
2.5.14 Synthesis of Compound [2-13][OTf] <sub>4</sub> .....	88
2.5.15 Synthesis of Compound [2-14][OTf] <sub>4</sub> .....	89
2.5.16 Synthesis of Compound [2-15] [OTf] <sub>4</sub> .....	94
2.5.17 Synthesis of Compound [2-16][OTf] <sub>4</sub> .....	98
2.5.18 Synthesis of Compound [2-17][OTf] <sub>4</sub> .....	102
CHAPTER 3 – <i>Improving Mesomorphism in [2]Rotaxanes</i> .....	106
3.1 INTRODUCTION .....	106
3.2 SYNTHESIS AND CHARACTERIZATION .....	107
3.2.1 Synthesis .....	107
3.2.2 Purification.....	110
3.2.3 <sup>1</sup> H NMR Spectroscopy.....	111

---

3.2.4 Mass Spectrometry.....	112
3.3 LIQUID CRYSTAL PHASE CHARACTERIZATION .....	114
3.3.1 Thermal Gravimetric Analysis (TGA).....	114
2.3.2 Defect Textures Observed by Polarized Optical Microscopy (POM) .....	115
3.3.3 Differential Scanning Calorimetry (DSC) .....	119
3.3.4 Variable Temperature X-Ray Diffraction (XRD).....	122
3.3.5 Processing of LC Materials.....	125
3.3.6 Calculated Packing Volumes Ratios and Molecular Lengths.....	126
3.3.7 Liquid Crystal Phase Determination .....	127
3.4 SUMMARY AND CONCLUSIONS .....	128
3.5 EXPERIMENTAL.....	130
3.5.1 General Comments.....	130
2.5.2 Synthesis of Compound <b>3-1</b> .....	132
3.5.3 Synthesis of Compound <b>3-2</b> .....	133
3.5.4 Synthesis of Compound <b>3-3</b> .....	134
3.5.5 Synthesis of Compound <b>3-4</b> .....	135
3.5.6 Synthesis of Compound <b>3-5</b> .....	137
3.5.7 Synthesis of Compound <b>3-6</b> .....	139
3.5.8 Synthesis of Compound <b>3-7</b> .....	141
3.5.9 Synthesis of Compound <b>3-8</b> .....	143
3.5.10 Synthesis of Compound <b>[3-9][OTf]<sub>4</sub></b> and <b>[3-10][OTf]<sub>4</sub></b> .....	145
3.5.11 Synthesis of Compound <b>[3-11][OTf]<sub>4</sub></b> .....	150
3.5.12 Synthesis of Compound <b>[3-12][OTf]<sub>4</sub></b> .....	154

---

3.5.13 Synthesis of Compound [3-13][OTf] <sub>4</sub> .....	158
CHAPTER 4 – A New Design: Liquid Crystal [2]Rotaxanes .....	162
4.1 INTRODUCTION .....	162
4.2 SYNTHESIS AND CHARACTERIZATION .....	164
4.2.1 Synthesis .....	164
4.2.1.1 Synthesis of the Four-Charged Design .....	164
4.2.1.2 Synthesis of the Two-Charged Design .....	166
4.2.2 <sup>1</sup> H NMR and <sup>13</sup> C NMR Spectroscopy .....	169
4.2.3 UV-Vis Spectroscopy .....	172
4.2.4 Single Crystal Structure .....	173
4.3 LIQUID CRYSTAL PHASE CHARACTERIZATION .....	176
4.3.1 Thermal Gravimetric Analysis (TGA).....	176
4.3.2 Defect Textures Observed by Polarized Optical Microscopy (POM) .....	177
4.3.3 Differential Scanning Calorimetry (DSC) .....	181
4.3.4 Variable Temperature X-Ray Diffraction (XRD).....	182
4.3.5 Alignment of LC Materials.....	184
4.3.6 Calculated Packing Volumes Ratios and Molecular Lengths.....	186
4.3.7 Liquid Crystal Phase Determination.....	188
4.4 SUMMARY AND CONCLUSIONS .....	189
4.5 EXPERIMENTAL.....	191
4.5.1 General Comments.....	191
4.5.2 Synthesis of Compound <b>4-1</b> .....	194
4.5.3 Synthesis of Compound <b>4-2</b> .....	197

---

4.5.4 Synthesis of Compound <b>4-3</b> .....	200
4.5.5 Synthesis of Compound <b>4-4</b> .....	202
4.5.6 Synthesis of Compound <b>[4-5][OTf]<sub>4</sub> and [4-6][OTf]<sub>4</sub></b> .....	204
4.5.7 Synthesis of Compound <b>4-7</b> .....	207
4.5.8 Synthesis of Compound <b>4-8</b> .....	208
4.5.9 Synthesis of Compound <b>[4-9][OTf]<sub>2</sub></b> .....	210
4.5.10 Synthesis of Compound <b>4-10</b> .....	214
4.5.11 Synthesis of Compound <b>4-11</b> .....	217
4.5.12 Synthesis of Compound <b>4-12</b> .....	219
4.5.13 Synthesis of Compound <b>4-13</b> .....	222
4.5.14 Synthesis of Compound <b>4-14</b> .....	224
4.5.15 Synthesis of Compound <b>4-15</b> .....	227
4.5.16 Synthesis of Compound <b>[4-16][OTf]<sub>2</sub></b> .....	230
4.5.17 Synthesis of Compound <b>[4-17][OTf]<sub>2</sub></b> .....	233
4.5.18 Synthesis of Compound <b>[4-18][OTf]<sub>2</sub></b> .....	235
4.5.19 Synthesis of Compound <b>[4-19][OTf]<sub>2</sub></b> .....	240
CHAPTER 5 - <i>Chirality in a Liquid Crystal [2]Rotaxane</i> .....	244
5.1 INTRODUCTION .....	244
5.2 SYNTHESIS AND CHARACTERIZATION .....	247
5.2.1 Synthesis .....	247
5.2.2 <sup>1</sup> H NMR Spectroscopy.....	249
5.2.3 Results and Discussion: Pseudorotaxane Studies .....	253
5.3 LIQUID CRYSTAL PHASE CHARACTERIZATION .....	257

---

5.3.1 Defect Textures Observed by Polarized Optical Microscopy (POM) .....	258
5.3.2 Differential Scanning Calorimetry (DSC) .....	260
5.3.3 Variable Temperature X-Ray Diffraction (XRD).....	261
5.3.4 Processing of LC Materials.....	263
5.3.5 Liquid Crystal Phase Determination.....	264
5.4 SUMMARY AND CONCLUSIONS .....	265
5.5 EXPERIMENTAL.....	267
5.5.1 General Comments.....	267
5.5.2 Synthesis of Compound [5-1][Cam(SO <sub>3</sub> ) <sub>2</sub> ].....	269
5.5.3 Synthesis of Compound 5-2.....	271
5.5.4 Synthesis of Compound 5-3.....	273
5.5.5 Synthesis of Compound [5-4][OTf] <sub>2</sub> .....	277
5.5.6 Synthesis of Compound [5-5][OTf] <sub>2</sub> .....	289
5.5.7 Synthesis of Compound [5-6][OTf] <sub>2</sub> .....	291
CHAPTER 6 - <i>Towards Liquid Crystalline Molecular Machines</i> .....	283
6.1 INTRODUCTION .....	283
6.1.1 [2]Rotaxane Molecular Shuttles .....	283
6.1.2 Mesogenic [2]Rotaxane Molecular Shuttles .....	284
6.1.3 Our Approach to a Mesogenic [2]Rotaxane Molecular Shuttle.....	287
6.2 SYNTHESIS AND CHARACTERIZATION .....	290
6.2.1 Synthesis .....	290
6.2.2 <sup>1</sup> H NMR Spectroscopy.....	295
6.3 SUMMARY AND CONCLUSIONS .....	298

---

6.4 EXPERIMENTAL.....	300
6.4.1 General Comments.....	300
6.4.2 Synthesis of Compound <b>6-1</b> .....	301
6.4.3 Synthesis of Compound <b>6-2</b> .....	302
6.4.4 Synthesis of Compound <b>6-3</b> .....	305
6.4.5 Synthesis of Compound <b>6-4</b> .....	308
6.4.6 Synthesis of Compound [ <b>6-5</b> ][ <b>BF<sub>4</sub></b> ] <sub>2</sub> .....	311
6.4.7 Synthesis of Compound [ <b>6-6</b> ][ <b>BF<sub>4</sub></b> ] <sub>3</sub> .....	314
6.4.8 Synthesis of Compound [ <b>6-7</b> ][ <b>OTf</b> ] <sub>4</sub> .....	317
6.4.9 Synthesis of Compound <b>6-8</b> .....	321
6.4.10 Synthesis of Compound [ <b>6-9</b> ][ <b>OTf</b> ] <sub>4</sub> .....	322
REFERENCES .....	323
VITA AUCTORIS .....	339



---

**LIST OF FIGURES**

Figure 1.1 – Examples from the works of C. Pedersen, J.-M. Lehn and D. Cram .....	1
Figure 1.2 - Various types of non-covalent interactions.....	2
Figure 1.3 – Illustration of complexed [2]pseudorotaxane and its uncomplexed components.....	4
Figure 1.4 – Templates for pseudorotaxane formation used by Stoddart .....	5
Figure 1.5 – Folding/Unfolding pseudorotaxane work by Kim <i>et al.</i> .....	5
Figure 1.6 – Formation of a [2]rotaxane by threading followed by stoppering.....	7
Figure 1.7 – [2]rotaxane as a molecular shuttle .....	8
Figure 1.8 – Mechanical switching of $\alpha$ -CD by photoisomerization of the encapsulated azobenzene based dumbbell.....	8
Figure 1.9 – Structural and graphical representation of a disulfide-tethered molecular muscle [3]rotaxane constructed by Stoddart <i>et al.</i> .....	9
Figure 1.10 – Graphical representations of the proposed bending action a cantilever coated with the disulfide-tethered molecular muscle.....	10
Figure 1.11 – Structural and graphical representation for generation of nano-meter scale elevator with pseudorotaxane formation between the trifurcated cationic guest and tritopic host followed by stoppering with 3,5-di-tert-butylbenzylbromide, constructed by Stoddart <i>et al.</i> .....	11
Figure 1.12 – Illustration for the operation of the nano-meter scale elevator.....	12
Figure 1.13 – Illustration for states of matter and two major classes of liquid crystals ...	13
Figure 1.14 – Examples of a) calamitic and b) discotic mesogens.....	14

---

Figure 1.15 – Illustration of crystalline (Cr), smectic C (SmC), smectic A (SmA), nematic (N) and isotropic liquid (I) phases exhibited by calamitic mesogens.....	15
Figure 1.16 – The general structural template for calamitic LCs .....	15
Figure 1.17 – Graphical and schematic representation of nematic phase.....	17
Figure 1.18 – a) Illustrations of molecular packing in SmA and SmC phases and b) layer shrinkage from SmA to SmC phase.....	19
Figure 1.19 – Plan views of molecular organization in SmB, SmI and SmF mesophases. The tilt is depicted by the direction of the triangle .....	20
Figure 1.20 – Schematic illustration of the helical superstructure of the chiral bulk SmC* phase and the direction of the director on the tilt cone .....	22
Figure 1.21 - A DSC plot showing the three typical phase transitions: $T_g$ , $T_m$ , $T_c$ .....	24
Figure 1.22 – POM of N phase with Schlieren textures featuring point defects with 2-brush and 4-brush disclinations. b) Shows defects with the corresponding s value .....	26
Figure 1.23 – POM of SmA phase showing fan-shaped texture and SmC phase showing broken fan-shaped texture.....	26
Figure 1.24 – Bragg reflection from a set of crystal planes with a spacing $d_{hkl}$ .....	27
Figure 1.25 – a) Structure of LCs used and b) time profile of the photoinduced inchworm walk of the LC laminated film by alternate irradiation with UV and visible light at room temperature.....	29
Figure 1.26 – a) Structure of mesogen-substituted polyrotaxane.....	31
Figure 1.27 – a) Structure of LC free [2]catenane, b) Possible organization into Sm phase and c) fan-shaped texture of non-aligned Cu(I) complexed LC [2]catenane.....	32

---

Figure 1.28 - A LC bistable [2]rotaxane molecular shuttle done by Kato and Stoddart <i>et al</i> .....	33
Figure 1.29 – a) [2]pseudorotaxane: paraquat <sup>2+</sup> /crown ether, by Stoddart. b) Comparison of N <sup>+</sup> ···N <sup>+</sup> distances between paraquat <sup>2+</sup> and 1,2-bis(pyridinium)ethane <sup>2+</sup> .....	34
Figure 1.30 – Newman projection top view (top) and side view (bottom) showing non-covalent interactions between a 1,2-bis(dipyridinium)ethane <sup>4+</sup> stoppered thread and DB24C8 macrocyclic ring .....	35
Figure 2.1 - Newman projection showing non-covalent interactions between a 1,2-bis(dipyridinium)ethane <sup>4+</sup> stoppered thread and DB24C8 macrocyclic ring.....	37
Figure 2.2 - Graphical representation of dumbbell and [2]rotaxane based on gemini surfactant and tetracatenar design for calamitic LCs.....	38
Figure 2.3 - Structural and graphical representation of a) gemini surfactant synthesized by Menger and Keiper <i>et al</i> ; b) tetracatenar generated from the design synthesized by Bruce and co-workers.....	39
Figure 2.4 - Colour of, a) free axle, b) free macrocycle, c) [2]pseudorotaxane and d) [2]rotaxane in MeCN.....	43
Figure 2.5 - <sup>1</sup> H NMR spectra of a) <b>2-11<sup>4+</sup></b> and b) <b>2-2<sup>2+</sup></b> in CD <sub>3</sub> CN at 500 MHz.. ..	44
Figure 2.6 - <sup>1</sup> H NMR spectra of a) <b>2-17<sup>4+</sup></b> , b) <b>2-2<sup>2+</sup></b> and c) <b>DB24C8</b> in CD <sub>3</sub> CN.....	45
Figure 2.7 - <sup>1</sup> H NMR spectra of a) <b>2-10<sup>4+</sup></b> , b) <b>2-14<sup>4+</sup></b> in CD <sub>3</sub> CN.....	46
Figure 2.8 - Single crystal of <b>2-14<sup>4+</sup></b> a) ball-and-stick view, b) space filling view.....	47
Figure 2.9 - TGA curves of dumbbells <b>2-10<sup>4+</sup></b> - <b>2-13<sup>4+</sup></b> at 2 °C/min under He .....	49
Figure 2.10 - TGA curves of [2]rotaxanes <b>2-14<sup>4+</sup></b> - <b>2-17<sup>4+</sup></b> at 2 °C/min under He .....	49

---

Figure 2.11 - POM of <b>2-11<sup>4+</sup></b> (crossed polarizers): a) crystallized from MeCN @ 25 °C, b) squeezed between glass slides @ 25 °C and c) @ 200 °C. ....	.51
Figure 2.12 - POM of <b>2-12<sup>4+</sup></b> (crossed polarizers): a) crystallized from MeCN @ 25 °C, b) squeezed between glass slides @ 25 °C and c) @ 200 °C .....	.51
Figure 2.13 - POM of <b>2-13<sup>4+</sup></b> (crossed polarizers): a) crystallized from MeCN @ 25 °C, b) squeezed between glass slides @ 25 °C and c) @ 25 °C upon cooling from 150 °C.....	.52
Figure 2.14 - POM of <b>2-15<sup>4+</sup></b> (crossed polarizers): a) crystallized from MeCN @ 25 °C, b) squeezed between glass slides @ 25 °C and c) @ 80 °C .....	.53
Figure 2.15 - POM of <b>2-16<sup>4+</sup></b> (crossed polarizers): a) crystallized from MeCN @ 25 °C, b) squeezed between glass slides @ 25 °C and c) @ 80 °C .....	.53
Figure 2.16 - POM of <b>2-17<sup>4+</sup></b> (crossed polarizers): a) precipitate from MeCN @ 25 °C, b) squeezed between glass slides @ 123 °C and c) @ 25 °C upon cooling from T <sub>i</sub> .....	.54
Figure 2.17 - Second heating DSC runs of dumbbells <b>2-10<sup>4+</sup></b> to <b>2-13<sup>4+</sup></b> at 5 °C/min under N <sub>2</sub> and first heating runs (dashed) of <b>2-12<sup>4+</sup></b> and <b>2-13<sup>4+</sup></b> .....	.55
Figure 2.18 - The second heating and cool DSC run of [2]rotaxane <b>2-17<sup>4+</sup></b> at 10 °C/min under N <sub>2</sub> .....	.56
Figure 2.19 - vt-XRD data of a) <b>2-10<sup>4+</sup></b> at 25 °C, b) <b>2-11<sup>4+</sup></b> (inset at 120 °C), c) <b>2-12<sup>4+</sup></b> (inset at 170 °C) and d) <b>2-13<sup>4+</sup></b> (inset at 50 °C on cooling).....	.58
Figure 2.20 - vt-XRD data of a) <b>2-14<sup>4+</sup></b> , b) <b>2-15<sup>4+</sup></b> , c) <b>2-16<sup>4+</sup></b> and d) <b>2-17<sup>4+</sup></b> , (insets are XRD on cool).....	.59

---

Figure 2.21 - 2D-XRD pattern (left) and POM (right) of <b>2-13<sup>4+</sup></b> as fibre drawn from the bulk material when submerged in decane/CH <sub>2</sub> Cl <sub>2</sub> at 25 °C (alignment shown with fibre rotated by 45 °, overlaid).....	.60
Figure 2.22 - POMs of <b>2-17<sup>4+</sup></b> a) shear alignment, b) rotated by 45°, c) in cells treated for homogeneous alignment with rubbed polyimide, and d) homeotropic alignment with cetyl-trimethylammonium bromide .....	.61
Figure 2.23 - Drawn fibre of <b>2-17<sup>4+</sup></b> , b) 2D-XRD pattern of drawn fibre at 25 ° C, and c) molecular modeling (MM3) diagram showing self-organization into a SmA phase. Alkyl chains were input in a disordered fashion to simulate packing.....	.62
Figure 2.24 - Phase transitions for dumbbells <b>2-11<sup>4+</sup></b> - <b>2-13<sup>4+</sup></b> (left) and [2]rotaxanes <b>2-15<sup>4+</sup></b> - <b>2-17<sup>4+</sup></b> (right) measured by DSC and POM on heating.....	.65
Figure 3.1 – Structural representation of [2]rotaxanes with the various aliphatic benzylic stoppers used in this chapter.....	107
Figure 3.2 - Colour of [2]pseudorotaxane (left) at t = 0 and of [2]rotaxane <b>3-5<sup>4+</sup></b> (right) at t = 5 h by applying microwave irradiation.....	110
Figure 3.3 - a) structure of <b>3-10<sup>4+</sup></b> and <b>3-9<sup>4+</sup></b> and b) <sup>1</sup> H NMR spectra of <b>3-10<sup>4+</sup></b> and <b>3-9<sup>4+</sup></b> in CD <sub>3</sub> CN .....	.112
Figure 3.4 - ESI-Mass spectra of experimental data for a) <b>3-9<sup>+</sup></b> , b) <b>3-9<sup>2+</sup></b> , c) <b>3-9<sup>3+</sup></b> and b) <b>3-9<sup>4+</sup></b> .....	.113
Figure 3.5 - TGA curves of [2]rotaxanes <b>3-9<sup>4+</sup></b> , <b>3-12<sup>4+</sup></b> and <b>3-13<sup>4+</sup></b> at 2 °C/min under He .....	.115

---

Figure 3.6 - POM of <b>3-9<sup>4+</sup></b> (crossed polarizers): a) crystallized from MeCN @ 25 °C, b) squeezed between glass slides @ 100 °C and c) @ 25 °C upon cooling from 190 °C... .116	
Figure 3.7 - POM of <b>3-11<sup>4+</sup></b> (crossed polarizers): a) precipitated from MeCN @ 25 °C, b) squeezed between glass slides @ 25 °C and c) @ 25 °C upon cooling from 190 °C..... .116	
Figure 3.8 - POM of <b>3-12<sup>4+</sup></b> (crossed polarizers): a) precipitated from MeCN @ 25 °C, b) squeezed between glass slides @ 150 °C, c) squeezed between glass slides @ 185 °C and d) @ 25 °C upon cooling from $T_i = 193$ °C ..... .117	
Figure 3.9 - POM of <b>3-13<sup>4+</sup></b> (crossed polarizers): a) crystallized from MeCN @ 25 °C, b) squeezed between glass slides @ 109 °C and c) @ 25 °C upon cooling from $T_i = 172$ °C ..... .118	
Figure 3.10 - First heating DSC runs of freshly crystallized (black) and dried (orange) [2]rotaxane <b>3-9<sup>4+</sup></b> at a rate of 10 °C/min under N <sub>2</sub> . ..... .120	
Figure 3.11 - Second heating and cool DSC run of [2]rotaxanes a) <b>3-9<sup>4+</sup></b> , b) <b>3-11<sup>4+</sup></b> , c) <b>3-12<sup>4+</sup></b> and d) <b>3-13<sup>4+</sup></b> at 10 °C/min under N <sub>2</sub> ..... .121	
Figure 3.12 - vt-XRD data of a) <b>3-9<sup>4+</sup></b> , b) <b>3-11<sup>4+</sup></b> , c) <b>3-12<sup>4+</sup></b> and d) molecular modeling (MM3) diagram showing self-organization of material into a SmA phase. Alkyl chains were input in a disordered fashion to simulate packing..... .123	
Figure 3.13 - vt-XRD data of <b>3-13<sup>4+</sup></b> , a) with layer spacing defined and b) with crystallinity defined ..... .124	
Figure 3.14 - POMs of <b>3-11<sup>4+</sup></b> a) shear alignment at 150 °C (in direction of arrow) and b) rotated by 45° ..... .125	
Figure 3.15 - Phase transition temperatures for [2]rotaxanes <b>3-9<sup>4+</sup></b> and <b>3-11<sup>4+</sup></b> through <b>3-13<sup>4+</sup></b> measured by DSC and POM on heating..... .128	

---

Figure 4.1 – Structural representation of [2]rotaxane: four-charge design (top) and [2]rotaxane: two-charge design (bottom) based on tetracatenar design for calamitic LCs .....	163
Figure 4.2 - Stacked $^{13}\text{C}$ NMR spectra of a) 3,5-dicarboxymethylbenzoic acid and b) <b>4-14</b> in the region between 120-175 ppm in $\text{CDCl}_3$ .....	169
Figure 4.3 - Stacked $^1\text{H}$ NMR spectra of a) dumbbell <b>4-6<math>^{4+}</math></b> and b) [2]rotaxane <b>4-5<math>^{4+}</math></b> in $\text{CD}_3\text{CN}$ .....	170
Figure 4.4 - Stacked $^1\text{H}$ NMR spectra of a) [2]rotaxane <b>4-18<math>^{2+}</math></b> , b) [2]rotaxane <b>4-19<math>^{2+}</math></b> , c) <b>2-9<math>^{2+}</math></b> and d) DB24C8 in $\text{CD}_3\text{CN}$ .....	171
Figure 4.5 - Stacked $^1\text{H}$ NMR spectra of a) dumbbell <b>4-16<math>^{2+}</math></b> and b) [2]rotaxane <b>4-17<math>^{2+}</math></b> in $\text{CD}_3\text{CN}$ .....	172
Figure 4.6 - UV-visible spectra of [2]rotaxanes <b>2-17<math>^{4+}</math></b> (orange) and <b>4-18<math>^{2+}</math></b> (black) in $\text{CH}_3\text{CN}$ .....	173
Figure 4.7 - Model of <b>4-17<math>^{2+}</math></b> generated from single crystal structure of the 3,5-dimethyl benzylated [2]rotaxane using MM3; a) ball-and-stick view and b) space filling view .	174
Figure 4.8 - TGA curves of four-charged [2]rotaxane <b>2-17<math>^{4+}</math></b> and two-charged [2]rotaxanes <b>4-18<math>^{2+}</math></b> and <b>4-19<math>^{2+}</math></b> obtained at rate of $2\text{ }^\circ\text{C}/\text{min}$ under He .....	177
Figure 4.9 - POM of <b>4-5<math>^{4+}</math></b> (crossed polarizers): a) crystallized from MeCN @ $25\text{ }^\circ\text{C}$ , b) squeezed between glass slides @ $25\text{ }^\circ\text{C}$ and c) @ $25\text{ }^\circ\text{C}$ upon cooling from $150\text{ }^\circ\text{C}$ .....	178
Figure 4.10 - POM of <b>4-18<math>^{2+}</math></b> (crossed polarizers): a) precipitated from MeCN @ $25\text{ }^\circ\text{C}$ , b) squeezed @ $25\text{ }^\circ\text{C}$ and c) @ $25\text{ }^\circ\text{C}$ upon cooling from $T_i = 111\text{ }^\circ\text{C}$ . .....	179
Figure 4.11 - POM of <b>4-19<math>^{2+}</math></b> (crossed polarizers), untreated glass (top filmstrip): a) precipitated from MeCN @ $25\text{ }^\circ\text{C}$ , b) at $146\text{ }^\circ\text{C}$ upon cooling from $T_i = 151\text{ }^\circ\text{C}$ and c) at	

---

25 °C upon cooling from $T_i$ . Freshly cleaned (hydrophilic) glass (bottom filmstrip): d) precipitated from MeCN @ 25 °C, e) at 146 °C upon cooling from $T_i = 151$ °C and f) at 25 °C upon cooling from $T_i$ .....	180
Figure 4.12 - Second heating and cool DSC run of [2]rotaxane <b>4-18</b> <sup>2+</sup> at 10 °C/min under N <sub>2</sub> . .....	182
Figure 4.13 - XRD of a) <b>4-5</b> <sup>4+</sup> and vt-XRD of b) <b>4-18</b> <sup>2+</sup> and c) <b>4-19</b> <sup>2+</sup> .....	183
Figure 4.14 - POMs of <b>4-5</b> <sup>4+</sup> a) shear alignment at 80 °C (in direction of arrow) and b) rotated by 45° .....	184
Figure 4.15 - POMs of <b>4-18</b> <sup>2+</sup> a) shear alignment at 75 °C (in direction of arrow) and b) rotated by 45°, c) in cell treated for parallel (homogeneous) alignment with rubbed polyimide, 4 μm gap .....	185
Figure 4.16 - POMs of <b>4-19</b> <sup>2+</sup> a) shear alignment at 120 °C (in direction of arrow), b) rotated by 45° and c) schlieren texture obtained after 15 seconds. d) Shear alignment of thin film pulled from teflon (in direction of arrow), e) rotated by 45°, and f) 2D-XRD pattern of thin film at 25 °C .....	186
Figure 4.17 - Phase transition temperatures for [2]rotaxanes <b>2-17</b> <sup>4+</sup> , <b>4-5</b> <sup>4+</sup> , <b>4-18</b> <sup>2+</sup> and <b>4-19</b> <sup>2+</sup> measured by DSC and POM on heating.....	189
Figure 5.1 – a) Schematic illustration of the symmetry elements of the achiral SmC phase, b) schematic illustrations of the helical superstructure of the chiral bulk SmC* phase and the direction of the director on the tilt cone and the corresponding direction of the vector of the spontaneous polarization ( $P_s$ ).....	245
Figure 5.2 – [2]Rotaxane [ <b>4-19</b> ][OTf] <sub>2</sub> chosen for the introduction of chirality.....	246



---

Figure 5.3 - $^1\text{H}$ NMR spectra of free $[(-)\text{CamSO}_3][\text{NH}_4]$ (top) and $[\mathbf{5-1}][(-)\text{CamSO}_3]_2$ in $\text{CD}_3\text{NO}_2$ .....	251
Figure 5.4 - $^1\text{H}$ NMR spectrum of $\mathbf{5-3}$ in $\text{CD}_3\text{CN}$ .....	252
Figure 5.5 - Stacked $^1\text{H}$ NMR spectra of a) dumbbell $[\mathbf{5-6}][\text{OTf}]_2$ and b) [2]rotaxane $[\mathbf{5-5}][\text{OTf}]_2$ in $\text{CD}_3\text{CN}$ .....	252
Figure 5.6 - $^1\text{H}$ NMR spectrum of $2 \times 10^{-3}$ M solution of $[\mathbf{5-4}][\text{OTf}]_2$ in $\text{CD}_3\text{CN}$ at 289K. The uncomplexed protons of the free components are designated by $u_x$ and the complexed [2]pseudorotaxane protons are designated by $c_x$ .....	254
Figure 5.7 - VT $^1\text{H}$ NMR spectra of $[\mathbf{5-4}][\text{OTf}]_2$ in $\text{CD}_3\text{CN}$ .....	256
Figure 5.8 - The van't Hoff plot for $[\mathbf{5-4}][\text{OTf}]_2$ plotted from $^1\text{H}$ NMR data.....	257
Figure 5.9 - Variation of $\Delta G^\circ$ , $\Delta H^\circ$ and $T\Delta S^\circ$ with temperature for $[\mathbf{5-4}][\text{OTf}]_2$ .....	257
Figure 5.10 - POM of $[\mathbf{5-1}][(-)\text{CamSO}_3]_2$ (crossed polarizers): a) squeezed between glass slides @ 25 °C, b) @ 90 °C upon heating, c) @ 135 °C upon heating and d) @ 25 °C upon cooling from $T_i = 153$ °C. All are shown at 50 X magnification .....	259
Figure 5.11 - POM of $[\mathbf{5-5}][\text{OTf}]_2$ (crossed polarizers): a) squeezed between glass slides @ 25 °C, b) @ 100 °C upon heating, c) @ 140 °C upon cooling from $T_i = 155$ °C, $t = 10$ s, d) @ 140 °C, $t = 45$ s and e, f) the two difference magnified areas of d .....	260
Figure 5.12 - Second heating and cooling DSC runs of [2]rotaxane $[\mathbf{5-5}][\text{OTf}]_2$ at 10 °C/min under $\text{N}_2$ .....	261
Figure 5.13 - vt-XRD data of a) $[\mathbf{5-1}][(-)\text{CamSO}_3]_2$ and b) $[\mathbf{5-5}][\text{OTf}]_2$ .....	263
Figure 5.14 - POMs of a) $[\mathbf{5-1}][(-)\text{CamSO}_3]_2$ mechanically sheared at 85 °C and b) rotated by 45°. c) Schlieren texture obtained for $[\mathbf{5-5}][\text{OTf}]_2$ after mechanically shearing at 120 °C, which remained throughout rotation of the sample.....	264

---

Figure 5.15 - Phase transition temperatures for [2]rotaxanes <b>[5-1][(-)CamSO<sub>3</sub>]<sub>2</sub></b> and <b>[5-5][OTf]<sub>2</sub></b> measured by DSC and POM on heating. ....	265
Figure 6.1 - Non degenerate [2]rotaxane molecular shuttle .....	284
Figure 6.2 - A LC switchable bistable [2]rotaxane molecular shuttle done by Kato and Stoddart <i>et al</i> .....	285
Figure 6.3 - Co-conformations of nematic [2]rotaxane molecular shuttle substituted with Fréchet polyaryl ether dendrons. Each sphere represents a generation .....	287
Figure 6.4 - Various components for the thread that will form a pseudorotaxane with the DB24C8 macrocycle.....	289
Figure 6.5 - Proposed design for a LC bistable [2]rotaxane molecular shuttle .....	290
Figure 6.6 - Stacked <sup>13</sup> C NMR spectra of a) <b>6-2</b> (acid) and b) <b>6-3</b> (anhydride) in the region between 100-180 ppm in CDCl <sub>3</sub> .....	295
Figure 6.7 - <sup>1</sup> H NMR spectrum of crown <b>6-4</b> in CDCl <sub>3</sub> .....	296
Figure 6.8 - Stacked <sup>1</sup> H NMR spectra of a) shuttle thread precursor <b>[6-6][OTf]<sub>3</sub></b> and b) shuttle thread <b>[6-7][OTf]<sub>4</sub></b> in CD <sub>3</sub> CN .....	297
Figure 6.9 - <sup>1</sup> H NMR spectrum of alternate shuttle thread <b>6-8</b> in CD <sub>2</sub> Cl <sub>2</sub> .....	298

---

**LIST OF TABLES**

Table 2.1 - Calculated weight % values for components of dumbbells and [2]rotaxanes along with actual weight % values for the first step losses.....	50
Table 2.2 - Transition temperatures (°C, midpoint) and enthalpies (kJ/mol) determined by DSC at scan rates of 5 °C/min for dumbbells and 10 °C/min for [2]rotaxanes.....	56
Table 2.3 - Obtained (XRD) layer spacings and calculated molecular lengths of dumbbells <b>2-11<sup>4+</sup></b> to <b>2-13<sup>4+</sup></b> and [2]rotaxanes <b>2-15<sup>4+</sup></b> to <b>2-17<sup>4+</sup></b> .....	64
Table 2.4 - <sup>1</sup> H NMR data of [ <b>2-1</b> ][Br] in D <sub>2</sub> O. MW <sub>Br</sub> = 344.058 g/mol.....	69
Table 2.5 - <sup>1</sup> H NMR data of [ <b>2-2</b> ][Br] <sub>2</sub> in D <sub>2</sub> O. MW <sub>Br</sub> = 500.229 g/mol.....	71
Table 2.6 - <sup>1</sup> H NMR data of [ <b>2-2</b> ][OTf] <sub>2</sub> in CD <sub>3</sub> CN. MW <sub>OTf</sub> = 638.559 g/mol.....	71
Table 2.7 - <sup>1</sup> H NMR data of <b>2-3</b> in CDCl <sub>3</sub> . MW= 364.476 g/mol.....	72
Table 2.8 - <sup>1</sup> H NMR data of <b>2-4</b> in CDCl <sub>3</sub> . MW= 448.635 g/mol.....	73
Table 2.9 - <sup>1</sup> H NMR data of <b>2-5</b> in CDCl <sub>3</sub> . MW= 532.795 g/mol.....	74
Table 2.10 - <sup>1</sup> H NMR data of <b>2-6</b> in CDCl <sub>3</sub> . MW= 287.107 g/mol.....	75
Table 2.11 - <sup>1</sup> H NMR data of <b>2-6</b> in CD <sub>3</sub> CN. MW= 287.107 g/mol.....	75
Table 2.12 - <sup>1</sup> H NMR data of <b>2-7</b> in CDCl <sub>3</sub> . MW= 427.374 g/mol.....	77
Table 2.13 - <sup>1</sup> H NMR data of <b>2-7</b> in CD <sub>3</sub> CN. MW= 427.374 g/mol.....	77
Table 2.14 - <sup>1</sup> H NMR data of <b>2-8</b> in CDCl <sub>3</sub> . MW= 511.532 g/mol.....	79
Table 2.15 - <sup>1</sup> H NMR data of <b>2-8</b> in CD <sub>3</sub> CN. MW= 511.532 g/mol.....	79
Table 2.16 - <sup>1</sup> H NMR data of <b>2-9</b> in CDCl <sub>3</sub> . MW= 595.691 g/mol.....	81
Table 2.17 - <sup>1</sup> H NMR data of <b>2-9</b> in CD <sub>3</sub> CN. MW= 595.691 g/mol.....	81
Table 2.18 - <sup>1</sup> H NMR data of [ <b>2-10</b> ][OTf] <sub>4</sub> in CD <sub>3</sub> CN. MW <sub>OTf</sub> = 1351.103 g/mol .....	82
Table 2.19 - <sup>13</sup> C NMR data of [ <b>2-10</b> ][OTf] <sub>4</sub> in CD <sub>3</sub> CN. MW <sub>OTf</sub> = 1351.103 g/mol.....	83

---

Table 2.20 - $^1\text{H}$ NMR data of <b>[2-11][OTf]<sub>4</sub></b> in $\text{CD}_3\text{CN}$ . $\text{MW}_{\text{OTf}} = 1631.634$ g/mol.....	.85
Table 2.21 - $^1\text{H}$ NMR data of <b>[2-12][OTf]<sub>4</sub></b> in $\text{CD}_3\text{CN}$ . $\text{MW}_{\text{OTf}} = 1799.533$ g/mol.....	.87
Table 2.22 - $^1\text{H}$ NMR data of <b>[2-13][OTf]<sub>4</sub></b> in $\text{CD}_3\text{CN}$ . $\text{MW}_{\text{OTf}} = 1968.277$ g/mol.....	.88
Table 2.23 - $^1\text{H}$ NMR data of <b>[2-14][OTf]<sub>4</sub></b> in $\text{CD}_3\text{CN}$ . $\text{MW}_{\text{OTf}} = 1799.610$ g/mol.....	.90
Table 2.24 - $^{13}\text{C}$ NMR data of <b>[2-14][OTf]<sub>4</sub></b> in $\text{CD}_3\text{CN}$ . $\text{MW}_{\text{OTf}} = 1799.610$ g/mol.....	.91
Table 2.25 - Crystal data/details: structure solution/refinement for <b>[2-14][OTf]<sub>4</sub></b> .....	.93
Table 2.26 - $^1\text{H}$ NMR data of <b>[2-15][OTf]<sub>4</sub></b> in $\text{CD}_3\text{CN}$ . $\text{MW}_{\text{OTf}} = 2080.145$ g/mol.....	.95
Table 2.27 - $^{13}\text{C}$ NMR data of <b>[2-15][OTf]<sub>4</sub></b> in $\text{CD}_3\text{CN}$ . $\text{MW}_{\text{OTf}} = 2080.145$ g/mol.....	.96
Table 2.28 - $^1\text{H}$ NMR data of <b>[2-16][OTf]<sub>4</sub></b> in $\text{CD}_3\text{CN}$ . $\text{MW}_{\text{OTf}} = 2248.464$ g/mol.....	.99
Table 2.29 - $^{13}\text{C}$ NMR data of <b>[2-16][OTf]<sub>4</sub></b> in $\text{CD}_3\text{CN}$ . $\text{MW}_{\text{OTf}} = 2248.464$ g/mol.....	.100
Table 2.30 - $^1\text{H}$ NMR data of <b>[2-17][OTf]<sub>4</sub></b> in $\text{CD}_3\text{CN}$ . $\text{MW}_{\text{OTf}} = 2416.782$ g/mol.....	.103
Table 2.31 - $^{13}\text{C}$ NMR data of <b>[2-17][OTf]<sub>4</sub></b> in $\text{CD}_3\text{CN}$ . $\text{MW}_{\text{OTf}} = 2416.782$ g/mol.....	.104
Table 3.1 - Calculated and found exact masses for [2]rotaxane <b>[3-9][OTf]<sub>4</sub></b> .....	.114
Table 3.2 - Calculated weight % values for components of [2]rotaxanes with actual weight % values for the first step losses.....	.115
Table 3.3 - Transition temperatures ( $^{\circ}\text{C}$ , midpoint) and enthalpies (kJ/mol) determined by DSC at scan rates of $10^{\circ}\text{C}/\text{min}$ for [2]rotaxanes.....	.120
Table 3.4 - Obtained (XRD) and calculated layer spacings of [2]rotaxanes <b>3-9<sup>4+</sup></b> and <b>3-11<sup>4+</sup></b> through <b>3-13<sup>4+</sup></b> .....	.127
Table 3.5 - $^1\text{H}$ NMR data of <b>3-1</b> in $\text{CDCl}_3$ . $\text{MW} = 616.954$ g/mol.....	.132
Table 3.6 - $^1\text{H}$ NMR data of <b>3-2</b> in $\text{CDCl}_3$ . $\text{MW} = 645.441$ g/mol.....	.133
Table 3.7 - $^1\text{H}$ NMR data of <b>3-3</b> in $\text{CDCl}_3$ . $\text{MW} = 645.007$ g/mol.....	.134
Table 3.8 - $^1\text{H}$ NMR data of <b>3-4</b> in $\text{CDCl}_3$ . $\text{MW} = 701.114$ g/mol.....	.136

---

Table 3.9 - $^1\text{H}$ NMR data of <b>3-5</b> in $\text{CDCl}_3$ . MW= 679.851 g/mol.....	.138
Table 3.10 - $^1\text{H}$ NMR data of <b>3-5</b> in $\text{CD}_3\text{CN}$ . MW= 679.851 g/mol.....	.138
Table 3.11 - $^1\text{H}$ NMR data of <b>3-6</b> in $\text{CDCl}_3$ . MW= 707.904 g/mol.....	.140
Table 3.12 - $^1\text{H}$ NMR data of <b>3-6</b> in $\text{CD}_3\text{CN}$ . MW= 707.904 g/mol.....	.140
Table 3.13 - $^1\text{H}$ NMR data of <b>3-7</b> in $\text{CDCl}_3$ . MW= 707.904 g/mol.....	.142
Table 3.14 - $^1\text{H}$ NMR data of <b>3-7</b> in $\text{CD}_3\text{CN}$ . MW= 707.904 g/mol.....	.142
Table 3.15 - $^1\text{H}$ NMR data of <b>3-8</b> in $\text{CDCl}_3$ . MW= 764.010 g/mol.....	.143
Table 3.16 - $^1\text{H}$ NMR data of <b>3-8</b> in $\text{CD}_3\text{CN}$ . MW= 764.010 g/mol.....	.144
Table 3.17 - $^1\text{H}$ NMR data of <b>[3-9][OTf]<sub>4</sub></b> in $\text{CD}_3\text{CN}$ . MW <sub>OTf</sub> = 2585.097 g/mol.....	.146
Table 3.18 - $^{13}\text{C}$ NMR data of <b>[3-9][OTf]<sub>4</sub></b> in $\text{CD}_3\text{CN}$ . MW <sub>OTf</sub> = 2585.097 g/mol.....	.147
Table 3.19 - $^1\text{H}$ NMR data of <b>[3-10][OTf]<sub>4</sub></b> in $\text{CD}_3\text{CN}$ . MW <sub>OTf</sub> = 2134.985 g/mol.....	.149
Table 3.20 - $^1\text{H}$ NMR data of <b>[3-11][OTf]<sub>4</sub></b> in $\text{CD}_3\text{CN}$ . MW <sub>OTf</sub> = 2641.204 g/mol.....	.151
Table 3.21 - $^{13}\text{C}$ NMR data of <b>[3-11][OTf]<sub>4</sub></b> in $\text{CD}_3\text{CN}$ . MW <sub>OTf</sub> = 2641.204 g/mol.....	.152
Table 3.22 - $^1\text{H}$ NMR data of <b>[3-12][OTf]<sub>4</sub></b> in $\text{CD}_3\text{CN}$ . MW <sub>OTf</sub> = 2641.204 g/mol.....	.155
Table 3.23 - $^{13}\text{C}$ NMR data of <b>[3-12][OTf]<sub>4</sub></b> in $\text{CD}_3\text{CN}$ . MW <sub>OTf</sub> = 2641.204 g/mol.....	.156
Table 3.24 - $^1\text{H}$ NMR data of <b>[3-13][OTf]<sub>4</sub></b> in $\text{CD}_3\text{CN}$ . MW <sub>OTf</sub> = 2753.416 g/mol.....	.159
Table 3.25 - $^{13}\text{C}$ NMR data of <b>[3-13][OTf]<sub>4</sub></b> in $\text{CD}_3\text{CN}$ . MW <sub>OTf</sub> = 2753.416 g/mol.....	.160
Table 4.1 - Summary of UV-vis data for [2]rotaxanes <b>2-17<sup>4+</sup></b> , <b>4-5<sup>4+</sup></b> , <b>4-18<sup>2+</sup></b> and <b>4-19<sup>2+</sup></b> .	.173
Table 4.2 - Calculated weight % values for components of [2]rotaxanes with measured weight % values for the first step losses. ....	.177
Table 4.3 - Transition temperatures ( $^{\circ}\text{C}$ , midpoint) and enthalpies (kJ/mol) determined by DSC at scan rates of $10^{\circ}\text{C}/\text{min}$ for [2]rotaxanes. Clearing into the isotropic liquid ( $T_i$ ) were determined by POM.....	.181

---

Table 4.4 - Obtained (XRD) layer spacings and calculated molecular lengths of [2]rotaxanes <b>2-17</b> <sup>4+</sup> , <b>4-5</b> <sup>4+</sup> , <b>4-18</b> <sup>2+</sup> and <b>4-19</b> <sup>2+</sup> .....	188
Table 4.5 - <sup>1</sup> H NMR data of <b>4-1</b> in CDCl <sub>3</sub> . MW = 304.338 g/mol. ....	194
Table 4.6 - <sup>13</sup> C NMR data of <b>4-1</b> in CDCl <sub>3</sub> . MW = 304.338 g/mol. ....	195
Table 4.7 - <sup>1</sup> H NMR data of <b>4-2</b> in CDCl <sub>3</sub> . MW= 749.347 g/mol.....	197
Table 4.8 - <sup>13</sup> C NMR data of <b>4-2</b> in CDCl <sub>3</sub> . MW= 749.347 g/mol.....	198
Table 4.9 - <sup>1</sup> H NMR data of <b>4-3</b> in CDCl <sub>3</sub> . MW= 812.244 g/mol.....	200
Table 4.10 - <sup>13</sup> C NMR data of <b>4-3</b> in CDCl <sub>3</sub> . MW= 812.244 g/mol.....	201
Table 4.11 - <sup>1</sup> H NMR data of <b>4-4</b> in CDCl <sub>3</sub> . MW= 827.438 g/mol.....	202
Table 4.12 - <sup>13</sup> C NMR data of <b>4-4</b> in CDCl <sub>3</sub> . MW= 827.438 g/mol.....	203
Table 4.13 - <sup>1</sup> H NMR data of [ <b>4-5</b> ][OTf] <sub>4</sub> in CD <sub>3</sub> CN. MW <sub>OTf</sub> = 2849.884 g/mol .....	205
Table 4.14 - <sup>1</sup> H NMR data of [ <b>4-6</b> ][OTf] <sub>4</sub> in CD <sub>3</sub> CN. MW <sub>OTf</sub> = 2401.378 g/mol .....	206
Table 4.15 - <sup>1</sup> H NMR data of <b>4-7</b> in CDCl <sub>3</sub> . MW = 183.206 g/mol.....	207
Table 4.16 - <sup>1</sup> H NMR data of <b>4-8</b> in CD <sub>3</sub> CN. MW = 185.222 g/mol .....	208
Table 4.17 - <sup>1</sup> H NMR data of [ <b>4-9</b> ][Br] <sub>2</sub> in D <sub>2</sub> O. MW <sub>Br</sub> = 558.305 g/mol.....	211
Table 4.18 - <sup>1</sup> H NMR data of [ <b>4-9</b> ][OTf] <sub>2</sub> in CD <sub>3</sub> CN. MW <sub>OTf</sub> = 696.103 g/mol .....	211
Table 4.19 - <sup>13</sup> C NMR data of [ <b>4-9</b> ][OTf] <sub>2</sub> in CD <sub>3</sub> CN. MW <sub>OTf</sub> = 696.103 g/mol.....	212
Table 4.20 - <sup>1</sup> H NMR data of <b>4-10</b> in CDCl <sub>3</sub> . MW= 546.778 g/mol.....	214
Table 4.21 - <sup>13</sup> C NMR data of <b>4-10</b> in CDCl <sub>3</sub> . MW= 546.778 g/mol.....	215
Table 4.22 - <sup>1</sup> H NMR data of <b>4-11</b> in CDCl <sub>3</sub> . MW = 318.321 g/mol. ....	217
Table 4.23 - <sup>13</sup> C NMR data <b>4-11</b> in CDCl <sub>3</sub> . MW = 318.321 g/mol .....	218
Table 4.24 - <sup>1</sup> H NMR of data <b>4-12</b> in CDCl <sub>3</sub> . MW= 763.331 g/mol.....	219
Table 4.25 - <sup>13</sup> C NMR data of <b>4-12</b> in CDCl <sub>3</sub> . MW= 763.331 g/mol.....	220

---

Table 4.26 - $^1\text{H}$ NMR data of <b>4-13</b> in $\text{CDCl}_3$ . MW= 458.372 g/mol.....	.222
Table 4.27 - $^{13}\text{C}$ NMR data of <b>4-13</b> in $\text{CDCl}_3$ . MW= 458.372 g/mol.....	.223
Table 4.28 - $^1\text{H}$ NMR data of <b>4-14</b> in $\text{CDCl}_3$ . MW= 1047.488 g/mol.....	.224
Table 4.29 - $^{13}\text{C}$ NMR data of <b>4-14</b> in $\text{CDCl}_3$ . MW= 1047.488 g/mol.....	.225
Table 4.30 - $^1\text{H}$ NMR data of <b>4-15</b> in $\text{CDCl}_3$ . MW= 1508.647 g/mol.....	.227
Table 4.31 - $^{13}\text{C}$ NMR data of <b>4-15</b> in $\text{CDCl}_3$ . MW= 1508.647 g/mol.....	.228
Table 4.32 - $^1\text{H}$ NMR data of <b>[4-16][OTf]<sub>2</sub></b> in $\text{CD}_3\text{CN}$ . MW <sub>OTf-</sub> = 1136.992 g/mol .....	.231
Table 4.33 - $^{13}\text{C}$ NMR data of <b>[4-16][OTf]<sub>2</sub></b> in $\text{CD}_3\text{CN}$ . MW <sub>OTf-</sub> = 1136.992 g/mol .....	.232
Table 4.34 - $^1\text{H}$ NMR data of <b>[4-17][OTf]<sub>2</sub></b> in $\text{CD}_3\text{CN}$ . MW <sub>OTf-</sub> = 1585.498 g/mol .....	.234
Table 4.35 - $^1\text{H}$ NMR data of <b>[4-18][OTf]<sub>2</sub></b> in $\text{CD}_3\text{CN}$ . MW <sub>OTf-</sub> = 2202.667 g/mol .....	.236
Table 4.36 - $^{13}\text{C}$ NMR data of <b>[4-18][OTf]<sub>2</sub></b> in $\text{CD}_3\text{CN}$ . MW <sub>OTf-</sub> = 2202.667 g/mol .....	.237
Table 4.37 - $^1\text{H}$ NMR data of <b>[4-19][OTf]<sub>2</sub></b> in $\text{CD}_3\text{CN}$ . MW <sub>OTf-</sub> = 2635.773 g/mol. ....	.241
Table 4.38 - $^{13}\text{C}$ NMR of data <b>[4-19][OTf]<sub>2</sub></b> in $\text{CD}_3\text{CN}$ . MW <sub>OTf-</sub> = 2635.773 g/mol .....	.242
Table 5.1 - Transition temperatures ( $^{\circ}\text{C}$ , midpoint) observed by DSC at scan rates of 10 $^{\circ}\text{C}/\text{min}$ for [2]rotaxanes.....	.261
Table 5.2 - vt-XRD data of <b>[5-1][(-)CamSO<sub>3</sub>]<sub>2</sub></b> and <b>[5-5][OTf]<sub>2</sub></b> on cool. The values are consistent over several heating and cooling cycles.....	.262
Table 5.3 - $^1\text{H}$ NMR data of <b>[5-1][(-)CamSO<sub>3</sub>]<sub>2</sub></b> in $\text{CD}_3\text{NO}_2$ . MW = 2800.212 g/mol. .	.269
Table 5.4 - $^1\text{H}$ NMR data of <b>5-2</b> in $\text{CDCl}_3$ . MW= 820.197 g/mol.....	.271
Table 5.5 - $^{13}\text{C}$ NMR data of <b>5-2</b> in $\text{CDCl}_3$ . MW= 820.197 g/mol.....	.272
Table 5.6 - $^1\text{H}$ NMR data of <b>5-3</b> in $\text{CD}_3\text{CN}$ . MW= 793.035 g/mol .....	.274
Table 5.7 - $^{13}\text{C}$ NMR data of <b>5-3</b> in $\text{CDCl}_3$ . MW= 793.035 g/mol.....	.275
Table 5.8 - $^1\text{H}$ NMR data of <b>[5-4][OTf]<sub>2</sub></b> in $\text{CD}_3\text{CN}$ . MW= 1489.670 g/mol .....	.278

---

Table 5.9 - $^1\text{H}$ NMR data of <b>[5-5][OTf]<sub>2</sub></b> in $\text{CD}_3\text{CN}$ . MW= 3144.741 g/mol .....	.279
Table 5.10 - $^1\text{H}$ NMR data of <b>[5-6][OTf]<sub>2</sub></b> in $\text{CDCl}_3$ . MW <sub>OTf</sub> = 2187.267 g/mol .....	.282
Table 6.1 - $^1\text{H}$ NMR spectral data of <b>6-1</b> in $\text{CD}_2\text{Cl}_2$ . MW= 969.635 g/mol. ....	301
Table 6.2 - $^1\text{H}$ NMR spectral data of <b>6-2</b> in $\text{CD}_2\text{Cl}_2$ . MW= 927.555 g/mol. ....	302
Table 6.3 - $^{13}\text{C}$ NMR spectral data of <b>6-2</b> in $\text{CD}_2\text{Cl}_2$ . MW= 927.555 g/mol. ....	303
Table 6.4 - $^1\text{H}$ NMR spectral data of <b>6-3</b> in $\text{CDCl}_3$ . MW= 1837.094 g/mol. ....	305
Table 6.5 - $^{13}\text{C}$ NMR spectral data of <b>6-3</b> in $\text{CD}_2\text{Cl}_2$ . MW= 1837.094 g/mol. ....	306
Table 6.6 - $^1\text{H}$ NMR spectral data of <b>6-4</b> in $\text{CDCl}_3$ . MW= 1578.524 g/mol. ....	309
Table 6.7 - $^{13}\text{C}$ NMR spectral data of <b>6-4</b> in $\text{CDCl}_3$ . MW= 1578.524 g/mol. ....	310
Table 6.8 - $^1\text{H}$ NMR spectral data of <b>[6-5][Br]<sub>2</sub></b> in $\text{D}_2\text{O}$ . MW <sub>Br</sub> = 451.198 g/mol. ....	311
Table 6.9 - $^1\text{H}$ NMR spectral data of <b>[6-5][BF<sub>4</sub>]<sub>2</sub></b> in $\text{CD}_3\text{CN}$ . MW <sub>BF<sub>4</sub></sub> = 464.999 g/mol. ....	312
Table 6.10 - $^{13}\text{C}$ NMR spectral data of <b>[6-5][BF<sub>4</sub>]<sub>2</sub></b> in $\text{CD}_3\text{CN}$ . MW <sub>BF<sub>4</sub></sub> = 464.999 g/mol .....	312
Table 6.11 - $^1\text{H}$ NMR spectral data of <b>[6-6][Br]<sub>3</sub></b> in $\text{D}_2\text{O}$ . MW <sub>Br</sub> = 639.059 g/mol. ....	315
Table 6.12 - $^1\text{H}$ NMR spectral data of <b>[6-6][BF<sub>4</sub>]<sub>3</sub></b> in $\text{CD}_3\text{CN}$ . MW <sub>BF<sub>4</sub></sub> = 659.791 g/mol. .....	315
Table 6.13 - $^1\text{H}$ NMR spectral data of <b>[6-6][OTf]<sub>3</sub></b> in $\text{CD}_3\text{CN}$ MW <sub>OTf</sub> = 846.555 g/mol .....	316
Table 6.14 - $^{13}\text{C}$ NMR spectral data of <b>[6-6][BF<sub>4</sub>]<sub>3</sub></b> in $\text{CD}_3\text{CN}$ . MW <sub>BF<sub>4</sub></sub> = 659.761 g/mol .....	316
Table 6.15 - $^1\text{H}$ NMR spectral data of <b>[6-7][Br]<sub>4</sub></b> in $\text{D}_2\text{O}$ . MW <sub>Br</sub> = 824.281 g/mol. ....	317
Table 6.16 - $^1\text{H}$ NMR spectral data of <b>[6-7][OTf]<sub>4</sub></b> in $\text{CD}_3\text{CN}$ . MW <sub>OTf</sub> = 1100.9416 g/mol .....	318



---

Table 6.17 - $^{13}\text{C}$ NMR spectral data of <b>[6-7][OTf]<sub>4</sub></b> in $\text{CD}_3\text{CN}$ . $\text{MW}_{\text{OTf}}$ = 1100.9416 g/mol .....	.319
Table 6.18 - $^1\text{H}$ NMR spectral data of <b>6-8</b> in $\text{CD}_2\text{Cl}_2$ . $\text{MW}$ = 1094.761 g/mol .....	.321
Table 6.19 - $^{13}\text{C}$ NMR spectral data of <b>6-8</b> in $\text{CD}_2\text{Cl}_2$ . $\text{MW}$ = 1094.761 g/mol .....	.322

---

**LIST OF SCHEMES**

Scheme 2.1 - Synthetic route to thread <b>2-2<sup>2+</sup></b> .....	40
Scheme 2.2 - Synthetic route for stoppers <b>2-3</b> through <b>2-9</b> .....	41
Scheme 2.3 - Synthetic route for [2]rotaxanes and dumbbells .....	42
Scheme 3.1 - Synthetic route for stoppers <b>3-1</b> through <b>3-8</b> .....	108
Scheme 3.2 - Improved synthetic route to [2]rotaxanes <b>3-9<sup>4+</sup></b> , <b>3-11<sup>4+</sup></b> - <b>3-13<sup>4+</sup></b> .....	109
Scheme 4.1 - Synthetic route to new stoppers <b>4-1</b> through <b>4-4</b> .....	165
Scheme 4.2 - Synthetic route for [2]rotaxanes <b>2-17<sup>4+</sup></b> and <b>4-5<sup>4+</sup></b> .....	166
Scheme 4.3 - Synthetic route for two-charged thread.....	167
Scheme 4.4 - Synthetic route for stoppers <b>4-10</b> through <b>4-15</b> .....	167
Scheme 4.5 - Synthetic route for [2]rotaxanes <b>4-17<sup>4+</sup></b> through <b>4-19<sup>4+</sup></b> .....	168
Scheme 5.1 - Synthetic route for [2]rotaxane <b>[5-1][(-)CamSO<sub>3</sub>]<sub>2</sub></b> .....	248
Scheme 5.2 - Synthetic route for tetra-substituted crowns <b>5-2</b> and <b>5-3</b> .....	249
Scheme 5.3 - Synthetic route for [2]rotaxane <b>[5-5][OTf]<sub>2</sub></b> .....	250
Scheme 6.1 - Synthetic route for stoppers <b>6-1</b> through <b>6-3</b> .....	291
Scheme 6.2 - Synthetic scheme for crown <b>6-4</b> .....	291
Scheme 6.3 - Synthetic route for thread <b>6-5<sup>2+</sup></b> through <b>6-7<sup>4+</sup></b> .....	292
Scheme 6.4 - Synthetic routes for molecular shuttle <b>6-9<sup>4+</sup></b> .....	293
Scheme 6.5 - Synthetic route for thread <b>6-8</b> .....	294

---

**LIST OF ABBREVIATIONS**

<b>Å</b>	Angstrom
<b>Bu<sub>3</sub>P</b>	Tributyl phosphine
<b>CD<sub>3</sub>CN</b>	Deuterated acetonitrile
<b>CD<sub>3</sub>Cl<sub>3</sub></b>	Deuterated chloroform
<b>CD<sub>2</sub>Cl<sub>2</sub></b>	Deuterated methylene chloride
<b>CT</b>	Charge Transfer
<b>CHCl<sub>3</sub></b>	Chloroform
<b>CH<sub>2</sub>Cl<sub>2</sub></b>	Methylene chloride
<b>COSY</b>	Correlation Spectroscopy
<b>Cr</b>	Crystalline state
<b>DB24C8</b>	Dibenzo-24-crown-8
<b>D<sub>2</sub>O</b>	Deuterated water
<b>DMF</b>	Dimethylformamide
<b>DMSO</b>	Dimethyl sulfoxide
<b>DSC</b>	Differential Scanning Calorimetry
<b>ESI-MS</b>	High resolution electrospray ionization mass spectrometry
<b>EtOH</b>	Ethanol
<b>EtOAc</b>	Ethyl acetate
<b>HETCOR</b>	Heteronuclear Correlation Spectroscopy
<b>Hz</b>	Hertz
<b>LC</b>	Liquid crystal
<b>K<sub>2</sub>CO<sub>3</sub></b>	Potassium carbonate
<b>MeCN</b>	Acetonitrile

---

<b>MeNO<sub>2</sub></b>	Nitromethane
<b>MeOH</b>	Methanol
<b>MgSO<sub>4</sub></b>	Magnesium sulphate
<b>MW</b>	Molecular weight
<b>N</b>	Nematic phase
<b>n</b>	Director
<b>NaHCO<sub>3</sub></b>	Sodium bicarbonate
<b>NaBH<sub>4</sub></b>	Sodium borohydride
<b>Na<sub>2</sub>CO<sub>3</sub></b>	Sodium carbonate
<b>NaH</b>	Sodium hydride
<b>NH<sub>4</sub>Cl</b>	Ammonium chloride
<b>NaOTf</b>	Sodium trifluoromethane sulfonate (sodium triflate)
<b>POM</b>	Polarized Optical Microscopy
<b>Pd(PPh<sub>3</sub>)<sub>4</sub></b>	Palladium-tetrakis-triphenylphosphine
<b>RP-C<sub>18</sub></b>	Reverse Phase C <sub>18</sub> silica gel
<b>SmA</b>	Smectic A phase
<b>SmC</b>	Smectic C phase
<b>TBAI</b>	Tetrabutylammonium iodide
<b>THF</b>	Tetrahydrofuran
<b>TGA</b>	Thermal gravimetric analysis
<b>TLC</b>	Thin layer chromatography
<b>Ti(O-<i>i</i>-Pr)<sub>4</sub></b>	Titanium isopropoxide
<b>Triflate</b>	Trifluoromethanesulfonate ion
<b>TsCl</b>	<i>Para</i> -toluenesulfonyl chloride

---

<b>VT-NMR</b>	Variable temperature NMR spectroscopy
<b>XRD</b>	X-ray diffraction

# CHAPTER 1

## *Introduction*

### 1.1 SUPRAMOLECULAR CHEMISTRY

Supramolecular chemistry is a mature and vigorous area of research, stemming from the fields of chemistry, biochemistry, physics and materials science. It was classically defined as the 'chemistry of molecular assemblies and of the intermolecular bond' and 'chemistry beyond the molecule', by Jean-Marie Lehn.<sup>1</sup> Its focus is on the non-covalent intermolecular interactions used to self-assemble separate molecular or ionic components into highly ordered structures.<sup>2,3</sup> Depending on the type of interactions a variety of terms for the process include: host-guest chemistry; molecular recognition; self assembly and template synthesis, just to name a few. The foundations for their origin have been set forth in the pioneering works of Pedersen<sup>4</sup>, Cram<sup>5</sup>, and Lehn<sup>6</sup>, for which they were awarded the Nobel Prize in Chemistry in 1987 (Figure 1.1).

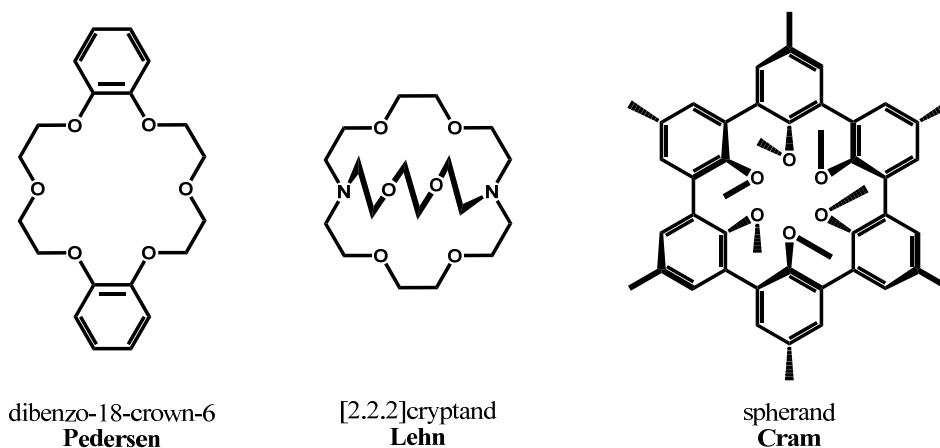


Figure 1.1 – Examples from the works of C. Pedersen<sup>4</sup>, J.-M. Lehn<sup>6</sup> and D. Cram<sup>5</sup>

## 1.2 SUPRAMOLECULAR INTERACTIONS

The defining feature of supramolecular chemistry is the types of interactions involved in holding these assemblies together. Molecular chemistry is concerned with individual molecules that are connected by traditional covalent bonds; with strengths of 200 - 400 kJ/mol. Supramolecular chemistry has the further complexity of involving the interactions of individual covalent entities through various types of non-covalent bonding interactions. Figure 1.2 shows examples of the types of non-covalent interactions observed and their relative strengths.<sup>7-12</sup> The individual interactions vary in strength and it is the co-operation of these numerous non-covalent interactions that provides the supramolecular complexes with their overall stability.

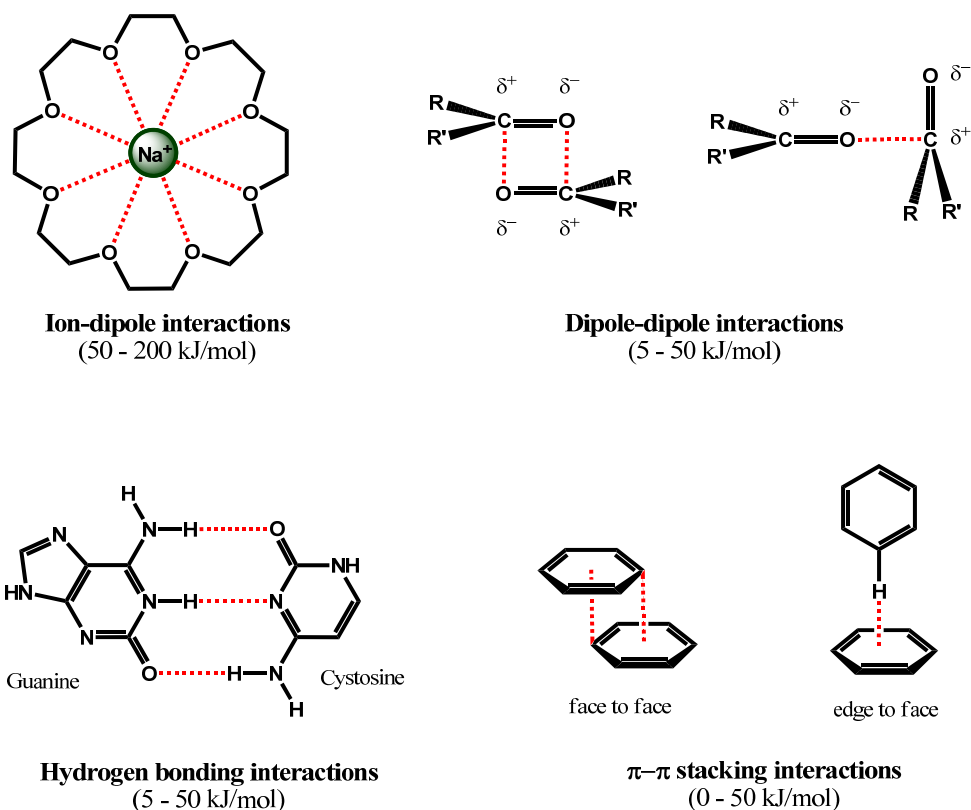


Figure 1.2 - Various types of non-covalent interactions.

Ion-dipole interactions result from electrostatic interactions between an ion and the lone pairs of a polar molecule, which is the driving force for the solvation of ions by polar molecules. Dipole-dipole interactions result from significant attractive interactions when dipoles align. The high boiling points of aldehydes and ketones compared to their hydrocarbon counterparts can be attributed to dipole-dipole interactions between carbonyl groups. Hydrogen bonding, responsible for holding the double helix of DNA together, is a particular kind of dipole-dipole interaction which is relatively strong and highly directional. Hydrogen bonds are considered as the 'masterkey interactions in supramolecular chemistry'.<sup>2</sup> Also responsible for stabilization of the DNA double helix,  $\pi$ - $\pi$  interactions are regarded as a weak electrostatic interaction between the negatively charged  $\pi$ -electron cloud of one ring and the positive  $\sigma$ -framework of another.<sup>2</sup>

### 1.3 INTERPENETRATED AND INTERLOCKED MOLECULES

Some of the most intriguing supramolecular complexes arise from a guest that is capable of threading through and occupying the cavity of a host. These interpenetrated complexes can further be modified such that the host and guest become permanently connected, through mechanical bonds, in an interlocked fashion. Much attention has been given to these types of compounds because of their potential applications which include the formation of sophisticated switchable molecular devices, development of materials with new physical properties and surface immobilization of catalytically photo or redox active species without the need to alter their properties by chemical modification.<sup>13-27</sup>



### 1.3.1 Threading and Dethreading of Pseudorotaxanes

Threading and dethreading movements refer to supramolecular complexes called pseudorotaxanes. These host-guest complexes are composed of at least two components, as illustrated in Figure 1.3. The complexes exist in equilibrium with their free components; a linear molecule, referred to as the thread, and a ring whose cavity is large enough to allow the thread to penetrate. Design of these host-guest systems requires that interactions exist between the two components that favour their complexation. Pseudorotaxanes are formed under thermodynamic control and are driven by the formation of one or a combination of the weak non-covalent interactions that define supramolecular complexes. The naming system adopted for pseudorotaxanes consists of placing a number in square brackets in front of the word pseudorotaxane. The number denotes the total number of individual components making up the complex, *i.e.* [n]pseudorotaxane.

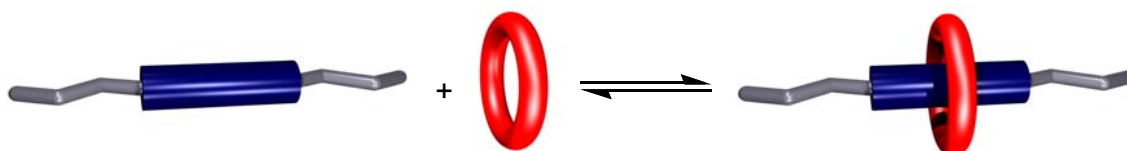


**Figure 1.3 – Illustration of a complexed [2]pseudorotaxane and its uncomplexed components.**

Incorporating the supramolecular interactions described above, a number of different recognition motifs have been developed. Each one contains a minimum of one complementary interaction and stability is increased when such interactions are numerous. Stoddart developed two systems; one uses hydrogen bonding between a dibenzylammonium centre and the polyether oxygen atoms of dibenzo-24-crown-8, **DB24C8** (Figure 1.4, left).<sup>28,29</sup> The other, uses  $\pi$ -stacking interactions between an

electron poor paraquat unit and electron rich aromatics such as a dioxynaphthalene or a tetrathiafulvalene group (Figure 1.4, right).<sup>30-33</sup>

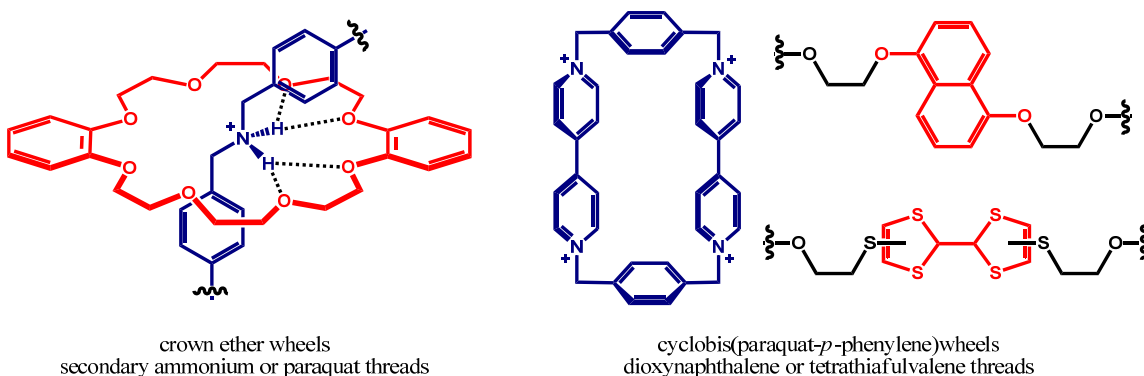


**Figure 1.4 – Templates for pseudorotaxane formation used by Stoddart.**

The octameric macrocycle cucurbituril (CB[8]) has been widely used as a templating motif by Kim *et al.*<sup>34</sup> For example this macrocycle can complex a hexamethylene bridged bis(viologen) thread *via* a combination of hydrophobic interactions between the bridging alkyl chain and the inner cavity of **CB[8]** and ion-dipole interactions between the pyridinium nitrogen atoms and the **CB[8]** oxygen atoms around the rims of the rings (Figure 1.5). The conformation of this pseudorotaxane was

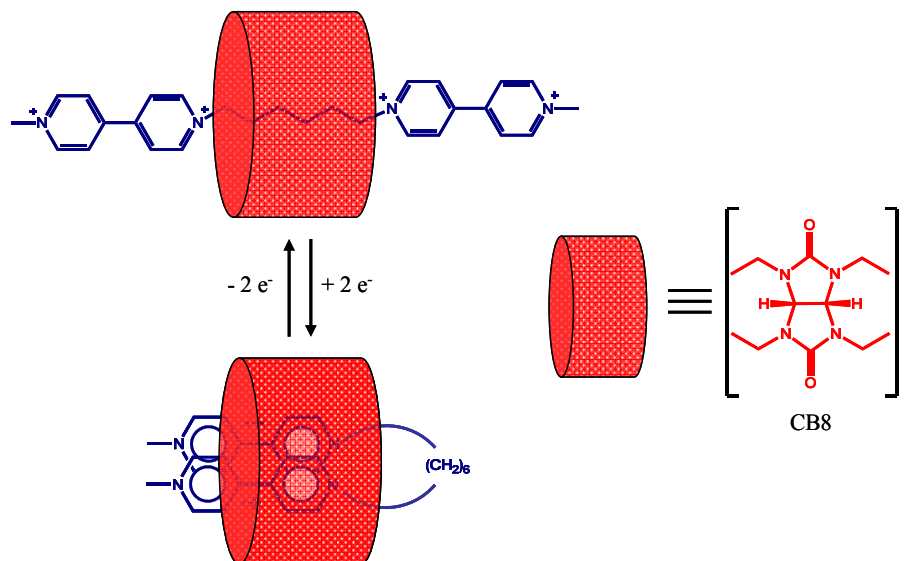


**Figure 1.5 – Folding/unfolding pseudorotaxane by Kim *et al.***

shown to be electrochemically controlled. Folding of the thread within the cavity of the macrocycle was observed with a two electron reduction of the bis(viologen) thread, resulting in two radical cation viologen terminal groups that intramolecularly pair inside the **CB[8]** ring. Unfolding of the thread is accomplished by a two-electron oxidation.

### 1.3.2 Rotaxanes

Rotaxanes are the interlocked analogue of pseudorotaxanes, consisting of a linear thread component that is stoppered on both ends with bulky groups and a macrocyclic ring. The bulky groups prevent dethreading and the ring and the stoppered thread are mechanically linked together. The naming system adopted for rotaxanes follows the same methodology as pseudorotaxanes.

There are three methods for the generation of rotaxanes: i) threading followed by stoppering,<sup>35</sup> ii) slipping<sup>36,37</sup> and iii) clipping<sup>38</sup>. All methods require the design to include the necessary components that are capable of the non-covalent interactions for the self-assembly of the thread and macrocycle, known as 'templating'. The threading followed by stoppering method involves pre-forming the pseudorotaxane between the thread and the macrocycle, followed by covalently attaching bulky stopper groups to either end of the thread to prevent dethreading. All of the [2]rotaxanes prepared in this thesis were synthesized by threading followed by stoppering (Figure 1.6).

### 1.3.3 Molecular Machines

A molecular machine is described as the assembly of a distinct number of components that are designed to perform machine-like movements as a result of an appropriate external stimulation.<sup>39</sup> This requires the ability to induce and control their

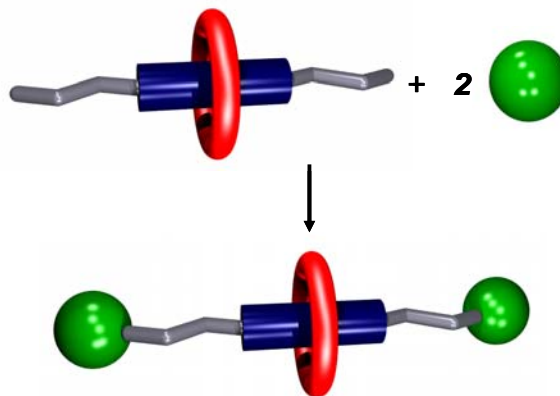


**Figure 1.6 – Formation of a [2]rotaxane by threading followed by stoppering.**

relative motion. Triggering mechanical movements, which can be simplified to rotational or translational, can be achieved by chemical,<sup>40,41</sup> electrochemical<sup>14,42,43</sup> or photochemical stimuli.<sup>40,43,44</sup>

A molecular shuttle is a rotaxane with two or more distinct recognition sites on the thread for the macrocyclic ring to occupy (Figure 1.7). Preferably, the macrocycle would reside at one site over the other, due to a large difference in the binding affinities for the macrocycle. A free energy difference of greater than 5.0 kJ/mol between the two translational isomers ensures that 90 % of the ring is positioned around one recognition site over the other, at room temperature.<sup>45</sup> This is a situation which gives rise to a highly preferred ground state co-conformation; State 0. The application of an external stimulus either destroys the interactions at this site or enhances the interactions at the other site, causing the ring to 'shuttle' to the other site which temporarily provides better stabilizing interactions; State 1. Reversing the effects caused by the external stimulus completes the full cycle of the machine-like movement of the bistable rotaxane, making them one of the most accessible molecular machines.

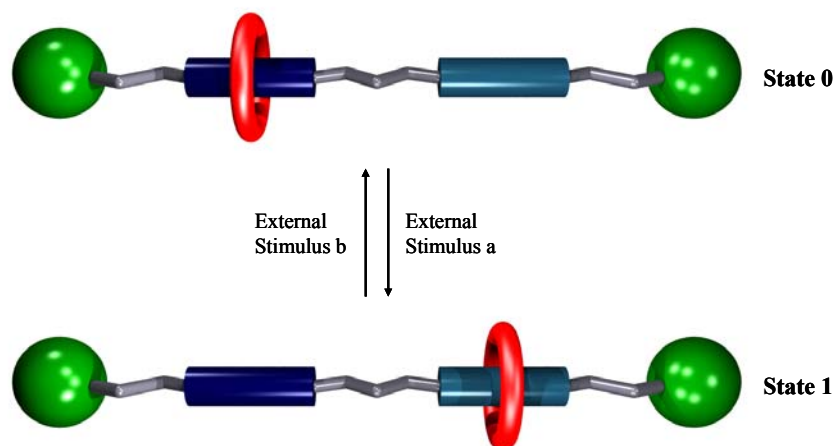


**Figure 1.7 – [2]Rotaxane as a molecular shuttle.**

The first photochemically driven molecular shuttle, seen in Figure 1.8, was composed of an  $\alpha$ -cyclodextrin macrocycle interlocked onto a dumbbell component containing an azobenzene unit.<sup>46</sup> In the ground state, the  $\alpha$ -cyclodextrin macrocycle preferentially encapsulates the *trans*-conformation of the azobenzene group. Upon irradiation with UV light ( $\lambda = 360$  nm), the macrocycle moves to one of the adjacent paraquat<sup>2+</sup> sites. The reverse is accomplished by irradiation with a different

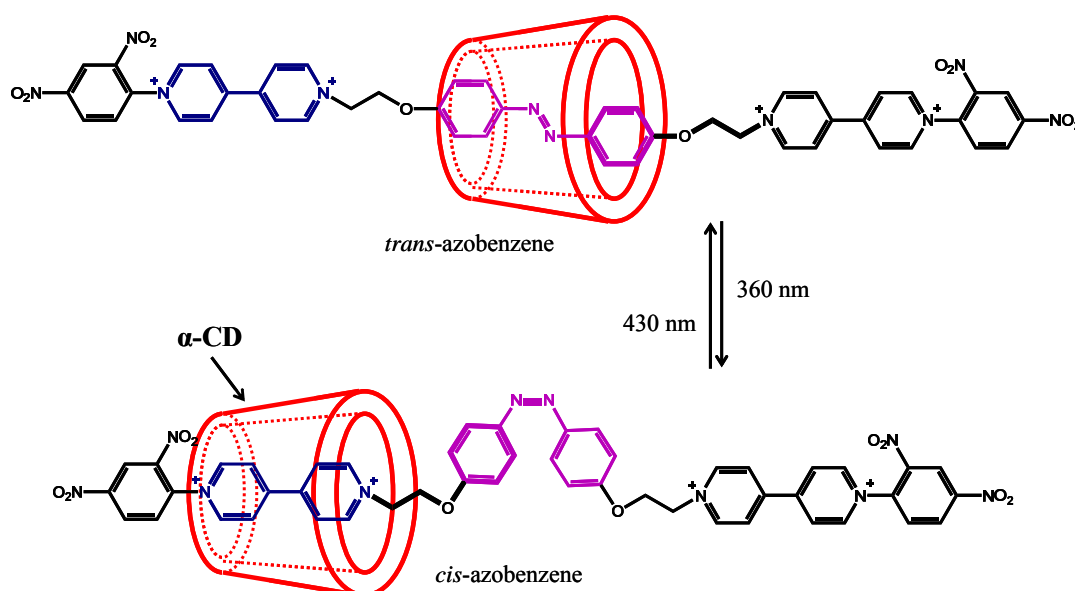


**Figure 1.8 – Mechanical switching of  $\alpha$ -CD by photoisomerization of the encapsulated azobenzene based dumbbell.**

wavelength ( $\lambda = 430$  nm) to restore the *trans*-conformation. This photochemically driven mechanical movement was verified by  $^1\text{H-NMR}$  and UV-Vis spectroscopy.

Skeletal muscles are natural linear motors possessing mechanical properties that are conferred to vertebrates. Focus has been aimed at reproducing some of the essential properties of muscles. A recent approach reported by Stoddart and co-workers<sup>24,19</sup> of a molecular machine performing measurable mechanical work, involved a self-assembled monolayer (SAM) of a bistable [3]rotaxane molecular shuttle on a gold surface of cantilever beams that would bend the beam by contraction and expansion of the shuttle. Figure 1.9 shows the palindromic molecular shuttling system.

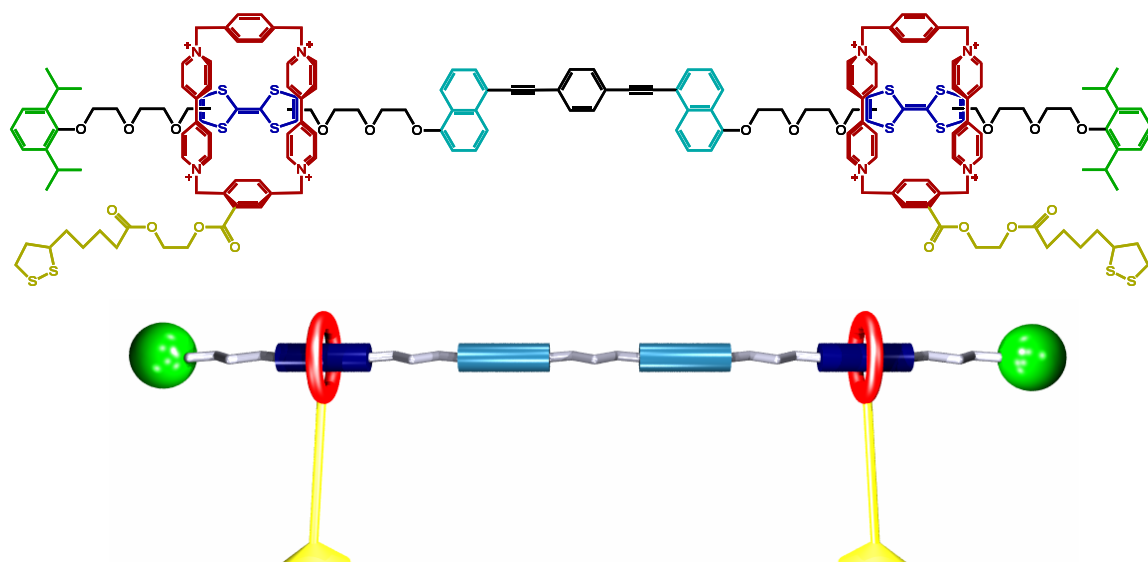


**Figure 1.9 – Structural and graphical<sup>47</sup> representation of a disulfide-tethered molecular muscle [3]rotaxane constructed by Stoddart *et al.***

The thread is composed of two pairs of distinct recognition sites for the cyclobis(paraquat-*p*-phenylene)<sup>4+</sup> (CBPQT<sup>4+</sup>) macrocyclic ring; the tetrathiafulvalene (TTF) and the naphthalene groups, both of which are electron rich. In its ground state, the electron poor CBPQT<sup>4+</sup> macrocycle has a higher affinity for the TTF recognition site. With a two-electron oxidation of TTF, electrostatic repulsion between the two forces the

macrocycle to the naphthalene site. The system is fully cycled by reduction of the dication  $\text{TTF}^{2+}$  back to its neutral state (Figure 1.10). The distance between the two macrocycles changes from 4.2 nm (fully extended state) to 1.4 nm (contracted state), upon oxidation/reduction of **TTF**. Control studies indicated that it is the contraction and extension of the surface-bound nanoscale molecular muscles that lead to the bending of the beam, which is five orders of magnitude larger in size than the [3]rotaxane molecular muscle.

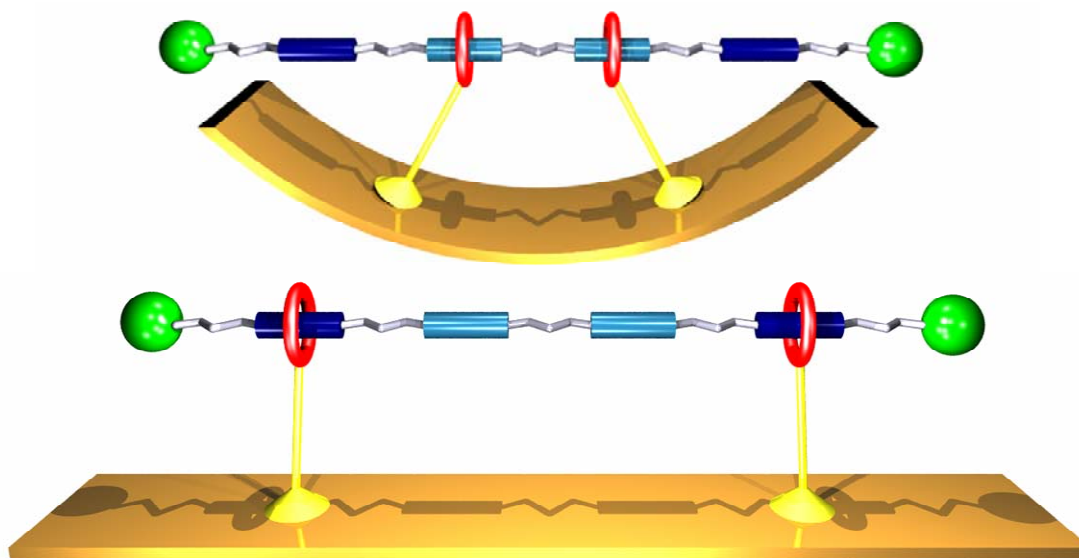


**Figure 1.10 – Graphical representations<sup>47</sup> of the proposed bending action a cantilever coated with the disulfide-tethered molecular muscle.**

Another example of a molecular machine performing measurable mechanical work, which exhibits clear on/off behaviour was the two-component molecular elevator reported by Stoddart and co-workers.<sup>18,39</sup> Figure 1.11 illustrates the molecular machine that undergoes movements reminiscent of an elevator. The trifurcated guest salt possesses diakylammonium sites (green) which are complexed by the tritopic host (red) through numerous hydrogen bonding and ion-dipole interactions. The interlocked [2]rotaxane

molecular elevator is generated with the addition 3,5-di-*tert*-butylbenzyl groups as the stoppers (grey) to form the additional recognition site of the bipyridinium group (blue).

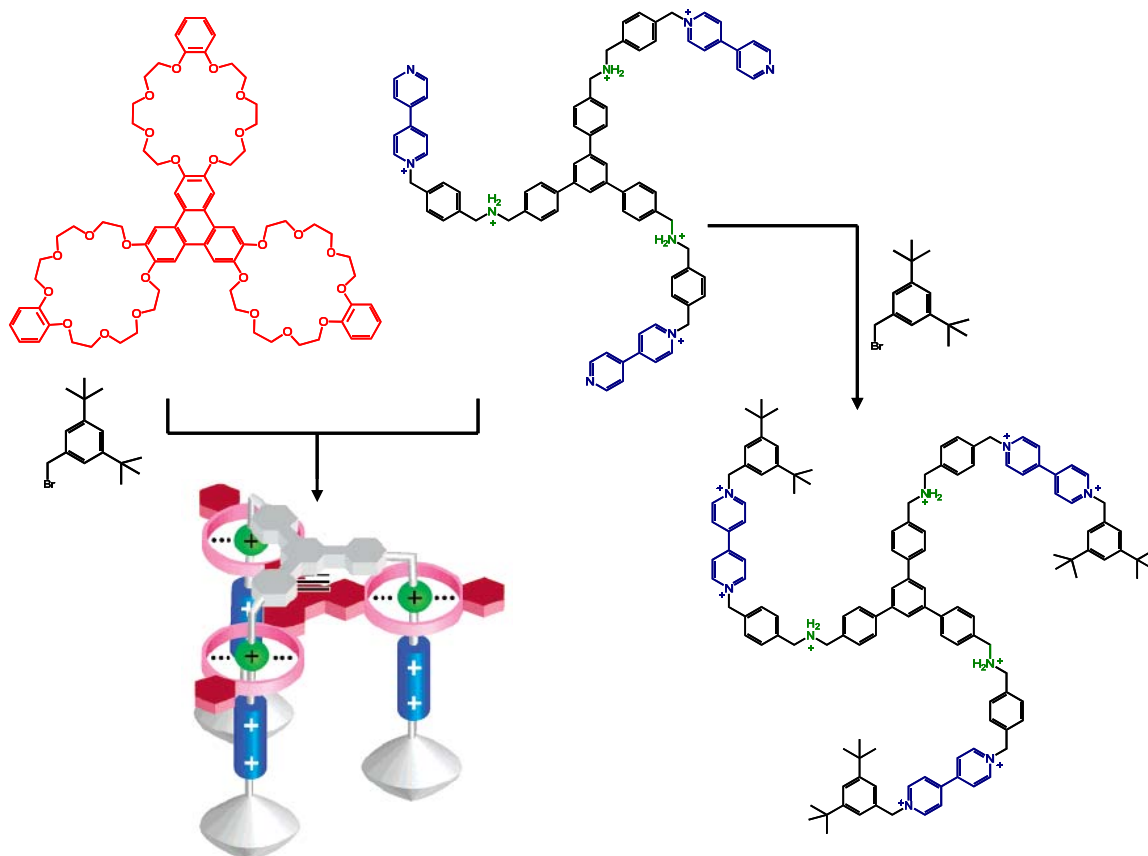


**Figure 1.11 – Structural and graphical<sup>39</sup> representation of nano-meter scale elevator with pseudorotaxane formation between the trifurcated cationic guest and tritopic host followed by stoppering with 3,5-di-*tert*-butylbenzylbromide, constructed by Stoddart *et al.***

The completely bistable acid-base molecular shuttle operation is illustrated in Figure 1.12. The host platform is situated on the upper level initially; State 0. Addition of the base causes the platform to shuttle to the lower level; State 1. Addition of the acid restores the platform to the upper level and the motion was shown to cycle repeatedly without any significant loss of reversibility. The distance travelled by the platform is 0.7 nm and the nanoactuator can potentially generate a force up to 200 pN in motion from the



upper level to the lower level. In contrast, the force generated by natural linear motors like myosin and kinesin are more than an order of magnitude smaller.

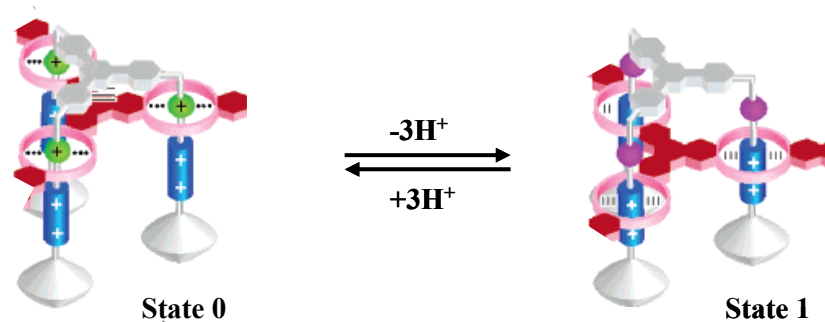


**Figure 1.12 – Illustration for the operation of the nano-meter scale elevator.<sup>18</sup>**

## 1.4 LIQUID CRYSTALS

### 1.4.1 General Introduction

Liquid crystals (LCs) are partially ordered, anisotropic fluids that are thermodynamically intermediate between that of three dimensionally ordered solid state crystals and the isotropic liquid. In these phases, the order of the crystalline state is only partly lost and the individual molecules have some degree of mobility. Because they can possess one or two dimensional ordering, they possess crystalline properties such as birefringence. Their discovery dates back to 1888, when the Austrian botanist Friedrich Reinitzer reported the observation of two compounds (cholesteryl benzoate and cholesteryl acetate) that apparently had two melting points.<sup>48</sup> These were later determined to be cholesteric liquid crystals by Lehmann, who coined the term “liquid crystal” to describe this new state of matter.<sup>49</sup>

Liquid crystalline materials are generally divided into two categories; the thermotropic and lyotropic mesophases (Figure 1.13). The term “Mesophase” stems from the Greek word *meso*, meaning “in between”. Mesophases are intermediate between that

of a crystal and liquid phases and they may or may not possess liquid crystallinity. However, compounds forming liquid crystal phases are described as mesomorphic, or said to possess mesogenic properties. Thermotropic liquid crystals are observed by a change in temperature, while lyotropic phases form in the presence of a suitable solvent. It follows that lyotropic liquid crystal phases are concentration dependent.

Liquid crystals are important in materials science and in the life sciences because they combine order and mobility. Important applications<sup>50</sup> of thermotropic liquid crystals are optoelectronic displays, temperature sensors and selective reflecting pigments<sup>51</sup>. On the other hand, lyotropic liquid crystals are incorporated in cleaning processes<sup>52</sup> and are important in the cosmetics industry, and are used as model systems for biomembranes<sup>53</sup> as well as templates for the preparation of mesoporous materials<sup>54</sup>. Only thermotropic liquid crystal materials will be considered here.

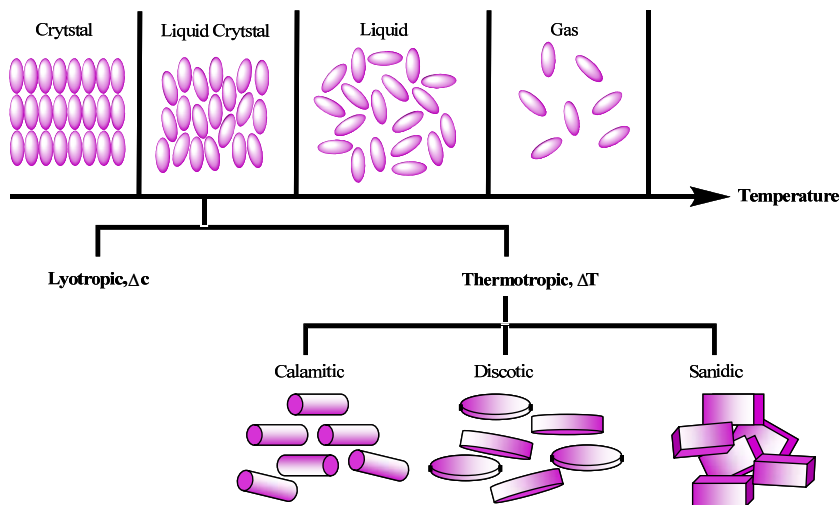


**Figure 1.13 – Illustration of states of matter and two major classes of liquid crystals.**

Thermotropic liquid crystals are classified further with respect to the molecular shape of the constituent molecules, being designated calamitic for rod-like, discotic for disk-like, and sanidic for brick or lath-like molecules (Figure 1.13). A common structural

feature of calamitic mesogens is a relatively rigid core, consisting of two or more ring structures which are substituted with two flexible end-groups, often alkyl or alkoxy chains (Figure 1.14a). Due to the elongated rigid core, one molecule axis is much longer than the other two. Discotic mesogens, on the other hand, are typically substituted with six flexible end-groups around a rigid, disk-like core (Figure 1.14b). From the disc-like nature, one molecule axis is much smaller than the other two. There are numerous variations of the general structures that may be implemented, leading to a vast variety of mesogenic compounds.

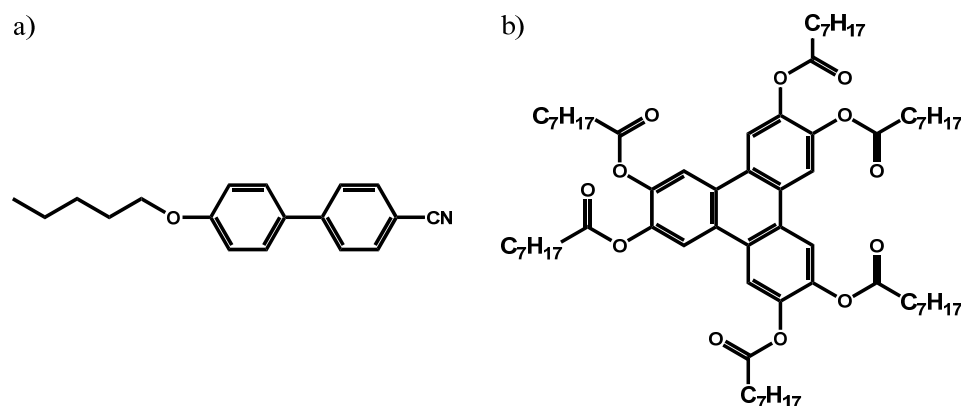


**Figure 1.14 – Examples of a) calamitic and b) discotic mesogens.**

Thermotropic mesomorphism is governed by molecular design. This not only includes the anisotropic shape but also microsegregation<sup>55</sup> effects of incompatible moieties in amphiphilic molecules including for example, perfluorinated side-chains<sup>56</sup> or organosiloxane groups<sup>57</sup>. Intermolecular interactions, such as dipole-dipole interactions, can also play a key role in the induction of mesomorphism.

### 1.4.2 Calamitic Liquid Crystals

A crystalline solid has long range order of the molecular positions in three dimensions. Upon heating of the solid to the isotropic liquid the process occurs through

one or more intermediate mesophases. Various degrees of positional order are broken which can lead to a liquid crystal phase. Generally, calamitic mesogens may form a nematic (N) or smectic (Sm) phase. Typically observed smectic phases are the smectic A (SmA) and the smectic C (SmC) phases. A typical thermotropic phase sequence is shown in Figure 1.15, illustrating the different types.<sup>58</sup>

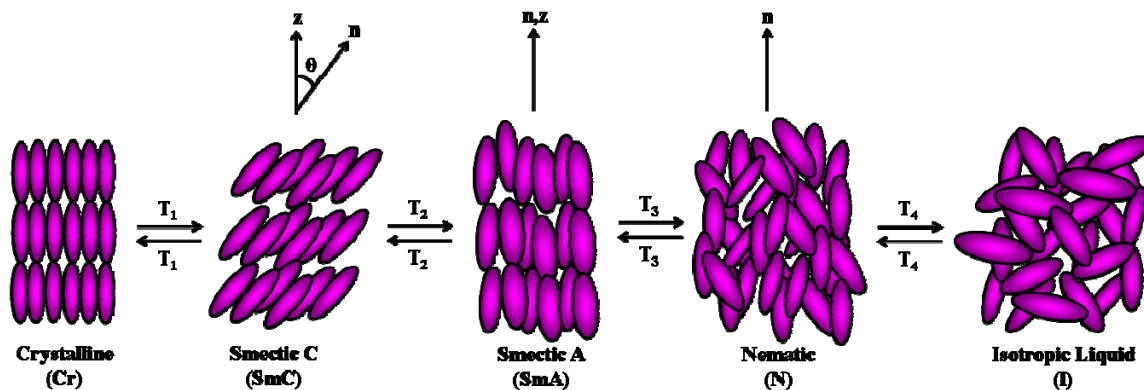


**Figure 1.15 – Illustration of crystalline (Cr), smectic C (SmC), smectic A (SmA), nematic (N) and isotropic liquid (I) phases exhibited by calamitic mesogens.**

The general structure template from which calamitic mesogens are generated follows the schematic representation shown in Figure 1.16. The groups labelled A and B (blue) represent linear rigid core groups and are typically aromatic. The central group C (teal) is an optional linker group and some examples are esters, stilbenes or azo groups. The end-groups R and R' are flexible terminal alkyl or alkoxy chains and these may be substituted via a linker as well, but typically are directly linked to the core.

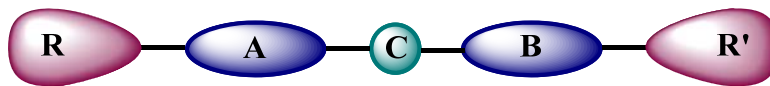


**Figure 1.16 – The general structural template for calamitic LCs.**

The molecular structure of calamitic liquid crystals can be tailored to generate specific liquid crystal phases at specific temperatures. Certain structural moieties confer a certain

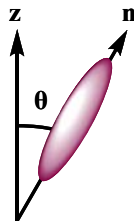
---

phase morphology and particular values of melting points and transition temperatures, as well as combinations of moieties for low molecular weight (LMW) systems. This becomes a crucial component when designing materials for specific applications. For application purposes, not only does the material require the necessary molecular structure to generate the desired liquid crystal phase at a specific temperature or range, but the material also needs to possess the necessary combination of physical properties for that application. Even still, the liquid crystal designed may not be suitable for the required application but valuable information based on the structure-property relations can be obtained. Since one molecule may form several different liquid crystal phases, it is difficult to establish conclusive trends.

#### 1.4.2.1 Nematic Liquid Crystals

The nematic phase is the least ordered phase; all positional order is lost and only long range orientational order in one dimension is exhibited. The long molecular axes are distributed around a particular direction, denoted the director  $\mathbf{n}$ , while the molecule, centers of mass are isotropically distributed in all three dimensions (Figure 1.17). The alignment of the molecule's long axes parallel to the director within the phase is only an approximate, time-averaged view of the molecular orientation. In actuality, the molecular orientation is more often described by angular distributions that the molecules assume with respect to the director. This distribution was described by Tsvetkov<sup>59</sup> and defined as the order parameter  $S$  (Equation 1.1).

$$S = 1/2 \langle 3 \cos^2\theta - 1 \rangle \quad \text{Eq. 1.1}$$



The brackets denote a statistical average of the molecules with their long molecular axis deviating from the director  $\mathbf{n}$  by an angle  $\theta$ . Thus, for perfectly orientated molecules the order parameter is  $S = 1$ , and for an isotropic liquid the order parameter is  $S = 0$ .

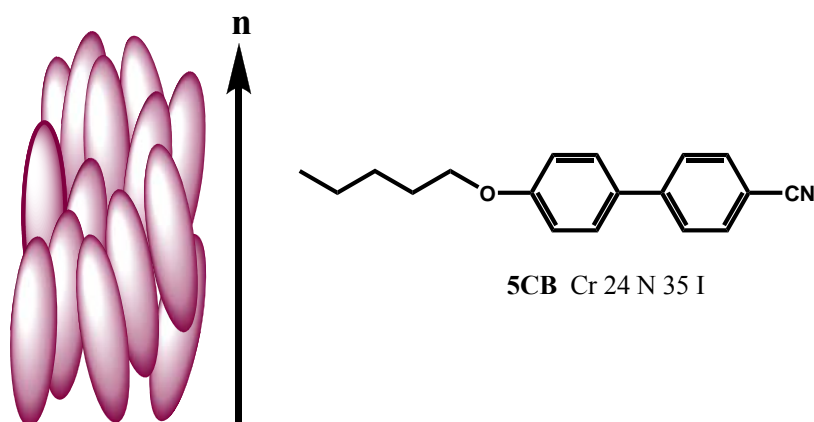


**Figure 1.17 – Graphical and schematic representation of a nematic phase.**

Due to the lack of positional order, the nematic phase is a fluid phase with viscosity approaching that of the isotropic liquid. Unsymmetrical molecules having one polar group and one short alkyl side-chain tend to generate a nematic phase. One of the most common LMW nematic LCs is 4-pentyl-4'-cyanobiphenyl, **5CB** (Figure 1.17). The phase transition behaviour is shown in Figure 1.17; **5CB** melts to an isotropic liquid at 24 °C and has a nematic phase stability of 35 °C, which gives a nematic range of 11 °C.

#### 1.4.2.2 Smectic Liquid Crystals

In the smectic A (**SmA**) phase molecules are free to rotate about their long axis, having orientational order and one-dimensional long-range positional order. Hence, they

---

form layers in which these layers are not clearly defined. The director  $\mathbf{n}$  and thus the optic axis is oriented perpendicular to the smectic layer plane (Figure 1.18a). This phase is typically generated from elongated molecules with a rigid non-polar aromatic core substituted with flexible terminal chains at both ends.

There also exists the possibility of various SmA layer arrangements. In simple monolayers, the smectic layer spacing  $d$  is approximately equal to the molecular length  $l$  ( $d \approx l$ ). Other possibilities are double layers, where the layer spacing  $d$  approximately equals double the length of the molecule ( $d \approx 2l$ ) or an interdigitated molecular arrangement can exist where the observed layer spacing is intermediate between the molecular length and double the molecular length ( $l < d < 2l$ ).<sup>60</sup>

The concept of microsegregation plays a key role in understanding the formation of lamellar structures in smectic phases. This involves the assembly of chemically incompatible components within the mesogens into distinct domains or sublayers.<sup>55</sup> Formation of smectic phases is partially driven by microsegregation of the rigid aromatic molecular core from the flexible aliphatic side-chains. It is well known that smectic phases are stabilized by elongation of the terminal aliphatic chains and hence the diameter of the core also plays an important role in the generation of smectic layers. The formation of smectic phases can be strongly promoted by designing calamitic mesogens that combine hydrophilic and lipophilic segments; for example fluorocarbon and hydrocarbon segments, or siloxane and hydrocarbon segments. If the different regions are mixed, the stability of the liquid crystal phases decreases.

If the director ( $\mathbf{n}$ ) of the SmA phase tilts by an angle ( $\theta$ ) with respect to the layer normal a tilted SmC phase results (Figure 1.18a). The tilt of the molecules long axis is the

only difference between the two phases. The formation of the SmC phase is favoured by molecules with unsymmetrical polar aromatic cores. The antiparallel coupling of terminal dipoles is thought to induce a tilt.<sup>61,62</sup> Also, the ability of mesogens to pack in a low energy zig-zag conformation results in a tilted structure.<sup>63</sup>

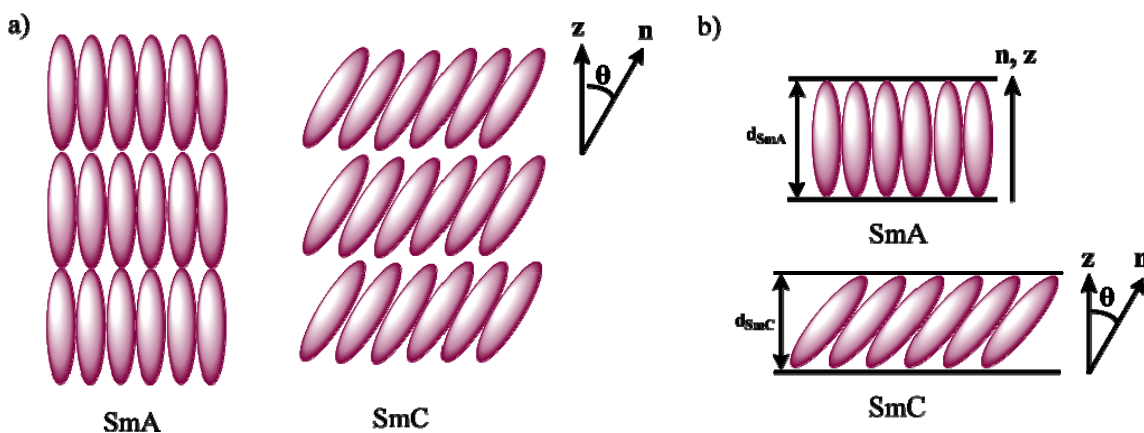


**Figure 1.18 – a) Illustrations of molecular packing in SmA and SmC phases and b) layer shrinkage from SmA to SmC phase.**

The amplitude of the tilt angle is determined by thermodynamic variables, such as temperature and pressure. However, the direction is not predetermined. With a uniform tilt direction, the transition from the SmA to the SmC phase results in a tilt angle that is temperature dependent, with increasing tilt with decreasing temperature. In the low temperature range of the SmC phase, the majority of single component materials exhibit tilt angles in the range of  $\theta \approx 25^\circ - 35^\circ$ .<sup>60</sup> A characteristic difference between the SmA and SmC phase is a substantial shrinkage (7- 10 %) in the smectic layer spacing upon tilting of the molecules long axis with respect to the layer normal (Figure 1.18b). Accordingly, the decrease in the layer spacing of the SmC ( $d_{\text{SmC}}$ ) phase relates to the SmA ( $d_{\text{SmA}}$ ) layer spacing by:

$$d_{\text{SmC}} = d_{\text{SmA}} \cos\theta \quad \text{Eqn. 1.2}$$

where  $\theta$  is the angle between the director ( $\mathbf{n}$ ) and the layer normal ( $\mathbf{z}$ ).



There are several other smectic phases which possess higher degrees of order than the SmA or SmC phase and they exhibit short-range positional ordering, in which layers are uncorrelated, but also long-range orientational ordering within the layers.<sup>58</sup> These include the hexatic B (SmB) phase which is similar to the SmA phase but with hexagonal packing. The SmF and SmI phases are tilted with pseudohexagonal packing; mesogens in the SmF phase tilt to the side of the hexagon while mesogens in the SmI phase tilt to the apex of the hexagon (Figure 1-19).

Additionally, crystal smectic phases exist, which have both long-range orientational and positional ordering leading to correlated layers, but still lack rotational order about the long molecular axes. These include the crystal B, E, G, H, J and K phases.

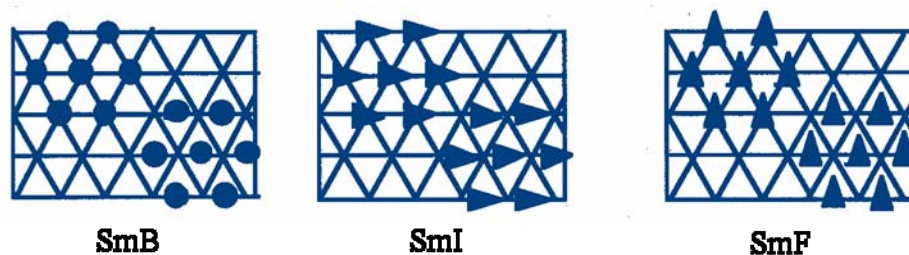


**Figure 1.19 – Plan views of molecular organization in SmB, SmI and SmF mesophases. The tilt is depicted by the direction of the triangle.<sup>58</sup>**

### 1.4.3 Chirality in Liquid Crystals

Chirality in soft matter can be present at both the molecular and supramolecular level. In liquid crystals, chirality can be introduced by several different avenues.<sup>64-68</sup> Chirality can be directly introduced within the molecule by incorporation of chiral elements, usually chiral centers which are thus single component chiral systems. Another popular way, especially for materials used in applications, is the addition of a small amount of a chiral guest (dopant) molecule to an achiral host phase. The amount of chiral

---

dopant is usually less than 5 %, and can themselves be mesogenic or non-mesogenic and induce chirality. Additionally, mixtures of chiral and achiral mesogenic materials can be prepared.

It has been well established that molecular chirality can give rise to helical supramolecular structures.<sup>69,70</sup> This is not restricted to nematic phases which are turned into cholesteric phases. Chirality can also modify ordered mesophases by distortion of the interfaces. Some examples of this phenomenon include twist grain boundary (TGB\*) phases and the blue phases (BP\*), which are only observed in chiral materials with large twisting power. Also, the physical properties of LC phases are modified by the loss of mirror symmetry. Tilted chiral smectic phases can exhibit a spontaneous polarization, and are thus pyroelectric.<sup>71</sup> This spontaneous polarization is switchable between two stable states by an applied electric field for several phases, SmC\*, SmI\* and SmF\*. Ferroelectricity can be observed when LCs are subjected to the appropriate geometry and boundary conditions.<sup>72</sup>

In the cholesteric nematic phase N\*, there is a spontaneous macroscopic helical superstructure with a twist axis that is perpendicular to the local director. The phase consists of local nematic 'layers', which are continually twisted with respect to each other. The helical superstructure is described by the temperature dependent pitch. The pitch can vary from 100 nm to 10  $\mu$ m and the twist can be right- or left-handed, depending on the configuration of the chiral element(s) within the molecule. In the N\* phase, due to the head-tail symmetry of the molecules, the periodicity L along the helix is given by half of the pitch,  $L = P/2$ .

In contrast to the  $N^*$  phase, where vertical boundary conditions result in a helical axis in the plane of the substrate, in the chiral smectic C ( $SmC^*$ ) helix lines are observed when the local director is oriented in the plane of the substrate. Unlike the  $N^*$  phases, where the identity period is  $P/2$ , the distance between two dark lines in the  $SmC^*$  phase gives the full pitch when the polarizer direction is along one of the in-plane director positions (Figure 1.20). An extensive overview on the effects of chirality in liquid crystals has recently been published by Kitzerow and Bahr.<sup>73</sup>

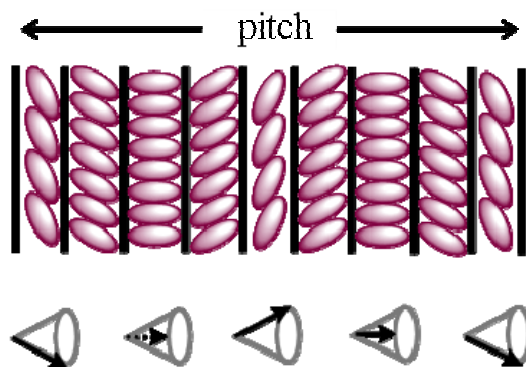


**Figure 1.20** – Schematic illustration of the helical superstructure of the chiral bulk  $SmC^*$  phase and the direction of the director on the tilt cone.

#### 1.4.4 Liquid Crystal Phase Characterization

There are various techniques which must be employed in order to classify the type of liquid crystal phase observed. The precise classification of each phase can sometimes be quite difficult when only small differences between phases exist. It is the combination of techniques that helps to elucidate the correct phase designation; these include, differential scanning calorimetry (DSC), polarizing optical microscopy (POM) and X-ray diffraction (XRD).<sup>58</sup>

#### 1.4.4.1 Differential Scanning Calorimetry (DSC)

Differential scanning calorimetry (DSC) is a thermo-analytical technique which is used to detect the enthalpy change associated with phase transitions, such as melting, crystallization, glass transitions, or LC to LC transitions, by measuring the heat either absorbed or released upon heating and cooling. This is accomplished by gradually heating and cooling a sample with respect to a reference, but keeping the sample and the reference maintained at nearly the same temperature throughout the experiment. DSC detects the energy changes or change in heat capacity for each transition with great sensitivity.<sup>74</sup> As a result, a curve of heat flux versus temperature or versus time can be created.

Transitions for melting or crystallization processes are relatively drastic and hence have a relatively high energy of transition (Figure 1.21). For example, melting from a crystalline solid to an isotropic liquid generates an enthalpy change of 30 - 50 kJ/mol. Glass transition ( $T_g$ ) refers to the transformation of a glass-forming liquid into a glass, which usually occurs upon rapid cooling. Figure 1.21 shows the plot for a glass transition, melting  $T_m$  (endothermic) and crystallization  $T_c$  (exothermic), of which  $T_m$  and  $T_c$  can be sharp or broad transitions depending upon the rate of heating or cooling. The glass transition is represented as a step in the DSC curve.

Glass transitions and LC-LC transitions result from smaller changes in structure and are reflected by relatively small enthalpy changes. For example, the SmA to isotropic liquid transition involves an enthalpy change of 4 - 6 kJ/mol. However, the nematic phase usually gives a smaller enthalpy change, 1 - 2 kJ/mol upon transition to the isotropic liquid. Enthalpy changes for transition between different liquid crystal phases can also

be extremely small. For example, the SmC to SmA transition is typically less than 300 J/mol. These changes can, however, be readily detected by POM.

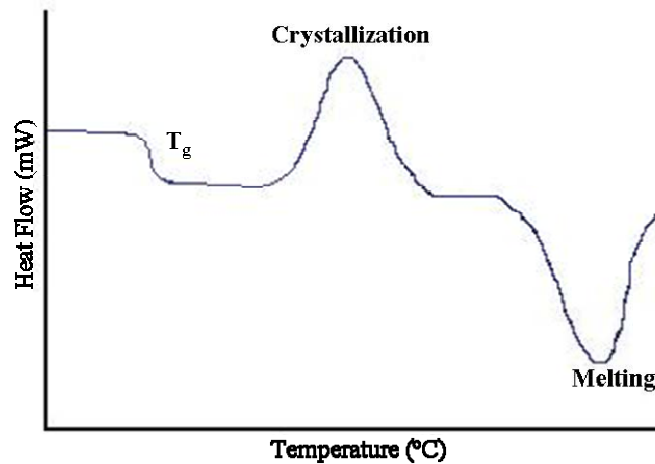


**Figure 1.21 - A DSC plot showing the three typical phase transitions:  $T_g$ ,  $T_m$ ,  $T_c$ .**<sup>74</sup>

The precise identity of the phase(s) cannot be determined, but the level of enthalpy change at that phase transition does provide some indication of the types of phases involved. Accordingly, DSC is used in conjunction with the other techniques to determine the type of mesophase that the material exhibits.

#### 1.4.4.2 Polarizing Optical Microscopy (POM)

Polarizing optical microscopy (POM) is a contrast-enhancing technique which improves the quality of the image acquired with birefringent (doubly refractive) materials and was developed to observe and photograph materials that are visible mainly due to their optically anisotropic property.<sup>60</sup> Primarily, POM enables the identification of the type of LC and other mesophases from the optical texture that is generated. This technique is also essential when evaluating the physical properties of LCs in particular phases over various temperature ranges.

---

The molecular arrangement of the molecules within a phase can be determined by careful analysis of the defect texture. These are studied when polarizers are crossed at  $90^\circ$  to each other. When no sample is in place light is extinguished and only black is seen. This is also the case with an isotropic liquid in place because no light passes through the analyzer (second polarizer). However, when birefringent medium is present, light is not extinguished and an optical texture is observed which conveys important information related to the molecular arrangement of the molecules. The observed textures are not only dependent upon the phase structure of the sample, but also upon the alignment of the sample. The two basic forms of alignment for LC compounds are homeotropic (vertical) and homogeneous (planar) alignment.<sup>58,60</sup> In planar alignment, the long axes of the molecules are in-plane with the substrate, and a texture is observed. In homeotropic alignment, the long axes of the molecules are normal to the substrate and parallel with the direction of the propagation of light. This results in no birefringence for any in-plane rotational position between the cross polarizers and the region appears black, this is termed pseudo-isotropic.

Nematics are easily identified by polarizing optical microscopy (POM), when viewed between crossed polarizers.<sup>60</sup> They typically show schlieren textures, due to the director orienting parallel to the substrates (Figure 1.22a,b). Schlieren textures exhibit characteristic sets of curved dark brushes, which corresponds to the extinction position of the nematic field, with director  $\mathbf{n}$  coinciding with the direction of either the polarizer or analyzer. The brushes come together in a singular point and can be twofold or fourfold (Figure 1.22b). These singularities are topological defects and are assigned a certain

strength  $s$ , with two-fold brushes  $s = \pm 1/2$ , and four-fold brushes  $s = \pm 1$ . Typically both  $s = \pm 1/2$  and  $s = \pm 1$  are observed for nematic LCs.

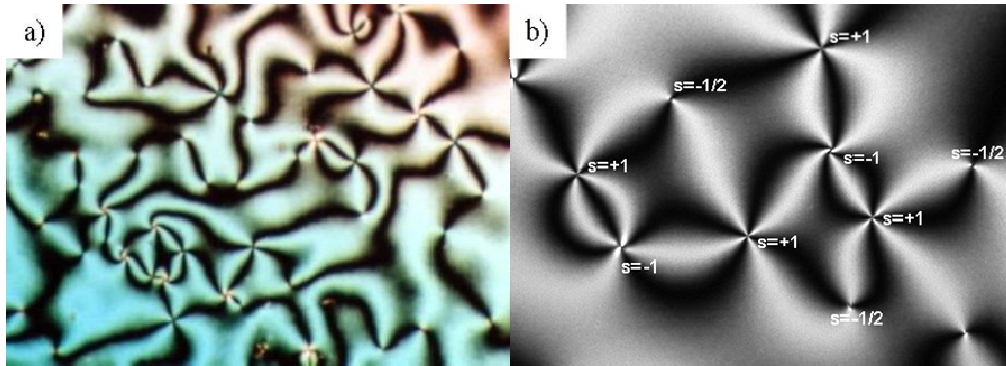


**Figure 1.22 – POM of N phase with schlieren textures featuring point defects with 2-brush and 4-brush disclinations. b) Shows defects with the corresponding  $s$  value.**

A typical texture characteristic of a SmA phase is a fan-shaped texture. Transition from a SmA to a SmC phase can be seen by the formation of a broken fan-shaped texture (Figure 1.23). Another characteristic feature of the SmC phase are schlieren textures in which singularities are resolved showing only four-fold defects, differing from the nematic schlieren textures that exhibit both. There are numerous characteristic defect textures for each phase, and classification requires a detailed analysis of these.<sup>60</sup>

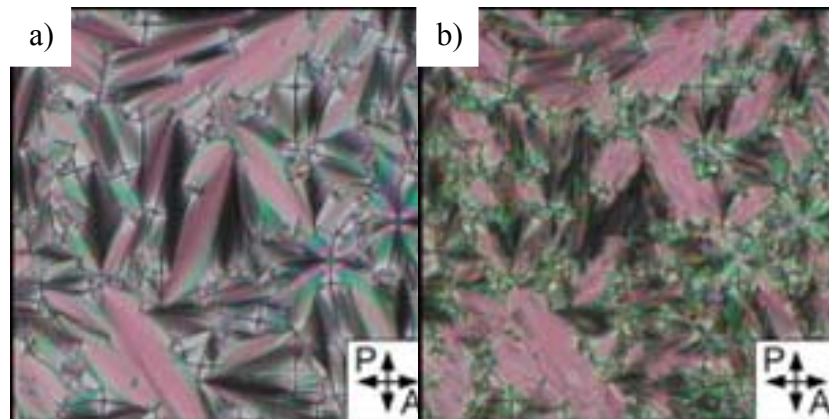


**Figure 1.23 – POM of a SmA phase (left) showing fan-shaped texture and of a SmC phase (right) showing a broken fan-shaped texture.<sup>75</sup>**

### 1.4.4.3 X-Ray Diffraction (XRD)

X-Ray diffraction (XRD) occurs when light of a suitable wavelength interacts with a crystal, and the crystal acts as a three dimensional diffraction grating due to the periodic nature of its internal structure.<sup>76</sup> XRD can be thought of as the ‘reflection’ of X-rays from the planes of atoms within a crystal. X-rays are ‘reflected’ from the planes only at specific orientations of the crystal and occur when the conditions for constructive interference are fulfilled.<sup>76</sup> The condition for the ‘reflection’ of X-rays by a crystal was outlined by W.H. Bragg and is illustrated in Figure 1.24. When a beam of monochromatic X-rays comes into contact with an atom in the plane at angle  $\theta$  and the X-ray is scattered. Bragg’s equation is given by:

$$\lambda = 2 d_{hkl} \sin \theta \quad \text{Eqn. 1.3}$$

The wavelength of the X-rays is given by  $\lambda$ . The equation relates the angle  $\theta$ , at which these reflections are observed, to the  $d_{hkl}$  spacing which occurs between the crystal planes.

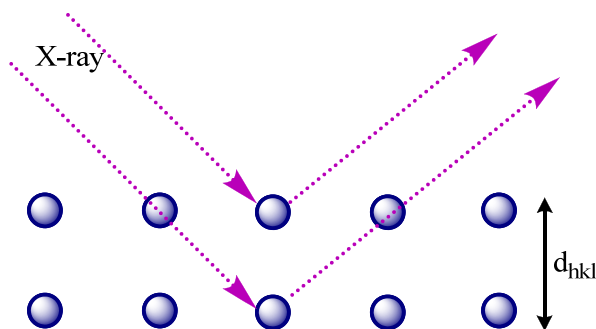


**Figure 1.24 – Bragg reflection from a set of crystal planes with a spacing  $d_{hkl}$ .**

Accordingly, XRD is the most definitive technique employed for the identification of mesophases. XRD analysis of a LC will map the positions of the molecules within each phase, thereby determining the phase structure and the



classification to which the phase belongs.<sup>58</sup> However, aligned samples are required to confirm phase designations. For example, the powder XRD profile for the bulk material of a SmA phase shows a diffuse outer ring and a sharp inner ring at a Bragg angle of  $2\theta$  corresponding to the smectic layer spacing, which is usually on the order of the molecular length. Due to the lack of positional ordering in nematics, a broad ring would be observed in the small angle region. The amorphous state of LCs is seen by diffuse reflections in the wide angle region. It follows then that if the material is crystalline there would be additional sharp reflections in this region.

## 1.5 THE COOPERATIVE EFFECT

Because liquid crystals are ordered condensed states of molecules, they can be used as dynamic materials which play significant roles in information transport, sensing, catalysis and as mentioned previously optoelectronic displays.<sup>77-81</sup> The ordering of liquid crystals is a cooperative phenomenon that is highly sensitive to small amounts of added dopant molecules. Over the past decade, stimuli-responsive bistable dopants have been employed as a means of controlling bulk LC properties as well as a way of amplifying molecular motion into mechanical work.<sup>82-85</sup> For example, stimuli-responsive materials can incorporate either light-, heat-, or redox-responsive components.<sup>86-88</sup>

A recent example of a light responsive LC was reported by Ikeda,<sup>89</sup> with the incorporation of an azobenzene chromophore into crossed-linked LC polymers (CLCPs). Incorporation of azobenzene groups into CLCPs causes large deformations induced by photoisomerization of the azobenzene. The types of movement observed by irradiation with UV light can include: bending, oscillating, twisting, swimming and rotational motions.<sup>90-93</sup> This work demonstrated three-dimensional movements such as an inchworm

walk and a flexible robotic arm motion from laminated films composed of a CLCP layer containing azobenzene.

The CLCP films were prepared from a 1:4 mixture of LC monomers (**1** and **2**) in a glass cell coated with rubbed polyimide alignment layers (Figure 1.25a). The CLCP film exhibited a smectic phase after photopolymerization. Conveniently, the glass transition of the CLCP films were close to room temperature, allowing the films to function at room temperature. Figure 1.25b shows the photoinduced motion of the CLCP laminated film having a curved shape. The azobenzene mesogens are aligned along the long axis of the film and the CLCP laminated parts are curled due to the difference in the thermal expansion coefficients between the two layers. Upon irradiation with UV light, the film extends to a flat shape and reverts back to the initial bent shape upon irradiation with visible light. This can be repeated at room temperature just by changing the wavelength of light.

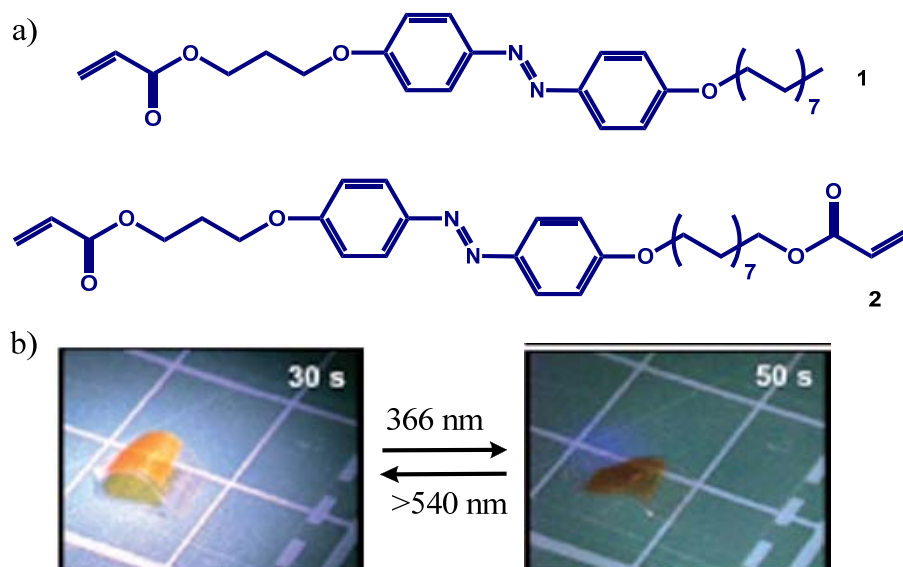


**Figure 1.25 – a) Structure of LCs used and b) time profile of the photoinduced inchworm walk of the LC laminated film by alternate irradiation with UV and visible light at room temperature.<sup>89</sup>**

---

A promising new approach towards nanoscale devices is the combination of molecular machines and liquid crystals. The liquid crystalline molecular order can provide the molecular machinery component with an organized dynamic environment. Furthermore, molecular machines have the capability to control the self-assembled behaviour of LC molecules. Very recent work has focused on the incorporation of LCs into polyrotaxanes, catenanes and rotaxanes for potential nanoscale devices.<sup>94-96</sup>

Polyrotaxanes are supramolecular polymers composed of a number of macrocycles which are threaded onto a linear polymer chain and are mechanically interlocked on the polymer chain by bulky groups.<sup>97-99</sup> The characteristic feature of polyrotaxanes is that each macrocycle can translate and rotate on the polymer chain. This feature enables the preparation of molecular materials such as molecular tubes, insulated molecular wires incorporating conductive polymers<sup>100-1</sup> and drug delivery systems.<sup>102-3</sup> Recently, a liquid crystalline polyrotaxane with mobile mesogenic side-chains was reported.<sup>94</sup> The thread component was composed of poly(ethyleneglycol) (PEG) and the macrocycle was a  $\alpha$ -cyclodextrin ( $\alpha$ -CD) ring which was substituted with the mesogenic cyanobiphenylhexanoate (CB5PR) groups, providing high mobility which allowed for translation and rotation of the macrocycle (Figure 1.26). The polyrotaxane was classified as a nematic LC from POM and XRD analysis. A schlieren texture was obtained by microscopy and by XRD a diffuse peak in the wide-angle region and a broad peak in the low-angle region characteristic of a nematic phase.

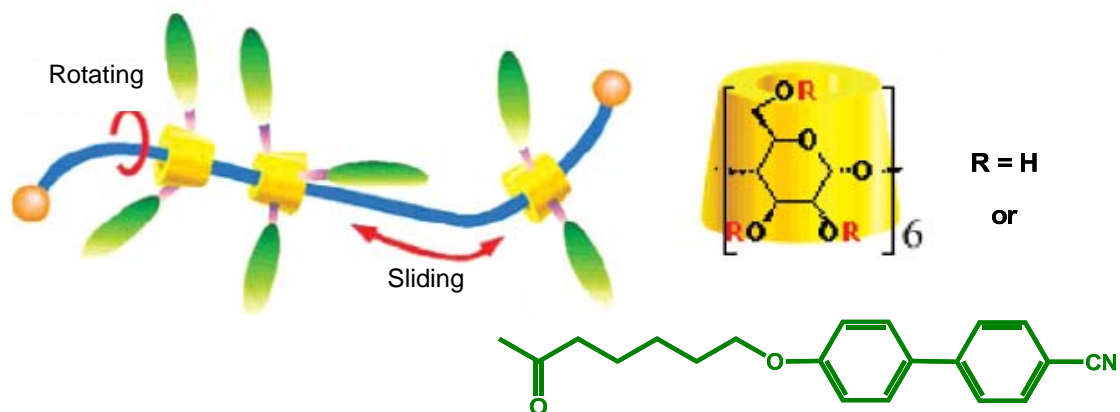


**Figure 1.26 – Structure of a mesogen-substituted polyrotaxane.<sup>94</sup>**

The first LC [2]catenane has been described from a collaboration between the groups of Kato and Sauvage.<sup>95</sup> They functionalized the [2]catenane with fork-like dendrons containing a fluorosubstituted cyclohexylbiphenyl unit, which tends to produce relatively wide smectic LC phases.<sup>81,104</sup> The structure of the free LC [2]catenane is shown in Figure 1.27a. The complexed [2]catenane differs from the free with the addition of copper(I) complexed to the central core. Both compounds exhibited smectic LC phases. Interestingly, both were observed to possess the same glass transition temperature. In contrast, the isotropization temperature of the complexed [2]catenane is 30 °C higher than that of the free [2]catenane. Hence, binding of the copper ion leads to thermal stabilization of the LC phase. This is likely due to an increase in rigidity in the central core upon complexation and stabilizes the assembled structure through inter ionic interactions. XRD analysis and POM studies suggested a SmA for both and a fan-shaped texture was obtained for the complexed non-aligned [2]catenane (Figure 1.27b,c).

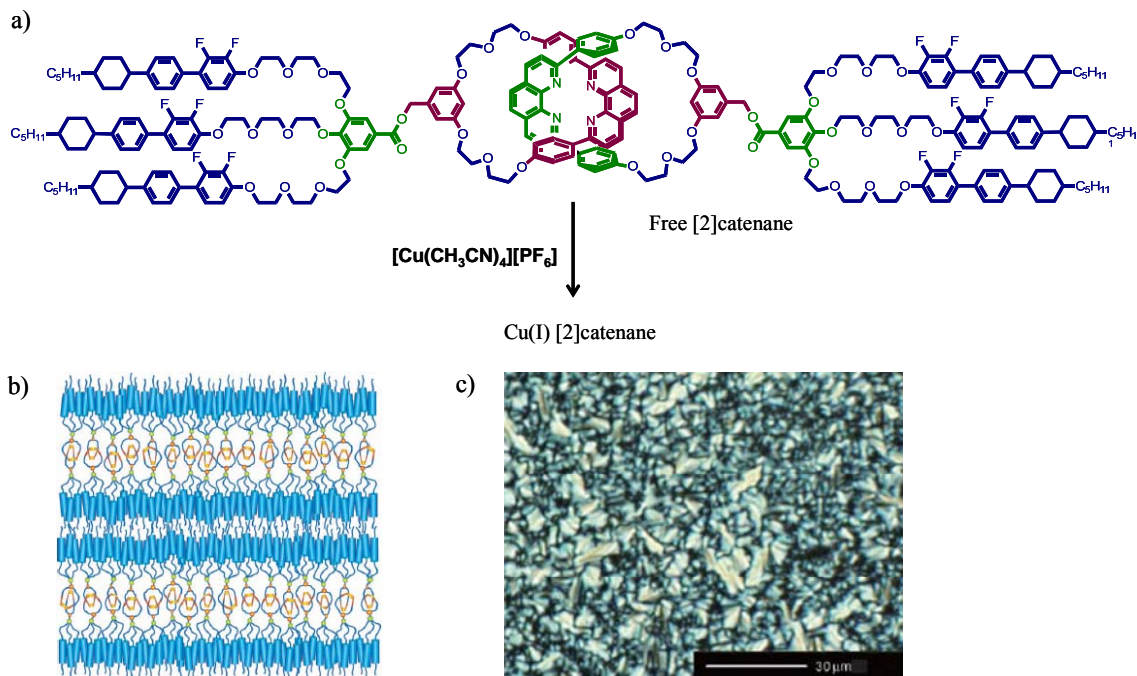


**Figure 1.27 – a) Structure of LC free [2]catenane, b) Possible organization into Sm phase and c) fan-shaped texture of non-aligned Cu(I) complexed LC [2]catenane.<sup>95</sup>**

The first bistable LC [2]rotaxane molecular shuttle had been described from a collaboration between the groups of Kato and Stoddart.<sup>96</sup> They designed an electrochemically switchable bistable [2]rotaxane molecular shuttle consisting of a tetracationic cyclobis(paraquat-*p*-phenylene) as the mobile macrocycle and two different recognition sites in the thread, containing tetrathiafulvalene (TTF) and 1,5-dioxynaphthalene groups (Figure 1.28). The macrocycle is shuttled by a two-electron oxidation of TTF followed by reduction of the dication  $\text{TTF}^{2+}$  back to its neutral state; similar to that discussed previously for the molecular muscle.<sup>47</sup>

Smectic A mesomorphism was introduced by the attachment of large liquid crystalline dendritic stoppers. Incorporation of a large number of ethylene glycol units lowered the melting temperature of the molecular shuttle, but the transition into the isotropic liquid still occurred *above* the decomposition temperature of the compound at

150 °C. This approach has been previously applied to other typical non-mesogens<sup>86,88,105-111</sup> and is generally successful if the dendritic mesomorphic groups are sufficiently large and numerous and dictate the self-organization of the entire compound. However, this basic methodology does have limits such as an increase in phase transition temperatures, an increase in viscosity and synthetic feasibility.

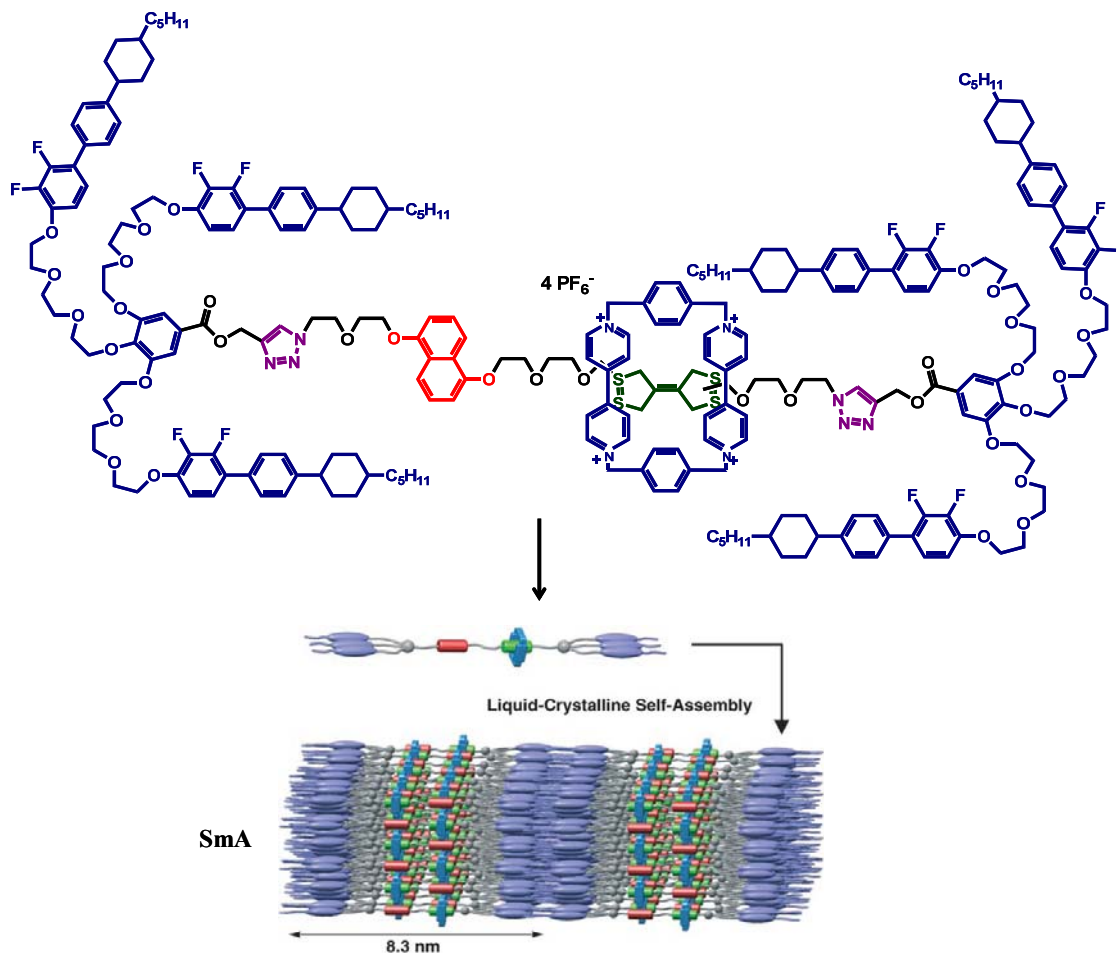


**Figure 1.28 - A LC bistable [2]rotaxane molecular shuttle reported by Kato and Stoddart *et al.*<sup>96</sup>**

### 1.6 THE LOEB MOTIF

It was reported early on by Stoddart and co-workers, that bis(paraphenylene)-34-crown-10 ether formed a [2]pseudorotaxane with the paraquat<sup>2+</sup> ion (Figure 1.29a).<sup>112</sup>

The binding of paraquat<sup>2+</sup> with the crown ether was primarily due to  $\pi$ - $\pi$  interactions between the hydroquinol rings of the crown and the pyridinium rings of the paraquat<sup>2+</sup>. Numerous ion-dipole interactions ( $N^+ \cdots O$ ) between the pyridinium nitrogen atoms and the crown ether oxygen atoms, as well as hydrogen bond interactions between the guest and the host also contributed to binding.

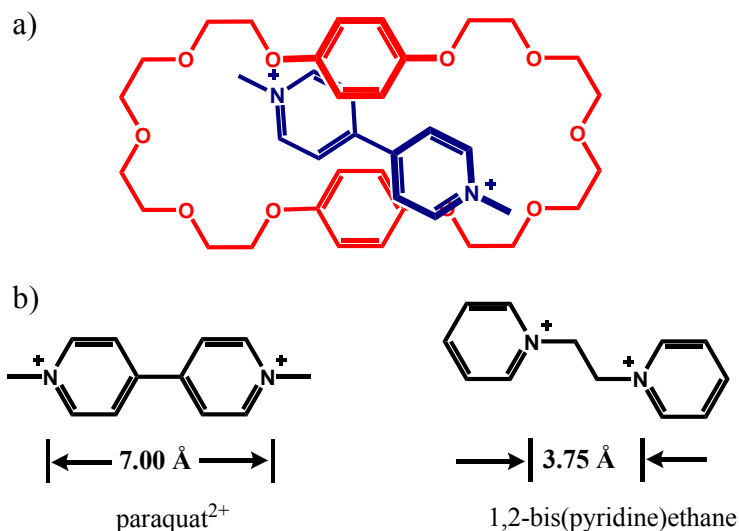


**Figure 1.29 – a) [2]Pseudorotaxane formed between paraquat<sup>2+</sup> and a crown ether. b) Comparison of the N<sup>+</sup>...N<sup>+</sup> distances in the paraquat<sup>2+</sup> cation and the 1,2-bis(pyridinium)ethane<sup>2+</sup> cation.**

Approximately 10 years later, Loeb and Wisner<sup>113</sup> synthesized an isomer of paraquat<sup>2+</sup>, namely 1,2-bis(pyridinium)ethane, containing a higher charge concentration between the pyridinium nitrogen atoms: the N<sup>+</sup>...N<sup>+</sup> distance was reduced from 7.00 Å in paraquat<sup>2+</sup> to 3.75 Å in 1,2-bis(pyridinium)ethane (Figure 1.29b). It was observed that the 1,2-bis(pyridinium)ethane cation was strongly complexed in the cavity of 24-crown-8 containing macrocycles. A combination of solution <sup>1</sup>H NMR spectroscopic studies and X-ray crystallographic data revealed that complexation was driven by several non-covalent interactions, namely: i) N<sup>+</sup>...O ion-dipole interactions, ii) eight weak C-H...O hydrogen bonds and iii) significant stacking interactions (Figure 1.30).<sup>113,114</sup>

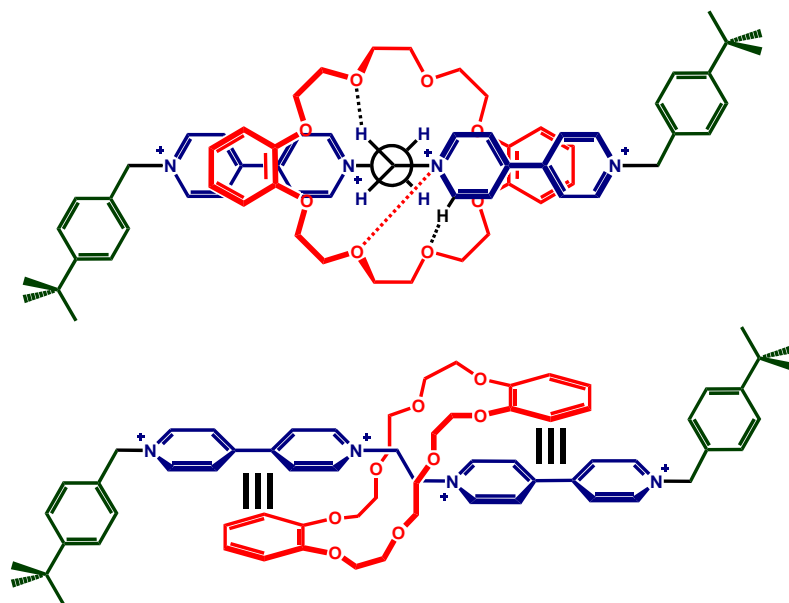


**Figure 1.30** – Newman projection top view (top) and side view (bottom) showing non-covalent interactions between a 1,2-bis(4,4'-bipyridinium)ethane<sup>4+</sup> thread and the DB24C8 macrocyclic ring.

Over the past decade, the 1,2-bis(pyridinium)ethane/24C8 motif has proven to be a versatile system. It has been used for the formation of [2]pseudorotaxanes,<sup>113-115</sup> [2]rotaxanes,<sup>116-119</sup> [3]rotaxanes,<sup>120</sup> [3]catenanes,<sup>121</sup> molecular shuttles,<sup>122-124</sup> branched [n]rotaxanes,<sup>125</sup> dendrimeric rotaxanes<sup>126</sup> and metal organic rotaxane frameworks (MORFs).<sup>127-128</sup>

## 1.7 SCOPE OF THE THESIS

Combining the self-assembly of supramolecular chemistry with self-organization inherent in liquid crystals has very recently become a focused area of research, since their cooperation has the potential to lead to a variety of functional nanoscale devices. That said, it is very unlikely that the well-established chemistry of low molecular weight liquid crystals will necessarily translate to complex interlocked systems and there is essentially nothing known about the structure-property relationship between rotaxane design and



---

mesomorphism. We also firmly believe that the control of molecular switches and the amplification of their cooperative motion to produce a macroscopic response within a mesophase can only be accomplished if there are contributions from *both* the shuttling macrocycle and the mesogenic groups. These types of materials have never been studied. Finally, it is essential that any new LC rotaxane can be prepared in large quantity and high purity and since any future application as a functional material will require good alignment in optical and/or electronic devices, the formation of an isotropic melt at temperatures below 200 °C is essential.

To address the above comments, this thesis describes a systematic approach to the design and synthesis as well as the structure-property relationships of mesomorphic [2]rotaxanes incorporating the 1,2-bis(pyridinium)ethane/**DB24C8** rotaxane motif. The thesis consists of two major parts: **Chapters 2, 3, and 4** describe the structure-property relationships for the designed systems and **Chapters 5 and 6** recount some preliminary experiments on areas of applicability; chirality in liquid crystals and mesomorphic molecular shuttles. In **Chapters 2 and 3** a systematic approach to introduce liquid crystallinity into the 1,2-bis(pyridinium)ethane/**DB24C8** rotaxane motif is described in which various purely aliphatic extended 3,5-disubstituted stoppers are introduced. The effect of applying groups typical for low molecular weight LCs to the Loeb motif is investigated in **Chapter 4** along with the introduction of a modified rotaxane design. The introduction of chirality into mesomorphic [2]rotaxanes is presented in **Chapter 5** along with the effect of chirality on the phase behavior. The design of a molecular shuttle based upon the structure-property relations determined from the previous chapters is presented in **Chapter 6**.

# CHAPTER 2

## *Discovery of a Liquid Crystal [2]Rotaxane*

### 2.1 INTRODUCTION

The (1,2-bis(dipyridinium)ethane)-(dibenzo-24-crown-8) or *Loeb* motif has proven to be a versatile recognition template for the formation of interlocked and interpenetrated molecules.<sup>113-128</sup> The interaction between a cationic 1,2-bis(dipyridinium)ethane thread and a dibenzo-24-crown-8 (**DB24C8**) macrocyclic ring occurs by three sets of complementary interactions: (i) ion-dipole interactions between the  $N^+$ -pyridinium and the oxygen atoms on the crown ether, (ii) a set of eight weak  $CH\cdots O$  hydrogen bonds between the *ortho*- $N^+$  hydrogen atoms and the oxygen atoms on the crown ether and (iii)  $\pi$ - $\pi$  stacking interactions between the electron-rich catechol rings of the crown ether and the electron-poor pyridinium rings of the thread (Figure 2.1).

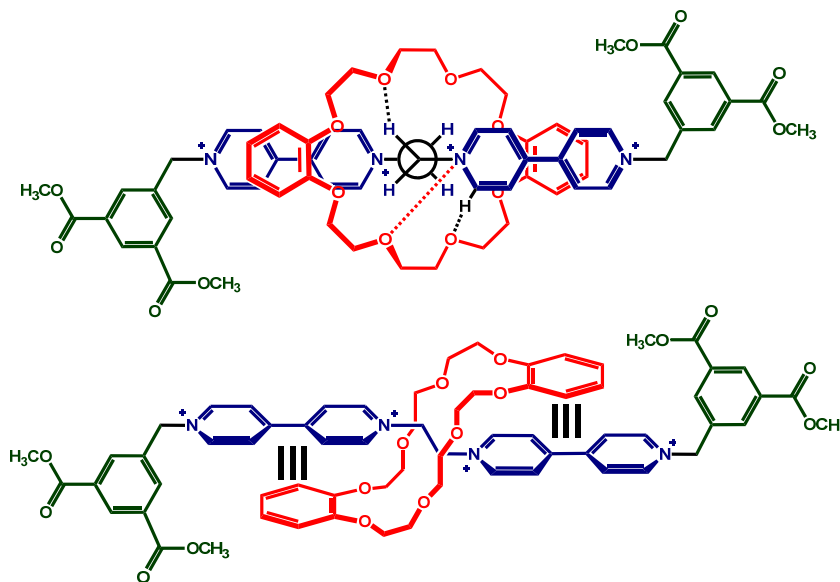


**Figure 2.1 – Newman projection top view (top) and side view (bottom) showing non-covalent interactions between a 1,2-bis(dipyridinium)ethane<sup>4+</sup> stoppered thread and DB24C8 macrocyclic ring.**

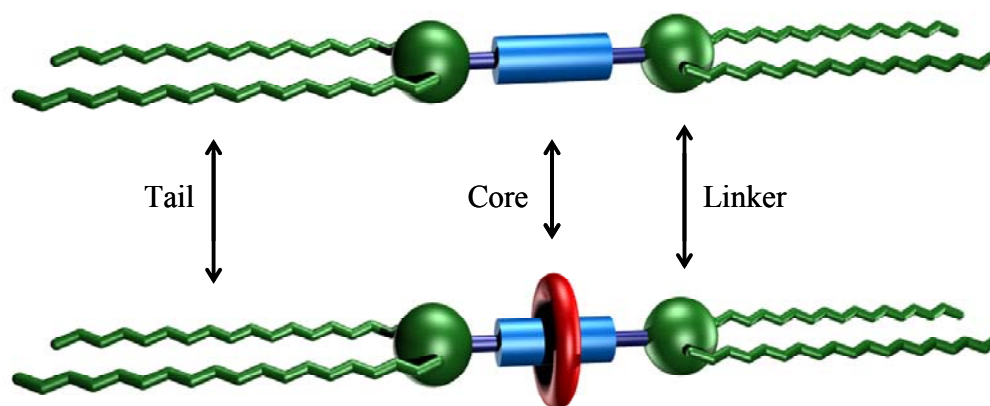


**Figure 2.2 – Graphical representation of dumbbell (top) and [2]rotaxane (bottom) based on gemini surfactant and tetracatenar design for calamitic LCs.**

This chapter describes the initial design of liquid crystalline materials incorporating this interaction. Mesomorphism can be introduced into our design by many avenues, the simplest of which was to incorporate non-mesogenic terminal stoppering units that contain long chain alkyl groups as part of an ester function (Figure 2.1 and Figure 2.2). The molecular weight was kept to a minimum, to avoid high melting clearing temperatures into the isotropic liquid, which is essential for processing and alignment of the materials. Comparative studies were done on the naked dumbbells (without a macrocycle) and ion sheltered [2]rotaxanes (with a macrocycle) to determine the effect of the macrocycle on mesomorphism (Figure 2.2).

The design of our system is similar to gemini surfactants<sup>129</sup>, which resembles the stoppered threads with a rod-like ionic aromatic core and long alkyl terminal chains (Figure 2.3a). The [2]rotaxanes are reminiscent of calamitic liquid crystalline polycatenars, namely tetracatenars, with a rigid polyaromatic rod-like core and four long terminal alkyl groups. A tetracatenar design was chosen for its potential to induce smectic (Sm) mesomorphism by providing sufficient packing volume of the side-chains to

counterbalance the large packing volume of the [2]rotaxane cores. Of all the reported tetracatenars only one tetracatenar presented by Bruce and Fazio *et al*<sup>130</sup> was ionic and is shown in Figure 2.3b. An anion containing a long aliphatic chain was chosen to lower melting temperatures. In this systematic approach the 3,5-disubstituted stoppers were employed instead of the traditional 3,4-disubstituted stoppers because the latter would not adequately fill space to compensate for the bulky ionic core. This chapter focuses on introducing mesomorphism via functionalized stoppers to form thermally stable liquid crystals that can be processed and aligned into thin films.

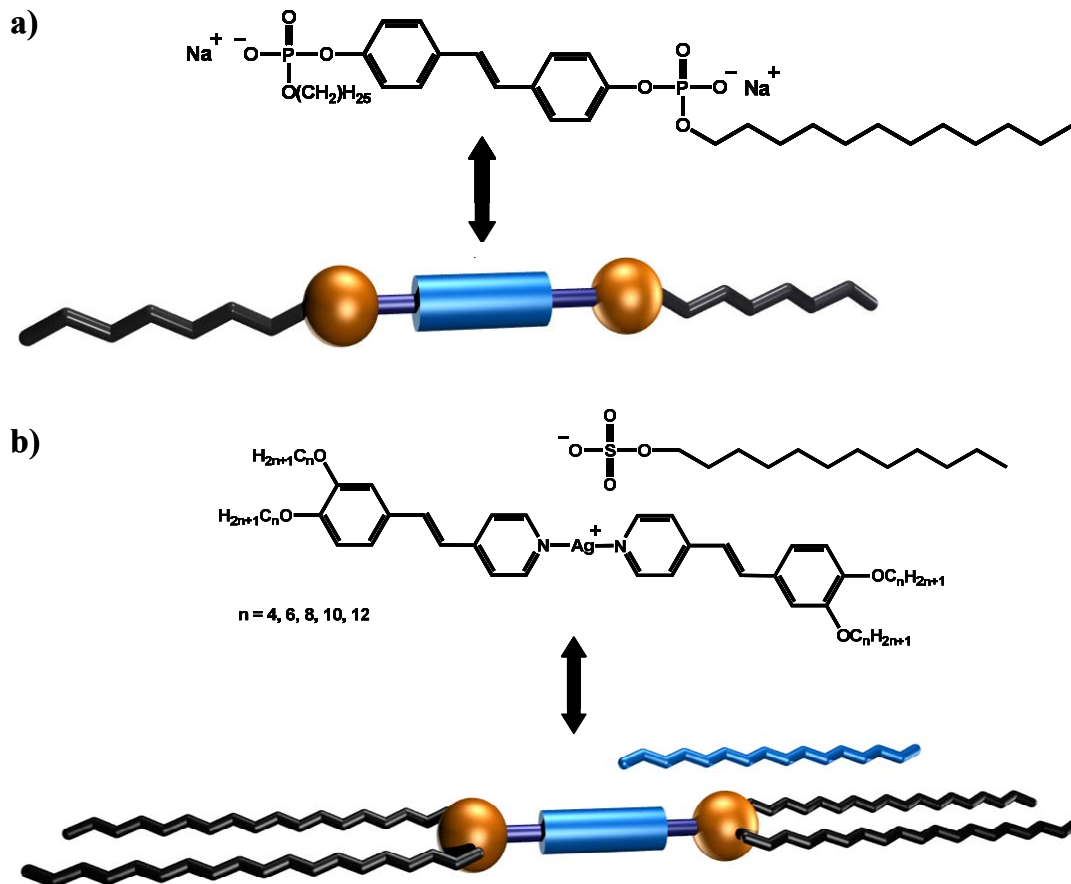
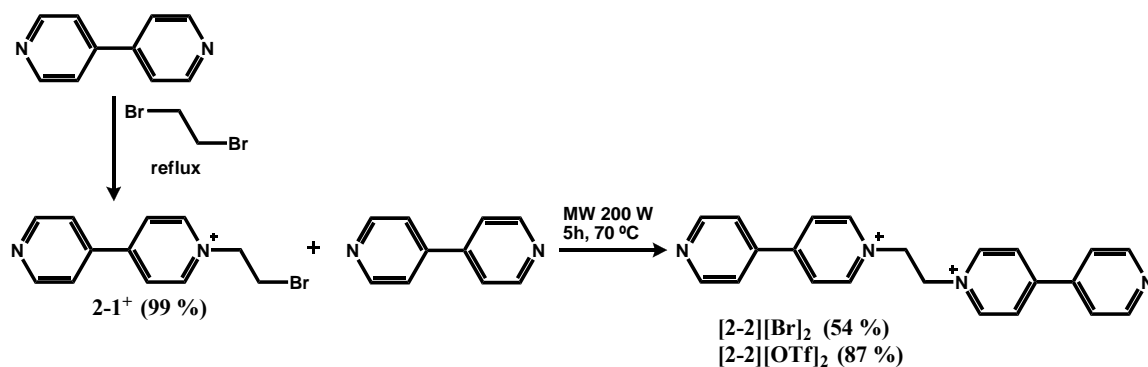


Figure 2.3 – Structural and graphical representation of a) a gemini surfactant synthesized by Menger and Keiper *et al*; b) a tetracatenar generated from the design synthesized by Bruce and co-workers.

## 2.2 SYNTHESIS AND CHARACTERIZATION

### 2.2.1 Synthesis

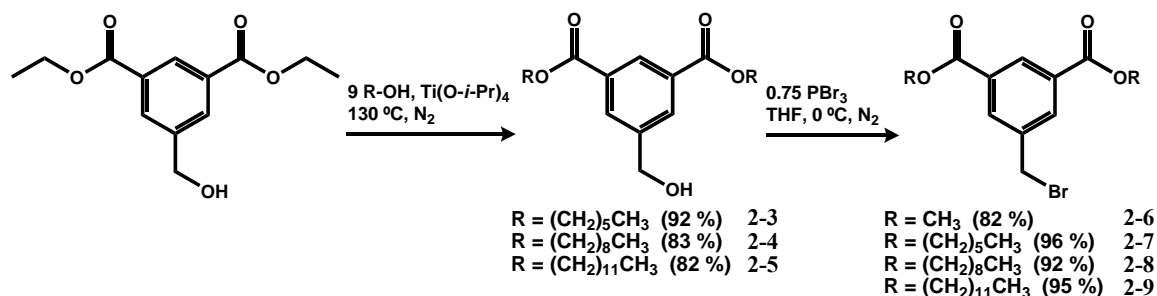
Compound **2-1**<sup>+</sup> was combined with 4,4'-bipyridine in butanol and subjected to microwave irradiation for 5 h at 70 °C to generate thread **2-2**<sup>2+</sup> (Scheme 2.1). The resulting crude mixture was then filtered hot and resulting precipitate washed with methanol. Formation of the thread does not go to completion, thus it was necessary to purify the residue by column chromatography. The thread was isolated as the bromide salt and subsequently anion exchanged to the triflate salt *via* a two-layer extraction with NaOTf (aq)/MeNO<sub>2</sub>.



**Scheme 2.1 - Synthetic route to thread **2-2**<sup>2+</sup>.**

In this initial study, we systematically introduced relatively short alkyl groups in order to determine the minimum packing volume of side-chains required to induce a smectic LC phase in [2]rotaxanes. Compound **2-3** was synthesized according to a modified literature procedure.<sup>131</sup> The new 3,5-bis(*n*-alkylcarboxy)benzylbromide stoppers were synthesized in two steps: 1) transesterification<sup>132</sup> of dimethyl-5-(hydroxymethyl)*isophthalate* with an excess of the *n*-alkyl alcohol in the presence of Ti(O-*i*-Pr)<sub>4</sub> as the catalyst to generate the corresponding benzyl alcohols, bis(hexyl) **2-4**,

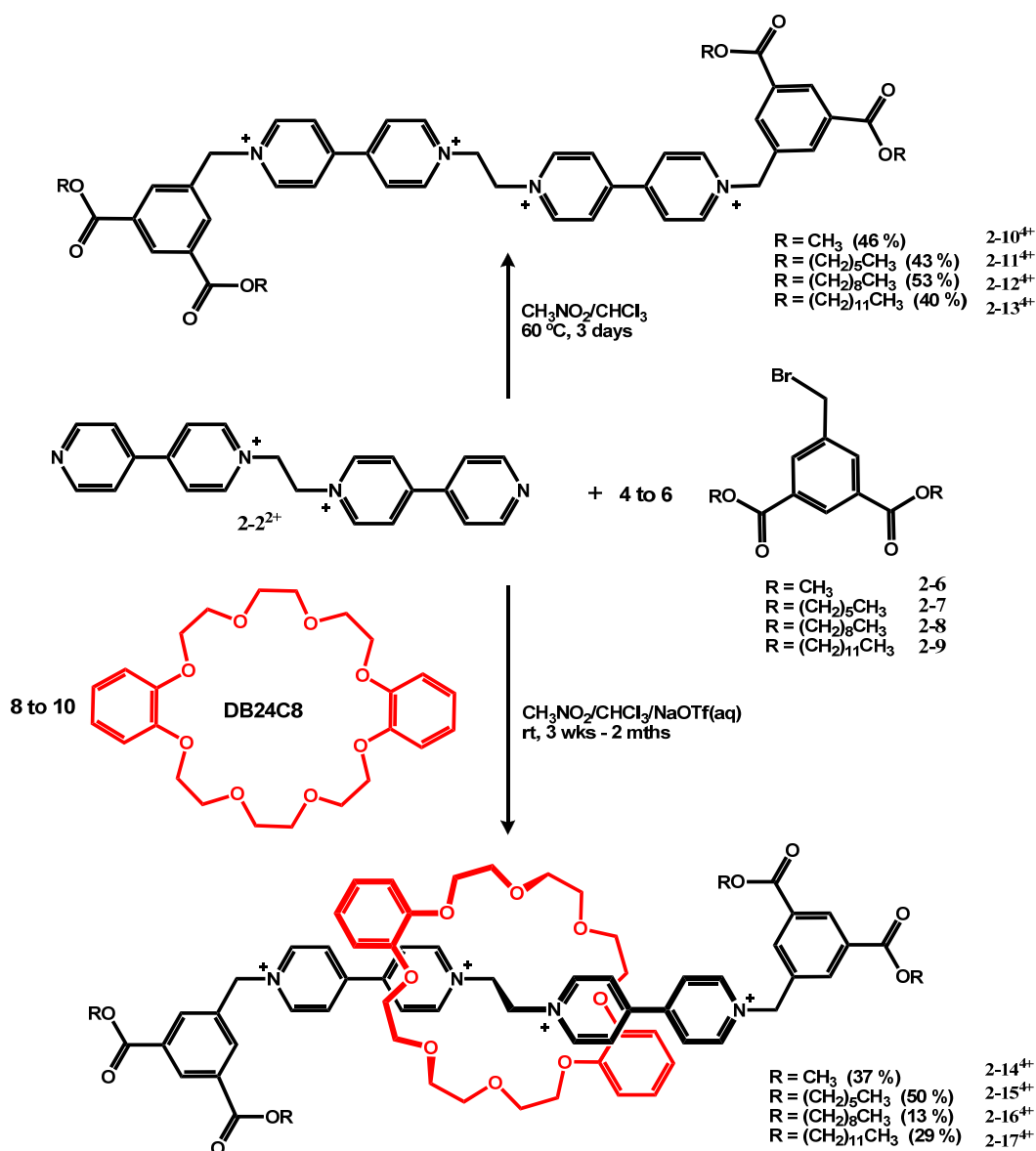
bis(nonyl) **2-6** and bis(dodecyl) **2-8**; 2) bromination of the benzyl alcohol with phosphorous tribromide to generate the bis(methyl) **2-3**, bis(hexyl) **2-5**, bis(nonyl) **2-7** and bis(dodecyl)benzyl bromide **2-9** stoppers (Scheme 2.2). Due to the high purity requirement for incorporation into [2]rotaxanes, each compound was further purified by column chromatography.



**Scheme 2.2 - Synthetic route to stoppers.**

As outlined in Scheme 2.3, both the [2]rotaxanes (**2-14**<sup>4+</sup>, **2-15**<sup>4+</sup>, **2-16**<sup>4+</sup> and **2-17**<sup>4+</sup>) and their analogous dumbbell shaped axles (**2-10**<sup>4+</sup>, **2-11**<sup>4+</sup>, **2-12**<sup>4+</sup> and **2-13**<sup>4+</sup>) were prepared by alkylating the terminal pyridine groups of axle **2-2**<sup>2+</sup> with 3,5-bis(*n*-alkylcarboxy)benzylbromides (**2-6**, **2-7**, **2-8** and **2-9**) in the presence (rotaxane) or absence (dumbbell) of the macrocycle dibenzo-24-crown-8, **DB24C8**. To synthesize the [2]rotaxanes, one equivalent of thread was reacted with eight to ten equivalents of crown ether and four to six equivalents of appropriate stopper and the mixtures were stirred at room temperature for three weeks to two months. Two different reaction conditions were used. [2]Rotaxanes **2-14**<sup>4+</sup> and **2-15**<sup>4+</sup> were synthesized by dissolving all reactants in a two phase mixture of MeNO<sub>2</sub>/NaOTf(aq), stirring at room temperature until all terminal pyridine groups were alkylated, whereas, [2]rotaxanes **2-16**<sup>4+</sup> and **2-17**<sup>4+</sup> were synthesized by initially dissolving the thread and crown in a minimum amount of hot

MeNO<sub>2</sub> and combining this with the stopper which was dissolved in a minimum amount of CHCl<sub>3</sub>, followed by addition of saturated NaOTf and stirred at room temperature until



**Scheme 2.3 - Synthetic route for [2]rotaxanes and dumbbells.**

all terminal pyridine groups were alkylated. The uncomplexed thread and macrocycle are colourless (Figure 2.4a and 2.4b, respectively), however, significant  $\pi$ - $\pi$  stacking interactions between the electron-rich catechol group of the crown and the electron-poor pyridinium rings of the axle give rise to a charge transfer interaction that imparts the

pseudorotaxane with a characteristic yellow colour and the rotaxane with a characteristic orange-red colour, (Figure 2.4c and 2.4d, respectively). This system introduced the further complexity of large solubility differences due to the large non-polar alkyl chains of the stopper with respect to the polar ionic core, and reaction times were longer with increasing amounts of  $\text{CHCl}_3$ . Due to small amounts of residual starting materials after many recrystallizations, all rotaxanes were further subjected to column chromatography employing assorted combinations of polar solvents with salt solutions to move the charged species. The typical eluant was a 7:1:2 mixture of MeOH, 2M  $\text{NH}_4\text{Cl}$  (aq) and  $\text{MeNO}_2$ . Once the [2]rotaxanes were recovered from the column they were anion exchanged back to the triflate salt by way of a two-layer  $\text{NaOTf}$  (aq)/ $\text{MeNO}_2$  extraction.

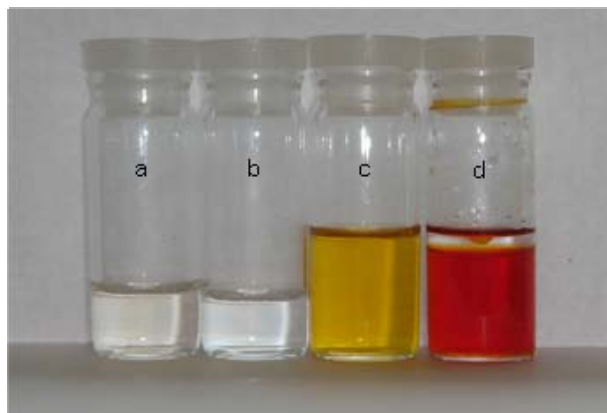


**Figure 2.4 – Typical colours of a) free axle, b) free macrocycle, c) [2]pseudorotaxane and d) [2]rotaxane in MeCN.**

Dumbbells were synthesized to study the effect of the macrocycle on mesomorphism from unsheltered ionic dumbbells to charge sheltered [2]rotaxanes. Dumbbells **2-10<sup>4+</sup>** and **2-11<sup>4+</sup>** were synthesized by stirring the thread and stopper in  $\text{MeNO}_2$ , where the alkylation was accelerated by heating to 60 °C for three days. Dumbbells **2-12<sup>4+</sup>** and **2-13<sup>4+</sup>** were synthesized in the same manner, but with the addition



of  $\text{CHCl}_3$  to ensure dissolution of the stopper. Synthesis of the dumbbells made the analysis of the non-covalent interactions in the [2]rotaxanes possible by comparing the  $^1\text{H}$  NMR chemical shifts of both species in the same solvent.

### 2.2.2 $^1\text{H}$ NMR Spectroscopy

Generation of dumbbells by alkylation of the terminal pyridine group causes small chemical shift differences compared to that of the free axle **2-2<sup>2+</sup>** in the  $^1\text{H}$  NMR spectra in  $\text{CD}_3\text{CN}$  (Figure 2.5). Protons **d** and **b** are deshielded while protons **c** are shielded by stoppering, and protons **a** and **e** are unaffected. All  $^1\text{H}$  NMR spectra of [2]rotaxanes were identical with the only difference being an increase in the intensity of the aliphatic protons at 1.3 ppm due to an increase in the number of carbons in the chain (Figure 2.6).

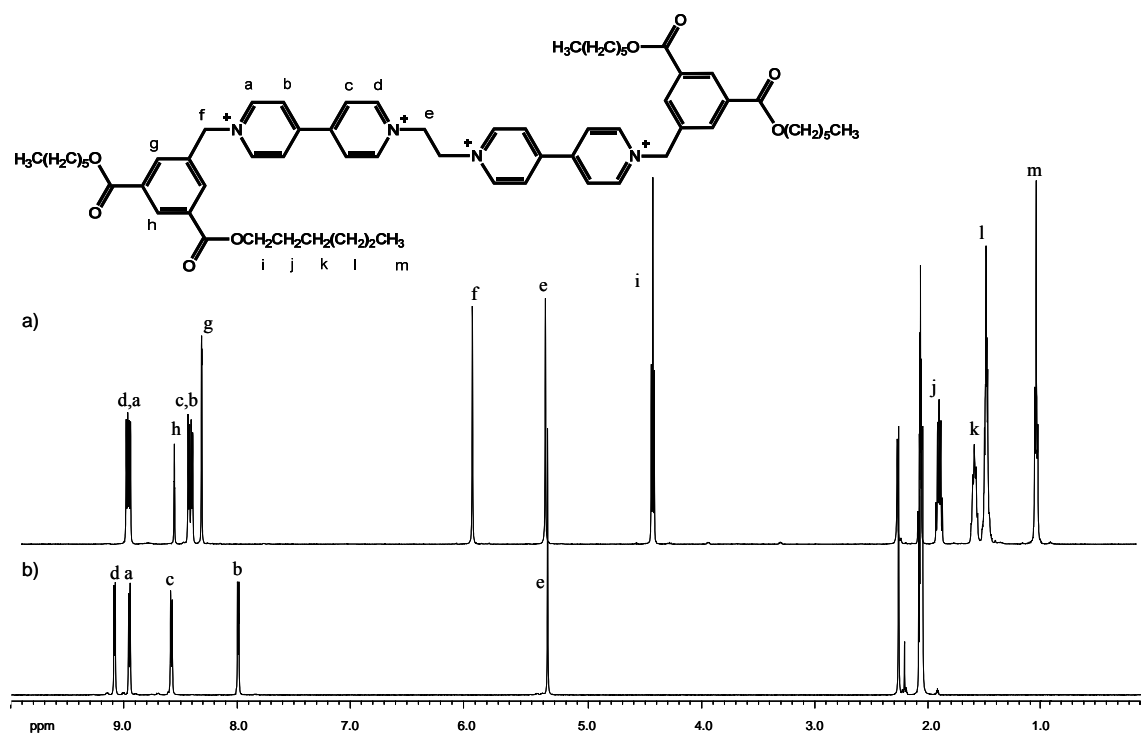
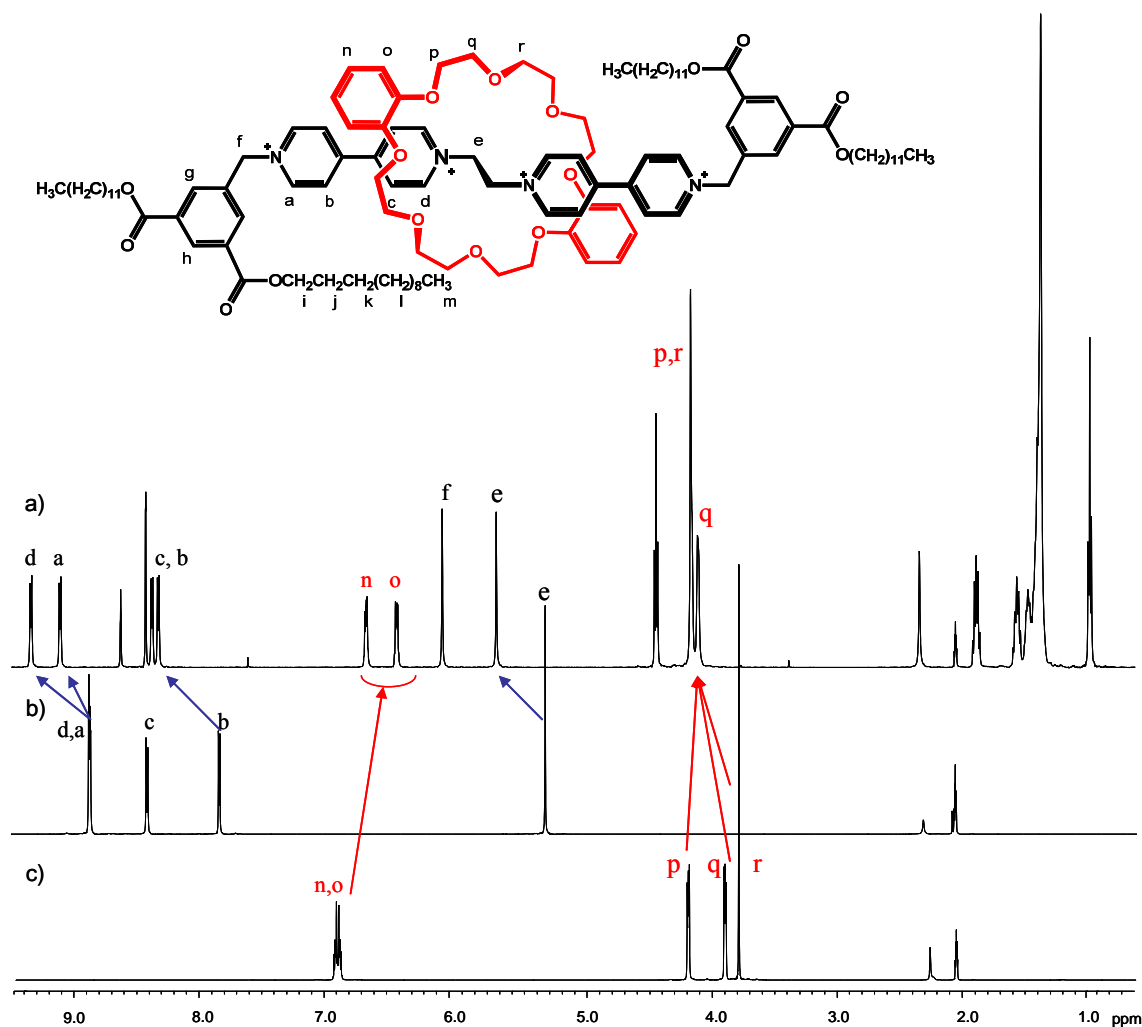


Figure 2.5 -  $^1\text{H}$  NMR spectra of a) **2-11<sup>4+</sup>** and b) **2-2<sup>2+</sup>** in  $\text{CD}_3\text{CN}$ .



**Figure 2.6 - <sup>1</sup>H NMR spectra of a) 2-17<sup>4+</sup>, b) 2-2<sup>2+</sup> and c) DB24C8 in CD<sub>3</sub>CN.**

The comparison of the <sup>1</sup>H NMR spectra of the naked dumbbell **2-10<sup>4+</sup>** to the [2]rotaxane **2-14<sup>4+</sup>** prepared with the bis(pyridinium)ethane-**DB24C8** binding motif clearly shows the effect of all three non-covalent interactions responsible for the initial self-assembly. Figure 2.7 shows that the ethylene protons of the recognition site, **e**, and  $\alpha$ -pyridinium protons, **d**, are deshielded due to hydrogen bonding with the oxygen atoms of the crown ether, while  $\beta$ -pyridinium protons, **b** and **c**, are shielded due to  $\pi$ - $\pi$  stacking interactions between the electron rich catechol rings of the crown ether and the electron poor pyridinium rings of the dumbbell. The crown ether catechol protons are shielded for

the same reason, and the other protons on the dumbbell, **g**, **h** and **f**, do not shift as they are not directly involved in any non-covalent interactions with the crown ether.

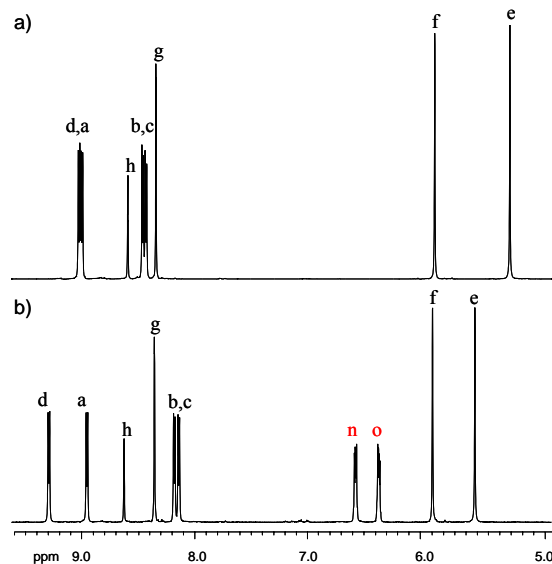


**Figure 2.7** -  $^1\text{H}$  NMR spectra of a)  $2-10^{4+}$ , b)  $2-14^{4+}$  in  $\text{CD}_3\text{CN}$ .

### 2.2.3 Single Crystal X-ray Structure

The methyl substituted [2]rotaxane  $2-14^{4+}$  was prepared as a model compound. Crystals suitable for single crystal X-ray structural determination were grown by slow diffusion of *iso*-propanol layered on top of a saturated solution of rotaxane in MeCN. Figures 2.8a and 2.8b show the ball-and-stick and space filling views, respectively. The ball-and-stick representation shows the atom numbering scheme and the triflate anions are omitted for clarity. The four triflate counterions are included in the side-on-view of the space-filling model of [2]rotaxane  $2-14^{4+}$ , where the pyridinium axle is blue, the crown ether wheel is red, the stoppering groups are green and the triflate anions are yellow. The interlocked nature of the [2]rotaxane can be seen clearly, with the crown ether arranged in an "S"-shaped conformation around the axle. The stoppering groups are

oriented almost perpendicular to the axle and wheel, which are parallel, giving the molecule an overall zigzag shape.

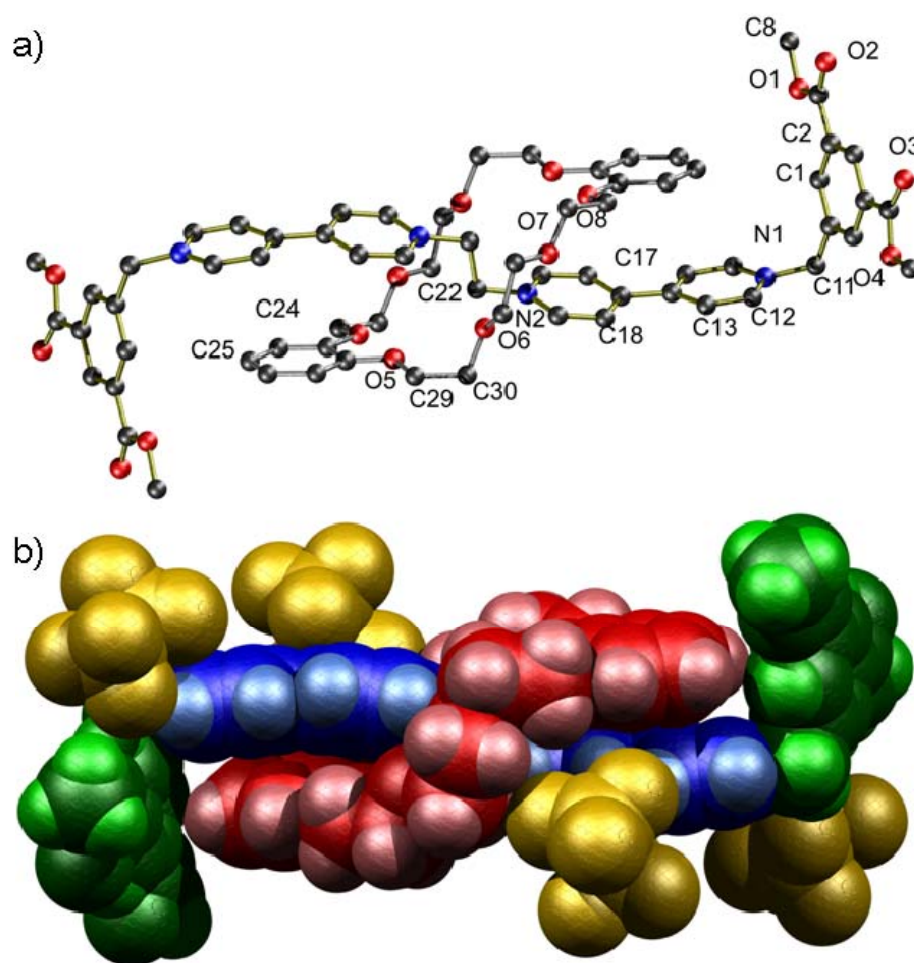


**Figure 2.8 - Single crystal structure of 2-14<sup>4+</sup>** a) ball-and-stick view (carbon = black, oxygen = red, nitrogen = blue) and b) space filling view with anions.

Eight hydrogen bonds are formed between  $\alpha$ -pyridinium and ethyl protons of the axle and oxygens of the **DB24C8** macrocycle. The N<sup>+</sup>⋯O distances vary from 3.83 Å (aliphatic oxygens) to 3.49 Å (aromatic oxygens). The C<sup>δ+</sup>⋯O distances vary from 2.36 Å (aliphatic oxygens) to 2.66 Å (aromatic oxygens). The oxygen atoms are also involved in ion-dipole interactions with N<sup>+</sup> and C<sup>δ+</sup> atoms. The distance between catechol and pyridinium aromatic rings range from 3.07 - 3.68 Å which is in the upper range for  $\pi$ - $\pi$

interactions.<sup>133-134</sup> The approximate dimensions of this tetra-cation are 27.4 Å along the long axis, 7.0 Å in depth through the  $\pi$ -stacking and 10.6 Å in width orthogonal to the  $\pi$ -stacking. However, when considering the counter ions the average width through the  $\pi$ -stacking increases to 9.0 Å.

The shape and dimensions of the [2]rotaxane **2-14**<sup>4+</sup> determined in this single crystal structure are used for modeling molecular packing in the mesophases discussed in the following sections. No significant colour difference is observed between the single crystal and the mesophase of the [2]rotaxanes, which verifies undisturbed  $\pi$ -stacking and supports the assumption that the packing of thread and core remain largely unchanged.

## 2.3 LIQUID CRYSTAL PHASE CHARACTERIZATION

### 2.3.1 Thermal Gravimetric Analysis (TGA)

The TGA curves for dumbbells and [2]rotaxanes were obtained at a rate of 2 °C/min under He (Figure 2.9 and Figure 2.10, respectively). Weight loss occurs in two distinct steps and the first step is attributed to the weight % values of the benzylic stoppers for all dumbbells and [2]rotaxanes. That the bond between the pyridinium group and benzylic stopper is thermally most labile is also supported by TGA coupled with mass spectrometry (TGA-MS) measurements on **2-14**<sup>4+</sup>. Fragment ion peaks characteristic for the stopper unit appear in the MS when the first weight loss occurs. The second step in the TGA curves of the rotaxanes was not as distinct and is caused by the loss of either macrocycle or thread. The calculated weight % values of the individual components for the dumbbells and [2]rotaxanes relative to the entire molecule, including the four triflate anions, are provided in Table 2.1.

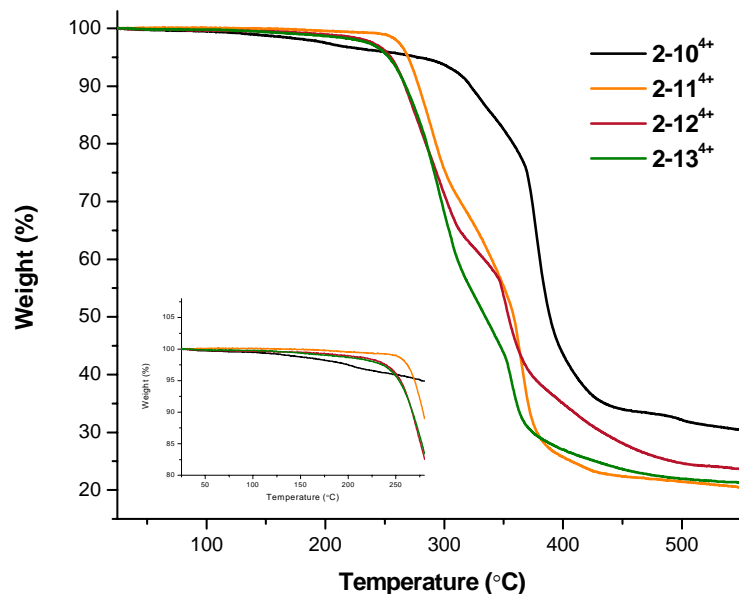


Figure 2.9 - TGA curves of dumbbells at 2 °C/min under He.

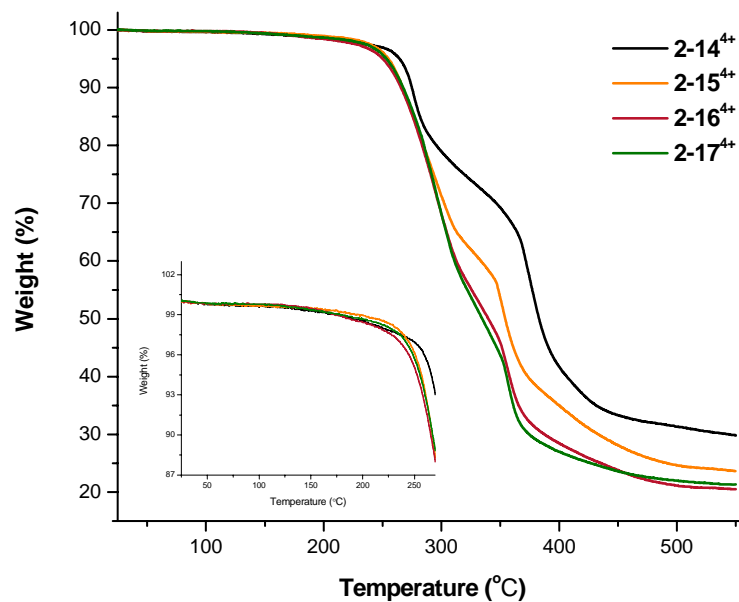


Figure 2.10 - TGA curves of [2]rotaxanes at 2 °C/min under He.

Decomposition of dumbbells and [2]rotaxanes occurs at temperatures above 200 °C as indicated by the first weight loss event in the TGA. In general, a thermal decomposition temperature determined by TGA is accurate if one of the generated

fragments easily evaporates at the given temperature and this may be questionable here. Both, the quasi independence of the onset of weight loss on the size of the stoppers and the absence of transitions in the DSC at temperatures below the decomposition temperatures determined by TGA confirm that the initial bond cleavage results in an immediate weight loss event.

**Table 2.1 - Calculated weight % values for components of dumbbells and [2]rotaxanes along with actual weight % values for the first step losses.**

Compound	2 Stoppers (actual %)	2 Stoppers (calc. %)	Axle (%)	4 OTf anions	DB24C8 (%)
<b>2-10<sup>4+</sup></b>	29.3	30.6	25.3	44.1	--
<b>2-11<sup>4+</sup></b>	43.1	42.6	20.9	36.5	--
<b>2-12<sup>4+</sup></b>	51.4	50.0	18.9	33.1	--
<b>2-13<sup>4+</sup></b>	51.9	52.4	17.3	30.2	--
<b>2-14<sup>4+</sup></b>	22.7	23.0	18.9	33.1	25.0
<b>2-15<sup>4+</sup></b>	34.7	33.4	16.4	28.7	21.5
<b>2-16<sup>4+</sup></b>	42.1	38.4	15.1	26.5	19.9
<b>2-17<sup>4+</sup></b>	44.2	42.7	14.0	24.7	18.6

### 2.3.2 Defect Textures Observed by Polarizing Optical Microscopy (POM)

All defect textures obtained by POM were viewed with crossed polarizers. The dumbbells and [2]rotaxanes were freshly crystallized from saturated MeCN solution onto microscope slides and dried under a flow of nitrogen gas. This procedure generates a maximum degree of crystallinity. Transfer of the samples was avoided because dumbbells **2-11<sup>4+</sup>** through **2-13<sup>4+</sup>** and [2]rotaxanes **2-15<sup>4+</sup>** through **2-17<sup>4+</sup>** formed soft crystal phases and the initially obtained crystallites are easily mechanically sheared to give liquid crystal-like textures. The softness of the crystallites was demonstrated by pressing/squeezing them with a cover glass slide. Sheared (squeezed) samples displayed

liquid crystal-like textures, which are probably not at equilibrium even though they are thermally stable due to the high viscosity of the materials. No crystallites are formed upon heating and cooling of the sheared bulk materials.

POM images of freshly crystallized and sheared dumbbells **2-11<sup>4+</sup>** through **2-13<sup>4+</sup>** are shown in Figures 2.11 - 2.13. The only change observed by POM was an increase in softness with increasing temperature, especially above 45 °C, and increasing length of the aliphatic chains but none of the dumbbells cleared into the isotropic liquid below 200 °C. They were not studied at higher temperatures because of the onset of decomposition.

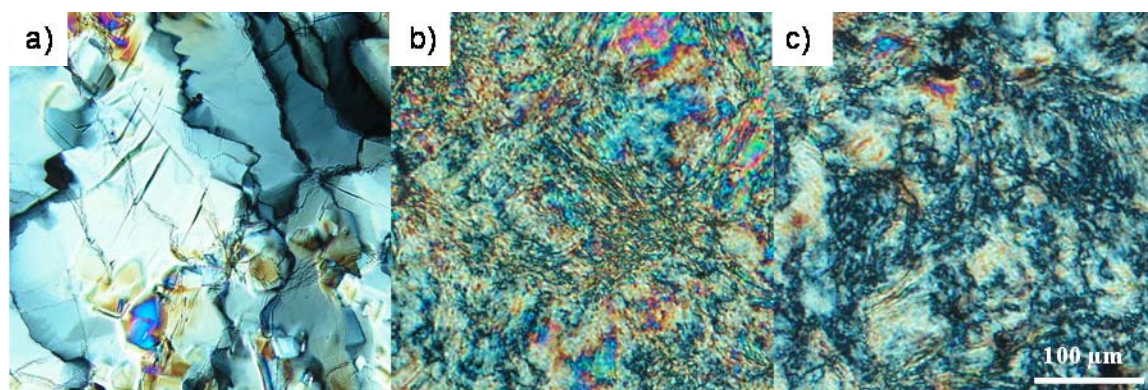


**Figure 2.11 - POM of 2-11<sup>4+</sup> (crossed polarizers): a) crystallized from MeCN @ 25 °C, b) squeezed between glass slides @ 25 °C and c) @ 200 °C.**

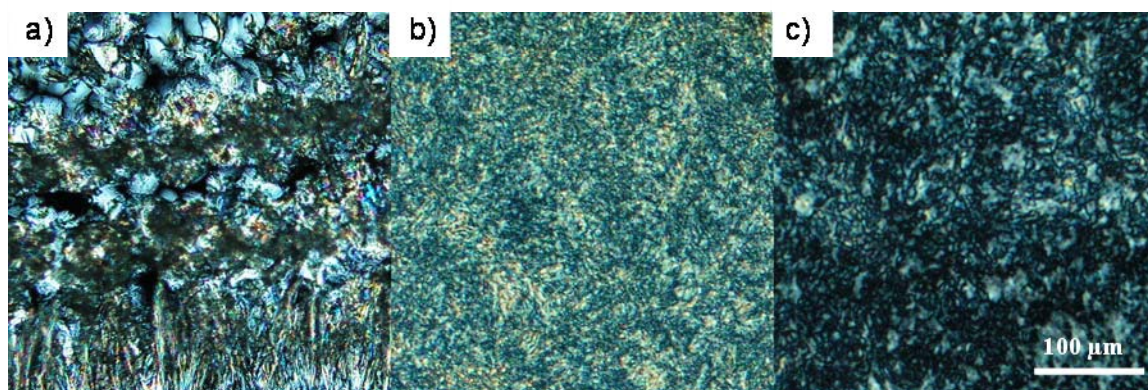


**Figure 2.12 - POM of 2-12<sup>4+</sup> (crossed polarizers): a) crystallized from MeCN @ 25 °C, b) squeezed between glass slides @ 25 °C and c) @ 200 °C.**



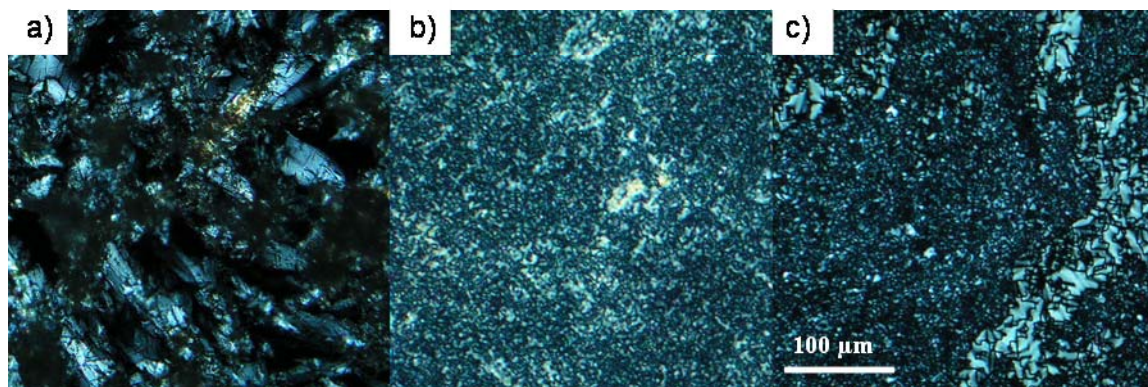


**Figure 2.13 - POM of 2-13<sup>4+</sup> (crossed polarizers): a) crystallized from MeCN @ 25 °C, b) squeezed between glass slides @ 25 °C and c) @ 25 °C upon cooling from 150 °C.**

Schlieren-type defect textures are observed for sheared phases of all three dumbbells and 2-13<sup>4+</sup>, the most fluid compound of the three, also displays fan-shaped defect textures. However, these textures are of little analytical value because they most likely represent non-equilibrium states and can not be obtained without the application of mechanical shear.

Addition of the **DB24C8** macrocycle induces major changes in the mesomorphism as sheltering of the ionic core reduces the crystallinity, viscosity and the phase transition temperatures of the materials. [2]Rotaxanes 2-15<sup>4+</sup> through 2-17<sup>4+</sup> clear into isotropic liquids ( $T_i$ ) upon heating well below their decomposition temperatures of 128, 118, and 137 °C, respectively. Clearing into the isotropic liquid was broad for all [2]rotaxanes which ranged between 8 to 10 °C, as observed by POM. Addition of the macrocycle clearly reduces the strength of the intermolecular interactions between the cores and the core's potential for inducing microphase segregation. This can be attributed to reduction of the strong interactions between the ionic axles which are considerably weakened upon complexation of the axle with the macrocycle. [2]Rotaxanes 2-15<sup>4+</sup> and 2-16<sup>4+</sup> still form crystallites, spherulites and plates when slowly crystallized from MeCN,

that are identified as soft crystal phases at room temperature by applying a mechanical shear force (Figure 2.14a and Figure 2.15a, respectively). **2-15<sup>4+</sup>** remains crystalline when squeezed between glass slides at 25 °C and **2-16<sup>4+</sup>** does not show any crystallinity under the same conditions, (Figure 2.14b and Figure 2.15b, respectively). Their textures become less birefringent with increasing temperature with no characteristic textures observed (Figure 2.14c and Figure 2.15c). The melting of these soft crystal phases into the isotropic liquids is thermally irreversible and isotropic soft solids are obtained upon cooling. This behaviour is likely a result of the high viscosity of the isotropic liquid phases even at 180 °C.

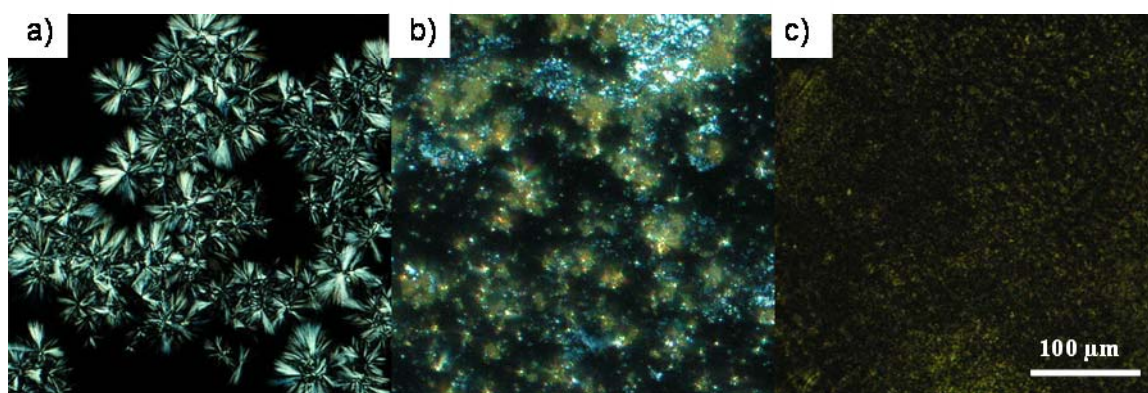


**Figure 2.14 - POM of 2-15<sup>4+</sup> (crossed polarizers): a) crystallized from MeCN @ 25 °C, b) squeezed between glass slides @ 25 °C and c) @ 80 °C upon cooling from T<sub>i</sub>.**

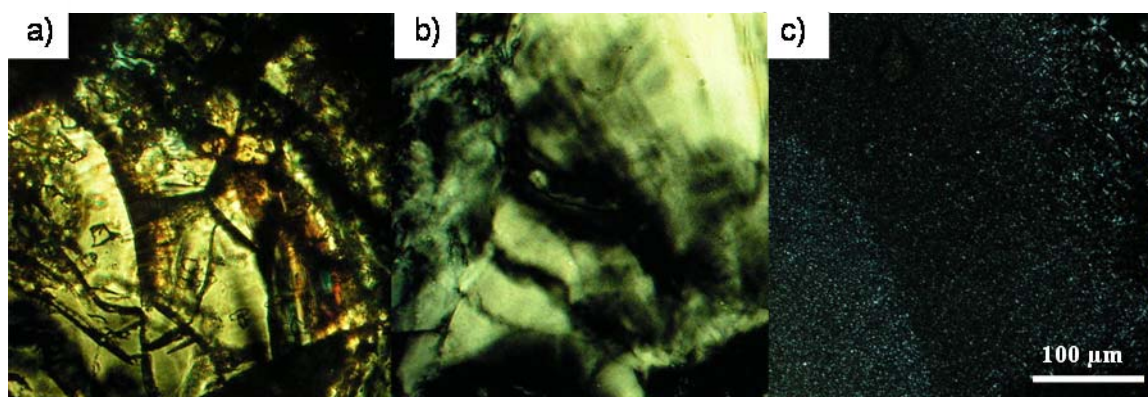


**Figure 2.15 - POM of 2-16<sup>4+</sup> (crossed polarizers): a) crystallized from MeCN @ 25 °C, b) squeezed between glass slides @ 25 °C and c) @ 80 °C upon cooling from T<sub>i</sub>.**

Ultimately, an optimal balance between intermolecular interactions and fluidity was reached with **2-17<sup>4+</sup>**. Unlike **2-15<sup>4+</sup>** and **2-16<sup>4+</sup>**, this material forms a LC phase rather than crystallites upon precipitation from MeCN and is significantly less viscous than the other two [2]rotaxanes, although its viscosity is still more comparable to a LC polymer than a small molecule LC (Figure 2.16a). When squeezed between glass slides a broken focal conic type texture with decreased birefringence is observed (Figure 2.16b). The natural texture obtained upon cooling from the  $T_i$  is a fan-like texture typical for smectic LC phases, confirming a preferential orientation of the molecule long axis parallel to the substrate (Figure 2.16c). No phase transitions other than the reversible clearing into the isotropic liquid were observed.

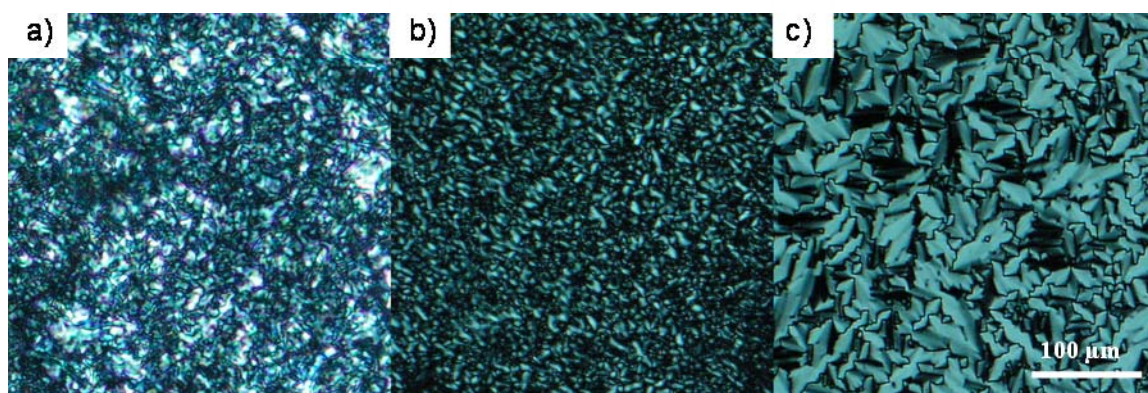


**Figure 2.16 - POM of 2-17<sup>4+</sup> (crossed polarizers): a) precipitate from MeCN @ 25 °C, b) squeezed between glass slides @ 123 °C and c) @ 25 °C upon cooling from  $T_i$ .**

### 2.3.3 Differential Scanning Calorimetry (DSC)

All samples for DSC analysis were freshly crystallized/precipitated from MeCN solution, exactly as previously described for POM studies and then dried under a stream of nitrogen gas before carefully being transferred into aluminum crucibles. Transition temperatures and calculated enthalpies are listed for all dumbbells and [2]rotaxanes in Table 2.2. Dumbbells **2-11<sup>4+</sup>** and **2-12<sup>4+</sup>** showed no transitions in subsequent heating and

cooling runs, after initial heating (Figure 2.17, orange and blue). In contrast, dumbbell **2-13<sup>4+</sup>** showed two reversible thermal transitions at -16 °C (only observed on heating) and 44 °C with enthalpies of -0.8 and -9.5 kJ/mol, respectively (Figure 2.17, red). Only the irreversible endothermic transition at 100 °C in the first heating run of **2-13<sup>4+</sup>** coincides with a texture change observed by POM; none of the other transitions were detected by POM. The origin of these transitions remains uncertain and they were not investigated further, but likely involve thermally reversible and irreversible transitions between different soft crystal phases.

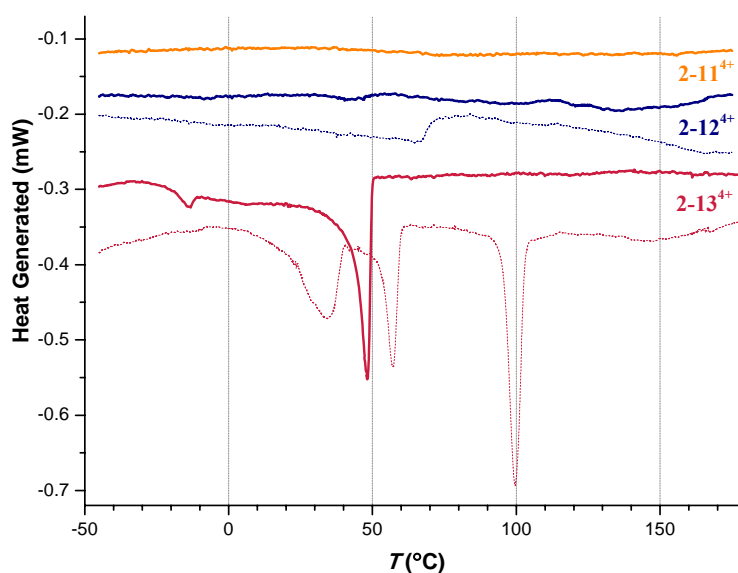


**Figure 2.17 - Second heating DSC runs of dumbbells **2-11<sup>4+</sup>**, **2-12<sup>4+</sup>** and **2-13<sup>4+</sup>** at 5 °C/min under N<sub>2</sub> and first heating runs (dashed) of **2-12<sup>4+</sup>** and **2-13<sup>4+</sup>**.**

The only transitions observed by DSC for [2]rotaxanes **2-15<sup>4+</sup>** through **2-17<sup>4+</sup>** are glass transitions ( $T_g$ ) between 30 and 90 °C that decrease in temperature with increasing length of the aliphatic chains. All three [2]rotaxanes display glass transitions on heating while a glass transition on cooling was only resolved for **2-17<sup>4+</sup>** (Figure 2.18). No transitions into the isotropic liquid were observed for any of the [2]rotaxanes that suggests they are broad and of low enthalpy.

**Table 2.2 - Transition temperatures (°C, midpoint) and enthalpies (kJ/mol) determined by DSC at scan rates of 5 °C/min for dumbbells and 10 °C/min for [2]rotaxanes.**

Compound	1 <sup>st</sup> Heating	2 <sup>nd</sup> Heating	Cooling
2-10 <sup>4+</sup>	171.7 (-0.93)	n.t.	n.t.
2-11 <sup>4+</sup>		n.t.	n.t.
2-12 <sup>4+</sup>	47.9 (-9.88)	n.t.	n.t.
2-13 <sup>4+</sup>	19.4 (-4.20)	-16.2 (-0.75)	37.1 (9.06)
	51.8 (-2.92)	44.3 (-9.49)	
	94.1 (-8.47)		
2-14 <sup>4+</sup>	66.9 (-1.30)	67.7 (-0.60)	63.1 (1.16)
2-15 <sup>4+</sup>		89 (T <sub>g</sub> )	n.t.
2-16 <sup>4+</sup>		66 (T <sub>g</sub> )	n.t.
2-17 <sup>4+</sup>		30 (T <sub>g</sub> )	18 (T <sub>g</sub> )

n.t. : no transition observed.

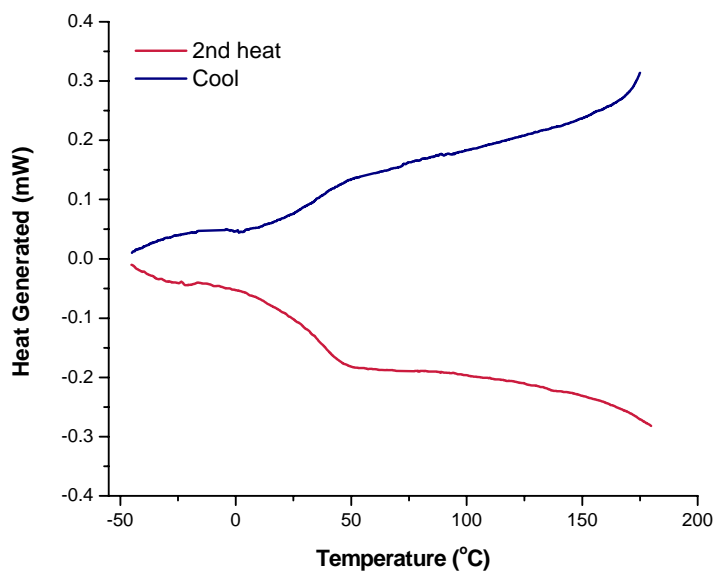


**Figure 2.18 - The second heating and cool DSC run of [2]rotaxane 2-17<sup>4+</sup> at 10 °C/min under N<sub>2</sub>.**

### 2.3.4 Variable Temperature X-Ray Diffraction (vt-XRD)

Model dumbbell **2-10<sup>4+</sup>** and model [2]rotaxane **2-14<sup>4+</sup>** were measured at room temperature and showed typical diffraction patterns of crystalline powders (Figure 2.19a and 2.20a, respectively) whereas the diffraction patterns of dumbbells **2-11<sup>4+</sup>** through **2-13<sup>4+</sup>** and [2]rotaxanes **2-15<sup>4+</sup>** through **2-17<sup>4+</sup>** have fewer and broadened peaks that are typical for disordered crystal phases and mesophases. Consequently, variable temperature X-ray diffraction experiments (vt-XRD) were performed on these compounds to monitor structural changes with temperature and determine the types of phases.

Dumbbells **2-11<sup>4+</sup>** through **2-13<sup>4+</sup>** and [2]rotaxanes **2-15<sup>4+</sup>** through **2-17<sup>4+</sup>** all show intense small angle reflections between 44 and 33 Å, which are attributed to layer spacings of lamellar phases because the spacings agree with the molecular lengths of the dumbbells and [2]rotaxanes. Peaks observed between 16 and 10 Å likely result from in-plane packing order because the spacings agree with the widths of the molecules and their values are independent of the length of the molecules. Reflections between 5 Å and 4 Å are associated with the packing of aliphatic chains and varied between sharp and broad. Sharp reflections indicate a crystalline state while one broad reflection (halo) indicates an amorphous state of the aliphatic chains.

Dumbbells **2-11<sup>4+</sup>** through **2-13<sup>4+</sup>** exhibit crystalline phases and also show a lamellar packing of the molecules with layer spacings of 33, 39 and 43 Å, respectively (Figure 2.19b - d). These lamellar phases are highly ordered as indicated by the presence of second order reflections ( $d_{20}$ ). These values are in good agreement with the dimensions of the molecules, and the formation of one molecule thick lamellar layers is proposed.

Increasing the number of aliphatic chains decreases the crystallinity in the mesophases, to the point where an amorphous state of the aliphatic side chains is observed over the entire temperature range for **2-13<sup>4+</sup>** (Figure 2.19d, inset). Unfortunately, the viscosity is still high and two lamellar phases could co-exist, with two separate small angle diffraction peaks at 64 and 43 Å. The two diffraction peaks may be explained by two different packing structures, since second order reflections are also observed for both at 32 and 21 Å, respectively; the phase could also potentially be columnar.

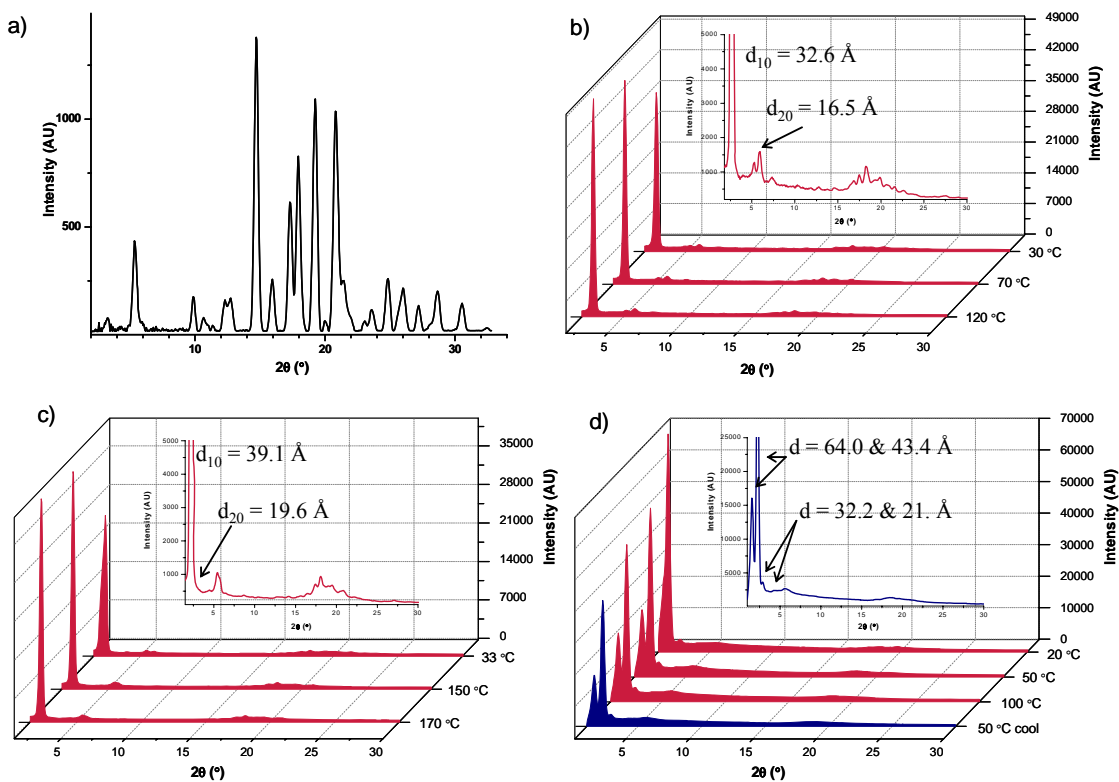


**Figure 2.19** - vt-XRD data for a) **2-10<sup>4+</sup>** at 25 °C, b) **2-11<sup>4+</sup>** (inset at 120 °C), c) **2-12<sup>4+</sup>** (inset at 170 °C) and d) **2-13<sup>4+</sup>** (inset at 50 °C on cooling).

[2]Rotaxanes **2-15<sup>4+</sup>** through **2-17<sup>4+</sup>** all display highly ordered lamellar phases with layer spacings of 30, 36 and 40 Å, respectively (Figure 2.20b - d), the second order

reflections for only  $2-16^{4+}$  were broad. The lamellar order in  $2-15^{4+}$  and  $2-16^{4+}$  is not thermally reversible, however, the lamellar order in  $2-17^{4+}$  remains over many cycles. Like the dumbbells, these values are in good agreement with the dimensions of the molecules, and formation of one molecule thick lamellar layers with a non-tilted SmA phase is proposed. The structure of the [2]rotaxanes, in contrast to the dumbbells, display a large decrease of lamellar packing order with increasing temperature; the largest between 40 °C and 90 °C.

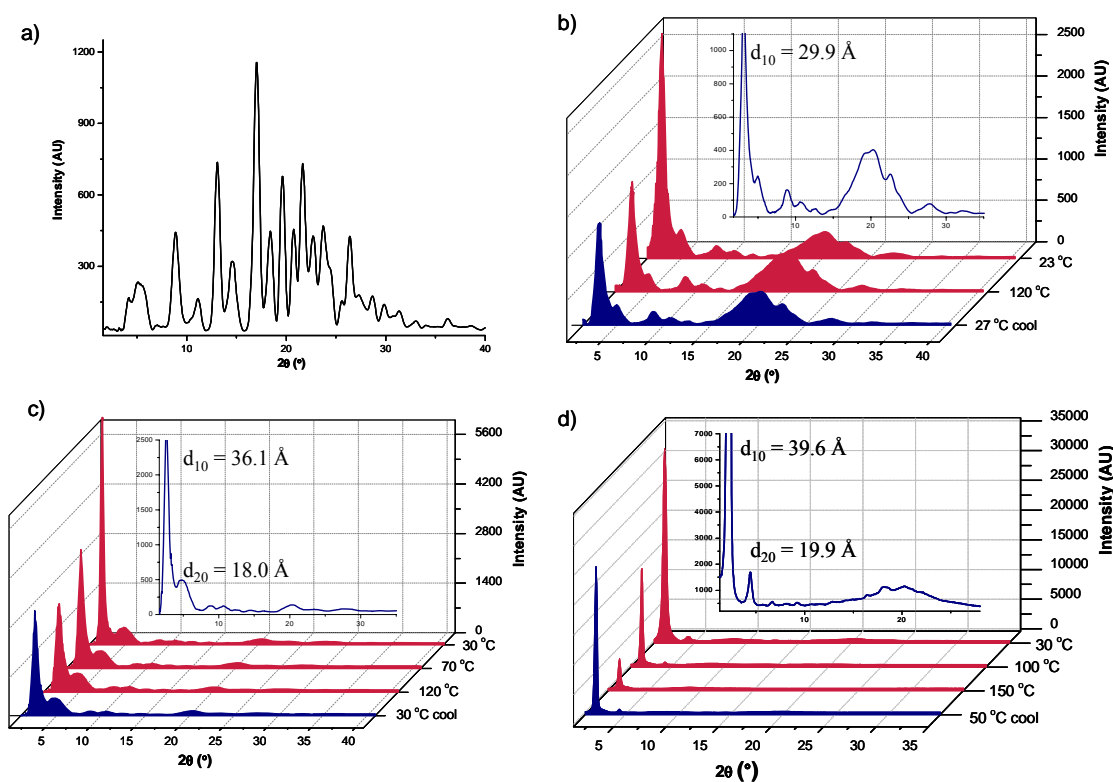


Figure 2.20 - vt-XRD data of a)  $2-14^{4+}$ , b)  $2-15^{4+}$ , c)  $2-16^{4+}$  and d)  $2-17^{4+}$ , (insets are XRD on cool).

### 2.3.5 Processing and Alignment of LC Materials

Only dumbbell  $2-13^{4+}$  and [2]rotaxane  $2-17^{4+}$  were investigated by processing and alignment due to the high viscosity and crystallinity of the other materials. Dumbbell  $2-$



$13^{4+}$  was not investigated in cells for parallel and perpendicular alignment because the material does not become fluid enough to enter a cell by capillary force. For a uniform planar SmA phase, the sample appears black when the optic axis is oriented along one of the polarizer directions, and maximum intensity is observed when the optic axis is oriented at  $45^\circ$  between polarizer and analyzer. We were able to draw fibres of  $2-13^{4+}$ , but only partial alignment was achieved. The overlaid fiber was rotated by  $45^\circ$  but did not completely change from bright to black (Figure 2.21, right). Only one layer reflection at  $43 \text{ \AA}$  is observed in the aligned fibre by 2D-XRD even though the fibre represents a non-equilibrium phase (Figure 2.21, left). This reflection correlates well to one of the first order reflections obtained from the XRD of the bulk material. The small angle reflection aligns orthogonal to the fiber direction, suggesting that the phase is either smectic or columnar which also agrees with POM studies.

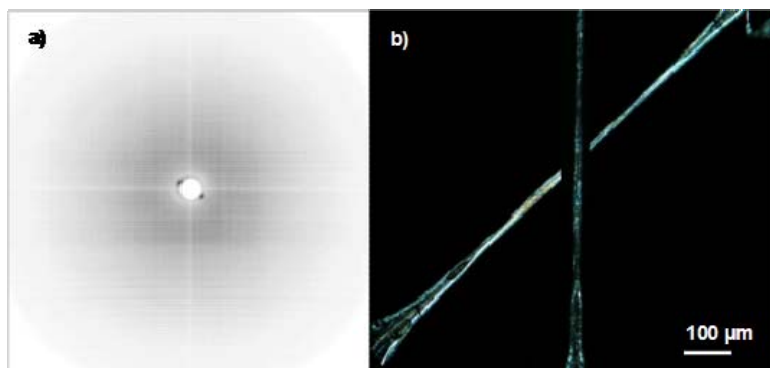


**Figure 2.21 - 2D-XRD pattern (left) and POM (right) of  $2-13^{4+}$  as fibre drawn from the bulk material when submerged in decane/ $\text{CH}_2\text{Cl}_2$  at  $25^\circ\text{C}$  (alignment shown with fibre rotated by  $45^\circ$ , overlaid).**

[2]Rotaxane  $2-17^{4+}$  was fluid enough to be mechanically sheared at  $120^\circ\text{C}$  producing nearly uniform planar alignment of its SmA phase in the direction of applied shear force; Figure 2.22a (arrow shows direction of shear force) and Figure 2.22b (rotated  $45^\circ$ ). Due to the high viscosity of the material,  $2-17^{4+}$  did not interact favorably with a

planar alignment layer in a cell, treated with rubbed polyimide. The formation of exclusively fan-like defect textures confirms a preferential orientation of the molecule long axis parallel to the substrates, but no uniformly aligned domains are generated in the cell (Figure 2.22c).

An optically-pseudo isotropic homeotropic monodomain was obtained when filled into a LC cell with vertical alignment layer (treated cetyl-trimethylammonium bromide), where there was no birefringence for any in-plane rotation of the sample, confirming the formation of a SmA phase with layers parallel to the substrate and molecular axis oriented perpendicular to the bounding glass plates (Figure 2.22d). Furthermore, diffraction patterns excluded the presence of higher ordered smectic phases such as SmB

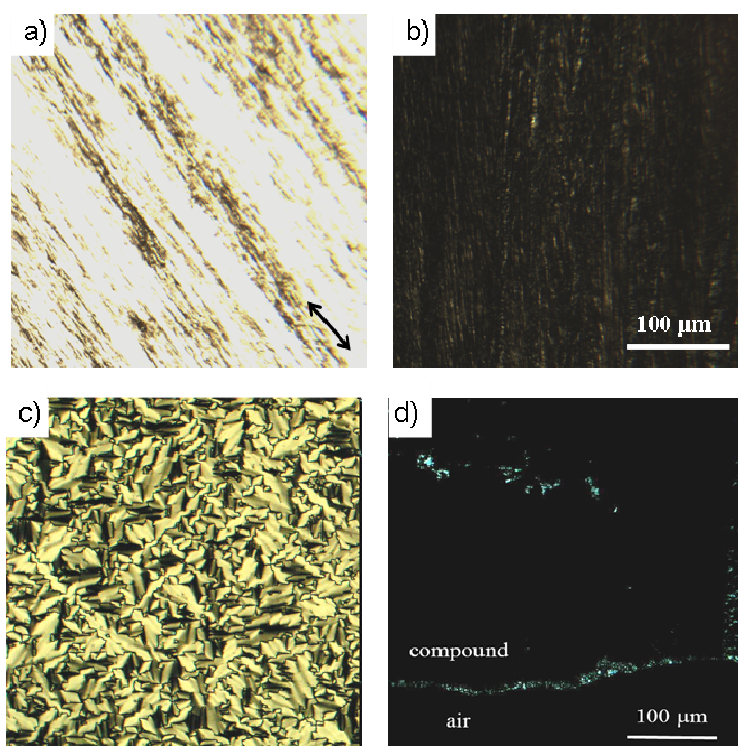


**Figure 2.22 - POMs of 2-17<sup>4+</sup> a) shear alignment (in direction of arrow) and b) rotated by 45°. POMs of 2-17<sup>4+</sup> c) in cells treated for parallel (homogeneous) alignment with rubbed polyimide, 4 μm gap (left) and d) vertical (homeotropic) alignment with cetyl-trimethylammonium bromide, 6 μm gap, both at 70 °C.**

and the lack of any schlieren textures observed by POM studies excludes the presence of a tilted SmC phase.

Aligned fibres of **2-17<sup>4+</sup>** were drawn, seen in Figure 2.23a, with fibre rotated by 45° overlaid. 2D-XRD analyses of drawn fibres are in excellent agreement with reflections obtained in the bulk material. The first order (10) and (20) reflections of the layer spacing are orthogonal to the long axis of the fibre confirming an alignment of the smectic layers parallel to the long axis of the fibre, seen overlaid in Figure 2.23b. Unlike the bulk material, the drawn fibre is not an equilibrium phase, so a clear distinction between smectic phases SmA and SmC is not possible. However, observed lengths are too long to support a tilt of the molecules long axis.

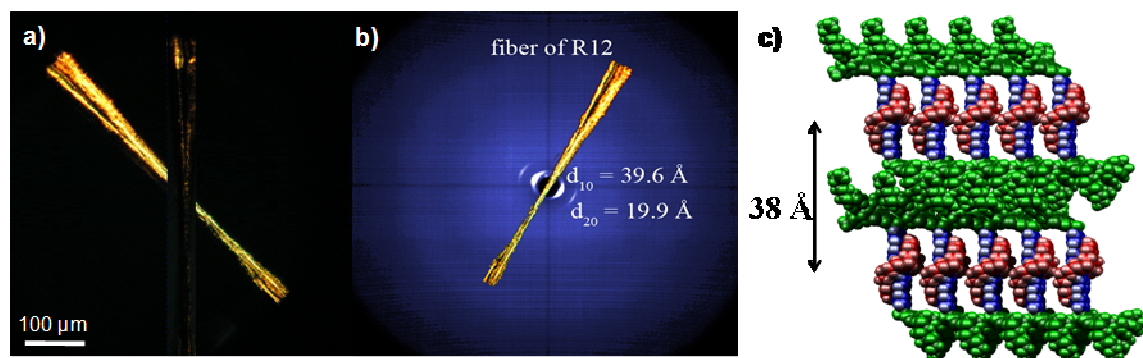


**Figure 2.23 - Drawn fibre of **2-17<sup>4+</sup>** (alignment shown with fibre rotated by 45 °, overlaid), b) 2D-XRD pattern of drawn fibre at 25 ° C, and c) molecular modeling (MM3) diagram showing self-organization of material into a SmA phase. Alkyl chains were input in a disordered fashion to simulate packing.**

A molecular modeling (MM3) diagram of **2-17<sup>4+</sup>** (Figure 2.23c), shows the self-organization of the material into a SmA phase with the calculated molecular length shown (38 Å). Alkyl chains were input in a disordered fashion to simulate packing. It is likely that the alignment of this material is dominated by the large core and the side chains solely and randomly fill the space between the layers.

### 2.3.6 Calculated Packing Volume Ratios & Molecular Lengths

Space filling calculations were performed to compare the molecular dimensions with the layer spacings obtained by XRD for dumbbells **2-11<sup>4+</sup>** to **2-13<sup>4+</sup>** and [2]rotaxanes **2-15<sup>4+</sup>** to **2-17<sup>4+</sup>**. The layer spacings are expectedly shorter than the extended length of these molecules, between 40 Å (dumbbells) and 50 Å ([2]rotaxanes), and agree well with calculations based on amorphous side chains and space filling considerations. The cylindrical volume of the core, without the **DB24C8** macrocycle, but including the four triflate anions is estimated to be 1350 Å<sup>3</sup>, based on a length of 27.4 Å and an average diameter of 8.1 Å. The cylindrical volume of the [2]rotaxane core, with **DB24C8** macrocycle, including the four triflate anions is estimated to be 2400 Å<sup>3</sup>, based on a length of 27.4 Å and an average diameter of 10.6 Å. The length and average diameter of the cores were calculated based on the dimensions of the [2]rotaxane core in the single crystal structure and free rotation over the long axis of the molecule (Figure 2.8).

The volumes occupied by the side chains of the benzyl dicarboxylate units are calculated to be 430, 640 and 850 Å<sup>3</sup>, for *n*-alkyl chains of 6, 9, and 12 carbon atoms respectively, based on established packing volumes in liquid phases.<sup>135,136</sup> Based on these volumes and the diameters of the cores, the lengths of the cylindrical spaces occupied by the side chains of the benzyl dicarboxylate units were calculated and added to the length of the core (27.4 Å), giving excellent agreement with the observed spacings for all six compounds (Table 2.3). These calculated molecular lengths also confirm the formation of a SmA phase for **2-17<sup>4+</sup>**, since the tilted SmC layer spacings would be markedly shorter than 39 Å. The layer spacings of the [2]rotaxanes are 3-4 Å shorter than the analogous

dumbbells due to the increase in average diameter of the core with addition of the **DB24C8** macrocycle, while packing volumes of aliphatic extended benzyl stoppers remain unchanged.

This model is independent of other packing considerations such as the degree of interdigitation between adjacent side-chains. Moreover, these calculations assume the presence of SmA phases but an average tilted orientation of the cores of the molecules with regard to the normal of the layers can not be excluded in all cases. Tilted Sm phases such as SmC would reduce the layer spacings and consequently disagree with the proposed model if the tilt angles are sufficiently large. Calculated packing volumes of the [2]rotaxanes suggest that formation of a stable and sufficiently fluid smectic LC phase requires a minimum 1:3 ratio of aliphatic chains of the extended benzylic stoppers to central [2]rotaxane core, which is important for the design of such materials for future synthesis and potential application in devices.

**Table 2.3 - Obtained (XRD) layer spacings and calculated molecular lengths of dumbbells 2-11<sup>4+</sup> to 2-13<sup>4+</sup> and [2]rotaxanes 2-15<sup>4+</sup> to 2-17<sup>4+</sup>**

Compound	$d_{10}$ (Å)	$l_{calc}$ (Å)
2-11 <sup>4+</sup>	32.6	35
2-12 <sup>4+</sup>	39.1	40
2-13 <sup>4+</sup>	43.4	44
2-15 <sup>4+</sup>	29.9	32
2-16 <sup>4+</sup>	36.1	35
2-17 <sup>4+</sup>	39.6	38

### 2.3.7 Liquid Crystal Phase Determination

The mesophases were fully characterized by POM observations, DSC analysis and vt-XRD analysis. The phase characterization and transition temperatures measured

by POM and DSC on heating are shown in Figure 2.24. Dumbbells **2-11<sup>4+</sup>** and **2-12<sup>4+</sup>** both form a lamellar soft crystal phase over the entire temperature range studied and neither cleared into the isotropic liquid phase before their decomposition temperature, above 200 °C. On the other hand, dumbbell **2-13<sup>4+</sup>** forms an unidentified mesophase that is either smectic or columnar. This material did not clear into the isotropic liquid phase before its decomposition either.

[2]Rotaxanes **2-15<sup>4+</sup>** and **2-16<sup>4+</sup>** also form lamellar soft crystal phases over their entire temperature range until clearing into the isotropic liquid phase at 128 and 118 °C. [2]Rotaxane **2-17<sup>4+</sup>** formed a SmA phase over the entire temperature range until clearing into the isotropic liquid phase at 137 °C. By POM, the absence of schlieren textures confirmed the presence of a SmA phase for **2-17<sup>4+</sup>**. Comparison of the experimental and calculated molecular lengths also agreed with the formation of a SmA phase. The initial decomposition for each compound is marked with a black line in Figure 2.24, with decomposition for all dumbbells and [2]rotaxanes occurring above 200 °C.

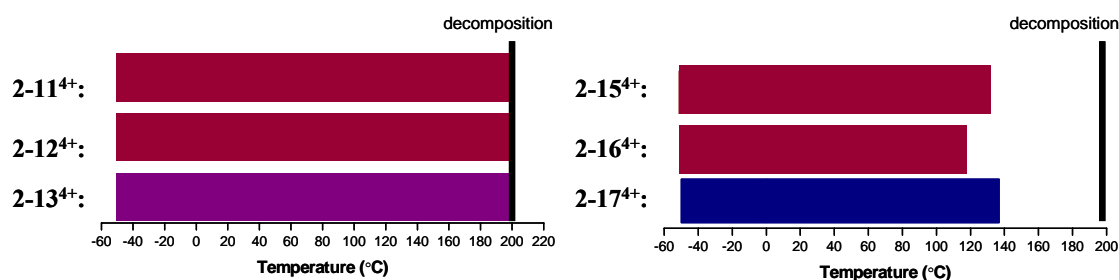


**Figure 2.24 - Phase transition temperatures for dumbbells 2-11<sup>4+</sup> through 2-13<sup>4+</sup> (left) and [2]rotaxanes 2-15<sup>4+</sup> through 2-17<sup>4+</sup> (right) measured by DSC and POM on heating. (navy, SmA; maroon, lamellar soft crystal; violet, unidentified mesophase). The start of decomposition is marked with a black line.)**

## 2.4 SUMMARY AND CONCLUSIONS

A smectic [2]rotaxane was obtained by using a tetracatenar design and attachment of stoppers containing aliphatic side-chains of sufficient length and number. Dumbbells **2-11<sup>4+</sup>**, **2-12<sup>4+</sup>** and [2]rotaxanes **2-15<sup>4+</sup>**, **2-16<sup>4+</sup>** all form lamellar soft crystal phases, whilst dumbbell **2-13<sup>4+</sup>** formed an unidentified mesophase and [2]rotaxane **2-17<sup>4+</sup>** was sufficiently soft to form a SmA phase, of which only the rotaxane was thermally reversible. This was confirmed by POM and vt-XRD. Addition of the **DB24C8** macrocycle to shelter the ionic core proved to be necessary for the formation of a true LC phase. Furthermore, **2-17<sup>4+</sup>** was successfully aligned as a SmA phase in LC cells treated for homeotropic alignment as well as in fibres drawn in the LC phase. Calculated packing volumes of [2]rotaxanes revealed that a minimum packing volume ratio of 1:3 for aliphatic chains of the extended benzylic stoppers to the central [2]rotaxane core, is required for the formation of a stable and sufficiently fluid smectic LC phase. Alignment of these unusual materials is significant since it is essential for any detailed study of their properties and potential for application in devices. Presently, the SmA phase of **2-17<sup>4+</sup>** is hampered by its high viscosity and hence is not easily aligned in thin films, by applying shear force or conventional LC alignment layers.

To improve on this system, the viscosity of these materials must be sufficiently reduced to improve processing and alignment in thin films. While keeping the (1,2-bis(dipyridinium)ethane)/**DB24C8** pseudorotaxane motif, this can be accomplished by either increasing the length of the aliphatic chains on the stopper, or by utilizing branched or hyperbranched aliphatic chains in order to increase the fluidity and stabilize the molecular packing of material, which is the focus of Chapter 3.

## 2.5 EXPERIMENTAL

### 2.5.1 General Comments

Sodium trifluoromethanesulfonate, 4,4'-bipyridine, 1,2-dibromomethane, diethyl-5-(hydroxymethyl)-*isophthalate*, 1-hexanol, 1-nonanol, 1-dodecanol, titanium isopropoxide, phosphorus tribromide, tetrabutyl ammonium iodide (TBAI) and **DB24C8** were purchased from Aldrich and used as received. Deuterated solvents were obtained from Cambridge Isotope Laboratories and used as received. Solvents were dried using an Innovative Technologies Solvent Purification System. Thin layer chromatography (TLC) was performed using Teledyne Silica gel 60 F<sub>254</sub> plates and viewed under UV light. Column chromatography was performed using Silicycle Ultra Pure Silica Gel (230 – 400 mesh). Flash column chromatography was performed using Teledyne Ultra Pure Silica/RP-C<sub>18</sub> Silica Gel (230 – 400 mesh) on a Teledyne Isco Combiflash R<sub>f</sub>. All flash chromatography was performed under pressure (120 mL/min. - 200 mL/min.) for normal phase silica and (10 mL/min. - 40 mL/min.) for RP-C<sub>18</sub> silica, with increasing pressure corresponding to larger columns. Unless otherwise stated, all flash chromatography involved applied gradient elution from 0 - 100 % with increasing polar solvent with respect to less polar solvent. Length of column (column volumes - CV) were determined by separations on preliminary TLC runs.

<sup>1</sup>H NMR, <sup>13</sup>C NMR and 2-D experiments were performed on a Brüker Avance 500 instrument, with a working frequency of 500.13 MHz for <sup>1</sup>H nuclei, and 125.7 MHz for <sup>13</sup>C nuclei. Chemical shifts are quoted in ppm relative to tetramethylsilane, using the residual solvent peak as a reference standard. Conventional 2-D NMR experiments (<sup>1</sup>H-<sup>1</sup>H COSY) and (<sup>1</sup>H-<sup>13</sup>C HETCOR) were conducted and used to help assign all peaks.



High resolution mass spectrometry (HR-MS) experiments were performed on a Micromass LCT electrospray (ESI) time-of-flight (TOF) mass spectrometer. Solutions of 50-100 ng/ $\mu$ L were prepared in CH<sub>3</sub>CN and injected for analysis at a rate of 5  $\mu$ L/min, using a syringe pump.

Calorimetric studies were performed on a Mettler Toledo DSC 822<sup>e</sup> instrument and thermal gravimetric analysis with mass spectrometric detection of evolved gases was performed on a Mettler Toledo TGA SDTA 851e instrument that was attached to a Pfeiffer Vacuum ThermoStar<sup>TM</sup> mass spectrometer (1-300 amu) *via* a thin glass capillary. Helium (99.99 %) was used to purge the system with a flow rate of 30 mL/min. Samples were held at 25 °C for 30 min before heating to 550 °C at 2 °C/min. A mass range between 16 m/z and 150 m/z was constantly scanned. All samples were run in aluminum crucibles. Powder XRD measurements were recorded on a Br $\ddot{u}$ ker D8 Discover diffractometer equipped with a Hi-Star area detector and GADDS software and operated at 40 kV and 40 mA. CuK $\alpha$ <sub>1</sub> radiation ( $\lambda = 1.54187 \text{ \AA}$ ) was used and the initial beam diameter was 0.5 mm. A custom made Instec hot stage (based on HS-400) was used for VT-XRD that covers a temperature range of -40 °C to 350 °C. Bulk samples for variable temperature XRD were filled into a 2 mm diameter hole in a 1 mm thick copper plate and covered with Kapton<sup>TM</sup> foil. This plate was mounted in an Instec hot-stage, aligned, and run at theta angles of 0°, and 15° for 30 or 60 min. Spectra were combined and evaluated in EVA and plotted with Origin. Polarized light microscopy was performed on an Olympus TPM51 polarized light microscope equipped with a Linkam variable temperature stage HCS410 and digital photographic imaging system (DITO1).

### 2.5.2 Synthesis of [2-1][OTf]

4,4'-Bipyridine (5.00 g, 0.0320 mol) was dissolved in 1,2-dibromoethane (150 mL) and refluxed for 3 h. The solution was filtered hot and the resulting precipitate washed with cold diethyl ether (3 x 50 mL). The precipitate was collected and recrystallized from ethanol to yield a yellow crystalline powder. Yield: 10.86 g, 99 %.

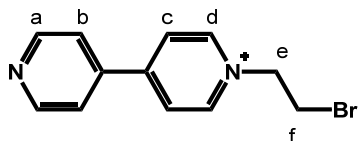
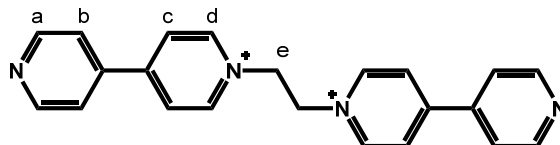


Table 2.4 -  $^1\text{H}$  NMR data of [2-1][Br] in  $\text{D}_2\text{O}$ .  $\text{MW}_{\text{Br}^-} = 344.058$  g/mol

Proton	$\delta$ (ppm)	Multiplicity	# Protons	$J$ (Hz)
<b>a</b>	8.68	d	2	$^3J_{ab} = 6.36$
<b>b</b>	7.87	d	2	$^3J_{ba} = 6.36$
<b>c</b>	8.35	d	2	$^3J_{cd} = 6.77$
<b>d</b>	8.93	d	2	$^3J_{dc} = 6.77$
<b>e</b>	4.99	t	2	$^3J_{ef} = 5.70$
<b>f</b>	3.92	t	2	$^3J_{fe} = 5.70$

### 2.5.3 Synthesis of [2-2][OTf]<sub>2</sub>

[2-1][Br] (5.00 g, 0.0145 mol) and 4,4'-bipyridine (6.81 g, 0.0436 mol) were dissolved in 1-butanol (70 mL) and added to a thick-walled 80 mL vessel with stir bar and microwaved for 1 h at 70 °C. The solution was filtered hot and the resulting precipitate washed with methanol. The precipitate was collected and recrystallized from H<sub>2</sub>O, first stirring with charcoal then filtering through celite followed by cooling on ice to yield colourless crystals. The product was then further purified and isolated by column chromatography on silica gel using a 7:1:2 mixture of MeOH, 2M NH<sub>4</sub>Cl (aq) and MeNO<sub>2</sub> (3.89 g, 54 %). The resulting transparent crystals, R<sub>f</sub> = 0.18, were anion exchanged to the triflate salt by way of a two layer NaOTf (aq)/MeNO<sub>2</sub> extraction. Yield: 4.32 g, 87 %.

Table 2.5 –  $^1\text{H}$  NMR data of [2-2][Br]<sub>2</sub> in D<sub>2</sub>O. MW<sub>Br-</sub> = 500.229 g/mol

Proton	$\delta$ (ppm)	Multiplicity	# Protons	$J$ (Hz)
a	8.77	d	4	$^3J_{ab} = 4.48$
b	7.90	d	4	$^3J_{ba} = 4.48$
c	8.48	d	4	$^3J_{cd} = 5.65$
d	8.98	d	4	$^3J_{dc} = 5.65$
e	5.40	s	4	--

Table 2.6 -  $^1\text{H}$  NMR data of [2-2][OTf]<sub>2</sub> in CD<sub>3</sub>CN. MW<sub>OTf-</sub> = 638.559 g/mol

Proton	$\delta$ (ppm)	Multiplicity	# Protons	$J$ (Hz)
a	8.76	d	4	$^3J_{ab} = 6.88$
b	8.38	d	4	$^3J_{ba} = 6.88$
c	7.81	d	4	$^3J_{cd} = 4.50$
d	8.87	d	4	$^3J_{dc} = 4.50$
e	5.16	s	4	--

### 2.5.4 Synthesis of 2-3

Diethyl-5-(hydroxymethyl)-isophthalate (3.00 g, 0.01153 mol), 1-hexanol (9.42 g, 0.0922 mol), and  $\text{Ti}(\text{O-}i\text{-Pr})_4$  (6.55 g, 0.0231 mol) were heated (130 °C) under a nitrogen atmosphere overnight. The EtOH bi-product was removed via a Dean Stark apparatus. The solution was neutralized with 0.1 M HCl yielding a waxy solid which was then filtered and washed with  $\text{H}_2\text{O}$ . The solid was taken up in  $\text{CHCl}_3$ , dried with  $\text{MgSO}_4$ , filtered and concentrated to a white solid. The product was then purified by column chromatography on silica gel with 99:1 ( $\text{CHCl}_3$ : MeOH) as eluant. The resulting white solid was collected. Yield: 3.87 g, 92 %.

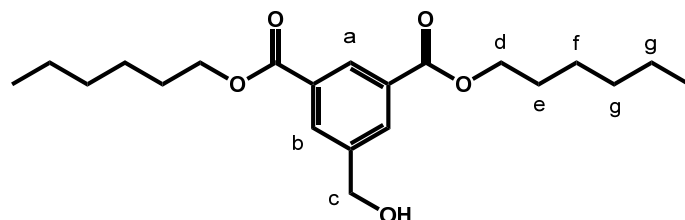


Table 2.7 –  $^1\text{H}$  NMR data of 2-3 in  $\text{CDCl}_3$ . MW= 364.476 g/mol

Proton	$\delta$ (ppm)	Multiplicity	# Protons	$J$ (Hz)
a	8.56	s	1	--
b	8.21	s	2	--
c	4.76	s	2	--
d	4.32	t	4	$^3J_{de} = 6.74$
e	1.76	tt	4	$^3J_{ed} = 6.74, ^3J_{ef} = 7.47$
f	1.41	tt	4	$^3J_{fe} = 7.47, ^3J_{fg} = 7.47$
g	1.32	m	8	--
h	0.88	t	6	$^3J_{hg} = 6.74$

## 2.5.5 Synthesis of 2-4

Diethyl-5-(hydroxymethyl)-isophthalate (2.00 g, 0.0077 mol), 1-nonanol (8.87 g, 0.0615 mol), and  $\text{Ti}(\text{O-}i\text{-Pr})_4$  (4.37 g, 0.0154 mol) were heated (130 °C) under a nitrogen atmosphere overnight. The EtOH bi-product was removed via a Dean Stark apparatus. The solution was neutralized with 0.1 M HCl yielding a waxy solid which was then filtered and washed with  $\text{H}_2\text{O}$ . The solid was taken up in  $\text{CHCl}_3$ , dried with  $\text{MgSO}_4$ , filtered and concentrated to a white solid. The product was then purified by column chromatography on silica gel with 99:1 ( $\text{CHCl}_3$ : MeOH) as eluant. The resulting white solid was collected. Yield: 2.87 g, 83 %.

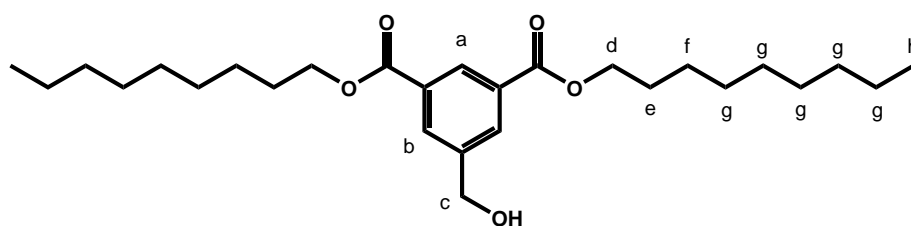


Table 2.8 –  $^1\text{H}$  NMR data of 2-4 in  $\text{CDCl}_3$ . MW= 448.635 g/mol

Proton	$\delta$ (ppm)	Multiplicity	# Protons	$J$ (Hz)
a	8.58	s	1	--
b	8.22	s	2	--
c	4.76	s	2	--
d	4.34	t	4	$^3J_{de} = 6.76$
e	1.78	tt	4	$^3J_{ed} = 6.76, ^3J_{ef} = 7.40$
f	1.43	tt	4	$^3J_{fe} = ^3J_{fg} = 7.40$
g	1.32	m	20	--
h	0.87	t	6	$^3J_{hg} = 6.76$

## 2.5.6 Synthesis of 2-5

Diethyl-5-(hydroxymethyl)-isophthalate (3.00 g, 0.0115 mol), 1-dodecanol (17.18 g, 0.0922 mol), and  $\text{Ti}(\text{O-}i\text{-Pr})_4$  (6.55 g, 0.0231 mol) were heated (130 °C) under a nitrogen atmosphere for 3 days. The EtOH bi-product was removed via a Dean Stark apparatus. The solution was neutralized with 0.1 M HCl yielding a waxy solid which was then filtered and washed with  $\text{H}_2\text{O}$ . The solid was taken up in  $\text{CHCl}_3$ , dried with  $\text{MgSO}_4$ , filtered and concentrated to a white solid. The product was then purified by flash column chromatography on silica gel with 99:1 ( $\text{CHCl}_3$ : MeOH) gradient as eluant. The resulting white solid was collected. Yield: 5.06 g, 82 %.

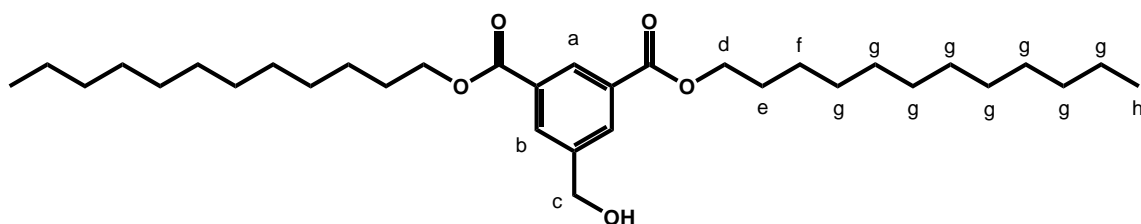
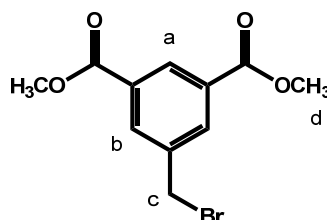


Table 2.9 –  $^1\text{H}$  NMR data of 2-5 in  $\text{CDCl}_3$ . MW= 532.795 g/mol

Proton	$\delta$ (ppm)	Multiplicity	# Protons	$J$ (Hz)
a	8.56	s	1	--
b	8.19	s	2	--
c	4.76	s	2	--
d	4.32	t	4	$^3J_{de} = 6.76$
e	1.75	tt	4	$^3J_{ed} = 6.76, ^3J_{ef} = 7.41$
f	1.37	tt	4	$^3J_{fe} = ^3J_{fg} = 7.41$
g	1.24	m	32	--
h	0.86	t	6	$^3J_{hg} = 6.76$

## 2.5.7 Synthesis of 2-6

Dimethyl-5-(hydroxymethyl)-isophthalate (4.26 g, 0.0190 mol) was dissolved in THF (100 mL) under nitrogen and cooled (0 °C) on ice. Phosphorus tribromide (14.25 mL, 0.0143 mol) 1.0 M in CH<sub>2</sub>Cl<sub>2</sub> was added dropwise over 15 min. and stirring continued for 4 h. The solution was concentrated and recrystallized from MeOH. Product purified by column chromatography on silica gel with 1:4 (hexanes: CH<sub>2</sub>Cl<sub>2</sub>) as eluant. The resulting white solid, R<sub>f</sub> = 0.89, was collected. Yield: 4.47 g, 82 %.

Table 2.10 – <sup>1</sup>H NMR data of 2-6 in CDCl<sub>3</sub>. MW= 287.107 g/mol

Proton	δ (ppm)	Multiplicity	# Protons	J (Hz)
a	8.83	s	1	--
b	8.25	s	2	--
c	4.54	s	2	--
d	3.95	s	6	--

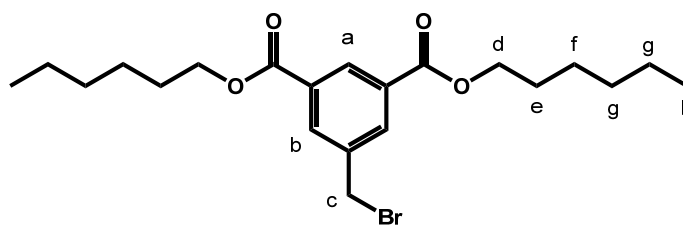
Table 2.11 – <sup>1</sup>H NMR data of 2-6 in CD<sub>3</sub>CN. MW= 287.107 g/mol

Proton	δ (ppm)	Multiplicity	# Protons	J (Hz)
a	8.69	s	1	--
b	8.21	s	2	--
c	4.33	s	2	--
d	3.92	s	6	--



**2.5.8 Synthesis of 2-7**

**2-3** (3.00 g, 0.0082 mol) was dissolved in THF (100 mL) under nitrogen and cooled (0 °C) on ice. Phosphorus tribromide (6.17 mL, 0.0062 mol) 1.0 M in CH<sub>2</sub>Cl<sub>2</sub> was added dropwise over 15 min. and stirring continued for 4 h. The solution was concentrated and recrystallized from MeOH. The product was purified by column chromatography on silica gel with 1:4 (hexanes: CH<sub>2</sub>Cl<sub>2</sub>) as eluant. The resulting white solid, R<sub>f</sub> = 0.93, was collected. Yield: 3.36 g, 96 %.

Table 2.12 –  $^1\text{H}$  NMR data of 2-7 in  $\text{CDCl}_3$ . MW= 427.374 g/mol

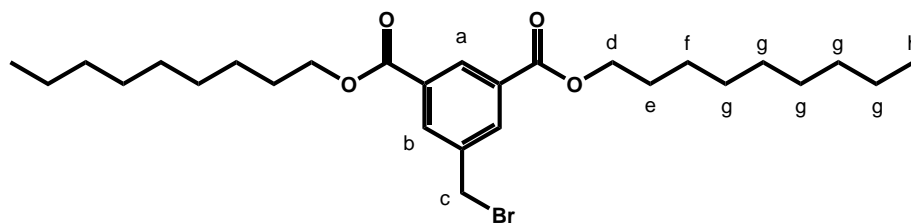
Proton	$\delta$ (ppm)	Multiplicity	# Protons	$J$ (Hz)
a	8.56	s	1	--
b	8.21	s	2	--
c	4.52	s	2	--
d	4.32	t	4	$^3J_{de} = 6.74$
e	1.76	tt	4	$^3J_{ed} = 6.74, ^3J_{ef} = 7.26$
f	1.41	tt	4	$^3J_{ed} = ^3J_{ef} = 7.26$
g	1.32	m	8	--
h	0.88	t	6	$^3J_{hg} = 6.74$

Table 2.13 –  $^1\text{H}$  NMR data of 2-7 in  $\text{CD}_3\text{CN}$ . MW= 427.374 g/mol

Proton	$\delta$ (ppm)	Multiplicity	# Protons	$J$ (Hz)
a	8.44	s	1	--
b	8.21	s	2	--
c	4.32	s	2	--
d	4.29	t	4	$^3J_{de} = 6.67$
e	1.74	tt	4	$^3J_{ed} = 6.67, ^3J_{ef} = 7.49$
f	1.44	tt	4	$^3J_{fe} = 7.49, ^3J_{fg} = 7.49$
g	1.32	m	8	--
h	0.88	t	6	$^3J_{hg} = 6.67$

**2.5.9 Synthesis of 2-8**

**2-4** (3.50 g, 0.0078 mol) was dissolved in THF (100 mL) under nitrogen and cooled (0 °C) on ice. Phosphorus tribromide (5.85 mL, 0.0059 mol) 1.0 M in CH<sub>2</sub>Cl<sub>2</sub> was added dropwise over 15 min. and stirring continued for 8 h. The solution was concentrated and recrystallized from MeOH. Product purified by column chromatography on silica gel with 1:4 (hexanes: CH<sub>2</sub>Cl<sub>2</sub>) as eluant. The resulting white solid, R<sub>f</sub> = 0.94, was collected. Yield: 3.69 g, 92 %.

Table 2.14 –  $^1\text{H}$  NMR data of 2-8 in  $\text{CDCl}_3$ . MW= 511.532 g/mol

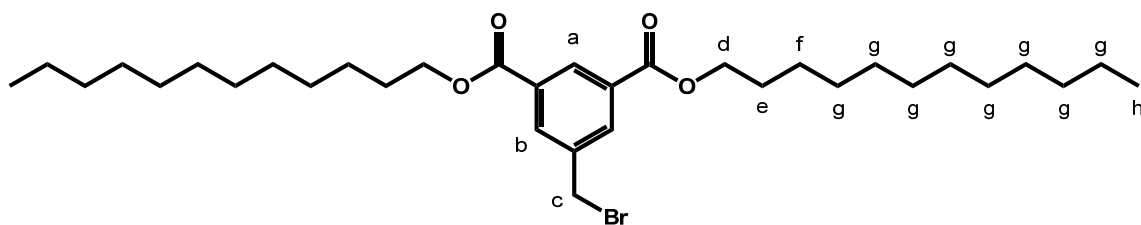
Proton	$\delta$ (ppm)	Multiplicity	# Protons	$J$ (Hz)
a	8.58	s	1	--
b	8.22	s	2	--
c	4.54	s	2	--
d	4.34	t	4	$^3J_{de} = 6.74$
e	1.78	tt	4	$^3J_{ed} = 6.74, ^3J_{ef} = 7.47$
f	1.43	tt	4	$^3J_{fe} = ^3J_{fg} = 7.47$
g	1.32	m	20	--
h	0.87	t	6	$^3J_{hg} = 6.74$

Table 2.15 –  $^1\text{H}$  NMR data of 2-8 in  $\text{CD}_3\text{CN}$ . MW= 511.532 g/mol

Proton	$\delta$ (ppm)	Multiplicity	# Protons	$J$ (Hz)
a	8.47	s	1	--
b	8.24	s	2	--
c	4.68	s	2	--
d	4.32	t	4	$^3J_{de} = 6.70$
e	1.76	tt	4	$^3J_{ed} = 6.70, ^3J_{ef} = 7.43$
f	1.45	tt	4	$^3J_{fe} = ^3J_{fg} = 7.43$
g	1.33	m	20	--
h	0.87	t	6	$^3J_{hg} = 6.70$

**2.5.10 Synthesis of 2-9**

**2-5** (4.50 g, 0.0084 mol) was dissolved in THF (200 mL) under nitrogen and cooled (0 °C) on ice. Phosphorus tribromide (6.33 mL, 0.0063 mol) 1.0 M in CH<sub>2</sub>Cl<sub>2</sub> was added dropwise over 15 min. and stirring continued overnight. The solution was concentrated and recrystallized from MeOH. Product purified by flash column chromatography on silica gel with 1:4 (hexanes: CH<sub>2</sub>Cl<sub>2</sub>) as eluant. The resulting white solid, R<sub>f</sub> = 0.92, was collected. Yield: 4.78 g, 95 %.

Table 2.16 –  $^1\text{H}$  NMR data of 2-9 in  $\text{CDCl}_3$ . MW= 595.691 g/mol

Proton	$\delta$ (ppm)	Multiplicity	# Protons	$J$ (Hz)
a	8.58	s	1	--
b	8.22	s	2	--
c	4.53	s	2	--
d	4.33	t	4	$^3J_{de} = 6.75$
e	1.77	tt	4	$^3J_{ed} = ^3J_{ef} = 7.37$
f	1.42	m	4	--
g	1.31	m	32	--
h	0.86	t	6	$^3J_{hg} = 6.90$

Table 2.17 –  $^1\text{H}$  NMR data of 2-9 in  $\text{CD}_3\text{CN}$ . MW= 595.691 g/mol

Proton	$\delta$ (ppm)	Multiplicity	# Protons	$J$ (Hz)
a	8.47	s	1	--
b	8.25	s	2	--
c	4.68	s	2	--
d	4.33	t	4	$^3J_{de} = 6.70$
e	1.67	tt	4	$^3J_{ed} = 6.70, ^3J_{ef} = 7.30$
f	1.44	tt	4	$^3J_{fe} = ^3J_{fg} = 7.30$
g	1.32	m	32	--
h	0.87	t	6	$^3J_{hg} = 6.70$

2.5.11 Synthesis of [2-10][OTf]<sub>4</sub>

[2-2][OTf]<sub>2</sub> (100.0 mg, 0.156 mmol) and **2-6** (179.0 mg, 0.626 mmol) were dissolved in MeNO<sub>2</sub> (60 mL) and the mixture was heated (60 °C) 3 days. The precipitate formed was filtered, washed with MeNO<sub>2</sub> and anion exchanged to the triflate salt. The ivory solid was dissolved in MeNO<sub>2</sub>, washed with H<sub>2</sub>O (3 x 10 mL), dried over MgSO<sub>4</sub> and the solvent removed. The product was isolated as a white solid. Yield: 98.2 mg, 46 %. **ESI-MS**: *m/z* 1201.1558 (calc.) for C<sub>47</sub>H<sub>42</sub>F<sub>9</sub>N<sub>4</sub>O<sub>17</sub>S<sub>3</sub> [M-3OTF]<sup>+</sup>, found 1201.1522. *m/z* 526.1016 (calc.) for C<sub>46</sub>H<sub>42</sub>F<sub>6</sub>N<sub>4</sub>O<sub>14</sub>S<sub>2</sub> [M-2OTF]<sup>2+</sup>, found 526.1039.

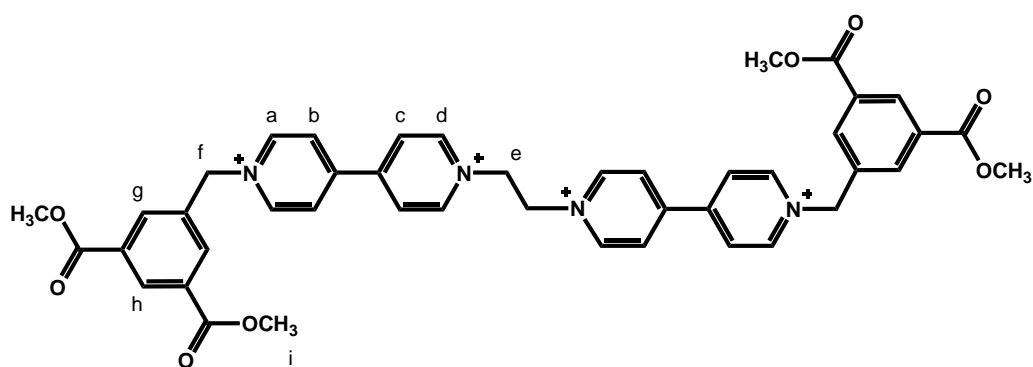
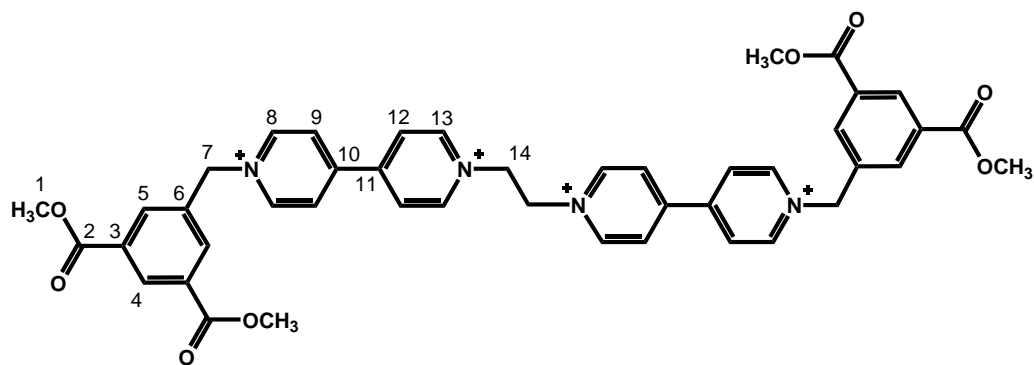


Table 2.18 – <sup>1</sup>H NMR data of [2-10][OTf]<sub>4</sub> in CD<sub>3</sub>CN. MW<sub>OTf</sub> = 1351.103 g/mol

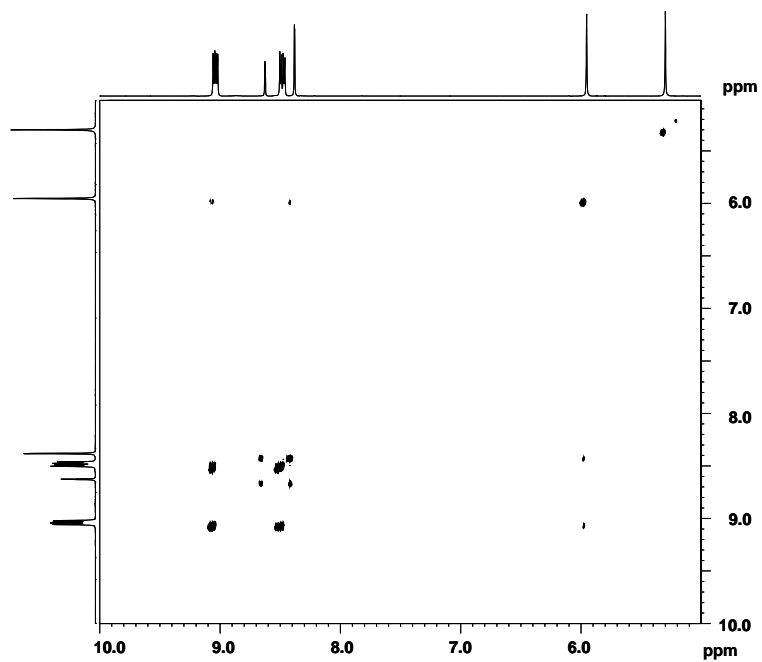
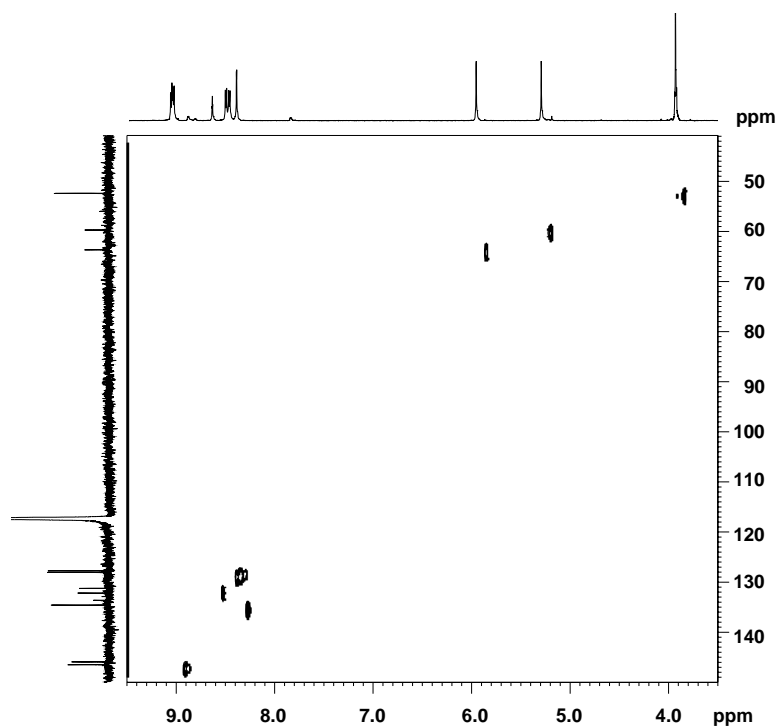
Proton	δ (ppm)	Multiplicity	# Protons	J (Hz)
<b>a,d</b>	9.03	dd	8	<sup>3</sup> J <sub>ab</sub> = <sup>3</sup> J <sub>dc</sub> = 6.77
<b>b</b>	8.46	d	4	<sup>3</sup> J <sub>ba</sub> = 6.77
<b>c</b>	8.49	d	4	<sup>3</sup> J <sub>cd</sub> = 6.77
<b>e</b>	5.29	s	4	--
<b>f</b>	5.95	s	4	--
<b>g</b>	8.38	s	4	--
<b>h</b>	8.63	s	2	--
<b>i</b>	3.93	s	12	--



**Table 2.19** –  $^{13}\text{C}$  NMR data of [2-10][OTf] $_4$  in  $\text{CD}_3\text{CN}$ .  $\text{MW}_{\text{OTf}} = 1351.103$  g/mol. Quaternary carbons assigned using software

Carbon	$\delta$ (ppm)	# Carbons
1	52.49	4
2	165.28	4
3	132.19	4
4	131.30	2
5	134.65	4
6	133.94	2
7	63.73	2
8	146.00	4
9	127.78	4
10	148.12	2
11	148.2	2
12	128.10	4
13	146.55	4
14	59.70	2



COSY of [2-10][OTf]<sub>4</sub> in CD<sub>3</sub>CN.HETCOR of [2-10][OTf]<sub>4</sub> in CD<sub>3</sub>CN.

2.5.12 Synthesis of [2-11][OTf]<sub>4</sub>

[2-2][OTf]<sub>2</sub> (80.0 mg, 0.125 mmol) and 2-7 (220.0 mg, 0.501 mmol) were dissolved in MeNO<sub>2</sub> (60 mL) and heated (60 °C) for 3 days. The precipitate formed was filtered, washed with MeNO<sub>2</sub> and anion exchanged to the triflate salt. The ivory solid was dissolved in MeNO<sub>2</sub>, washed with H<sub>2</sub>O (3 x 10 mL), dried over MgSO<sub>4</sub> and the solvent removed. The product was isolated as a white solid. Yield: 86.8 mg, 43 %. **ESI-MS**: *m/z* 666.2581 (calc.) for C<sub>66</sub>H<sub>82</sub>F<sub>6</sub>N<sub>4</sub>O<sub>14</sub>S<sub>2</sub> [M-2OTF]<sup>2+</sup>, found 666.2599.

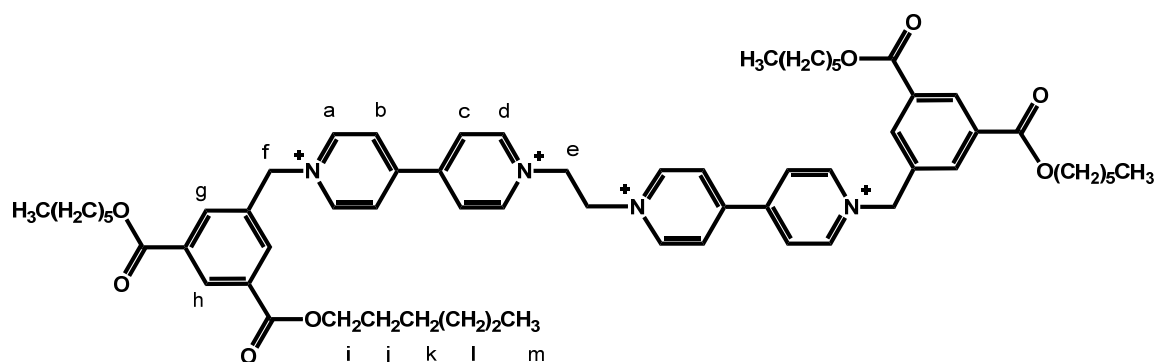
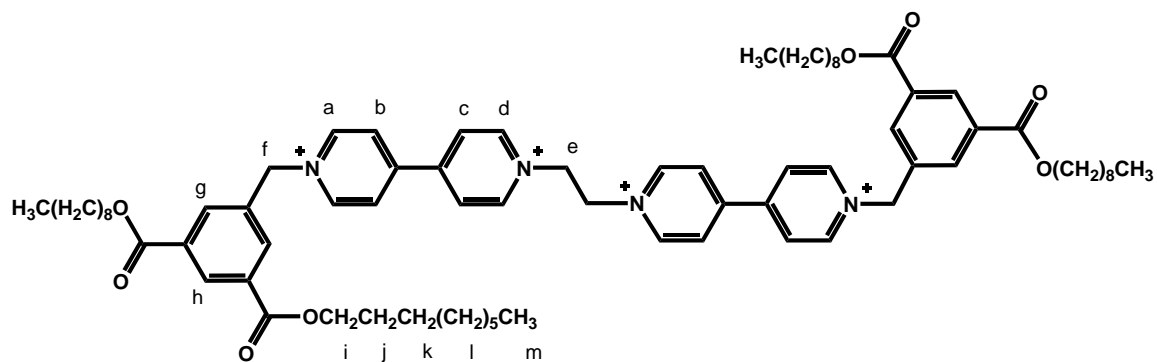


Table 2.20 – <sup>1</sup>H NMR data of [2-11][OTf]<sub>4</sub> in CD<sub>3</sub>CN. MW<sub>OTf</sub> = 1631.634 g/mol

Proton	δ (ppm)	Multiplicity	# Protons	J (Hz)
a,d	9.03	dd	8	<sup>3</sup> J <sub>ab</sub> = <sup>3</sup> J <sub>dc</sub> = 6.84
b	8.47	d	4	<sup>3</sup> J <sub>ba</sub> = 6.84
c	8.50	d	4	<sup>3</sup> J <sub>cd</sub> = 6.84
e	5.3	s	4	--
f	5.95	s	4	--
g	8.38	s	4	--
h	8.63	s	2	--
i	4.34	t	8	<sup>3</sup> J <sub>ij</sub> = 6.65
j	1.77	tt	8	<sup>3</sup> J <sub>ji</sub> = 6.65, <sup>3</sup> J <sub>jk</sub> = 7.48
k	1.45	tt	8	<sup>3</sup> J <sub>kj</sub> = <sup>3</sup> J <sub>kl</sub> = 7.48
l	1.35	m	16	--
m	0.90	t	12	<sup>3</sup> J <sub>ml</sub> = 6.65

### 2.5.13 Synthesis of [2-12][OTf]<sub>4</sub>

[2-2][OTf]<sub>2</sub> (76.0 mg, 0.118 mmol) and **2-8** (242.0 mg, 0.473 mmol) were dissolved in MeNO<sub>2</sub> (60 mL) and the mixture was heated (60 °C) for 3 days. The precipitate formed was filtered, washed with MeNO<sub>2</sub> and anion exchanged to the triflate salt. The ivory solid was dissolved in MeNO<sub>2</sub>, washed with H<sub>2</sub>O (3 x 10 mL), dried over MgSO<sub>4</sub> and the solvent removed. The product was isolated as a white solid. Yield: 112.0 mg, 53 %. **ESI-MS**:  $m/z$  750.3520 (calc.) for C<sub>78</sub>H<sub>106</sub>F<sub>6</sub>N<sub>4</sub>O<sub>14</sub>S<sub>2</sub> [M-2OTF]<sup>2+</sup>, found 750.3519.

Table 2.21 –  $^1\text{H}$  NMR data of [2-12][OTf] $_4$  in  $\text{CD}_3\text{CN}$ .  $\text{MW}_{\text{OTf}} = 1799.533$  g/mol

Proton	$\delta$ (ppm)	Multiplicity	# Protons	$J$ (Hz)
a	9.02	d	4	$^3J_{ab} = 6.83$
b	8.46	d	4	$^3J_{ba} = 6.83$
c	8.49	d	4	$^3J_{cd} = 6.83$
d	9.05	d	4	$^3J_{dc} = 6.83$
e	5.29	s	4	--
f	5.95	s	4	--
g	8.38	s	4	--
h	8.63	s	2	--
i	4.33	t	8	$^3J_{ij} = 6.65$
j	1.77	tt	8	$^3J_{ji} = 6.65, ^3J_{jk} = 7.40$
k	1.44	tt	8	$^3J_{kj} = ^3J_{kl} = 7.40$
l	1.32	m	40	--
m	0.87	t	12	$^3J_{ml} = 6.65$

2.5.14 Synthesis of [2-13][OTf]<sub>4</sub>

[2-2][OTf]<sub>2</sub> (80.0 mg, 0.125 mmol) and **2-9** (298.0 mg, 0.501 mmol) were dissolved in MeNO<sub>2</sub> (60 mL) and the mixture was heated (60 °C) for 4 days. The precipitate formed was filtered, washed with MeNO<sub>2</sub> and anion exchanged to the triflate salt. The ivory solid was dissolved in MeNO<sub>2</sub>, washed with H<sub>2</sub>O (3 x 10 mL), dried over MgSO<sub>4</sub> and the solvent removed. The product was isolated as a white solid. Yield: 97.2 mg, 40 %. **ESI-MS**: *m/z* 834.4459 (calc.) for C<sub>90</sub>H<sub>130</sub>F<sub>6</sub>N<sub>4</sub>O<sub>14</sub>S<sub>2</sub> [M-2OTf]<sup>2+</sup>, found 834.4457, *m/z* 506.6464 (calc.) for C<sub>89</sub>H<sub>130</sub>F<sub>3</sub>N<sub>4</sub>O<sub>11</sub>S [M-OTf]<sup>3+</sup>, found 506.6479.

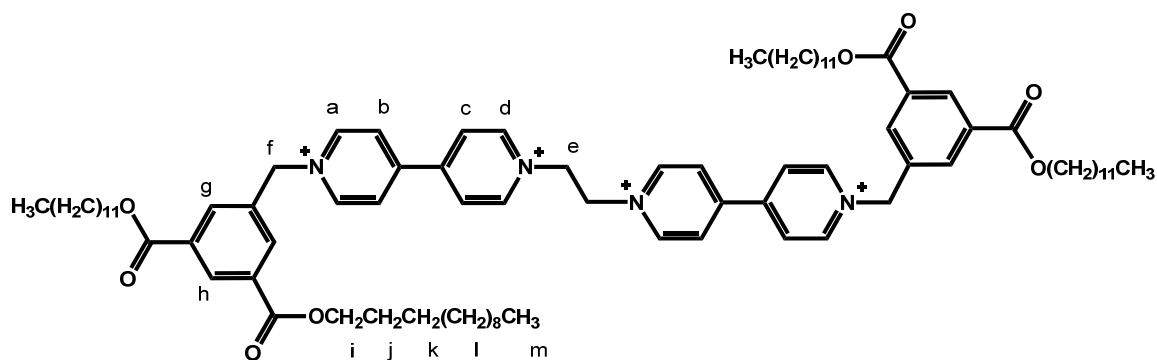
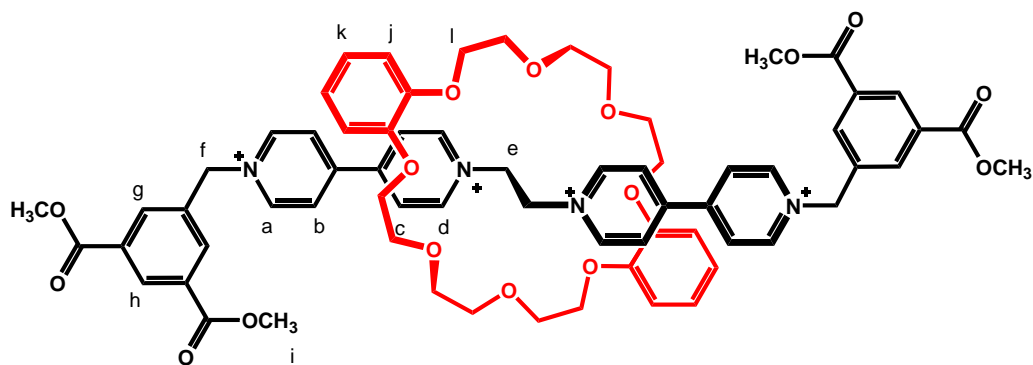


Table 2.22 – <sup>1</sup>H NMR data of [2-13][OTf]<sub>4</sub> in CD<sub>3</sub>CN. MW<sub>OTf</sub> = 1968.277 g/mol

Proton	δ (ppm)	Multiplicity	# Protons	J (Hz)
<b>a,d</b>	9.02	dd	8	<sup>3</sup> J <sub>ab</sub> = <sup>3</sup> J <sub>dc</sub> = 6.85
<b>b</b>	8.45	d	4	<sup>3</sup> J <sub>ba</sub> = 6.85
<b>c</b>	8.48	d	4	<sup>3</sup> J <sub>cd</sub> = 6.85
<b>e</b>	5.28	s	4	--
<b>f</b>	5.95	s	4	--
<b>g</b>	8.38	s	4	--
<b>h</b>	8.62	s	2	--
<b>i</b>	4.33	t	8	<sup>3</sup> J <sub>ij</sub> = 6.85
<b>j</b>	1.77	tt	8	<sup>3</sup> J <sub>ji</sub> = 6.85, <sup>3</sup> J <sub>jk</sub> = 7.42
<b>k</b>	1.44	tt	8	<sup>3</sup> J <sub>kj</sub> = <sup>3</sup> J <sub>kl</sub> = 7.42
<b>l</b>	1.31	m	64	--
<b>m</b>	0.87	t	12	<sup>3</sup> J <sub>ml</sub> = 6.85

### 2.5.15 Synthesis of [2-14][OTf]<sub>4</sub>

[2-2][OTf]<sub>2</sub> (70.0 mg, 0.110 mmol) and **DB24C8** (491.0 mg, 1.100 mmol) were dissolved in a two-phase NaOTf (aq)/MeNO<sub>2</sub> (1 and 30 mL) mixture. **2-6** (157.0 mg, 0.548 mmol) was added and the mixture stirred at RT for 21 days. The MeNO<sub>2</sub> was washed with H<sub>2</sub>O (3 x 10 mL), dried over MgSO<sub>4</sub> and the solvent removed. The residue was stirred in toluene and remaining solid filtered. The resulting solid was stirred in CHCl<sub>3</sub> and remaining solid filtered. Product was purified and isolated by column chromatography on silica gel using a 7:1:2 mixture of MeOH, 2M NH<sub>4</sub>Cl (aq) and MeNO<sub>2</sub>. The resulting deep orange solid, R<sub>f</sub> = 0.515, was anion exchanged back to the triflate salt and collected. Yield: 72.0 mg, 37 %. **ESI-MS**: *m/z* 1649.3655 (calc.) for C<sub>71</sub>H<sub>74</sub>F<sub>9</sub>N<sub>4</sub>O<sub>25</sub>S<sub>3</sub> [M-3OTF]<sup>+</sup>, found 1649.3715, *m/z* 750.2064 (calc.) for C<sub>70</sub>H<sub>74</sub>F<sub>6</sub>N<sub>4</sub>O<sub>22</sub>S<sub>2</sub> [M-2OTF]<sup>2+</sup>, found 750.2049.

Table 2.23 –  $^1\text{H}$  NMR data of [2-14][OTf]<sub>4</sub> in CD<sub>3</sub>CN. MW<sub>OTf</sub> = 1799.610 g/mol

Proton	$\delta$ (ppm)	Multiplicity	# Protons	$J$ (Hz)
<b>a</b>	8.98	d	4	$^3J_{ab} = 6.78$
<b>b</b>	8.19	d	4	$^3J_{ba} = 6.78$
<b>c</b>	8.23	d	4	$^3J_{cd} = 6.78$
<b>d</b>	9.31	d	4	$^3J_{dc} = 6.78$
<b>e</b>	5.61	s	4	--
<b>f</b>	5.97	s	4	--
<b>g</b>	8.39	s	4	--
<b>h</b>	8.65	s	2	--
<b>i</b>	3.94	s	12	--
<b>j</b>	6.45	dd	4	$^3J_{\text{meta}} = 3.56; ^3J_{\text{ortho}} = 5.93$
<b>k</b>	6.64	dd	4	$^3J_{\text{meta}} = 3.56; ^3J_{\text{ortho}} = 5.93$
<b>l</b>	4.05	m	24	--

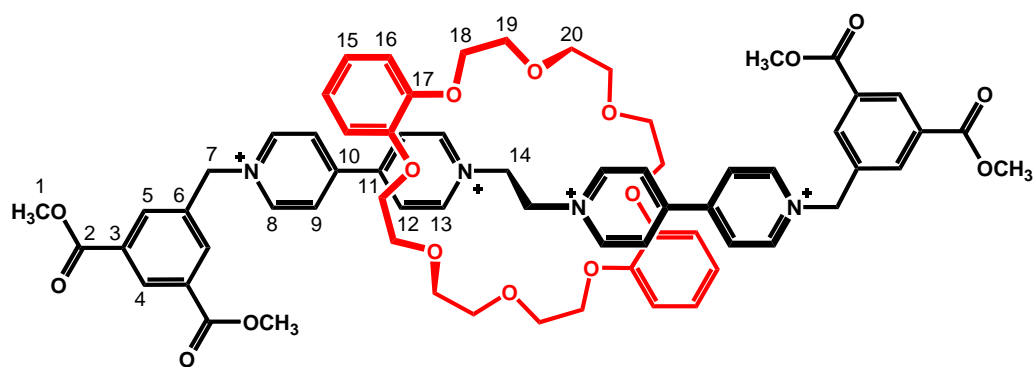
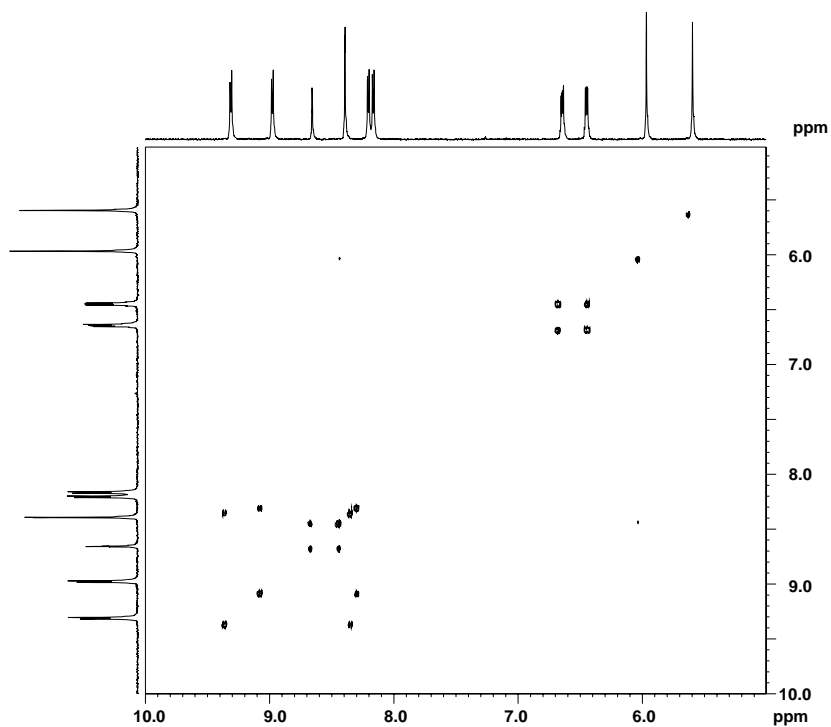
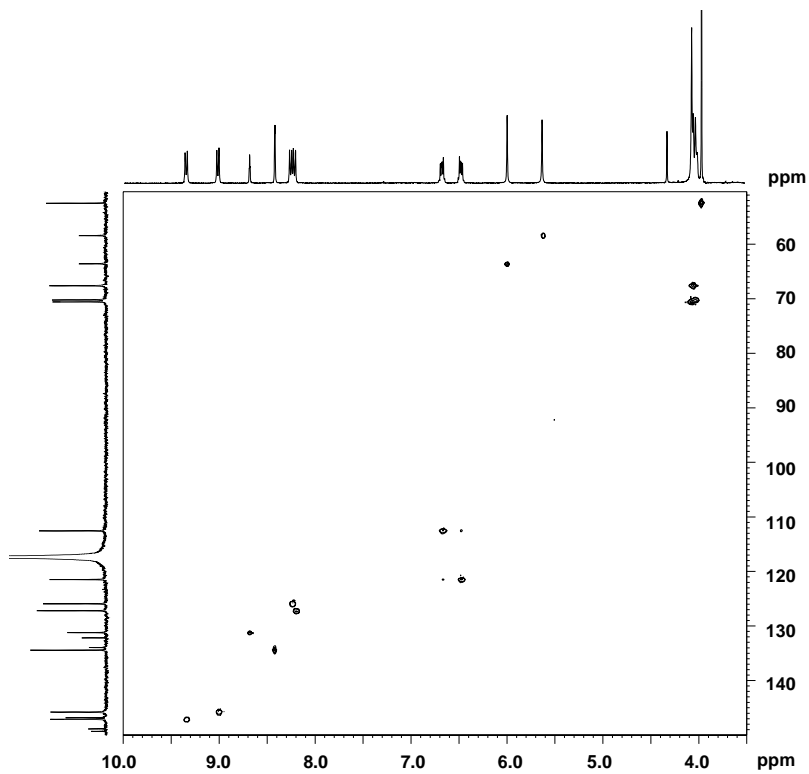


Table 2.24 –  $^{13}\text{C}$  NMR data of [2-14][OTf] $_4$  in  $\text{CD}_3\text{CN}$ .  $\text{MW}_{\text{OTf}} = 1799.610$  g/mol. Quaternary carbons assigned by software

Carbon	$\delta$ (ppm)	# Carbons
1	52.47	4
2	165.27	4
3	132.19	4
4	131.23	2
5	134.43	4
6	133.95	2
7	63.59	2
8	145.78	4
9	127.22	4
10	149.31	2
11	148.87	2
12	125.95	4
13	147.10	4
14	58.43	2
15	121.50	4
16	112.57	4
17	146.82	4
18	70.22	4
19	67.63	4
20	70.58	4



COSY of [2-14][OTf]<sub>4</sub> in CD<sub>3</sub>CN.HETCOR of [2-14][OTf]<sub>4</sub> in CD<sub>3</sub>CN.

**Single Crystal - X-ray Information:**

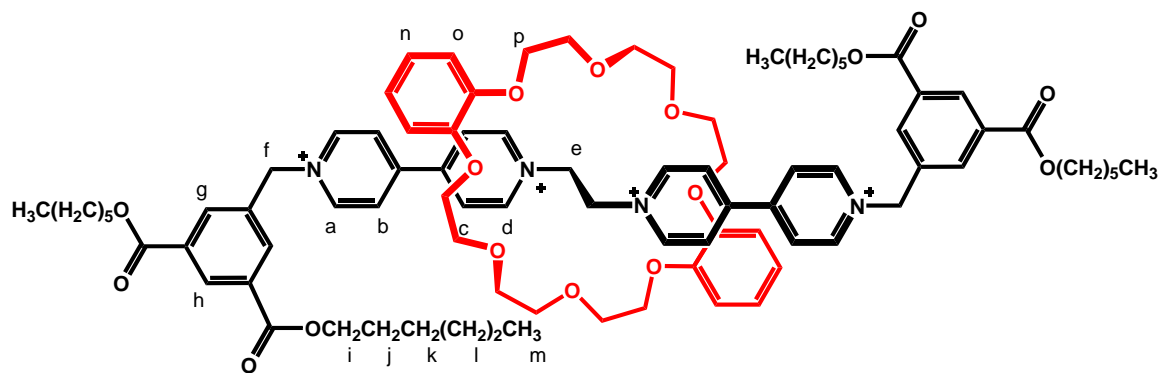
The crystals were frozen in paratone oil inside a cryoloop. Reflection data was integrated from frame data obtained from hemisphere scans on a Brüker APEX diffractometer with a CCD detector. Decay was monitored by 50 standard data frames measured at the beginning and end of data collection. Diffraction data and unit-cell parameters were consistent with assigned space groups. Lorentzian polarization corrections and empirical absorption corrections, based on redundant data at varying effective azimuthal angles, were applied to the data series. The structure was solved by direct methods, completed by subsequent Fourier syntheses and refined using full-matrix least-squares methods against  $|F^2|$  data. All non-hydrogen atoms were refined anisotropically. Hydrogen atoms were treated as idealized contributions. Scattering factors and anomalous dispersion coefficients are contained in the SHELXTL 5.03 program library.<sup>137</sup> Ball-and-stick and space-filling models were generated using the program DIAMOND.<sup>138</sup>

**Table 2.25 – Crystal data/details: structure solution/refinement for [2-14][OTf]<sub>4</sub>.**

Formula	C <sub>74</sub> H <sub>77</sub> F <sub>12</sub> N <sub>5</sub> O <sub>29</sub> S <sub>4</sub>	Collection Temp [K]	173.0(2)
Formula Weight	1856.7	$\rho_{\text{calcd}}$ [g.cm <sup>-3</sup> ]	1.523
Crystal System	Triclinic	$\mu$ (MoK $\alpha$ ) [mm <sup>-1</sup> ]	0.231
Space Group	P-1	Min/max trans.	0.8535/1.0000
a [Å]	12.442(3)	Total reflections	38473
b [Å]	16.488(4)	R(int)	0.437
c [Å]	20.443(5)	R1 [I>2 $\sigma$ I]	0.0808
$\alpha$ [°]	104.939(3)	R1 [all data]	0.0981
$\beta$ [°]	90.035(3)	wR2 [I>2 $\sigma$ I]	0.2165
$\gamma$ [°]	91.766(3)	wR2 [all data]	0.2277
V [Å <sup>3</sup> ]	4049.8(17)	Data/variables	14147/11118
Z	2	GoF (F <sup>2</sup> )	1.072

### 2.5.16 Synthesis of [2-15][OTf]<sub>4</sub>

[2-2][OTf]<sub>2</sub> (40.0 mg, 0.063 mmol) and **DB24C8** (281.0 mg, 0.626 mmol) were dissolved in a two-phase NaOTf (aq)/MeNO<sub>2</sub> (1 and 30 mL) mixture. **2-7** (107.0 mg, 0.251 mmol) and a catalytic amount of TBAI (10 mg) was added and the mixture stirred at RT for 1 month. The MeNO<sub>2</sub> was washed with H<sub>2</sub>O (3 x 10 mL), dried over MgSO<sub>4</sub> and the solvent removed. The residue was stirred in toluene and remaining solid filtered. Product was purified and isolated by column chromatography on silica gel using a 7:1:2 mixture of MeOH, 2M NH<sub>4</sub>Cl (aq) and MeNO<sub>2</sub>. The resulting deep orange solid, R<sub>f</sub> = 0.72, was anion exchanged back to the triflate salt and collected. Yield: 65.0 mg, 50 %. **ESI-MS:** *m/z* 890.3629 (calc.) for C<sub>90</sub>H<sub>114</sub>F<sub>6</sub>N<sub>4</sub>O<sub>22</sub>S<sub>2</sub> [M-2OTF]<sup>2+</sup>, found 890.3621.

Table 2.26 –  $^1\text{H}$  NMR data of [2-15][OTf]<sub>4</sub> in CD<sub>3</sub>CN. MW<sub>OTf</sub> = 2080.145 g/mol

Proton	$\delta$ (ppm)	Multiplicity	# Protons	$J$ (Hz)
a	9.00	d	4	$^3J_{ab} = 6.62$
b	8.25	d	4	$^3J_{ba} = 6.62$
c	8.27	d	4	$^3J_{cd} = 6.62$
d	9.32	d	4	$^3J_{dc} = 6.62$
e	5.61	s	4	--
f	5.98	s	4	--
g	8.39	s	4	--
h	8.65	s	2	--
i	4.35	t	8	$^3J_{ij} = 6.62$
j	1.78	tt	8	$^3J_{ji} = 6.62$ $^3J_{jk} = 7.42$
k	1.46	tt	8	$^3J_{kj} = ^3J_{kl} = 7.42$
l	1.35	m	16	--
m	0.90	t	12	$^3J_{ml} = 6.68$
n	6.43	dd	4	$^3J_{meta} = 3.75$ ; $^3J_{ortho} = 5.74$
o	6.65	dd	4	$^3J_{meta} = 3.75$ ; $^3J_{ortho} = 5.74$
p	4.02	m	24	--

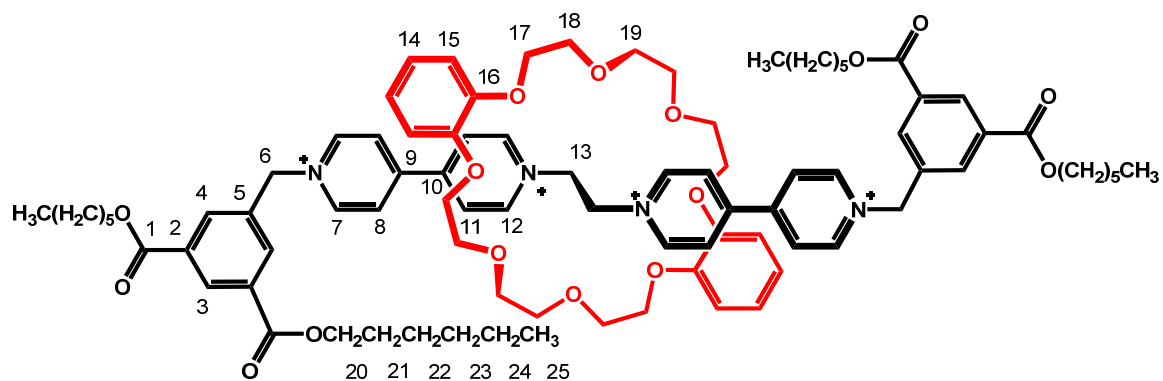


Table 2.27 –  $^{13}\text{C}$  NMR data of [2-15][OTf] $_4$  in  $\text{CD}_3\text{CN}$ .  $\text{MW}_{\text{OTf}} = 2080.145$  g/mol. Quaternary carbons assigned by software

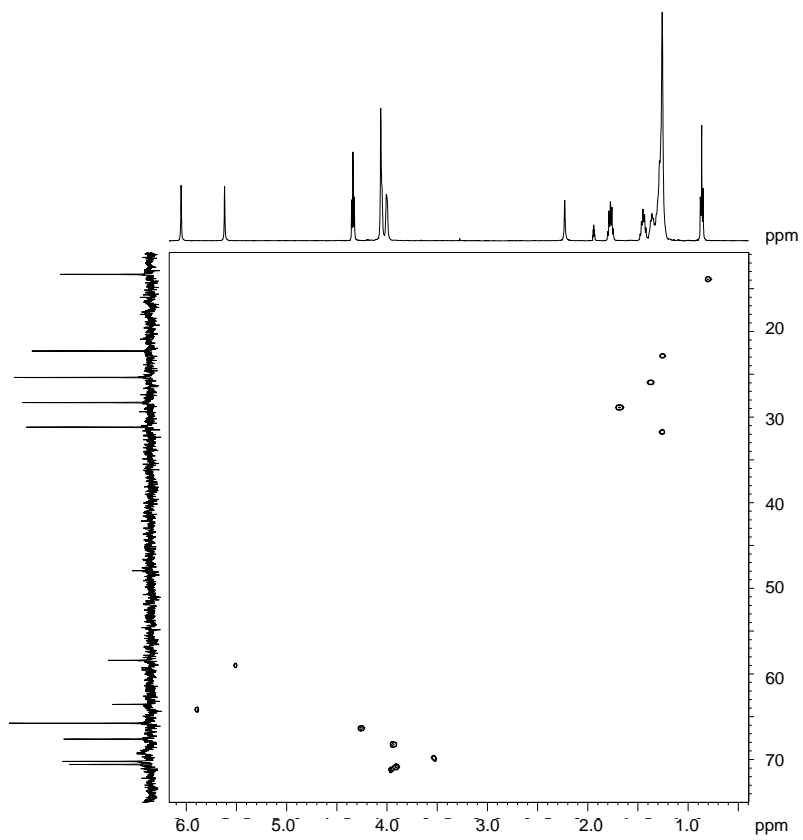
Carbon	$\delta$ (ppm)	# Carbons
1	164.82	4
2	131.06	4
3	132.47	2
4	134.44	4
5	133.86	2
6	63.56	2
7	145.73	4
8	127.17	4
9	149.24	2
10	148.80	2
11	125.95	4
12	147.06	4
13	58.42	2
14	121.46	4
15	112.55	4
16	146.83	4
17	67.62	4
18	70.22	4
19	70.58	4
20	65.76	4
21	28.30	4
22	25.37	4
23	31.17	4

---

24	22.28	4
25	13.33	4

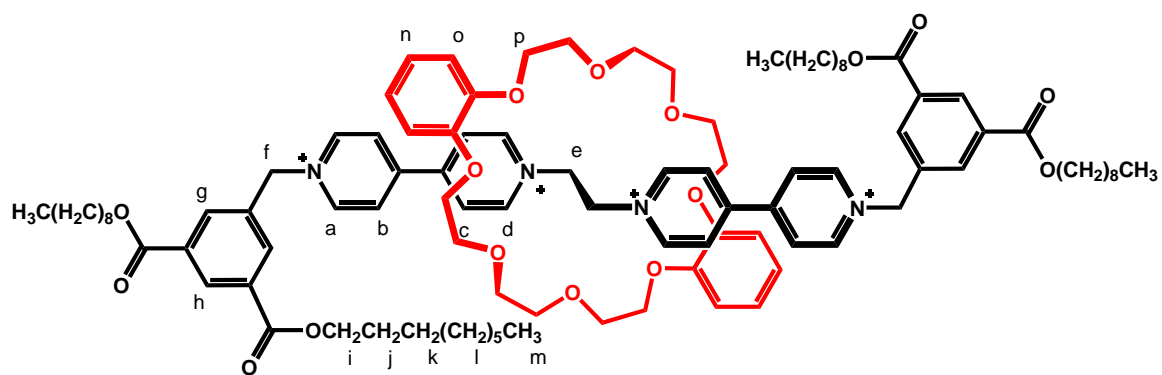
---

HETCOR of [2-15][OTf]<sub>4</sub> in CD<sub>3</sub>CN.



### 2.5.17 Synthesis of [2-16][OTf]<sub>4</sub>

[2-2][OTf]<sub>2</sub> (70.0 mg, 0.110 mmol) and **DB24C8** (491.0 mg, 1.100 mmol) were dissolved in a two-phase NaOTf (aq)/MeNO<sub>2</sub> (1 and 30 mL) mixture. **2-8** (224.0 mg, 0.438 mmol) was added, then CHCl<sub>3</sub> was added dropwise until solid dissolved and a catalytic amount of TBAI (10 mg) was added and the mixture was stirred at RT for 45 days. The MeNO<sub>2</sub> was washed with H<sub>2</sub>O (3 x 10 mL), dried over MgSO<sub>4</sub> and the solvent removed. The residue was stirred in cold toluene and remaining solid filtered. Product was purified and isolated by column chromatography on silica gel using a 7:1:2 mixture of MeOH, 2M NH<sub>4</sub>Cl (aq) and MeNO<sub>2</sub>. The resulting orange soft solid, R<sub>f</sub> = 0.68, was anion exchanged to the triflate salt and collected. Yield: 31.0 mg, 13 %. **ESI-MS**: *m/z* 974.4569 (calc.) for C<sub>102</sub>H<sub>138</sub>F<sub>6</sub>N<sub>4</sub>O<sub>22</sub>S<sub>2</sub> [M-2OTF]<sup>2+</sup>, found 974.4568.

Table 2.28 –  $^1\text{H}$  NMR data of [2-16][OTf] $_4$  in  $\text{CD}_3\text{CN}$ .  $\text{MW}_{\text{OTf}} = 2248.464$  g/mol

Proton	$\delta$ (ppm)	Multiplicity	# Protons	$J$ (Hz)
a	8.98	d	4	$^3J_{ab} = 6.69$
b	8.18	d	4	$^3J_{ba} = 6.69$
c	8.22	d	4	$^3J_{cd} = 6.69$
d	9.31	d	4	$^3J_{dc} = 6.69$
e	5.60	s	4	--
f	5.97	s	4	--
g	8.40	s	4	--
h	8.65	s	2	--
i	4.35	t	8	$^3J_{ij} = 6.63$
j	1.78	tt	8	$^3J_{ji} = 6.63$ $^3J_{jk} = 7.39$
k	1.45	tt	8	$^3J_{kj} = ^3J_{kl} = 7.39$
l	1.32	m	40	--
m	0.87	t	12	$^3J_{ml} = 6.69$
n	6.43	dd	4	$^3J_{\text{meta}} = 3.57$ ; $^3J_{\text{ortho}} = 5.86$
o	6.65	dd	4	$^3J_{\text{meta}} = 3.57$ ; $^3J_{\text{ortho}} = 5.86$
p	4.02	m	24	--



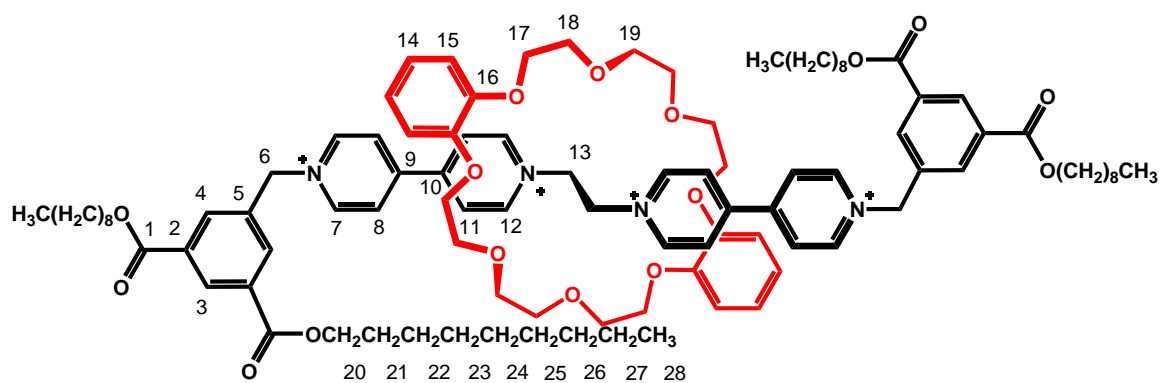


Table 2.29 –  $^{13}\text{C}$  NMR data of [2-16][OTf] $_4$  in  $\text{CD}_3\text{CN}$ .  $\text{MW}_{\text{OTf}} = 2248.464$  g/mol. Quaternary carbons assigned by software

Carbon	$\delta$ (ppm)	# Carbons
1	164.79	4
2	131.06	4
3	132.43	2
4	134.51	4
5	134.07	2
6	63.60	2
7	145.76	4
8	127.21	4
9	149.23	2
10	148.75	2
11	125.99	4
12	147.08	4
13	58.44	2
14	121.49	4
15	112.54	4
16	146.85	4
17	68.15	4
18	70.21	4
19	70.60	4
20	65.98	4
21	28.31	4
22	25.79	4
23	29.35	4

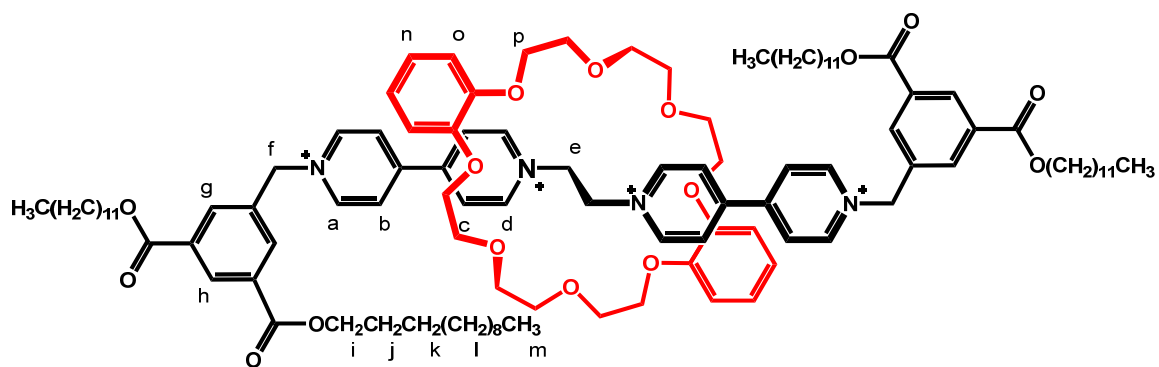
---

<b>24</b>	28.97	4
<b>25</b>	29.31	4
<b>26</b>	31.54	4
<b>27</b>	22.24	4
<b>28</b>	13.51	4

---

### 2.5.18 Synthesis of [2-17][OTf]<sub>4</sub>

[2-2][OTf]<sub>2</sub> (80.0 mg, 0.125 mmol) and **DB24C8** (562.0 mg, 1.253 mmol) were dissolved in a two-phase NaOTf (aq)/MeNO<sub>2</sub> (1 and 40 mL) mixture and placed in an 80 mL reaction vessel. **2-9** (298.0 mg, 0.501 mmol) was dissolved in CHCl<sub>3</sub> (20 mL) and a catalytic amount of TBAI (10 mg) was added to 80 mL vessel with stir bar and microwaved for 30 h at 50 °C. The MeNO<sub>2</sub> was washed with H<sub>2</sub>O (3 x 10 mL), dried over MgSO<sub>4</sub> and the solvent removed. The residue was stirred in MeCN, white solid filtered off and remaining solution concentrated. The orange residue was dissolved in cold EtOH, white solid filtered off and remaining solution concentrated. Product was purified and isolated by flash column chromatography on RP-C<sub>18</sub> silica gel using MeOH as eluant, yielding a deep red/orange brittle solid. Yield: 98.0 mg, 29 %. **ESI-MS**: *m/z* 1058.5508 (calc.) for C<sub>114</sub>H<sub>162</sub>F<sub>6</sub>N<sub>4</sub>O<sub>22</sub>S<sub>2</sub> [M-2OTF]<sup>2+</sup>, found 1058.5515. *m/z* 656.0497 (calc.) for C<sub>113</sub>H<sub>162</sub>F<sub>3</sub>N<sub>4</sub>O<sub>19</sub>S [M-OTF]<sup>3+</sup>, found 656.0518.

Table 2.30 –  $^1\text{H}$  NMR data of [2-17][OTf] $_4$  in  $\text{CD}_3\text{CN}$ .  $\text{MW}_{\text{OTf}} = 2416.782$  g/mol

Proton	$\delta$ (ppm)	Multiplicity	# Protons	$J$ (Hz)
<b>a</b>	8.97	d	4	$^3J_{ab} = 6.73$
<b>b</b>	8.18	d	4	$^3J_{ba} = 6.73$
<b>c</b>	8.22	d	4	$^3J_{cd} = 6.73$
<b>d</b>	9.31	d	4	$^3J_{dc} = 6.73$
<b>e</b>	5.59	s	4	--
<b>f</b>	5.96	s	4	--
<b>g</b>	8.39	s	4	--
<b>h</b>	8.65	s	2	--
<b>i</b>	4.35	t	8	$^3J_{ij} = 6.65$
<b>j</b>	1.78	tt	8	$^3J_{ji} = 6.65; ^3J_{jk} = 7.40$
<b>k</b>	1.45	tt	8	$^3J_{kj} = ^3J_{kl} = 7.40$
<b>l</b>	1.32	m	64	--
<b>m</b>	0.87	t	12	$^3J_{ml} = 6.69$
<b>n</b>	6.63	dd	4	$^3J_{\text{meta}} = 3.64; ^3J_{\text{ortho}} = 5.87$
<b>o</b>	6.42	dd	4	$^3J_{\text{meta}} = 3.64; ^3J_{\text{ortho}} = 5.87$
<b>p</b>	4.02	m	24	--

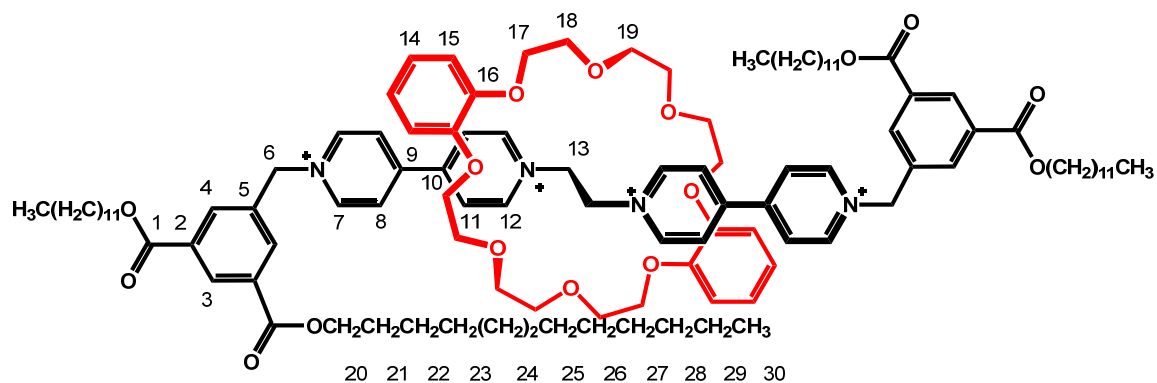


Table 2.31 –  $^{13}\text{C}$  NMR data of [2-17][OTf] $_4$  in  $\text{CD}_3\text{CN}$ .  $\text{MW}_{\text{OTf}} = 2416.782$  g/mol. Quaternary carbons assigned by software

Carbon	$\delta$ (ppm)	# Carbons
1	164.79	4
2	131.03	4
3	132.44	2
4	134.46	4
5	133.92	2
6	63.49	2
7	145.76	4
8	127.18	4
9	149.20	2
10	148.79	2
11	126.04	4
12	147.02	4
13	58.40	2
14	121.46	4
15	112.55	4
16	146.82	4
17	67.62	4
18	70.24	4
19	70.60	4
20	65.74	4
21	28.34	4
22	25.72	4
23	29.33	4

---

<b>24</b>	29.38	8
<b>25</b>	29.29	4
<b>26</b>	28.98	4
<b>27</b>	29.09	4
<b>28</b>	31.66	4
<b>29</b>	22.41	4
<b>30</b>	13.41	4

---

# CHAPTER 3

## *Improving Mesomorphism in [2]Rotaxanes*

### 3.1 INTRODUCTION

Self-assembly and self-organization<sup>1,6,28-33,139</sup> represent powerful means for the spontaneous and programmed generation of nanoscale architectures based upon instructions stored in the building block components. This involves the formation of organized, discrete assemblies and the collective behaviour of ensembles such as liquid crystals.<sup>140</sup> The successful design of a liquid crystalline rotaxane assembly depends primarily on the choice of a suitable rotaxane core, but an often underestimated aspect is the influence of the substituents of the building blocks, where even the smallest changes can lead to unexpected consequences for the superstructure.

As shown in Chapter 2, a [2]rotaxane incorporating the 1,2-bis(dipyridinium)ethane/**DB24C8** motif and based upon a tetracatenar design, substituted with dodecane aliphatic chains, demonstrated liquid crystallinity over a wide temperature range with formation of a lamellar SmA phase. This material is however, hampered by a high viscosity making processing and alignment in thin films quite challenging. This chapter describes the use of terminal benzylic stoppers with longer straight aliphatic chains, a branching chain and a hyperbranched chain in order to decrease crystallinity and increase the fluidity of these materials. The effect of odd versus even chain length will also be investigated, as well as comparison of straight chains to branching, to determine the ability of the stopper to efficiently fill space and the resulting effect this has on the resulting mesomorphism.

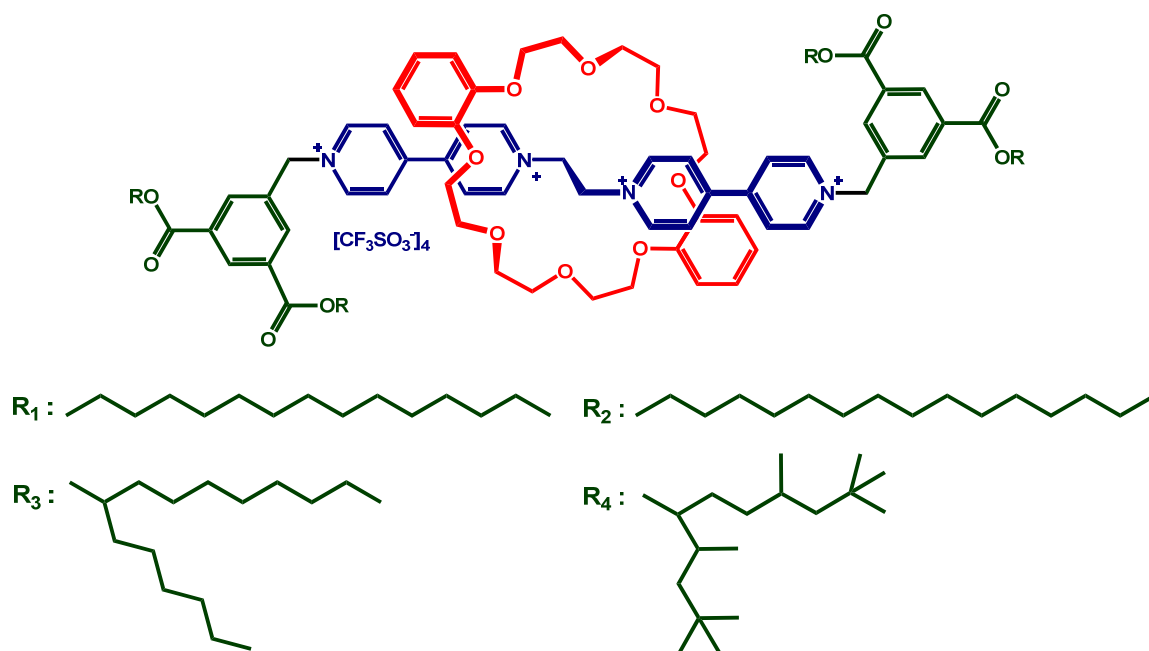


**Figure 3.1 – Structural representation of [2]rotaxanes with the various aliphatic benzylic stoppers introduced in this chapter.**

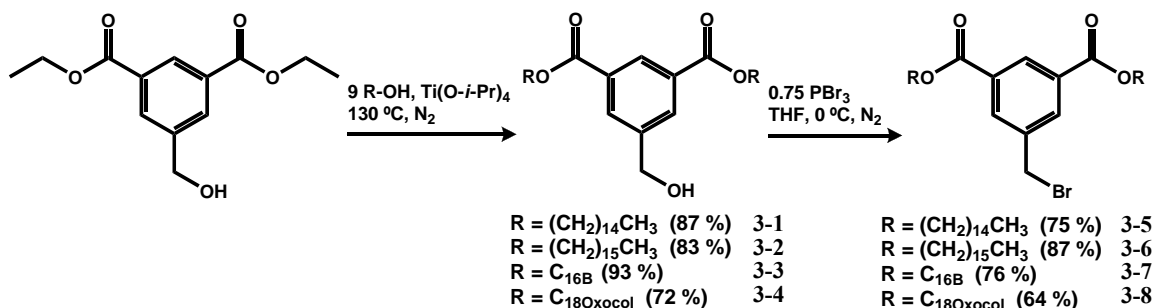
## 3.2 SYNTHESIS AND CHARACTERIZATION

### 3.2.1 Synthesis

In Chapter 2, it was shown that the minimum packing volume of side-chains required to induce a smectic LC phase in [2]rotaxanes was achieved using straight dodecane chains. Hence, increasing the number of carbons in the chain and/or how they are distributed should still induce a smectic LC phase. The new 3,5-bis(carboxyalkyl)benzyl bromide stoppers were synthesized in two steps. The first was a transesterification<sup>132</sup> of dimethyl-5-(hydroxymethyl)-*isophthalate* with an excess of the appropriate alkyl alcohol in the presence of  $\text{Ti}(i\text{-PrO})_4$  as the catalyst to generate the corresponding benzyl alcohol as bis(pentadecyl) **3-1**, bis(hexadecyl) **3-2**, bis(2-hexyl-1-decyl) **3-3** and bis(1-octyl,5,7,7-trimethyl-2-(1,3,3-trimethylbutane)) (oxocol) **3-4**. Next



was the bromination of the benzyl alcohol with phosphorous tribromide to generate the corresponding benzyl bromide stoppers **3-5**, **3-6**, **3-7** and **3-8** (Scheme 3.1). Due to the high purity requirement for incorporation into [2]rotaxanes, each compound was purified by flash column chromatography.

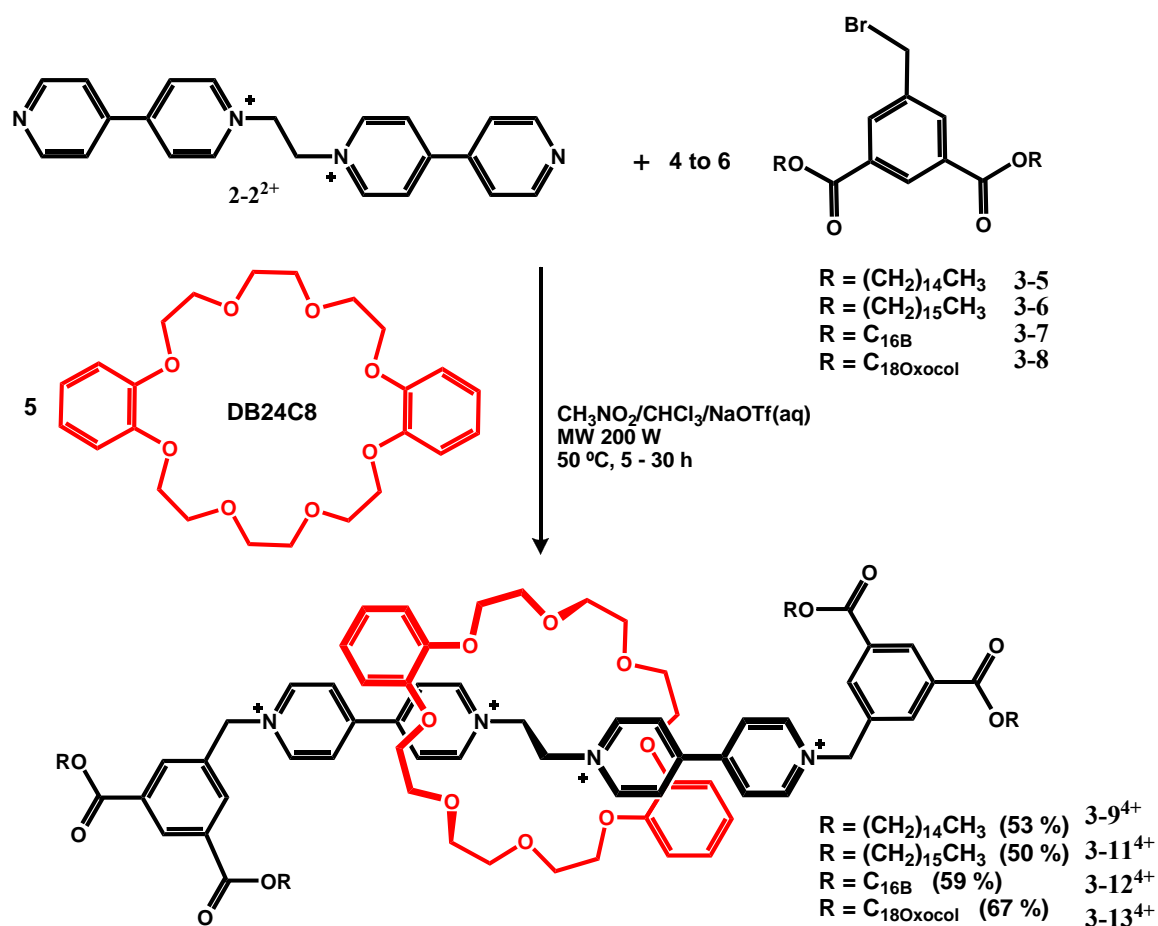


**Scheme 3.1 – Synthetic route for stoppers.**

The [2]rotaxanes based on our well established templating motif, incorporating 1,2-bis(pyridinium)ethane threads and **DB24C8** macrocycles,<sup>113-128</sup> were synthesized in a fashion similar to that described in Chapter 2. However, some modifications were introduced that proved to be marked advances in the synthesis of these complex structures. As outlined in Chapter 2, the preparation of the rotaxanes comprised some challenges, mainly time constraints. Due to the solubility differences between the thread and stoppers with increased alkyl chain lengths, reaction times were long with stirring at room temperature from three weeks to nearly two months, usually resulting in incomplete rotaxane formation. Our efforts to decrease reactions times by heating were thwarted by a marked decrease in pseudorotaxane formation.

In recent years, an area of growing interest is that of microwave assisted organic synthesis.<sup>141-145</sup> Due to the internal heating by microwaves, this technology can shorten reaction times, simplify work up procedures and improve overall efficiency. In our attempts to decrease reaction times and increase product yields, microwave irradiation

was employed in place of room temperature stirring. Microwave synthesis was employed at temperatures as high as 60 °C and yielded nearly complete rotaxane formation (80-90 %) on a gram-scale in 5 to 30 h. To synthesize the [2]rotaxanes **3-9<sup>4+</sup>** and **3-11<sup>4+</sup>** through **3-13<sup>4+</sup>** one equivalent of thread and five equivalents of the **DB24C8** macrocycle were dissolved in a minimum amount of hot MeNO<sub>2</sub> to form the pseudorotaxane and then this solution combined with the appropriate stopper dissolved in a minimum amount of CHCl<sub>3</sub>. The two solvent mixture was then subjected to microwave irradiation at 60 °C for 5h, followed by addition of saturated NaOTf (aq), and continued microwaving until all terminal pyridine groups were alkylated (Scheme 3.2).



Scheme 3.2 - Improved synthetic route to [2]rotaxanes **3-9<sup>4+</sup>**, **3-11<sup>4+</sup>**, **3-12<sup>4+</sup>** and **3-13<sup>4+</sup>**.

Significant  $\pi$ -stacking interactions between the electron-rich catechol of the crown and the electron-poor pyridinium rings of the axle give rise to a charge transfer interaction that imparts the pseudorotaxane with a characteristic yellow colour and the rotaxane with a characteristic orange-red colour. Rotaxane formation was monitored by  $^1\text{H}$  NMR spectroscopy or more simply by a colour change before (yellow), and after 5h of microwaving (orange-red); see Figure 3.2. Since the different components have very different solubility properties, there are still some problems which prevent the reaction time from being shortened even further.

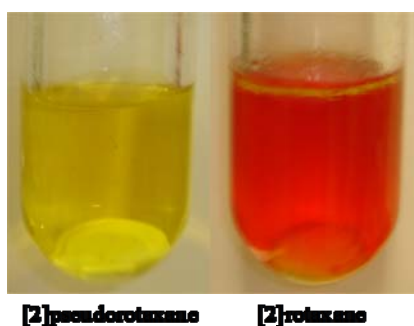


**Figure 3.2 - Colour of [2]pseudorotaxane at  $t = 0$  (left) and of [2]rotaxane 3-9<sup>4+</sup> at  $t = 5$  h after applying microwave irradiation (right).**

### 3.2.2 Purification

Rotaxanes were typically purified by numerous recrystallizations followed by column chromatography employing assorted combinations of polar solvents with salt solutions to move the charged species.<sup>28-33,113-128</sup> This particular system introduces the further complexity of large solubility differences for the reactants due to the large non-polar alkyl chains of the stopper and the polar ionic core. For [2]rotaxanes purified in Chapter 2, decomposition in some manner was suspected due to the small amounts of product recovered from both bench top columns and preparative TLC plates with 7:1:2 (MeOH: 2M  $\text{NH}_4\text{Cl}$ :  $\text{MeNO}_2$ ) as eluant on ultrapure normal phase silica gel. It was also

observed that when employing automated flash chromatography with a Combiflash R<sub>f</sub> system, cleavage at the quaternary pyridinium ethyl bridge was identified. This was noted by the recovery of the mono stoppered 4-4'-bipyridine in large quantities. This type of cleavage has been previously reported for methyl viologens with cleavage occurring through cation-radical formation in the presence of aqueous base.<sup>146-149</sup>

We are still uncertain as to the mechanism through which this cleavage occurs, since the reduction to the cation-radical usually requires a pH below 10, but are convinced that the silica gel facilitates its formation. We believe this occurs with all stoppered systems having the 1,2-bis(pyridinium)ethane bridge which is reflected in the low yields reported over the years. However, the product and cleaved species were chemically different enough not to have ever been isolated. Interestingly, we have yet to recover any 4-4'-bipyridine and assume this must be due to the stabilizing effects of the stopper. This hurdle was overcome by employing MeOH as the eluant on fully end-capped RP-C<sub>18</sub> silica gel, with full recovery of the rotaxane. The present issue with the RP-C<sub>18</sub> silica is once any end capping groups are removed, for example after one to two uses, the cleaved species is once again detected.

### 3.2.3 <sup>1</sup>H NMR Spectroscopy

Comparison of the <sup>1</sup>H NMR spectra of the naked dumbbell **3-10**<sup>4+</sup> to the [2]rotaxane **3-9**<sup>4+</sup> prepared with the 1,2-bis(pyridinium)ethane/**DB24C8** binding motif clearly shows the effect of all three non-covalent interactions with the introduction of the **DB24C8** macrocycle (Figure 3.3). Ethylene protons of the recognition site, **e**, and α-pyridinium protons, **d**, are deshielded due to hydrogen bonding with the oxygen atoms of the crown ether. Conversely, β-pyridinium protons, **b** and **c**, are shielded due to π-

stacking interactions between the electron rich catechol rings of the crown ether and the electron poor pyridinium rings of the thread. Other protons **g**, **h** and **f**, do not shift as they are not directly involved in any non-covalent interactions with the crown ether.

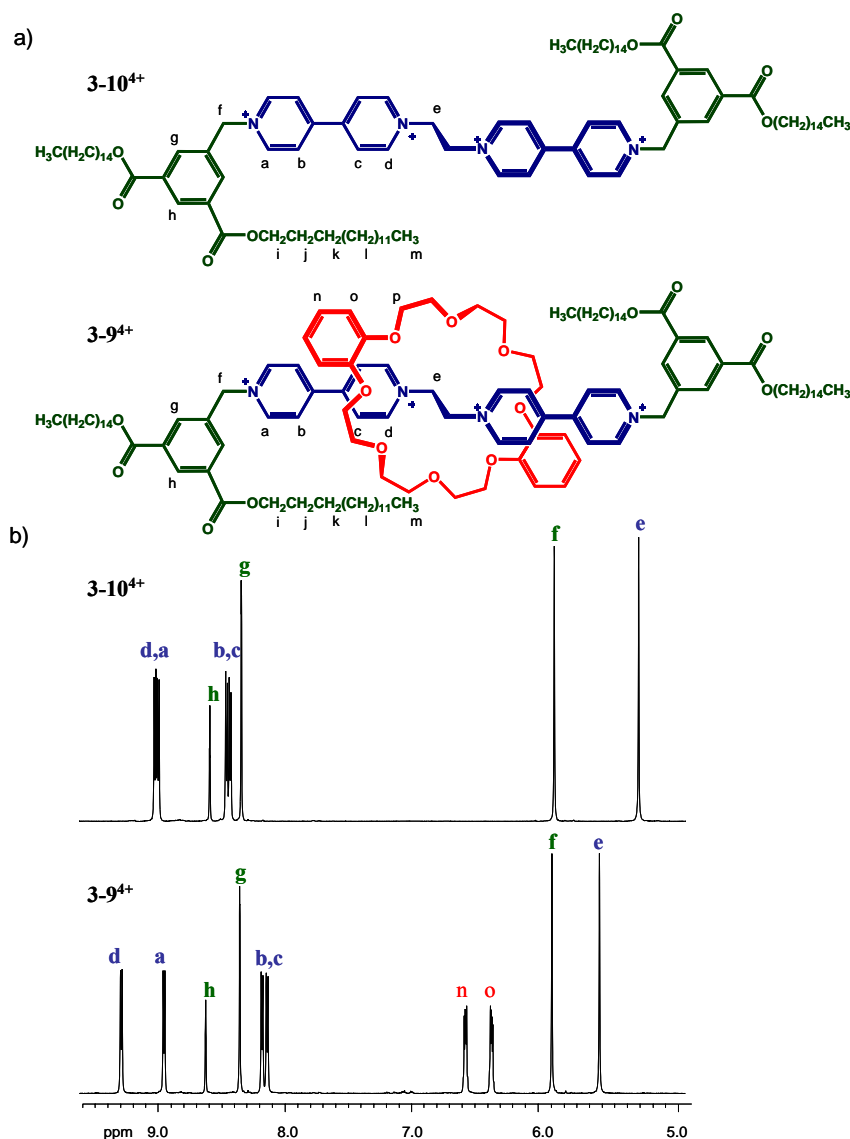


Figure 3.3 - a) Structure of  $3-10^{4+}$  and  $3-9^{4+}$  and b)  $^1\text{H}$  NMR spectra of  $3-10^{4+}$  and  $3-9^{4+}$  in  $\text{CD}_3\text{CN}$ .

### 3.2.4 Mass Spectrometry

Mass spectrometry was used as an analytical tool to confirm the formation of all molecular ions for [2]rotaxanes  $3-9^{4+}$  and  $3-11^{4+}$  through  $3-13^{4+}$  (Section 3.6). For

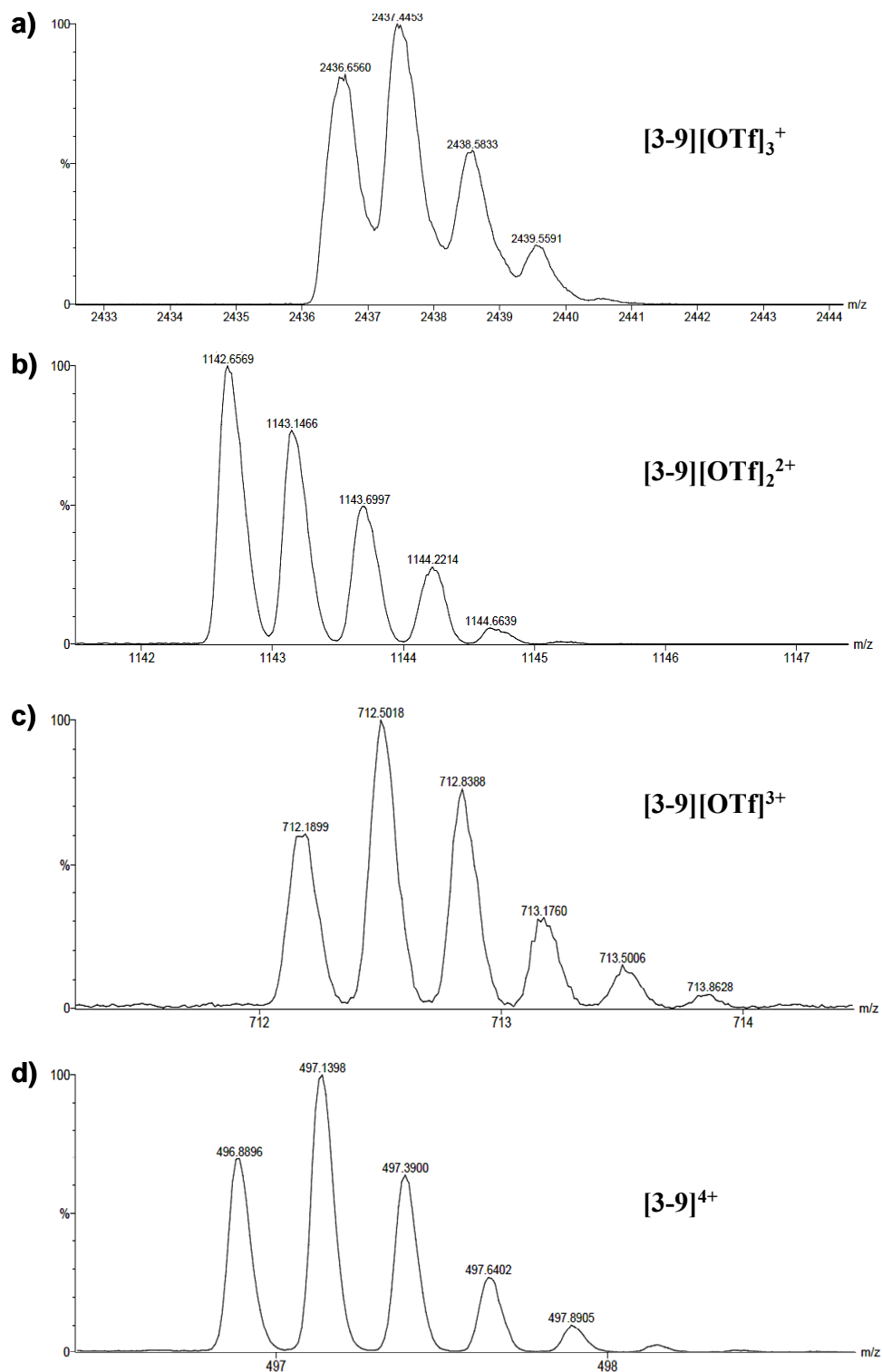


Figure 3.4 - ESI-Mass spectra of experimental data for a)  $3-9^+$ , b)  $3-9^{2+}$ , c)  $3-9^{3+}$  and d)  $3-9^{4+}$ .

example, a sample of [3-9][OTf]<sub>4</sub> was analyzed in a solution of acetonitrile and the spectra for the 1+, 2+, 3+ and 4+ molecular ions are shown in Figure 3.4. Sufficient resolution allowed for exact mass measurements to within 5 ppm of the calculated exact masses for all except the 1+ species, confirming the molecular formula of [3-9][OTf]<sub>4</sub>. Table 3.1 summarizes these MS values. The spectra show the typical splitting patterns for multiply charged species.

**Table 3.1 - Calculated and found exact masses for [2]rotaxane [3-9][OTf]<sub>4</sub>.**

Molecular Ion	Calc. m/z (g/mol)	Expt. m/z (g/mol)	Δ (ppm)
3-9 <sup>+</sup>	2434.2419	2436.6560	-
3-9 <sup>2+</sup>	1142.6447	1142.6486	3.4
3-9 <sup>3+</sup>	712.1123	712.1154	4.5
3-9 <sup>4+</sup>	496.8460	496.8460	0

### 3.3 LIQUID CRYSTAL PHASE CHARACTERIZATION

#### 3.3.1 Thermal Gravimetric Analysis (TGA)

The TGA curves for all [2]rotaxanes were obtained at a rate of 2 °C/min under He (Figure 3.5). Decomposition occurs in the same manner as discussed in Chapter 2 with two distinct steps of weight loss. The first step loss is attributed to the stoppers, indicating that the bond between the pyridinium and benzylic stopper is thermally most labile with decomposition occurring above 200 °C. The second step weight % loss is due to the **DB24C8** macrocycle with decomposition occurring at temperatures above 325 °C. The weight % values of the individual components for the [2]rotaxanes with regard to the entire molecule including the four triflate anions were calculated and are in good agreement with the separate steps in weight loss observed (Table 3.2).

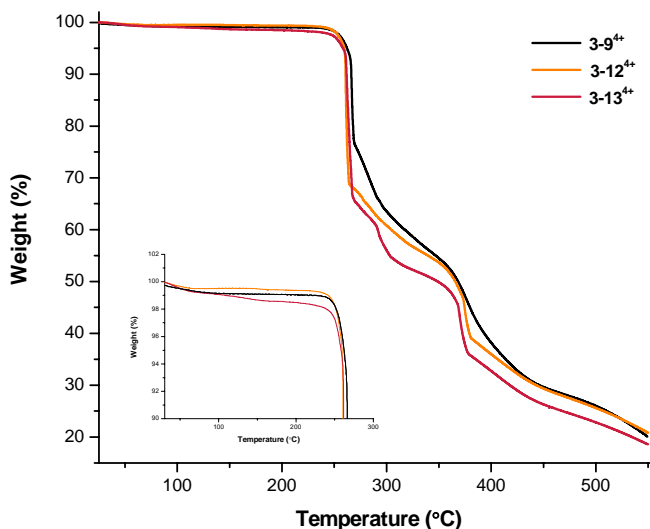


Figure 3.5 - TGA curves of [2]rotaxanes 3-9<sup>4+</sup>, 3-12<sup>4+</sup> and 3-13<sup>4+</sup> at 2 °C/min under He.

Table 3.2 - Calculated weight % values for components of [2]rotaxanes with actual weight % values for the first step losses.

Compound	2 Stoppers (actual %)	2 Stoppers (calc. %)	Axle (%)	4 OTf anions	DB24C8 (%)
3-9 <sup>4+</sup>	45.2	46.5	13.2	23.1	17.3
3-11 <sup>4+</sup>	45.4	47.6	12.9	22.6	17.0
3-12 <sup>4+</sup>	46.8	47.6	12.9	22.6	17.0
3-13 <sup>4+</sup>	50.4	49.8	12.4	22.6	17.0

### 3.3.2 Defect Textures Observed by Polarizing Optical Microscopy (POM)

The POMs observed for all [2]rotaxanes 3-9<sup>4+</sup> and 3-11<sup>4+</sup> through 3-13<sup>4+</sup> did not show any characteristic textures, making classification difficult, although some exhibited some similarities to textures reported for small molecule LCs. Clearing into the isotropic liquid was broad for all [2]rotaxanes which ranged between 8 to 10 °C, as observed by POM. [2]Rotaxanes 3-9<sup>4+</sup> and 3-11<sup>4+</sup> did not clear into the isotropic liquid phase before their decomposition at temperatures above 200 °C, as determined by TGA, and thus their



textures were not studied above 190 °C. Both showed similar behaviour upon heating and cooling cycles, with the exception that **3-9<sup>4+</sup>** crystallized from MeCN with the formation of plates, and **3-11<sup>4+</sup>** precipitated from MeCN forming a liquid crystalline phase (Figure 3.6a and 3.7a, respectively). This difference is due to how the straight chains pack; the so called odd-even effect of aliphatic chains. Both materials demonstrated high birefringence across the entire temperature range from 15 to 190 °C with a large number of disclination lines, which is a defect in the orientation of the director. The viscosity of these [2]rotaxanes were not significantly reduced compared to the [2]rotaxane **2-17<sup>4+</sup>**

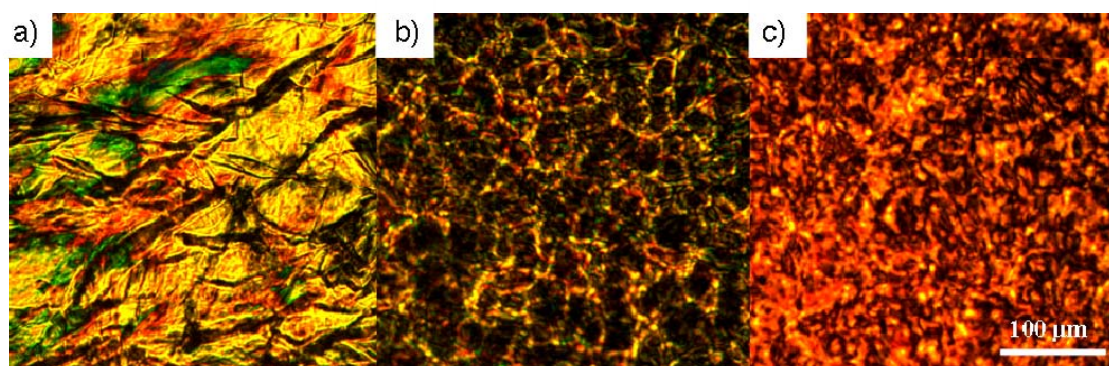


**Figure 3.6 - POM of 3-9<sup>4+</sup> (crossed polarizers): a) crystallized from MeCN @ 25 °C, b) squeezed between glass slides @ 100 °C and c) @ 25 °C upon cooling from 190 °C.**

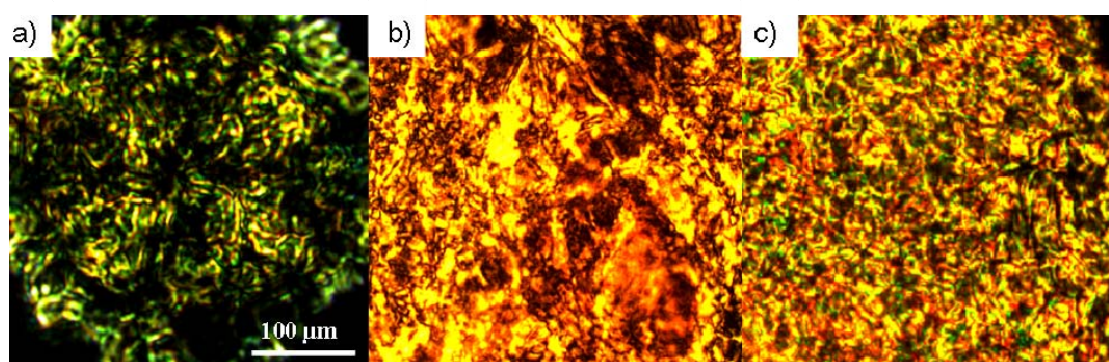


**Figure 3.7 - POM of 3-11<sup>4+</sup> (crossed polarizers): a) precipitated from MeCN @ 25 °C, b) squeezed between glass slides @ 25 °C and c) @ 25 °C upon cooling from 190 °C.**

discussed in Chapter 2. The natural textures of **3-9<sup>4+</sup>** and **3-11<sup>4+</sup>** are shown in Figure 3.6c and 3.7c, respectively.

[2]Rotaxane **3-12<sup>4+</sup>** precipitated from MeCN forming a smectic schlieren-like texture with curvature and with singularities resolved showing four-fold brushes, typical of a tilted SmC phase (Figure 3.8a). Upon heating and softening of the material the texture changed to that of a less birefringent crystalline-like material between approximately 110 and 165 °C, at which point the birefringence nearly disappeared with an increase in fluidity at 170 °C (Figure 3.8b). A broken focal conic type texture grew in at 175 °C and remained until clearing into the isotropic liquid phase at 193 °C. The

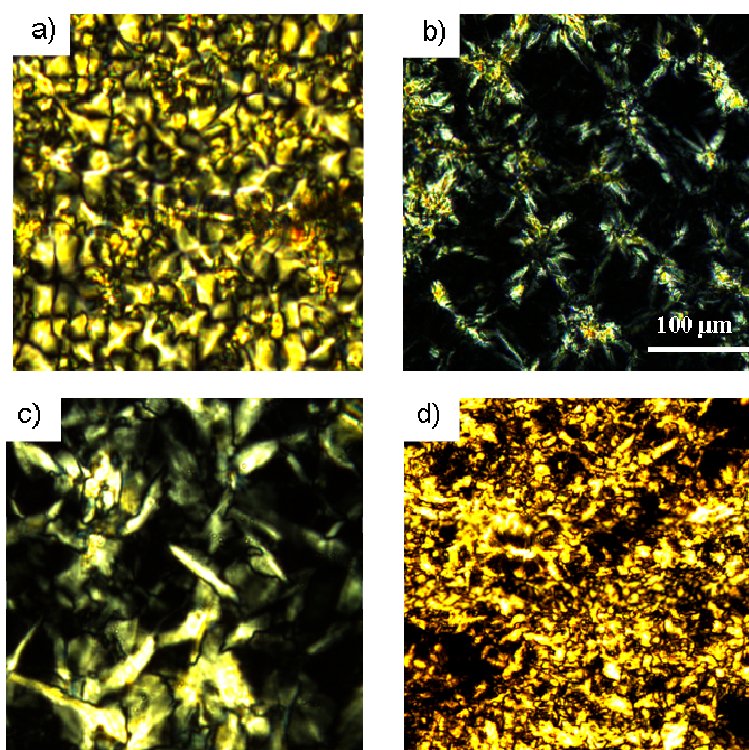


**Figure 3.8 - POM of 3-12<sup>4+</sup> (crossed polarizers): a) precipitated from MeCN @ 25 °C, b) squeezed between glass slides @ 150 °C, c) squeezed between glass slides @ 185 °C and d) @ 25 °C upon cooling from T<sub>i</sub> = 193 °C.**

broken focal conic type texture returned upon cooling at 182 °C and remained when cooled to room temperature. All textural changes were reversible by POM with the exception of the schlieren texture with the four-fold brushes that was only observed when the material was precipitated from solution and hence the alignment was influenced by the solvent. The formation of broken focal conic defect textures confirms a preferential orientation in which the smectic layers are perpendicular to the substrate plane.

[2]Rotaxane **3-13<sup>4+</sup>** crystallized from MeCN forming a soft crystalline phase with highly birefringent crystalline domains as well as smectic schlieren domains with singularities resolved showing four-fold brushes, again typical of a tilted SmC phase (Figure 3.9a). Upon heating and softening of the material the texture changed to that of a less birefringent oily-streak texture at 105 °C and remained until clearing into the isotropic liquid phase at 172 °C. As seen with all these [2]rotaxanes, upon cooling from the isotropic liquid a broken focal conic defect texture was observed, with many disclination lines, indicative of a lamellar phase. All textural changes were reversible by POM with the exception of the schlieren texture with the four-fold brushes that was only

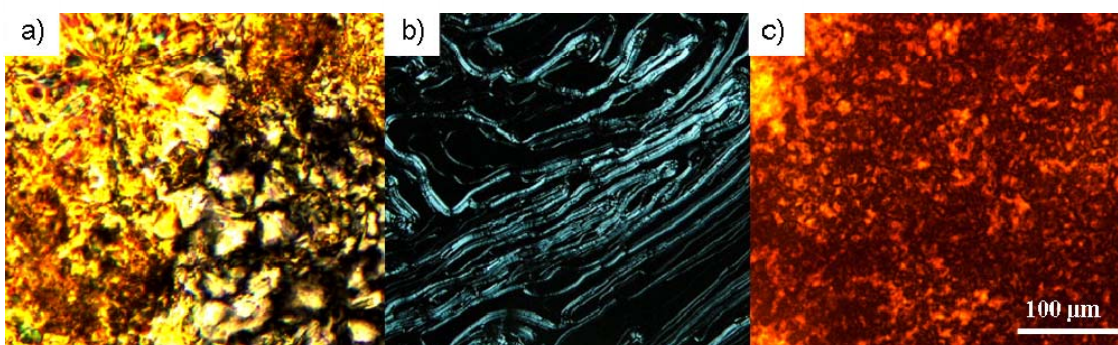


**Figure 3.9 - POM of 3-13<sup>4+</sup> (crossed polarizers): a) crystallized from MeCN @ 25 °C, b) squeezed between glass slides @ 109 °C and c) @ 25 °C upon cooling from  $T_i = 172$  °C.**

ever observed when the material was crystallized from solution and hence is a result of the effect of solvent on molecular packing.

### 3.3.3 Differential Scanning Calorimetry (DSC)

DSC analysis of both freshly crystallized and dried samples were recorded in order to observe the effect of the solvent on the changes in molecular packing within the soft crystal/liquid crystal phase(s). All crystallized samples were freshly crystallized/precipitated from an MeCN solution and then dried under a stream of nitrogen gas and carefully transferred into aluminum crucibles. All dried samples were heated to 85 °C under vacuum for at least 8 h and then transferred into aluminum crucibles. All [2]rotaxanes showed polymorphism upon heating the crystallized samples, with additional peaks that were not observed upon subsequent heating of the crystallized samples and were never observed with the dried samples. This behaviour is a result of the materials ability to organize into an equilibrium state with increased fluidity upon increasing the temperature, which is supported by these additional transitions occurring at temperatures above 50 °C coinciding with melting of the aliphatic side chains (Figure 3.10).

Transition temperatures and calculated enthalpies are listed in Table 3.3 for the dried [2]rotaxanes. All showed glass transitions ( $T_g$ ) upon heating and were not resolved on cooling for **3-11**<sup>4+</sup> and **3-13**<sup>4+</sup> (Figure 3.11). Melting into the isotropic liquid was only observed for **3-13**<sup>4+</sup>, coinciding with what was observed by POM. The odd straight chain [2]rotaxane **3-9**<sup>4+</sup> showed thermally reversible melting transitions upon heating and crystallization transitions upon cooling centered at 21 °C, the largest with an enthalpy of 19.6 kJ/mol. Not surprisingly, the even straight chain [2]rotaxane **3-11**<sup>4+</sup> showed similar

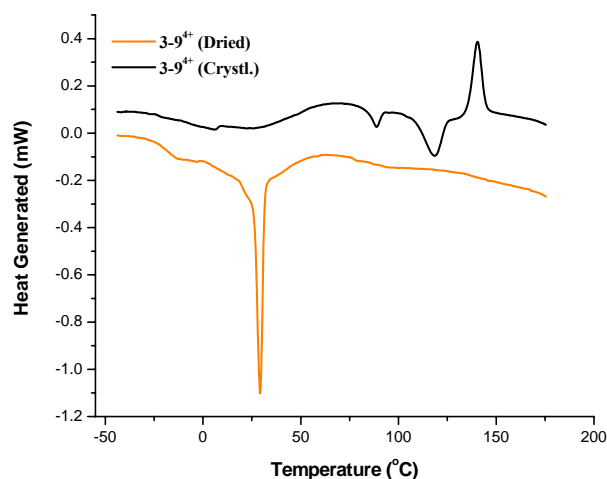


**Figure 3.10** - First heating DSC runs of freshly crystallized (black) and dried (orange) [2]rotaxane 3-9<sup>4+</sup> at a rate of 10 °C/min under N<sub>2</sub>.

transitions with the largest enthalpy of 34.7 kJ/mol, occurring at approximately the same temperature as 3-9<sup>4+</sup>. Small textural changes observed by POM for both 3-9<sup>4+</sup> and 3-11<sup>4+</sup> between 15 and 50 °C coincide with transitions observed by DSC.

**Table 3.3** - Transition temperatures (°C, midpoint) and enthalpies (kJ/mol) determined by DSC at scan rates of 10 °C/min for [2]rotaxanes.

Compound	2 <sup>nd</sup> Heating	Cooling
3-9 <sup>4+</sup>	-15 (T <sub>g</sub> )	-18 (T <sub>g</sub> )
	12.5 (-19.60)	17.8 (16.56)
	17.8 (-16.22)	21.9 (9.96)
		28.1 (5.96)
3-11 <sup>4+</sup>	16.4 (-34.75)	13.1 (31.81)
	35.2 (-5.18)	22.6 (2.44)
	83 (T <sub>g</sub> )	30.1 (3.06)
3-12 <sup>4+</sup>	67 (T <sub>g</sub> )	51 (T <sub>g</sub> )
	129.6 (6.53)	
	155.3 (-4.58)	
3-13 <sup>4+</sup>	74 (T <sub>g</sub> )	n.t.
	167.7 (-1.94)	

n.t. : no transition observed.

The branched [2]rotaxane **3-12<sup>4+</sup>** showed a broad reversible glass transition with the midpoint just over 50 °C. Only upon heating is there an exothermic transition at 129.6 °C with an enthalpy of 6.53 kJ/mol, followed by an endothermic transition at 155.3 °C with an enthalpy of 4.58 kJ/mol. The exothermic transition is a cold crystallization followed by the endothermic melting transition. Cold crystallization is a kinetic effect and occurs when the material does not have adequate time or mobility upon cooling from the isotropic liquid and hence does not fully crystallize. However upon heating, the material becomes mobile enough to crystallize further before the melting transition. These reversible transitions were confirmed by POM.

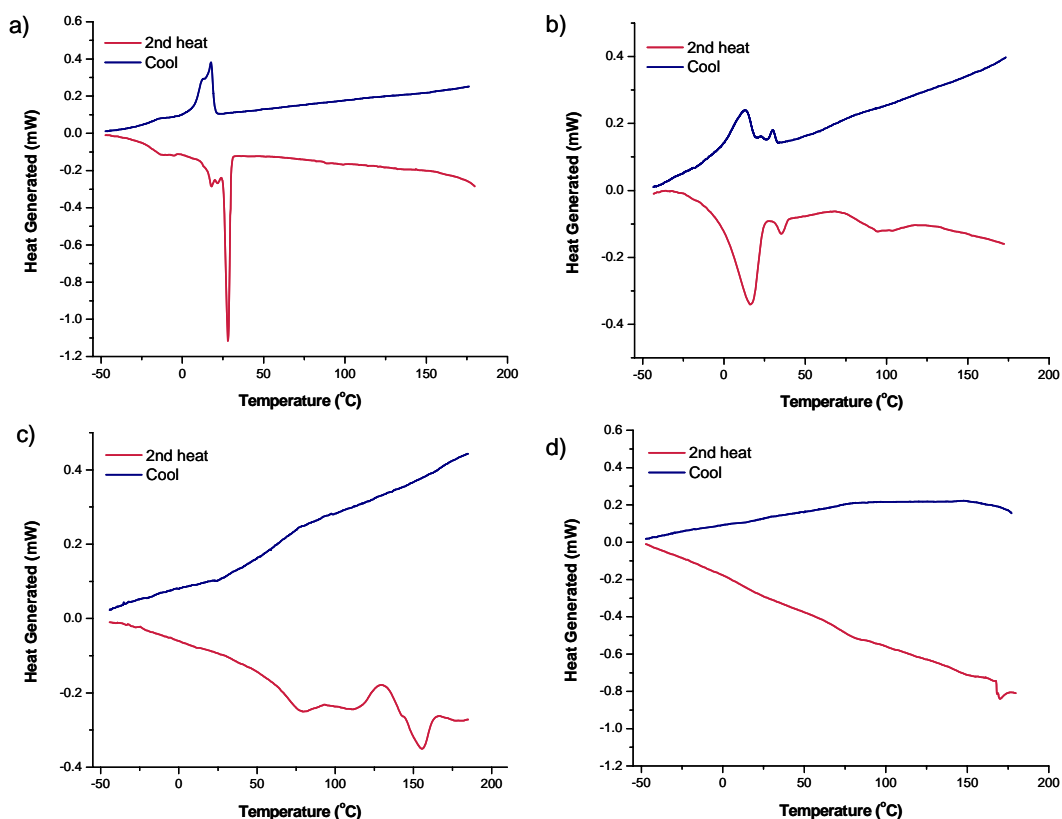


Figure 3.11 - Second heating and cool DSC runs of [2]rotaxanes a) **3-9<sup>4+</sup>**, b) **3-11<sup>4+</sup>**, c) **3-12<sup>4+</sup>** and d) **3-13<sup>4+</sup>** at 10 °C/min under N<sub>2</sub>.

### 3.3.4 Variable Temperature X-Ray Diffraction (vt-XRD)

Bulk samples for variable temperature X-ray diffraction (vt-XRD) were initially heated to 190 °C for [2]rotaxanes **3-9**<sup>4+</sup> and **3-11**<sup>4+</sup> and to the isotropic liquid for [2]rotaxanes **3-12**<sup>4+</sup> and **3-13**<sup>4+</sup> and then cooled back to room temperature in order to allow the materials to self-organize into thermally controlled states. Hence, data for vt-XRD were collected for the second heating and cooling in order to study their transitions. All [2]rotaxanes show intense small angle reflections between 47 and 32 Å which are attributed to the layer spacing of lamellar phases, several peaks between 16 and 10 Å which likely result from in-plane packing order as well as sharp or broad reflections between 6 and 4 Å which indicate a crystalline or amorphous state of the aliphatic chains. The results obtained from the vt-XRD coincide with that obtained from DSC and POM.

Large differences are observed in the reflections for the odd and even straight chain substituted [2]rotaxanes **3-9**<sup>4+</sup> and **3-11**<sup>4+</sup> (Figure 3.12a and 3.12b, respectively). The odd chain [2]rotaxane **3-9**<sup>4+</sup> forms a soft crystalline phase over the entire temperature range from -25 to 190 °C with a reflection of 45.1 Å with moderate intensity and a reflection of 32.7 Å with strong intensity in the small angle region. The phase was not investigated further for the determination of the structure. However, 45.1 Å agrees with the length of the molecule.

On the contrary, the even [2]rotaxane **3-11**<sup>4+</sup> forms an amorphous phase over the entire temperature range. A SmA phase is observed below 100 °C with a layer spacing of 46.6 Å and a second order reflection at 23.3 Å (Figure 3.12b). This layer spacing is in good agreement with the length of the molecule, and formation of approximately one molecule thick lamellar layers is proposed (Figure 3.12d). An additional mesophase is

observed above 100 °C with intense reflections in the small angle region at 46.5 and 55.3 Å. This unknown phase was not investigated further. However, both reflections are longer than the length of the molecule, suggesting that the phase is not lamellar. Hence, by increasing the length of the chain by only one carbon the ability of the molecules to adequately pack results in a smectic liquid crystal over the highly crystalline lamellar mesophase. Unfortunately, neither compound clears into the isotropic liquid before decomposition above 200 °C.

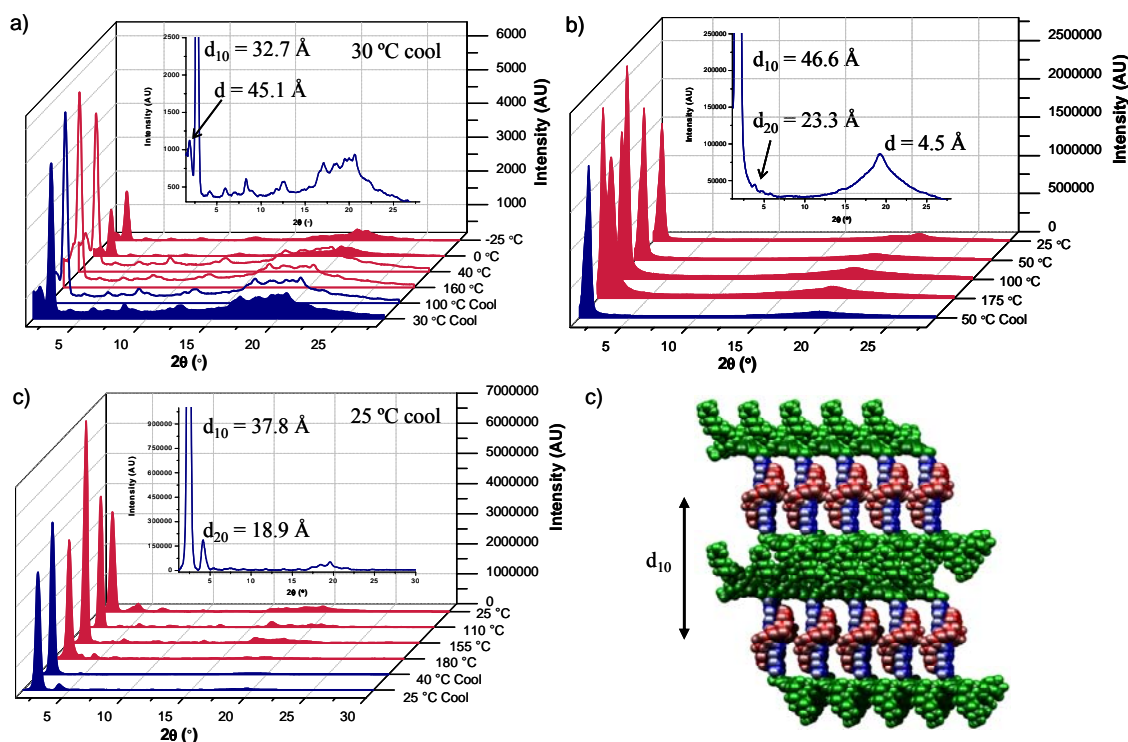


**Figure 3.12 - vt-XRD data for a) 3-9<sup>4+</sup>, b) 3-11<sup>4+</sup> and c) 3-12<sup>4+</sup>; d) molecular modeling (MM3) diagram showing self-organization of material into a SmA phase (alkyl chains were input in a disordered fashion to simulate packing.)**

The branched hexadecane substituted [2]rotaxane 3-12<sup>4+</sup> forms a highly ordered lamellar phase as indicated by the presence of a second order reflection ( $d_{20}$ ). The layer spacing is 37.8 Å with the second order peak at 18.9 Å (Figure 3.12c). This layer spacing is in good agreement with the length of the molecule and formation of one molecule thick



lamellar layers is proposed. The branching chains pack well enough to allow crystallization, with a small amount of crystallinity being observed over the entire temperature range between 6 and 4 Å. An amorphous smectic phase is only observed upon cooling from the isotropic liquid and is shown in Figure 3.12c at 40 °C upon cooling. This is a kinetic effect because crystallinity reoccurs in the side-chain region after several days at room temperature (Figure 3.12c, inset).

The introduction of a liquid hyperbranched chain (oxocol) was expected to avoid the crystallization of the side-chains due to the decreased likelihood that they could pack effectively. Surprisingly, this material was not only less fluid than [2]rotaxane **3-12<sup>4+</sup>**, but was highly crystalline over the entire temperature range (Figure 3.13b, inset). The structure may be lamellar because the smallest angle reflection with d-spacing of 36.8 Å has, by far, the highest intensity and this layer spacing agrees with the length of the molecule. None of these changes were observed by DSC but various textures were observed by POM coinciding with these changes observed by vt-XRD.

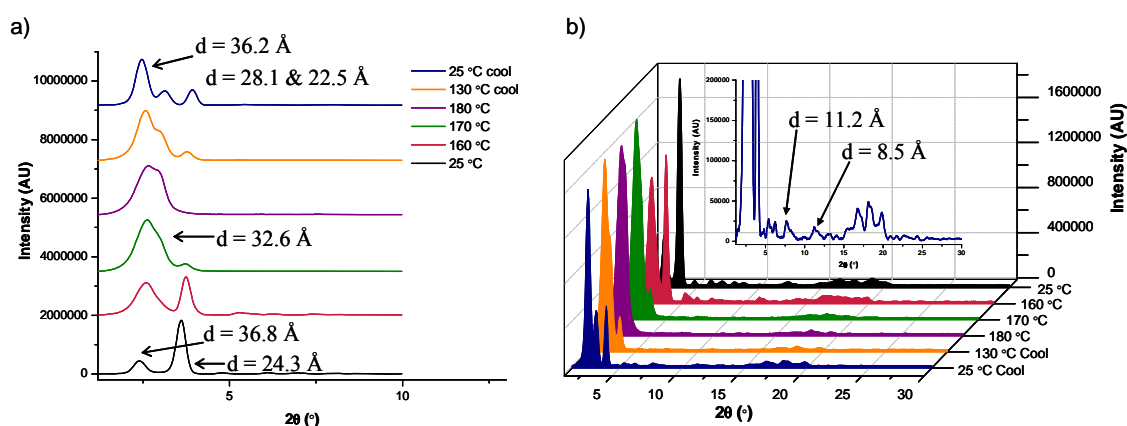
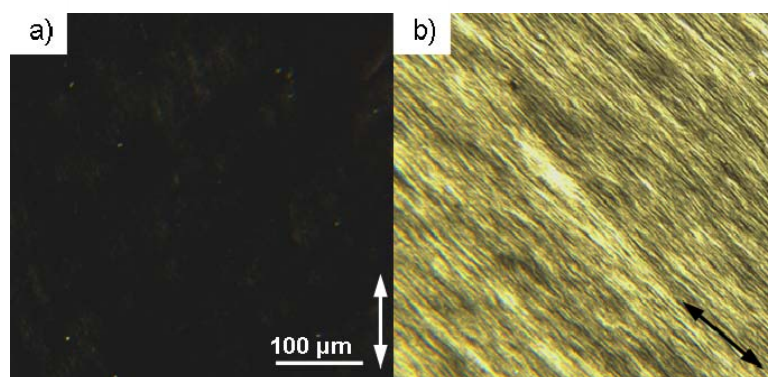


Figure 3.13 - vt-XRD data for 3-13<sup>4+</sup>, a) with layer spacing defined and b) with crystallinity defined.

### 3.3.5 Processing of LC Materials

Due to the high viscosity of the [2]rotaxanes and high degree of crystallinity in [2]rotaxanes **3-9<sup>4+</sup>** and **3-13<sup>4+</sup>**, alignment of these materials was not investigated. Since only **3-11<sup>4+</sup>** and **3-12<sup>4+</sup>** displayed lamellar phase behaviour, these were processed by applying shear force to determine the ease of alignment and relative viscosity compared to the highly viscous [2]rotaxane **2-17<sup>4+</sup>**. For a uniform planar SmA phase, the sample appears black when the optic axis is oriented along one of the polarizer directions, and maximum intensity is observed when the optic axis is oriented at 45° between polarizer and analyzer. Both [2]rotaxanes **3-11<sup>4+</sup>** and **3-12<sup>4+</sup>** were relatively fluid and mechanically sheared between glass slides at 150 and 160 °C respectively, producing partial alignment with many domains in the direction of the applied shear force, Figure 3.14a (arrow shows direction of shear force) and Figure 3.14b (rotated by 45°). This would suggest a forced SmA phase with a preferential orientation of the molecule long axis parallel to the substrate and layers oriented orthogonal to the substrate. In contrast, these materials were not as fluid as the [2]rotaxane **2-17<sup>4+</sup>** which was mechanically sheared at 120 °C, 30 to 40 °C lower with an obvious reduced viscosity.



**Figure 3.14 - POMs of 3-11<sup>4+</sup> a) shear alignment at 150 °C (in direction of arrow) and b) rotated by 45°.**

### 3.3.6 Calculated Packing Volumes and Molecular Lengths

Space filling calculations were performed to compare the molecular dimensions with the layer spacings obtained by XRD for [2]rotaxanes **3-9<sup>4+</sup>** and **3-11<sup>4+</sup>** through **3-13<sup>4+</sup>**. The layer spacings are comparable to the length of these molecules, and agree well with calculations based on amorphous side chains and space filling considerations. As mentioned in Chapter 2, the cylindrical volume of the [2]rotaxane core, with **DB24C8** macrocycle, including the four triflate anions is estimated to be 2400 Å<sup>3</sup>, based on a length of 27.4 Å and an average diameter of 10.6 Å. The length and average diameter of the cores were calculated based on the dimensions of the [2]rotaxane core in the single crystal structure and free rotation over the long axis of the molecule (Figure 2.8).

The volumes occupied by the side chains of the benzyl dicarboxylate units are calculated to be 1190, 1270, 1275 and 1360 Å<sup>3</sup>, for alkyl chains of 15, 16, 16 (branched) and 18 (hyperbranched) carbon atoms respectively, based on established packing volumes in liquid phases.<sup>135-136</sup> Based on these volumes and the diameters of the cores, the lengths of the cylindrical spaces occupied by the side chains of the benzyl dicarboxylate units were calculated and added to the length of the core (27.4 Å), giving reasonable agreement with the observed spacings for all four compounds (Table 3.4). Due to branching and hyperbranching of the chains, the calculated lengths are approximately 5 to 6 Å longer than the actual lengths of the molecules for [2]rotaxanes **3-12<sup>4+</sup>** and **3-13<sup>4+</sup>**, respectively. The molecular length for **3-9<sup>4+</sup>** was found to be 41 Å, but this crystalline phase is not likely a lamellar phase.

**Table 3.4 - Obtained (XRD) and calculated layer spacings of [2]rotaxanes 3-9<sup>4+</sup> and 3-11<sup>4+</sup> through 3-13<sup>4+</sup>.**

Compound	d <sub>10</sub> (Å)	l <sub>calc</sub> (Å)
3-9 <sup>4+</sup>	32.7	41
	45.1	
3-11 <sup>4+</sup>	46.6	42
3-12 <sup>4+</sup>	37.8	42
3-13 <sup>4+</sup>	36.2	43
	28.1	
	22.5	

These calculated molecular lengths confirm the likelihood of a SmA phase for 3-11<sup>4+</sup> (below 100 °C) and 3-12<sup>4+</sup>, since the tilted SmC layer spacing would be markedly shorter than the observed spacing. Consequently, the shorter observed layer spacings at 28.1 Å and 22.5 Å with larger layer spacing at 36.2 Å for 3-13<sup>4+</sup> could be lamellar in nature but the phase was not investigated further.

### 3.3.7 Liquid Crystal Phase Determination

The mesophases formed by [2]rotaxanes 3-9<sup>4+</sup> and 3-11<sup>2+</sup> through 3-13<sup>2+</sup> were fully characterized by POM observations, DSC analysis and vt-XRD analysis. The phase characterization and transition temperatures measured by POM and DSC on heating are shown in Figure 3.15. The aliphatic straight [2]rotaxanes 3-9<sup>4+</sup> and 3-11<sup>4+</sup> both showed similar transitions by DSC with melting transitions on heating at approximately 15 °C, however, by POM and vt-XRD there was no change at this temperature. Neither cleared into the isotropic liquid before decomposition occurring above 200 °C, with the odd chain [2]rotaxane 3-9<sup>4+</sup> forming an unidentified crystalline mesophase over the entire temperature range. The even chain [2]rotaxane formed a SmA phase, below 100 °C and a unidentified phase over 100 °C.

By applying a branching extension of the stoppers [2]rotaxane **3-12<sup>4+</sup>** did melt into the isotropic liquid at 193 °C, but there was a small amount of crystallinity in the side-chain region over the entire range by XRD until forming a SmA phase above 165 °C. The hyperbranched extended [2]rotaxane **3-13<sup>4+</sup>** showed similar behaviour, showing a high degree of crystallinity and was highly viscous and the phase was also designated as a lamellar soft crystal. The branching of the alkyl chains did lower the temperature for melting into the isotropic liquid for the [2]rotaxanes, over the straight chains, but they exhibited crystallinity in the side-chain region over their entire temperature range studied and showed increased viscosity. The initial decomposition for each compound is marked with a black line in Figure 3.15, with decomposition for all occurring above 200 °C.

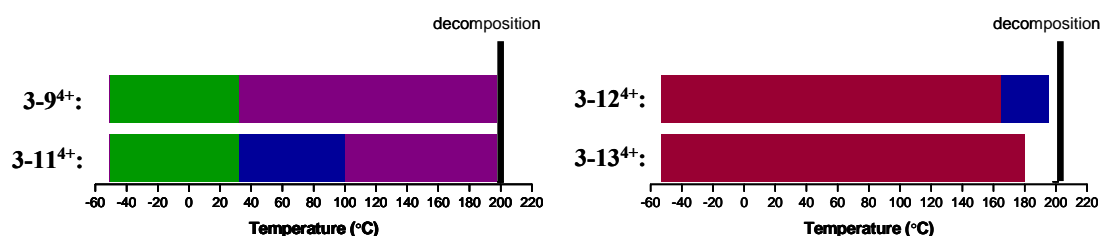


**Figure 3.15 - Phase transition temperatures for [2]rotaxanes 3-9<sup>4+</sup> and 3-11<sup>4+</sup> through 3-13<sup>4+</sup> measured by DSC and POM on heating. (green, crystalline; violet, unidentified mesophase; navy, SmA; maroon, lamellar soft crystal. The start of decomposition is marked with a black line.)**

### 3.4 SUMMARY AND CONCLUSIONS

A reduction in the viscosity of liquid crystalline [2]rotaxanes incorporating the (1,2-bis(dipyridinium)ethane)/DB24C8 pseudorotaxane motif by increasing the length of the aliphatic chains on the stopper, and by utilizing a branched and hyperbranched aliphatic chain was attempted. The odd straight chain substituted [2]rotaxane **3-9<sup>4+</sup>** was a soft crystalline material and its mesophase not identified. The even chain substituted [2]rotaxane **3-11<sup>4+</sup>** formed a SmA liquid crystal below 100 °C and an unidentified

amorphous mesophase above 100 °C, with the SmA phase being confirmed by POM and vt-XRD. The branched [2]rotaxane **3-12**<sup>4+</sup> formed a non-tilted lamellar phase with a small degree of crystallinity in the side-chain region with SmA phase above 165 °C. The hyperbranched [2]rotaxane **3-13**<sup>4+</sup> formed a lamellar crystalline mesophase. All showed slightly lower viscosity than [2]rotaxane **2-17**<sup>4+</sup> at high temperatures, but increasing the overall molecular weight increased the clearing temperatures into the isotropic liquid phase and the odd and even straight chain [2]rotaxanes **3-9**<sup>4+</sup> and **3-11**<sup>4+</sup> did not clear into the isotropic liquid phase before their decomposition temperatures. Due to the small reduction in viscosity, the fluidity was not markedly increased and alignment of these materials was not investigated.

This design is at the mercy of high viscosity and high clearing temperatures into the isotropic liquid with increasing size. These setbacks can be overcome by employing two different approaches. One approach would be to employ stoppers extended with functionalities that are typical in small molecule calamitic liquid crystals; that is, something other than purely aliphatic chains. The other approach would focus on increasing the thermal stability of the system by removing the thermally labile pyridinium benzylic bond which breaks above 200 °C. This requires new rotaxane designs which will be discussed in Chapter 4.

### 3.5 EXPERIMENTAL

#### 3.5.1 General Comments

Sodium trifluoromethanesulfonate, diethyl-5-(hydroxymethyl)-isophthalate, 1-pentadecanol, 1-hexadecanol, 2-hexyl-1-decanol, titanium isopropoxide, phosphorus tribromide, tetrabutyl ammonium iodide (TBAI) and **DB24C8** were purchased from Aldrich and used as received. 1-Octanol, 5,7,7-trimethyl-2-(1,3,3-trimethylbutane) (oxocol) was purchased from Nissan Chemical Industries and used as received. Deuterated solvents were obtained from Cambridge Isotope Laboratories and used as received. Solvents were dried using an Innovative Technologies Solvent Purification System. Thin layer chromatography (TLC) was performed using Teledyne Silica gel 60 F<sub>254</sub> plates and viewed under UV light. Column chromatography was performed using Silicycle Ultra Pure Silica Gel (230 – 400 mesh). Flash column chromatography was performed using Teledyne Ultra Pure Silica/RP-C<sub>18</sub> Silica Gel (230 – 400 mesh) on a Teledyne Isco Combiflash R<sub>f</sub>. All flash chromatography was performed under pressure (120 mL/min. - 200 mL/min.) for normal phase silica and (10 mL/min. - 40 mL/min.) for RP-C<sub>18</sub> silica, with increasing pressure corresponding to larger columns. Unless otherwise stated, all flash chromatography involved applied gradient elution from 0 - 100 % with increasing polar solvent with respect to less polar solvent. Length of column (column volumes - CV) were determined by separations on preliminary TLC runs. <sup>1</sup>H NMR, <sup>13</sup>C NMR and 2-D experiments were performed on a Brüker Avance 500 instrument, with working frequency of 500.13 MHz for <sup>1</sup>H nuclei, and 125.7 MHz for <sup>13</sup>C nuclei. Chemical shifts are quoted in ppm relative to tetramethylsilane, using the residual solvent peak as a reference standard. Conventional 2-D NMR experiments (<sup>1</sup>H-<sup>1</sup>H

COSY) and ( $^1\text{H}$ - $^{13}\text{C}$  HETCOR) were conducted and used to help assign all peaks. High resolution mass spectrometry (HR-MS) experiments were performed on a Micromass LCT Electrospray (ESI) time-of-flight (TOF) Mass Spectrometer. Solutions of 50-100 ng/ $\mu\text{L}$  were prepared in  $\text{CH}_3\text{CN}$  and injected for analysis at a rate of 5  $\mu\text{L}/\text{min}$  using a syringe pump. Thermal gravimetric analysis was conducted on a Mettler Toledo TGA SDTA 851e. Helium (99.99 %) was used to purge the system with a flow rate of 30 mL/min. Samples were held at 25  $^\circ\text{C}$  for 30 min before heated to 550  $^\circ\text{C}$  at 2  $^\circ\text{C}/\text{min}$ . A mass range between 16 m/z and 150 m/z was constantly scanned. All samples were run in aluminum crucibles. Powder XRD measurements were recorded on a Br $\ddot{u}$ ker D8 Discover diffractometer equipped with a Hi-Star area detector and GADDS software operated at 40 kV and 40 mA.  $\text{CuK}\alpha_1$  radiation ( $\lambda = 1.54187 \text{ \AA}$ ) was used and the initial beam diameter was 0.5 mm. A custom made Instec hot stage (based on HS-400) was used for vt-XRD that covers a temperature range of -40 to 350  $^\circ\text{C}$ . Bulk samples for variable temperature XRD were filled into a 2 mm diameter hole in a 1 mm thick copper plate. This plate was mounted in an Instec hot-stage, aligned, and run at theta angle 11 $^\circ$  for 60 min. Spectra were combined and evaluated in EVA and plotted with Origin. Polarized light microscopy was performed on an Olympus TPM51 polarized light microscope equipped with a Linkam variable temperature stage HCS410 and digital photographic imaging system (DITO1).



### 3.5.2 Synthesis of 3-1

Diethyl-5-(hydroxymethyl)-isophthalate (2.79 g, 0.0111 mol), 1-pentadecanol (20.21 g, 0.0885 mol), and  $\text{Ti}(\text{O-}i\text{-Pr})_4$  (4.71 g, 0.0166 mol) were heated (130 °C) under a nitrogen atmosphere for 3 days. The EtOH bi-product was removed via a Dean Stark apparatus. The solution was neutralized with 0.1 M HCl yielding a waxy solid which was then filtered and washed with  $\text{H}_2\text{O}$ . The solid was taken up in  $\text{CHCl}_3$ , dried with  $\text{MgSO}_4$ , filtered and concentrated to a white solid. The product was then purified by flash column chromatography on silica gel with ( $\text{CHCl}_3$ : MeOH) gradient (0 - 5 % MeOH) as eluant. The resulting white solid was collected. Yield: 5.94 g, 87 %.

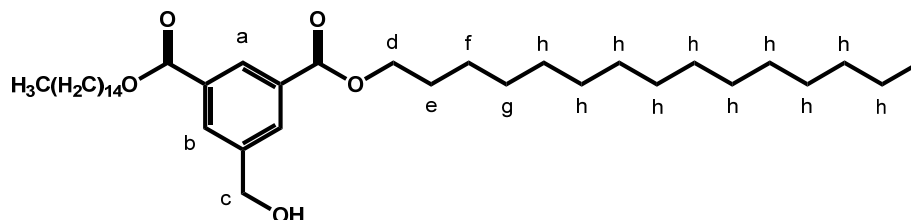


Table 3.5 –  $^1\text{H}$  NMR data of 3-1 in  $\text{CDCl}_3$ . MW= 616.954 g/mol

Proton	$\delta$ (ppm)	Multiplicity	# Protons	$J$ (Hz)
a	8.56	s	1	--
b	8.19	s	2	--
c	4.73	s	2	--
d	4.30	t	4	$^3J_{de} = 6.79$
e	1.75	tt	4	$^3J_{ed} = 6.79, ^3J_{ef} = 7.25$
f	1.52	tt	4	$^3J_{fe} = ^3J_{fg} = 7.25$
g	1.40	tt	4	$^3J_{gf} = ^3J_{gh} = 7.25$
h	1.25	m	40	--
i	0.85	t	6	$^3J_{hg} = 6.87$

## 3.5.3 Synthesis of 3-2

Diethyl-5-(hydroxymethyl)-isophthalate (3.00 g, 0.0119 mol), 1-hexadecanol (23.06 g, 0.0951 mol), and  $\text{Ti}(\text{O-}i\text{-Pr})_4$  (5.07 g, 0.0178 mol) were heated (130 °C) under a nitrogen atmosphere for 4 days. The EtOH bi-product was removed via a Dean Stark apparatus. The solution was neutralized with 0.1 M HCl yielding a waxy solid which was then filtered and washed with  $\text{H}_2\text{O}$ . The solid was taken up in  $\text{CHCl}_3$ , dried with  $\text{MgSO}_4$ , filtered and concentrated to a white solid. The product was then purified by flash column chromatography on silica gel with ( $\text{CHCl}_3$ : MeOH) gradient (0 - 5 % MeOH) as eluant. The resulting white solid was collected. Yield: 6.37 g, 83 %.

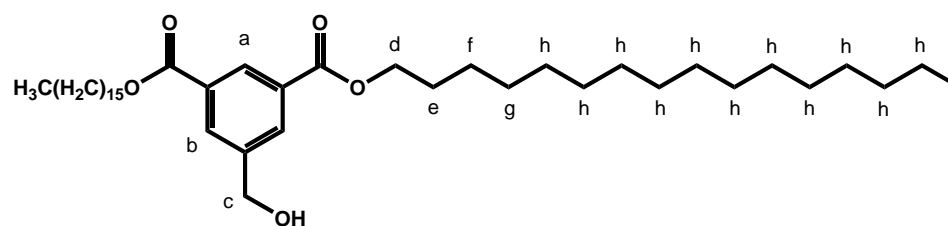


Table 3.6 –  $^1\text{H}$  NMR data of 3-2 in  $\text{CDCl}_3$ . MW= 645.441 g/mol

Proton	$\delta$ (ppm)	Multiplicity	# Protons	$J$ (Hz)
a	8.56	s	1	--
b	8.24	s	2	--
c	4.83	s	2	--
d	4.33	t	4	$^3J_{de} = 6.74$
e	1.77	tt	4	$^3J_{ed} = 6.74, ^3J_{ef} = 7.66$
f	1.44	tt	4	$^3J_{fe} = ^3J_{fg} = 7.66$
g	1.33	tt	4	$^3J_{gf} = ^3J_{gh} = 7.25$
h	1.25	m	44	--
i	0.85	t	6	$^3J_{hg} = 6.91$

### 3.5.4 Synthesis of 3-3

Diethyl-5-(hydroxymethyl)-isophthalate (3.00 g, 0.0115 mol), 2-hexyl-1-decanol (11.18 g, 0.0461 mol), and  $\text{Ti}(\text{O-}i\text{-Pr})_4$  (6.55 g, 0.0231 mol) were heated (130 °C) under a nitrogen atmosphere for 3 days. The EtOH bi-product was removed via a Dean Stark apparatus. The solution was neutralized with 0.1 M HCl yielding a waxy solid which was then filtered and washed with  $\text{H}_2\text{O}$ . The solid was taken up in  $\text{CHCl}_3$ , dried with  $\text{MgSO}_4$ , filtered and concentrated to a white solid. The product was then purified by flash column chromatography on silica gel with ( $\text{CHCl}_3$ : MeOH) gradient (0 - 5 % MeOH) as eluant. The resulting white solid was collected. Yield: 6.92 g, 93 %.

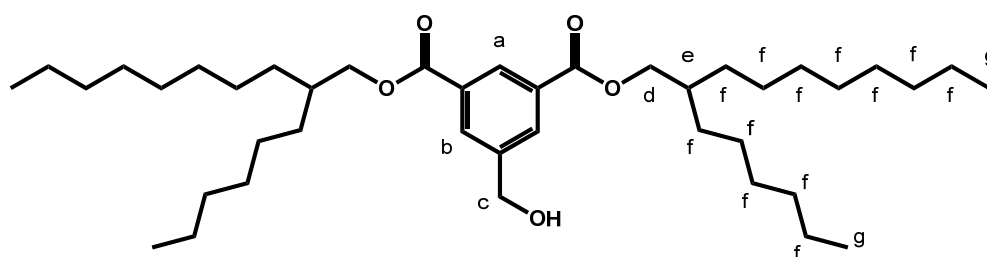
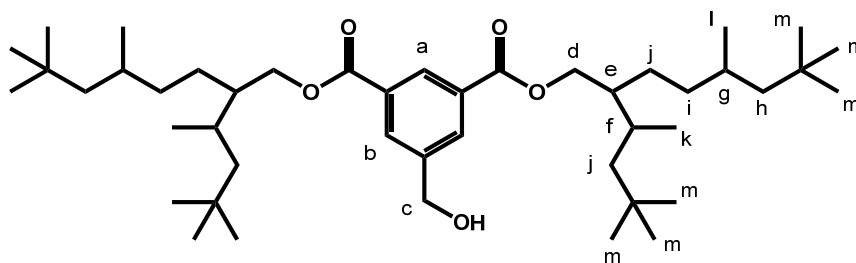


Table 3.7 –  $^1\text{H}$  NMR data of 3-3 in  $\text{CDCl}_3$ . MW= 645.007 g/mol

Proton	$\delta$ (ppm)	Multiplicity	# Protons	$J$ (Hz)
a	8.61	s	1	--
b	8.22	s	2	--
c	4.77	s	2	--
d	4.25	d	4	$^3J_{de} = 5.54$
e	1.78	tt	4	$^3J_{ed} = 5.54, ^3J_{ef} = 5.68$
f	1.37	m	48	--
g	0.86	t	6	$^3J_{fg} = 5.51$

### 3.5.5 Synthesis of 3-4

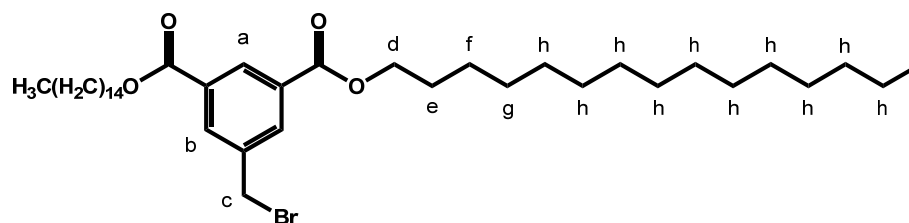
Diethyl-5-(hydroxymethyl)-isophthalate (3.00 g, 0.0115 mol), 1-oxocol (24.95 g, 0.0922 mol), and Ti(O-*i*-Pr)<sub>4</sub> (4.91 g, 0.0173 mol) were heated (130 °C) under a nitrogen atmosphere for 3 days. The EtOH bi-product was removed via a Dean Stark apparatus. The solution was neutralized with 0.1 M HCl yielding a waxy solid which was then filtered and washed with H<sub>2</sub>O. The solid was taken up in CHCl<sub>3</sub>, dried with MgSO<sub>4</sub>, filtered and concentrated to a white solid. The product was then purified by flash column chromatography on silica gel with (CHCl<sub>3</sub>: MeOH) gradient (0 - 5 % MeOH) as eluant. The resulting white solid was collected. Yield: 5.82 g, 72 %.

Table 3.8 –  $^1\text{H}$  NMR data of 3-4 in  $\text{CDCl}_3$ . MW= 701.114 g/mol

Proton	$\delta$ (ppm)	Multiplicity	# Protons	$J$ (Hz)
a	8.56	s	1	--
b	8.22	s	2	--
c	4.79	s	2	--
d	4.25	m	2	--
e	1.83	m	1	--
f	1.71	m	1	--
g	1.40	m	1	--
h	1.12	m	2	--
i	1.23	m	2	--
j	1.44	m	2	--
k	0.97	m	3	--
l	0.91	m	3	--
m	0.88	m	18	--

**3.5.6 Synthesis of 3-5**

**3-1** (3.50 g, 0.0057 mol) was dissolved in THF (100 mL) under nitrogen and cooled (0 °C) on ice. Phosphorus tribromide (4.25 mL, 0.0043 mol) 1.0 M in CH<sub>2</sub>Cl<sub>2</sub> was added dropwise over 15 min and stirring continued overnight. The solution was concentrated and recrystallized from MeOH. Product purified by flash column chromatography on silica gel with (hexanes: CH<sub>2</sub>Cl<sub>2</sub>) gradient (30 - 100% CH<sub>2</sub>Cl<sub>2</sub>) as eluant. The resulting white solid, was collected. Yield: 2.91 g, 75 %.

Table 3.9 –  $^1\text{H}$  NMR data of 3-5 in  $\text{CDCl}_3$ . MW= 679.851 g/mol

Proton	$\delta$ (ppm)	Multiplicity	# Protons	$J$ (Hz)
a	8.59	s	1	--
b	8.23	s	2	--
c	4.54	s	2	--
d	4.34	t	4	$^3J_{de} = 6.76$
e	1.78	tt	4	$^3J_{ed} = ^3J_{ef} = 7.10$
f	1.43	tt	4	$^3J_{fe} = ^3J_{fg} = 7.10$
g	1.31	m	44	--
h	0.87	t	6	$^3J_{hg} = 6.93$

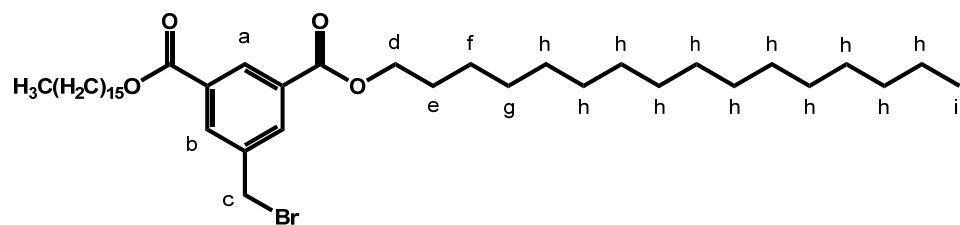
Table 3.10 –  $^1\text{H}$  NMR data of 3-5 in  $\text{CD}_3\text{CN}$ . MW= 679.851 g/mol

Proton	$\delta$ (ppm)	Multiplicity	# Protons	$J$ (Hz)
a	8.47	s	1	--
b	8.25	s	2	--
c	4.68	s	2	--
d	4.33	t	4	$^3J_{de} = 6.70$
e	1.67	tt	4	$^3J_{ed} = 6.70, ^3J_{ef} = 7.30$
f	1.44	tt	4	$^3J_{fe} = ^3J_{fg} = 7.30$
g	1.32	m	20	--
h	0.87	t	6	$^3J_{hg} = 6.70$

**3.5.7 Synthesis of 3-6**

**3-2** (3.67 g, 0.0057 mol) was dissolved in THF (150 mL) under nitrogen and cooled (0 °C) on ice. Phosphorus tribromide (4.28 mL, 0.0043 mol) 1.0 M in CH<sub>2</sub>Cl<sub>2</sub> was added dropwise over 15 min and stirring continued overnight. The solution was concentrated and recrystallized from MeOH. Product purified by flash column chromatography on silica gel with (hexanes: CH<sub>2</sub>Cl<sub>2</sub>) gradient (30 - 100 % CH<sub>2</sub>Cl<sub>2</sub>) as eluant. The resulting white waxy solid was collected. Yield: 3.50 g, 87 %.



Table 3.11 –  $^1\text{H}$  NMR data of 3-6 in  $\text{CDCl}_3$ . MW= 707.904 g/mol

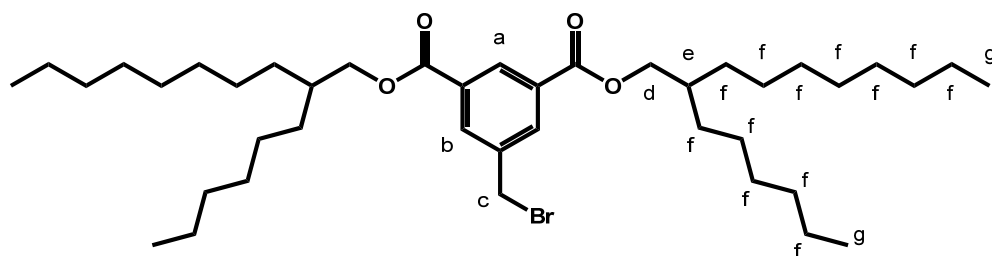
Proton	$\delta$ (ppm)	Multiplicity	# Protons	$J$ (Hz)
a	8.59	s	1	--
b	8.23	s	2	--
c	4.54	s	2	--
d	4.34	t	4	$^3J_{de} = 6.75$
e	1.78	tt	4	$^3J_{ed} = ^3J_{ef} = 7.37$
f	1.42	m	4	--
g	1.31	m	48	--
h	0.86	t	6	$^3J_{hg} = 6.90$

Table 3.12 –  $^1\text{H}$  NMR data of 3-6 in  $\text{CD}_3\text{CN}$ . MW= 707.904 g/mol

Proton	$\delta$ (ppm)	Multiplicity	# Protons	$J$ (Hz)
a	8.47	s	1	--
b	8.25	s	2	--
c	4.68	s	2	--
d	4.33	t	4	$^3J_{de} = 6.70$
e	1.67	tt	4	$^3J_{ed} = 6.70, ^3J_{ef} = 7.30$
f	1.44	tt	4	$^3J_{fe} = ^3J_{fg} = 7.30$
g	1.32	m	48	--
h	0.87	t	6	$^3J_{hg} = 6.70$

**3.5.8 Synthesis of 3-7**

**3-3** (4.53 g, 0.0070 mol) was dissolved in THF (175 mL) under nitrogen and cooled (0 °C) on ice. Phosphorus tribromide (5.27 mL, 0.0053 mol) 1.0 M in CH<sub>2</sub>Cl<sub>2</sub> was added dropwise over 15 min and stirring continued overnight. The solution was concentrated and product was purified by column chromatography on silica gel with (hexanes: CH<sub>2</sub>Cl<sub>2</sub>) gradient (30 - 100 % CH<sub>2</sub>Cl<sub>2</sub>) as eluant. The resulting beige oil was collected. Yield: 3.78 g, 76 %.

Table 3.13 –  $^1\text{H}$  NMR data of 3-7 in  $\text{CDCl}_3$ . MW= 707.904 g/mol

Proton	$\delta$ (ppm)	Multiplicity	# Protons	$J$ (Hz)
a	8.58	s	1	--
b	8.23	s	2	--
c	4.54	s	2	--
d	4.26	d	4	$^3J_{de} = 5.68$
e	1.78	ttt	2	$^3J_{ed} = ^3J_{ef} = 8.61$
f	1.33	m	48	--
g	0.88	t	6	$^3J_{hg} = 9.85$

Table 3.14 –  $^1\text{H}$  NMR data of 3-7 in  $\text{CD}_3\text{CN}$ . MW= 707.904 g/mol

Proton	$\delta$ (ppm)	Multiplicity	# Protons	$J$ (Hz)
a	8.47	s	1	--
b	8.25	s	2	--
c	4.68	s	2	--
d	4.33	d	4	$^3J_{de} = 6.70$
e	1.67	ttt	2	$^3J_{ed} = 6.70, ^3J_{ef} = 7.30$
f	1.44	m	48	--
h	0.87	t	6	$^3J_{hg} = 6.70$

## 3.5.9 Synthesis of 3-8

**3-4** (5.78 g, 0.0082 mol) was dissolved in THF (200 mL) under nitrogen and cooled (0 °C) on ice. Phosphorus tribromide (6.18 mL, 0.0062 mol) 1.0 M in CH<sub>2</sub>Cl<sub>2</sub> was added dropwise over 15 min and stirring continued overnight. The solution was concentrated and product was purified by column chromatography on silica gel with (hexanes: CH<sub>2</sub>Cl<sub>2</sub>) gradient (30 - 100 % CH<sub>2</sub>Cl<sub>2</sub>) as eluant. The resulting pale yellow oil was collected. Yield: 4.03 g, 64 %.

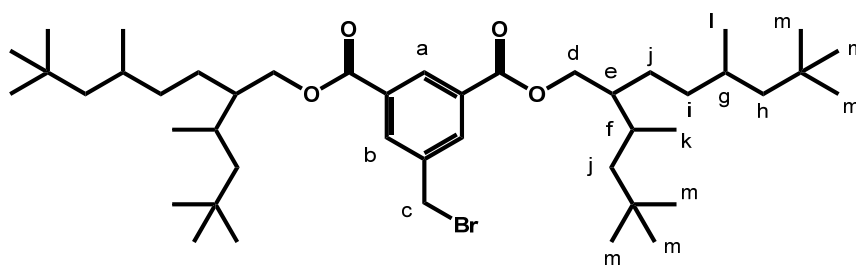


Table 3.15 – <sup>1</sup>H NMR data of 3-8 in CDCl<sub>3</sub>. MW= 764.010 g/mol

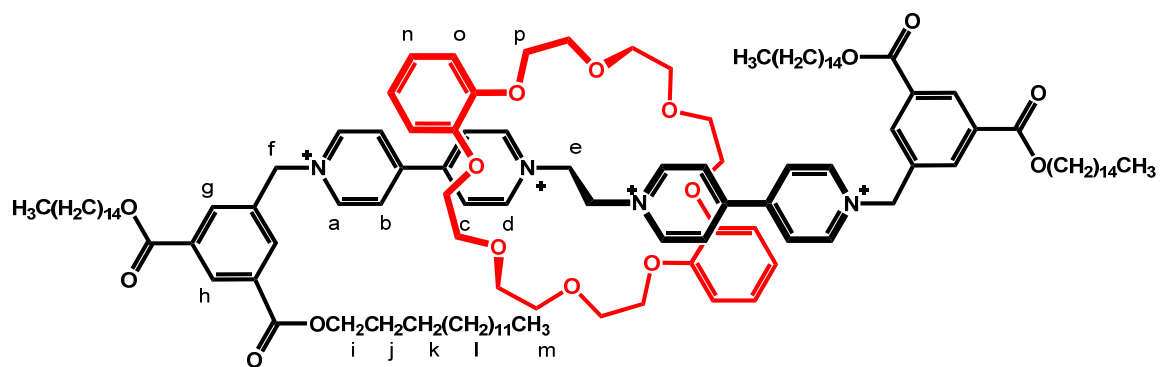
Proton	δ (ppm)	Multiplicity	# Protons	J (Hz)
a	8.60	s	1	--
b	8.23	s	2	--
c	4.53	s	2	--
d	4.26	m	4	--
e	1.83	m	2	--
f	1.69	m	2	--
g	1.39	m	2	--
h	1.11	m	4	--
i	1.23	m	4	--
j	1.42	m	8	--
k	0.96	m	6	--
l	0.90	m	6	--
m	0.87	m	36	--

Table 3.16 –  $^1\text{H}$  NMR data of 3-8 in  $\text{CD}_3\text{CN}$ . MW= 764.010 g/mol

Proton	$\delta$ (ppm)	Multiplicity	# Protons	$J$ (Hz)
<b>a</b>	8.60	s	1	--
<b>b</b>	8.23	s	2	--
<b>c</b>	4.53	s	2	--
<b>d</b>	4.26	m	4	--
<b>e</b>	1.83	m	2	--
<b>f</b>	1.69	m	2	--
<b>g</b>	1.39	m	2	--
<b>h</b>	1.11	m	4	--
<b>i</b>	1.23	m	4	--
<b>j</b>	1.42	m	8	--
<b>k</b>	0.96	m	6	--
<b>l</b>	0.90	m	6	--
<b>m</b>	0.87	m	36	--

### 3.5.10 Synthesis of [3-9][OTf]<sub>4</sub> and [3-10][OTf]<sub>4</sub>

[2-2][OTf]<sub>2</sub> (271.0 mg, 0.424 mmol) and **DB24C8** (952.0 mg, 2.122 mmol) were dissolved in a two-phase NaOTf (aq)/MeNO<sub>2</sub> (1 and 35 mL) mixture and placed in a thick-walled 80 mL reaction vessel. **3-5** (1.15 g, 1.697 mmol) was dissolved in CHCl<sub>3</sub> (45 mL) and a catalytic amount of TBAI (10 mg) was added to 80 mL vessel with stir bar and microwaved for 30 h at 60 °C. The MeNO<sub>2</sub> was washed with H<sub>2</sub>O (3 x 10 mL), dried over MgSO<sub>4</sub> and the solvent removed. The residue was stirred in cold MeCN, solid filtered off and remaining solution concentrated. The orange residue was dissolved in cold EtOAc, solid filtered off and remaining solution concentrated. The orange residue was dissolved in cold toluene, solid filtered off and remaining solution concentrated. Product **3-9**<sup>4+</sup> was purified and isolated by flash column chromatography on RP-C<sub>18</sub> silica gel using MeOH as eluant, yielding a red soft solid. Yield: 581.5 mg, 53 %. **ESI-MS**: *m/z* 1142.6447 (calc.) for C<sub>126</sub>H<sub>186</sub>F<sub>6</sub>N<sub>4</sub>O<sub>22</sub>S<sub>2</sub> [M-2OTF]<sup>2+</sup>, found 1142.6486. *m/z* 712.1123 (calc.) for C<sub>125</sub>H<sub>186</sub>F<sub>3</sub>N<sub>4</sub>O<sub>19</sub>S [M-OTF]<sup>3+</sup>, found 712.1154. *m/z* 496.8461 (calc.) for C<sub>124</sub>H<sub>186</sub>N<sub>4</sub>O<sub>16</sub> [M]<sup>4+</sup>, found 496.8460. The dumbbell **3-10**<sup>4+</sup> (without **DB24C8** macrocycle) was also isolated from the column. The product was isolated as a waxy pale beige solid. Yield: 72.48 mg, 8 %. **ESI-MS**: *m/z* 918.5398 (calc.) for C<sub>102</sub>H<sub>154</sub>F<sub>6</sub>N<sub>4</sub>O<sub>14</sub>S<sub>2</sub> [M-2OTF]<sup>2+</sup>, found 918.5396, *m/z* 562.7090 (calc.) for C<sub>101</sub>H<sub>154</sub>F<sub>3</sub>N<sub>4</sub>O<sub>11</sub>S [M-OTF]<sup>3+</sup>, found 562.7088.

Table 3.17 –  $^1\text{H}$  NMR data of [3-9][OTf] $_4$  in  $\text{CD}_3\text{CN}$ .  $\text{MW}_{\text{OTf}} = 2585.097$  g/mol

Proton	$\delta$ (ppm)	Multiplicity	# Protons	$J$ (Hz)
<b>a</b>	9.01	d	4	$^3J_{ab} = 6.85$
<b>b</b>	8.22	d	4	$^3J_{ba} = 6.85$
<b>c</b>	8.26	d	4	$^3J_{cd} = 6.85$
<b>d</b>	9.33	d	4	$^3J_{dc} = 6.85$
<b>e</b>	5.61	s	4	--
<b>f</b>	5.98	s	4	--
<b>g</b>	8.40	s	4	--
<b>h</b>	8.65	s	2	--
<b>i</b>	4.35	t	8	$^3J_{ij} = 6.58$
<b>j</b>	1.78	tt	8	$^3J_{ji} = ^3J_{jk} = 7.41$
<b>k</b>	1.45	tt	8	$^3J_{kj} = ^3J_{kl} = 7.41$
<b>l</b>	1.32	m	88	--
<b>m</b>	0.87	t	12	$^3J_{ml} = 6.88$
<b>n</b>	6.43	dd	4	$^3J_{\text{meta}} = 3.63$ ; $^3J_{\text{ortho}} = 5.90$
<b>o</b>	6.65	dd	4	$^3J_{\text{meta}} = 3.63$ ; $^3J_{\text{ortho}} = 5.90$
<b>p</b>	4.01	m	24	--

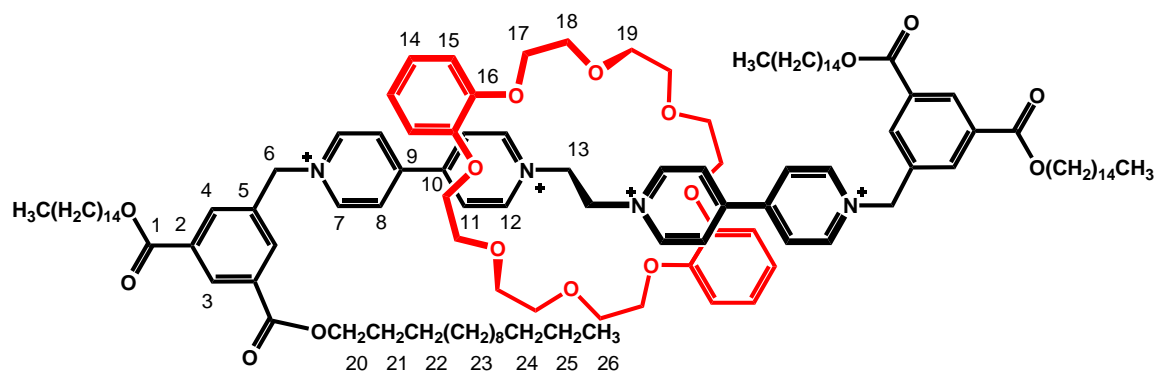


Table 3.18 –  $^{13}\text{C}$  NMR data of [3-9][OTf]<sub>4</sub> in CD<sub>3</sub>CN. MW<sub>OTf</sub> = 2585.097 g/mol. Quaternary carbons assigned by software

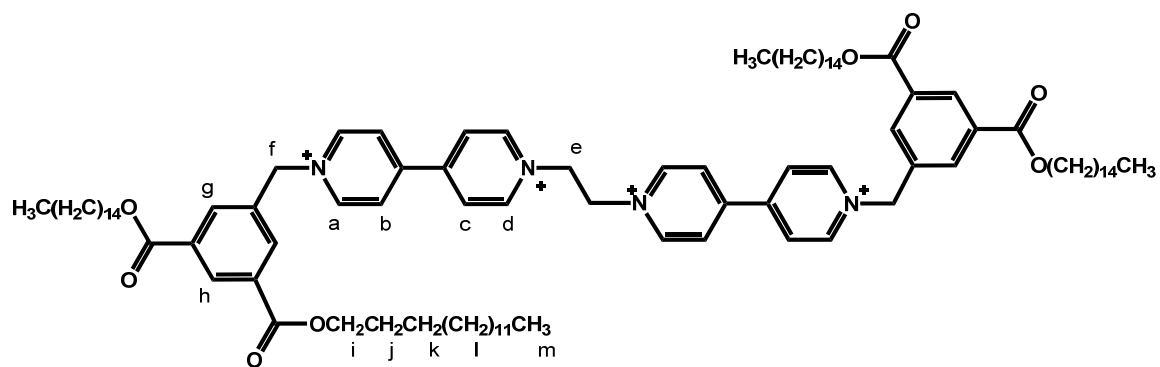
Carbon	$\delta$ (ppm)	# Carbons
1	164.86	4
2	132.53	4
3	131.11	2
4	134.52	4
5	133.94	2
6	63.64	2
7	145.82	4
8	127.25	4
9	149.31	2
10	148.90	2
11	126.03	4
12	147.14	4
13	58.49	2
14	121.55	4
15	112.61	4
16	146.89	4
17	67.68	4
18	70.29	4
19	70.65	4
20	65.83	4
21	28.41	4
22	25.81	4
23	29.47	4
24	31.74	4



---

<b>25</b>	22.49	32
<b>26</b>	13.50	4

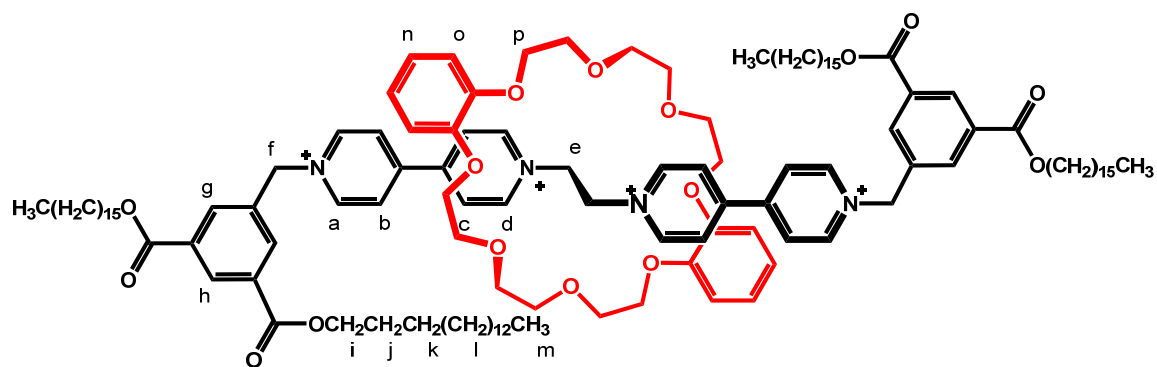
---

Table 3.19 –  $^1\text{H}$  NMR data of [3-10][OTf] $_4$  in  $\text{CD}_3\text{CN}$ .  $\text{MW}_{\text{OTf}} = 2134.985$  g/mol

Proton	$\delta$ (ppm)	Multiplicity	# Protons	$J$ (Hz)
<b>a</b>	9.07	d	4	$^3J_{ab} = 6.81$
<b>b</b>	8.46	d	4	$^3J_{ba} = 6.81$
<b>c</b>	8.49	d	4	$^3J_{cd} = 6.81$
<b>d</b>	9.01	d	4	$^3J_{dc} = 6.81$
<b>e</b>	5.29	s	4	--
<b>f</b>	5.96	s	4	--
<b>g</b>	8.38	s	4	--
<b>h</b>	8.67	s	2	--
<b>i</b>	4.33	t	8	$^3J_{ij} = 6.60$
<b>j</b>	1.76	tt	8	$^3J_{ji} = ^3J_{jk} = 7.39$
<b>k</b>	1.44	tt	8	$^3J_{kj} = ^3J_{kl} = 7.39$
<b>l</b>	1.32	m	88	--
<b>m</b>	0.88	t	12	$^3J_{ml} = 6.86$

### 3.5.11 Synthesis of [3-11][OTf]<sub>4</sub>

[2-2][OTf]<sub>2</sub> (257.5 mg, 0.403 mmol) and **DB24C8** (1.44 g, 3.226 mmol) were dissolved in a two-phase NaOTf (aq)/MeNO<sub>2</sub> (1 and 35 mL) mixture and placed in a thick-walled 80 mL reaction vessel. **3-6** (910.0 mg, 1.613 mmol) was dissolved in CHCl<sub>3</sub> (45 mL) and a catalytic amount of TBAI (10 mg) was added to 80 mL vessel with stir bar and microwaved for 20 h at 50 °C. The MeNO<sub>2</sub> was washed with H<sub>2</sub>O (3 x 10 mL), dried over MgSO<sub>4</sub> and the solvent removed. The residue was stirred in cold MeCN, solid filtered off and remaining solution concentrated. The orange residue was dissolved in cold EtOAc, solid filtered off and remaining solution concentrated. The orange residue was dissolved in cold toluene, solid filtered off and remaining solution concentrated. Product was purified and isolated by flash column chromatography on RP-C<sub>18</sub> silica gel using MeOH as eluant, yielding a red soft solid. Yield: 532.5 mg, 50 %. **ESI-MS:** *m/z* 730.7998 (calc.) for C<sub>129</sub>H<sub>194</sub>F<sub>3</sub>N<sub>4</sub>O<sub>19</sub>S [M-OTf]<sup>3+</sup>, found 730.7989. *m/z* 510.8617 (calc.) for C<sub>128</sub>H<sub>194</sub>N<sub>4</sub>O<sub>16</sub> [M]<sup>4+</sup>, found 510.8642.

Table 3.20 –  $^1\text{H}$  NMR data of [3-11][OTf]<sub>4</sub> in CD<sub>3</sub>CN. MW<sub>OTf</sub> = 2641.204 g/mol

Proton	$\delta$ (ppm)	Multiplicity	# Protons	$J$ (Hz)
<b>a</b>	8.98	d	4	$^3J_{ab} = 6.54$
<b>b</b>	8.17	d	4	$^3J_{ba} = 6.54$
<b>c</b>	8.21	d	4	$^3J_{cd} = 6.54$
<b>d</b>	9.31	d	4	$^3J_{dc} = 6.54$
<b>e</b>	5.60	s	4	--
<b>f</b>	5.97	s	4	--
<b>g</b>	8.39	s	4	--
<b>h</b>	8.65	s	2	--
<b>i</b>	4.35	t	8	$^3J_{ij} = 6.58$
<b>j</b>	1.78	tt	8	$^3J_{ji} = ^3J_{jk} = 7.36$
<b>k</b>	1.42	tt	8	$^3J_{kj} = ^3J_{kl} = 7.36$
<b>l</b>	1.33	m	96	--
<b>m</b>	0.88	t	12	$^3J_{ml} = 6.89$
<b>n</b>	6.43	dd	4	$^3J_{meta} = 3.61; ^3J_{ortho} = 5.87$
<b>o</b>	6.64	dd	4	$^3J_{meta} = 3.61; ^3J_{ortho} = 5.87$
<b>p</b>	4.04	m	24	--

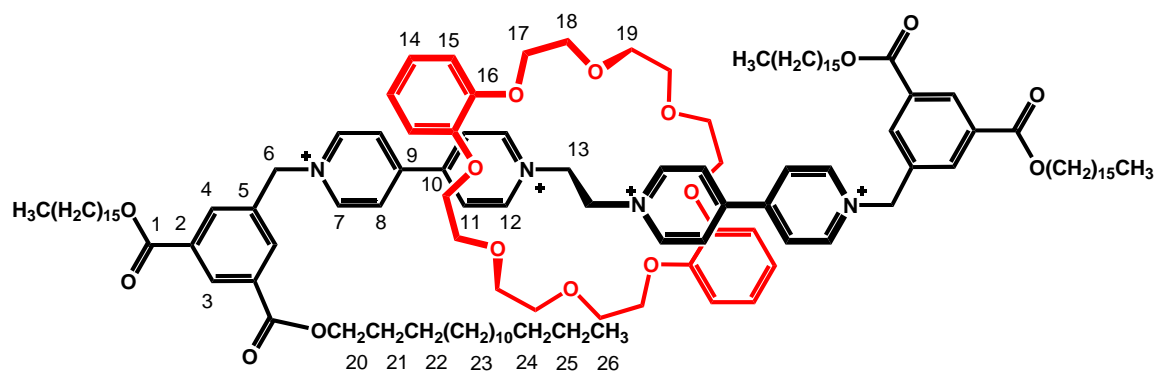


Table 3.21 - <sup>13</sup>C NMR data of [3-11][OTf]<sub>4</sub> in CD<sub>3</sub>CN. MW<sub>OTf</sub> = 2641.204 g/mol. Quaternary Carbons assigned by software

Carbon	δ (ppm)	# Carbons
1	164.83	4
2	132.51	4
3	131.09	2
4	134.50	4
5	135.98	2
6	63.61	2
7	145.80	4
8	127.22	4
9	149.31	2
10	149.23	2
11	126.05	4
12	147.12	4
13	58.41	2
14	121.52	4
15	112.57	4
16	146.86	4
17	67.65	4
18	70.25	4
19	70.61	4
20	65.82	4
21	28.39	4
22	25.80	4
23	29.46	40
24	31.34	4

---

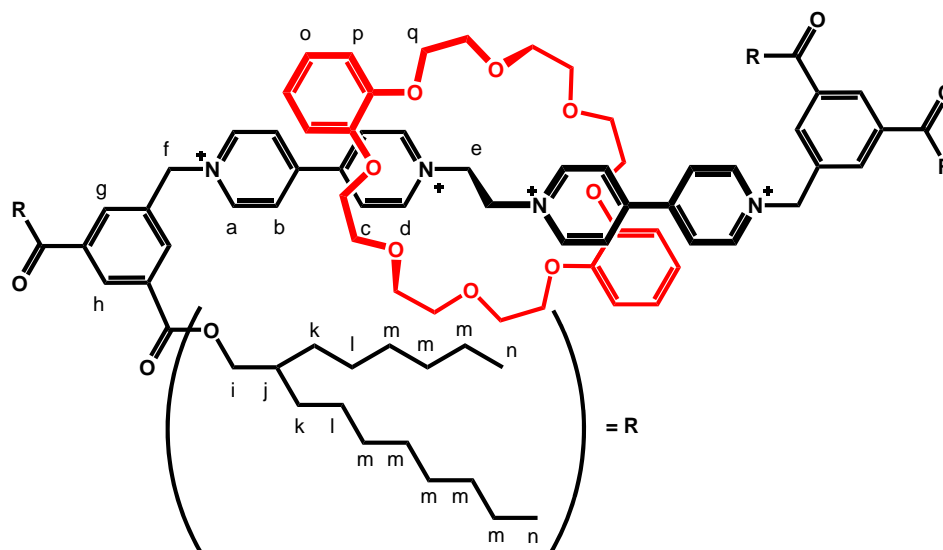
<b>25</b>	22.49	4
<b>26</b>	13.50	4

---

### 3.5.12 Synthesis of [3-12][OTf]<sub>4</sub>

[2-2][OTf]<sub>2</sub> (197.0 mg, 0.309 mmol) and **DB24C8** (1.11 g, 2.468 mmol) were dissolved in a two-phase NaOTf (aq)/MeNO<sub>2</sub> (1 and 25 mL) mixture and placed in a thick-walled 80 mL reaction vessel. **3-7** (875.0 mg, 1.234 mmol) was dissolved in CHCl<sub>3</sub> (20 mL) and a catalytic amount of TBAI (10 mg) was added to 80 mL vessel with stir bar and microwaved for 25 h at 50 °C. The MeNO<sub>2</sub> was washed with H<sub>2</sub>O (3 x 10 mL), dried over MgSO<sub>4</sub> and the solvent removed. The residue was stirred in cold MeCN, solid filtered off and remaining solution concentrated. The orange residue was dissolved in cold EtOAc, solid filtered off and remaining solution concentrated. The orange residue was dissolved in cold toluene, solid filtered off and remaining solution concentrated. Product was purified and isolated by flash column chromatography on RP-C<sub>18</sub> silica gel using MeOH as eluant, yielding a bright red/orange brittle solid. Yield: 480.7 mg, 59 %.

**ESI-MS:** *m/z* 1170.6760 (calc.) for C<sub>130</sub>H<sub>194</sub>F<sub>6</sub>N<sub>4</sub>O<sub>22</sub>S<sub>2</sub> [M-2OTF]<sup>2+</sup>, found 1170.6970.  
*m/z* 730.7998 (calc.) for C<sub>129</sub>H<sub>194</sub>F<sub>3</sub>N<sub>4</sub>O<sub>19</sub>S [M-OTF]<sup>3+</sup>, found 730.8020.

Table 3.22 -  $^1\text{H}$  NMR data of [3-12][OTf] $_4$  in  $\text{CD}_3\text{CN}$ .  $\text{MW}_{\text{OTf}^-} = 2641.204$  g/mol

Proton	$\delta$ (ppm)	Multiplicity	# Protons	$J$ (Hz)
a	9.06	d	4	$^3J_{ab} = 6.76$
b	8.33	d	4	$^3J_{ba} = 6.76$
c	8.31	d	4	$^3J_{cd} = 6.76$
d	9.34	d	4	$^3J_{dc} = 6.76$
e	5.61	s	4	--
f	6.02	s	4	--
g	8.44	s	4	--
h	8.65	s	2	--
i	4.27	d	8	$^3J_{ij} = 5.31$
j	1.79	ttt	4	$^3J_{ji} = 5.89, ^3J_{jk} = 5.80$
k	1.42	dt	16	$^3J_{kj} = 6.58, ^3J_{kl} = 6.28$
l	1.36	tt	16	--
m	1.27	m	64	--
n	0.85	tt	24	--
o	6.42	dd	4	$^3J_{\text{meta}} = 3.17; ^3J_{\text{ortho}} = 6.25$
p	6.63	dd	4	$^3J_{\text{meta}} = 3.17; ^3J_{\text{ortho}} = 6.25$
q	4.02	m	24	--



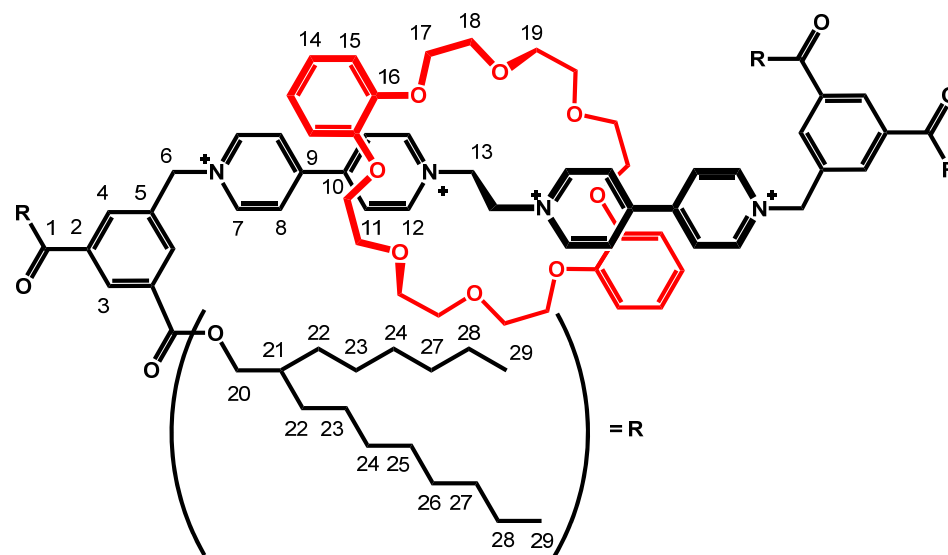


Table 3.23 -  $^{13}\text{C}$  NMR data of [3-12][OTf]<sub>4</sub> in CD<sub>3</sub>CN. MW<sub>OTf</sub> = 2641.204 g/mol. Quaternary Carbons assigned by software

Carbon	$\delta$ (ppm)	# Carbons
1	165.76	4
2	132.39	4
3	130.90	2
4	134.53	4
5	134.07	2
6	63.60	2
7	145.76	4
8	127.21	4
9	149.23	2
10	148.75	2
11	125.99	4
12	147.08	4
13	58.44	2
14	121.49	4
15	112.54	4
16	146.85	4
17	70.25	4
18	67.61	4
19	70.60	4
20	67.98	4

---

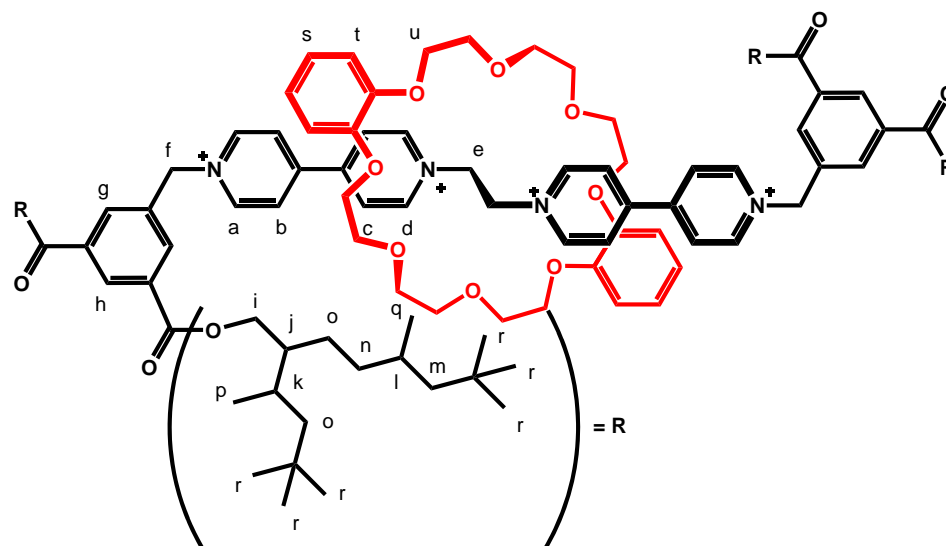
<b>21</b>	37.27	4
<b>22</b>	31.65	8
<b>23</b>	26.55	8
<b>24</b>	29.37	8
<b>25</b>	20.55	4
<b>26</b>	29.13	4
<b>27</b>	31.72	8
<b>28</b>	22.46	8
<b>29</b>	13.51	8

---

### 3.5.13 Synthesis of [3-13][OTf]<sub>4</sub>

[2-2][OTf]<sub>2</sub> (189.0 mg, 0.296 mmol) and **DB24C8** (1.06 g, 2.368 mmol) were dissolved in a two-phase NaOTf (aq)/MeNO<sub>2</sub> (1 and 20 mL) mixture and placed in a thick-walled 80 mL reaction vessel. **3-8** (904.0 mg, 1.184 mmol) was dissolved in CHCl<sub>3</sub> (10 mL) and a catalytic amount of TBAI (10 mg) was added to 80 mL vessel with stir bar and microwaved for 30 h at 50 °C. The MeNO<sub>2</sub> was washed with H<sub>2</sub>O (3 x 10 mL), dried over MgSO<sub>4</sub> and the solvent removed. The residue was stirred in cold MeCN, solid filtered off and remaining solution concentrated. The orange residue was dissolved in cold EtOAc, solid filtered off and remaining solution concentrated. The orange residue was dissolved in cold toluene, solid filtered off and remaining solution concentrated. Product was purified and isolated by flash column chromatography on RP-C<sub>18</sub> silica gel using MeOH as eluant, yielding a bright red/orange brittle solid. Yield: 546.0 mg, 67 %.

**ESI-MS:** *m/z* 1226.7385 (calc.) for C<sub>138</sub>H<sub>210</sub>F<sub>6</sub>N<sub>4</sub>O<sub>22</sub>S<sub>2</sub> [M-2OTF]<sup>2+</sup>, found 1226.7382. *m/z* 538.8930 (calc.) for C<sub>136</sub>H<sub>210</sub>N<sub>4</sub>O<sub>16</sub> [M]<sup>4+</sup>, found 538.8929.

Table 3.24 -  $^1\text{H}$  NMR data of [3-13][OTf]<sub>4</sub> in CD<sub>3</sub>CN. MW<sub>OTf</sub> = 2753.416 g/mol

Proton	$\delta$ (ppm)	Multiplicity	# Protons	$J$ (Hz)
a	9.00	d	4	$^3J_{ab} = 6.60$
b	8.24	d	4	$^3J_{ba} = 6.60$
c	8.27	d	4	$^3J_{cd} = 6.60$
d	9.33	d	4	$^3J_{dc} = 6.60$
e	5.61	s	4	--
f	5.99	s	4	--
g	8.39	s	4	--
h	8.68	s	2	--
i	4.31	m	8	--
j	1.82	m	4	--
k	1.71	m	4	--
l	1.41	m	4	--
m	1.12	m	8	--
n	1.24	m	8	--
o	1.41	m	16	--
p	0.97	m	12	--
q	0.90	m	12	--
r	0.87	m	72	--
s	6.42	dd	4	$^3J_{\text{meta}} = 3.90; ^3J_{\text{ortho}} = 5.59$
t	6.63	dd	4	$^3J_{\text{meta}} = 3.90; ^3J_{\text{ortho}} = 5.59$
u	4.03	m	24	--



**Table 3.25 -  $^{13}\text{C}$  NMR data of [3-13][OTf] $_4$  in  $\text{CD}_3\text{CN}$ .  $\text{MW}_{\text{OTf}} = 2753.416$  g/mol. Quaternary Carbons assigned by software**

Carbon	$\delta$ (ppm)	# Carbons
1	164.77	4
2	132.48	4
3	130.86	2
4	134.45	4
5	133.94	2
6	63.60	2
7	145.76	4
8	127.22	4
9	149.33	2
10	148.80	2
11	125.98	4
12	147.09	4
13	58.44	2
14	121.49	4
15	112.59	4
16	146.88	4
17	70.25	4
18	67.69	4
19	70.63	4
20	66.99	4
21	51.09	4

---

<b>22</b>	24.80	4
<b>23</b>	26.55	8
<b>24</b>	22.11	4
<b>25</b>	26.43	4
<b>26</b>	49.60	4
<b>27</b>	30.61	4
<b>28</b>	29.34	12
<b>29</b>	30.82	8
<b>30</b>	18.16	4

---

# CHAPTER 4

## *A New Design: Liquid Crystal [2]Rotaxanes*

### 4.1 INTRODUCTION

Control over the relative position and motion of components in interpenetrated or interlocked molecules can impart machine-like properties at the molecular level, such as translation of the macrocycle in a [2]rotaxane molecular shuttle.<sup>39-43,123-124,150-151</sup> The possibility of integrating molecular machines into self-organized materials arises from interest in the potential to control molecular switches with amplification of their cooperative motion to produce a macroscopic response within a mesophase.

As mentioned in Chapters 2 and 3, a number of [2]rotaxanes based upon a tetracatenar motif have demonstrated liquid crystallinity over a wide temperature range. However, this [2]rotaxane design has only produced materials with a high viscosity that would not be useful for incorporation into a functional material based on a molecular shuttle. The high viscosity of the material renders the possibility of shuttling in the material at elevated temperatures nearly impossible. The system is also at the mercy of high clearing temperatures into the isotropic liquid with increasing size. As mentioned in Chapters 2 and 3, although the [2]rotaxanes are thermally stable to 200 °C, the isotropization temperatures for the larger [2]rotaxanes are presently within 10 °C of this making reversibility an issue due to decomposition.

Two approaches were taken to address these shortcomings. The first, was to employ stoppers extended with functionalities that are typical in small molecule calamitic liquid crystals. Use of fluid siloxanes in place of entirely aliphatic chains, for example,

has the possibility to reduce the viscosity of the material and lower glass transition temperatures because of the greater flexibility of the siloxane backbone.<sup>152-156</sup> It was also hoped that the presence of the siloxane tail might lead to lower clearing temperatures and more interesting physical properties.<sup>157</sup> The second approach focuses on increasing the thermal stability of the system and reducing its ionic character. This new design incorporates stoppering by ester formation, previously reported by Takata *et al.*,<sup>158,159</sup>

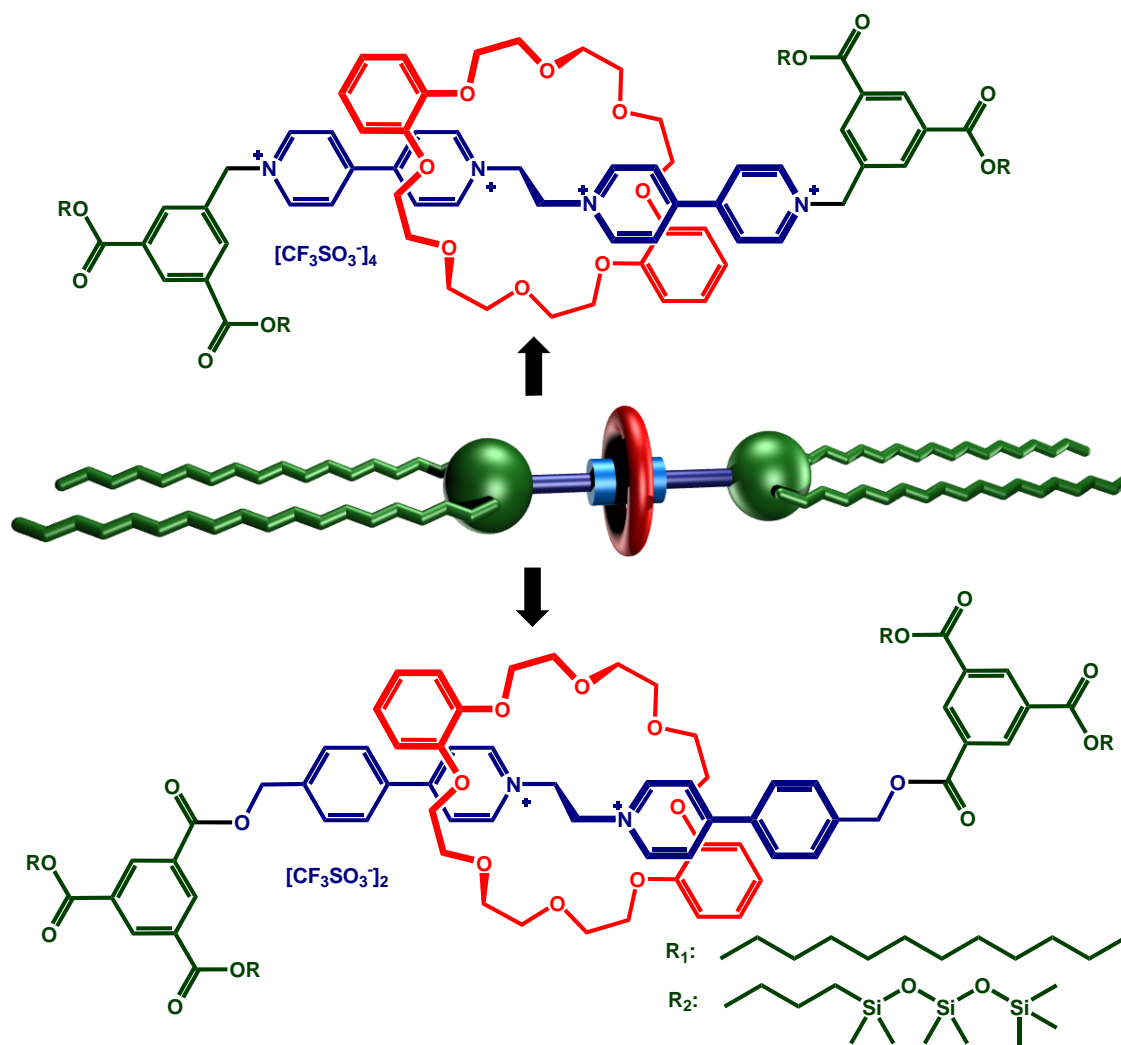


Figure 4.1 – Structural representation of [2]rotaxane: four-charge design (top) and [2]rotaxane: two-charge design (bottom) based on tetracatenar design for calamitic LCs.



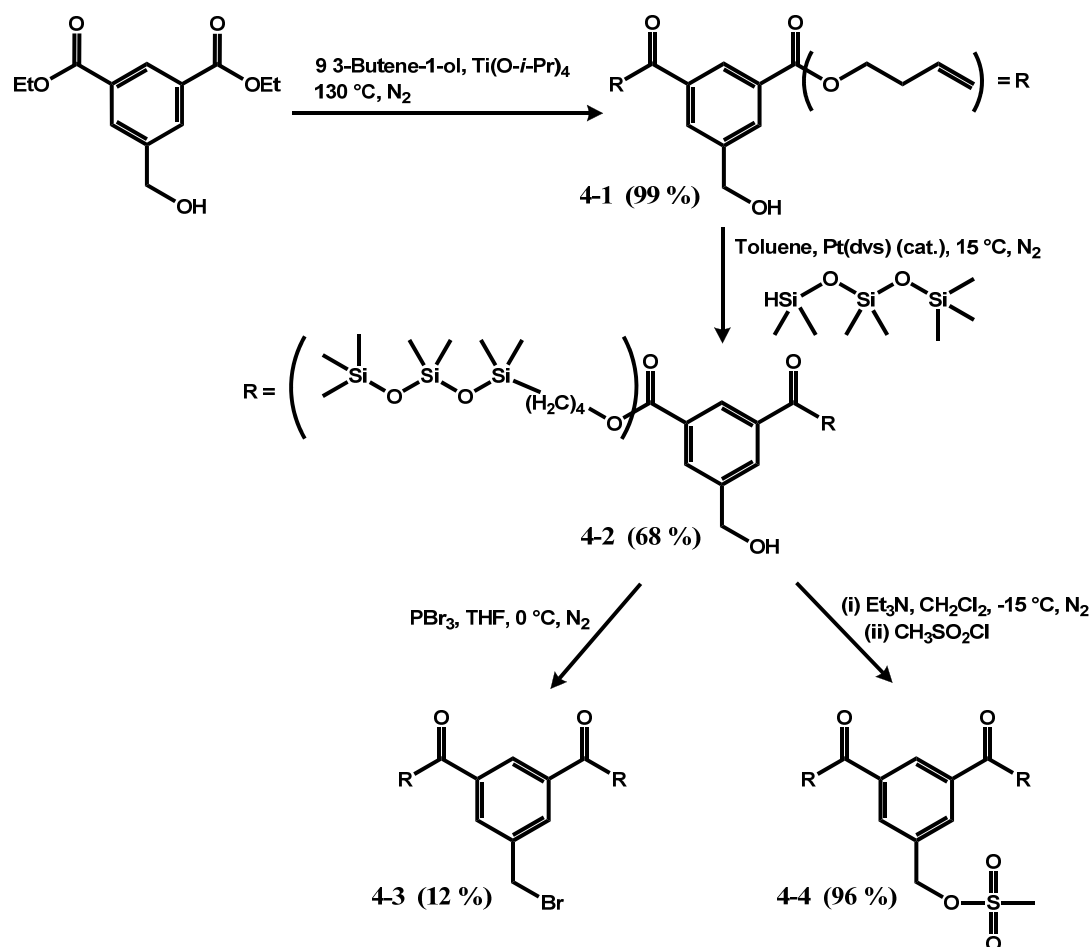
which are thermally more stable than the bond between the pyridinium group and benzylic stopper. This structural change also reduces the ionic charge of the core from four to two. Comparative studies were carried out on the [2]rotaxanes with the aliphatic dodecane chain and [2]rotaxanes with an aliphatic extended siloxane functionality to determine the effect of these design changes on mesomorphism (Figure 4.1).

## 4.2 SYNTHESIS AND CHARACTERIZATION

### 4.2.1 Synthesis

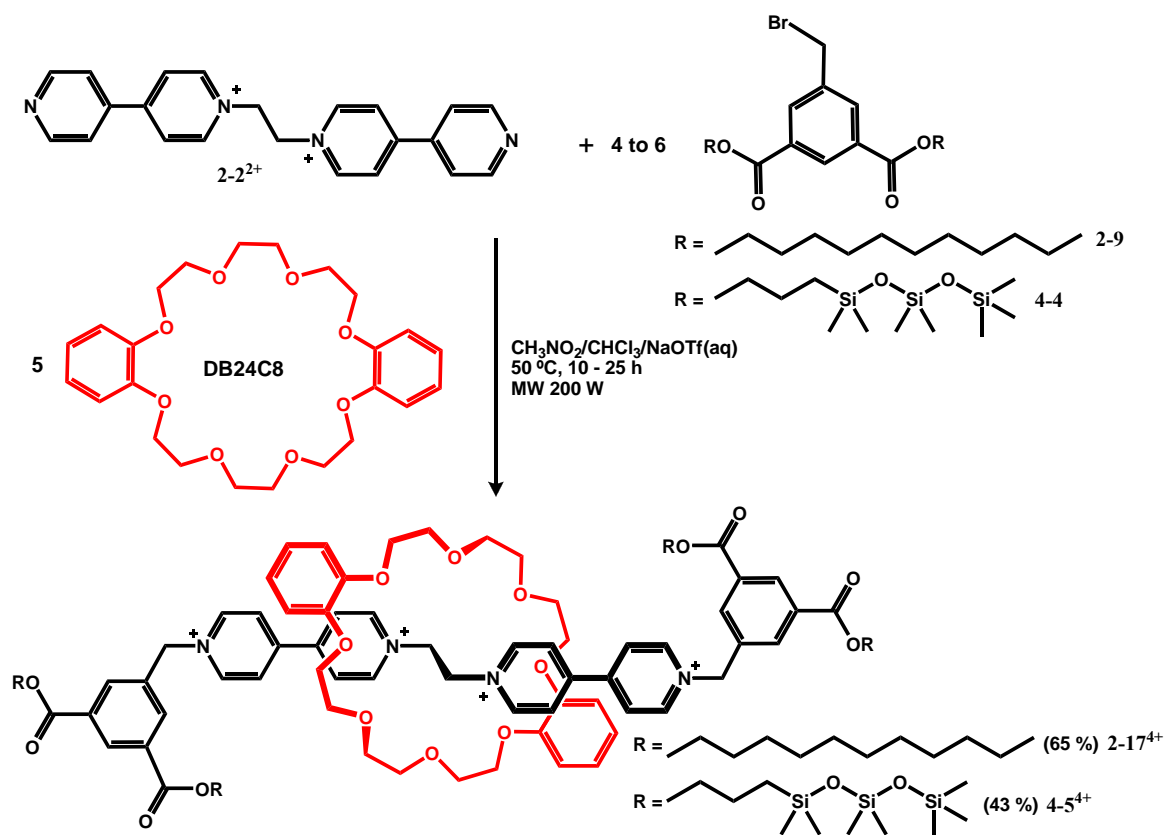
#### 4.2.1.1 Synthesis: Four-Charge Design

The new aliphatic extended siloxane stopper was constructed first (Scheme 4.1). This begins with the transesterification of dimethyl-5-(hydroxymethyl)-*isophthalate* with an excess of the alkene 3-butene-1-ol in the presence of  $\text{Ti}(\text{O-}i\text{-Pr})_4$  as the catalyst to generate the corresponding benzyl alcohol (**4-1**). Subsequent hydrosilylation of **4-1** in the presence of a Pt(0) catalyst gave the bis(siloxane) **4-2**. The reaction was monitored by  $^1\text{H}$  NMR spectroscopy and stopped after full formation. This was important to limit the amount of *beta*-elimination. Repeated attempts at bromination of **4-2** via the method employed in Chapters 2 and 3 by addition of  $\text{PBr}_3$  in a 1.0 M  $\text{CH}_2\text{Cl}_2$  solution yielded a mere 5-12 % of the bis(siloxane)benzylbromide (**4-3**). **4-2** was most likely destroyed with the formation of hydrobromic acid by hydrolysis/condensation of siloxane groups due to the acidic environment.<sup>160,161</sup> Alternatively, the alcohol was converted to the mesylate in the presence of triethylamine to give the product (**4-4**) in near quantitative yield. Compounds **4-1** through **4-4** were oils and were all purified by flash column chromatography.



**Scheme 4.1 - Synthetic route to new stoppers 4-1 through 4-4.**

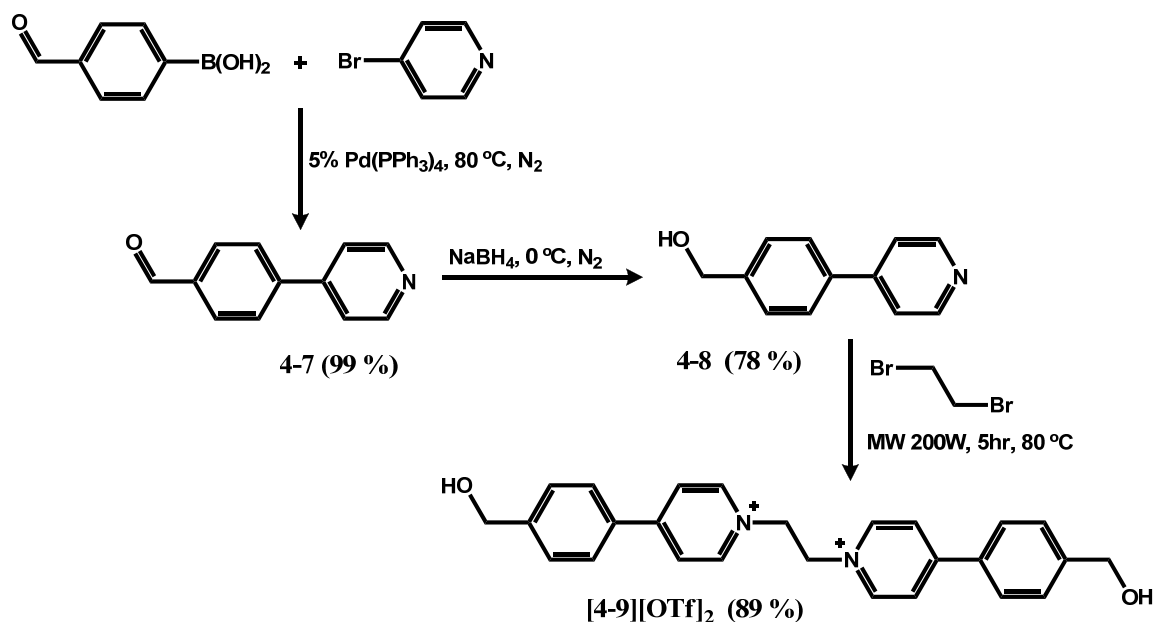
Processing and alignment studies require liquid crystalline rotaxanes that can be prepared in larger quantities and with high purity. Synthesis and isolation of four-charged [2]rotaxanes **2-17**<sup>4+</sup> and **4-5**<sup>4+</sup> were performed in a similar manner to the [2]rotaxanes described in Chapter 3. Use of microwave synthesis for **2-17**<sup>4+</sup> allowed isolation of larger quantities with higher purity in a fraction of the original time. Scheme 4.2 outlines this synthetic methodology. Microwave synthesis was employed at  $50\text{ }^\circ\text{C}$  and 200 W and yielded near complete rotaxane formation on a gram scale in 25 h for **2-17**<sup>4+</sup> and 10 h for **4-5**<sup>4+</sup>. As in Chapter 3, the [2]rotaxanes were purified by column chromatography on reverse phase  $\text{C}_{18}$  silica gel at a flow rate of 10 mL/min.



Scheme 4.2 - Synthetic route for [2]rotaxanes 2-17<sup>4+</sup> and 4-5<sup>4+</sup>.

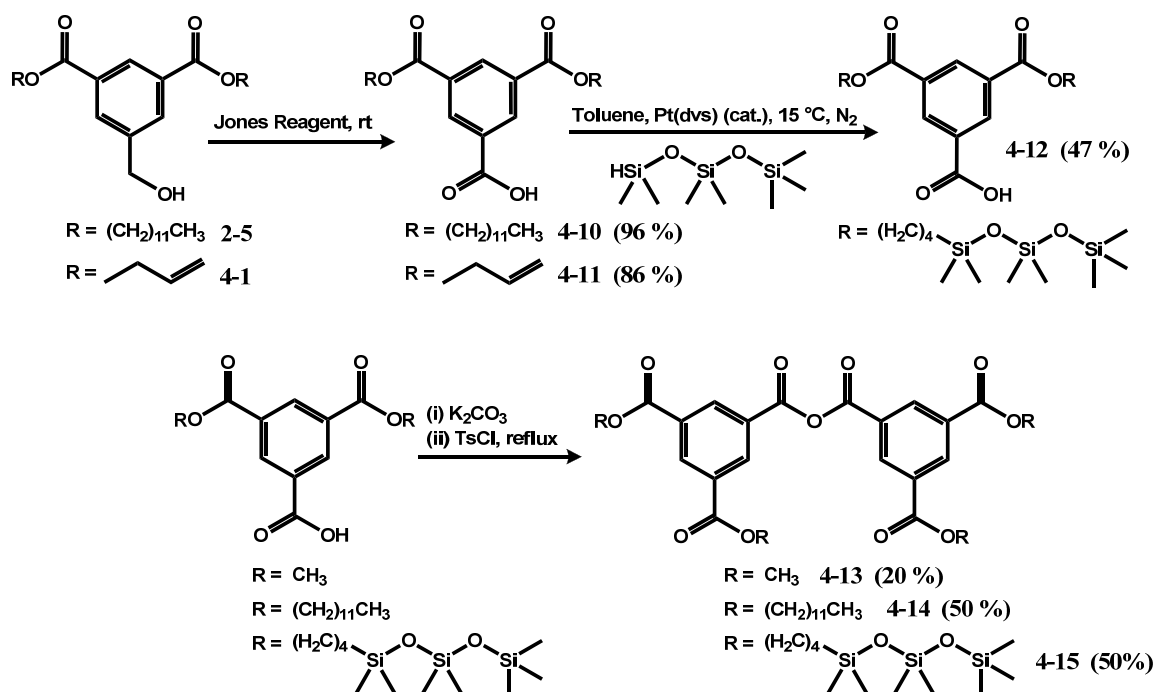
#### 4.2.1.2 Synthesis: Two-Charge Design

The 1,2-bis(4-pyridinium-4-benzylalcohol)ethane two-charged thread was previously synthesized in our group<sup>162</sup> with an improved version of that synthesis shown in Scheme 4.3. A Suzuki coupling reaction was used to synthesize **4-7** in near quantitative yield and this was subsequently reduced in the presence of  $\text{NaBH}_4$  to generate **4-8** in a yield of 78 %. Further reaction of **4-8** with 1,2-dibromoethane under microwave irradiation at  $80\text{ }^\circ\text{C}$  and 200 W for 5 h, gave **4-9**<sup>2+</sup> which was then anion exchanged to the triflate salt.



Scheme 4.3 - Synthetic route for two-charged thread.

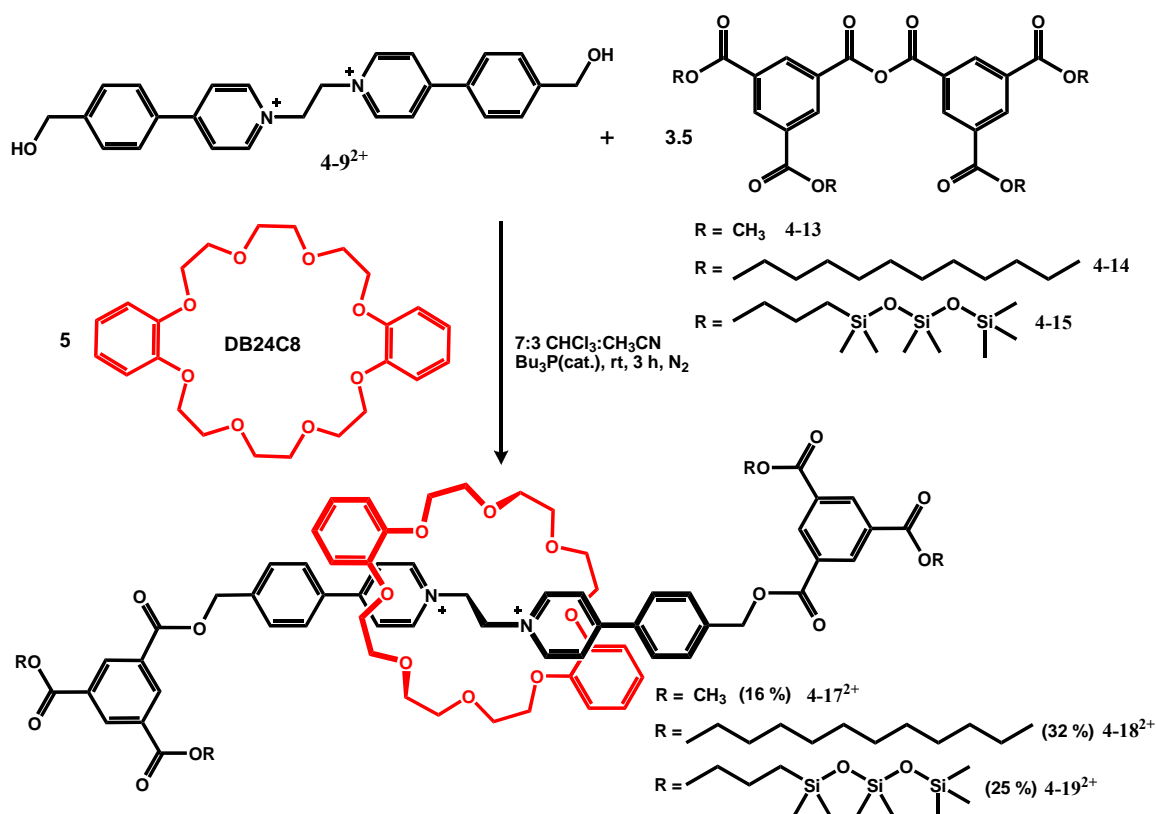
The anhydride stoppers were synthesized according to Scheme 4.4. Precursors **2-5** and **4-1** were first oxidized in the presence of Jones reagent, converting the alcohols to acids **4-10** and **4-11**. Hydrosilylation, under conditions mentioned previously gave the



Scheme 4.4 - Synthetic route for stoppers 4-10 through 4-15.

bis(siloxane) as the benzoic acid **4-12**. Formation of the anhydrides<sup>163</sup> (**4-13** through **4-15**) from their corresponding acids was achieved quantitatively using half of an equivalent of tosyl chloride and excess base. Reaction completion was monitored by <sup>1</sup>H NMR and <sup>13</sup>C NMR spectroscopy.

Part of the synthetic attractiveness of this system lies in the ability to incorporate different properties into the [2]rotaxane simply by changing the benzyl stoppering group. This compact design permits the gram-scale preparation of a range of different rotaxanes for systematic studies of their mesomorphism and provides access to liquid crystalline rotaxanes that can be processed and aligned more easily. The methyl substituted [2]rotaxane **4-17<sup>2+</sup>** was prepared as a simple model compound. As outlined in Scheme 4.5, both the [2]rotaxanes **4-17<sup>2+</sup>** and **4-19<sup>2+</sup>** were synthesized by ester formation under

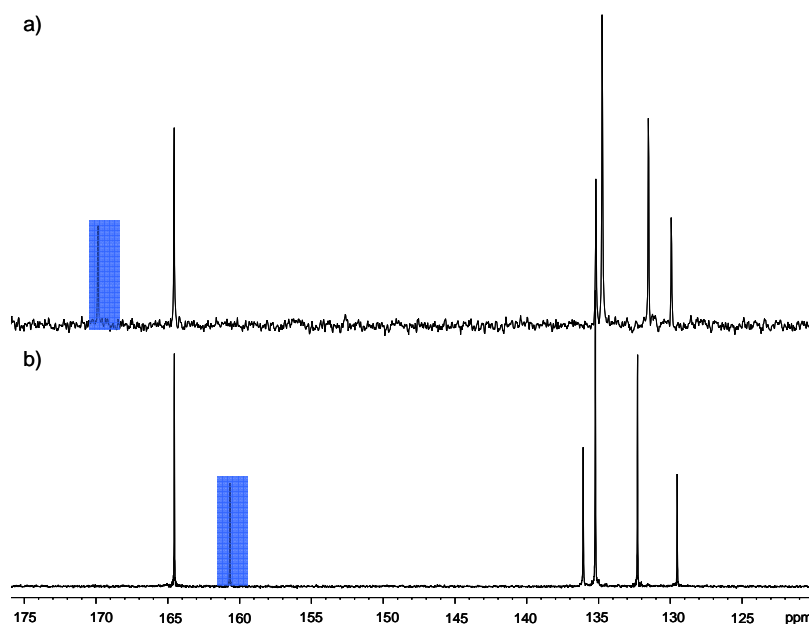


Scheme 4.5 - Synthetic route for [2]rotaxanes **4-17<sup>4+</sup>** through **4-19<sup>4+</sup>**.

modified conditions reported by Takata *et al.*<sup>158,159</sup>, with Bu<sub>3</sub>P as the catalyst. Significant synthetic improvements were noted; in particular, for this two-charge design the full rotaxane formation was complete in 3 h. Interestingly, there is no formation of the usual dumbbell side-product (without **DB24C8** macrocycle) using this method for which there is no apparent explanation.

#### 4.2.2 <sup>1</sup>H NMR and <sup>13</sup>C NMR Spectroscopy

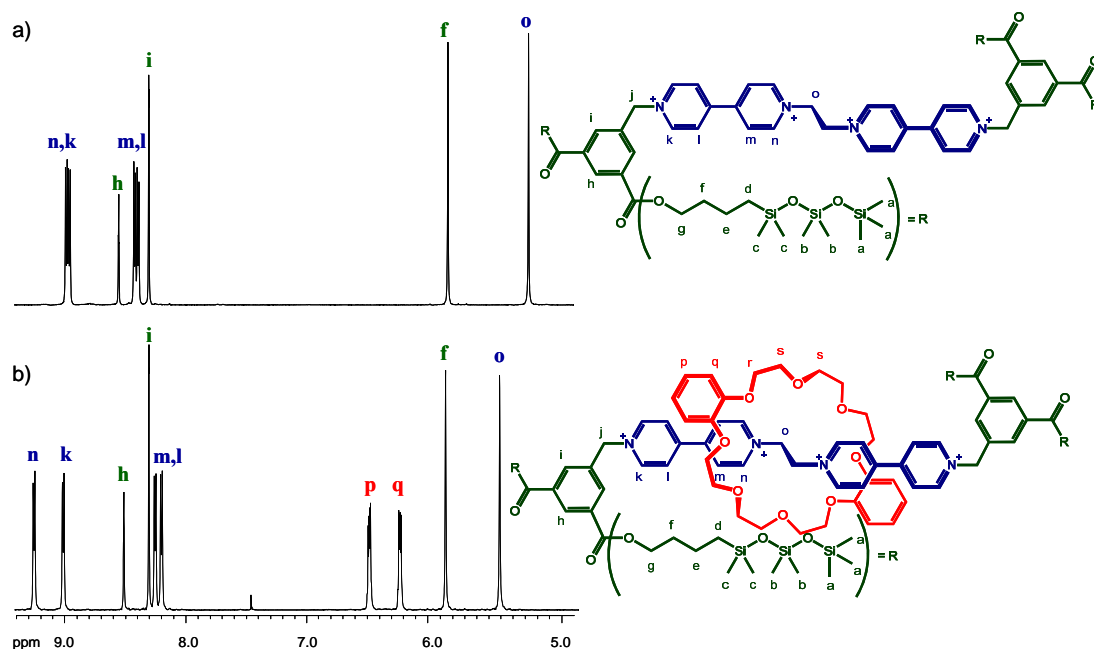
The formation of anhydride stoppers **4-13** through **4-15** were monitored by both <sup>1</sup>H NMR and <sup>13</sup>C NMR spectroscopy, since fourier transform infrared (FT-IR) spectroscopy was not extremely definitive. Due to symmetry, the <sup>1</sup>H NMR spectra of the acid and the anhydride are identical, though the <sup>1</sup>H NMR spectra does show the complete disappearance of the TsCl protons upon complete anhydride formation. <sup>13</sup>C NMR spectroscopy proved to be the best analytical tool for proving that only the anhydride was



**Figure 4.2 - Stacked <sup>13</sup>C NMR spectra of a) 3,5-dicarboxymethylbenzoic acid and b) 4-14 in the region between 120-175 ppm in CDCl<sub>3</sub>.**

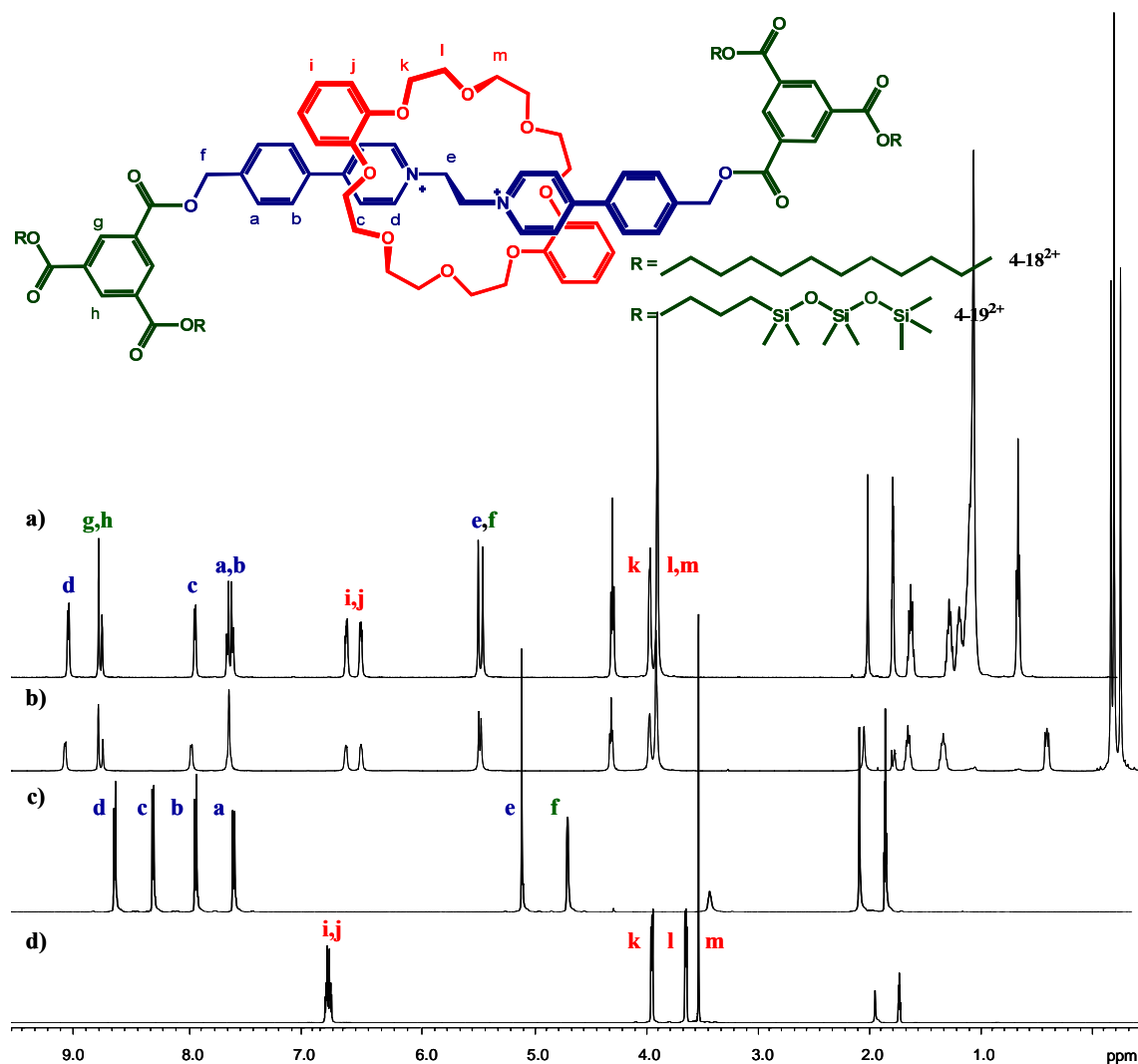
present. The anhydride synthesis was confirmed by a shift in the carbonyl carbon peak from  $\sim 170$  ppm, for the benzoic acids, to  $\sim 160$  ppm, for the benzyl anhydrides. The  $^{13}\text{C}$  NMR spectra for the di-methyl substituted benzoic acid and anhydride are shown in Figure 4.2.

Figure 4.3 shows the  $^1\text{H}$  NMR spectra of dumbbell **4-6** $^{4+}$  and [2]rotaxane **4-5** $^{4+}$  in  $\text{CD}_3\text{CN}$  illustrating typical 1,2-bis(pyridinium)ethane interactions with **DB24C8**. The ethylene protons of the recognition site, **o**, and  $\alpha$ -pyridinium protons, **n**, are deshielded due to hydrogen bonding with the oxygen atoms of the crown ether, while  $\beta$ -pyridinium protons, **m** and **l**, are shielded due to  $\pi$ -stacking interactions caused by the ring currents of the aromatic rings on the crown ether. The crown ether catechol protons are shielded for the same reason. Other protons on the dumbbell, **f**, **h** and **i**, do not shift as they are not directly involved in any non-covalent interactions with the crown ether.



**Figure 4.3 - Stacked  $^1\text{H}$  NMR spectra of a) dumbbell **4-6** $^{4+}$  and b) [2]rotaxane **4-5** $^{4+}$  in  $\text{CD}_3\text{CN}$ .**

As expected, [2]rotaxanes **4-18**<sup>2+</sup> and **4-19**<sup>2+</sup> exhibited large chemical shift differences compared to that of the free thread **4-9**<sup>2+</sup> and uncomplexed **DB24C8** macrocycle (Figure 4.4).



**Figure 4.4** - Stacked <sup>1</sup>H NMR spectra of a) [2]rotaxane **4-18**<sup>2+</sup>, b) [2]rotaxane **4-19**<sup>2+</sup>, c) **2-9**<sup>2+</sup> and d) **DB24C8** in CD<sub>3</sub>CN.

Though this design lacks the strong  $\pi$ - $\pi$  interactions of the four-charged design, comparison of the <sup>1</sup>H NMR spectra of the naked dumbbell **4-16**<sup>2+</sup> to the [2]rotaxane **4-17**<sup>2+</sup> clearly shows the same effect of all three non-covalent interactions responsible for the initial self-assembly (Figure 4.5). Where ethylene protons of the recognition site, **i**,



and  $\alpha$ -pyridinium protons, **h**, are deshielded due to hydrogen bonding with the oxygen atoms of the crown ether and the  $\beta$ -pyridinium protons **g** and **f**, are shielded due to  $\pi$ -stacking interactions caused by the ring currents of the aromatic rings on the crown ether.

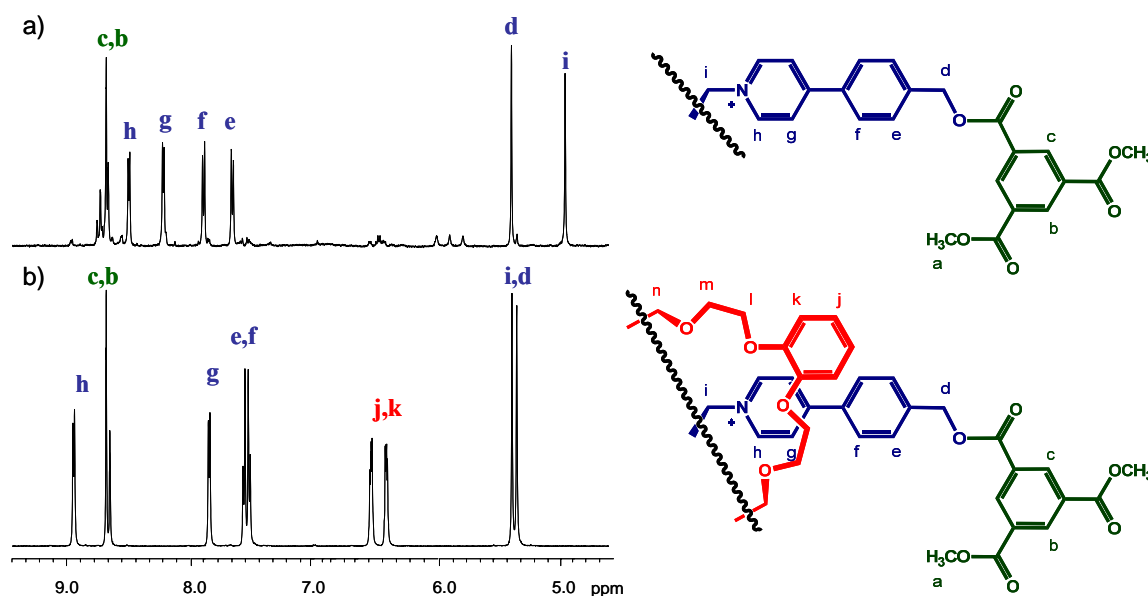


**Figure 4.5 - Stacked  $^1\text{H}$  NMR spectra of a) dumbbell  $4-16^{2+}$  and b) [2]rotaxane  $4-17^{2+}$  in  $\text{CD}_3\text{CN}$ .**

#### 4.2.3 UV-Visible Spectroscopy

The UV-visible spectra of  $2-17^{4+}$  and  $4-18^{2+}$  were obtained using  $1 \times 10^{-3}$  M solutions in MeCN (Figure 4.6). The  $\lambda_{\text{max}}$  and absorbance values are listed in Table 4.1. The molar extinction coefficients were calculated using the Beer-Lambert Law. [2]Rotaxanes  $2-17^{4+}$  and  $4-5^{4+}$  are both deep orange in solution, having their  $\lambda_{\text{max}}$  at 415 nm in the visible region of the spectrum. The large absorption is due the intramolecular charge transfer between the catechol of the macrocycle and the viologen-like, dipyridinium groups on the recognition site. [2]Rotaxanes  $4-18^{2+}$  and  $4-19^{2+}$  lack the strong CT transfer interaction of the four-charged compounds and are both pale yellow in

solution, with their  $\lambda_{\max}$  at  $< 400$  nm; presumably in the UV range obscured by the other absorbances of the molecule.

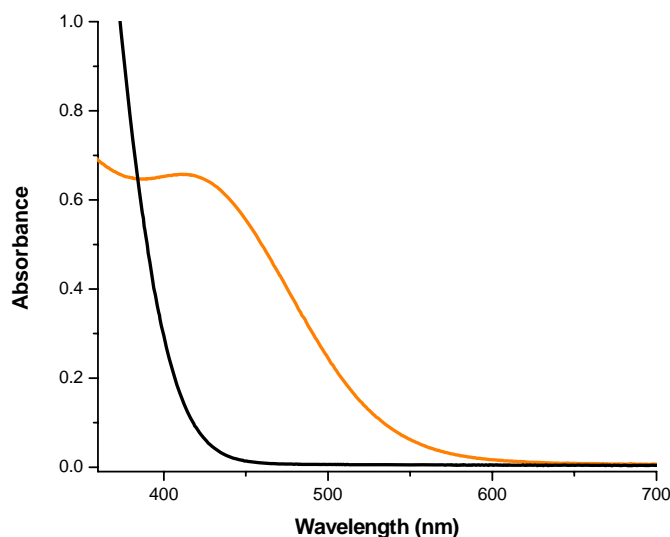


Figure 4.6 - UV-visible spectra of [2]rotaxanes 2-17<sup>4+</sup> (orange) and 4-18<sup>2+</sup> (black) in CH<sub>3</sub>CN.

Table 4.1 - Summary of UV-vis data for [2]rotaxanes 2-17<sup>4+</sup>, 4-5<sup>4+</sup>, 4-18<sup>2+</sup> and 4-19<sup>2+</sup>.

Compound	Concentration	$\lambda_{\max}$	Absorbance	$\epsilon$ (L cm <sup>-1</sup> mol <sup>-1</sup> )
2-17 <sup>4+</sup>	1 x 10 <sup>-3</sup>	415	0.657	657
4-5 <sup>4+</sup>	1 x 10 <sup>-3</sup>	415	0.657	657
4-18 <sup>2+</sup>	1 x 10 <sup>-3</sup>	< 400	--	--
4-19 <sup>2+</sup>	1 x 10 <sup>-3</sup>	< 400	--	--

#### 4.2.4 Single Crystal Structure

Single crystal growth of the model compound 4-17<sup>2+</sup> would aid in packing volume and aspect ratio considerations in the liquid crystalline [2]rotaxane molecular shuttle design. Unfortunately, the growth of good quality crystals for 4-17<sup>2+</sup> was unsuccessful. However, crystals were grown of the 3,5-dimethyl substituted [2]rotaxane, by another group member.<sup>162</sup> Figure 4.7 shows a structural model obtained from the

combination of the crystal structure of the 3,5-dimethyl substituted [2]rotaxane and molecular modeling (MM3) calculations after changing the methyl substituents to carboxymethyl groups. This was done in order to estimate packing volumes and molecular lengths. The [2]rotaxane was crystallized with tetrafluoroborate as the counter anion.

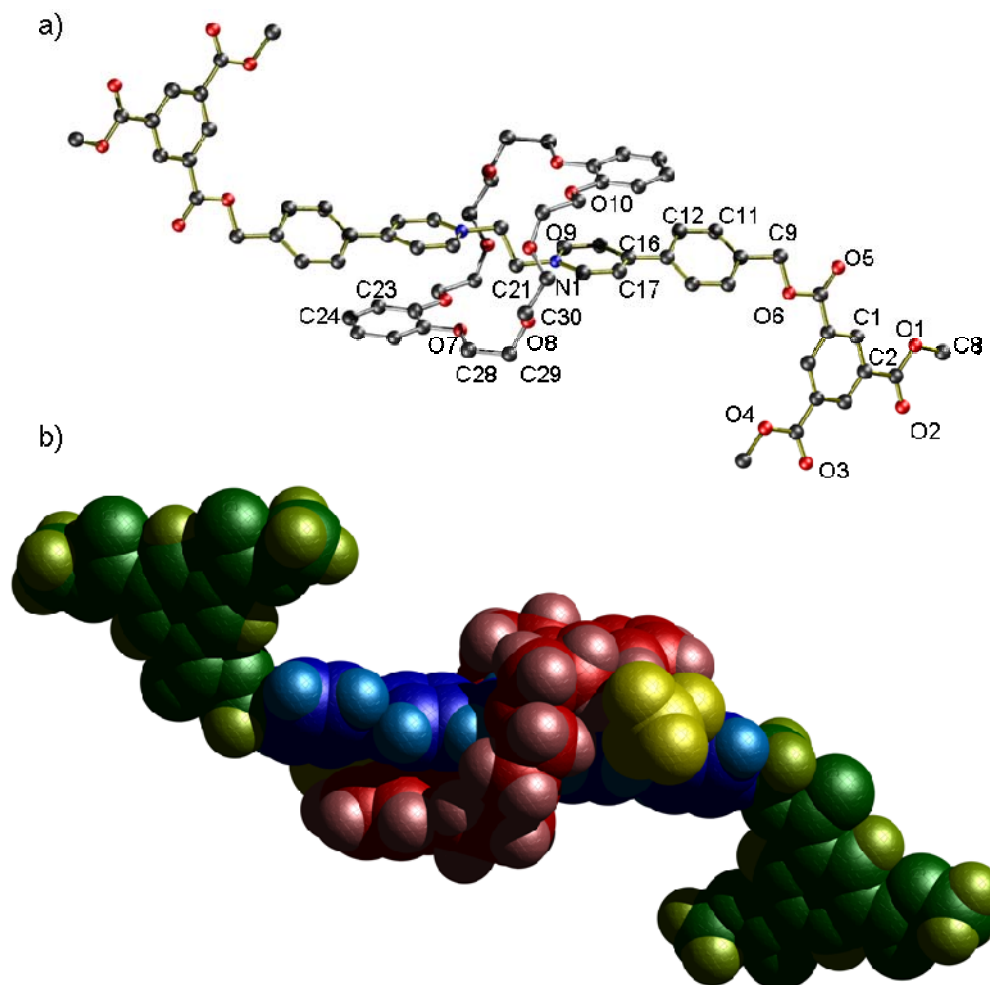


**Figure 4.7 - Model of 4-17<sup>2+</sup> generated from single crystal structure of the 3,5-dimethyl benzylated [2]rotaxane using MM3; a) ball-and-stick view (carbon = black, oxygen = red, nitrogen = blue) and b) space filling view with anions.**

Figures 4.7a and 4.7b show the ball-and-stick and space filling views, respectively. The ball-and-stick representation shows the atom numbering scheme and the counter anions omitted for clarity. The two tetrafluoroborate counter ions are included

in the side-on-view of the space-filling model of [2]rotaxane **4-17**<sup>2+</sup>, where the benzyropyridinium thread is blue, the crown ether macrocycle is red, the stoppering groups are green and the anions are yellow. The interlocked nature of the [2]rotaxane can be seen clearly, with the crown ether arranged in the typical "S"-shaped conformation around the thread. The stoppering groups in the two-charged model are oriented with a zigzag shape, as was observed for the four-charged compound **2-14**<sup>4+</sup>, however the stoppering groups are extended and rotated outward resulting in a longer length. The near planarity of the bipyridine rings in the four-charged model is lost in the two-charged model, resulting in a twisting of the benzyl pyridinium rings with a dihedral angle C14-C13-C16-C17 of 29.6°. Eight hydrogen bonds are formed between the  $\alpha$ -pyridinium and ethyl protons of the thread and the oxygen atoms of the **DB24C8** macrocycle. The N $\cdots$ O distances vary from 4.36 Å (aliphatic oxygens) to 3.43 Å (aromatic oxygens). The C $\cdots$ O distances vary from 4.09 Å (aliphatic oxygens) to 3.19 Å (aromatic oxygens). The oxygen atoms are also involved in ion-dipole interactions with N<sup>+</sup> and C $\delta^+$ . The ring distance ranges between 3.46 - 3.73 Å between the catechol of the crown ether and benzyl of the dumbbell, which are in the upper range for  $\pi$ - $\pi$  interactions.<sup>133,134</sup>

Large differences in shape and orientation are observed in changing the design from four-charges to two-charges. The overall extended molecular length is increased with the incorporation of the ester function on the stoppers. From a space filling perspective, the rectangular cylindrical shape of the [2]rotaxane four-charged core changes to a tilted oblique cylindrical shape in the two-charged core, suggesting that a tilt of the molecules long axis might be obtained in liquid crystal phases as long as the cores pack in the same fashion. The approximate dimensions of this di-cation are 36.8 Å along

the long axis, 9.6 Å in depth through the  $\pi$ -stacking and 10.7 Å in width. Assuming the cores pack the same in mesogenic materials, the approximate dimensions of the cores in the crystal lattice can be used to calculate volumes occupied and molecular lengths which will aid in phase determination for the mesogenic materials.

### 4.3 LIQUID CRYSTAL PHASE CHARACTERIZATION

#### 4.3.1 Thermal Gravimetric Analysis (TGA)

The TGA curves for [2]rotaxanes **2-17<sup>4+</sup>**, **4-18<sup>2+</sup>** and **4-19<sup>2+</sup>** were obtained at a rate of 2 °C/min under He (Figure 4.8). As mentioned in Chapter 2, the first step loss of **2-17<sup>4+</sup>** was the stoppers, indicating that the bond between the pyridinium and benzylic stopper is thermally most labile with decomposition occurring above 200 °C. By replacing this bond with an ester, in **4-18<sup>2+</sup>** the thermal stability is increased to 260 °C which is 60 °C higher than the four-charged **2-17<sup>4+</sup>**. Surprisingly, for **4-19<sup>2+</sup>** the siloxane moiety is the most thermally labile with decomposition occurring at 158 °C which is 42 °C below that of the [2]rotaxane **2-17<sup>4+</sup>**. Hence, the first two step losses are both attributed to the stopper in **4-19<sup>2+</sup>** and the subsequent step weight % losses for all [2]rotaxanes is due to loss of the **DB24C8** macrocycle with decomposition occurring at temperatures above 325 °C. The weight % values of the individual components for the [2]rotaxanes relative to the entire molecule including the triflate anions were calculated and are in good agreement with the separate steps in weight loss observed by TGA (Table 4.2). Only the first step weight loss observed by TGA are tabulated with the calculated weight losses of all individual components since we are only concerned with the initial decomposition of these materials.

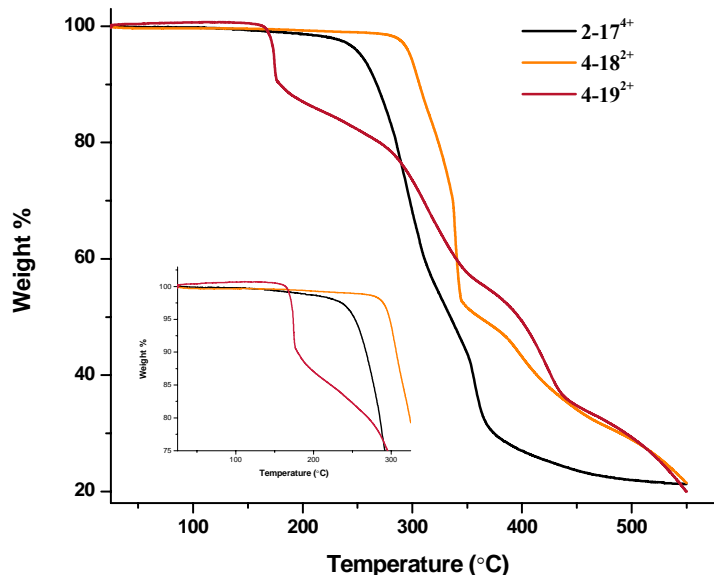


Figure 4.8 - TGA curves of four-charged [2]rotaxane  $2-17^{4+}$  and two-charged [2]rotaxanes  $4-18^{2+}$  and  $4-19^{2+}$  obtained at rate of  $2\text{ }^{\circ}\text{C}/\text{min}$  under He.

Table 4.2 - Calculated weight % values for components of [2]rotaxanes with measured weight % values for the first step losses.

Compound	2 Stoppers (measured %)	2 Stoppers (calc. %)	Thread (%)	OTf anions	DB24C8 (%)
$2-17^{4+}$	44.2	42.7	14.0	14.0	18.6
$4-18^{2+}$	49.23	48.2	18.1	13.5	20.4
$2-19^{2+}$	51.3	56.7	15.1	11.3	17.0

#### 4.3.2 Defect Textures by Optical Polarizing Microscopy (POM)

As previously mentioned in Chapter 2, [2]rotaxane  $2-17^{4+}$  formed a LC phase that was relatively viscous. The fan-like texture obtained, typical for smectics, confirmed a preferential orientation of the molecule long axis parallel to the substrates and layers orthogonal to the substrate (Figure 2.16c). By replacing the aliphatic chains with an alkane-siloxane moiety in [2]rotaxane  $4-5^{4+}$ , a decrease in viscosity for the material was expected. [2]Rotaxane  $4-5^{4+}$  precipitated from MeCN as a birefringent glass, and when

squeezed between glass slides the material softened which was observed by POM (Figure 4.9a and 4.9b, respectively). Interestingly, [2]rotaxane **4-5<sup>4+</sup>** showed increased viscosity upon heating and did not melt into the isotropic liquid phase before its decomposition temperature of 158 °C. No textures of analytical quality were observed (Figure 4.9c). Attempts to re-dissolve the material resulted in a plastic-like precipitate that was now insoluble in all common organic solvents. Even more surprisingly, this peculiar behaviour was only observed when the material was heated. A likely reason for these drastic changes in properties is cross-linking of the siloxane groups. This occurs when the Si-O bond is hydrolyzed, which facilitates polymerization.

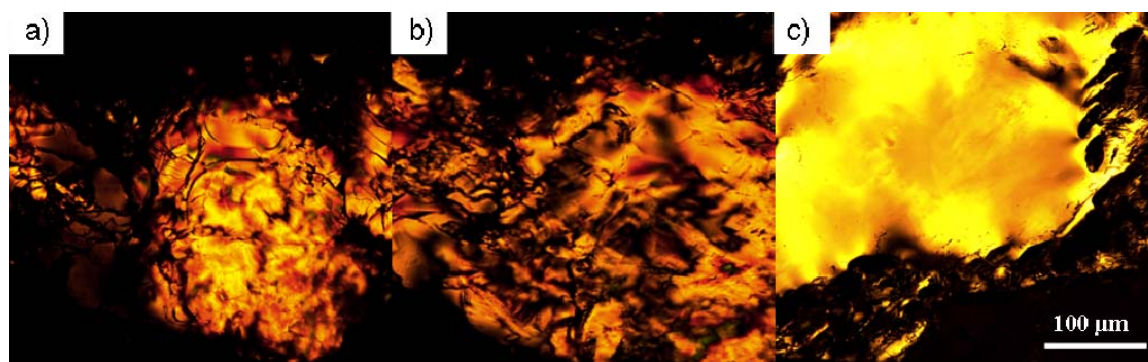


**Figure 4.9 - POM of 4-5<sup>4+</sup> (crossed polarizers): a) crystallized from MeCN @ 25 °C, b) squeezed between glass slides @ 25 °C and c) @ 25 °C upon cooling from 150 °C.**

In reducing the charges on the core from four to two, there was a substantial reduction in viscosity for both [2]rotaxanes **4-18<sup>2+</sup>** and **4-19<sup>2+</sup>**. The [2]rotaxane **4-18<sup>2+</sup>** forms a soft LC phase upon precipitation from MeCN and is significantly less viscous than the four-charged [2]rotaxane **2-17<sup>4+</sup>** (Figure 4.10a). When squeezed between glass slides the texture changes but the birefringence remains (Figure 4.10b). The natural texture obtained upon cooling from the isotropic liquid ( $T_i = 111$  °C) is a schlieren texture typical for tilted smectic LC phases (SmC), where the director points along a direction

that is tilted with respect to the smectic layer, the so-called tilt angle (Figure 4.10c). Reduction of the charges from  $2-17^{4+}$  to  $4-18^{2+}$  not only reduced the viscosity of the material, but also decreased the clearing into the isotropic liquid by 26 °C. No phase transitions were observed upon further heating and cooling cycles other than the reversible transition into the  $T_i$ .

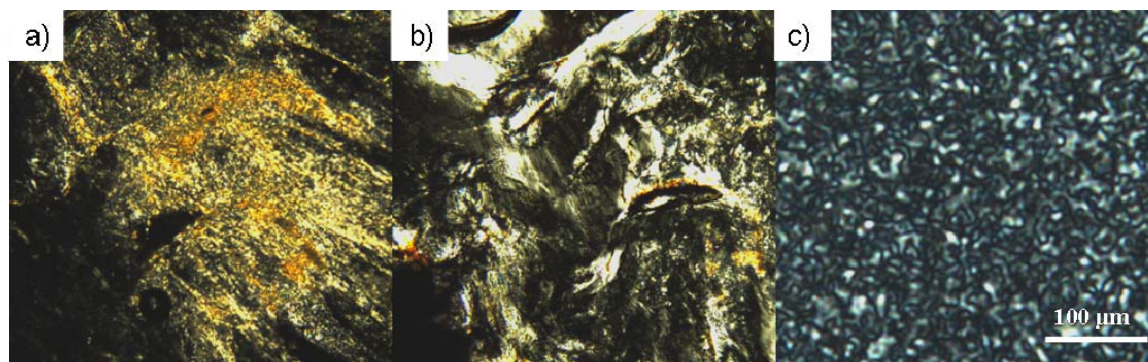


**Figure 4.10 - POM of  $4-18^{2+}$  (crossed polarizers): a) precipitated from MeCN @ 25 °C, b) squeezed between glass slides @ 25 °C and c) @ 25 °C upon cooling from  $T_i = 111$  °C.**

The natural texture obtained by POM for [2]rotaxane  $4-19^{2+}$  was dependent on the type of glass surface employed. When squeezed between untreated glass slides,  $4-19^{2+}$  forms an unspecific texture (Figure 4.11a) and elongated germs, also called smectic *bâtonnets*<sup>60</sup>, grow in at 146 °C when the sample was cooled from its isotropic liquid ( $T_i = 151$  °C). A fan-like texture (Figure 4.11b) is obtained as natural texture upon further cooling and remained at room temperature. The texture is very similar to that obtained for the four-charged  $2-17^{4+}$  and indicates a preferential orientation of the molecules long axis parallel to the substrates.

On freshly cleaned glass, which was washed with water to give a hydrophilic surface the initial texture looked similar to that observed for untreated glass (Figure 4.11d). Significant changes to the sample were observed when the material was cooled



from the isotropic liquid phase where resolved singularities showed four-fold brushes typical of a tilted SmC phase. These were fully resolved when cooled back to room temperature (Figure 4.11e and 4.11f). From these observations we conclude that **4-19<sup>2+</sup>** must form a SmC phase and not a SmA phase. Again, no other phase transitions were observed upon further heating and cooling cycles other than the reversible transition into the **T<sub>i</sub>**.

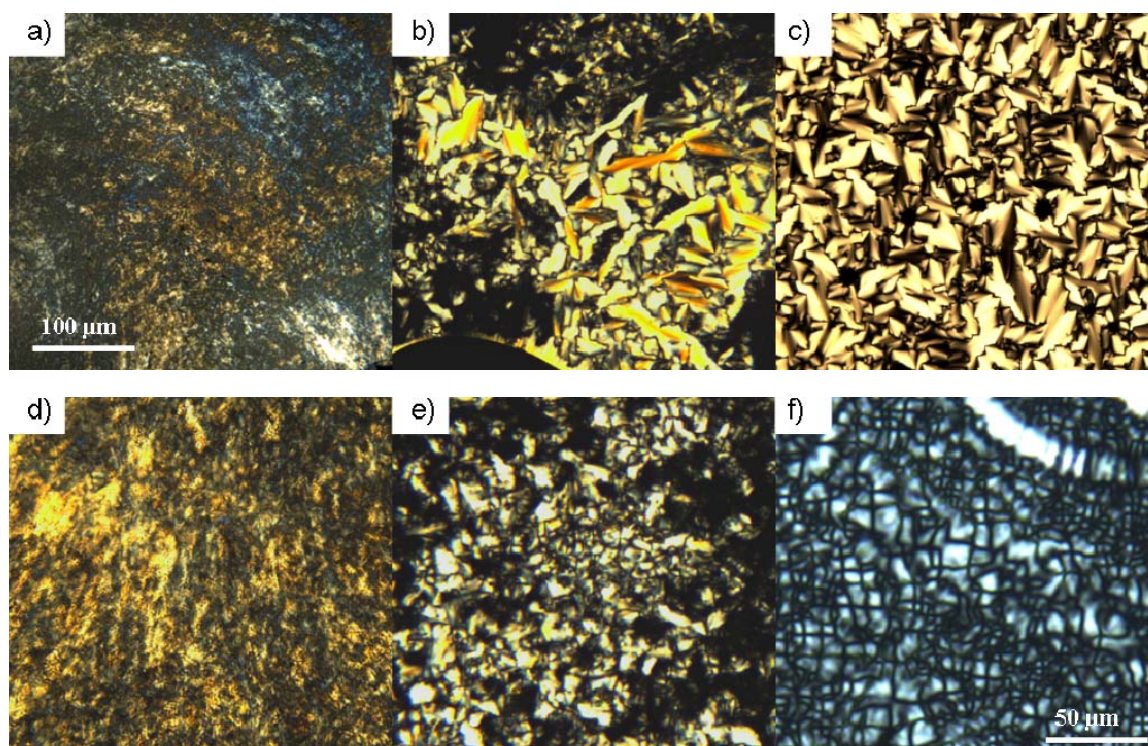


**Figure 4.11 - POM of 4-19<sup>2+</sup> (crossed polarizers), untreated glass (top strip): a) precipitated from MeCN @ 25 °C, b) at 146 °C upon cooling from T<sub>i</sub> = 151 °C and c) at 25 °C upon cooling from T<sub>i</sub>. Freshly cleaned (hydrophilic) glass (bottom strip): d) precipitated from MeCN @ 25 °C, e) at 146 °C upon cooling from T<sub>i</sub> = 151 °C and f) at 25 °C upon cooling from T<sub>i</sub>.**

Both two-charged [2]rotaxanes were equally fluid at elevated temperatures, which should improve processing and alignment in thin films. Interestingly, introduction of the siloxane moiety (**4-19<sup>2+</sup>**) over the fully aliphatic group (**4-18<sup>2+</sup>**) increased the transition temperature into the isotropic liquid by 40 °C. Both two-charged [2]rotaxanes exhibit

schlieren textures with exclusively fourfold brushes, which are indicative of the formation of tilted SmC phases.

### 4.3.3 Differential Scanning Calorimetry (DSC)

All samples for DSC analysis were freshly crystallized/precipitated from MeCN, dried over a stream of nitrogen gas and carefully transferred into aluminum crucibles. First heating runs showed several transitions that were not thermally reversible and will not be discussed here. Transition temperatures and calculated enthalpies of the 2<sup>nd</sup> and subsequent heating runs as well as cooling runs are listed in Table 4.3. The only reversible transitions observed were glass transitions,  $T_g$ , occurring between 30 and 70 °C for [2]rotaxanes **4-5<sup>4+</sup>**, **4-18<sup>2+</sup>** and **4-19<sup>2+</sup>** which is consistent with behaviour seen in Chapter 2, in that they are amorphous solids. These transitions coincide with softening observed by POM above the glass transition temperature. The glass transitions were resolved on cooling only for **4-19<sup>2+</sup>**, with a midpoint at approximately 45 °C upon heating and cooling. Compound **4-18<sup>2+</sup>** showed an additional broad exothermic peak at -38 °C (19.0 kJ/mol), which is likely a transition from an amorphous solid to a crystalline solid but was not resolved on heating and not investigated further (Figure 4.12). Clearing into the isotropic liquid observed by POM were not resolved by DSC analysis.

**Table 4.3 - Transition temperatures (°C, midpoint) and enthalpies (kJ/mol) determined by DSC at scan rates of 10 °C/min for [2]rotaxanes. Clearing into the isotropic liquid ( $T_i$ ) were determined by POM.**

Compound	2 <sup>nd</sup> Heating	Cooling	$T_i$
<b>2-17<sup>4+</sup></b>	30 ( $T_g$ )	18 ( $T_g$ )	137
<b>4-5<sup>4+</sup></b>	39 ( $T_g$ )	n.t.	>158
<b>4-18<sup>2+</sup></b>	40 ( $T_g$ )	-37.5 (19.0)	111
<b>4-19<sup>2+</sup></b>	42 ( $T_g$ )	48 ( $T_g$ )	151

n.t. : no transition observed.

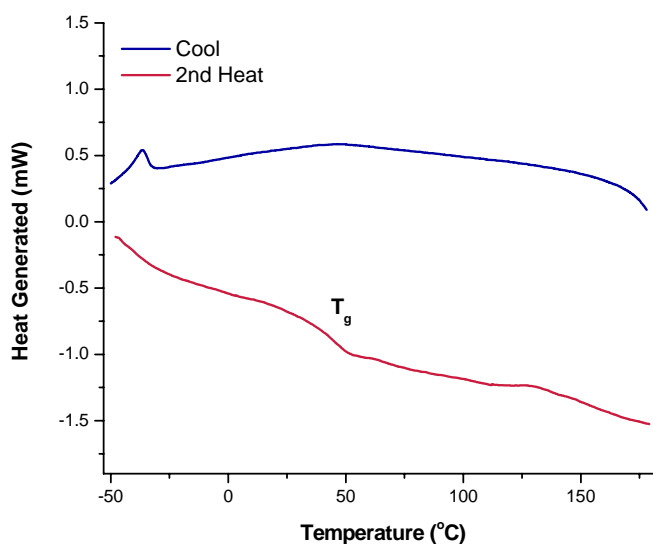


**Figure 4.12 - Second heating and cooling DSC runs of [2]rotaxane 4-18<sup>2+</sup> at 10 °C/min under N<sub>2</sub>.**

#### 4.3.4 Variable Temperature X-Ray Diffraction (vt-XRD)

Data for vt-XRD were collected for the second heating and cooling. [2]Rotaxanes 2-17<sup>4+</sup>, 4-5<sup>4+</sup>, 4-18<sup>2+</sup> and 4-19<sup>2+</sup> all displayed lamellar phases with layer spacings of 40, 33, 40 and 40 Å, respectively (Figure 4.13a - c). All four rotaxanes show a broad reflection (halo) at about 4.5 Å that is indicative of aliphatic chains in an amorphous state and verify the presence of liquid crystal phases. The aliphatic-siloxane substituted [2]rotaxanes 4-5<sup>4+</sup> and 4-19<sup>2+</sup> both showed an additional broad reflection centered between 5 and 6 Å, which is the reported packing distances between siloxane chains.<sup>157,164</sup> Similarly, due to the ability of [2]rotaxane 4-5<sup>4+</sup> to form a plastic-like material upon heating, only the room temperature XRD of the bulk material was recorded in order to confirm the formation of a lamellar phase and to retrieve layer spacings for comparison with the two-charged siloxane extended [2]rotaxane 4-19<sup>2+</sup>. The lamellar order in 4-18<sup>2+</sup> and 4-19<sup>2+</sup> is thermally reversible.

For the dodecane substituted [2]rotaxanes **2-17<sup>4+</sup>** and **4-18<sup>2+</sup>**, the overall molecular length of the core increases from the four-charged design to the two-charged design by approximately 7 Å. The difference between the first order reflections, responsible for the layer to layer spacing, is less than one angstrom between the two (39.6 and 40.3 Å, respectively). With **2-17<sup>4+</sup>** confirmed to form a SmA phase in Chapter 2, the molecules long axis must tilt in **4-18<sup>2+</sup>** to account for such a small difference in the layer spacing. The formation of a SmC phase is supported by the observed schlieren textures and the change in preferred molecular conformation based on single crystal structures.

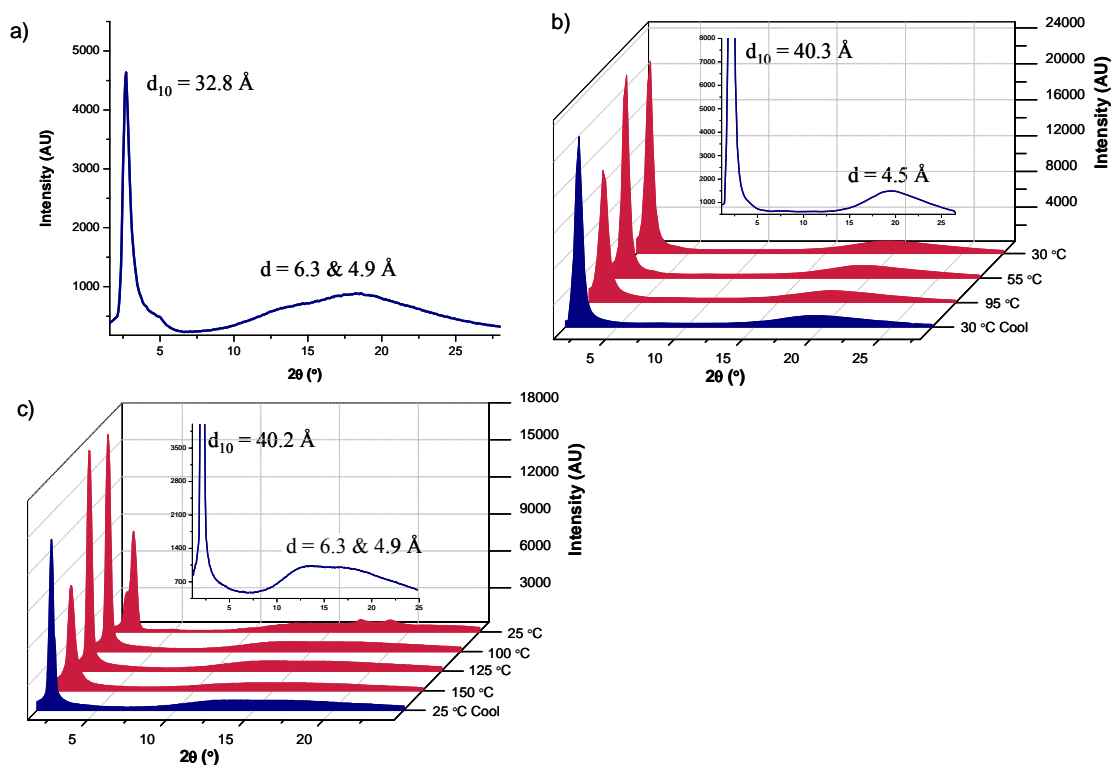


**Figure 4.13** - XRD of a) **4-5<sup>4+</sup>** and vt-XRD of b) **4-18<sup>2+</sup>** and c) **4-19<sup>2+</sup>**.

When comparing the aliphatic-siloxane substituted [2]rotaxanes **4-5<sup>4+</sup>** and **4-19<sup>2+</sup>**, the overall core molecular length again increases by approximately 7 Å. The layer spacing increases from 32.8 to 40.2 Å for **4-5<sup>4+</sup>** and **4-19<sup>2+</sup>**, respectively, with a difference

of 7.4 Å. This suggests that both the four-charged **4-5<sup>4+</sup>** and two-charged **4-19<sup>2+</sup>** molecules exhibit SmC phases. A definitive distinction between a tilted and non-tilted phase by XRD requires alignment of the compounds, but comparison of the calculated molecular lengths of 40 Å, 47 Å, and 50 Å for **4-5<sup>4+</sup>**, **4-18<sup>2+</sup>**, and **4-19<sup>2+</sup>**, respectively (see Section 4.3.6), with observed spacings of 33, 40, and 40 Å *strongly* suggests that all three compounds form SmC phases.

#### 4.3.5 Alignment of LC Materials

Alignment of [2]rotaxanes **4-5<sup>4+</sup>**, **4-18<sup>2+</sup>** and **4-19<sup>2+</sup>** is essential for detailed structural analysis of their mesophases and important for potential applications. All three rotaxanes require elevated temperatures for alignment because of their high viscosity. [2]Rotaxane **4-5<sup>4+</sup>** is the most viscous of the three rotaxanes and was only investigated by shear alignment at 80 °C. Reasonably uniform planar alignment in the direction of the applied shear force (Figure 4.14) was achieved but higher temperatures are required for more uniform mechanical alignments. Temperatures above 80 °C unfortunately, trigger cross-linking and formation of a polymeric material as mentioned above.

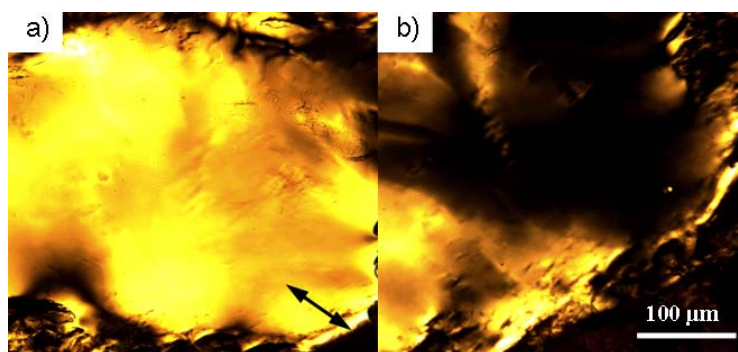


**Figure 4.14 - POMs of 4-5<sup>4+</sup> a) shear alignment at 80 °C (in direction of arrow) and b) rotated by 45°.**

The [2]rotaxane **4-18<sup>2+</sup>** was mechanically sheared between sheets of Teflon at 75 °C producing nearly uniform planar alignment of the optic axis in the direction of applied shear force (Figure 4.15). If the material is sheared at higher temperatures, the initially obtained texture of planar alignment immediately relaxes into a schlieren texture (Figure 4.10c). This suggests that **4-18<sup>2+</sup>** prefers a homeotropic orientation on Teflon. Planar alignment in a cell treated with rubbed polyimide was unsuccessful because only schlieren textures were formed that did not change in light transmission when rotated (Figure 4.15c).

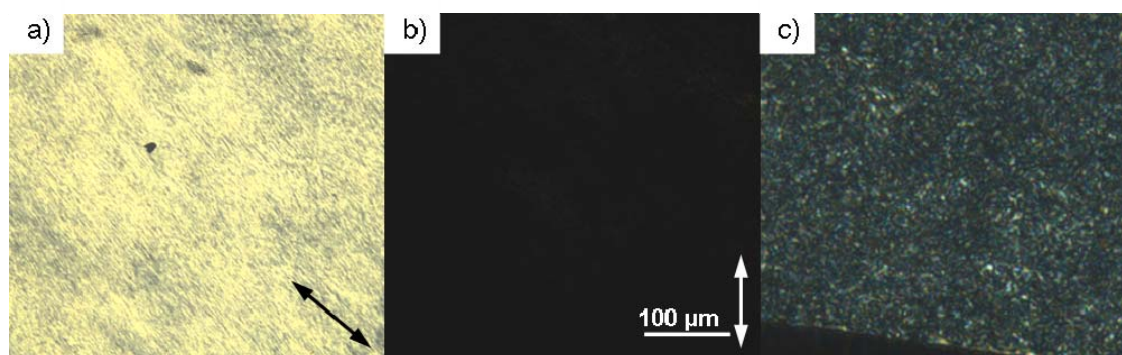


**Figure 4.15 - POMs of 4-18<sup>2+</sup> a) shear alignment at 75 °C (in direction of arrow) and b) rotated by 45°, c) in cell treated for parallel (homogeneous) alignment with rubbed polyimide, 4 μm gap.**

[2]Rotaxane **4-19<sup>2+</sup>** behaved in much the same way as **4-18<sup>2+</sup>** when subjected to identical conditions. The material was aligned by applying shear force giving near planar alignment between sheets of Teflon at 120 °C with the optic axis pointing in the direction of the applied shear force (Figure 4.16). However, due to the high temperature, the material reorients into a homeotropic alignment within 10 - 15 seconds evidenced by the formation of a schlieren texture (Figure 4.16c). Attempts to cool the forced SmA planar alignment were successful when sheared between Teflon at 100 °C and then quickly cooled to room temperature. 2D-XRD of this film shows that the layers are well aligned

orthogonally to the direction of shear. The layer spacing is 42 Å, which is 2 Å longer than that seen in the bulk. A weak reflection at 14 Å, parallel to the layer spacing, corresponds to the approximate distance between the siloxane chains and the core of the [2]rotaxane.

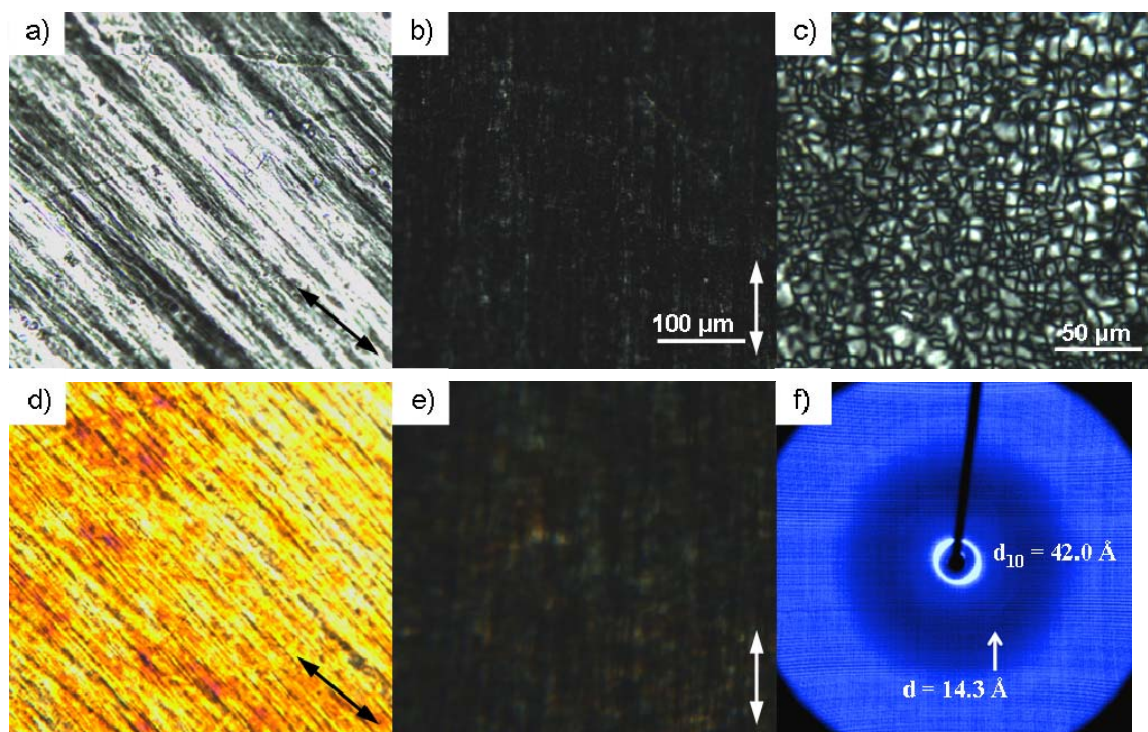


**Figure 4.16 - POMs of 4-19<sup>2+</sup>** a) shear alignment at 120 °C (in direction of arrow), b) rotated by 45° and c) schlieren texture obtained after 15 seconds. d) Shear alignment of thin film pulled from teflon (in direction of arrow), e) rotated by 45°, and f) 2D-XRD pattern of thin film at 25 °C

#### 4.3.6 Calculated Packing Volume Ratios & Molecular Lengths

Space filling calculations were performed to compare the molecular dimensions with the layer spacings obtained by XRD for the four-charged [2]rotaxanes **2-17<sup>4+</sup>**, **4-5<sup>4+</sup>** and the two-charged [2]rotaxanes **4-18<sup>2+</sup>** and **4-19<sup>2+</sup>**. As expected, the layer spacings are shorter than the extended length of these molecules and agree well with calculations based on amorphous side chains and space filling considerations described below.

As previously mentioned in Chapters 2 and 3, the cylindrical volume of the four-charged core, including the **DB24C8** macrocycle and the four triflate anions is estimated to be  $2400 \text{ \AA}^3$  based on a length of  $27.4 \text{ \AA}$  and an average diameter of  $10.6 \text{ \AA}$ . With the ester function, the cylindrical volume of the two-charged core, including the **DB24C8** macrocycle and the two triflate anions, is estimated to be  $3280 \text{ \AA}^3$  based on a length of  $36.8 \text{ \AA}$  and an average diameter of  $10.6 \text{ \AA}$ . The length and average diameter of the cores were calculated based on the dimensions of the cores in the single crystal structures and a free rotation over the long axis of the molecule (Figure 2.8 and Figure 4.7).

The volume occupied by the dodecane aliphatic side chains of the benzyl dicarboxylate stoppers was calculated to be  $850 \text{ \AA}^3$ , and the volume occupied by the butyl-siloxane side chains was calculated to be  $1200 \text{ \AA}^3$ , based on established packing volumes in liquid phases.<sup>135,136</sup> Based on these volumes and the diameters of the cores, the lengths of the cylindrical spaces occupied by the side chains of the benzyl dicarboxylate stoppers were calculated and added to the length of the core, giving excellent agreement with the observed spacing for **2-17<sup>4+</sup>**. The calculated total lengths are larger for **4-5<sup>4+</sup>** and both two-charged compounds (Table 4.4). These calculated molecular lengths also confirm the formation of a SmA phase for **2-17<sup>4+</sup>**, since a tilted SmC layer spacing would be markedly shorter than the observed spacing. Consequently, the markedly shorter observed layer spacings for **4-5<sup>4+</sup>**, **4-18<sup>2+</sup>** and **4-19<sup>2+</sup>**, compared to their calculated molecular lengths, confirm the formation of SmC phases for all three.

The calculated length of the molecule was used to calculate the approximate tilt angle for [2]rotaxanes **4-18<sup>2+</sup>** and **4-19<sup>2+</sup>**, with the long axis of the molecule tilted with respect to the director. The angles were determined to be  $31^\circ$  and  $36^\circ$ , respectively.



**Table 4.4 - Obtained (XRD) layer spacings and calculated molecular lengths of [2]rotaxanes 2-17<sup>4+</sup>, 4-5<sup>4+</sup>, 4-18<sup>2+</sup> and 4-19<sup>2+</sup>.**

Compound	d <sub>10</sub> (Å)	l <sub>calc</sub> (Å)
2-17 <sup>4+</sup>	39.6	38
4-5 <sup>4+</sup>	32.8	40
4-18 <sup>2+</sup>	40.3	47
4-19 <sup>2+</sup>	40.2	50

The applied model of cylindrical space filling is independent of other packing considerations such as the degree of interdigitation between adjacent side-chains. The calculated ratios are very similar to those mentioned in Chapter 2, confirming the formation of a stable and sufficiently fluid smectic LC phase for all [2]rotaxanes 4-5<sup>4+</sup>, 4-18<sup>2+</sup> and 4-19<sup>2+</sup>.

#### 4.3.7 Liquid Crystal Phase Determination

The mesophases formed by [2]rotaxanes 4-5<sup>4+</sup>, 4-18<sup>2+</sup> and 4-19<sup>2+</sup> were fully characterized by POM observations, DSC analysis and vt-XRD analysis and characterization of the [2]rotaxane 2-17<sup>4+</sup> was included for comparison. The phase characterization and transition temperatures measured by POM and DSC on heating are shown in Figure 4.17. [2]Rotaxanes 2-17<sup>4+</sup>, 4-5<sup>4+</sup> and 4-19<sup>2+</sup> form a single mesophase over the entire temperature range studied; 2-17<sup>4+</sup> forms a SmA phase, 4-5<sup>4+</sup> forms a lamellar gel and 4-19<sup>2+</sup> forms a SmC phase. [2]Rotaxane 4-18<sup>2+</sup> formed a SmC phase and DSC analysis revealed a transition below -29 °C which is likely due to crystallization. By POM the absence of schlieren textures confirmed the presence of a SmA phase for 2-17<sup>4+</sup> and the presence of schlieren textures for 4-18<sup>2+</sup> and 4-19<sup>2+</sup> confirmed the presence of a SmC phase. The approximate tilt angles for [2]rotaxanes 4-18<sup>2+</sup> and 4-19<sup>2+</sup> were

determined to be 31° and 36°. Comparison of the experimental and calculated molecular lengths also agreed with these phase designations. Thus, in reducing the charge on the core from four to two, there is an obvious increase in the fluidity for both the *n*-alkyl and alkyl-siloxane systems and this was also observed when processing these materials. In addition, clearing into the isotropic liquid phase occurred at lower temperatures for the two-charged systems over the four-charged. The thermal stability was increased by stoppering with ester formation, however the alkyl-siloxane systems showed decreased thermal stability due to hydrolysis of the siloxane moiety. The initial decomposition for each compound is marked with a black line in Figure 4.17, with decomposition for **2-17<sup>4+</sup>** occurring above 200 °C, **4-18<sup>2+</sup>** above 260 °C and both **4-5<sup>4+</sup>** and **4-19<sup>2+</sup>** above 158 °C.

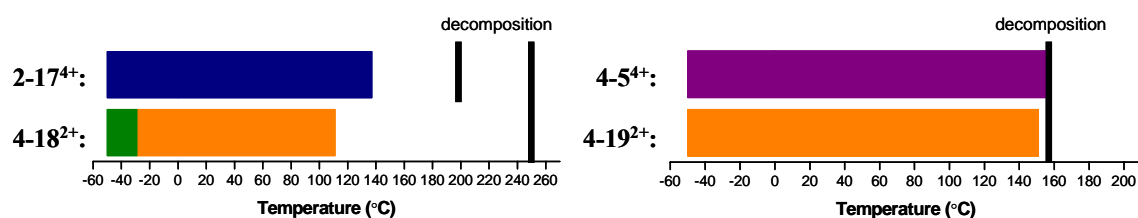


**Figure 4.17 - Phase transition temperatures for [2]rotaxanes 2-17<sup>4+</sup>, 4-5<sup>4+</sup>, 4-18<sup>2+</sup> and 4-19<sup>2+</sup> measured by DSC and POM on heating. (green, Cr; navy, SmA; orange, SmC; violet, lamellar gel. The start of decomposition is marked with a black line.)**

#### 4.4 SUMMARY AND CONCLUSIONS

The viscosity of the four-charged [2]rotaxane design was decreased by appending a siloxane moiety to the stoppers in place of the entirely aliphatic chains previously discussed. This [2]rotaxane formed a lamellar phase, as confirmed by XRD, but the material polymerized at elevated temperatures. By employing stoppering by formation of an ester, the ionic charge of the core was reduced from four positive charges to two, and this design showed not only a reduction in viscosity but cleared into the isotropic liquid

---

phase at lower temperatures and displayed increased thermal stability. The two-charged aliphatic stoppered [2]rotaxane showed increased thermal stability up to 260 °C, 60 °C higher than that of the four-charged material. This material formed a highly ordered SmC phase, which was confirmed by POM and vt-XRD. Clearing temperatures into the isotropic phase were lowered by 26 °C when comparing the four-charged to the two-charged material for the entirely aliphatic [2]rotaxanes. However, the siloxane moiety proved to be the most thermally labile with decomposition occurring at 158 °C in the two-charged material, which was 42 °C below that of the four-charged material. However, this [2]rotaxane did form a highly ordered SmC phase which was also confirmed by POM and vt-XRD. Both the four-charged and two-charged [2]rotaxanes exhibited improvements in ease of processing and alignment in thin films.

## 4.5 EXPERIMENTAL

### 4.5.1 General Comments

Sodium trifluoromethanesulfonate, 1,2-dibromoethane, diethyl-5-(hydroxymethyl)-isophthalate, 3-butene-1-ol, titanium isopropoxide, platinum(0)-1,3-divinyl-1,1,3,3-tetramethyldisiloxane complex, **Pt(dvs)**, solution in xylenes (~2 % Pt), phosphorus tribromide, methanesulfonyl chloride (mesylchloride), triethylamine, 4-bromopyridine, 4-formylphenyl boronic acid, palladium triphenylphosphine, chromium trioxide, 3,5-dicarboxymethylbenzoic acid, *p*-toluenesulfonylchloride, tributylphosphine and **DB24C8** were purchased from Aldrich and used as received. 1,1,1,3,3,5,5-Heptamethylsiloxane was purchased from Gelest Inc. and used as received. Deuterated solvents were obtained from Cambridge Isotope Laboratories and used as received. Solvents were dried using an Innovative Technologies Solvent Purification System. Microwave synthesis was carried out in either a 10 mL or 80 mL vessel on a CEM Discover microwave at 200W. Thin layer chromatography (TLC) was performed using Teledyne Silica gel 60 F<sub>254</sub> plates and viewed under UV light. Column chromatography was performed using Silicycle Ultra Pure Silica Gel (230 – 400 mesh). Flash column chromatography was performed using Teledyne Ultra Pure Silica/RP-C<sub>18</sub> Silica Gel (230 – 400 mesh) on a Teledyne Isco Combiflash R<sub>f</sub>. All flash chromatography was performed under pressure (120 mL/min. - 200 mL/min.) for normal phase silica and (10 mL/min. - 40 mL/min.) for RP-C<sub>18</sub> silica, with increasing pressure corresponding to larger columns. Unless otherwise stated, all flash chromatography applied gradient elution from 0 - 100 % with increasing polar solvent with respect to less polar solvent. Length of column (column volumes - CV) was determined by separation seen by TLC.

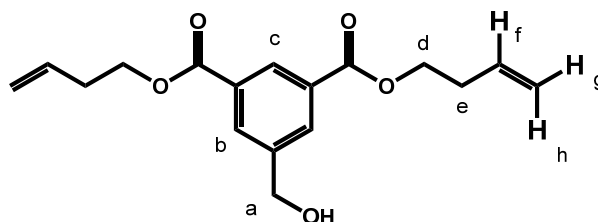
$^1\text{H}$  NMR,  $^{13}\text{C}$  NMR and 2-D experiments were performed on a Bruker Avance 500 instrument, with working frequency of 500.13 MHz for  $^1\text{H}$  nuclei, and 125.7 MHz for  $^{13}\text{C}$  nuclei, respectively. Chemical shifts are quoted in ppm relative to tetramethylsilane, using the residual solvent peak as a reference standard. Conventional 2-D NMR experiments ( $^1\text{H}$ - $^1\text{H}$  COSY) and ( $^1\text{H}$ - $^{13}\text{C}$  HETCOR) were conducted and used to help assign all peaks. High resolution mass spectrometry (HR-MS) experiments were performed on a Micromass LCT Electrospray (ESI) time-of-flight (TOF) Mass spectrometer. Solutions of 50-100 ng/ $\mu\text{L}$  were prepared in  $\text{CH}_3\text{CN}$  and injected for analysis at a rate of 5  $\mu\text{L}/\text{min}$  using a syringe pump.

Calorimetric studies were performed on a Mettler Toledo DSC 822 $^\circ$  and thermal gravimetric analysis with mass spectrometric detection of evolved gases was performed on a Mettler Toledo TGA SDTA 851e that was attached to a Pfeiffer Vacuum ThermoStar<sup>TM</sup> mass spectrometer (1-300 amu) *via* a thin glass capillary. Helium (99.99 %) was used to purge the system with a flow rate of 30 mL/min. Samples were held at 25  $^\circ\text{C}$  for 30 min before heating to 550  $^\circ\text{C}$  at 2  $^\circ\text{C}/\text{min}$ . A mass range between 16 m/z and 150 m/z was constantly scanned. All samples were run in aluminum crucibles. Powder XRD measurements were recorded on a Bruker D8 Discover diffractometer equipped with a Hi-Star area detector and GADDS software and operated at 40 kV and 40 mA.  $\text{CuK}\alpha_1$  radiation ( $\lambda = 1.54187 \text{ \AA}$ ) was used and the initial beam diameter was 0.5 mm. A custom made Instec hot stage (based on HS-400) was used for VT-XRD that covers a temperature range of -40  $^\circ\text{C}$  to 350  $^\circ\text{C}$ . Bulk samples for variable temperature XRD were filled into a 2 mm diameter hole in a 1 mm thick copper plate and covered with Kapton<sup>TM</sup> foil. This plate was mounted in an Instec hot-stage, aligned, and run at theta angles of 0 $^\circ$ ,

and 15° for 30 or 60 min. Spectra were combined and evaluated in EVA and plotted with Origin. Polarized light microscopy was performed on an Olympus TPM51 polarized light microscope equipped with a Linkam variable temperature stage HCS410 and digital photographic imaging system (DITO1).

## 4.5.2 Synthesis of 4-1

Diethyl-5-(hydroxymethyl)-isophthalate (5.63 g, 0.0223 mol), 3-butene-1-ol (12.87 g, 0.1785 mol), and  $\text{Ti}(\text{O-}i\text{-Pr})_4$  (6.34 g, 0.0223 mol) were heated (130 °C) under a nitrogen atmosphere for three days. The EtOH bi-product was removed via a Dean Stark apparatus. The solution was neutralized with 0.1 M HCl and the product extracted with  $\text{CH}_2\text{Cl}_2$ . The organic layer was washed with  $\text{H}_2\text{O}$ , dried with  $\text{MgSO}_4$ , filtered and concentrated to yellow oil. The product was then purified by flash column chromatography on silica gel with (hexanes: EtOAc) gradient (0 - 100 % EtOAc) as eluant. The resulting colorless oil was collected. Yield: 6.72 g, 99 %.

Table 4.5 -  $^1\text{H}$  NMR data of 4-1 in  $\text{CDCl}_3$ . MW = 304.338 g/mol

Proton	$\delta$ (ppm)	Multiplicity	# Protons	$J$ (Hz)
a	4.74	s	2	--
b	8.15	s	2	--
c	8.50	s	1	--
d	4.35	t	4	$^3J_{de} = 6.74$
e	2.50	dt	4	$^3J_{ed} = 6.74$ ; $^3J_{ef} = 6.99$
f	5.83	dtd	2	$^3J_{fh} = 10.28$ ; $^3J_{fe} = ^3J_{fg} = 6.99$
g	5.08	dd	2	$^3J_{gf} = 10.28$ ; $^2J_{gh} = 1.45$
h	5.13	dd	2	$^3J_{hf} = 17.15$ ; $^2J_{hg} = 1.45$

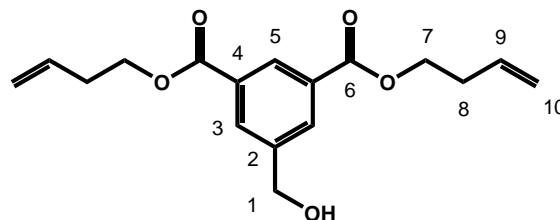
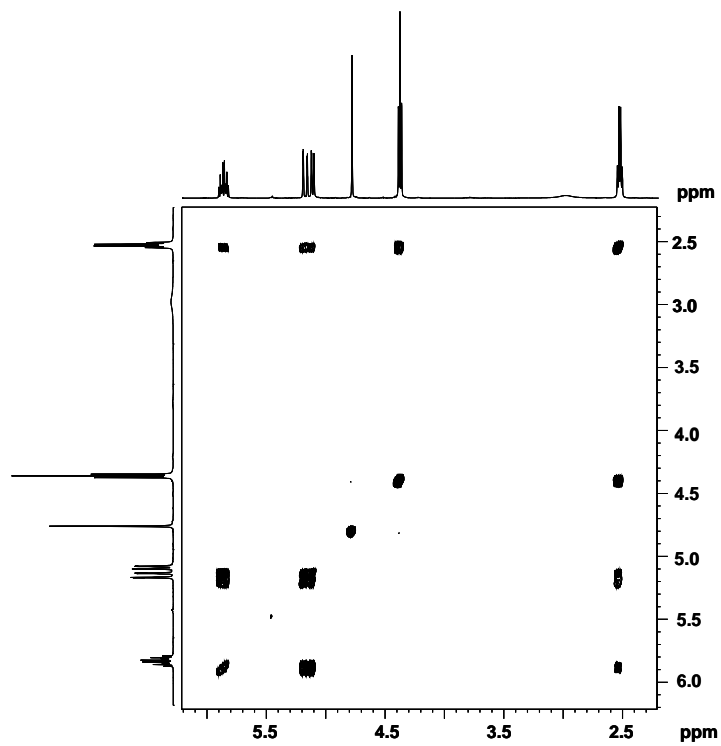


**Table 4.6 – <sup>13</sup>C NMR data of 4-1 in CDCl<sub>3</sub>. MW = 304.338 g/mol. Quaternary carbons assigned by software**

Carbon	$\delta$ (ppm)	# Carbons
1	68.27	1
2	140.95	1
3	133.81	2
4	131.69	2
5	128.20	1
6	164.73	2
7	64.82	2
8	33.54	2
9	135.49	2
10	17.02	2

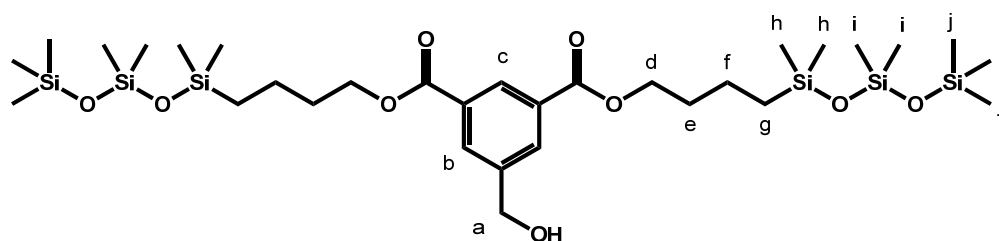


COSY of 4-1 in CD<sub>3</sub>CN.



## 4.5.3 Synthesis of 4-2

4-1 (3.97 g, 0.0130 mol) was dissolved in dry toluene in a schlenk flask, under nitrogen at 15 °C. 1,1,1,3,3,5,5-Heptamethylsiloxane (7.85 mL, 0.0287 mol) was added via glass syringe, followed by Pt(dvs) (0.50 mL). The mixture was then stirred until the reaction was complete (5 - 15 min). Solvents were evaporated via vacuum line. The product was then purified by flash column chromatography on silica gel with (hexanes: EtOAc) gradient (0 - 10 % EtOAc) as eluant. The resulting colorless oil was collected. Yield: 6.64 g, 68 %.

Table 4.7 – <sup>1</sup>H NMR data of 4-2 in CDCl<sub>3</sub>. MW= 749.347 g/mol

Proton	δ (ppm)	Multiplicity	# Protons	J (Hz)
a	4.80	s	2	--
b	8.21	s	2	--
c	8.58	s	1	--
d	4.34	t	4	<sup>3</sup> J <sub>de</sub> = 6.75
e	1.81	tt	4	<sup>3</sup> J <sub>ed</sub> = 6.75; <sup>3</sup> J <sub>ef</sub> = 7.35
f	1.48	tt	4	<sup>3</sup> J <sub>fe</sub> = <sup>3</sup> J <sub>fg</sub> = 7.35
g	0.61	t	4	<sup>3</sup> J <sub>gf</sub> = 8.40
h	0.01	s	12	--
i	0.08	s	12	--
j	0.07	s	18	--

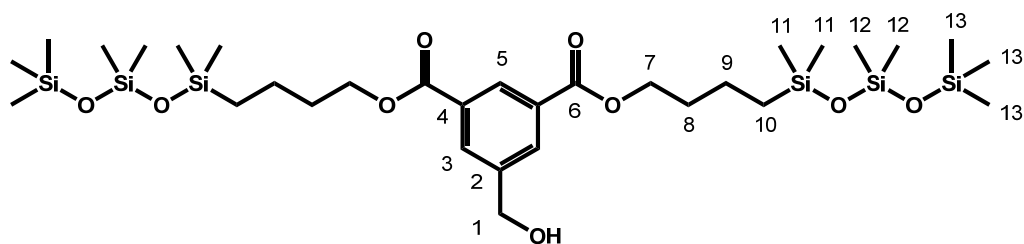
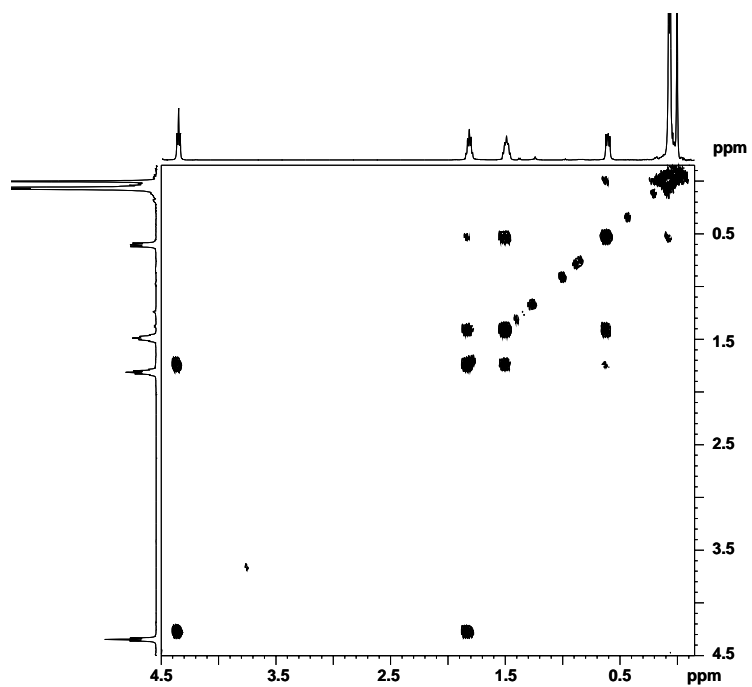


**Table 4.8** –  $^{13}\text{C}$  NMR data of 4-2 in  $\text{CDCl}_3$ . MW= 749.347 g/mol. Quaternary carbons assigned by software

Carbon	$\delta$ (ppm)	# Carbons
1	67.36	1
2	139.11	1
3	133.89	2
4	131.65	2
5	129.98	1
6	165.43	2
7	65.28	2
8	32.13	2
9	17.37	2
10	18.61	2
11	0.47	4
12	1.32	4
13	1.96	6

**COSY of 4-2 in CDCl<sub>3</sub>.**



## 4.5.4 Synthesis of 4-3

4-2 (3.12 g, 0.0042 mol) was dissolved in dry THF (80 mL) under nitrogen and cooled (0 °C) on ice. Phosphorus tribromide (3.12 mL, 0.0031 mol) 1.0 M in CH<sub>2</sub>Cl<sub>2</sub> was added dropwise over 15 min. and stirring continued for 4 h. The solution was concentrated and product purified by flash column chromatography on silica gel with (hexanes: EtOAc) gradient (0 - 30 % EtOAc) as eluant. The resulting colorless oil was collected. Yield: 0.41 g, 12 %.

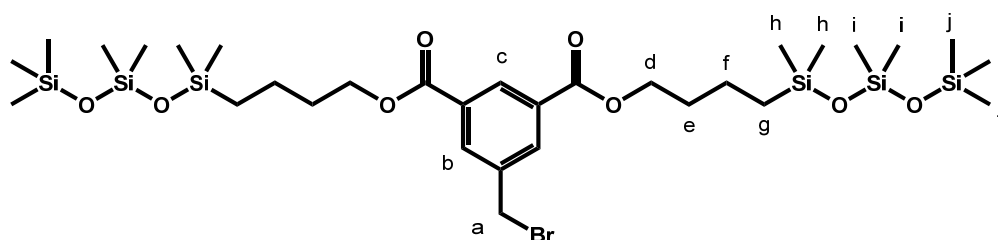
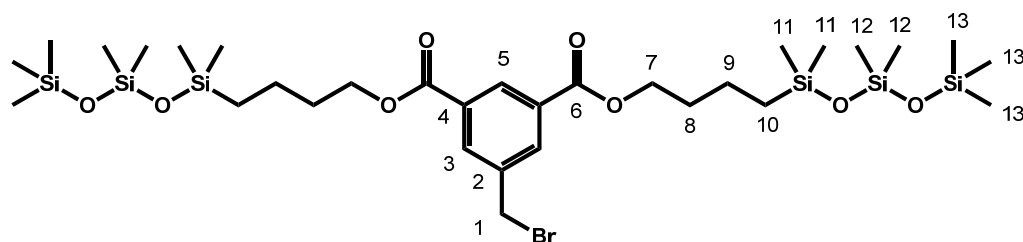


Table 4.9 – <sup>1</sup>H NMR data of 4-3 in CDCl<sub>3</sub>. MW= 812.244 g/mol

Proton	δ (ppm)	Multiplicity	# Protons	J (Hz)
a	4.53	s	2	--
b	8.23	s	2	--
c	8.59	s	1	--
d	4.35	t	4	<sup>3</sup> J <sub>de</sub> = 6.75
e	1.82	tt	4	<sup>3</sup> J <sub>ed</sub> = 6.75; <sup>3</sup> J <sub>ef</sub> = 7.29
f	1.49	tt	4	<sup>3</sup> J <sub>fe</sub> = <sup>3</sup> J <sub>fg</sub> = 7.29
g	0.61	t	4	<sup>3</sup> J <sub>gf</sub> = 8.43
h	0.01	s	12	--
i	0.08	s	12	--
j	0.07	s	18	--

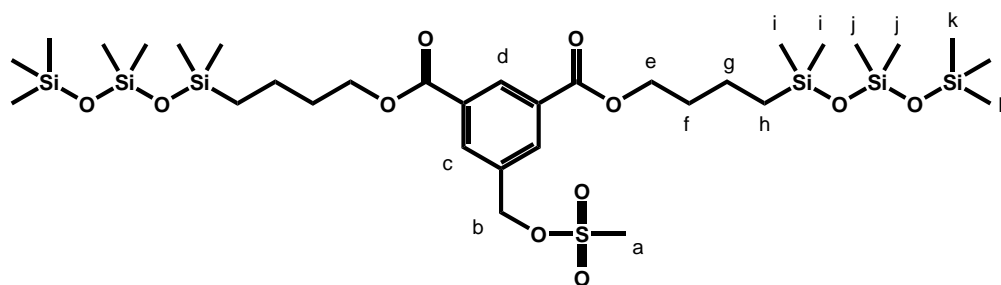


**Table 4.10** –  $^{13}\text{C}$  NMR data of 4-3 in  $\text{CDCl}_3$ . MW= 812.244 g/mol. Quaternary carbons assigned by software

Carbon	$\delta$ (ppm)	# Carbons
1	31.54	1
2	138.69	1
3	134.01	2
4	131.71	2
5	130.46	1
6	165.32	2
7	65.39	2
8	32.12	2
9	17.86	2
10	19.75	2
11	0.17	4
12	1.27	4
13	1.81	6

## 4.5.5 Synthesis of 4-4

4-2 (3.38 g, 0.0045 mol) was dissolved in dry  $\text{CH}_2\text{Cl}_2$  (~ 0.2 M) containing 50 % molar excess of triethylamine (31.74 mL, 0.2259 mol) and the reaction vessel was cooled (-15 °C) with MeOH/NaCl bath. A 10 % excess of mesyl chloride (3.50 mL, 0.0452 mol) was added dropwise over 15 min. and stirring continued for 15 min. The solution was transferred to a separatory funnel and washed with ice water followed by 10 % HCl, saturated  $\text{NaHCO}_3$  brine and water. The organic layer was concentrated and crude orange oil purified by flash column chromatography on silica gel with (hexanes: EtOAc) gradient (5 - 30 % EtOAc) as eluant. The resulting pale yellow oil was collected. Yield: 3.52 g, 96 %.

Table 4.11 –  $^1\text{H}$  NMR data of 4-4 in  $\text{CDCl}_3$ . MW= 827.438 g/mol

Proton	$\delta$ (ppm)	Multiplicity	# Protons	$J$ (Hz)
a	3.03	s	3	--
b	5.30	s	2	--
c	8.25	s	2	--
d	8.68	s	1	--
e	4.36	t	4	$^3J_{ef} = 6.78$
f	1.82	tt	4	$^3J_{fe} = 6.78; ^3J_{fg} = 7.13$
g	1.48	tt	4	$^3J_{gf} = ^3J_{gh} = 7.13$
h	0.61	t	4	$^3J_{hf} = 8.38$
i	0.01	s	12	--
j	0.08	s	12	--
j	0.07	s	18	--

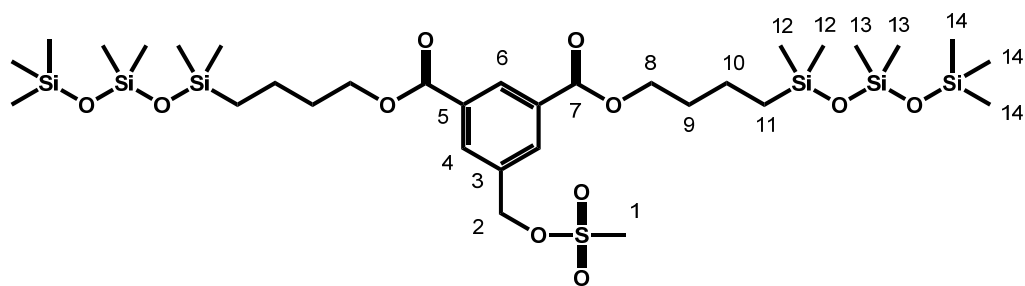


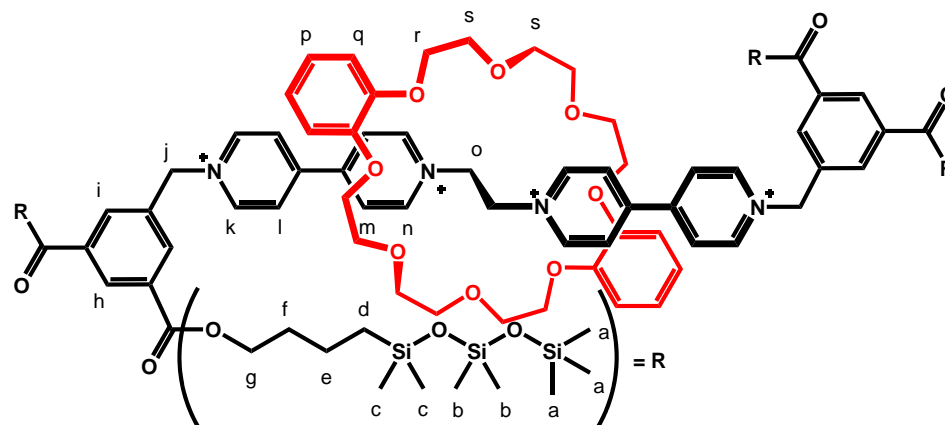
**Table 4.12** –  $^{13}\text{C}$  NMR data of 4-4 in  $\text{CDCl}_3$ . MW= 827.438 g/mol. Quaternary carbons assigned by software

Carbon	$\delta$ (ppm)	# Carbons
1	38.34	1
2	69.60	1
3	134.52	1
4	133.59	2
5	131.89	2
6	131.39	1
7	165.31	2
8	65.61	2
9	32.19	2
10	17.93	2
11	19.80	2
12	0.16	4
13	1.23	4
14	1.87	6

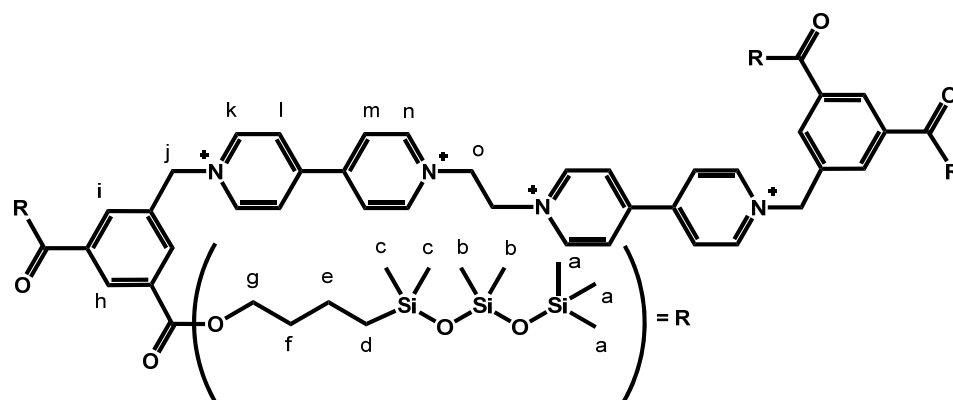


#### 4.5.6 Synthesis of Compound [4-5][OTf]<sub>4</sub> and [4-6][OTf]<sub>4</sub>

[2-2][OTf]<sub>2</sub> (61.49 mg, 0.0963 mmol) and **DB24C8** (215.94 mg, 0.4815 mmol) were dissolved in a two-phase NaOTf (aq)/MeNO<sub>2</sub> (0.5 and 25 mL) mixture and placed in a thick-walled 80 mL reaction vessel. **4-4** (312.54 mg, 0.3852 mmol) was dissolved in CHCl<sub>3</sub> (10 mL) and a catalytic amount of TBAI (5 mg) was added to the 80 mL vessel with a stir bar and microwaved for 10 h at 50 °C. The MeNO<sub>2</sub> layer was washed with H<sub>2</sub>O (3 x 10 mL), dried over MgSO<sub>4</sub> and the solvent removed. The orange residue was recrystallized from EtOAc several times. Excess crown precipitated out first followed by rotaxane with small amounts of crown. The product was then purified and isolated by flash column chromatography on RP-C<sub>18</sub> silica gel using MeOH as eluant, yielding a deep red/orange glassy solid. Yield: 118.02 mg, 43 %. **ESI-MS**:  $m/z$  1274.4546 (calc.) for C<sub>110</sub>H<sub>178</sub>F<sub>6</sub>N<sub>4</sub>O<sub>30</sub>S<sub>2</sub>Si<sub>12</sub> [M-2OTF]<sup>2+</sup>, found 1274.4545.  $m/z$  562.751 (calc.) for C<sub>110</sub>H<sub>178</sub>N<sub>4</sub>O<sub>26</sub>Si<sub>12</sub> [M]<sup>4+</sup>, found 562.748. The dumbbell (without **DB24C8** macrocycle) was also isolated from the column. The product was isolated as a waxy pale beige solid. Yield: 26.31 mg, 12 %. **ESI-MS**:  $m/z$  1050.3497 (calc.) for C<sub>86</sub>H<sub>146</sub>F<sub>6</sub>N<sub>4</sub>O<sub>22</sub>S<sub>2</sub>Si<sub>12</sub> [M-2OTF]<sup>2+</sup>, found 1050.3503,  $m/z$  650.5823 (calc.) for C<sub>85</sub>H<sub>146</sub>F<sub>3</sub>N<sub>4</sub>O<sub>19</sub>SSi<sub>12</sub> [M-OTF]<sup>3+</sup>, found 650.5612.

Table 4.13 –  $^1\text{H}$  NMR data of [4-5][OTf] $_4$  in  $\text{CD}_3\text{CN}$ .  $\text{MW}_{\text{OTf}} = 2849.884$  g/mol

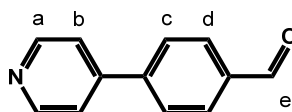
Proton	$\delta$ (ppm)	Multiplicity	# Protons	$J$ (Hz)
a	0.06	s	4	--
b	0.08	s	36	--
c	0.01	s	24	--
d	0.63	t	8	$^3J_{de} = 8.35$
e	1.51	tt	8	$^3J_{ef} = ^3J_{ed} = 7.25$
f	1.82	tt	8	$^3J_{fg} = 6.68; ^3J_{fe} = 7.25$
g	4.36	t	8	$^3J_{gf} = 6.68$
h	8.63	s	2	--
i	8.40	s	4	--
j	5.98	s	4	--
k	9.02	d	4	$^3J_{kl} = 6.64$
l	8.24	d	4	$^3J_{lk} = 6.64$
m	8.28	d	4	$^3J_{mn} = 6.64$
n	9.34	d	4	$^3J_{nm} = 6.64$
o	5.59	s	4	--
p	6.66	dd	4	$^3J_{\text{meta}} = 3.58; ^3J_{\text{ortho}} = 5.75$
q	6.42	dd	4	$^3J_{\text{meta}} = 3.58; ^3J_{\text{ortho}} = 5.75$
r	3.99	t	8	--
s	4.15	m	16	--

Table 4.14 –  $^1\text{H}$  NMR data of [4-6][OTf] $_4$  in  $\text{CD}_3\text{CN}$ .  $\text{MW}_{\text{OTf}} = 2401.378$  g/mol

Proton	$\delta$ (ppm)	Multiplicity	# Protons	$J$ (Hz)
<b>a</b>	0.06	s	36	--
<b>b</b>	0.08	s	24	--
<b>c</b>	0.01	s	24	--
<b>d</b>	0.63	t	8	$^3J_{\text{de}} = 8.33$
<b>e</b>	1.51	tt	8	$^3J_{\text{ed}} = ^3J_{\text{ef}} = 3.89$
<b>f</b>	1.81	tt	8	$^3J_{\text{fe}} = ^3J_{\text{fg}} = 6.87$
<b>g</b>	4.35	t	8	$^3J_{\text{gf}} = 6.87$
<b>h</b>	8.62	s	2	--
<b>i</b>	8.39	s	4	--
<b>j</b>	5.95	s	4	--
<b>k</b>	9.04	d	4	$^3J_{\text{kl}} = 6.45$
<b>l</b>	8.48	d	4	$^3J_{\text{lk}} = 6.45$
<b>m</b>	8.51	d	4	$^3J_{\text{mn}} = 6.45$
<b>n</b>	9.07	d	4	$^3J_{\text{nm}} = 6.45$
<b>o</b>	5.31	s	4	--

## 4.5.7 Synthesis of 4-7

This compound was synthesized according to literature<sup>165</sup> with slight modification of the published procedure. 4-Bromopyridine (5.00 g, 0.0257 mol), 4-formylphenyl boronic acid (3.86 g, 0.0257 mol) and NaCO<sub>3</sub> (4.24 g, 0.0511 mol) were dissolved in MeCN (200 mL) and degassed water (100 mL) under nitrogen. The Pd(PPh<sub>3</sub>)<sub>4</sub> catalyst was then added and the reaction refluxed for 20 h. The reaction mixture was cooled to room temperature, filtered and washed with MeCN. The product was extracted with CHCl<sub>3</sub> (3 x 100 mL), washed with H<sub>2</sub>O (2 x 100 mL) and then dried with MgSO<sub>4</sub>. The solvent was removed by a rotary evaporator and the resulting solid was subjected to column chromatography with CHCl<sub>3</sub>:MeOH gradient (0-5 % MeOH) as eluant. The product was obtained as a white powder. Yield: 4.71 g, 99 %.



**Table 4.15** - <sup>1</sup>H NMR data of 4-7 in CDCl<sub>3</sub>. MW = 183.206 g/mol

Proton	δ (ppm)	Multiplicity	# Protons	J (Hz)
<b>a</b>	8.70	d	2	<sup>3</sup> J <sub>ab</sub> = 6.01
<b>b</b>	7.53	d	2	<sup>3</sup> J <sub>ba</sub> = 6.01
<b>c</b>	7.78	d	2	<sup>3</sup> J <sub>cd</sub> = 8.15
<b>d</b>	7.99	d	2	<sup>3</sup> J <sub>dc</sub> = 8.15
<b>e</b>	10.08	s	1	--

#### 4.5.8 Synthesis of 4-8

4-7 (5.50 g, 0.0300 mol) was dissolved in EtOH (250 mL) under nitrogen and cooled on ice (0 °C). NaBH<sub>4</sub> (2.273 g, 0.0601 mol) was added very slowly and the reaction was left to stir over night. The NaBH<sub>4</sub> was neutralized by slow addition of 1.0 M HCl (~80 mL), and the reaction filtered and washed with CH<sub>2</sub>Cl<sub>2</sub>. The organic layer was washed with NaHCO<sub>3</sub> (2 x 100 mL), followed by H<sub>2</sub>O (2 x 100 mL) and then dried with MgSO<sub>4</sub>. The solvent was evaporated using a rotary evaporator and the product was then purified by flash column chromatography on silica gel with (CHCl<sub>3</sub>: MeOH) gradient (0 - 5 % MeOH) as eluant. The resulting white solid was collected. Yield: 4.34 g, 78 %.

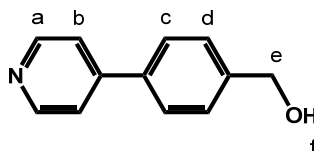
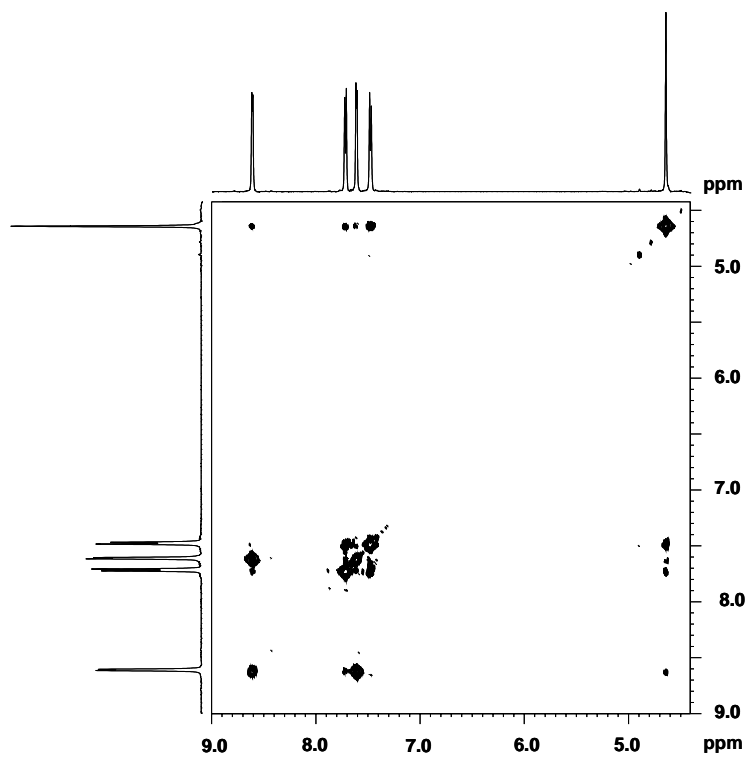


Table 4.16 - <sup>1</sup>H NMR data of 4-8 in CD<sub>3</sub>CN. MW = 185.222 g/mol

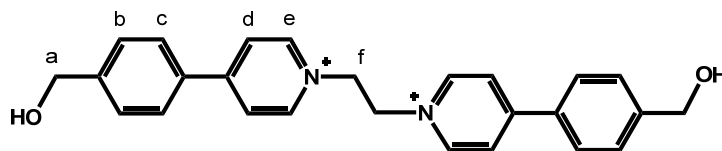
Proton	δ (ppm)	Multiplicity	# Protons	J (Hz)
<b>a</b>	8.61	d	2	<sup>3</sup> J <sub>ab</sub> = 5.83
<b>b</b>	7.60	d	2	<sup>3</sup> J <sub>ba</sub> = 5.83
<b>c</b>	7.47	d	2	<sup>3</sup> J <sub>cd</sub> = 8.17
<b>d</b>	7.71	d	2	<sup>3</sup> J <sub>dc</sub> = 8.17
<b>e</b>	4.64	s	2	--
<b>f</b>	2.19	s	1	--

COSY of 4-8 in CD<sub>3</sub>CN.



#### 4.5.9 Synthesis of [4-9][OTf]<sub>2</sub>

Was synthesized according to a previous method with modification.<sup>162</sup> **4-8** (1.42 g, 0.0077 mol) and 1,2-dibromoethane (0.33 mL, 0.0038 mol) were dissolved in hot MeNO<sub>2</sub> (50mL) in a thick-walled 80 mL vessel and microwaved for 5 h at 80 °C. The precipitate was filtered hot and washed with hot MeNO<sub>2</sub>. The white solid was anion exchanged to the triflate salt by two layer hot NaOTf (aq)/MeNO<sub>2</sub>. The hot MeNO<sub>2</sub> was washed with H<sub>2</sub>O (2 x 10 mL) and concentrated to yield white powder. Yield: 2.38 g, 89 % **ESI-MS**: *m/z* 547.1509 (calc.) for C<sub>27</sub>H<sub>26</sub>F<sub>3</sub>N<sub>2</sub>O<sub>5</sub>S [M-OTF]<sup>+</sup>, found 547.1517.

Table 4.17 -  $^1\text{H}$  NMR data of [4-9][Br]<sub>2</sub> in D<sub>2</sub>O. MW<sub>Br-</sub> = 558.305 g/mol

Proton	$\delta$ (ppm)	Multiplicity	# Protons	$J$ (Hz)
a	4.63	s	4	--
b	7.85	d	4	$^3J_{bc} = 7.83$
c	7.50	d	4	$^3J_{cb} = 7.83$
d	8.25	d	4	$^3J_{de} = 6.15$
e	8.66	d	4	$^3J_{ed} = 6.15$
f	5.19	s	4	--

Table 4.18 -  $^1\text{H}$  NMR data of [4-9][OTf]<sub>2</sub> in CD<sub>3</sub>CN. MW<sub>OTf-</sub> = 696.103 g/mol

Proton	$\delta$ (ppm)	Multiplicity	# Protons	$J$ (Hz)
a	4.70	s	4	--
b	7.94	d	4	$^3J_{bc} = 8.30$
c	7.61	d	4	$^3J_{cb} = 8.30$
d	8.31	d	4	$^3J_{de} = 6.91$
e	8.64	d	4	$^3J_{ed} = 6.91$
f	5.10	s	4	--



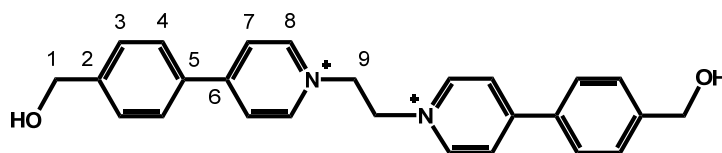
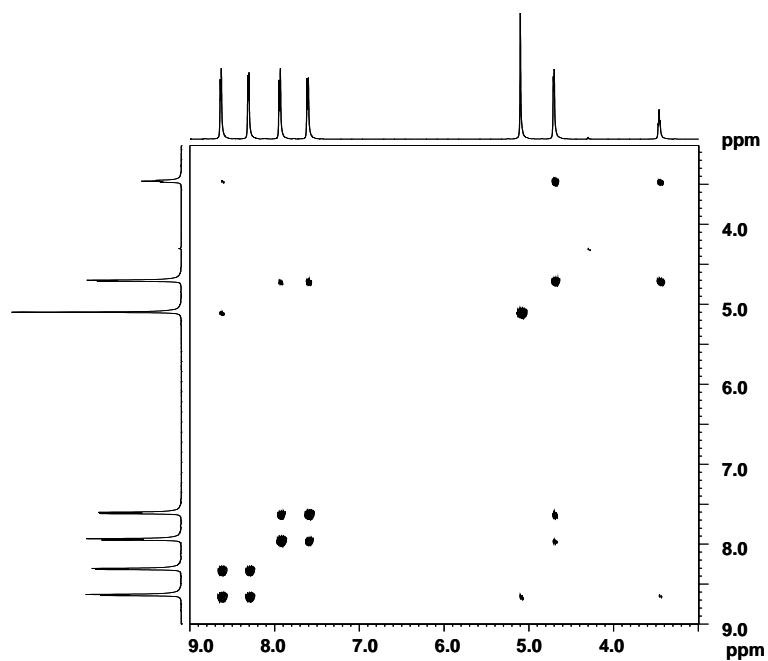


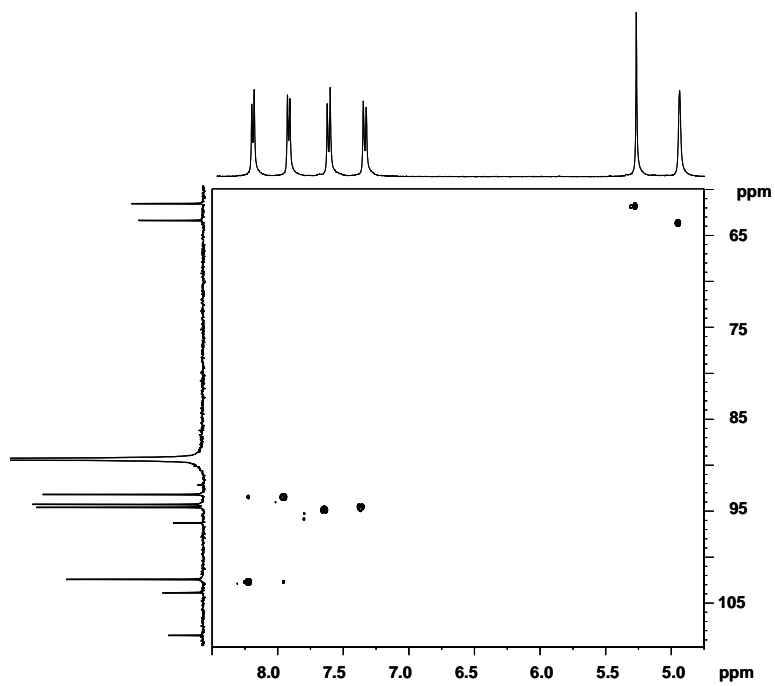
Table 4.19 –  $^{13}\text{C}$  NMR data of [4-9][OTf] $_2$  in  $\text{CD}_3\text{CN}$ .  $\text{MW}_{\text{OTf}} = 696.103$  g/mol. Quaternary carbons assigned by software

Carbon	$\delta$ (ppm)	# Carbons
1	62.97	2
2	147.88	2
3	127.75	4
4	128.42	4
5	131.97	2
6	157.62	2
7	125.48	4
8	144.85	4
9	59.12	2

COSY of [4-9][OTf] $_2$  in  $\text{CD}_3\text{CN}$ .



HETCOR of [4-9][OTf]<sub>2</sub> in CD<sub>3</sub>CN.



## 4.5.10 Synthesis of 4-10

**2-5** (4.78 g, 0.0090 mol) was dissolved in acetone (200 mL), treated with Jones reagent (18.67 mL, 0.0233 mol) added dropwise, and stirred for 2 - 3 h. The reaction mixture was quenched with 1-isopropanol (100 mL) and the precipitate filtered off. The solvent was concentrated to yield a crude white solid. The product was purified by flash column chromatography on silica gel with (CH<sub>2</sub>Cl<sub>2</sub>: MeOH) gradient (1 - 10 % MeOH) as eluant. The resulting waxy white solid was collected. Yield: 4.76 g, 96 %.

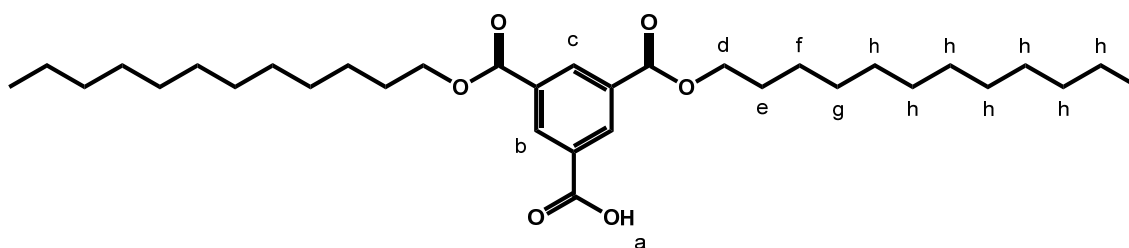


**Table 4.20** – <sup>1</sup>H NMR data of 4-10 in CDCl<sub>3</sub>. MW= 546.778 g/mol

Proton	δ (ppm)	Multiplicity	# Protons	J (Hz)
<b>a</b>	11.32	s	1	--
<b>b</b>	8.92	s	2	--
<b>c</b>	8.91	s	1	--
<b>d</b>	4.38	t	4	<sup>3</sup> J <sub>de</sub> = 6.76
<b>e</b>	1.80	tt	4	<sup>3</sup> J <sub>ed</sub> = 6.76, <sup>3</sup> J <sub>ef</sub> = 7.13
<b>f</b>	1.43	tt	4	<sup>3</sup> J <sub>fe</sub> = <sup>3</sup> J <sub>fg</sub> = 7.13
<b>g</b>	1.36	m	4	--
<b>h</b>	1.28	m	28	--
<b>i</b>	0.86	t	6	<sup>3</sup> J <sub>hg</sub> = 6.61

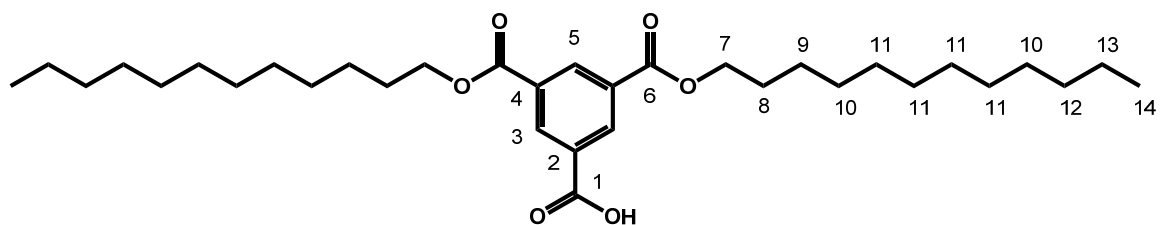
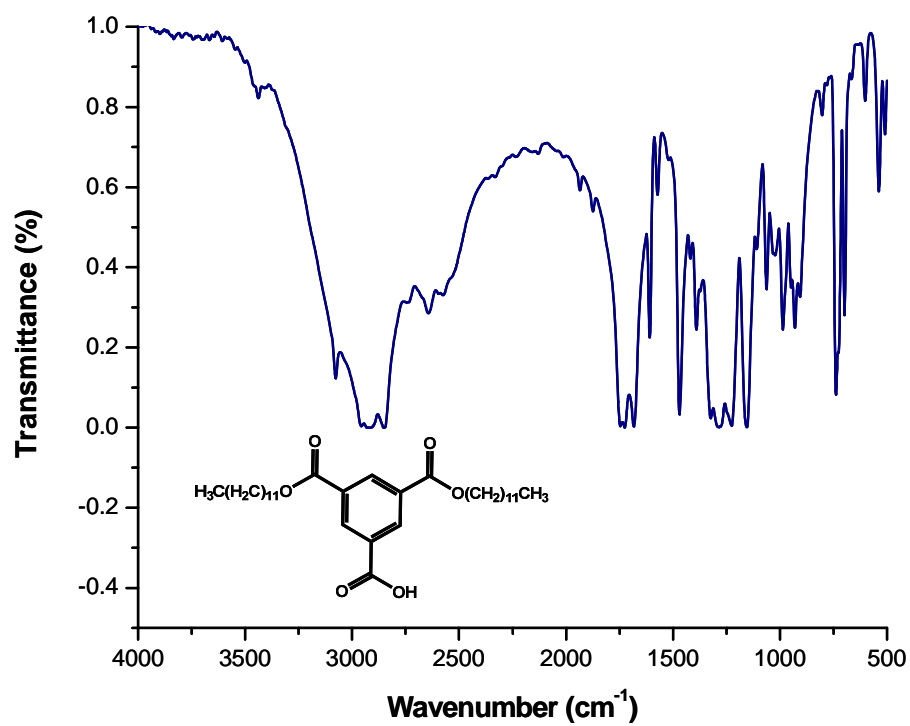


**Table 4.21** –  $^{13}\text{C}$  NMR data of 4-10 in  $\text{CDCl}_3$ . MW= 546.778 g/mol. Quaternary carbons assigned by software

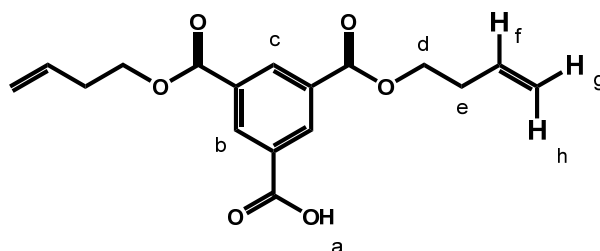
Carbon	$\delta$ (ppm)	# Carbons
1	170.35	1
2	130.27	1
3	135.10	2
4	131.87	2
5	135.54	1
6	165.02	2
7	66.11	2
8	28.74	2
9	26.07	2
10	29.41	4
11	29.69	8
12	32.01	2
13	22.79	2
14	14.21	2

## IR of 4-10



## 4.5.11 Synthesis of 4-11

**4-1** (6.07 g, 0.0199 mol) was dissolved in acetone (300 mL), treated with Jones reagent (41.44 mL, 0.0519 mol) added dropwise, and stirred for 2 - 3 h. The reaction mixture was quenched with 1-isopropanol (200 mL) and precipitate filtered off. The solvent was concentrated to a crude colorless oil. The product was purified by flash column chromatography on RP-C<sub>18</sub> silica gel with (H<sub>2</sub>O: MeOH) gradient (10 - 100 % MeOH) as eluant. The resulting colorless oil was collected. Yield: 5.46 g, 86 %.

Table 4.22 - <sup>1</sup>H NMR data of 4-11 in CDCl<sub>3</sub>. MW = 318.321 g/mol

Proton	δ (ppm)	Multiplicity	# Protons	J (Hz)
<b>a</b>	8.04	s	1	--
<b>b</b>	8.90	s	2	--
<b>c</b>	8.88	s	1	--
<b>d</b>	4.44	t	4	<sup>3</sup> J <sub>de</sub> = 6.68
<b>e</b>	2.56	dt	4	<sup>3</sup> J <sub>ed</sub> = 6.68; <sup>3</sup> J <sub>ef</sub> = 6.88
<b>f</b>	5.88	dtd	2	<sup>3</sup> J <sub>fh</sub> = 10.18; <sup>3</sup> J <sub>fe</sub> = <sup>3</sup> J <sub>fg</sub> = 6.88
<b>g</b>	5.19	dd	2	<sup>3</sup> J <sub>gf</sub> = 10.18; <sup>2</sup> J <sub>gh</sub> = 1.37
<b>h</b>	5.13	dd	2	<sup>3</sup> J <sub>hf</sub> = 17.16; <sup>2</sup> J <sub>hg</sub> = 1.37

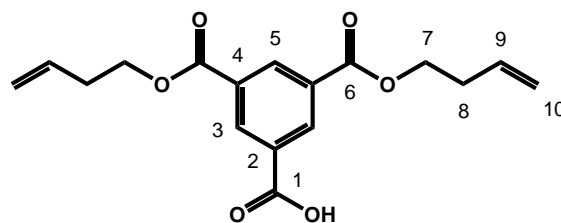
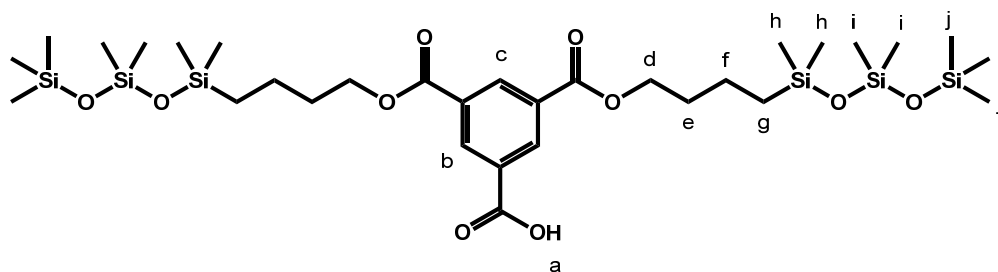


Table 4.23 –  $^{13}\text{C}$  NMR data 4-11 in  $\text{CDCl}_3$ . MW = 318.321 g/mol. Quaternary carbons assigned by software

Carbon	$\delta$ (ppm)	# Carbons
1	170.28	1
2	130.53	1
3	133.73	2
4	131.66	2
5	135.46	1
6	164.90	2
7	64.85	2
8	33.18	2
9	135.19	2
10	117.81	2

## 4.5.12 Synthesis of 4-12

**4-11** (6.73 g, 0.0212 mol) was dissolved in dry toluene (100 mL) in a schlenk flask, under nitrogen at 15 °C. 1,1,1,3,3,5,5-Heptamethylsiloxane (12.74 mL, 0.0465 mol) was added via a glass syringe, followed by Pt(dvs) (2.0 mL), and the reaction mixture was stirred until the reaction was complete (5 - 15 min). Solvents were evaporated via vacuum line. The product was then purified by column chromatography on silica gel with (hexanes: EtOAc) gradient (0 - 10 % EtOAc) as eluant. The resulting milky oil was collected. Yield: 7.64 g, 47 %.



**Table 4.24 – <sup>1</sup>H NMR of data 4-12 in CDCl<sub>3</sub>. MW= 763.331 g/mol**

Proton	δ (ppm)	Multiplicity	# Protons	J (Hz)
<b>a</b>	11.72	s	1	--
<b>b</b>	8.92	s	2	--
<b>c</b>	8.91	s	1	--
<b>d</b>	4.40	t	4	<sup>3</sup> J <sub>de</sub> = 6.93
<b>e</b>	1.85	tt	4	<sup>3</sup> J <sub>ed</sub> = 6.93; <sup>3</sup> J <sub>ef</sub> = 7.92
<b>f</b>	1.51	tt	4	<sup>3</sup> J <sub>fe</sub> = <sup>3</sup> J <sub>fg</sub> = 7.92
<b>g</b>	0.62	t	4	<sup>3</sup> J <sub>gf</sub> = 8.40
<b>h</b>	0.01	s	12	--
<b>i</b>	0.09	s	12	--
<b>j</b>	0.07	s	18	--



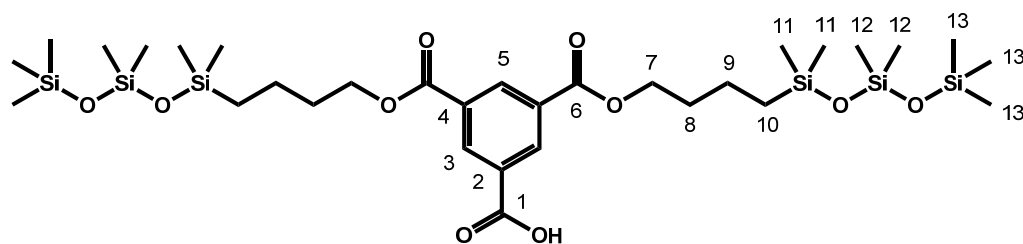
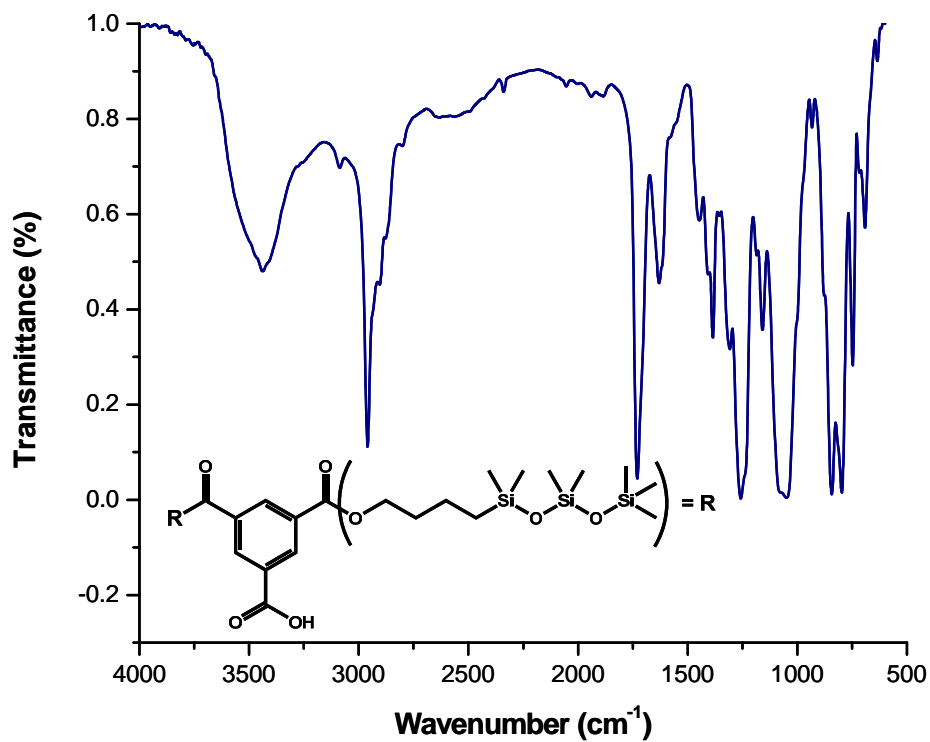


Table 4.25 –  $^{13}\text{C}$  NMR data of 4-12 in  $\text{CDCl}_3$ . MW= 763.331 g/mol. Quaternary carbons assigned by software

Carbon	$\delta$ (ppm)	# Carbons
1	170.72	1
2	130.34	1
3	139.09	2
4	131.86	2
5	135.50	1
6	165.01	2
7	65.73	2
8	32.17	2
9	17.92	2
10	19.82	2
11	1.89	4
12	0.24	4
13	1.34	6

## IR of 4-12



### 4.5.13 Synthesis of 4-13

3,5-Dicarboxymethylbenzoic acid (3.00 g, 0.0126 mol), TsCl (1.20 g, 0.0063 mol) and  $K_2CO_3$  (10.44 g, 0.0756 mol) was refluxed in 50:50 (MeCN: toluene) for 12 h. The crude mixture was filtered and concentrated to a white solid. The solid was taken up in  $CH_2Cl_2$  and washed with 1.0 M  $NaHCO_3$  (1 x 30 mL),  $H_2O$  (2 x 10 mL), dried over  $MgSO_4$ , and the solvent removed. The product was isolated as a white powder. Yield: 1.17 g, 20 %.

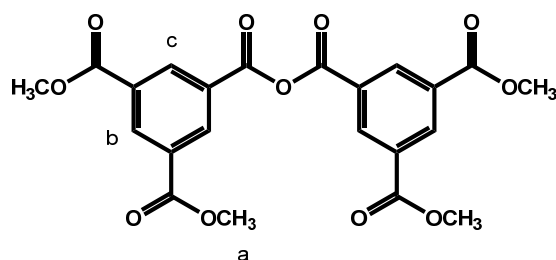


Table 4.26 –  $^1H$  NMR data of 4-13 in  $CDCl_3$ . MW= 458.372 g/mol

Proton	$\delta$ (ppm)	Multiplicity	# Protons	$J$ (Hz)
a	4.03	s	12	--
b	9.01	s	2	--
c	8.99	s	4	--

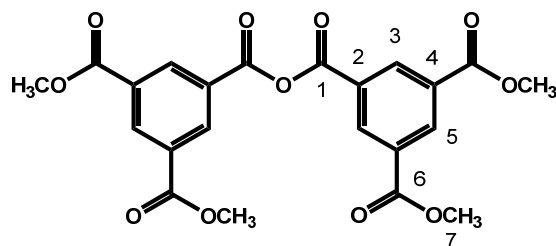
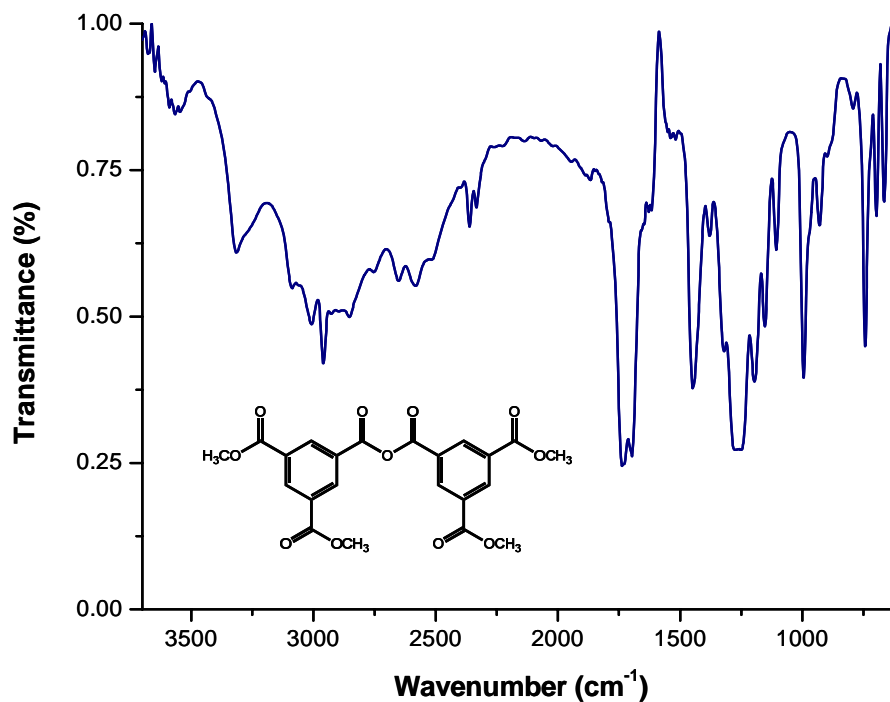


Table 4.27 –  $^{13}\text{C}$  NMR data of 4-13 in  $\text{CDCl}_3$ . MW= 458.372 g/mol. Quaternary carbons assigned by software

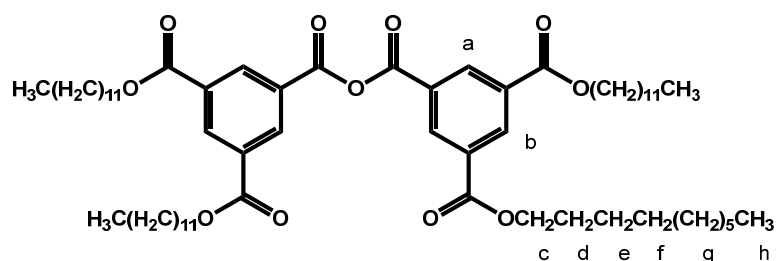
Carbon	$\delta$ (ppm)	# Carbons
1	160.57	2
2	129.63	2
3	135.41	4
4	131.97	4
5	136.21	2
6	164.97	4
7	52.89	4

#### IR of 4-13



## 4.5.14 Synthesis of 4-14

**4-10** (2.00 g, 0.0037 mol), TsCl (0.35 g, 0.0018 mol), and K<sub>2</sub>CO<sub>3</sub> (3.03 g, 0.0219 mol) was refluxed in CHCl<sub>3</sub> for 2 h. The crude mixture was filtered and concentrated to a white solid. The solid was taken up in CH<sub>2</sub>Cl<sub>2</sub> and washed with 1.0 M NaHCO<sub>3</sub> (1 x 50 mL), H<sub>2</sub>O (2 x 50 mL), dried over MgSO<sub>4</sub>, and the solvent removed. The product was isolated as a white waxy solid. Yield: 2.00 g, 50 %.

Table 4.28 – <sup>1</sup>H NMR data of 4-14 in CDCl<sub>3</sub>. MW= 1047.488 g/mol

Proton	δ (ppm)	Multiplicity	# Protons	J (Hz)
a	8.92	s	4	--
b	8.91	s	2	--
c	4.39	t	8	<sup>3</sup> J <sub>de</sub> = 6.69
d	1.81	tt	8	<sup>3</sup> J <sub>ed</sub> = 6.69, <sup>3</sup> J <sub>ef</sub> = 7.07
e	1.42	tt	8	<sup>3</sup> J <sub>fe</sub> = <sup>3</sup> J <sub>fg</sub> = 7.07
f	1.28	m	32	--
g	0.87	t	12	<sup>3</sup> J <sub>hg</sub> = 6.45

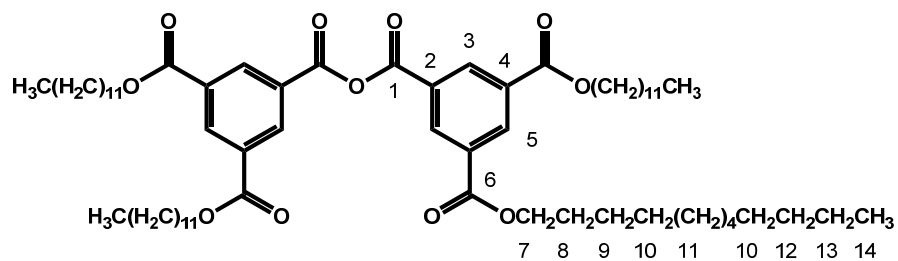
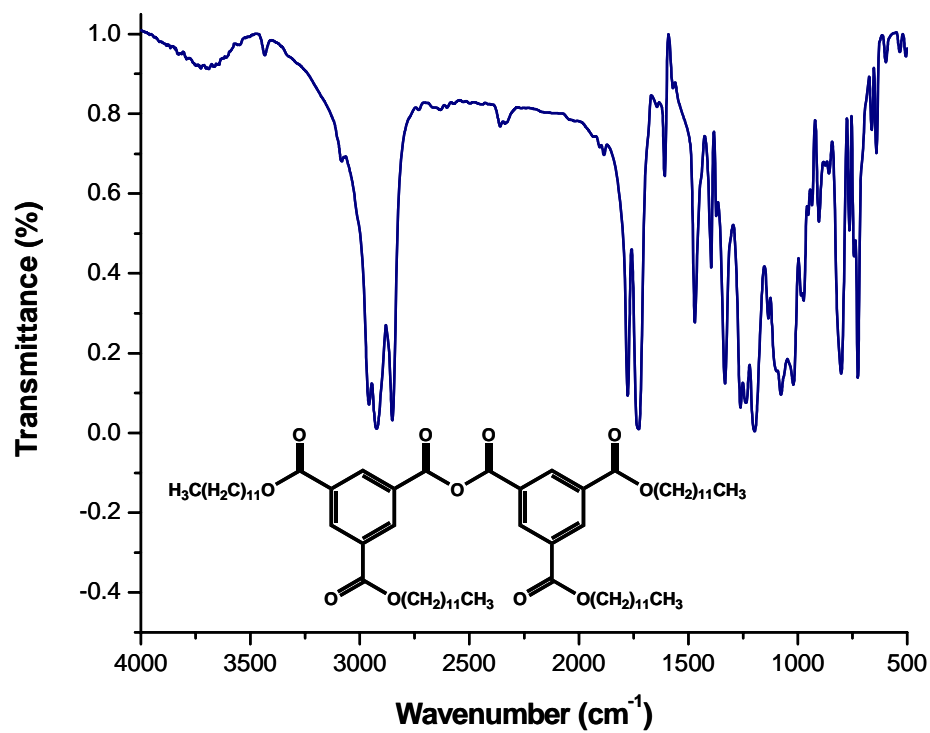


Table 4.29 –  $^{13}\text{C}$  NMR data of 4-14 in  $\text{CDCl}_3$ . MW= 1047.488 g/mol. Quaternary carbons assigned by software

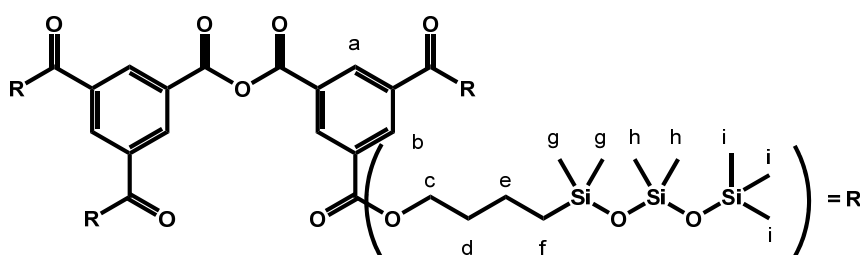
Carbon	$\delta$ (ppm)	# Carbons
1	160.68	2
2	129.52	2
3	135.22	4
4	132.29	4
5	136.07	2
6	164.55	4
7	66.16	4
8	28.66	4
9	25.99	4
10	29.42	8
11	31.92	16
12	31.99	4
13	22.69	4
14	14.11	4

## IR of 4-14



## 4.5.15 Synthesis of 4-15

4-12 (3.67 g, 0.0048 mol), TsCl (0.46 g, 0.0024 mol) and K<sub>2</sub>CO<sub>3</sub> (3.99 g, 0.0289 mol) was refluxed in CHCl<sub>3</sub> for 1.5 h. The crude mixture was filtered and concentrated to a colorless oil. The oil was taken up in CH<sub>2</sub>Cl<sub>2</sub> and washed with 1.0 M NaHCO<sub>3</sub> (1 x 50 mL), H<sub>2</sub>O (2 x 50 mL), dried over MgSO<sub>4</sub>, and the solvent removed. The product was isolated as a colorless oil. Yield: 3.61 g, 50 %.

Table 4.30 – <sup>1</sup>H NMR data of 4-15 in CDCl<sub>3</sub>. MW= 1508.647 g/mol

Proton	δ (ppm)	Multiplicity	# Protons	J (Hz)
a	8.98	s	4	--
b	8.93	s	2	--
c	4.40	t	8	<sup>3</sup> J <sub>cd</sub> = 7.98
d	1.85	tt	8	<sup>3</sup> J <sub>dc</sub> = 7.98; <sup>3</sup> J <sub>de</sub> = 7.18
e	1.51	tt	8	<sup>3</sup> J <sub>ed</sub> = <sup>3</sup> J <sub>ef</sub> = 7.18
f	0.62	t	8	<sup>3</sup> J <sub>fe</sub> = 8.31
g	0.02	s	24	--
h	0.10	s	24	--
i	0.09	s	36	--



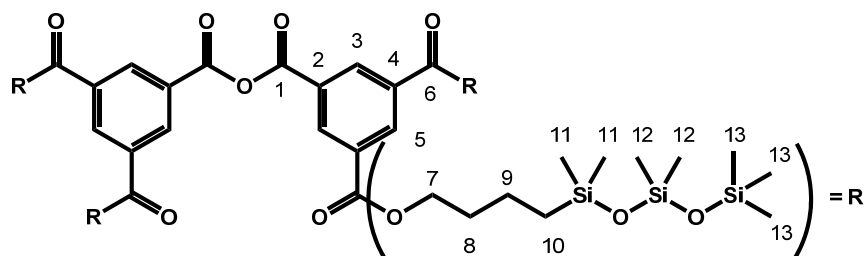
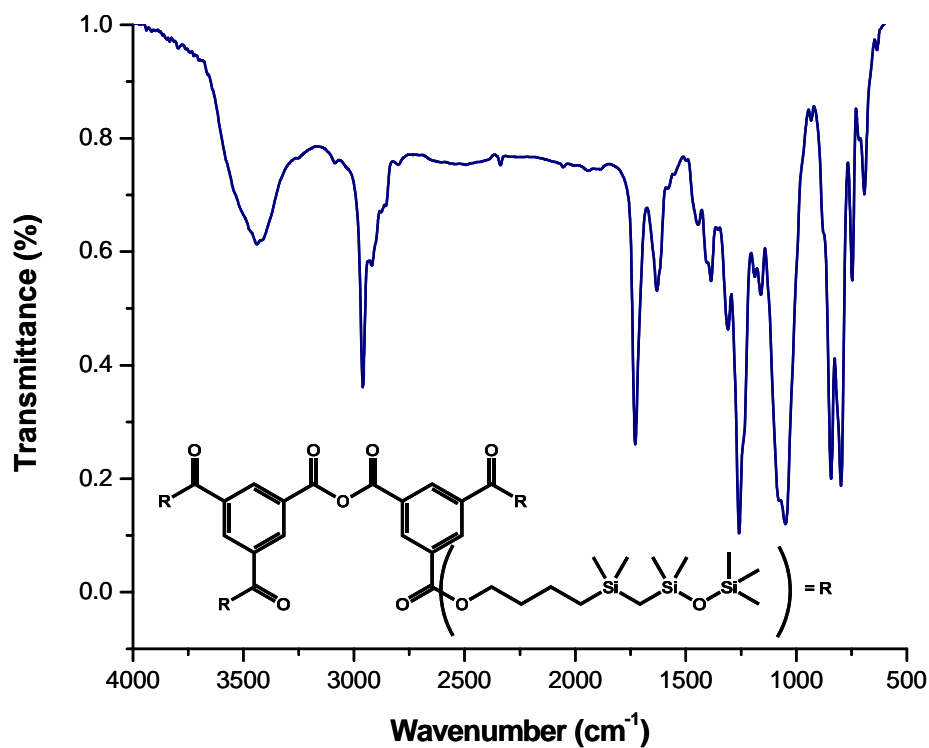


Table 4.31 –  $^{13}\text{C}$  NMR data of 4-15 in  $\text{CDCl}_3$ . MW= 1508.647 g/mol. Quaternary carbons assigned by software

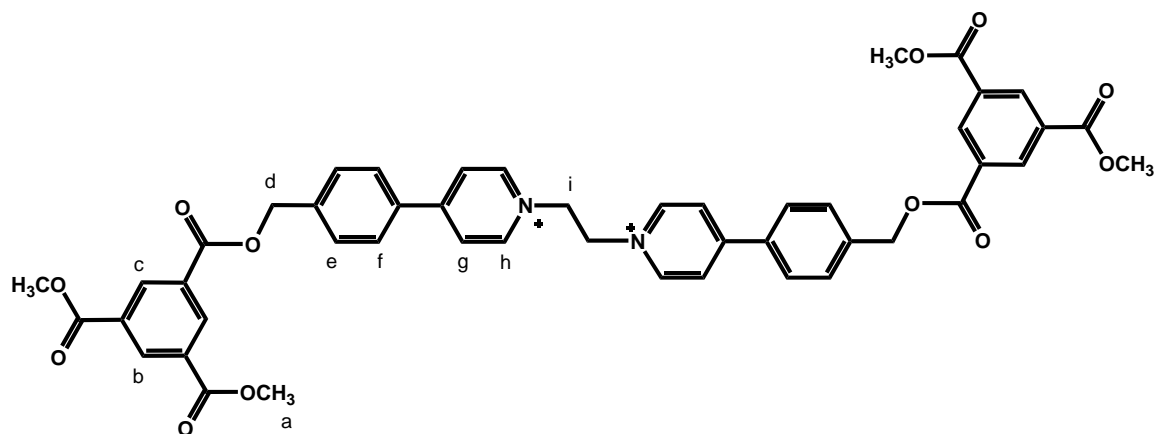
Carbon	$\delta$ (ppm)	# Carbons
1	160.88	2
2	129.58	2
3	135.09	4
4	132.32	4
5	136.10	2
6	164.67	4
7	65.92	4
8	32.16	4
9	17.92	4
10	19.79	4
11	1.90	8
12	0.24	8
13	1.35	12

## IR of 4-15



#### 4.5.16 Synthesis of [4-16][OTf]<sub>2</sub>

[4-9][OTf]<sub>2</sub> (93.17 mg, 0.1337 mmol) and **4-13** (503.47 mg, 0.4681 mmol) were dissolved in dry 1:1 (CHCl<sub>3</sub>: MeCN) (40 mL) under a nitrogen atmosphere. A catalytic amount of tributylphosphine (20 μL) was added via glass syringe and stirring continued until the reaction was complete (3 - 4 h.). The solvent was removed under reduced pressure, and the product stirred in CHCl<sub>3</sub> overnight. The precipitate formed was filtered and washed with CHCl<sub>3</sub>. The product was isolated as a pale beige waxy solid. Yield: 44.10 mg, 29 %. **ESI-MS**: *m/z* 987.2253 (calc.) for C<sub>49</sub>H<sub>42</sub>F<sub>3</sub>N<sub>2</sub>O<sub>15</sub>S [M-OTf]<sup>+</sup>, found 987.2250, *m/z* 419.1364 (calc.) for C<sub>48</sub>H<sub>42</sub>N<sub>2</sub>O<sub>12</sub> [M]<sup>2+</sup>, found 419.1361.

Table 4.32 –  $^1\text{H}$  NMR data of [4-16][OTf] $_2$  in  $\text{CD}_3\text{CN}$ .  $\text{MW}_{\text{OTf}} = 1136.992$  g/mol

Proton	$\delta$ (ppm)	Multiplicity	# Protons	$J$ (Hz)
a	4.34	t	8	$^3J_{\text{fe}} = 6.33$
b	8.74	s	2	--
c	8.76	s	4	--
d	5.52	s	4	--
e	7.75	d	4	$^3J_{\text{ef}} = 8.10$
f	7.98	d	4	$^3J_{\text{fe}} = 8.10$
g	8.32	d	4	$^3J_{\text{gh}} = 6.57$
h	8.58	d	4	$^3J_{\text{hg}} = 6.57$
i	5.08	s	4	--

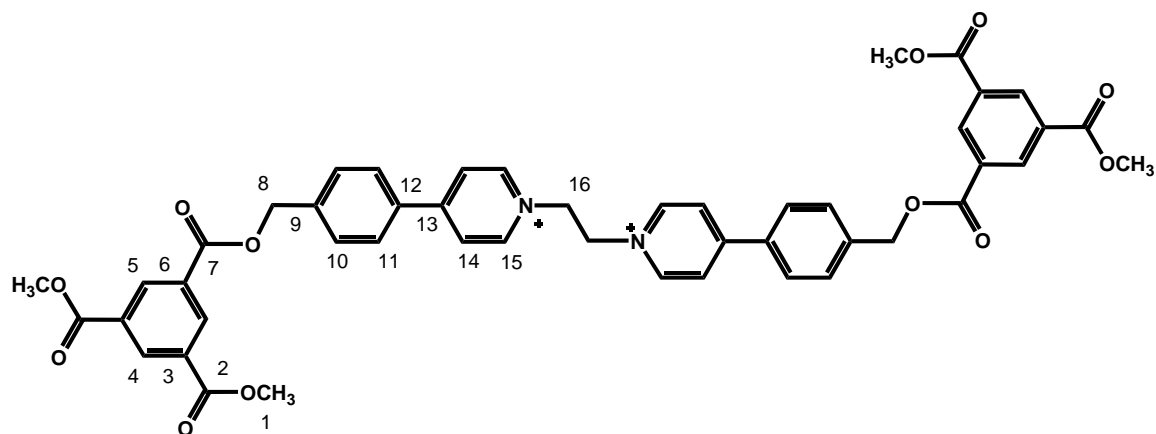
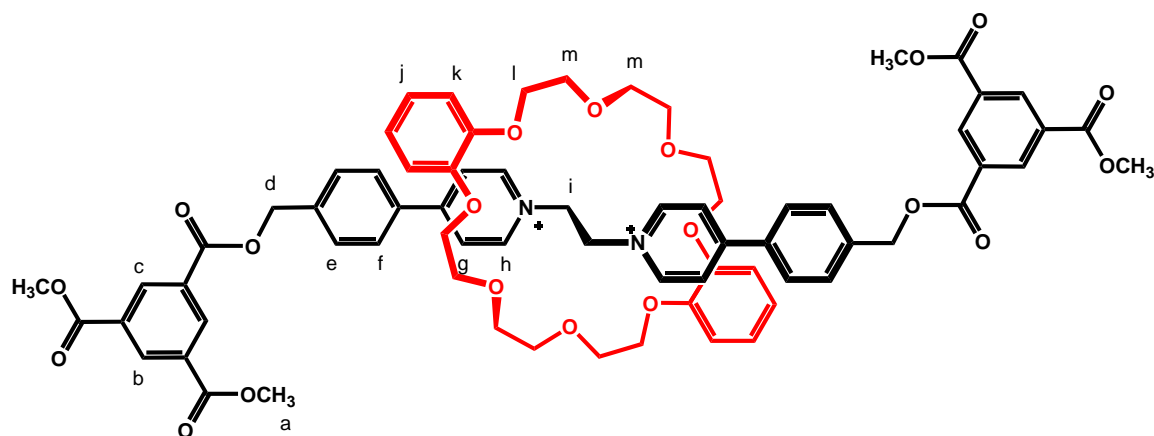


Table 4.33 –  $^{13}\text{C}$  NMR data of [4-16][OTf] $_2$  in  $\text{CD}_3\text{CN}$ .  $\text{MW}_{\text{OTf}} = 1136.992$  g/mol. Quaternary carbons assigned using software

Carbon	$\delta$ (ppm)	# Carbons
1	66.02	4
2	164.97	4
3	131.78	4
4	134.84	2
5	134.59	4
6	130.64	2
7	164.77	2
8	66.14	2
9	133.28	2
10	128.45	4
11	129.58	4
12	141.05	2
13	157.49	2
14	125.46	4
15	146.14	4
16	58.24	2

#### 4.5.17 Synthesis of [4-17][OTf]<sub>2</sub>

[4-9][OTf]<sub>2</sub> (119.23 mg, 0.1712 mmol), **DB24C8** (383.82 mg, 0.8558 mmol) and **4-13** (274.59 mg, 0.5990 mmol) were dissolved in dry 7:3 (CHCl<sub>3</sub>: MeCN) (100 mL) under nitrogen atmosphere. A catalytic amount of tributylphosphine (30 μL) was added via glass syringe and stirring continued overnight. The solvent was removed under reduced pressure, and the product stirred in toluene. The precipitate formed was filtered, washed with toluene several times and dried under reduced pressure. The resulting solid was dissolved in minimum hot MeCN (10 mL) and then cold EtOAc (10 mL) was added and cooled in fridge overnight. The pale yellow precipitate was collected. Yield: 43.61 mg, 16 %. **ESI-MS**:  $m/z$  1450.4584 (calc.) for C<sub>74</sub>H<sub>77</sub>F<sub>3</sub>N<sub>2</sub>O<sub>23</sub>S [M-OTF]<sup>+</sup>, found 1450.4579,  $m/z$  650.7529 (calc.) for C<sub>73</sub>H<sub>77</sub>N<sub>2</sub>O<sub>20</sub> [M]<sup>2+</sup>, found 650.7520.

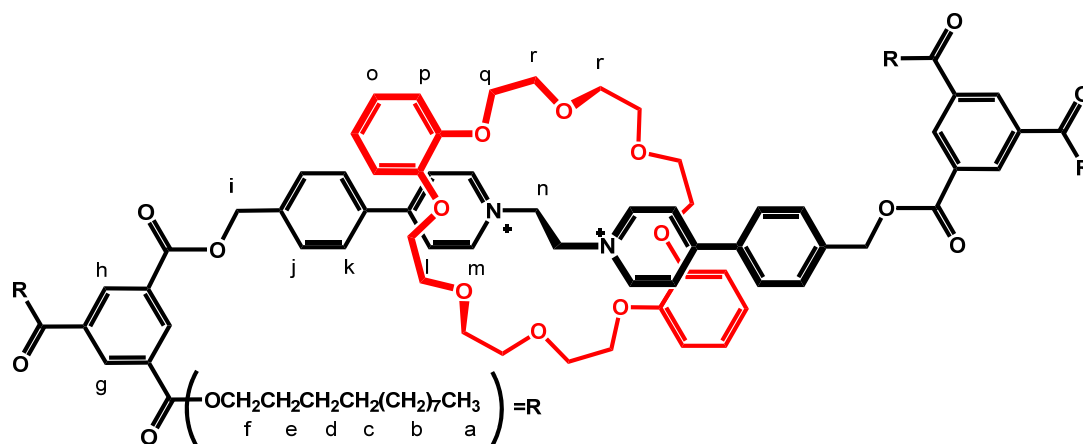
Table 4.34 –  $^1\text{H}$  NMR data of [4-17][OTf] $_2$  in  $\text{CD}_3\text{CN}$ .  $\text{MW}_{\text{OTf}} = 1585.498$  g/mol

Proton	$\delta$ (ppm)	Multiplicity	# Protons	$J$ (Hz)
a	3.95	s	12	--
b	8.76	s	2	--
c	8.80	s	4	--
d	5.50	s	4	--
e	8.02	d	4	$^3J_{\text{ef}} = 8.02$
f	7.65	d	4	$^3J_{\text{fe}} = 8.02$
g	7.67	d	4	$^3J_{\text{gh}} = 6.81$
h	9.09	d	4	$^3J_{\text{hg}} = 6.81$
i	5.54	s	4	--
j	6.53	dd	4	$^3J_{\text{meta}} = 3.72; ^3J_{\text{ortho}} = 6.55$
k	6.65	dd	4	$^3J_{\text{meta}} = 3.72; ^3J_{\text{ortho}} = 6.55$
l	4.04	t	8	--
m	3.99	m	16	--

#### 4.5.18 Synthesis of [4-18][OTf]<sub>2</sub>

[4-9][OTf]<sub>2</sub> (253.66 mg, 0.3641 mmol), **DB24C8** (816.54 mg, 1.8206 mmol) and **4-14** (1.37 g, 1.2744 mmol) were dissolved in dry 7:3 (CHCl<sub>3</sub>: MeCN) (125 mL) under nitrogen atmosphere. A catalytic amount of tributylphosphine (40 μL) was added via glass syringe and stirring continued until the reaction was complete (3.5 h.). The solvent was removed under reduced pressure and the product was stirred in MeCN. The insoluble solid was filtered off and MeCN concentrated to a pale yellow solid. This solid was then recrystallized from EtOAc multiple times to recover the excess **DB24C8**, then the yellow waxy solid was purified by flash column chromatography with RP-C<sub>18</sub> silica gel with 80:20 (MeCN: MeOH) isocratic elution initially followed by gradient (20 - 100 % MeOH) as eluant. The yellow glassy solid was collected. Yield: 256.71 mg, 32 %. **ESI-MS**:  $m/z$  951.5855 (calc.) for C<sub>116</sub>H<sub>162</sub>N<sub>2</sub>O<sub>20</sub> [M]<sup>2+</sup>, found 951.5851.



Table 4.35 –  $^1\text{H}$  NMR data of [4-18][OTf]<sub>2</sub> in CD<sub>3</sub>CN. MW<sub>OTf</sub> = 2202.667 g/mol

Proton	$\delta$ (ppm)	Multiplicity	# Protons	$J$ (Hz)
a	0.85	t	12	$^3J_{ab} = 6.93$
b	1.23	m	56	--
c	1.35	tt	8	$^3J_{cd} = 6.88$
d	1.44	tt	8	$^3J_{dc} = 6.88; ^3J_{de} = 7.15$
e	1.77	tt	8	$^3J_{ed} = 7.15; ^3J_{ef} = 6.50$
f	4.34	t	8	$^3J_{fe} = 6.50$
g	8.74	s	2	--
h	8.77	s	4	--
i	5.51	s	4	--
j	7.98	d	4	$^3J_{jk} = 8.10$
k	7.65	d	4	$^3J_{kj} = 8.10$
l	7.67	d	4	$^3J_{lm} = 6.86$
m	9.07	d	4	$^3J_{ml} = 6.86$
n	5.49	s	4	--
o	6.53	dd	4	$^3J_{meta} = 3.74; ^3J_{ortho} = 6.52$
p	6.65	dd	4	$^3J_{meta} = 3.74; ^3J_{ortho} = 6.52$
q	4.04	t	8	$^3J_{qr} = 5.09$
r	3.99	m	16	--

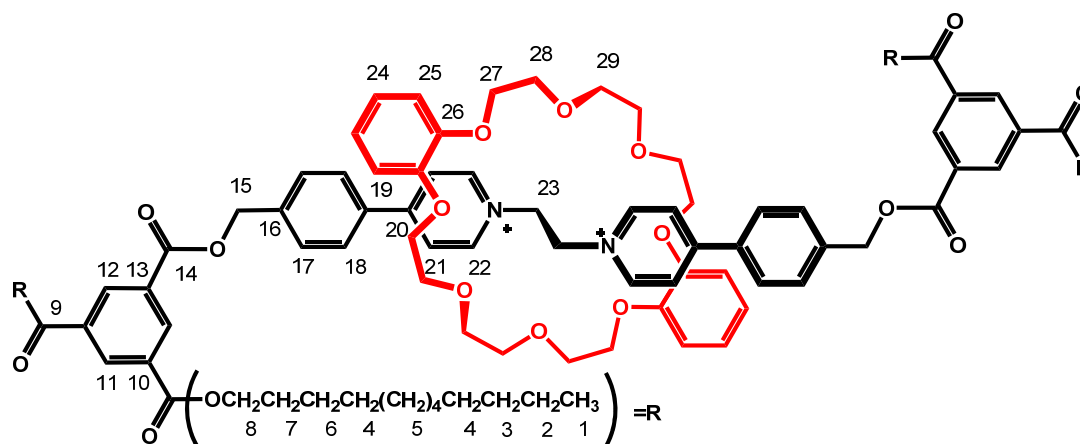


**Table 4.36** –  $^{13}\text{C}$  NMR data of [4-18][OTf]<sub>2</sub> in CD<sub>3</sub>CN. MW<sub>OTf</sub> = 2202.667 g/mol. Quaternary carbons assigned using software

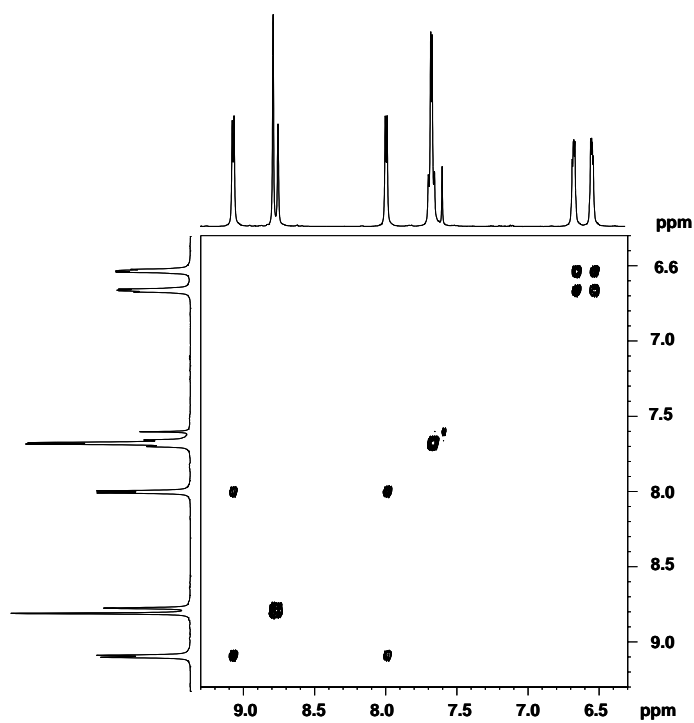
Carbon	$\delta$ (ppm)	# Carbons
1	13.53	4
2	22.51	4
3	31.76	4
4	28.37	8
5	29.47	16
6	25.83	4
7	29.04	4
8	65.83	4
9	164.69	4
10	131.32	4
11	132.00	2
12	133.97	4
13	133.89	2
14	164.60	2
15	66.45	2
16	133.48	2
17	128.97	4
18	128.57	4
19	140.49	2
20	155.71	2
21	124.13	4
22	145.71	4

---

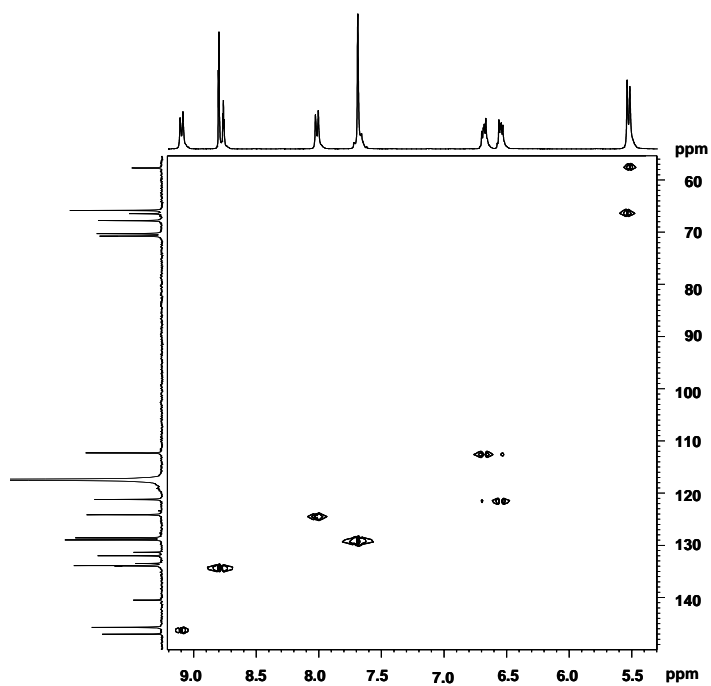
<b>23</b>	57.71	2
<b>24</b>	119.14	4
<b>25</b>	112.31	4
<b>26</b>	147.01	4
<b>27</b>	61.62	4
<b>28</b>	70.24	4
<b>29</b>	70.60	4

---

COSY of [4-18][OTf]<sub>2</sub> in CD<sub>3</sub>CN.

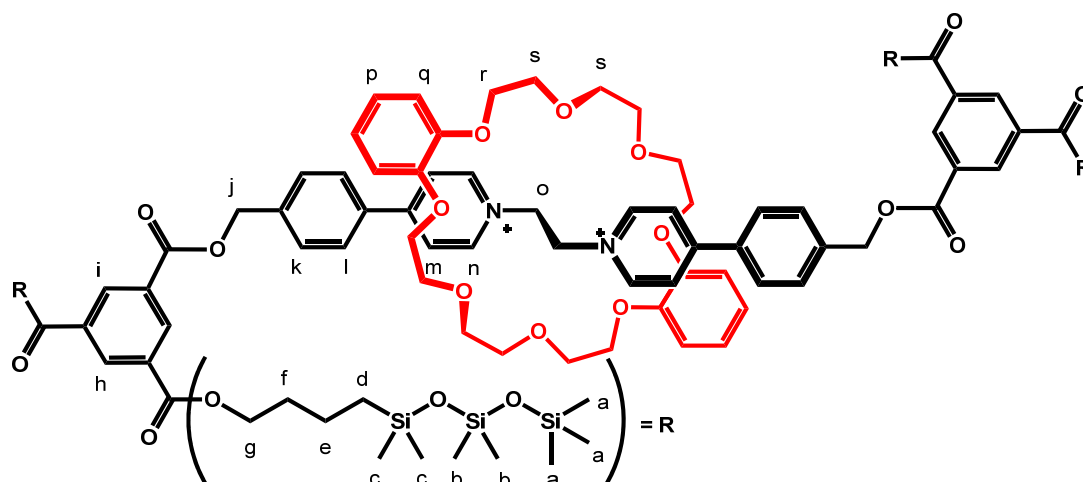


HETCOR of [4-18][OTf]<sub>2</sub> in CD<sub>3</sub>CN.



#### 4.5.19 Synthesis of [4-19][OTf]<sub>2</sub>

[4-9][OTf]<sub>2</sub> (193.79 mg, 0.2782 mmol), **DB24C8** (623.83 mg, 1.3909 mmol) and **4-15** (1.47 g, 0.9736 mmol) were dissolved in dry 7:3 (CHCl<sub>3</sub>: MeCN) (150 mL) under a nitrogen atmosphere. A catalytic amount of tributylphosphine (50 μL) was added via glass syringe, and stirring continued until the reaction was complete (3 h). The solvent was removed under reduced pressure. The crude yellow waxy solid was then recrystallized from EtOAc multiple times to recover the excess **DB24C8** and then the yellow waxy solid was purified by flash column chromatography with RP-C<sub>18</sub> silica gel with 90:10 (MeCN: MeOH) isocratic elution followed by gradient (10 - 100 % MeOH) as eluant. The soft yellow waxy solid was collected. Yield: 186.22 mg, 25 %. **ESI-MS**: *m/z* 1168.4893 (calc.) for C<sub>112</sub>H<sub>178</sub>N<sub>2</sub>O<sub>28</sub>Si<sub>12</sub> [M]<sup>2+</sup>, found 1168.4980.

Table 4.37 –  $^1\text{H}$  NMR data of [4-19][OTf] $_2$  in  $\text{CD}_3\text{CN}$ .  $\text{MW}_{\text{OTf}} = 2635.773$  g/mol

Proton	$\delta$ (ppm)	Multiplicity	# Protons	$J$ (Hz)
a	0.06	s	36	--
b	0.09	s	24	--
c	0.01	s	24	--
d	0.64	t	8	$^3J_{de} = 6.55$
e	1.53	tt	8	$^3J_{ed} = 6.55$ ; $^3J_{ef} = 6.87$
f	1.83	tt	8	$^3J_{fe} = 6.87$ ; $^3J_{fg} = 8.20$
g	4.39	t	8	$^3J_{gf} = 8.20$
h	8.76	s	2	--
i	8.80	s	4	--
j	5.53	s	4	--
k	7.67	d	4	$^3J_{kl} = 8.20$
l	7.65	d	4	$^3J_{kl} = 8.20$
m	8.00	d	4	$^3J_{mn} = 6.53$
n	9.08	d	4	$^3J_{nm} = 6.53$
o	5.51	s	4	--
p	6.66	dd	4	$^3J_{meta} = 3.70$ ; $^3J_{ortho} = 6.47$
q	6.54	dd	4	$^3J_{meta} = 3.70$ ; $^3J_{ortho} = 6.47$
r	4.05	m	8	--
s	4.00	m	16	--

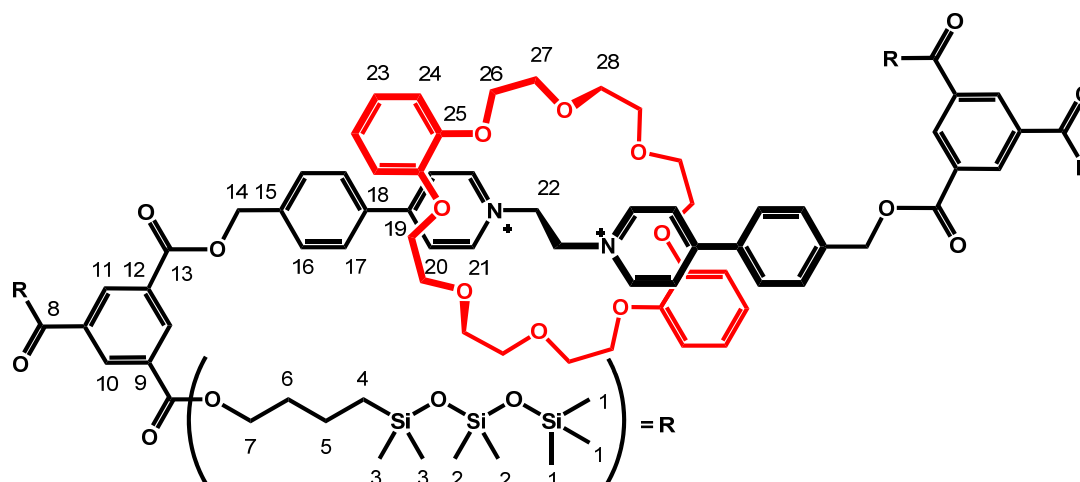


Table 4.38 –  $^{13}\text{C}$  NMR of data [4-19][OTf] $_2$  in  $\text{CD}_3\text{CN}$ .  $\text{MW}_{\text{OTf}} = 2635.773$  g/mol. Quaternary carbons assigned using software

Carbon	$\delta$ (ppm)	# Carbons
1	0.32	12
2	0.16	8
3	0.53	8
4	19.56	4
5	17.34	4
6	31.89	4
7	65.40	4
8	164.66	4
9	131.28	4
10	131.96	2
11	133.84	4
12	133.91	2
13	164.54	2
14	66.38	2
15	133.43	2
16	128.90	4
17	128.52	4
18	140.46	2
19	155.70	2
20	124.11	4
21	145.65	4
22	57.66	2

---

<b>23</b>	121.17	4
<b>24</b>	112.30	4
<b>25</b>	146.99	4
<b>26</b>	67.80	4
<b>27</b>	70.75	4
<b>28</b>	70.27	4

---



# CHAPTER 5

## *Chirality in a Liquid Crystal [2]Rotaxane*

### 5.1 INTRODUCTION

Chirality in soft matter can be present at the molecular and supramolecular level. In liquid crystals, chirality can be introduced by several different avenues.<sup>64-68</sup> Chirality can be directly introduced within the liquid crystalline molecule by incorporation of chiral elements, usually chiral centers which are thus single component chiral systems. Another popular way, especially for materials used in applications, is the addition of a small amount of a chiral guest (dopant) molecule to an achiral host phase. The amount of chiral dopant is usually less than 5 %, and the ability of the dopant to induce chirality does not depend on it being mesogenic or non-mesogenic. Additionally, mixtures of chiral and achiral mesogenic materials can be prepared.

Introduction of chirality into mesogenic materials introduces large changes in the molecular self-organization and thus on the respective liquid crystal behaviour. By introducing chirality a spontaneous macroscopic helical superstructure with a twist axis perpendicular to the local director is observed. This twist can be right- or left-handed, depending on the configuration of the chiral element(s) within the molecule. For example, when the molecules of a SmC phase are chiral the phase structure is basically the same except that the molecular chirality causes a small and gradual change in the direction of the molecular tilt. There is no change in the tilt angle with respect to the layer normal and this change in tilt direction from layer to layer describes the helix (Figure 5.1b). The achiral SmC phase symmetry consists of a two-fold rotation axis ( $C_2$ ) parallel

to the layers, a mirror plane ( $m$ ) orthogonal to the layers, and an inversion center ( $i$ ) (Figure 5.1a). When the tilted molecules of the SmC phase become chiral, the symmetry is reduced to solely a two-fold axis of rotation. Hence, the chiral tilted SmC\* phases all exhibit a local spontaneous polarization,  $\mathbf{P}_s$ , and this spontaneous polarization can be reoriented between two stable states by applying an electric field.<sup>166-169</sup> The  $\mathbf{P}_s$  is reduced to zero throughout a bulk sample and the SmC\* phase is hence defined as helielectric. The attractiveness of this phase is its promising properties for applications in fast switching, high contrast, and large viewing displays, as well as other non-display items. Figure 5.1b illustrates the helical superstructure of the chiral bulk SmC\* phase (left) and the corresponding direction of the vector for the spontaneous polarization together with the respective direction of the director on the tilt cone (right).

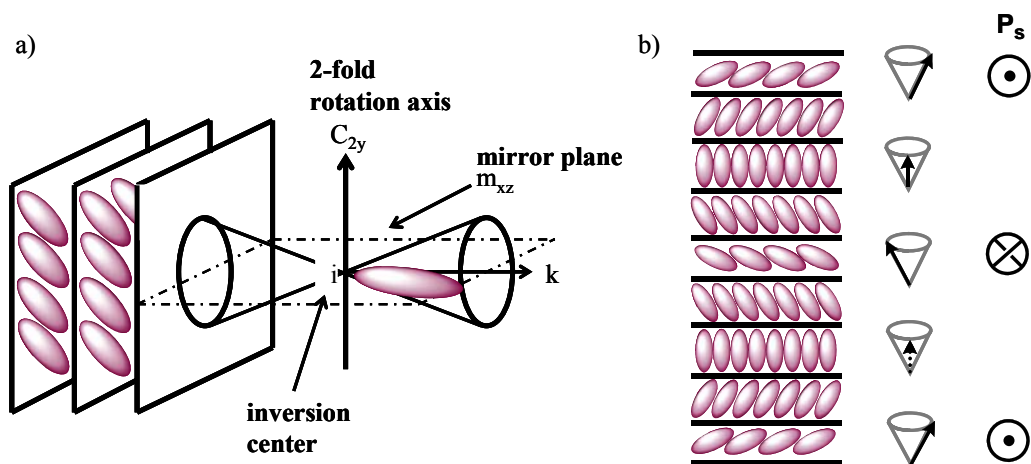


**Figure 5.1 – a) Schematic illustration of the symmetry elements of the achiral SmC phase, b) schematic illustrations of the helical superstructure of the chiral bulk SmC\* phase and the direction of the director on the tilt cone and the corresponding direction of the vector of the spontaneous polarization ( $\mathbf{P}_s$ ).**

This chapter focuses on the possibility of introducing chirality into a liquid crystal [2]rotaxane. Observations to changes in the superstructure, depending on the approach to introduce chirality will also be addressed. Of interest, with a charged LC [2]rotaxane, is

the possibility of introducing chirality in several ways: core structure (chiral thread, chiral macrocycle or chiral anions), end groups (chiral side-chains), and doping, as well as any combination of the three. This chapter focuses on the introduction of chirality *via* a chiral anion and a chiral macrocycle, which should be the least disruptive to the LC phase. The liquid crystalline [2]rotaxane chosen for this study was the alkyl-siloxane extended two-charge [2]rotaxane [4-19][OTf]<sub>2</sub> discussed in Chapter 4, which formed a SmC liquid crystal phase (Figure 5.2). The ultimate goal was to determine if there was an observable chiral induction by introducing chirality into the [2]rotaxane, via the core of the rotaxane and/or to the ends of the stoppers.

The simplest approach to introduce chirality into the core was to anion exchange the trifluoromethane sulfonate counter ions with a chiral anion. The chiral anion chosen for this work was (-)-camphor-10-sulfonate, which was commercially available. This particular anion was chosen because it was similar in size and functionality to the

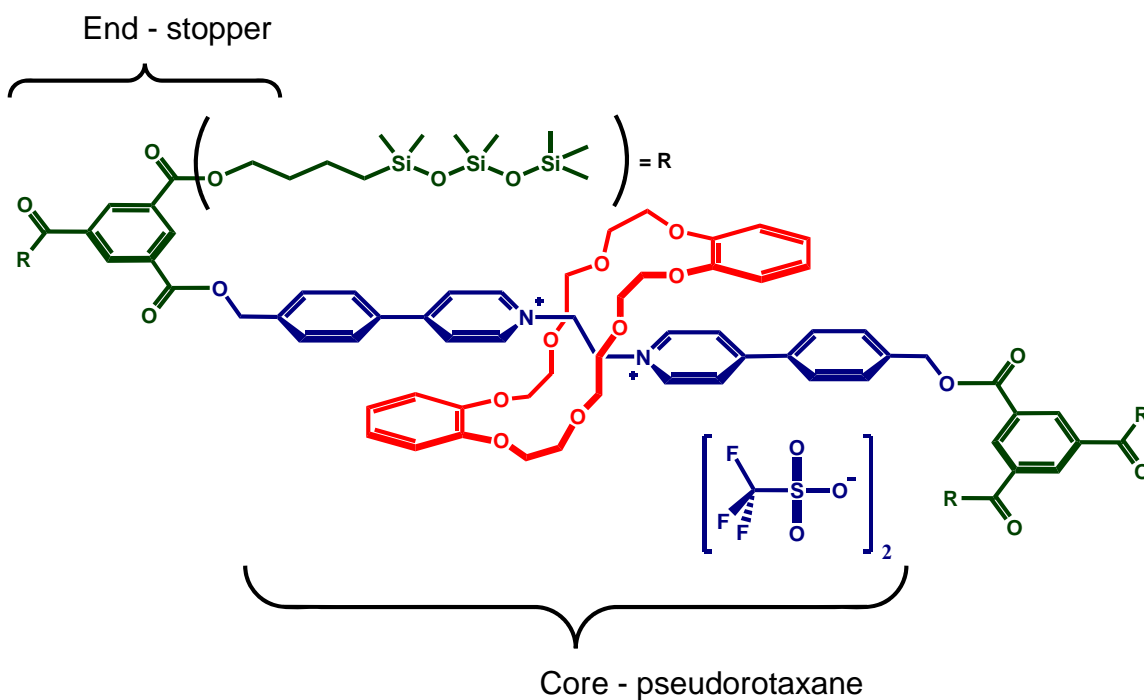


Figure 5.2 – [2]Rotaxane [4-19][OTf]<sub>2</sub> chosen for the introduction of chirality.

trifluoromethane sulfonate (triflate) anion and thus no large disruptions in the core to core packing of the molecules were expected.

The other approach would be to synthetically incorporate chirality into each individual interlocked molecular core. The initial design involves the incorporation of a chiral **DB24C8** macrocycle into the [2]rotaxane. By appending the chiral group to the macrocycle, the collective non-covalent interactions favoring pseudorotaxane formation are not disrupted. Another widely used approach to introduce chirality is to use a chiral dopant. Although this concept was not explored during this thesis work, an appropriate chiral dopant could be either a chiral siloxane, to interact with the side-chains, or a synthesized chiral mesogenic [2]rotaxane, to mix with the achiral mesogenic [2]rotaxane.

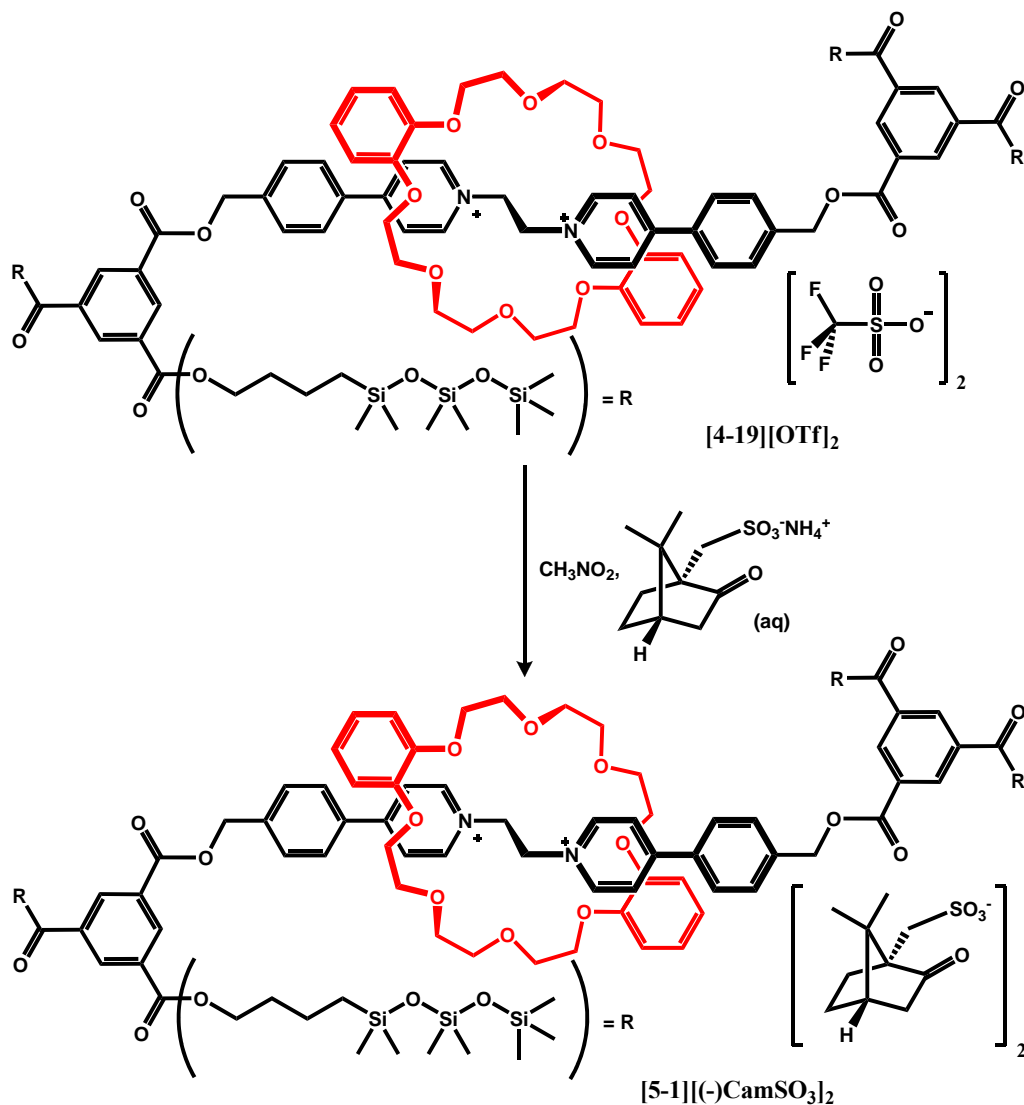
## 5.2 SYNTHESIS AND CHARACTERIZATION

### 5.2.1 Synthesis

In order to introduce chirality into the [2]rotaxane core via a chiral anion, the triflate anion of [2]rotaxane **[4-19][OTf]<sub>2</sub>** was anion exchanged for (-)-camphor-10-sulfonate (-)**CamSO<sub>3</sub>** (Scheme 5.1). This procedure was repeated multiple times to ensure all anions had been converted.

Chirality was incorporated into the crown at the 3- and 4- positions of the catechol ring as this was thought to cause the least disruption to [2]pseudorotaxane formation. An added bonus was that incorporation of ether groups makes the catechol rings on the crown more electron rich and increased the association constant for [2]pseudorotaxane formation relative to **DB24C8**. The chiral crown was synthesized in two steps (Scheme 5.2). Bromomethylation<sup>170-173</sup> of the **DB24C8** macrocycle was carried out with an excess of paraformaldehyde and a 40 % hydrobromic acid solution in acetic

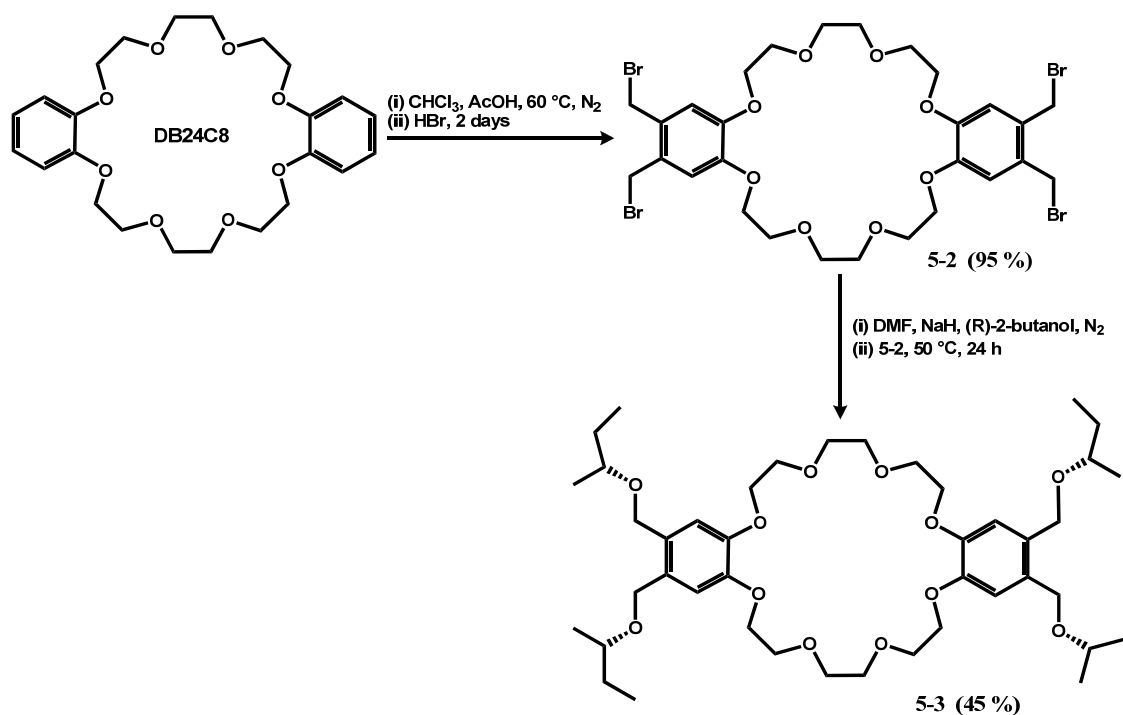
acid/ $\text{CHCl}_3$  to generate the corresponding tetra(bromomethyl) derivative **5-2** in 95 % yield. Alkylation with (R)-2-butanol and sodium hydride provided the tetrakis((R)-2-butyl-oxymethyl) derivative **5-3** in 45 % yield.



**Scheme 5.1** – Synthetic route for [2]rotaxane [5-1][(-)CamSO<sub>3</sub>]<sub>2</sub>.

As mentioned in Chapter 4, the synthesis of the two-charged [2]rotaxanes by ester formation follows a modified version of that reported by Takata *et al.*<sup>158,159</sup> [2]Rotaxane [5-5][OTf]<sub>2</sub> was synthesized by combining one equivalent of the thread [4-9][OTf]<sub>2</sub> with an excess of both the anhydride stopper **4-15** and the new tetrasubstituted chiral **DB24C8**

macrocycle **5-3** (Scheme 5.3). **[5-5][OTf]<sub>2</sub>** was then purified by column chromatography on reverse phase C<sub>18</sub> silica gel. In order to avoid cross-linking of siloxane groups as discussed in Chapter 4, the material collected from the column was never fully concentrated to dryness but anion exchanged to the triflate anion by a two-layer MeNO<sub>2</sub>/NaOTf (aq) mixing and washed with copious amounts of water before concentrating to a solid.

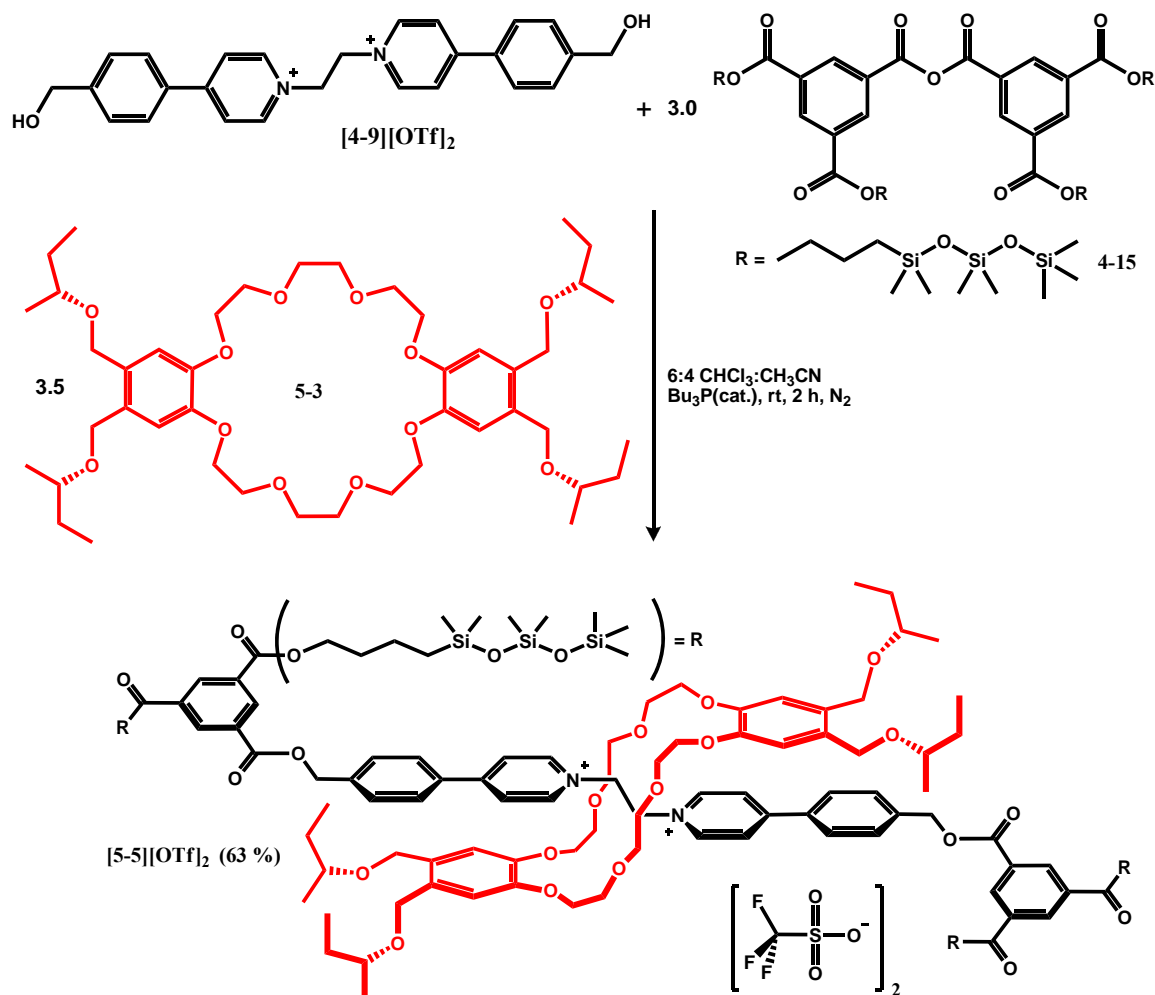


Scheme 5.2 – Synthetic route to tetra-substituted crowns **5-2** and **5-3**.

### 5.2.2 <sup>1</sup>H NMR Spectroscopy

The conversion of [2]rotaxane **[4-19][OTf]<sub>2</sub>** to **[5-1][(-)CamSO<sub>3</sub>]<sub>2</sub>** was conveniently monitored by <sup>1</sup>H NMR spectroscopy due to the presence of eleven chemically inequivalent protons on the chiral anion (Figure 5.3). The strained ring system in the chiral anion has a favorable geometry for overlapping orbitals and the complex <sup>1</sup>H NMR spectrum for the anion shows long-range coupling. The diastereotopic **x** and **x'**

protons of the chiral anion are slightly shielded when in close proximity to the [2]rotaxane due to ion-ion interactions between the sulfonate group of the anion and the pyridinium groups on the thread. By integration, the number of protons were appropriate for two anions to one [2]rotaxane molecule, consistent with all the triflate anions being exchanged to the chiral anions in this new material.



**Scheme 5.3** - Synthetic route to [2]rotaxane [5-5][OTf]<sub>2</sub>.

The <sup>1</sup>H NMR spectrum of chiral crown **5-3** shows the effect of the chiral center on neighboring protons (Figure 5.4). Protons **e**, **e'**, **b** and **b'** are diastereotopic, having different chemical shifts and split each other with a geminal coupling constant. All other protons show typical splitting patterns and are not affected by the chiral center.

Comparison of the  $^1\text{H}$  NMR spectra of the naked dumbbell [5-6][OTf] $_2$  and the [2]rotaxane [5-5][OTf] $_2$  clearly shows the effect of the three non-covalent interactions responsible for the initial self-assembly, as previously discussed in Chapter 4 (Figure 4.5). Ethylene protons of the recognition site, **o**, and  $\alpha$ -pyridinium protons, **n**, are deshielded due to hydrogen bonding with the oxygen atoms of the crown ether and the  $\beta$ -pyridinium protons **m** and **l**, are shielded due to  $\pi$ - $\pi$  interactions between the electron rich rings on the crown ether and the electron poor pyridinium rings on the thread.

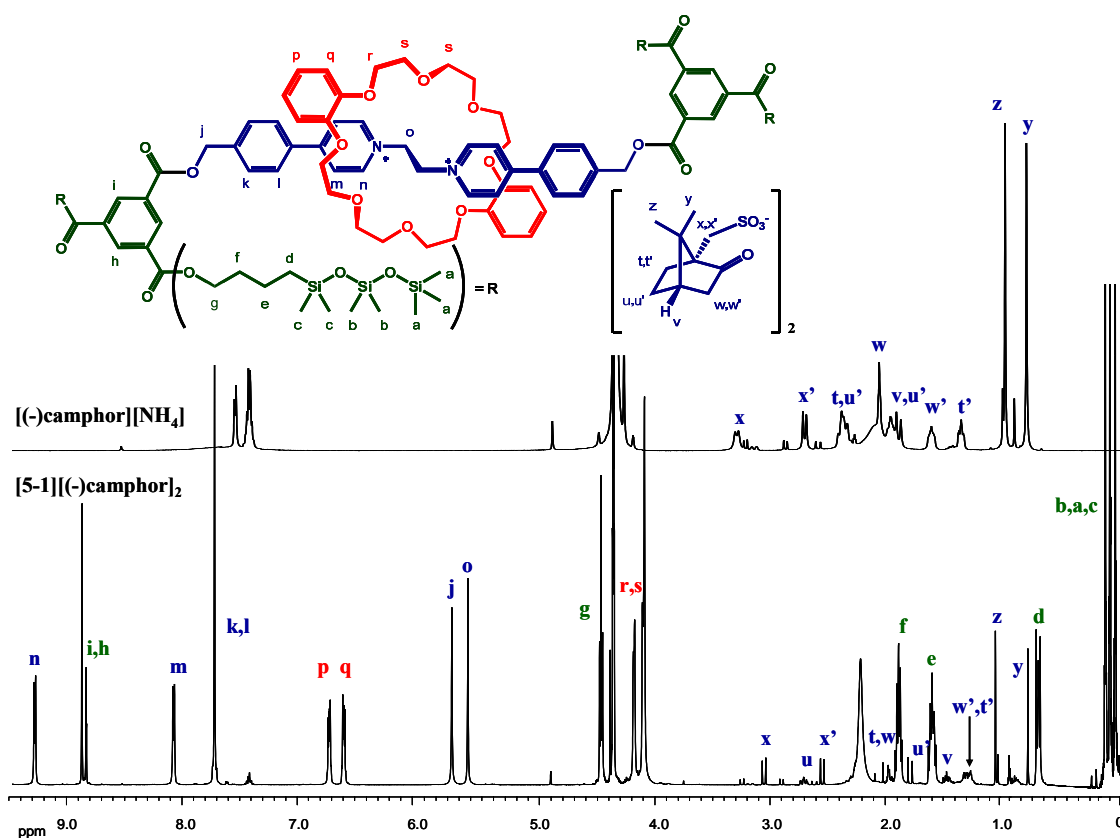


Figure 5.3 -  $^1\text{H}$  NMR spectra of free [NH<sub>4</sub>][(-)CamSO<sub>3</sub>](top) and [5-1][(-)CamSO<sub>3</sub>]<sub>2</sub> (bottom) in CD<sub>3</sub>NO<sub>2</sub>.



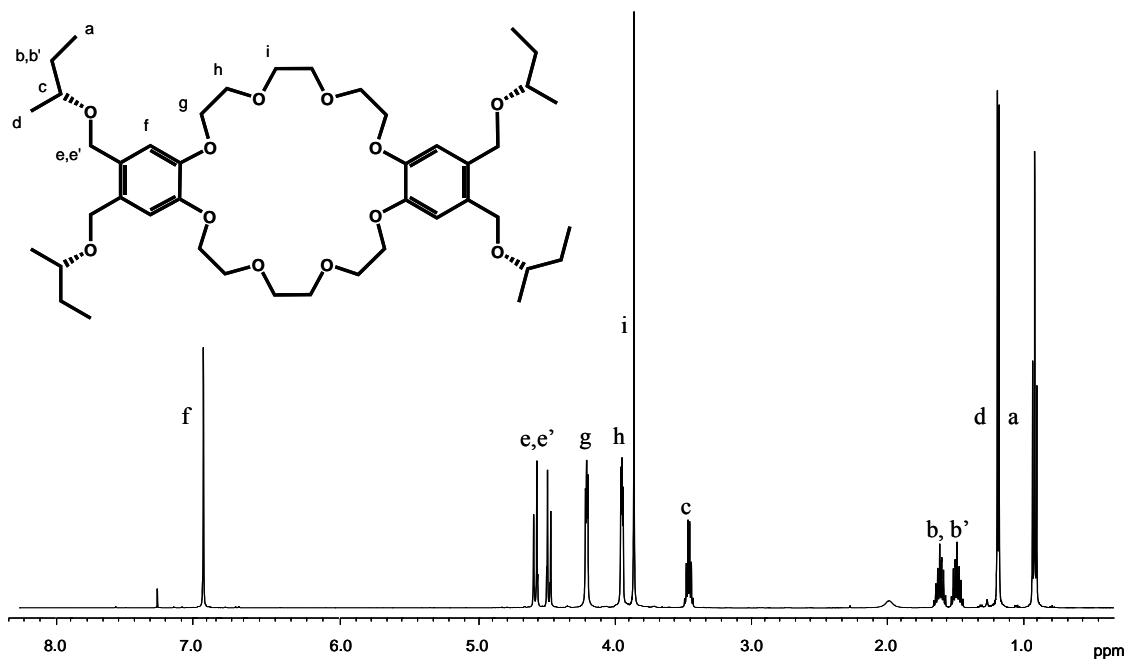


Figure 5.4 -  $^1\text{H}$  NMR spectrum of 5-3 in  $\text{CD}_3\text{CN}$ .

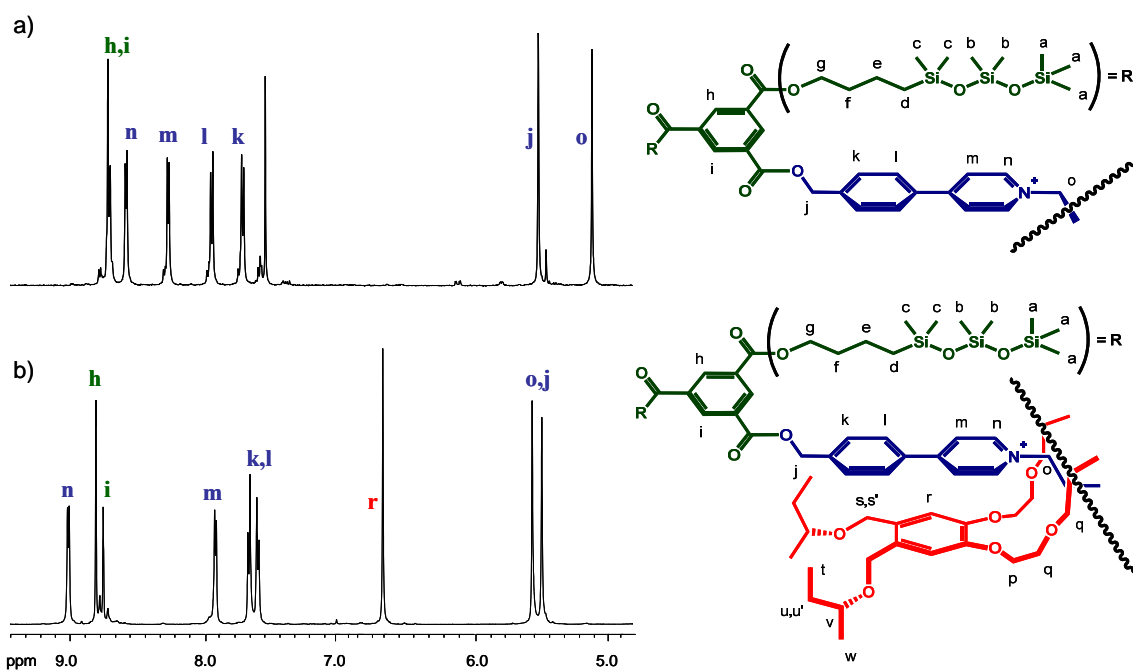
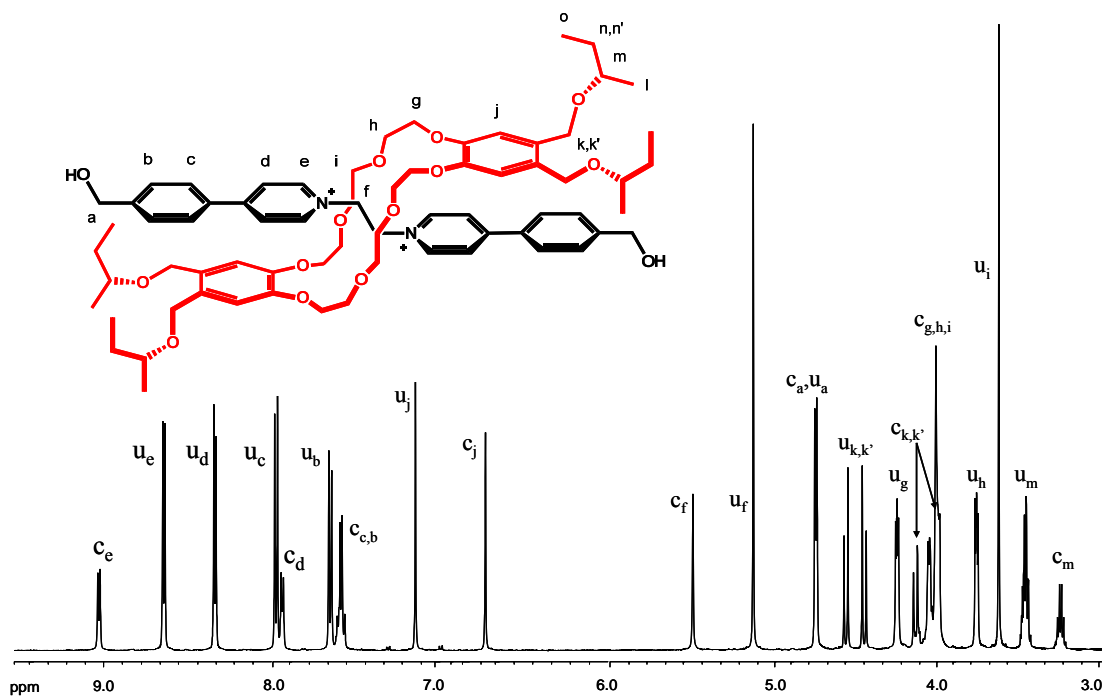


Figure 5.5 - Stacked  $^1\text{H}$  NMR spectra of a) dumbbell [5-6][ $\text{OTf}$ ] $_2$  and b) [2]rotaxane [5-5][ $\text{OTf}$ ] $_2$  in  $\text{CD}_3\text{CN}$ .

### 5.2.3 Results and Discussion: Pseudorotaxane Studies

The [2]pseudorotaxane formation between [4-9][OTf]<sub>2</sub> and 5-3 was studied in order to determine an association constant and indirectly to provide a guide to the appropriate amount of excess crown ether required to ensure full [2]pseudorotaxane formation for the eventual synthesis of [2]rotaxane [5-5][OTf]<sub>2</sub>. The [2]pseudorotaxane was formed when equimolar solutions of the thread [4-9][OTf]<sub>2</sub> and chiral macrocycle 5-3 were mixed at 25 °C in CD<sub>3</sub>CN. Equilibrium was rapidly attained and a new set of peaks, in addition to those assigned to the free components, were observed in the <sup>1</sup>H NMR spectrum (Figure 5.6). The chemical shifts of the new resonances were consistent with the formation of a [2]pseudorotaxane complex in solution with a rate of association-dissociation that was slow compared to the NMR timescale. Evidence for [2]pseudorotaxane formation was observed not only in solution, but also in the "gas phase" using electrospray mass spectrometry.

The ethylene protons of the recognition site, **f**, and  $\alpha$ -pyridinium protons, **e**, are deshielded due to hydrogen bonding with the oxygen atoms of the crown ether, while  $\beta$ -pyridinium protons, **d** and **c**, are shielded due to  $\pi$ - $\pi$  stacking interactions between the aromatic rings on the crown ether and the pyridinium rings of the thread. The crown ether catechol proton **j** and protons of the chiral group, **k**, **k'**, **l**, **m**, **n**, **n'** and **o**, are shielded for the same reason. Variable temperature <sup>1</sup>H NMR experiments were also performed in order to determine thermodynamic parameters for the interaction of [4-9][OTf]<sub>2</sub> with 5-3 in CD<sub>3</sub>CN (2 x 10<sup>-3</sup> M) at 298 K. The spectra at various temperatures, in the range 3 - 8 ppm, are shown in Figure 5.7, and a van't Hoff plot is shown in Figure 5.8.



**Figure 5.6** -  $^1\text{H}$  NMR spectrum of a  $2 \times 10^{-3}$  M solution of  $[5-4][\text{OTf}]_2$  in  $\text{CD}_3\text{CN}$  at 289 K. The uncomplexed protons of the free components are designated by  $u_x$  and the complexed [2]pseudorotaxane protons are designated by  $c_x$ .

Since the rate of threading/unthreading is slow on the NMR timescale, calculation of the concentrations of complexed and uncomplexed species is possible by integration. The single-point method can be used to calculate  $K_{\text{assoc}}$ .<sup>174</sup> This method uses the known initial concentrations of crown ether and thread and the signal integrals of a complexed and uncomplexed NMR signal representing the same proton. The equation for  $K_{\text{assoc}}$  is:



using notation of host (H) and guest (G).

Plots of  $\Delta G^\circ$ ,  $\Delta H^\circ$  and  $T\Delta S^\circ$  versus T are shown in Figure 5.9;  $\Delta G^\circ$  is relatively insensitive to temperature, whereas at high temperatures this process is enthalpy driven, and at low temperatures the process becomes entropy driven. The association constant  $K_{\text{assoc}}$  for  $[5-4][\text{OTf}]_2$  is  $327 \text{ M}^{-1}$  and  $\Delta G^\circ$  is  $-19.1 \text{ kJ/mol}$  at 298 K.

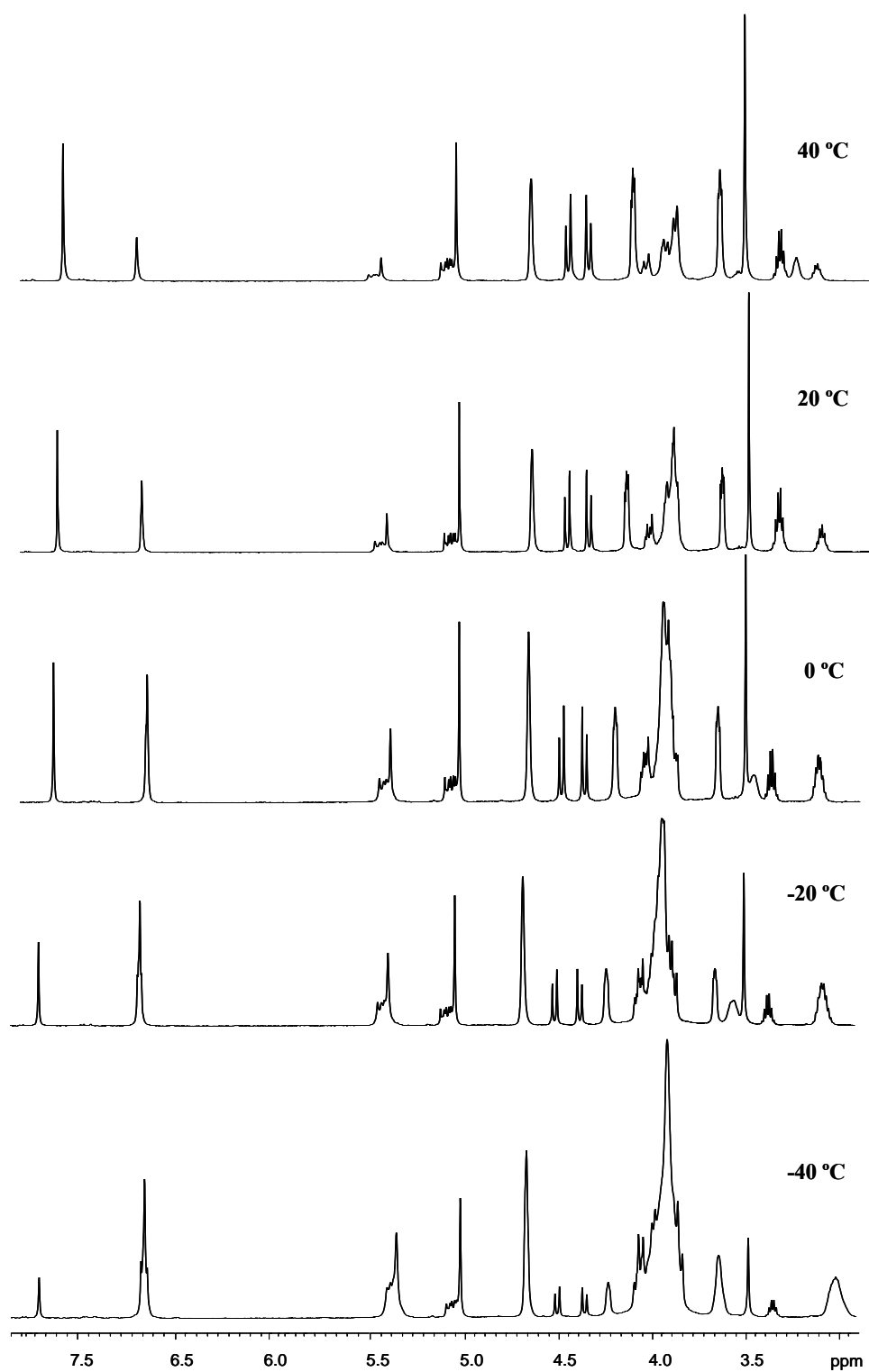


Figure 5.7 - VT  $^1\text{H}$  NMR spectra of [5-4][OTf]<sub>2</sub> in CD<sub>3</sub>CN.

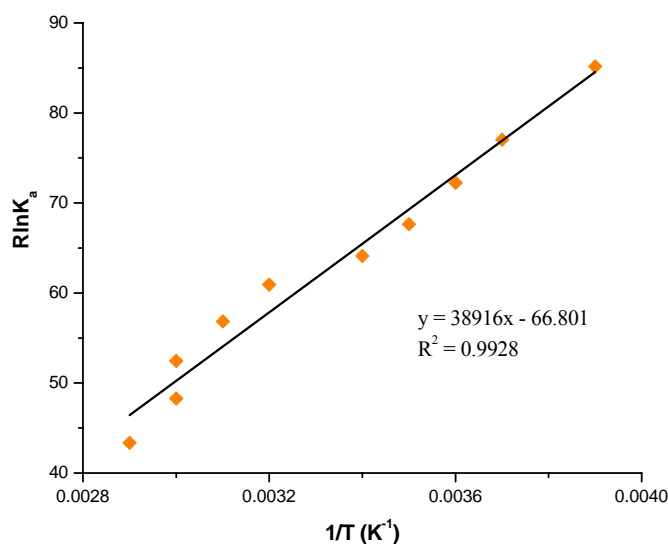


Figure 5.8 - The van't Hoff plot for [5-4][OTf]<sub>2</sub> plotted from <sup>1</sup>H NMR data.

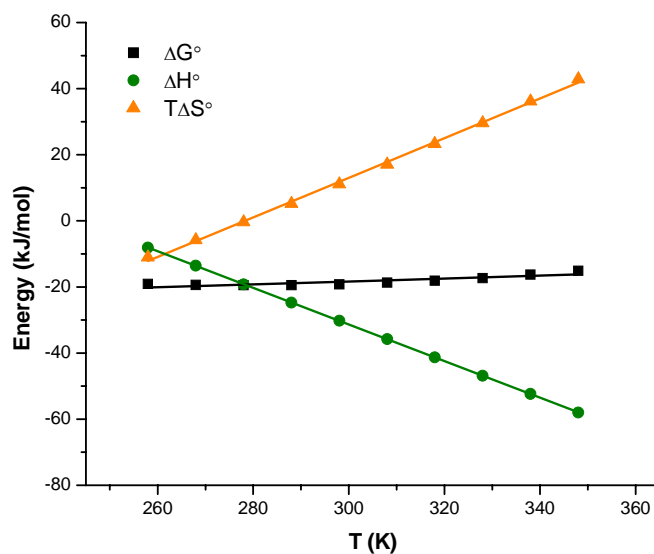


Figure 5.9 - Variation of  $\Delta G^\circ$ ,  $\Delta H^\circ$  and  $T\Delta S^\circ$  with temperature for [5-4][OTf]<sub>2</sub>.

### 5.3 LIQUID CRYSTAL PHASE CHARACTERIZATION

Thermal gravimetric analysis (TGA) was not performed on any of these compounds as the thermal lability is at the mercy of the siloxane moiety on the stoppers, as shown in Chapter 4, with decomposition occurring at temperatures above 158 °C.

### 5.3.1 Defect Textures Observed by Polarizing Optical Microscopy (POM)

The POM studies of both chiral [2]rotaxanes presented here are preliminary experiments to look at the reproducibility of the textures. All defect textures obtained by POM were viewed with crossed polarizers. The same type of schlieren texture observed for the achiral siloxane extended [2]rotaxane **[4-19][OTf]<sub>2</sub>** was also observed for both chiral [2]rotaxanes **[5-1][(-)CamSO<sub>3</sub>]<sub>2</sub>** and **[5-5][OTf]<sub>2</sub>**, suggesting that the long axis of the molecule is still tilted with respect to the director, even though the chemical makeup of each molecule has changed (Figure 5.10c,d and 5.11b, respectively). No visible crystallinity was detected by POM for either chiral [2]rotaxanes when squeezed between glass slides. Both were soft, strongly birefringent solids.

The [2]rotaxane **[5-1][(-)CamSO<sub>3</sub>]<sub>2</sub>** displayed several textural changes upon heating. Above 85 °C, the material became increasingly fluid and reorganized to a oily-streak texture with birefringent lines (Figure 5.10b). This texture remained until 130 °C, when a schlieren texture was observed until clearing into the isotropic liquid at 151 °C (Figure 5.10c). Where singularities are resolved, the typical four-fold brushes observed with tilted smectics were seen. Upon cooling from the isotropic liquid, the schlieren texture returns forming small domains, with many disclination lines typical for highly viscous materials.

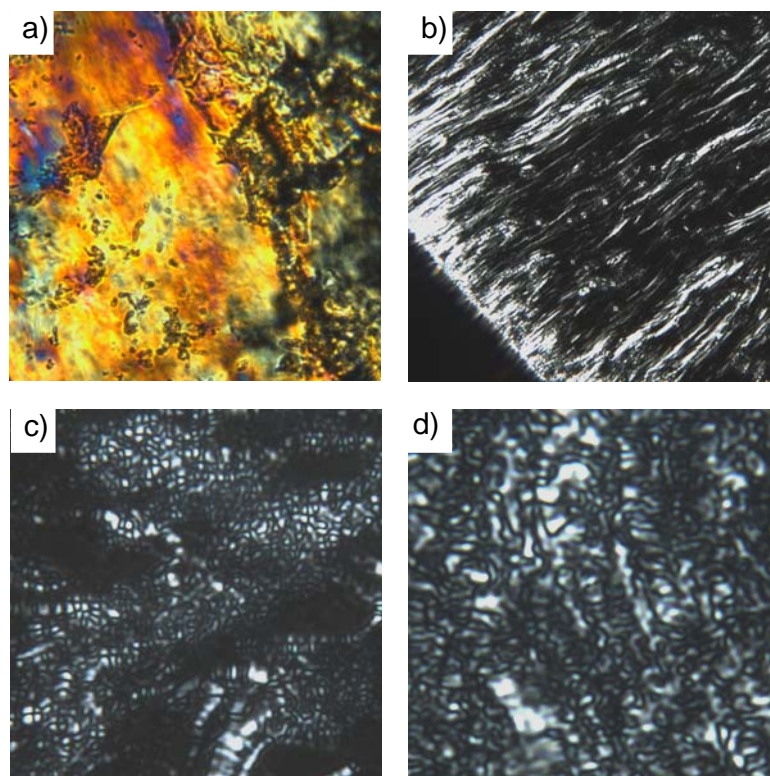


**Figure 5.10 - POM of [5-1][(-)CamSO<sub>3</sub>]<sub>2</sub> (crossed polarizers): a) squeezed between glass slides @ 25 °C, b) @ 90 °C upon heating, c) @ 135 °C upon heating and d) @ 25 °C upon cooling from  $T_i = 153$  °C. All are shown at 50x magnification.**

The chiral crown [2]rotaxane [5-5][OTf]<sub>2</sub> showed a decrease in fluidity, compared to [5-1][(-)CamSO<sub>3</sub>]<sub>2</sub> and little change was observed upon heating until 100 °C, at which point a schlieren texture was observed and remained until clearing into the isotropic liquid at 155 °C (Figure 5.11b), which is close to its decomposition temperature. Upon cooling from the isotropic liquid, there were domains of spherulites that grew in at 150 °C and other domains of a fan-like texture were observed after 30 seconds to 1 minute (Figure 5.11c, d). If the pitch of the helix is on the order of several micrometers, it can be observed by POM as an equidistant line pattern superimposed on the SmC\* fans. This equidistant line pattern, due to the helical superstructure, is observed in the magnified images of each domain (Figure 5.11e, f). The lines are parallel to the smectic layer planes and the distance between two adjacent dark lines provides the pitch of the helix; the helix

axis is perpendicular to the lines. So in the SmC\* phase, the helix line pattern follows the smectic layer planes, while the helix axis gives the local direction of the smectic layer normal. From the natural texture of the SmC\* phase, the pitch was estimated to be between 1.3 and 1.4  $\mu\text{m}$ .

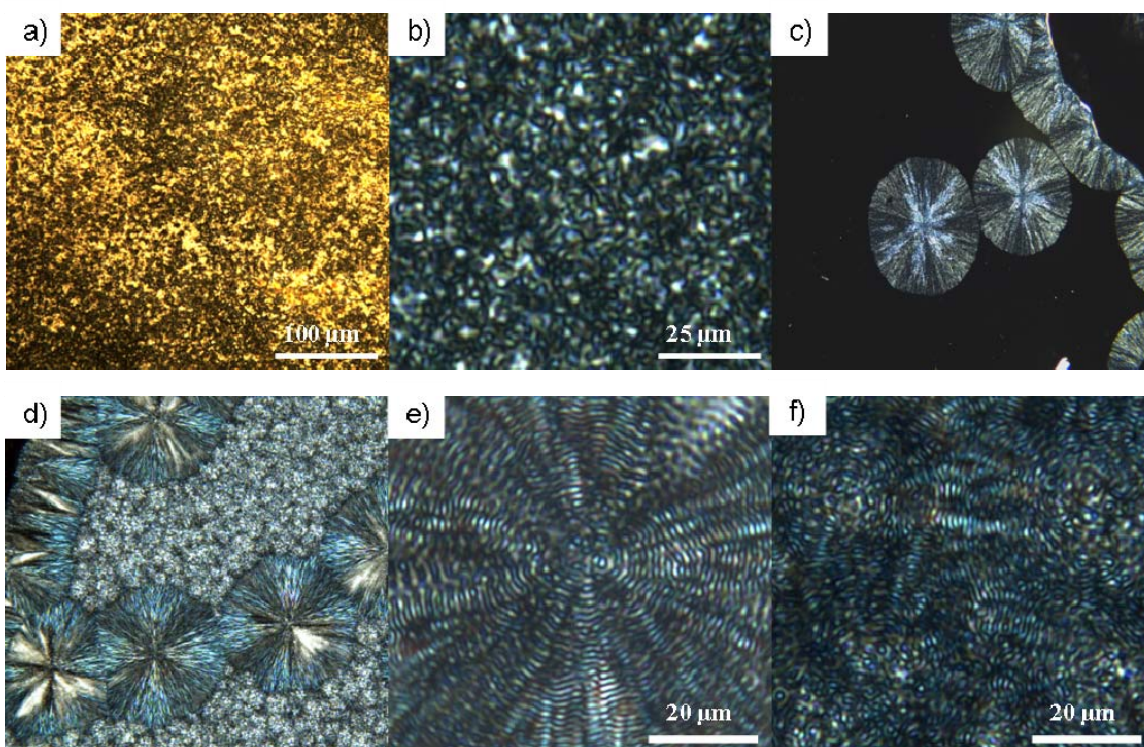


**Figure 5.11 - POM of [5-5][OTf]<sub>2</sub> (crossed polarizers): a) squeezed between glass slides @ 25 °C, b) @ 100 °C upon heating, c) @ 140 °C upon cooling from T<sub>i</sub> = 155 °C, t = 10 s, d) @ 140 °C, t = 45 s and e, f) the two difference magnified areas of d.**

### 5.3.2 Differential Scanning Calorimetry (DSC)

DSC analysis of both chiral [2]rotaxanes [5-1][(-)CamSO<sub>3</sub>]<sub>2</sub> and [5-5][OTf]<sub>2</sub> only displayed glass transitions; which was reversible upon cooling for [2]rotaxane [5-1][(-)CamSO<sub>3</sub>]<sub>2</sub> (Figure 5.12). The midpoint temperatures for the glass transitions are listed in Table 5.1.



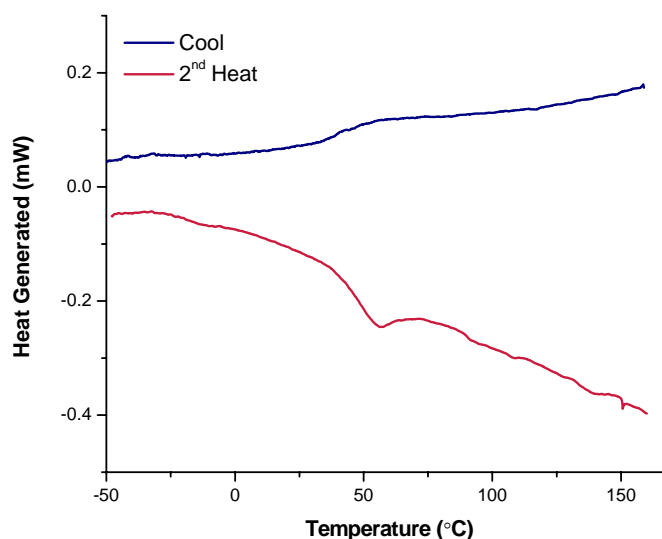


Figure 5.12 - Second heating and cooling DSC runs of [2]rotaxane [5-5][OTf]<sub>2</sub> at 10 °C/min under N<sub>2</sub>.

Table 5.1 - Transition temperatures (°C, midpoint) observed by DSC at scan rates of 10 °C/min for [2]rotaxanes.

Compound	2 <sup>nd</sup> Heating	Cooling
5-1 <sup>2+</sup>	32 (T <sub>g</sub> )	44 (T <sub>g</sub> )
5-5 <sup>2+</sup>	65 (T <sub>g</sub> )	n.t.

n.t. : no transition observed.

### 5.3.3 Variable Temperature X-Ray Diffraction (vt-XRD)

Data for vt-XRD were collected for the second heating and cooling cycles. [2]Rotaxanes [5-1][(-)CamSO<sub>3</sub>]<sub>2</sub> and [5-5][OTf]<sub>2</sub> displayed highly ordered lamellar phases with a near identical layer spacing of 41 Å, similar to that observed for the achiral [2]rotaxane [4-19][OTf]<sub>2</sub>. Neither of these exhibited second order reflections in the bulk material (Figure 5.13a and b). This confirms that the chiral [2]rotaxanes [5-1][(-)CamSO<sub>3</sub>]<sub>2</sub> and [5-5][OTf]<sub>2</sub> also have tilted smectic phases. POM studies for both [2]rotaxanes showed schlieren textures that are characteristic for a SmC phase. The

calculated lengths of the molecules for both chiral [2]rotaxanes remains nearly unchanged from the achiral [2]rotaxane [4-19][OTf]<sub>2</sub> and the tilt angles for [5-1][(-)CamSO<sub>3</sub>]<sub>2</sub> and [5-5][OTf]<sub>2</sub> were estimated to be 36° and 34°, with the long axis of the molecule tilted with respect to the director.

The [2]rotaxane [5-1][(-)CamSO<sub>3</sub>]<sub>2</sub> showed a very broad reflection centered between 5 and 6 Å, corresponding to the disordered lateral arrangement of the alkyl extended siloxane groups within each layer.<sup>157,164</sup> In contrast, the [2]rotaxane [5-5][OTf]<sub>2</sub> showed a higher degree of order over the entire range studied (Table 5.2). This suggests a more efficient packing of the molecules in the mesophase of [5-5][OTf]<sub>2</sub> compared to [5-1][(-)CamSO<sub>3</sub>]<sub>2</sub>. The reflections resulting in distances at 15 and 10 Å are within the range of core to core distances based on estimated molecular lengths and are likely due to in-plane packing order.

**Table 5.2 – vt-XRD data for [5-1][(-)CamSO<sub>3</sub>]<sub>2</sub> and [5-5][OTf]<sub>2</sub> upon cooling. The values are consistent over several heating and cooling cycles.**

Compound	d <sub>meas</sub> (Å)	Indexation k	2θ	Intensity
5-1 <sup>2+</sup>	40.5	10	2.18	vs
	5.61		2.14	br
5-5 <sup>2+</sup>	41.32	10	2.14	vs
	15.4		5.75	m
	9.97		8.88	sh
	7.46		11.90	sh
	5.53		15.82	sh
	4.77		18.50	sh
	4.49		19.73	sh

vs, very strong; m, medium; br, broad; sh, sharp.

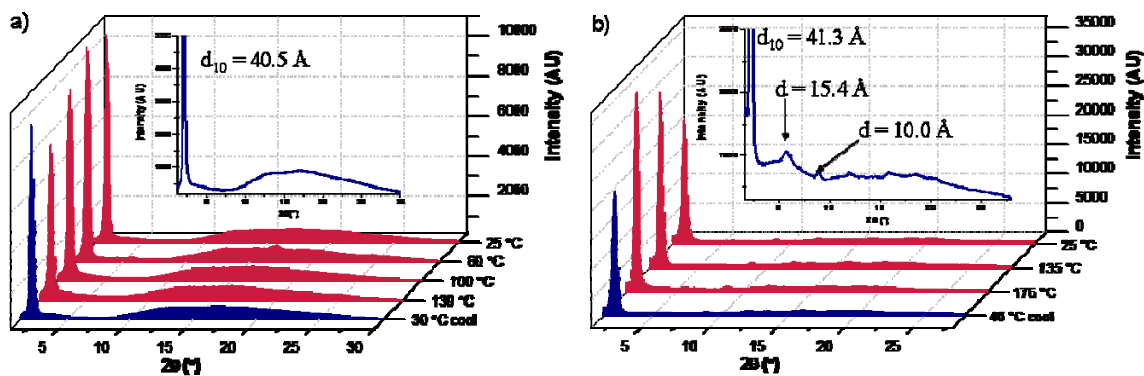


Figure 5.13 - vt-XRD data of a) [5-1][(-)CamSO<sub>3</sub>]<sub>2</sub> and b) [5-5][OTf]<sub>2</sub>.

### 5.3.4 Processing of LC Materials

An attempt at parallel alignment of these materials on glass by applying shear force was undertaken and the polarized micrographs are shown in Figure 5.14. [2]Rotaxane [5-1][(-)CamSO<sub>3</sub>]<sub>2</sub> was relatively fluid above 50 °C and the material was sheared at 85 °C, which appeared to align at low magnification. However, when magnified further the textures showed a moderately developed unidirectional line pattern (Figure 5.14a). This may suggest a long pitch SmC\* under planar anchoring conditions, and from this the pitch was estimated to be between 4.0 and 7.0 μm, which is nearly three times larger than the pitch for [5-5][OTf]<sub>2</sub>. Interestingly, when this material was rotated by 45° the birefringent areas between the lines showed only four-fold brushes (Figure 5.14b). From this polarized micrograph the pitch was estimated to be between 2.0 and 6.0 μm, which is still quite a bit larger than [5-5][OTf]<sub>2</sub>.

The chiral crown [2]rotaxane [5-5][OTf]<sub>2</sub> is less fluid than [5-1][(-)CamSO<sub>3</sub>]<sub>2</sub>, but became reasonably fluid above 100 °C. Mechanical shear alignment was attempted at 120 °C but only a schlieren texture of small domain size and many disclination lines was

observed. Brightness remained unchanged when the sample was rotated suggesting that no macroscopic alignment of one of the optic axes occurred (Figure 5.14c).

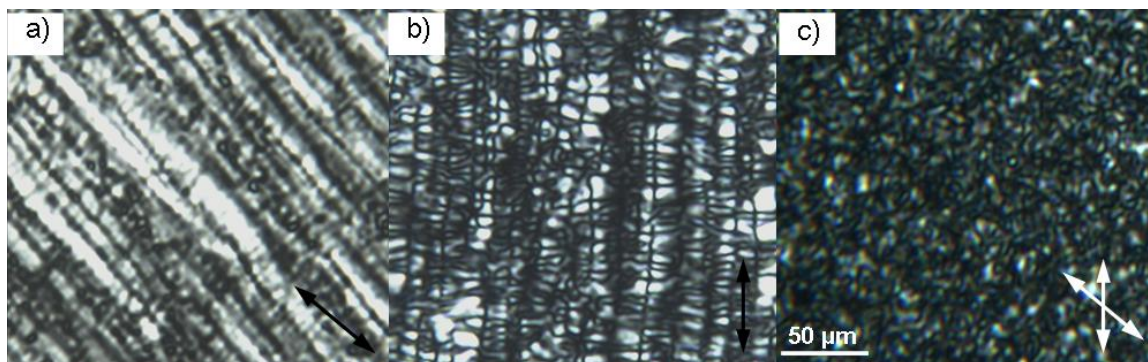


**Figure 5.14 - POMs of a) [5-1][(-)CamSO<sub>3</sub>]<sub>2</sub> mechanically sheared at 85 °C (in direction of arrow) and b) rotated by 45°. c) Schlieren texture obtained for [5-5][OTf]<sub>2</sub> after mechanically shearing at 120 ° C, which remained throughout rotation of the sample.**

### 5.3.6 Liquid Crystal Phase Determination

The mesophases formed by [2]rotaxanes [5-1][(-)CamSO<sub>3</sub>]<sub>2</sub> and [5-5][OTf]<sub>2</sub> have thus far been characterized by initial POM observations, DSC analysis and vt-XRD analysis. The phase characterization and transition temperatures measured by POM and DSC on heating are shown in Figure 5.15. Both formed chiral lamellar phases that cleared into the isotropic liquid just before their decomposition temperatures of 151 °C and 155 °C for [2]rotaxanes [5-1][(-)CamSO<sub>3</sub>]<sub>2</sub> and [5-5][OTf]<sub>2</sub>, respectively. [2]Rotaxane [5-1][(-)CamSO<sub>3</sub>]<sub>2</sub> remained amorphous over the entire temperature range and was thus a SmC\* liquid crystal. The chiral crown [2]rotaxane [5-5][OTf]<sub>2</sub> showed additional peaks in the wide angle region of the XRD over the entire temperature range and could be classified as a higher ordered chiral smectic phase SmX\*. The long axis of the molecule was tilted with respect to the layers and this was supported by textures observed by POM and by comparison to the calculated and experimentally determined molecular lengths. The approximate tilt angles for [2]rotaxanes [5-1][(-)CamSO<sub>3</sub>]<sub>2</sub> and

[5-5][OTf]<sub>2</sub> were determined to be 36° and 34°. The initial decomposition for each compound is marked with a black line in Figure 5.15, with decomposition for both occurring above 158 °C.

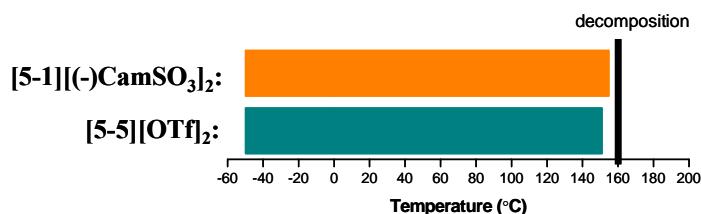


**Figure 5.15 - Phase transition temperatures for [2]rotaxanes [5-1][(-)CamSO<sub>3</sub>]<sub>2</sub> and [5-5][OTf]<sub>2</sub> measured by DSC and POM on heating. (orange, SmC\*; cyan, SmX\*. The start of decomposition is marked with a black line.)**

#### 5.4 SUMMARY AND CONCLUSIONS

In this preliminary study, chirality was introduced into the siloxane extended SmA [2]rotaxane [4-19][OTf]<sub>2</sub> by two different avenues. Avenue one is based on anion exchange of the triflate anion with the chiral (-)-camphor-10-sulfonate anion. This produced a SmC\* phase for [2]rotaxane [5-1][(-)CamSO<sub>3</sub>]<sub>2</sub> with an estimated pitch range between 2.0 and 7.0 μm, determined from applying shear force to induce parallel alignment. The tilt angle was estimated to be 36° with respect to the director based on XRD data and the calculated molecular length.

Avenue two introduces chirality into each [2]rotaxane by using a chiral crown. This formed a SmX\* phase for [2]rotaxane [5-5][OTf]<sub>2</sub> with an estimated pitch range between 1.4 and 1.3 μm, determined from the natural defect texture by POM. The tilt angle was estimated to be 34° with respect to the director based on XRD data and the calculated molecular length.

Due to time constraints further analysis required was not completed; variable temperature circular dichroism (vt-CD) in solution and on thin films to determine if there

---

is an amplification in the CD spectrum in the thin film and alignment in a wedge cell in an attempt to calculate the pitch. Also, future projects on doping the achiral [2]rotaxane with a chiral dopant to induce a chiral [2]rotaxane liquid crystal should be undertaken.

## 5.5 EXPERIMENTAL

### 5.5.1 General Comments

(-)-Camphor-10-sulfonic acid ammonium salt, paraformaldehyde, hydrobromic acid, sodium hydride, (R)-2-butanol and **DB24C8** were purchased from Aldrich and used as received. Deuterated solvents were obtained from Cambridge Isotope Laboratories and used as received. Thin layer chromatography (TLC) was performed using Teledyne Silica gel 60 F<sub>254</sub> plates and viewed under UV light. Column chromatography was performed using Silicycle Ultra Pure Silica Gel (230 – 400 mesh). Flash column chromatography was performed using Teledyne Ultra Pure Silica/RP-C<sub>18</sub> Silica Gel (230 – 400 mesh) on a Teledyne Isco Combiflash R<sub>f</sub>. All flash chromatography was performed under pressure (120 mL/min. - 200 mL/min.) for normal phase silica and (10 mL/min. - 40 mL/min.) for RP-C<sub>18</sub> silica, with increasing pressure corresponding to larger columns. Unless otherwise stated, all flash chromatography involved applied gradient elution from 0 - 100 % with increasing polar solvent with respect to less polar solvent. Length of column (column volumes - CV) were determined by separations on preliminary TLC runs.

<sup>1</sup>H NMR, <sup>13</sup>C NMR and 2-D experiments were performed on a Brüker Avance 500 instrument, with a working frequency of 500.13 MHz for <sup>1</sup>H nuclei, and 125.7 MHz for <sup>13</sup>C nuclei. Chemical shifts are quoted in ppm relative to tetramethylsilane, using the residual solvent peak as a reference standard. Conventional 2-D NMR experiments (<sup>1</sup>H-<sup>1</sup>H COSY) and (<sup>1</sup>H-<sup>13</sup>C HETCOR) were conducted and used to help assign all peaks. High resolution mass spectrometry (HR-MS) experiments were performed on a Micromass LCT Electrospray (ESI) time-of-flight (TOF) Mass Spectrometer. Solutions

of 50-100 ng/ $\mu$ L were prepared in CH<sub>3</sub>CN and injected for analysis at a rate of 5  $\mu$ L/min using a syringe pump.

Calorimetric studies were performed on a Mettler Toledo DSC 822<sup>e</sup> and thermal gravimetric analysis with mass spectrometric detection of evolved gases was performed on a Mettler Toledo TGA SDTA 851e that was attached to a Pfeiffer Vacuum ThermoStar<sup>TM</sup> mass spectrometer (1-300 amu) *via* a thin glass capillary. Helium (99.99 %) was used to purge the system with a flow rate of 30 mL/min. Samples were held at 25 °C for 30 min before heating to 550 °C at 2 °C/min. A mass range between 16 m/z and 150 m/z was constantly scanned. All samples were run in aluminum crucibles. Powder XRD measurements were recorded on a Brüker D8 Discover diffractometer equipped with a Hi-Star area detector and GADDS software and operated at 40 kV and 40 mA. CuK $\alpha_1$  radiation ( $\lambda = 1.54187 \text{ \AA}$ ) was used and the initial beam diameter was 0.5 mm. A custom made Instec hot stage (based on HS-400) was used for VT-XRD that covers a temperature range of -40 °C to 350 °C. Bulk samples for variable temperature XRD were filled into a 2 mm diameter hole in a 1 mm thick copper plate and covered with Kapton<sup>TM</sup> foil. This plate was mounted in an Instec hot-stage, aligned, and run at theta angles of 0°, and 15° for 30 or 60 min. Spectra were combined and evaluated in EVA and plotted with Origin. Polarized light microscopy was performed on an Olympus TPM51 polarized light microscope equipped with a Linkam variable temperature stage HCS410 and digital photographic imaging system (DITO1).



5.5.2 Synthesis of compound 5-1<sup>2+</sup>

[4-19][OTf]<sub>2</sub> (70.0 mg, 0.0266 mmol) was dissolved in MeNO<sub>2</sub> (4 mL) and stirred for one day after addition of saturated (-)-camphor-10-sulfonic acid ammonium (100.0 mg, 0.5 mL) solution. The MeNO<sub>2</sub> was washed with H<sub>2</sub>O (20 x 3 mL), dried over MgSO<sub>4</sub> and the solvent removed yielding a bright yellow glassy solid (62.0 mg).

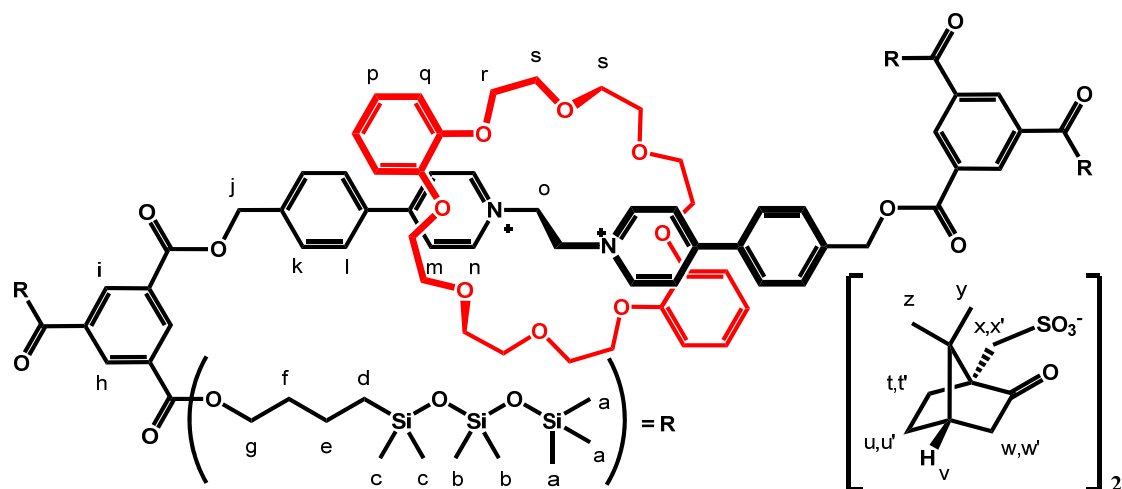


Table 5.3 - <sup>1</sup>H NMR data of [5-1][(-)CamSO<sub>3</sub>]<sub>2</sub> in CD<sub>3</sub>NO<sub>2</sub>. MW = 2800.212 g/mol

Proton	δ (ppm)	Multiplicity	# Protons	J (Hz)
a	0.13	s	36	--
b	0.16	s	24	--
c	0.77	s	24	--
d	0.73	t	8	<sup>3</sup> J <sub>de</sub> = 8.40
e	1.64	tt	8	<sup>3</sup> J <sub>ed</sub> = 8.40; <sup>3</sup> J <sub>ef</sub> = 6.96
f	1.93	tt	8	<sup>3</sup> J <sub>fe</sub> = 6.96; <sup>3</sup> J <sub>fg</sub> = 6.50
g	4.47	t	8	<sup>3</sup> J <sub>gf</sub> = 6.50
h	8.87	s	2	--
i	8.91	s	4	--
j	5.75	s	4	--
k	7.78	m	4	--
l	7.76	m	4	--
m	8.12	d	4	<sup>3</sup> J <sub>mn</sub> = 6.65

---

<b>n</b>	9.30	d	4	${}^3J_{nm} = 6.65$
<b>o</b>	5.61	s	4	--
<b>p</b>	6.79	dd	4	${}^3J_{meta} = 3.68; {}^3J_{ortho} = 6.53$
<b>q</b>	6.67	dd	4	${}^3J_{meta} = 3.68; {}^3J_{ortho} = 6.53$
<b>r</b>	4.19	m	8	--
<b>s</b>	4.12	m	16	--
<b>t</b>	2.01	m	2	--
<b>t'</b>	1.33	m	2	--
<b>u</b>	1.83	d	2	${}^2J_{u,u'} = 18.10$
<b>u'</b>	2.74	m	2	--
<b>v</b>	1.52	m	2	--
<b>w</b>	2.01	m	2	--
<b>w'</b>	1.36	m	2	--
<b>x</b>	3.07	d	2	${}^2J_{x,x'} = 14.70$
<b>x'</b>	2.57	d	2	${}^2J_{x',x} = 14.70$
<b>y</b>	0.82	s	6	--
<b>z</b>	1.10	s	6	--

---

## 5.5.3 Synthesis of compound 5-2

**DB24C8** (2.00 g, 4.4592 mmol) and paraformaldehyde (10.601 g, 6.6885mmol) were added to a 125 mL flask with stir bar which was then evacuated and backfilled, N<sub>2</sub> (g). Then 15 mL of degassed CHCl<sub>3</sub> was added to the flask, followed by 60 mL of acetic acid and heated to 60 °C. Once the temperature had reached 60 °C 30 mL of hydrogen bromide was added with heating continued for two days. The resulting beige precipitate was filtered and washed with copious amounts of H<sub>2</sub>O. The solid was then stirred in hot CHCl<sub>3</sub> and filtered and dried via vacuum line. The resulting light beige solid was collected. Yield: 3.47 g, 95 %.

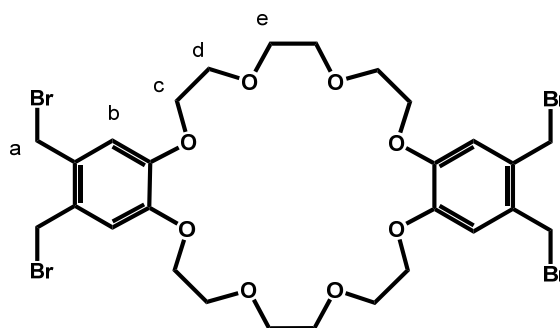


Table 5.4 – <sup>1</sup>H NMR data of 5-2 in CDCl<sub>3</sub>. MW= 820.197 g/mol

Proton	δ (ppm)	Multiplicity	# Protons	J (Hz)
<b>a</b>	4.58	s	8	--
<b>b</b>	6.83	s	4	--
<b>c</b>	4.15	t	8	<sup>3</sup> J <sub>cd</sub> = 4.23
<b>d</b>	3.89	t	8	<sup>3</sup> J <sub>dc</sub> = 4.23
<b>e</b>	3.79	s	16	--

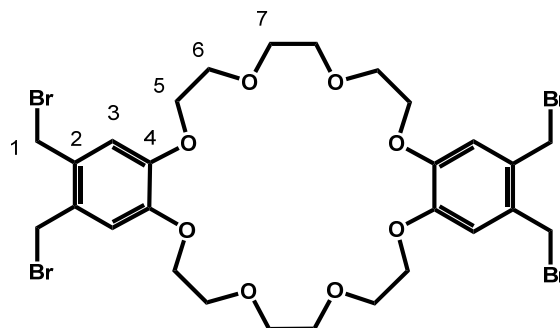
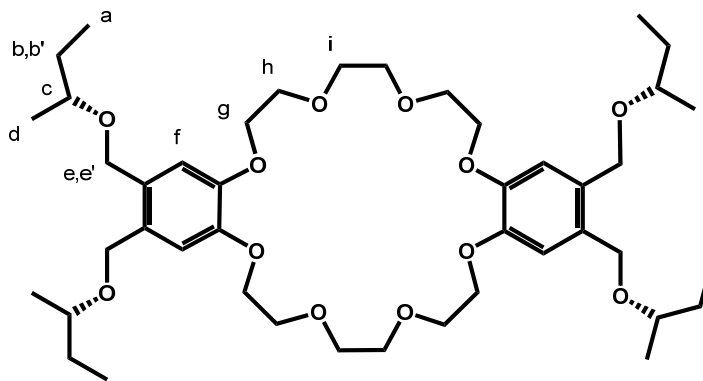


Table 5.5 –  $^{13}\text{C}$  NMR data of 5-2 in  $\text{CDCl}_3$ . MW= 820.197 g/mol

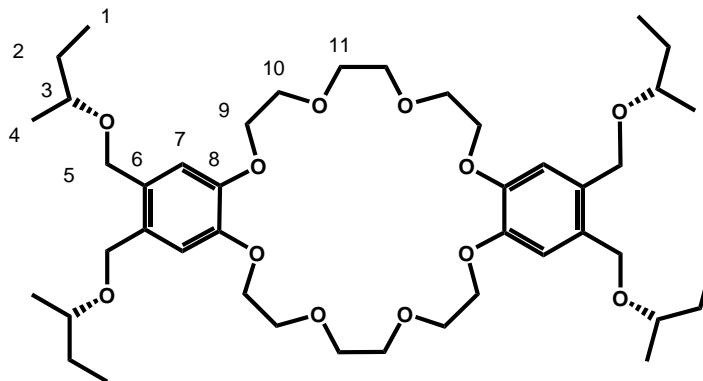
Carbon	$\delta$ (ppm)	# Carbons
1	31.63	4
2	130.19	4
3	113.97	4
4	148.11	4
5	69.48	4
6	70.62	4
7	71.25	4

#### 5.5.4 Synthesis of compound 5-3

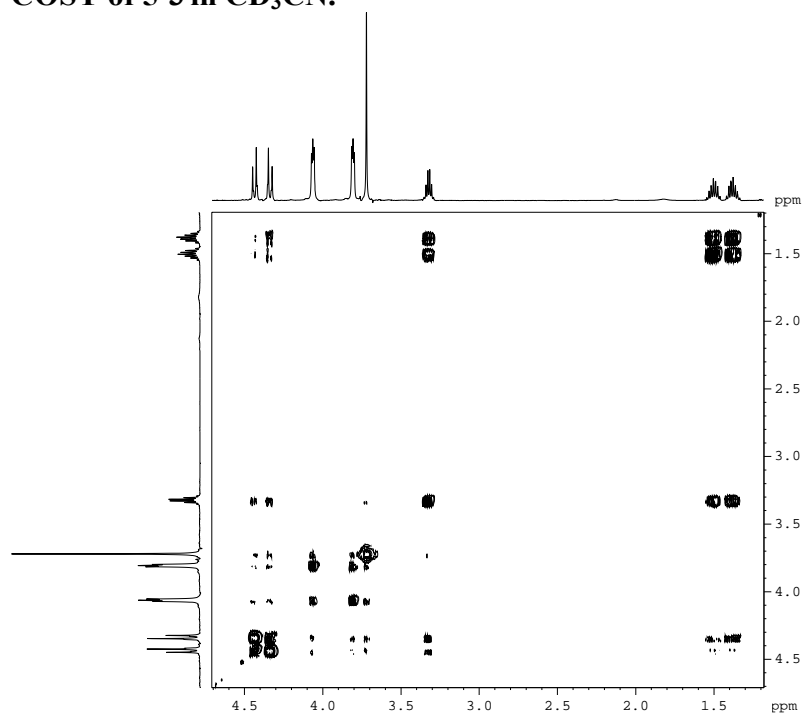
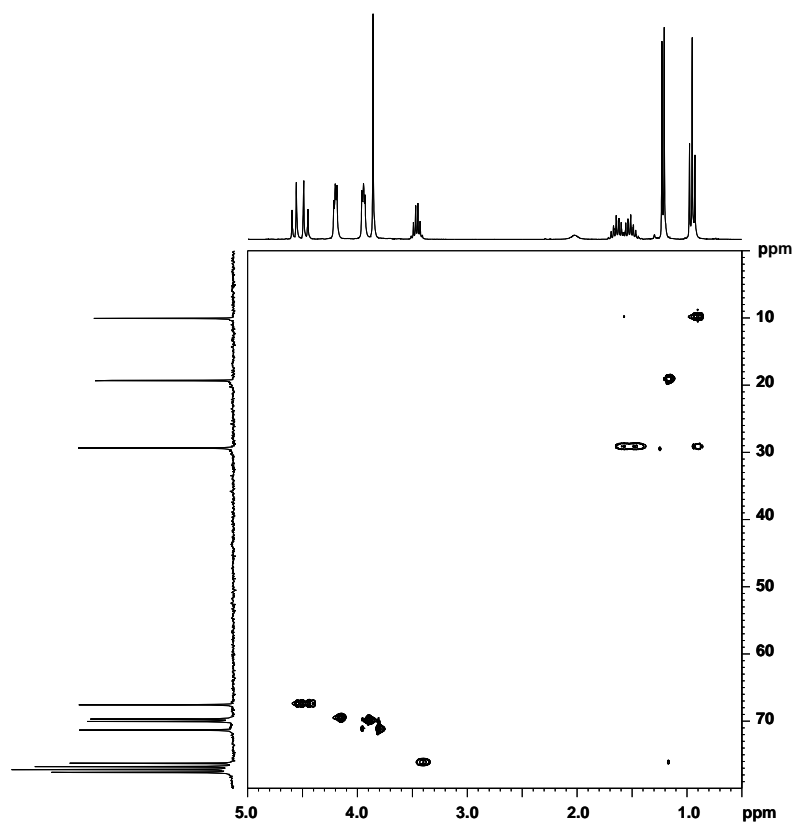
NaH (3.36 g, 0.1400 mol) and (R)-2-butanol (3.82 g, 0.0515 mol) were added to 100 mL of dry DMF in a 500 mL Schlenk flask under a nitrogen atmosphere which was stirred for 1 h. An additional 150 mL of dry DMF was added followed by addition of **5-2** (8.454 g, 0.0103 mol). The mixture was heated at 50 °C and stirring continued for 24 h. Reaction mixture was cooled to room temperature and the NaH was neutralized by slow addition of 2.0 M NH<sub>4</sub>Cl (aq) then basified with 1.0 M Na<sub>2</sub>CO<sub>3</sub>. The formed precipitate was filtered and washed with CHCl<sub>3</sub> (~200 mL). The aqueous layer was discarded and the organic layer was washed with H<sub>2</sub>O (2 x 150 mL), dried over MgSO<sub>4</sub> and concentrated to a crude yellow solid. The product was purified by flash column chromatography on RP-C<sub>18</sub> silica gel with H<sub>2</sub>O: MeOH gradient elution. The resulting white solid was collected. Yield: 3.65 g, 45 %.

Table 5.6 –  $^1\text{H}$  NMR data of 5-3 in  $\text{CD}_3\text{CN}$ . MW= 793.035 g/mol

Proton	$\delta$ (ppm)	Multiplicity	# Protons	$J$ (Hz)
a	0.90	t	12	$^3J_{ab,b'} = 7.47$
b	1.56	dq	4	$^3J_{ba} = ^3J_{bc} = 6.03, ^2J_{b,b'} = 51.89$
b'	1.46	dq	4	$^3J_{b'a} = ^3J_{b'c} = 6.03$
c	3.42	qt	4	$^3J_{cb} = ^3J_{cd} = 6.03$
d	1.14	d	12	$^3J_{dc} = 6.13$
e	4.50	d	4	$^2J_{e,e'} = ^2J_{e',e} = 11.59, ^2J_{e,e'} = 43.22$
e'	4.39	d	4	$^2J_{e,e'} = ^2J_{e',e} = 11.59$
f	6.96	s	4	--
g	4.09	t	8	$^3J_{gh} = 4.29$
h	3.79	t	8	$^3J_{hg} = 4.29$
i	3.68	s	8	--

Table 5.7 –  $^{13}\text{C}$  NMR data of 5-3 in  $\text{CDCl}_3$ . MW= 793.035 g/mol

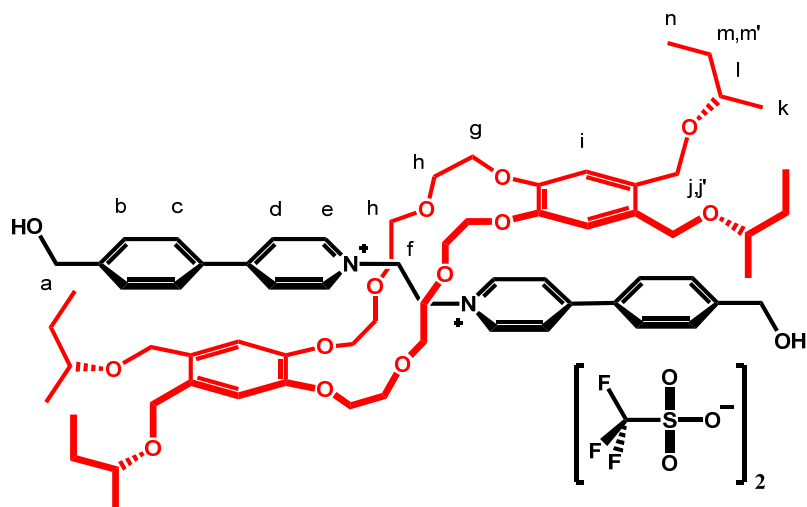
Carbon	$\delta$ (ppm)	# Carbons
1	19.89	4
2	76.44	4
3	29.15	4
4	10.17	4
5	70.62	4
6	129.23	4
7	114.92	4
8	145.71	4
9	68.03	4
10	69.42	4
11	70.09	4

COSY of 5-3 in CD<sub>3</sub>CN.HETCOR of 5-3 in CD<sub>3</sub>CN.



### 5.5.5 Synthesis of compound **5-4**<sup>2+</sup>

[**4-9**][OTf]<sub>2</sub> (1.39 mg, 0.0020 mmol) and **5-3** (4.75 mg, 0.0060 mmol) were stirred in MeNO<sub>2</sub> (1.0 mL) until solution turned yellow. The solution was evaporated to yield the crude yellow solid which was not purified further. **ESI-MS**: *m/z* 1339.6533 (calc.) for C<sub>71</sub>H<sub>98</sub>F<sub>3</sub>N<sub>2</sub>O<sub>17</sub>S<sup>+</sup> [M-OTF]<sup>+</sup>, found 1339.6537, *m/z* 595.3504 (calc.) for C<sub>70</sub>H<sub>98</sub>N<sub>2</sub>O<sub>14</sub><sup>2+</sup> [M]<sup>2+</sup>, found 595.3503. Yield: 2.92 mg, 98 %.

Table 5.8 –  $^1\text{H}$  NMR data of [5-4][OTf]<sub>2</sub> in CD<sub>3</sub>CN. MW= 1489.670 g/mol

Proton	$\delta$ (ppm)	Multiplicity	# Protons	$J$ (Hz)
a	4.72	s	4	--
b	7.54	d	4	$^3J_{bc} = 8.43$
c	7.57	d	4	$^3J_{cb} = 8.43$
d	7.91	d	4	$^3J_{de} = 6.82$
e	9.01	d	4	$^3J_{ed} = 6.82$
f	5.45	s	4	--
g	4.04	m	8	--
h	3.98	m	16	--
i	6.7	s	4	--
j	4.11	d	4	$^2J_{jj'} = ^2J_{j',j} = 11.96, ^2J_{jj'} = 48.79$
j'	3.38	d	4	$^2J_{j,j'} = ^2J_{j',j} = 11.96$
k	1.09	d	12	$^3J_{kl} = 6.06$
l	3.26	qt	4	$^3J_{lm} = ^3J_{lk} = 6.01$
m	1.43	dq	4	$^3J_{mn} = ^3J_{ml} = 6.01, ^2J_{m,m'} = 49.62$
m'	1.41	dq	4	$^3J_{m'n} = ^3J_{m'l} = 6.01$
n	0.92	t	12	$^3J_{nm,m'} = 7.48$

5.5.6 Synthesis of compound 5-5<sup>2+</sup>

[4-9][OTf]<sub>2</sub> (45.0 mg, 0.0646 mmol), 5-3 (179.3 mg, 0.2261 mmol) and 4-15 (292.4 mg, 0.1938 mmol) were dissolved in dry 6:4 (CHCl<sub>3</sub>: MeCN) (50 mL) under a nitrogen atmosphere. A catalytic amount of tributylphosphine (25 μL) was added via glass needle syringe and stirring continued until reaction complete (2 h). The solvent was removed under pressure. The crude yellow waxy solid was then purified by flash column chromatography with RP-C<sub>18</sub> silica gel with 90:10 (MeCN: MeOH) isocratic elution followed by gradient (10 - 100 % MeOH) as eluant. The soft yellow waxy solid was collected. Yield: 128.0 mg, 63 %. **ESI-MS**: *m/z* 1339.6356 (calc.) for C<sub>132</sub>H<sub>218</sub>N<sub>2</sub>O<sub>32</sub>Si<sub>2</sub><sup>2+</sup> [M]<sup>2+</sup>, found 1339.6350.

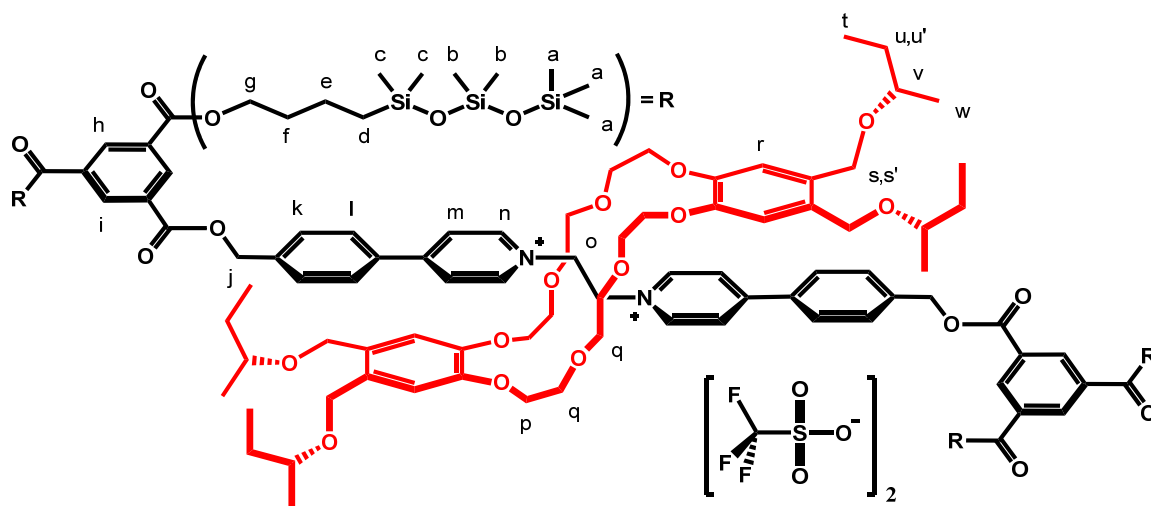


Table 5.9 – <sup>1</sup>H NMR data of [5-5][OTf]<sub>2</sub> in CD<sub>3</sub>CN. MW= 3144.741 g/mol

Proton	δ (ppm)	Multiplicity	# Protons	J (Hz)
a	0.07	s	36	--
b	0.09	s	24	--
c	0.01	s	24	--
d	0.65	t	8	<sup>3</sup> J <sub>de</sub> = 8.36
e	1.54	tt	8	<sup>3</sup> J <sub>ed</sub> = 8.36; <sup>3</sup> J <sub>ef</sub> = 7.59
f	1.84	tt	8	<sup>3</sup> J <sub>fe</sub> = 7.59; <sup>3</sup> J <sub>fg</sub> = 6.50

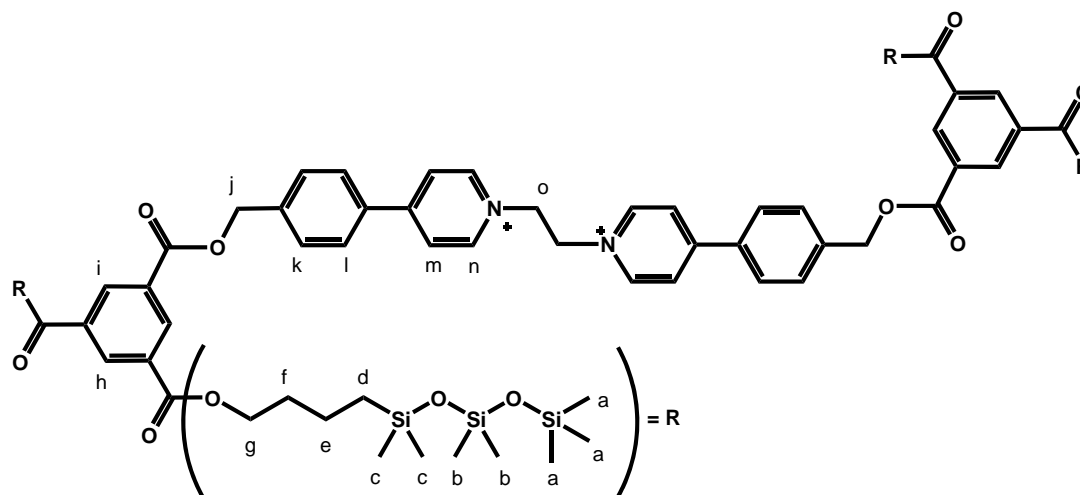
---

<b>g</b>	4.40	t	8	${}^3J_{gf} = 6.50$
<b>h</b>	8.84	s	4	--
<b>i</b>	8.78	s	2	--
<b>j</b>	5.55	s	4	--
<b>k</b>	7.68	d	4	${}^3J_{kl} = 8.15$
<b>l</b>	7.62	d	4	${}^3J_{lk} = 8.15$
<b>m</b>	7.93	d	4	${}^3J_{mn} = 6.50$
<b>n</b>	9.05	d	4	${}^3J_{nm} = 6.50$
<b>o</b>	5.48	s	4	--
<b>p</b>	4.00	m	8	--
<b>q</b>	4.03	m	16	--
<b>r</b>	6.68	s	4	--
<b>s</b>	4.04	d	4	${}^2J_{s,s'} = 11.85$
<b>s'</b>	3.89	d	4	${}^2J_{s',s} = 11.85$
<b>t</b>	0.82	t	12	${}^3J_{tu} = {}^3J_{tu'} = 7.45$
<b>u</b>	1.43	dq	4	${}^3J_{ut} = {}^3J_{uv} = 6.71, {}^2J_{u,u'} = 44.61$
<b>u'</b>	1.34	dq	4	${}^3J_{u',t} = {}^3J_{u',v} = 6.71$
<b>v</b>	3.15	qt	4	${}^3J_{vu} = {}^3J_{vw} = 6.01$
<b>w</b>	1.00	d	12	${}^3J_{vw} = 6.05$

---

### 5.5.7 Synthesis of 5-6<sup>2+</sup>

[4-9][OTf]<sub>2</sub> (32.16 mg, 0.0461 mmol) and 4-15 (243.8 mg, 0.1616 mmol) were dissolved in dry 7:3 (CH<sub>2</sub>Cl<sub>2</sub>: MeCN) (30 mL) under nitrogen atmosphere. A catalytic amount of tributylphosphane (15 μL) was added via glass needle syringe and stirring continued until reaction complete (3 - 4 h). The solvent was removed under pressure yielding the crude yellow oil. The oil was purified by flash column chromatography on RP-C<sub>18</sub> silica gel with CH<sub>2</sub>Cl<sub>2</sub> as eluant followed by MeOH. The product was isolated as a pale beige oil. Yield: 73.70 mg, 73 %. **ESI-MS**: m/z 943.3445 (calc.) for C<sub>88</sub>H<sub>146</sub>N<sub>2</sub>O<sub>20</sub>Si<sub>12</sub> [M]<sup>2+</sup>, found 943.3449.

Table 5.10 –  $^1\text{H}$  NMR data of [5-6][OTf] $_2$  in  $\text{CDCl}_3$ .  $\text{MW}_{\text{OTf}} = 2187.267$  g/mol

Proton	$\delta$ (ppm)	Multiplicity	# Protons	$J$ (Hz)
a	0.07	s	36	--
b	0.08	s	24	--
c	0.01	s	24	--
d	0.61	t	8	$^3J_{de} = 7.21$
e	1.50	tt	8	$^3J_{ed} = 7.21; ^3J_{ef} = 7.52$
f	1.81	tt	8	$^3J_{fe} = ^3J_{fg} = 7.52$
g	4.38	t	8	$^3J_{gf} = 8.34$
h	8.83	s	2	--
i	8.86	s	4	--
j	5.53	s	4	--
k	7.72	d	4	$^3J_{kl} = 8.05$
l	7.85	d	4	$^3J_{lk} = 8.05$
m	8.27	d	4	$^3J_{mn} = 6.43$
n	9.66	d	4	$^3J_{nm} = 6.43$
o	5.42	s	4	--

# CHAPTER 6

## *Towards Liquid Crystalline Molecular Machines*

### 6.1 INTRODUCTION

#### 6.1.1 [2]Rotaxane Molecular Shuttles

Supramolecular architectures such as rotaxanes have generated great attention, particularly because of their dynamic properties.<sup>175-181</sup> Many molecular machines and motors have been proposed over the last decade which incorporate such interlocking or threaded molecular systems<sup>39-43,114-123</sup> as well as non-interlocking complexes.<sup>182-184</sup> In a [2]rotaxane molecular shuttle, there are two recognition sites on the thread for the macrocycle to occupy. As a result, the complex possesses translational isomerism. Initial work done in our group incorporated the bis(dipyridinium)ethane/**DB24C8** motif into a molecular shuttle, where both recognition sites were based upon 1,2-bis(pyridinium)ethanes.<sup>116,120,122</sup> A non-degenerate shuttle consisting of a 1,2-bis(4,4'-dipyridinium)ethane site stoppered with a *t*-butylbenzyl group and a 1-(4,4'-dipyridinium) site stoppered with a *t*-butylpyridine group and incorporating the **DB24C8** macrocycle is shown in Figure 6.1. At room temperature, the <sup>1</sup>H NMR spectrum showed that the crown ether was rapidly shuttling between the two sites and there was only one set of averaged proton resonances. vt-<sup>1</sup>H NMR spectroscopy determined coalescence to occur at 0 °C and the rate of exchange between the two populated co-conformational states was calculated to be 222 s<sup>-1</sup> with a  $\Delta G^\ddagger = 54$  kJ/mol. Integration of the peaks in the limiting spectrum allowed determination of the isomer ratio which was found to be 2:1, with the 1,2-

bis(4,4'-dipyridinium)ethane site (blue) being favoured over the 1-(4,4'-dipyridinium)-2-(*t*-butylpyridinium)ethane site (green). This preference was attributed primarily to the 4-*t*-butylpyridine methyl group preventing the crown ether catechol group from  $\pi$ -stacking efficiently over the pyridinium ring.

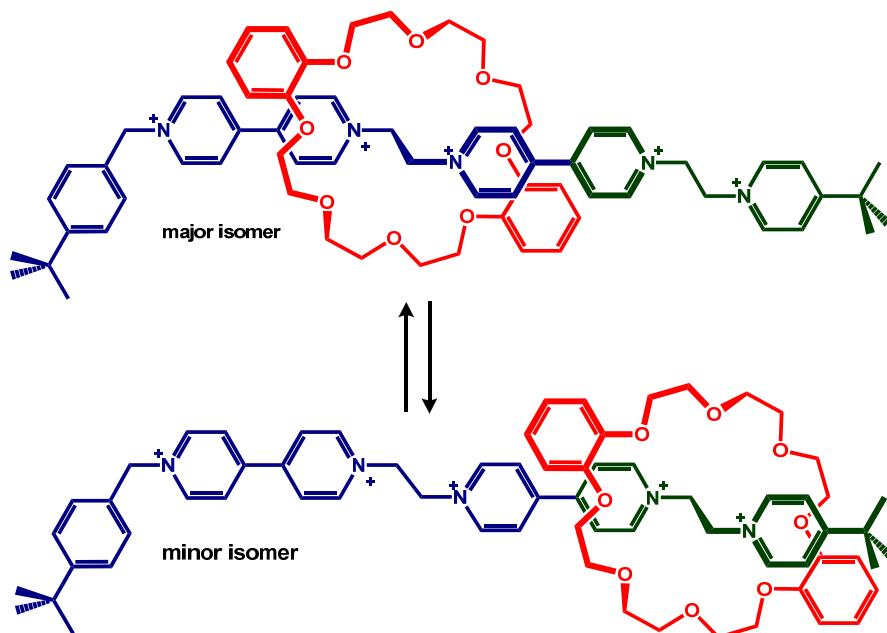


**Figure 6.1 - Non degenerate [2]rotaxane molecular shuttle.**

### 6.1.2 Mesogenic [2]Rotaxane Molecular Shuttles

A promising new approach towards nanoscale devices is the combination of molecular machines and liquid crystals, which are mobile and ordered condensed states. At the same time, the study of such compounds in solution is interesting in itself. The liquid crystalline molecular order can provide the molecular machinery component with an organized dynamic environment. Furthermore, molecular machines have the capability to control the self-assembled behaviour of LC molecules.

Only recently has the first bistable LC [2]rotaxane molecular shuttle been described by a collaboration between the groups of Kato and Stoddart.<sup>96</sup> They designed an



electrochemically switchable bistable [2]rotaxane molecular shuttle consisting of the tetra-cationic cyclobis(paraquat-*p*-phenylene) as the mobile macrocycle and two different recognition sites in the thread, containing tetrathiafulvalene and 1,5-dioxynaphthalene groups (Figure 6.2). Smectic A mesomorphism was introduced by the attachment of large liquid crystalline dendritic stoppers. Incorporation of a large number of ethylene glycol units lowered the melting temperature of the molecular shuttle, but tedious purification procedures were required and isotropization still occurred above the decomposition temperature of the complex at 150 °C.

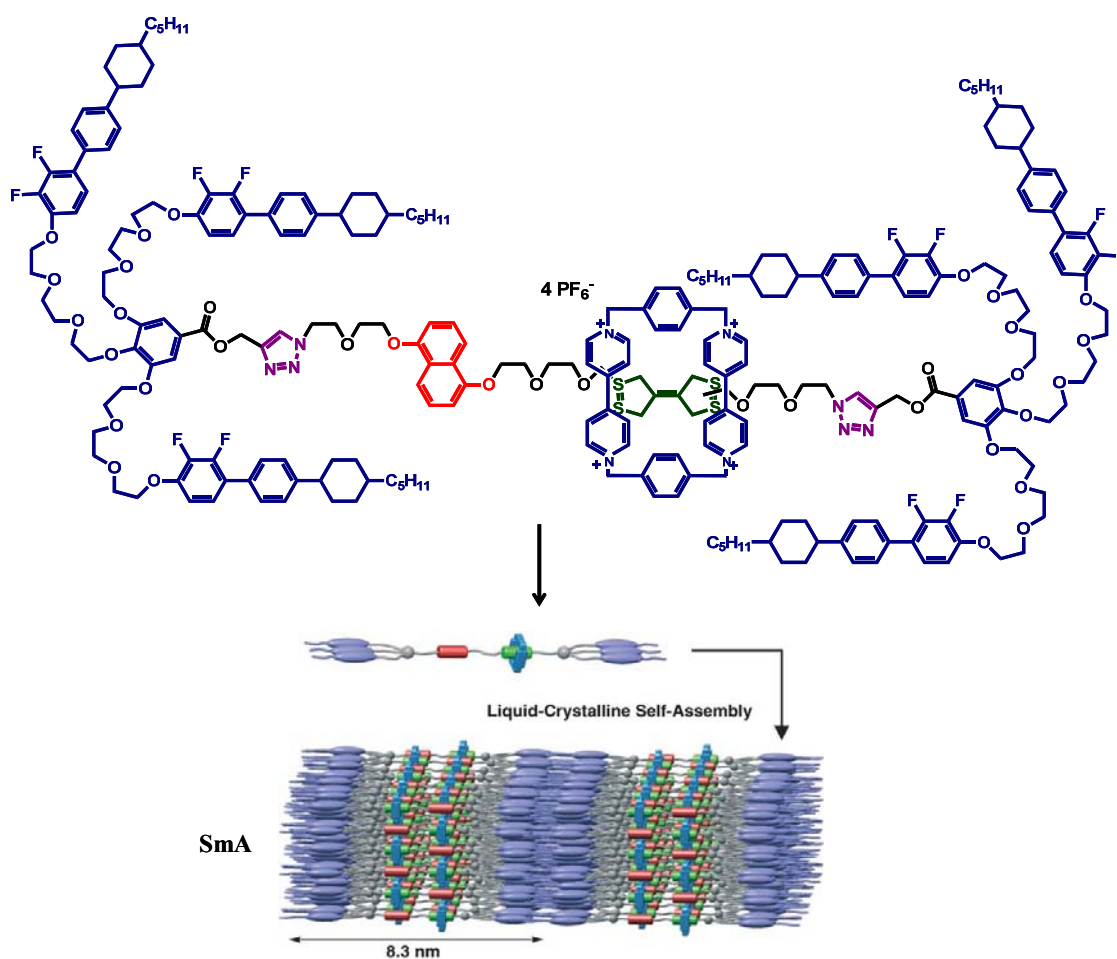


**Figure 6.2** - A LC bistable [2]rotaxane molecular shuttle done by Kato and Stoddart *et al.*

This approach has been previously applied to other typical non-mesogens<sup>86,88,105-111</sup> and is generally successful if the dendritic mesomorphic groups are sufficiently large and numerous and dictate the self-organization of the entire compound. However, this methodology does have limits such as an increase in phase transition temperatures, an increase in viscosity and synthetic feasibility.

Control of molecular switches and the amplification of their cooperative motion to produce a macroscopic response within a mesophase can only be accomplished by contributions from both the shuttling macrocycle and the mesogenic groups. These types of studies also require LC rotaxanes that can be prepared in large quantities and with high purity. Future applications such as functional materials also require a good alignment of these compounds in optical and/or electronic devices, which usually requires the formation of an isotropic melt at temperatures below 200 °C.

It has recently been shown in the Loeb group that incorporation of Fréchet's polyaryl ether dendrons into the components of a molecular shuttle based upon the 1,2-bis(dipyridinium)ethane/**DB24C8** motif increases the barrier to shuttling and biases the distribution of co-conformations in favor of a single recognition site.<sup>124</sup> The dendrons were employed as both a stopper and an appendage of the **DB24C8** macrocycle. In this system, it was observed that as the size of the dendritic moiety increased in generation on either the stopper or the macrocycle, the barrier to shuttling increased and the rate of shuttling decreased. There was a preference for the more compact "short" co-conformation of the complex with the macrocycle occupying the bis(4,4'-bipyridinium)ethane recognition site. This is illustrated in Figure 6.3, where each sphere indicates the number of generations of the aryl ether unit. These complexes formed a

nematic mesophase over the entire temperature range and cleared into the isotropic liquid well before their decomposition temperature, which was above 200 °C; all possessed a high degree of viscosity.

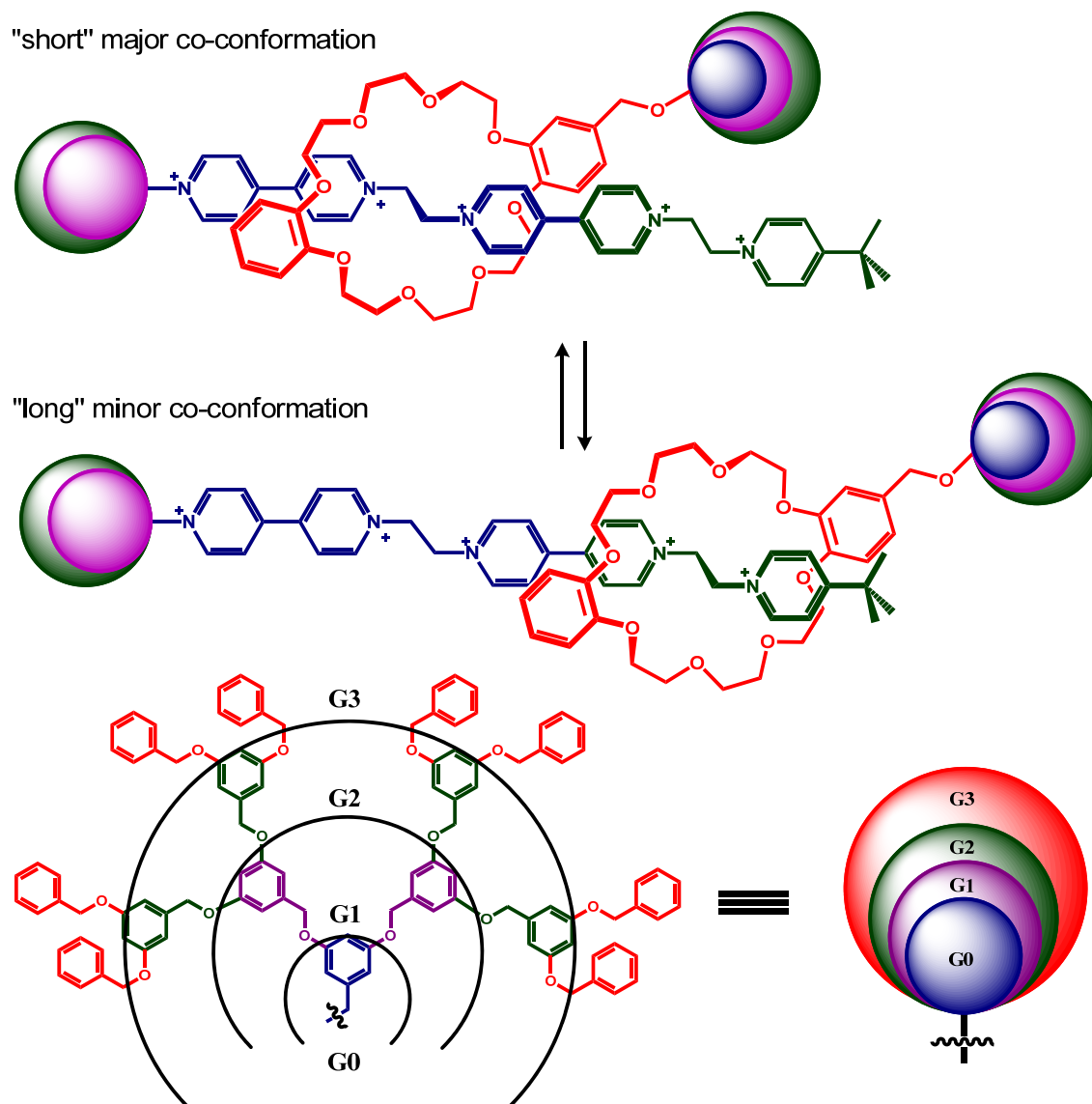


**Figure 6.3 - Co-conformations of nematic [2]rotaxane molecular shuttle substituted with Fréchet polyaryl ether dendrons. Each sphere represents a generation.**

### 6.1.3 Our Approach to a Mesogenic [2]Rotaxane Molecular Shuttle

Based upon the body of knowledge that we have gained from the mesogenic [2]rotaxanes discussed in the previous chapters, the approach to our design for a bistable

LC molecular shuttle incorporates components that have been shown to induce mesomorphism while possessing the fluidity required at high temperatures for processing. There are various types of recognition sites that can be incorporated into the shuttle thread in order to form a pseudorotaxane. Some possible groups are shown in Figure 6.4. These were chosen for their ease of synthesis or simply because they are commercially available and they have been shown to interact with the **DB24C8** macrocycle.<sup>114-123</sup> These play an important role depending upon the perturbation desired to shuttle the macrocycle from one site to the other. For example, the bis(dipyridinium) and diazapyrene components can be oxidized producing Coulombic charge-charge repulsion with the macrocycle and shuttle the macrocycle to the alternate site and can be reversed by reduction (Figure 6.4a, b). It may be possible to overcome the base sensitivity of the bis(dipyridinium) and diazapyrene components by introducing an alkyl bridge (Figure 6.4c, d). The alkyl bridge also introduces flexibility in the [2]rotaxane core. Components that undergo *cis-trans* isomerization upon irradiation, such as azobenzene derivatives, are also a convenient way to change the conformation of the complex and cause shuttling. The *trans* form is generally more stable than the *cis* form, which reverts thermally to the *trans* form on time scales ranging from milliseconds to months depending upon the particular system.<sup>185</sup>

It was decided that our new unsymmetrical [2]rotaxane molecular shuttle design would contain a bis(4,4'-bipyridinium)ethane stoppered with 3,5-lutidine on one end and a 4,4'-pyridinebenzyl group that is stoppered by ester formation (Figure 6.5). A triether octadecane substituted benzene was chosen as the stopper because the additional chain

length and number of chains should aid in fluidity. Only one end was stoppered with the mesogenic group to create a truly unsymmetrical thread where translation of the

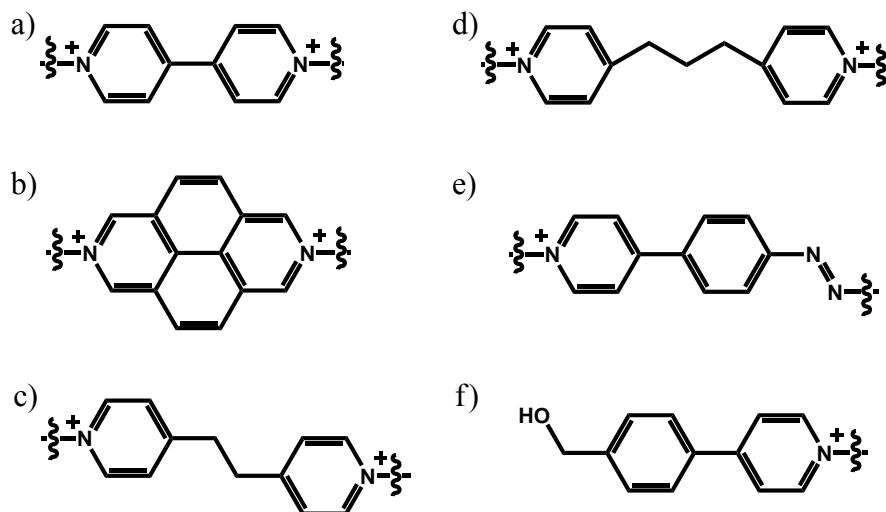


**Figure 6.4 - Various components for the thread that will form a pseudorotaxane with the DB24C8 macrocycle.**

macrocycle from one site to the other should create large differences in the size of the molecule, which we hope to observe macroscopically. For reasons discussed in Chapter 5, the macrocycle chosen was a tetra-substituted **DB24C8** crown ether which was extended with octadecane chains. The aliphatic chains should shelter the ionic core, keeping the viscosity of the material as low as possible.

This material is expected to induce layered self-assembled structures with smectic LC phases. From an electronic perspective, the macrocycle will occupy the site closest to the stopper and additional interactions with the alkyl chains on the stopper and macrocycle could further stabilize this interaction. This should be the major co-conformation in solution and may also be in the solid state. If upon heating the material and the chains possess enough fluidity, the macrocycle may shuttle to the other site, producing a longer molecule where the alkyl chains of both the stopper and macrocycle

could reorganize to give efficient microphase segregation. If there is preference for one co-conformation over the other, we should also observe a colour change due to the difference in aromatic interactions for each site. This shuttling can be studied by VT analysis both in solution and in thin films using  $^1\text{H}$  NMR spectroscopy, UV-Vis spectroscopy, XRD and POM analysis.

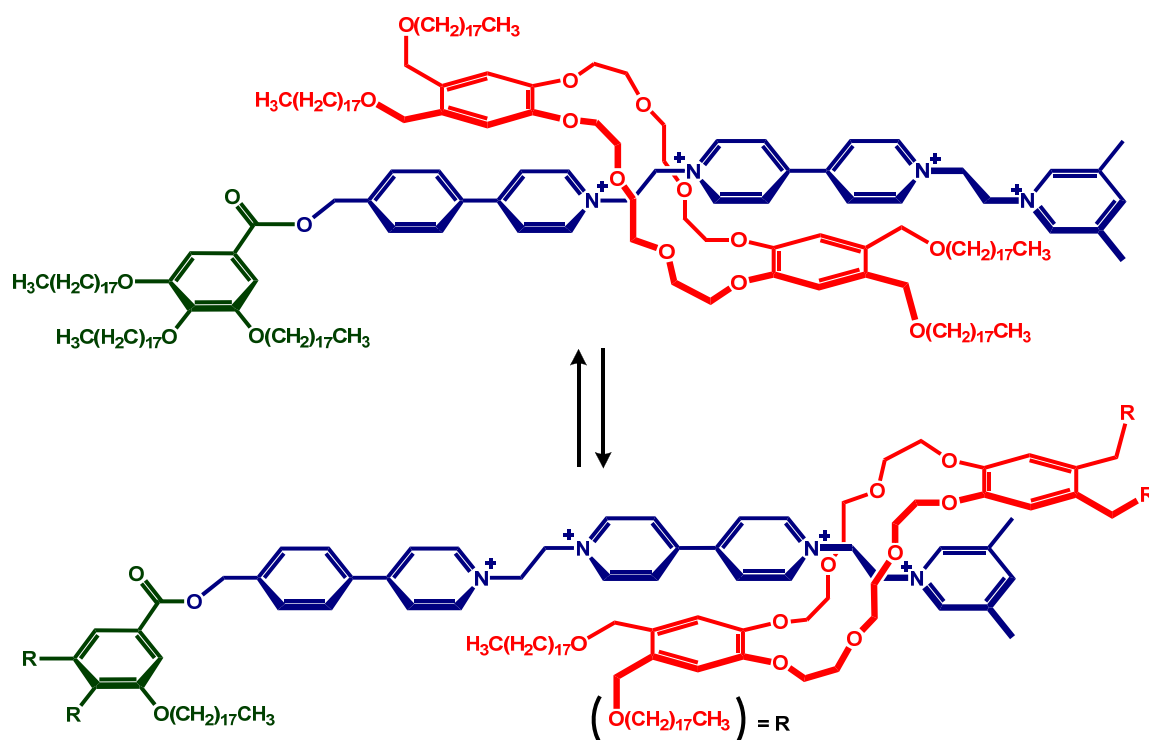


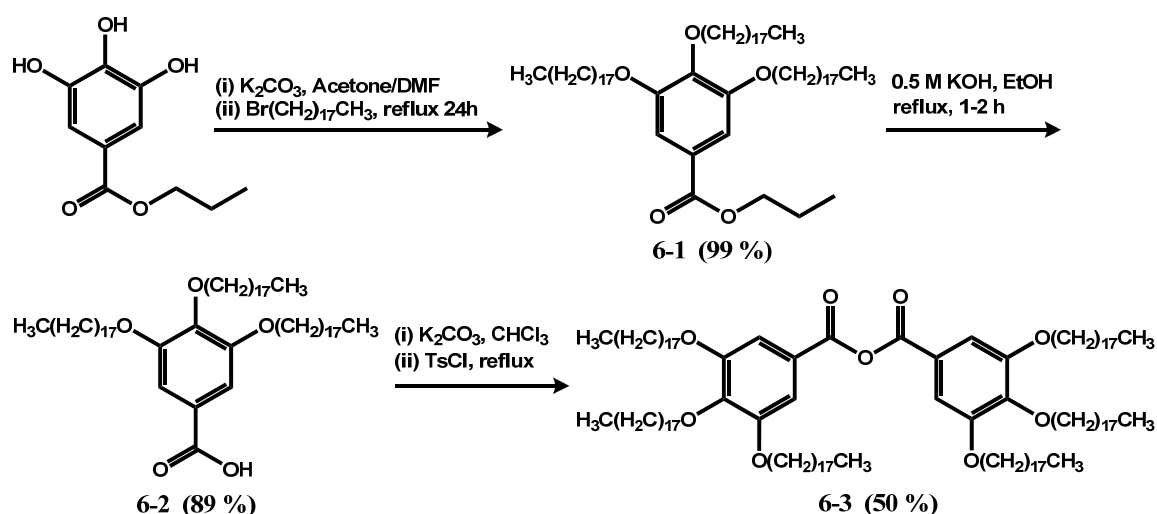
Figure 6.5 - Proposed design for a LC bistable [2]rotaxane molecular shuttle.

## 6.2 SYNTHESIS AND CHARACTERIZATION

### 6.2.1 Synthesis

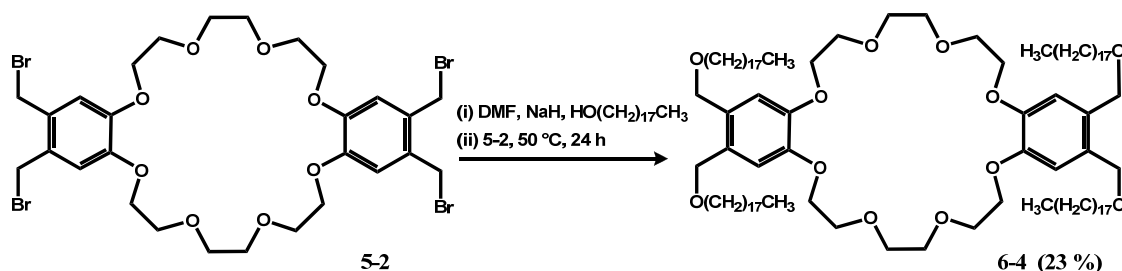
The benzoic acid **6-2** was prepared using a modified version of a previously reported procedure<sup>186</sup> for the alkylation of propyl gallate. This produced **6-1** quantitatively and was followed by deprotection of the propyl group to give **6-2** in 89 % yield (Scheme 6.1). The anhydride **6-3** was generated from the corresponding acid **6-2**

quantitatively using half of an equivalent of tosyl chloride and excess base. Reaction completion was monitored by  $^1\text{H}$  NMR and  $^{13}\text{C}$  NMR spectroscopy.



**Scheme 6.1 - Synthetic route for stoppers 6-1 through 6-3.**

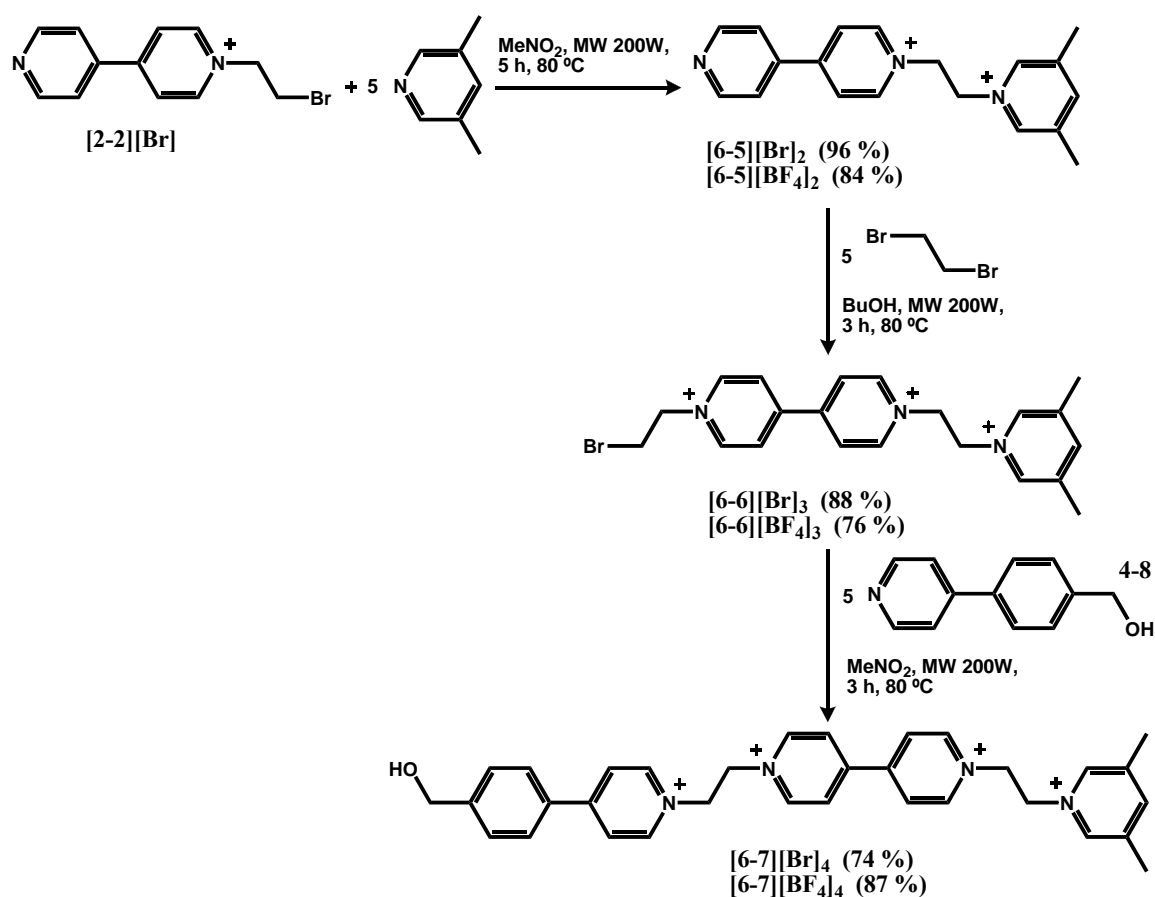
Synthesis of the tetrakis(oxyoctadecyl)-DB24C8 macrocycle followed similar conditions described in Chapter 5, by alkylation of **5-2** with 1-octadecanol to generate **6-4** in 23 % yield. Due to the insolubility of **5-2**, it was used without purification and hence the low yield of **6-4** was due primarily to the many variations of multiply substituted products and possible isomers of **5-2**. All of which were recovered by column chromatography on reverse phase silica gel.



**Scheme 6.2 - Synthetic scheme for crown 6-4.**

The shuttle thread compounds **6-5**<sup>2+</sup> through **6-7**<sup>4+</sup> were synthesized by alkylation *via* microwave synthesis to give the products as the bromide salt. Each was subsequently

anion exchanged, to the tetrafluoroborate salt for **6-5<sup>2+</sup>** and **6-6<sup>3+</sup>**, and to the triflate salt for **6-7<sup>4+</sup>** via a two-layer extraction. Compound **2-2<sup>+</sup>** was combined with an excess of 3,5-lutidine and subjected to microwave irradiation to generate thread precursor **6-5<sup>2+</sup>** (Scheme 6.3). This thread precursor was subjected to the same conditions with an excess of 1,2-dibromoethane to generate **6-6<sup>3+</sup>**. Then thread precursor **6-6<sup>3+</sup>** and an excess of **4-8** were dissolved in MeNO<sub>2</sub> and microwaved for 3h under the same conditions to give **6-7<sup>4+</sup>**.

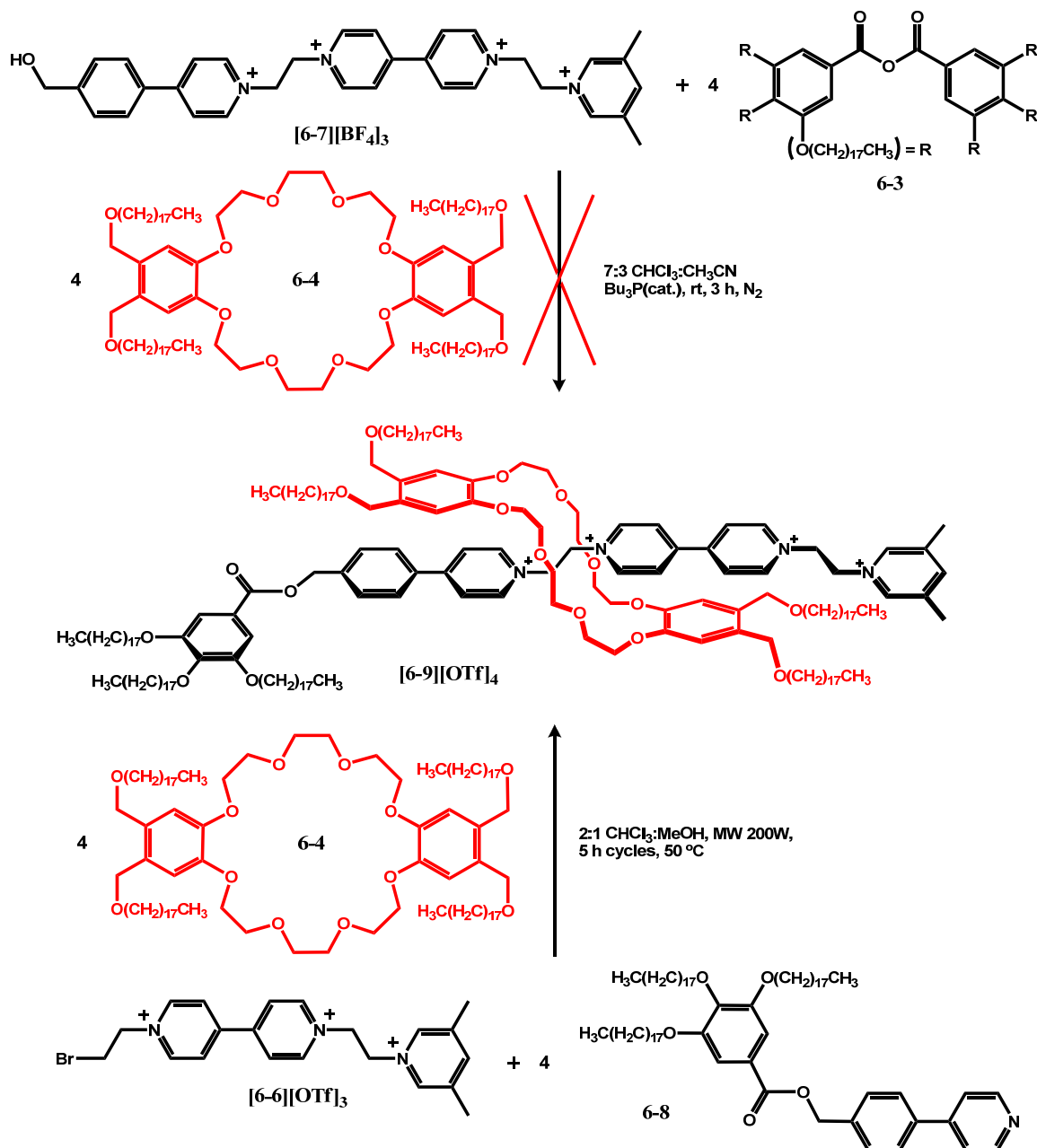


Scheme 6.3 - Synthetic route for thread **6-5<sup>2+</sup>** through **6-7<sup>4+</sup>**.

The first attempt at synthesizing the molecular shuttle was by ester formation of thread **6-7<sup>4+</sup>** with an excess of the anhydride stopper **6-3** and an excess of the tetra-substituted **DB24C8** macrocycle **6-4** with Bu<sub>3</sub>P as the catalyst. Surprisingly, once the



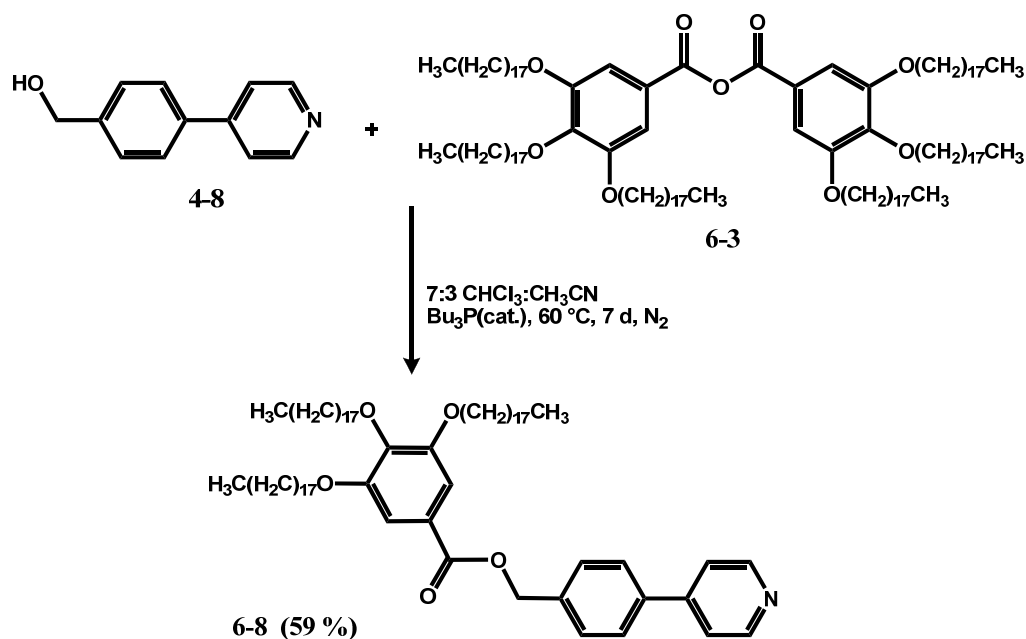
catalyst was added to the mixture of free components the reaction immediately turned yellow, then green and within minutes dark royal blue. This indicates radical formation of the paraquat<sup>146-149</sup> unit in the thread, which in turn cleaved every ethyl bridge, generating all of the single components of the shuttle thread; 4,4'-bipyridine, 3,5-lutidine and the



Scheme 6.4 - Synthetic routes for molecular shuttle  $6-9^{4+}$ .

4,4'-pyridinebenzyl alcohol. This radical formation was facilitated by the basicity of the  $\text{Bu}_3\text{P}$ , having a  $\text{pK}_a$  of 8.43. Hence, an alternate synthetic route *via* microwave synthesis was attempted.

Alternatively, the new stopper **6-8** was synthesized by ester formation under modified conditions discussed in Chapters 4 and 5, with  $\text{Bu}_3\text{P}$  as the catalyst (Scheme 6.5). Due to solubility differences in the starting materials the reaction time was long and required heating with the product formation coming to a halt just under 50 % conversion. With this as the stopper, the complementary thread to synthesize the molecular shuttle is now **6-6<sup>3+</sup>**.



Scheme 6.5 - Synthetic route for thread **6-8**.

To synthesize the molecular shuttle **6-9<sup>4+</sup>** by microwave synthesis one equivalent of thread **6-6<sup>3+</sup>** and five equivalents of the tetra-substituted **DB24C8** macrocycle **6-4** were dissolved in a hot  $\text{CHCl}_3/\text{MeOH}$  solution to ensure dissolution and pseudorotaxane

formation, followed by the addition of excess stopper 6-8 and microwaved continuously for 5 h cycles at 50 °C until all of **6-6**<sup>3+</sup> was alkylated (Scheme 6.4).

### 6.2.2 <sup>1</sup>H NMR Spectroscopy

The formation of anhydride stopper **6-3** was monitored by both <sup>1</sup>H NMR and <sup>13</sup>C NMR spectroscopy, since fourier transform infrared (FT-IR) spectroscopy did not allow for unambiguous distinction between the acid and anhydride. As mentioned in Chapter 4, due to symmetry, the <sup>1</sup>H NMR spectra of the acid and the anhydride are also identical though the <sup>1</sup>H NMR spectra does show the complete disappearance of the TsCl protons upon complete anhydride formation. <sup>13</sup>C NMR spectroscopy proved to be the best analytical tool for proving that only the anhydride was present. The anhydride synthesis was confirmed by a shift in the carbonyl carbon peak from ~172 ppm, for the benzoic acid, to ~163 ppm, for the benzyl anhydrides (Figure 6.6).

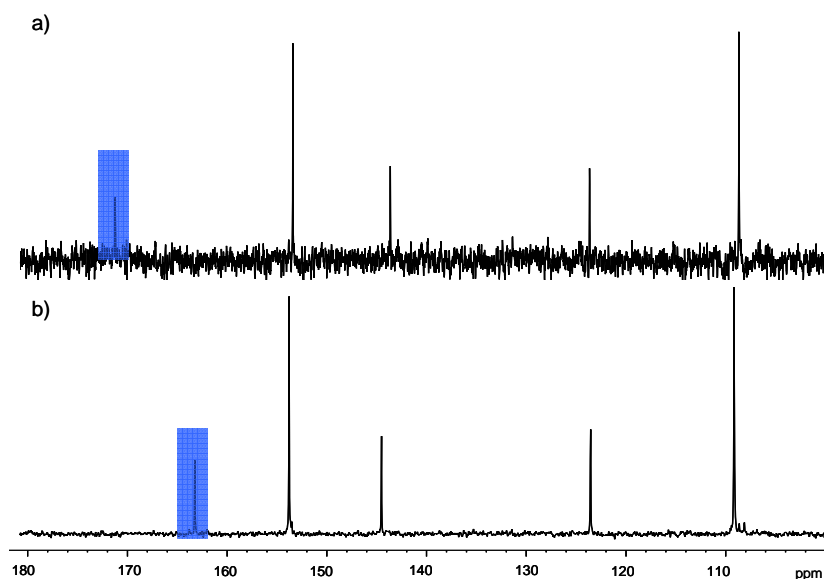


**Figure 6.6 - Stacked <sup>13</sup>C NMR spectra of a) 6-2 (acid) and b) 6-3 (anhydride) in the region between 100-180 ppm in CDCl<sub>3</sub>.**

The labeled  $^1\text{H}$  NMR spectrum of the tetra-substituted crown ether **6-4** is shown in Figure 6.7, with a singlet at 6.9 ppm due to the equivalent aromatic protons **f**, followed by the singlet at 4.5 ppm for the protons labeled **e** which are shielded by 0.3 ppm with the formation of the ether group from. The ethylene glycol protons **g**, **h**, and **i** are unaffected by the alkylation and appear in the range of 3.8 to 4.2 ppm. Also, the characteristic aliphatic protons **a**, **b** and **c** are unaffected and appear within the range of 0.8 to 1.6 ppm.

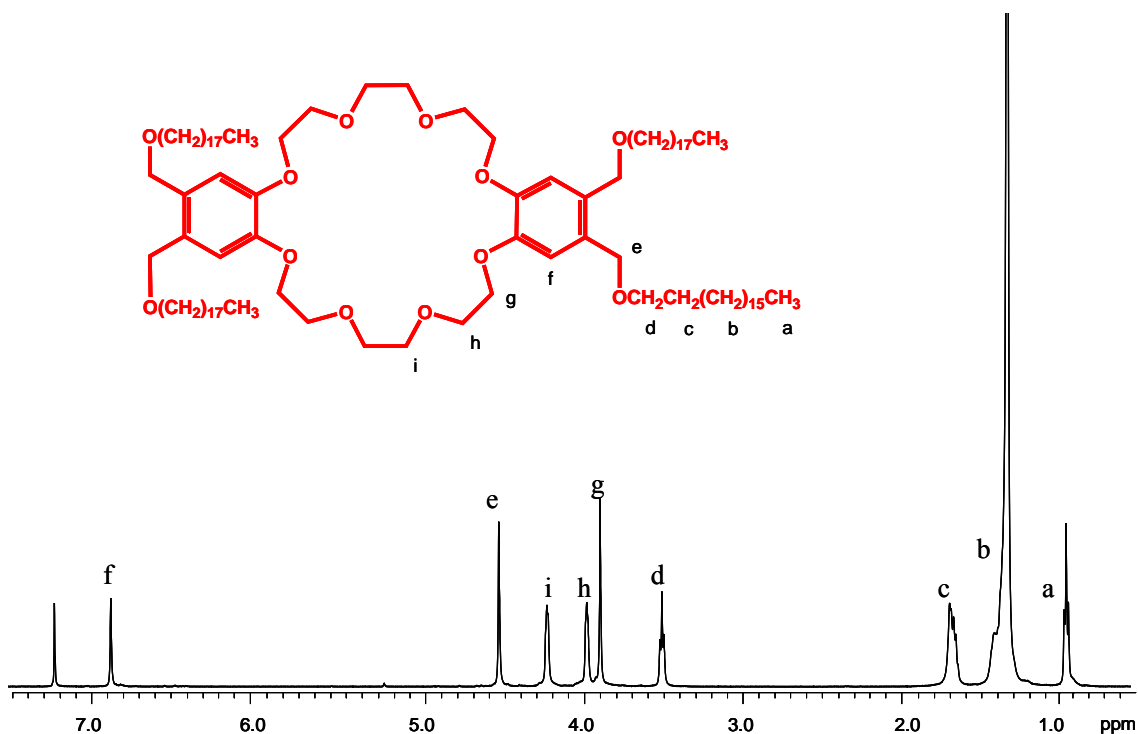


**Figure 6.7** -  $^1\text{H}$  NMR spectrum of crown **6-4** in  $\text{CDCl}_3$ .

The stacked  $^1\text{H}$  NMR spectra of the two shuttle threads **6-6<sup>3+</sup>** and **6-7<sup>4+</sup>** are shown in Figure 6.8. There were no differences observed for any of the pyridinium protons upon the formation of **6-7<sup>4+</sup>** from **6-6<sup>3+</sup>** other than the expected deshielding of protons **j** by 1.4 ppm due to the new pyridinium group. The molecular shuttle reaction progress was monitored by  $^1\text{H}$  NMR spectroscopy with full alkylation confirmed by the complete transference of protons **j** from 4.1 ppm in **6-6<sup>3+</sup>** to 5.3 ppm in **6-7<sup>4+</sup>**.

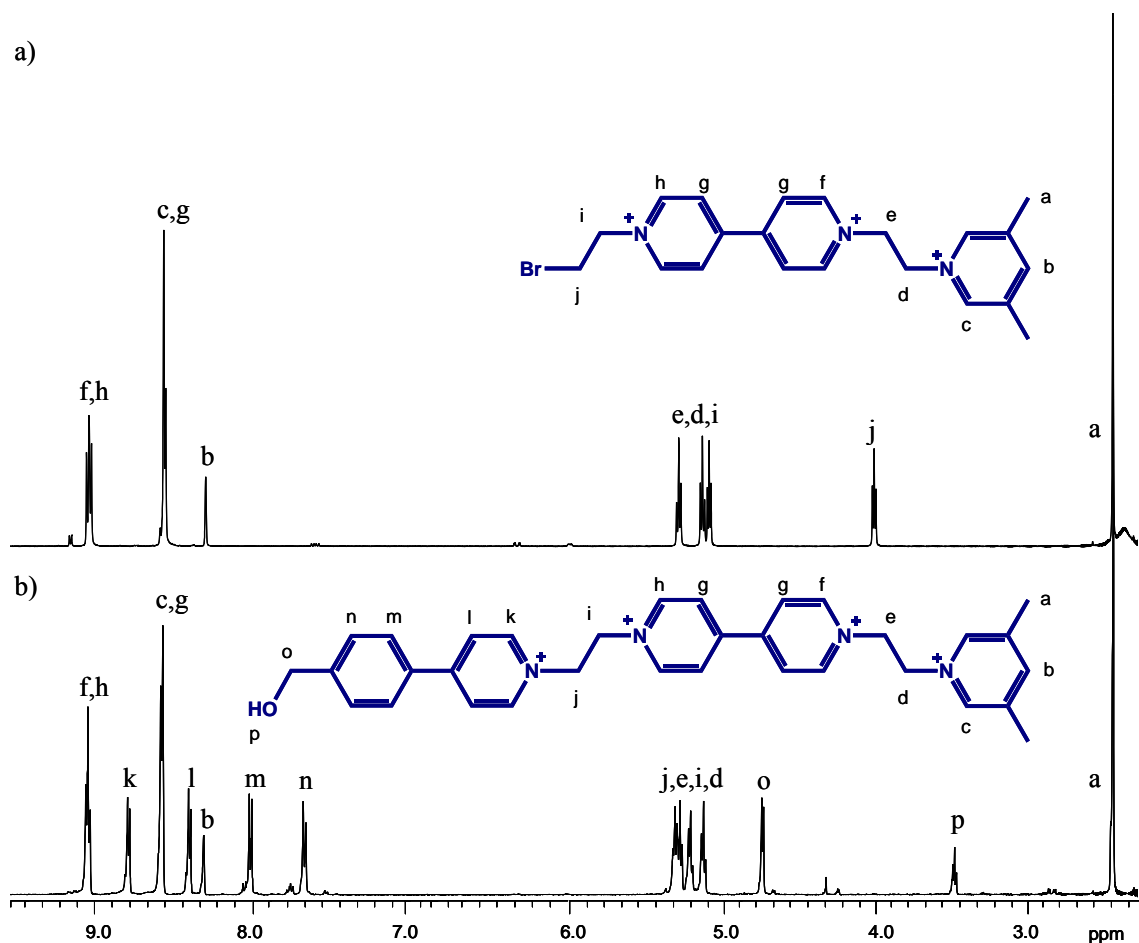


**Figure 6.8 - Stacked  $^1\text{H}$  NMR spectra of a) shuttle thread precursor [6-6][OTf]<sub>3</sub> and b) shuttle thread [6-7][OTf]<sub>4</sub> in  $\text{CD}_3\text{CN}$ .**

Due to the solubility differences amongst the thread, stopper and macrocycle, monitoring the reaction progress is complex. In polar solvents, such as  $\text{CD}_3\text{CN}$  the pseudorotaxane formation is broad and upon cooling the sample all but the thread become insoluble and it is difficult to predict the solubility of the complex. However, in organic solvents such as  $\text{CD}_2\text{Cl}_2$  all components except for the thread will dissolve and variable temperature experiments are employed. In  $\text{CD}_2\text{Cl}_2$ , another proton needs to be monitored for generation of the molecular shuttle. The proton spectrum for the alternate stopper **6-8** in  $\text{CD}_2\text{Cl}_2$  is shown in Figure 6.9. The proton **l** is monitored for product formation, which will be deshielded from 8.7 ppm to 9.1 - 9.3 ppm upon alkylation

and/or complexation with the macrocycle. Because this stopper is in excess the disappearance of protons **j** from **6-6<sup>3+</sup>** are also monitored in CD<sub>3</sub>CN at the same time.

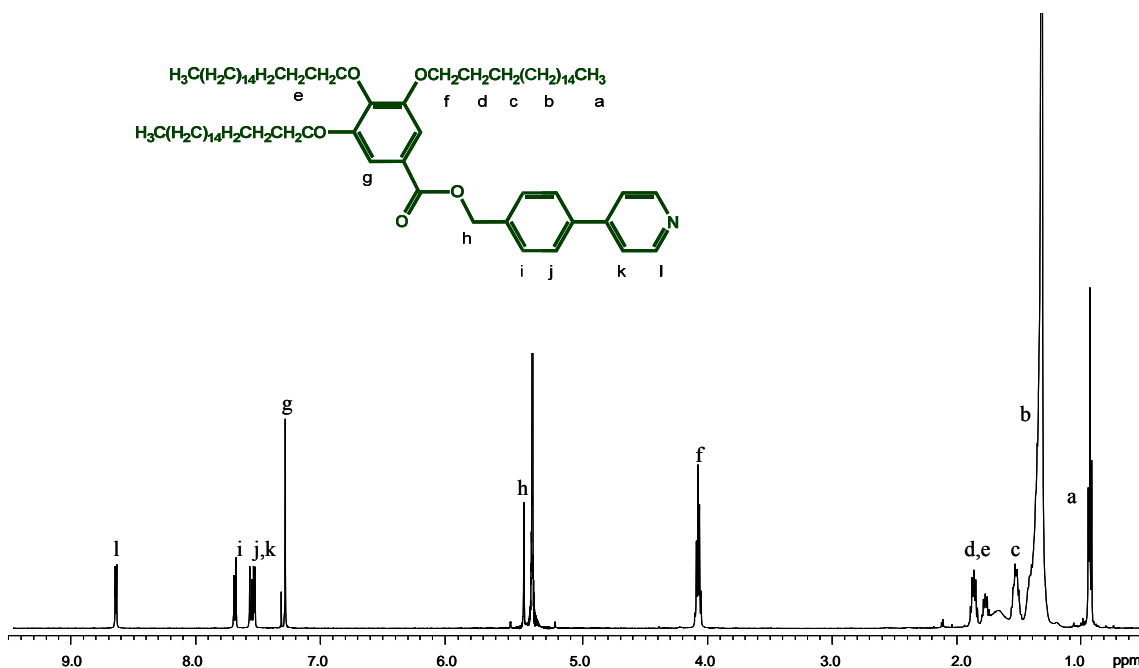


**Figure 6.9** - <sup>1</sup>H NMR spectrum of alternate shuttle thread **6-8** in CD<sub>2</sub>Cl<sub>2</sub>.

### 6.3 SUMMARY AND CONCLUSIONS

Two synthetic approaches for the generation of a single type of LC [2]rotaxane molecular shuttle have been described. This methodology makes use of simple modifications of pre-existing systems to change the properties of the material. However, many issues need to be addressed and studied.

For these complexes to be considered for functional materials there are still some fundamental questions that need to be answered. Will the macrocycle be easily shuttled in thin films? If the macrocycle does shuttle in a thin film, how thick can the film be without affecting the movement of the macrocycle between sites? How do we know if it is a combination of the liquid crystal and molecular machine that are contributing to any

visible macroscopic change? How can the motion be monitored and controlled in thin films? How can the number of counterions be reduced to further decrease viscosity, if required?

The answers to these and other important questions could lead to the future development of nanosegregated LC molecular machines that can be controlled to produce a macroscopic response within a mesophase.

## 6.4 EXPERIMENTAL

### 6.4.1 General Comments

Propyl gallate, potassium carbonate, formic acid, 1-bromooctadecane, 1-octadecanal, sodium hydride, p-toluenesulfonylchloride, 3,5-lutidine, sodium trifluoromethanesulfonate, sodium tetrafluoroborate, 1,2-dibromoethane and **DB24C8** were purchased from Aldrich and used as received. Deuterated solvents were obtained from Cambridge Isotope Laboratories and used as received. Solvents were dried using an Innovative Technologies Solvent Purification System. Thin layer chromatography (TLC) was performed using Teledyne Silica gel 60 F<sub>254</sub> plates and viewed under UV light. Column chromatography was performed using Silicycle Ultra Pure Silica Gel (230 – 400 mesh). Flash column chromatography was performed using Teledyne Ultra Pure Silica Gel (230 – 400 mesh) on a Teledyne Isco Combiflash R<sub>f</sub>. <sup>1</sup>H NMR, <sup>13</sup>C NMR and 2-D experiments were performed on a Brüker Avance 500 instrument, with working frequency of 500.13 MHz for <sup>1</sup>H nuclei, and 125.7 MHz for <sup>13</sup>C nuclei, respectively. Chemical shifts are quoted in ppm relative to tetramethylsilane, using the residual solvent peak as a reference standard. Conventional 2-D NMR experiments (<sup>1</sup>H-<sup>1</sup>H COSY) and (<sup>1</sup>H-<sup>13</sup>C HETCOR) were conducted and used to help assign all peaks. High resolution mass spectrometry (HR-MS) experiments were performed on a Micromass LCT Electrospray (ESI) time-of-flight (TOF) Mass Spectrometer. Solutions of 50-100 ng/μL were prepared in CH<sub>3</sub>CN and injected for analysis at a rate of 5 μL/min using a syringe pump.



### 6.4.2 Synthesis of 6-1

Potassium carbonate (35.16 g, 0.2544 mol) and propyl gallate (6.00 g, 0.02827 mol), were suspended in a mixture of acetone/DMF (90:10 mL) and stirred for 1h. The 1-bromooctadecane (32.99 g, 0.0990 mol) was then added and the mixture was refluxed overnight. The reaction mixture was then poured into 1.5 L of H<sub>2</sub>O and pH brought to 5-6 with the addition of 2.0 M formic acid. The product was extracted with CH<sub>2</sub>Cl<sub>2</sub> (200 mL) and the organic layer dried with MgSO<sub>4</sub> and the solvent evaporated. The resulting syrup was purified by flash column chromatography on basic alumina with CH<sub>2</sub>Cl<sub>2</sub> as the eluant. The resulting white waxy solid was collected. Yield: 27.27 g, 99 %.

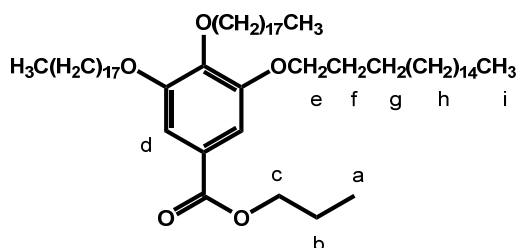


**Table 6.1 – <sup>1</sup>H NMR spectral data of 6-1 in CD<sub>2</sub>Cl<sub>2</sub>. MW= 969.635 g/mol**

Proton	δ (ppm)	Multiplicity	# Protons	J (Hz)
<b>a</b>	1.02	t	3	<sup>3</sup> J <sub>ab</sub> = 7.45
<b>b</b>	1.72	q	2	<sup>3</sup> J <sub>ba</sub> = 6.71
<b>c</b>	4.23	t	2	<sup>3</sup> J <sub>cb</sub> = 6.71
<b>d</b>	7.27	s	2	--
<b>e</b>	4.00	t	6	<sup>3</sup> J <sub>ef</sub> = 7.15
<b>f</b>	1.80	tt	6	<sup>3</sup> J <sub>fe</sub> = <sup>3</sup> J <sub>fg</sub> = 7.15
<b>g</b>	1.48	tt	6	<sup>3</sup> J <sub>gf</sub> = 7.15
<b>h</b>	1.35	m	84	--
<b>i</b>	0.89	t	9	<sup>3</sup> J <sub>ih</sub> = 6.91

## 6.4.3 Synthesis of 6-2

**6-1** (27.27 g, 0.0281 mol) was suspended in a solution 0.5 M KOH in EtOH:H<sub>2</sub>O (600: 10 mL) and refluxed for 1-2 h, or until reaction complete. The reaction mixture was then cooled to room temperature and acidified with 2.0 M formic acid to pH ~6. The product precipitated with the addition of 200-300 mL of H<sub>2</sub>O and was filtered off and dried *in vacuo* to give the product was a colourless solid. Yield: 23.27 g, 89 %.

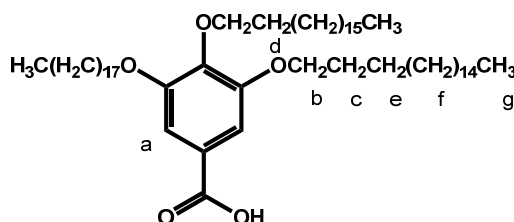


Table 6.2 – <sup>1</sup>H NMR spectral data of 6-2 in CD<sub>2</sub>Cl<sub>2</sub>. MW= 927.555 g/mol

Proton	δ (ppm)	Multiplicity	# Protons	J (Hz)
a	7.31	s	2	--
b	4.02	t	6	<sup>3</sup> J <sub>bc</sub> = 6.52
c	1.82	tt	4	<sup>3</sup> J <sub>cb</sub> = <sup>3</sup> J <sub>ce</sub> = 6.99
d	1.73	tt	2	<sup>3</sup> J <sub>db</sub> = <sup>3</sup> J <sub>de</sub> = 6.99
e	1.51	tt	6	<sup>3</sup> J <sub>ec</sub> = 6.99
f	1.29	m	84	--
g	0.89	t	9	<sup>3</sup> J <sub>gf</sub> = 6.90

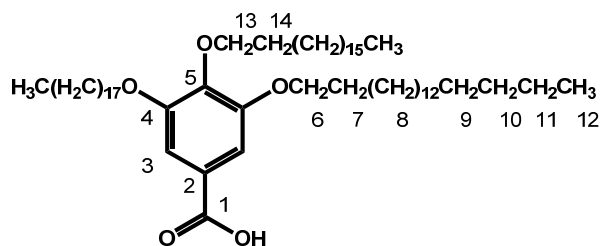
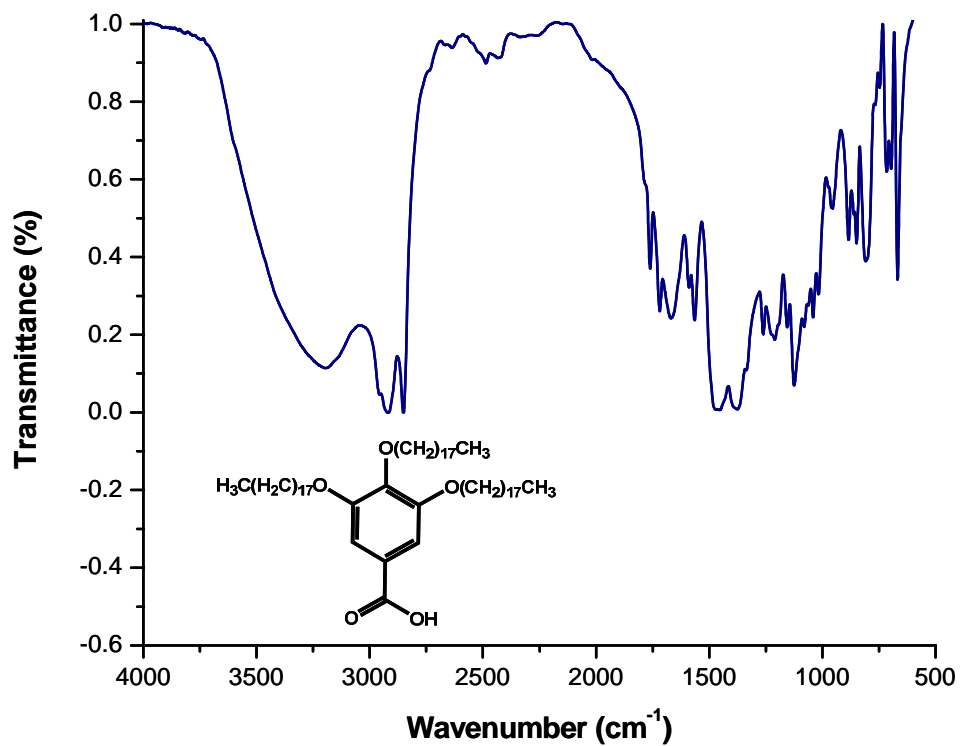


Table 6.3 –  $^{13}\text{C}$  NMR spectral data of 6-2 in  $\text{CD}_2\text{Cl}_2$ . MW= 927.555 g/mol.  
Quaternary carbons assigned by software

Carbon	$\delta$ (ppm)	# Carbons
1	171.67	1
2	123.52	1
3	108.70	2
4	152.94	2
5	143.27	1
6	69.30	2
7	29.37	2
8	29.78	36
9	26.15	3
10	31.99	3
11	22.75	3
12	14.16	3
13	73.62	1
14	30.41	1

## IR of 6-2



## 6.4.4 Synthesis of 6-3

**6-2** (8.00 g, 0.0082 mol), TsCl (838.4 mg, 4.3124 mmol), and  $K_2CO_3$  (6.83 g, 0.0493 mol) was refluxed in  $CHCl_3$  for 2-4 h. The crude mixture was filtered and concentrated to a white solid. The solid was taken up in  $CH_2Cl_2$  and washed with 1.0 M  $NaHCO_3$  (1 x 50 mL),  $H_2O$  (2 x 50 mL), dried over  $MgSO_4$ , and the solvent removed. The product was isolated as a white waxy solid. Yield: 8.00 g, 50 %.

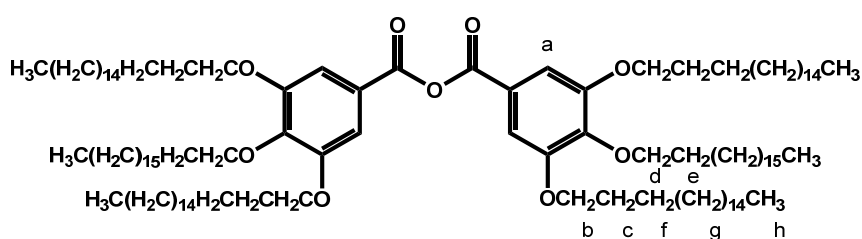


Table 6.4 –  $^1H$  NMR spectral data of 6-3 in  $CDCl_3$ . MW= 1837.094 g/mol

Proton	$\delta$ (ppm)	Multiplicity	# Protons	$J$ (Hz)
<b>a</b>	7.36	s	4	--
<b>b</b>	4.03	t	8	$^3J_{bc} = 6.47$
<b>c</b>	1.83	tt	8	$^3J_{cb} = ^3J_{cf} = 7.35$
<b>d</b>	4.09	t	4	$^3J_{de} = 6.47$
<b>e</b>	1.79	tt	4	$^3J_{ed} = ^3J_{eg} = 7.35$
<b>f</b>	1.49	tt	8	$^3J_{fc} = 7.35$
<b>g</b>	1.28	m	172	--
<b>h</b>	0.90	t	18	$^3J_{hg} = 6.87$

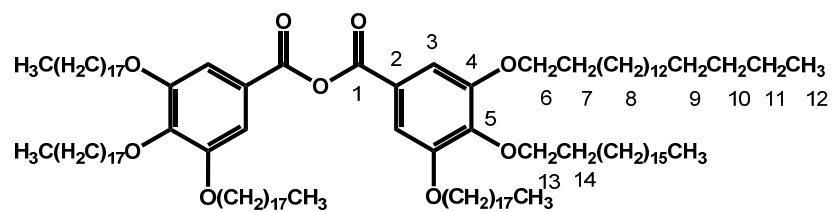
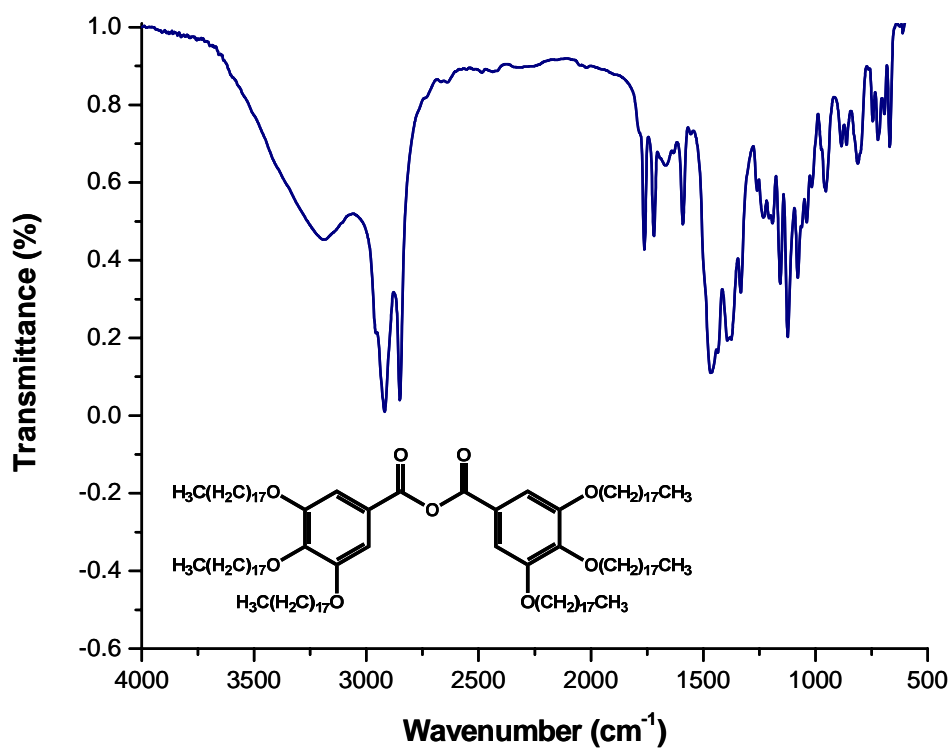


Table 6.5 –  $^{13}\text{C}$  NMR spectral data of 6-3 in  $\text{CD}_2\text{Cl}_2$ . MW= 1837.094 g/mol.  
Quaternary carbons assigned by software

Carbon	$\delta$ (ppm)	# Carbons
1	162.56	2
2	123.52	2
3	108.70	4
4	152.94	4
5	143.27	2
6	69.30	4
7	29.37	4
8	29.78	72
9	26.15	6
10	31.99	6
11	22.75	6
12	14.16	6
13	73.62	2
14	30.41	2

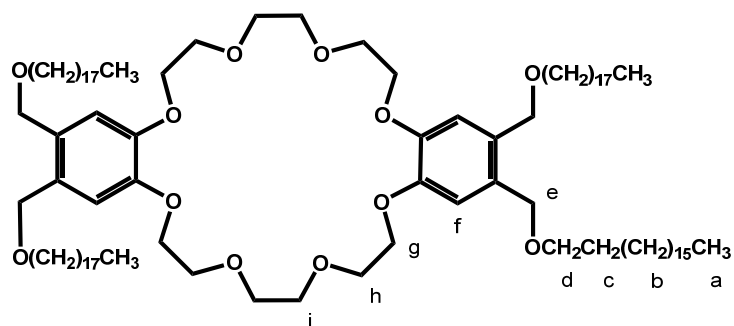
## IR of 6-3



#### 6.4.5 Synthesis of compound 6-4

NaH (2.40 g, 0.1000 mol) and 1-octadecanol (23.69 g, 0.0876 mol) were added to 300 mL of dry DMF in a 1 L shlienk flask under a nitrogen atmosphere which was stirred for 1 h at 50 °C. An additional 200 mL of dry DMF was added followed by slow addition of **5-2** (10.26 g, 0.0125 mol). The mixture was heated at 50 °C and stirring continued for 24 h. Reaction mixture was cooled to room temperature and the NaH was neutralized by slow addition of 2.0 M NH<sub>4</sub>Cl (aq) then basified with 1.0 M Na<sub>2</sub>CO<sub>3</sub>. The precipitate formed was filtered and washed with CHCl<sub>3</sub> (~200 mL). The aqueous layer was discarded and the organic layer was washed with H<sub>2</sub>O (2 x 150 mL), dried over MgSO<sub>4</sub> and concentrated to a crude dark brown waxy solid. The product was purified by flash column chromatography on RP-C<sub>18</sub> silica gel with MeOH as eluant, and product was forced off the column by hexane elution. The product was then further purified by flash column chromatography on silica gel with 99:1 (CHCl<sub>3</sub>: MeOH) isocratic elution to yield product was a dark brown waxy solid. The dark brown solid was dissolved in CHCl<sub>3</sub>, stirred in charcoal and then filtered through celite and solvent evaporated. The resulting white solid was collected. Yield: 4.54 g, 23 %.



Table 6.6 –  $^1\text{H}$  NMR spectral data of 6-4 in  $\text{CDCl}_3$ . MW= 1578.524 g/mol.

Proton	$\delta$ (ppm)	Multiplicity	# Protons	$J$ (Hz)
<b>a</b>	0.88	t	12	$^3J_{ab} = 6.61$
<b>b</b>	1.25	m	120	--
<b>c</b>	1.57	tt	8	$^3J_{cd} = 6.66$
<b>d</b>	3.43	t	8	$^3J_{dc} = 6.66$
<b>e</b>	4.46	s	8	--
<b>f</b>	6.90	s	8	--
<b>g</b>	4.15	t	8	$^3J_{gh} = 4.06$
<b>h</b>	3.90	t	8	$^3J_{hg} = 4.06$
<b>i</b>	3.82	s	8	--

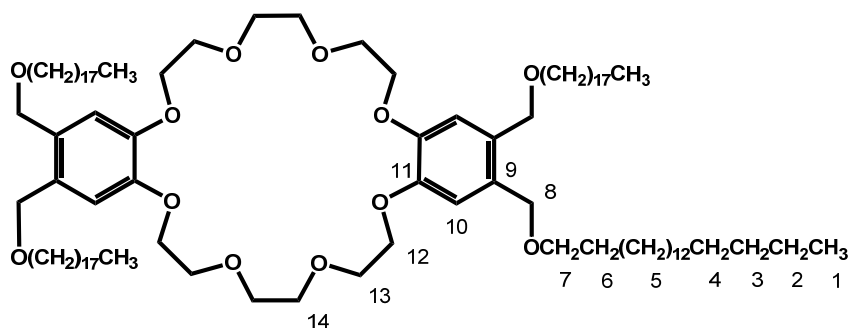
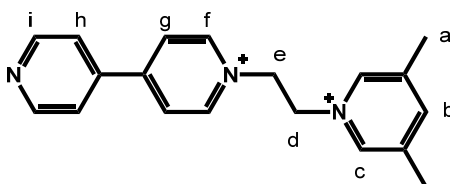


**Table 6.7 –  $^{13}\text{C}$  NMR spectral data of 6-4 in  $\text{CDCl}_3$ . MW= 1578.524 g/mol. Quaternary carbons assigned by software**

Carbon	$\delta$ (ppm)	# Carbons
1	14.14	4
2	22.72	4
3	31.96	4
4	26.36	4
5	29.76	48
6	29.39	4
7	69.83	4
8	71.27	4
9	129.96	4
10	115.09	4
11	148.13	4
12	69.64	4
13	70.02	4
14	70.55	4

6.4.6 Synthesis of [6-5][BF<sub>4</sub>]<sub>2</sub>

[2-1][Br] (6.00 g, 0.0174 mol) and 3,5-lutidine (9.92 mL, 0.0892 mol) were dissolved in MeNO<sub>2</sub> (70mL) in a thick-walled 80 mL vessel and microwaved for 5 h at 80 °C. The reaction mixture was cooled in the fridge and resulting precipitate was filtered and stirred in CHCl<sub>3</sub> (7.77 g, 96 %). The beige precipitate was filtered off and was then anion exchanged to the tetrafluoroborate salt by two layer NaOTf(aq)/MeNO<sub>2</sub>. The MeNO<sub>2</sub> was washed with H<sub>2</sub>O (2 x 10 mL) and concentrated to yield a beige powder. Yield: 6.73 g, 84 % **ESI-MS**: *m/z* 440.1250 (calc.) for C<sub>20</sub>H<sub>21</sub>F<sub>3</sub>N<sub>3</sub>O<sub>3</sub>S [M-OTF]<sup>+</sup>, found 440.1247, *m/z* 145.5962 (calc.) for C<sub>19</sub>H<sub>21</sub>N<sub>3</sub> [M]<sup>2+</sup>, found 145.5959.

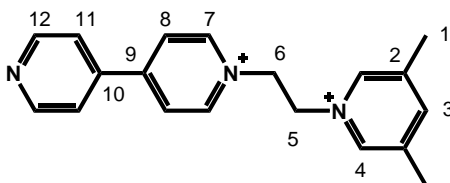


**Table 6.8** - <sup>1</sup>H NMR spectral data of [6-5][Br]<sub>2</sub> in D<sub>2</sub>O. MW<sub>Br-</sub> = 451.198 g/mol

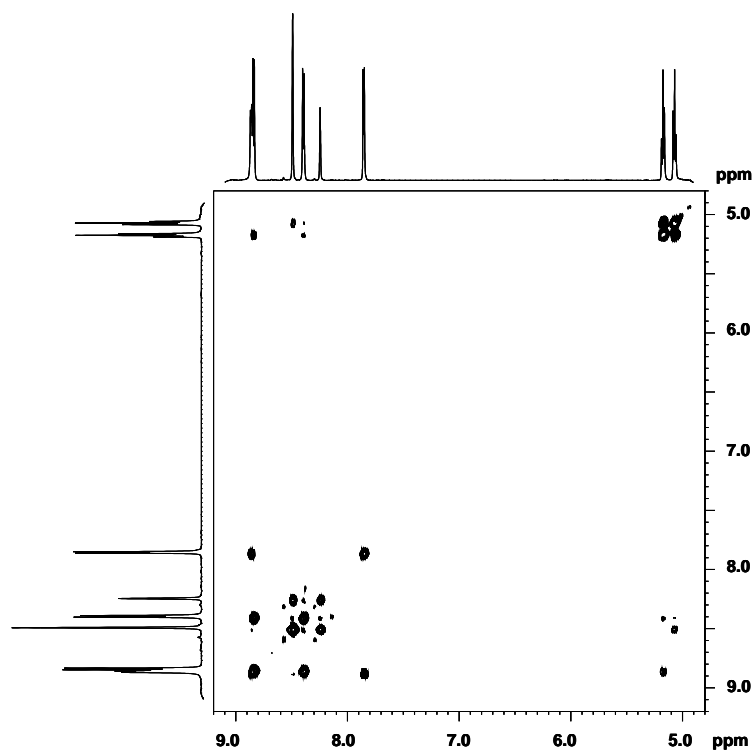
Proton	δ (ppm)	Multiplicity	# Protons	<i>J</i> (Hz)
<b>a</b>	2.33	s	6	--
<b>b</b>	8.19	s	1	--
<b>c</b>	8.38	s	2	--
<b>d</b>	5.12	t	2	<sup>3</sup> <i>J</i> <sub>de</sub> = 6.08
<b>e</b>	5.21	t	2	<sup>3</sup> <i>J</i> <sub>ed</sub> = 6.08
<b>f</b>	8.77	d	2	<sup>3</sup> <i>J</i> <sub>fg</sub> = 6.79
<b>g</b>	8.34	d	2	<sup>3</sup> <i>J</i> <sub>gf</sub> = 6.79
<b>h</b>	7.78	d	2	<sup>3</sup> <i>J</i> <sub>hi</sub> = 6.23
<b>i</b>	8.65	d	2	<sup>3</sup> <i>J</i> <sub>ih</sub> = 6.23

Table 6.9 -  $^1\text{H}$  NMR spectral data of [6-5][BF<sub>4</sub>]<sub>2</sub> in CD<sub>3</sub>CN. MW<sub>BF<sub>4</sub><sup>-</sup></sub> = 464.999 g/mol

Proton	$\delta$ (ppm)	Multiplicity	# Protons	$J$ (Hz)
<b>a</b>	2.03	s	6	--
<b>b</b>	9.04	s	1	--
<b>c</b>	9.23	s	2	--
<b>d</b>	5.13	t	2	$^3J_{de} = 7.91$
<b>e</b>	5.25	t	2	$^3J_{ed} = 7.91$
<b>f</b>	9.80	d	2	$^3J_{fg} = 7.05$
<b>g</b>	9.20	d	2	$^3J_{gf} = 7.05$
<b>h</b>	8.54	d	2	$^3J_{hi} = 6.88$
<b>i</b>	9.63	d	2	$^3J_{ih} = 6.88$

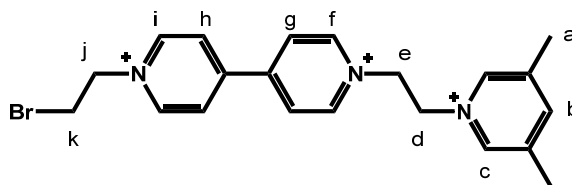
Table 6.10 –  $^{13}\text{C}$  NMR spectral data of [6-5][BF<sub>4</sub>]<sub>2</sub> in CD<sub>3</sub>CN. MW<sub>BF<sub>4</sub><sup>-</sup></sub> = 464.999 g/mol. Quaternary carbons assigned using software

Carbon	$\delta$ (ppm)	# Carbons
<b>1</b>	17.43	2
<b>2</b>	148.29	2
<b>3</b>	140.03	1
<b>4</b>	142.01	2
<b>5</b>	60.21	1
<b>6</b>	59.62	1
<b>7</b>	146.29	2
<b>8</b>	128.09	2
<b>9</b>	152.23	1
<b>10</b>	148.72	1
<b>11</b>	125.40	2
<b>12</b>	149.18	2

COSY of [6-5][BF<sub>4</sub>]<sub>2</sub> in CD<sub>3</sub>CN.

#### 6.4.7 Synthesis of [6-6][BF<sub>4</sub>]<sub>3</sub>

[6-5][BF<sub>4</sub>]<sub>2</sub> (1.621 g, 0.0035 mol) and 1,2-dibromoethane (4.48 mL, 0.052 mol) were dissolved in butanol (50mL) in a thick-walled 80 mL vessel and microwaved for 3 h at 80 °C. The reaction mixture was cooled in the fridge and resulting precipitate was filtered and washed with cold MeNO<sub>2</sub>. The purple brown solid was dissolved in H<sub>2</sub>O, stirred in charcoal and then filtered through celite and solvent evaporated. The white solid was then anion exchanged to the tetrafluoroborate salt by two layer NaOTf(aq)/MeNO<sub>2</sub>, for synthesis of [6-7][OTf]<sub>4</sub> (2.01 g, 88 %), and anion exchanged to the triflate salt in the same way, for the synthesis of the shuttle [6-9][OTf]<sub>4</sub>. The MeNO<sub>2</sub> layers were washed with H<sub>2</sub>O (4 x 10 mL) and concentrated to yield white powder. Yield: 1.70 g, 82 %, [BF<sub>4</sub>] and 1.65 g, 76 %, [OTf]. **ESI-MS:**  $m/z$  696.0267 (calc.) for C<sub>23</sub>H<sub>25</sub>BrF<sub>6</sub>N<sub>3</sub>O<sub>6</sub>S<sub>2</sub> [M-2OTF]<sup>+</sup>, found 696.0264,  $m/z$  273.5371 (calc.) for C<sub>22</sub>H<sub>25</sub>BrF<sub>3</sub>N<sub>3</sub>O<sub>3</sub>S [M-OTF]<sup>2+</sup>, found 273.0740.

Table 6.11 -  $^1\text{H}$  NMR spectral data of [6-6][Br] $_3$  in  $\text{D}_2\text{O}$ .  $\text{MW}_{\text{Br}^-} = 639.059$  g/mol

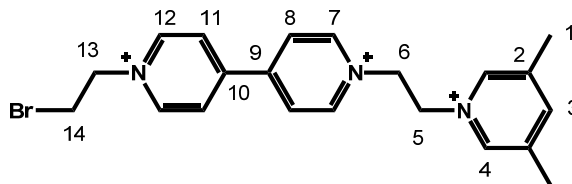
Proton	$\delta$ (ppm)	Multiplicity	# Protons	$J$ (Hz)
<b>a</b>	2.33	s	6	--
<b>b</b>	8.18	s	1	--
<b>c</b>	8.40	s	2	--
<b>d</b>	5.12	t	2	$^3J_{\text{de}} = 6.12$
<b>e</b>	5.26	t	2	$^3J_{\text{ed}} = 6.12$
<b>f</b>	9.05	d	2	$^3J_{\text{fg}} = 6.29$
<b>g</b>	8.48	d	2	$^3J_{\text{gf}} = 6.29$
<b>h</b>	8.45	d	2	$^3J_{\text{hi}} = 6.38$
<b>i</b>	8.95	d	2	$^3J_{\text{ih}} = 6.38$
<b>j</b>	5.03	t	2	$^3J_{\text{jk}} = 5.40$
<b>k</b>	3.91	t	2	$^3J_{\text{kj}} = 5.40$

Table 6.12 -  $^1\text{H}$  NMR spectral data of [6-6][BF $_4$ ] $_3$  in  $\text{CD}_3\text{CN}$ .  $\text{MW}_{\text{BF}_4^-} = 659.791$  g/mol

Proton	$\delta$ (ppm)	Multiplicity	# Protons	$J$ (Hz)
<b>a</b>	2.48	s	6	--
<b>b</b>	8.27	s	1	--
<b>c</b>	8.47	s	2	--
<b>d</b>	5.08	t	2	$^3J_{\text{de}} = 6.32$
<b>e</b>	5.24	t	2	$^3J_{\text{ed}} = 6.32$
<b>f</b>	9.01	d	2	$^3J_{\text{fg}} = 6.26$
<b>g,h</b>	8.51	d	4	$^3J_{\text{gf}} = ^3J_{\text{hi}} = 6.26$
<b>i</b>	8.92	d	2	$^3J_{\text{ih}} = 6.26$
<b>j</b>	5.06	t	2	$^3J_{\text{jk}} = 5.70$
<b>k</b>	4.00	t	2	$^3J_{\text{kj}} = 5.70$

Table 6.13 -  $^1\text{H}$  NMR spectral data of [6-6][OTf]<sub>3</sub> in CD<sub>3</sub>CN MW<sub>OTf-</sub> = 846.555 g/mol

Proton	$\delta$ (ppm)	Multiplicity	# Protons	$J$ (Hz)
<b>a</b>	2.51	s	6	--
<b>b</b>	8.28	s	1	--
<b>c</b>	8.57	s	2	--
<b>d</b>	5.12	t	2	$^3J_{de} = 6.58$
<b>e</b>	5.27	t	2	$^3J_{ed} = 6.58$
<b>f</b>	9.03	d	2	$^3J_{fg} = 6.96$
<b>g,h</b>	8.51	d	4	$^3J_{gf} = ^3J_{hi} = 6.96$
<b>i</b>	9.00	d	2	$^3J_{ih} = 6.96$
<b>j</b>	5.07	t	2	$^3J_{jk} = 5.85$
<b>k</b>	4.02	t	2	$^3J_{kj} = 5.85$

Table 6.14 –  $^{13}\text{C}$  NMR spectral data of [6-6][BF<sub>4</sub>]<sub>3</sub> in CD<sub>3</sub>CN. MW<sub>BF<sub>4</sub>-</sub> = 659.761 g/mol. Quaternary carbons assigned using software

Carbon	$\delta$ (ppm)	# Carbons
<b>1</b>	17.49	2
<b>2</b>	148.32	2
<b>3</b>	140.05	1
<b>4</b>	141.99	2
<b>5</b>	60.17	1
<b>6</b>	59.59	1
<b>7</b>	146.27	2
<b>8</b>	128.14	2
<b>9</b>	151.20	1
<b>10</b>	150.73	1
<b>11</b>	127.42	2
<b>12</b>	146.16	2
<b>13</b>	62.37	1
<b>14</b>	30.32	1



6.4.8 Synthesis of [6-7][OTf]<sub>4</sub>

[6-6][BF<sub>4</sub>]<sub>3</sub> (226.1 mg, 0.3427 mmol) and 4-8 (317.4 mg, 1.7314 mmol) were dissolved in hot MeNO<sub>2</sub> (40mL) in a thick-walled 80 mL vessel and microwaved for 3 h at 80 °C. The mixture was cooled to room temperature and resulting precipitate was filtered and washed with cold MeNO<sub>2</sub>. The dark brown solid was dissolved in H<sub>2</sub>O, stirred in charcoal and then filtered through celite and solvent evaporated (279.2 mg, 74 %). The white solid was then anion exchanged to the triflate salt by two layer NaOTf(aq)/MeNO<sub>2</sub>. The MeNO<sub>2</sub> was washed with H<sub>2</sub>O (4 x 10 mL) and concentrated to yield white powder. Yield: 331.9 mg, 87 % **ESI-MS**: *m/z* 951.1444 (calc.) for C<sub>36</sub>H<sub>36</sub>F<sub>9</sub>N<sub>4</sub>O<sub>10</sub>S<sub>3</sub> [M-3OTF]<sup>+</sup>, found 951.1443, *m/z* 401.0959 (calc.) for C<sub>35</sub>H<sub>36</sub>F<sub>6</sub>N<sub>4</sub>O<sub>7</sub>S<sub>2</sub> [M-2OTF]<sup>2+</sup>, found 401.0962.

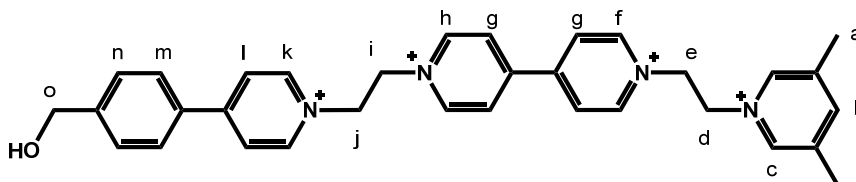


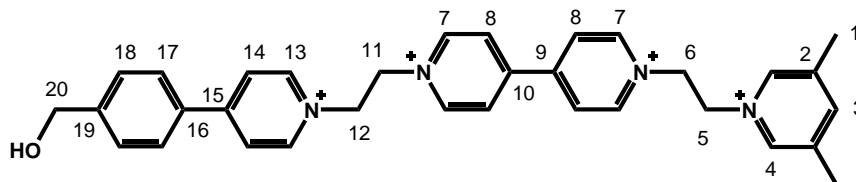
**Table 6.15** - <sup>1</sup>H NMR spectral data of [6-7][Br]<sub>4</sub> in D<sub>2</sub>O. MW<sub>Br-</sub> = 824.281 g/mol

Proton	δ (ppm)	Multiplicity	# Protons	J (Hz)
<b>a</b>	2.38	s	6	--
<b>b</b>	8.23	s	1	--
<b>c</b>	8.46	s	2	--
<b>d</b>	5.17	t	2	<sup>3</sup> J <sub>de</sub> = 6.73
<b>e</b>	5.31	t	2	<sup>3</sup> J <sub>ed</sub> = 6.73
<b>f</b>	9.09	d	2	<sup>3</sup> J <sub>fg</sub> = 6.92
<b>g</b>	8.54	d	4	<sup>3</sup> J <sub>gf</sub> = <sup>3</sup> J <sub>gh</sub> = 6.92
<b>h</b>	9.02	d	2	<sup>3</sup> J <sub>hg</sub> = 6.92
<b>i</b>	5.26	t	2	<sup>3</sup> J <sub>ij</sub> = 6.25
<b>j</b>	5.38	t	2	<sup>3</sup> J <sub>ji</sub> = 6.25

<b>k</b>	8.74	d	2	${}^3J_{kl} = 6.97$
<b>l</b>	8.30	d	2	${}^3J_{lk} = 6.97$
<b>m</b>	7.52	d	2	${}^3J_{mn} = 8.34$
<b>n</b>	7.88	d	2	${}^3J_{nm} = 8.34$
<b>o</b>	4.65	s	2	--

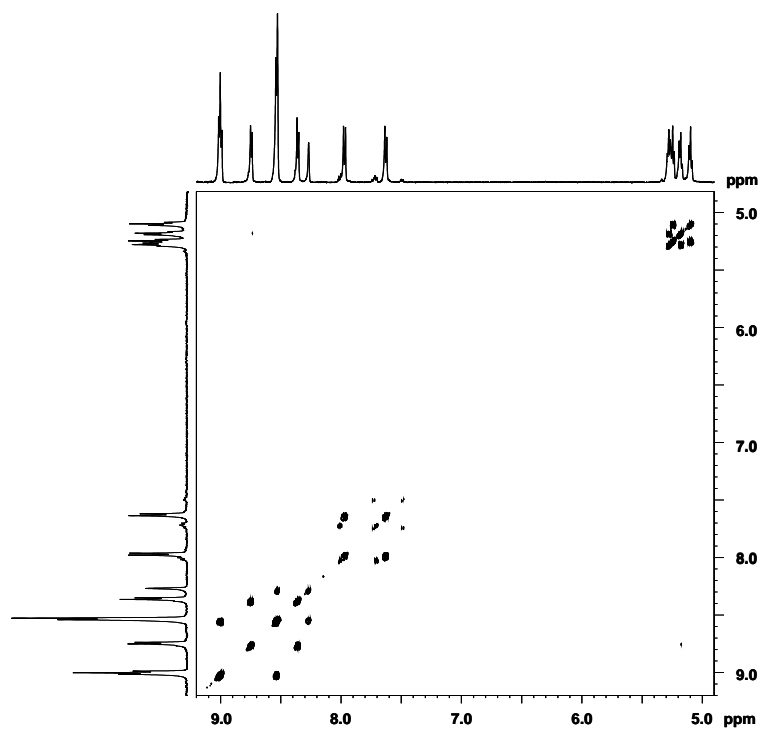
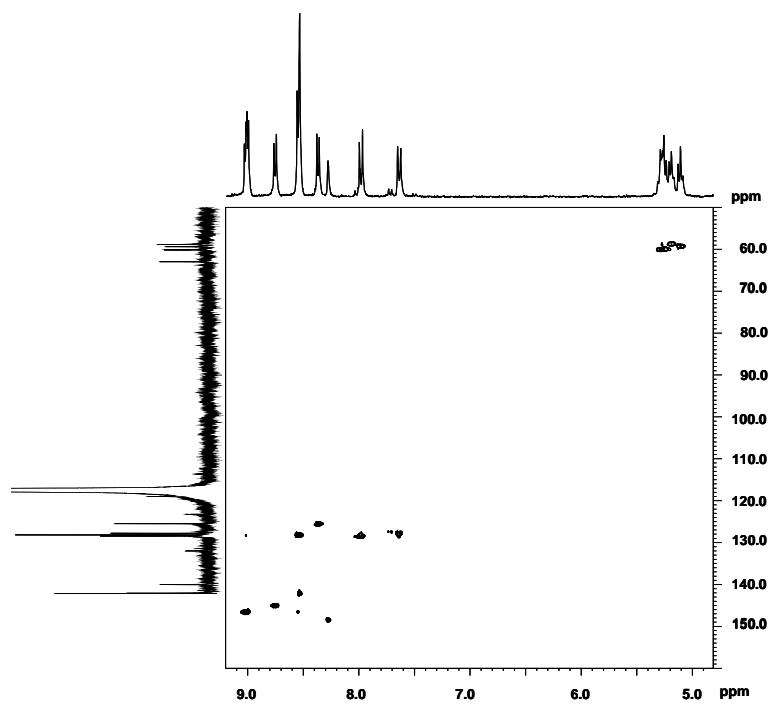
**Table 6.16 -  ${}^1\text{H}$  NMR spectral data of [6-7][OTf]<sub>4</sub> in CD<sub>3</sub>CN. MW<sub>OTf</sub> = 1100.9416 g/mol**

<b>Proton</b>	<b><math>\delta</math> (ppm)</b>	<b>Multiplicity</b>	<b># Protons</b>	<b><math>J</math> (Hz)</b>
<b>a</b>	2.51	s	6	--
<b>b</b>	8.27	s	1	--
<b>c</b>	8.53	s	2	--
<b>d</b>	5.10	t	2	${}^3J_{de} = 6.56$
<b>e</b>	5.28	t	2	${}^3J_{ed} = 6.56$
<b>f</b>	9.01	d	2	${}^3J_{fg} = 6.97$
<b>g</b>	8.53	d	4	${}^3J_{gf} = {}^3J_{gh} = 6.97$
<b>h</b>	8.99	d	2	${}^3J_{hg} = 6.97$
<b>i</b>	5.18	t	2	${}^3J_{ij} = 6.54$
<b>j</b>	5.32	t	2	${}^3J_{ji} = 6.54$
<b>k</b>	8.75	d	2	${}^3J_{kl} = 6.93$
<b>l</b>	8.36	d	2	${}^3J_{lk} = 6.93$
<b>m</b>	7.63	d	2	${}^3J_{mn} = 8.23$
<b>n</b>	7.97	d	2	${}^3J_{nm} = 8.23$
<b>o</b>	4.71	d	2	${}^3J_{op} = 5.74$
<b>p</b>	3.50	t	1	${}^3J_{po} = 5.74$



**Table 6.17 –  $^{13}\text{C}$  NMR spectral data of [6-7][OTf]<sub>4</sub> in CD<sub>3</sub>CN. MW<sub>OTf</sub> = 1100.9416 g/mol. Quaternary carbons assigned using software**

Carbon	$\delta$ (ppm)	# Carbons
1	17.49	2
2	131.99	2
3	148.37	1
4	142.06	2
5	58.83	1
6	60.06	1
7	146.49	4
8	128.16	4
9	151.11	1
10	151.07	1
11	59.38	1
12	60.17	1
13	144.99	2
14	125.51	2
15	157.67	1
16	140.01	1
17	127.75	2
18	128.42	2
19	147.88	1
20	62.99	1

COSY of [6-7][OTf]<sub>4</sub> in CD<sub>3</sub>CN.HETCOR of [6-7][OTf]<sub>4</sub> in CD<sub>3</sub>CN.

## 6.4.9 Synthesis of 6-8

**4-8** (253.00 mg, 1.3660 mmol) and **6-3** (2.509 g, 1.3660 mmol) were dissolved in dry 7:3 (CHCl<sub>3</sub>: MeCN) (120 mL) under nitrogen atmosphere. A catalytic amount of tributylphosphine (80 μL) was added via glass syringe and stirring continued at 60 °C for seven days. The solvent was removed under reduced pressure and the product was stirred in cold CHCl<sub>3</sub> and resulting precipitate filtered off. The crude CHCl<sub>3</sub> mixture was adsorbed onto silica and product was purified by flash column chromatography with normal phase silica gel with CHCl<sub>3</sub> as eluant for 10 column volumes, followed by 99:1 (CHCl<sub>3</sub>:MeOH) isocratic elution. The colourless waxy solid was collected. Yield: 871.3 mg, 59 %.

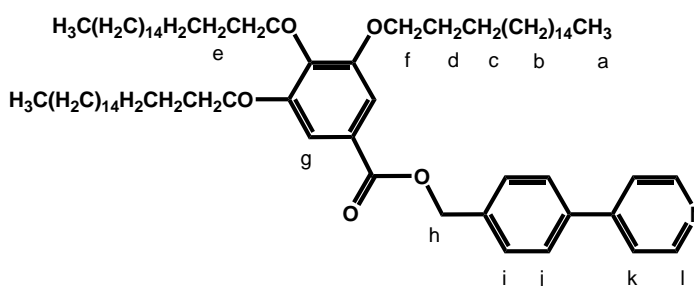


**Table 6.18** - <sup>1</sup>H NMR spectral data of **6-8** in CD<sub>2</sub>Cl<sub>2</sub>. MW = 1094.761 g/mol

Proton	δ (ppm)	Multiplicity	# Protons	J (Hz)
<b>a</b>	0.90	t	9	<sup>3</sup> J <sub>ab</sub> = 6.88
<b>b</b>	1.28	m	42	--
<b>c</b>	1.49	tt	6	<sup>3</sup> J <sub>cb</sub> = <sup>3</sup> J <sub>cd</sub> = 7.23
<b>d</b>	1.83	tt	4	<sup>3</sup> J <sub>dc</sub> = <sup>3</sup> J <sub>df</sub> = 7.23
<b>e</b>	1.75	tt	2	<sup>3</sup> J <sub>ec</sub> = <sup>3</sup> J <sub>ef</sub> = 7.73
<b>f</b>	4.03	t	6	<sup>3</sup> J <sub>fd</sub> = <sup>3</sup> J <sub>fe</sub> = 6.12
<b>g</b>	7.32	s	2	--
<b>h</b>	5.41	s	2	--
<b>i</b>	7.71	d	4	<sup>3</sup> J <sub>ij</sub> = 8.21
<b>j</b>	7.59	d	4	<sup>3</sup> J <sub>ji</sub> = 8.21
<b>k</b>	7.56	d	4	<sup>3</sup> J <sub>kl</sub> = 6.15
<b>l</b>	8.66	d	2	<sup>3</sup> J <sub>lk</sub> = 6.15

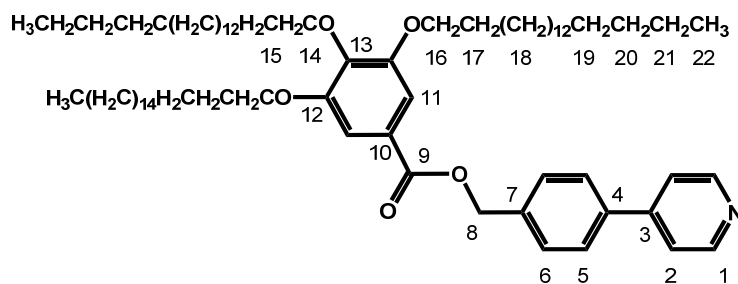
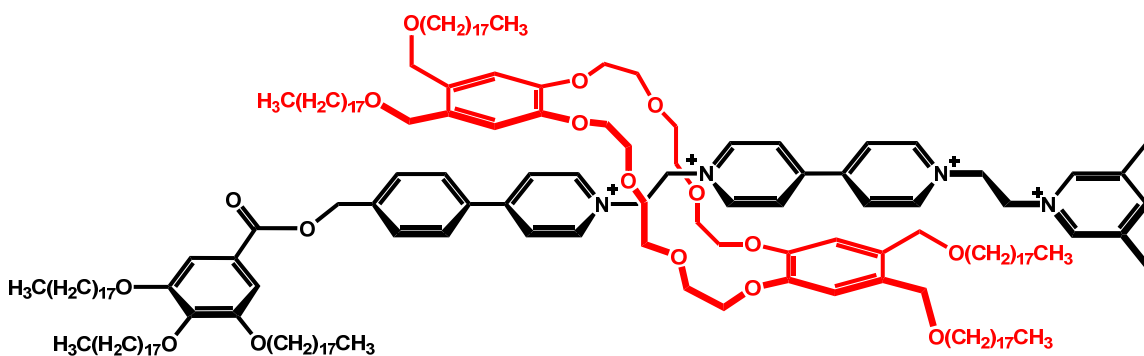


**Table 6.19 –  $^{13}\text{C}$  NMR spectral data of 6-8 in  $\text{CD}_2\text{Cl}_2$ . MW= 1094.761 g/mol. Quaternary carbons assigned by software**

Carbon	$\delta$ (ppm)	# Carbons
1	146.11	2
2	125.45	2
3	157.49	1
4	141.03	1
5	129.59	2
6	128.45	2
7	133.26	1
8	66.11	1
9	164.79	1
10	130.66	1
11	109.31	2
12	153.78	2
13	144.45	1
14	74.11	1
15	30.39	1
16	69.33	2
17	29.37	2
18	29.78	36
19	26.14	3
20	32.03	3
21	22.81	3
22	14.12	3

#### 6.4.10 Synthesis of [6-9][OTf]<sub>4</sub>

**6-6** (84.70 mg, 0.1284 mmol) and **6-4** (810.53 mg, 0.5135 mmol) were dissolved in a hot 1:1 CHCl<sub>3</sub>: MeOH solution (20 mL) in a thick-walled 80 mL reaction vessel, to form the pseudorotaxane. Then **6-8** (562.13 mg, 0.5135 mmol) in 10 mL of hot CHCl<sub>3</sub> was added to the vessel with a stir bar and microwaved continuously for 5 h cycles at 50 °C until all of **6-6** was alkylated. Presently, the alkylation has not yet gone to completion.



---

**REFERENCES**

1. J.-M. Lehn, *Supramolecular Chemistry: Concepts and Perspectives*, VCH, Weinheim, 1995.
2. J. W. Steed, J. L. Atwood, *Supramolecular Chemistry*, John Wiley & Sons, 2000.
3. P. Beer, P. Gale, D. Smith, *Supramolecular Chemistry*, Oxford Chemistry Primers, England, 1998.
4. C. J. Pedersen, The Discovery of Crown Ethers, *Angewandte Chemie*, **1988**, 100, (8), 1053-1059.
5. D. J. Cram, Molecular Hosts and Guests, and their Complexes, *Angewandte Chemie*, **1988**, 100, (8), 1041-1052.
6. J.-M. Lehn, *Supramolecular Chemistry - Molecules, Supermolecules, and Molecular Functional Units*, *Angewandte Chemie*, **1988**, 100, (1), 91-116.
7. J.-M. Lehn, Chemistry - From the Lock and Key to Molecular Recognition and Instructed Chemistry, *Pharmaceutica Acta Helveticae*, **1995**, 69, (4), 205-11.
8. M. C. F. Fyfe, J. F. Stoddart, Synthetic Supramolecular Chemistry, *Accounts of Chemical Research*, **1997**, 30, (10), 393-401.
9. M. Albrecht, Dicatechol Ligands: Novel Building-Blocks for Metallo-Supramolecular Chemistry, *Chemical Society Reviews*, **1998**, 27, (4), 281-288.
10. J.-M. Lehn, Programmed Chemical Systems: Multiple Subprograms and Multiple Processing/Expression of Molecular Information, *Chemistry, A European Journal*, **2000**, 6, (12), 2097-2102.
11. J.-M. Lehn, Toward Complex Matter: Supramolecular Chemistry and Self-Organization, *Proceedings of the National Academy of Sciences of the United States of America*, **2002**, 99, (8), 4763-4768.
12. F. M. Menger, Supramolecular Chemistry and Self-Assembly, *Proceedings of the National Academy of Sciences of the United States of America*, **2002**, 99(8), 4818-22.
13. M. C. Jimenez, C. Dietrich-Buchecker, J.-P. Sauvage, Towards Synthetic Molecular Muscles : Contraction and Stretching of a Linear Rotaxane Dimer. *Angewandte Chemie, International Edition*, **2000**, 39,(18), 3284-3287.



14. J. P. Collin, C. Dietrich-Buchecker P. Gavina, M. C. Jimenez-Molero, J.-P. Sauvage, Shuttles and Muscles : Linear Molecular Machines Based on Transition Metals. *Accounts of chemical research*, **2001**, 34, (6), 477-87.
15. P. R. Ashton, R. Ballardini, V. Balzani, I. Baxter, A. Credi, M. C. T. Fyfe, M. T. Gandolfi, M. Gómez-López, M. V. Martínez-Díaz, A. Piersanti, N. Spencer, J. F. Stoddart, M. Venturi, A. J. P. White, D. J. Williams, Acid-Base Controllable Molecular Shuttles, *Journal of the American Chemical Society*, **1998**, 120, 11932-11942.
16. P. R. Ashton, R. Ballardini, V. Balzani, I. Baxter, A. Credi, K. R. Dress, E. Ishow, C. J. Kleverlaan, O. Kocian, J. A. Preece, N. Spencer, J. F. Stoddart, M. Venturi, M. Wenger, A photochemically driven molecular-level abacus, *Chemistry - A European Journal*, **2000**, 6, 3558
17. Ishow, E.; Credi, A.; Balzani, V.; Spadola, F.; Mandolini, L., A molecular-level plug/socket system: electronic energy transfer from a binaphthyl unit incorporated into a crown ether to an anthracenyl unit linked to an ammonium ion. *Chemistry--A European Journal* **1999**, 5, (3), 984-989.
18. J. D. Badjic, V. Balzani, A. Credi, S. Silvi, J. F. Stoddart, A Molecular Elevator. *Science (New York, N.Y.)*, **2004**, 303, (5665), 1845-9.
19. Y. Liu, A. H. Flood, P. A. Bonvallet, S. A. Vignon, B. H. Northrop, H.-R. Tseng, J. O. Jeppesen, T. J. Huang, B. Brough, M. Baller, S. Magonov, S. D. Solares, W. A. Goddard, C.-M. Ho, J. F. Stoddart, Linear Artificial Molecular Muscles. *Journal of the American Chemical Society*, **2005**, 127, (27), 9745-59.
20. B. Gorodetsky, N. R. Branda, Electrochemically Induced Dethreading of a 2-Pseudorotaxane Based on the 1,2-bis(4,4'-pyridinium)ethane/24-crown-8 ether motif, *Tetrahedron Letters*, **2005**, 46, 6761-6763.
21. F. Durola, J.-P. Sauvage, Fast Electrochemically Induced Translation of the Ring in a Copper-Complexed [2]Rotaxane: the Biisoquinoline Effect. *Angewandte Chemie, International Edition*, **2007**, 46, (19), 3537-3540.
22. S. Saha, J. F. Stoddart, J. Fraser, Photodriven Molecular Devices, *Chemical Society Reviews*, **2007**, 36, (1), 77-92.
23. G. Fioravanti, N. Haraszkiewicz, E. R. Kay, S. M. Mendoza, C. Bruno, M. Marcaccio, P. G. Wiering, F. Paolucci, R. Rudolf, A. M. Brouwer, D. A. Leigh, Three State Redox-Active Molecular Shuttle That Switches in Solution and on a Surface. *Journal of the American Chemical Society*, 2008, 130, (8), 2593-2601.
24. B. K. Juluri, A. S. Kumar, Y. Liu, T. Ye, Y.-W. Yang, A. H. Flood, L. Fang, J. F. Stoddart, P. S. Weiss, T. J. Huang, A Mechanical Actuator Driven Electrochemically by Artificial Molecular Muscles. *ACS Nano*, **2009**, 3, (2), 291-300.

25. A. Coskun, D. C. Friedman, H. Li, K. K. Patel, A. Hussam, J. F. Stoddart, A Light-Gated STOP-GO Molecular Shuttle. *Journal of the American Chemical Society*, **2009**, 131, (7), 2493-2495.
26. L. Fang, M. Hmadeh, J. Wu, M. A. Olson, J. M. Spruell, A. Trabolsi, Y.-W. Yang, M. Elhabiri, A.-M. Albrecht-Gary, J. F. Stoddart, Acid-Base Actuation of [c2]Daisy Chains. *Journal of the American Chemical Society*, **2009**, 131, (20), 7126-7134.
27. J. M. Spruell, W. F. Paxton, J.-C. Olsen, D. Benitez, E. Tkatchouk, C. L. Stern, A. Trabolsi, D. C. Friedman, W. A. Goddard, J. F. Stoddart, A Push-Button Molecular Switch, *Journal of the American Chemical Society*, **2009**, 131, (32), 11571-11580.
28. P. R. Ashton, P. J. Campbell, E. J. T. Chrystal, P. T. Glinke, S. Menzer, D. Philp, N Spencer, J. F. Stoddart, P. A. Tasker, D. J. Williams, Dialkylammonium Ion/Crown Ether Complexes: The Forerunners of a New Family of Interlocked Molecules. *Angewandte Chemie, International Edition in English*, **1995**, 34,(17), 1865-9.
29. P. R. Ashton, P. J. Campbell, E. J. T. Chrystal, P. T. Glinke, S. Menzer, D. Philp, N Spencer, J. F. Stoddart, P. A. Tasker, D. J. Williams, C. Schiavo, Doubly Encircled and Double-Stranded Pseudorotaxanes. *Angewandte Chemie, International Edition in English*, **1995**, 34, (17), 1869-71.
30. P. R. Ashton, D. Philp, N Spencer, J. F. Stoddart, The Self-Assembly of [n]Pseudorotaxanes. *Journal of the Chemical Society, Chemical Communications*, **1991**, (23), 1677-9.
31. P. R. Ashton, C. L. Brown, J. Cao, J.-Y. Lee, S. P. Newton, F. M. Raymo, J. F. Stoddart, A. J. P. White, D. J. Williams, Molecular Meccano, 62. Azopyridinium-Containing [2]Pseudorotaxanes and Hydrazopyridinium-Containing [2]Catenanes. *European Journal of Organic Chemistry*, **2001**, (5), 957-965.
32. S. J. Cantrill, D. A. Fulton, A. M. Heiss, A. R. Pease, J. F. Stoddart, A. J. P. White, D. J. Williams, The Influence of Macrocyclic Polyether Constitution Upon Ammonium Ion/Crown Ether Recognition Processes. *Chemistry - A European Journal*, **2000**, 6, (12), 2274-2287.
33. M. Asakawa, P. R. Ashton, S. E. Boyd, C. L. Brown, R. E. Gillard, O. Kocian, F. M. Raymo, J. F. Stoddart, M. S. Tolley, Recognition of Bipyridinium-Based Derivatives by Hydroquinone- and/or Dioxynaphthalene-Based Macrocyclic Polyethers: From Inclusion Complexes to the Self-Assembly of [2]Catenanes. *Journal of Organic Chemistry*, **1997**, 62, (1), 26-37.
34. W. S. Jeon, A. Y. Ziganshina, J. W. Lee, Y. H. Ko, J.-K. Kang, C. Lee, K. Kim, K. A [2]pseudorotaxane-Based Molecular Machine: Reversible Formation of a Molecular Loop Driven by Electrochemical and Photochemical Stimuli. *Angewandte Chemie*,

---

*International Edition* **2003**, 42, (34), 4097-4100.

35. F. M. Raymo, J. F. Stoddart, Interlocked Macromolecules. *Chemical Reviews* (Washington, D. C.) **1999**, 99, (7), 1643-1663.
36. F. M. Raymo, K. N. Houk, J. F. Stoddart, The Mechanism of the Slippage Approach to Rotaxanes. Origin of the "All-or-Nothing" Substituent Effect. *Journal of the American Chemical Society* **1998**, 120, (36), 9318-9322.
37. A. M. Elizarov, T. Chang, S.-H. Chiu, J. F. Stoddart, Self-Assembly of Dendrimers by Slippage. *Organic Letters* **2002**, 4, (21), 3565-3568.
38. M. Horn, J. Ihringer, P. T. Glink, J. F. Stoddart, Kinetic Versus Thermodynamic Control During the Formation of [2]Rotaxanes by a Dynamic Template-Directed Clipping Process. *Chemistry--A European Journal* **2003**, 9, (17), 4046-4054.
39. V. Balzani, A. Credi, F. M. Raymo, J. F. Stoddart, A Molecular Elevator *Angewandte Chemie, International Edition*, **2000**, 39, 3348.
40. D.-H. Qu, Q.-C. Wang, J. Ren, H. Tian, A Light-Driven Rotaxane Molecular Shuttle with Dual Fluorescence Addresses. *Organic Letters*, **2004**, 6, (13), 2085-2088.
41. A. Altieri, F. G. Gatti, E. R. Kay, D. A. Leigh, D. Martel, F. Paolucci, S. M. Slawin, J. K. Wong. Electrochemically Switchable Hydrogen-Bonded Molecular Shuttles. *Journal of the American Chemical Society*, **2003**, 125, 8644-8654.
42. P. R. Ashton, R. Ballardini, V. Balzani, A. Credi, K. R. Dress, E. Ishow, C. J. Kleverlaan, O. Kocian, J. A. Preece, N. Spencer, J. F. Stoddart, M. Venturi, S. Wenger, A photochemically driven molecular-level abacus. *Chemistry - A European Journal*, **2000**, 6, 3558-3574.
43. P. R. Ashton, R. Ballardini, V. Balzani, A. Credi, M. C. T. Fyfe, M. T. Gandolfi, M. Gomez-Lopez, M.-V. Martinez-Diaz, A. Piersanti, N. Spencer, J. F. Stoddart, M. Venturi, A. J. P. White, D. J. Williams, Acid-Base Controllable Molecular Shuttles. *Journal of the American Chemical Society*, **1998**, 120, (46), 11932-11942.
44. A. Altieri, G. Bottari, F. Dehez, D. A. Leigh, J. K. Y. Wong, F. Zerbetto, F. Remarkable positional discrimination in bistable light- and heat-switchable hydrogen-bonded molecular shuttles. *Angewandte Chemie (International ed. in English)*, **2003**, 42, (20), 2296-300.
45. J.-P. Collin, J.-M. Kern, L. Raehm, J.-P. Sauvage. *Molecular Switches*, Wiley-VCH: Weinheim, 2000, 249-280.

- 
46. H. Murakami, A. Kawabuchi, K. Kotoo, M. Kunitake, N. Nakashima, A Light-Driven Molecular Shuttle Based on a Rotaxane, *Journal of the American Chemical Society*, **1997**, 1, 7605-7606.
47. S. J. Vella, *New Interlocked Molecular Machines*, University of Windsor, Windsor, **2006**.
48. F. M. Reinitzer, *Chemistry.*, **1988**, 9, 421.
49. O. Lehmann, *Journal of Physical Chemistry*, **1989**, 4, 462.
50. B. Bahadur, *Liquid Crystal - Applications and Uses*, vol. 1-3, World Scientific Publishing Co. Pte. Ltd. Singapore, **1990**.
51. T. J. Bunning, F. H. Kreuzer, Cyclosiloxane-Based Liquid Crystalline Materials. *Trends in Polymer Science (Cambridge, United Kingdom)*, **1995**, 3, (10), 318-23.
52. F. Schambil, S. Paacsh, M. J. Schwuger, Liquid crystals from surfactants, *Fette Ole Fettderivate Folgerprodukte*, **1988**, 114, 295-300.
53. H. Ringsdorf, B. Schlarb, J. Venzmer, Molecular Architecture and Function in Polymeric Oriented Systems. Models for the Study of Organization, Surface Recognition, and Dynamics in Biomembranes. *Angewandte Chemie*, **1988**, 100,(1), 117-62.
54. C. G. Goltner, M. Antonietti, Mesoporous Materials by Templating of Liquid Crystalline Phases. *Advanced Materials (Weinheim, Germany)*, **1997**, 9, (5), 431-436.
55. C. Tschierske, Non-Conventional Liquid Crystals: The Importance of Micro-Segregation for Self-Organization, *Journal of Materials Chemistry*, **1998**, 8, (7), 1485-1508.
56. B. E. Smart, *Organofluorine Chemistry Principles and Commercial Applications*, Plenum Press, New York, **1994**.
57. K. Kuschel, A. Maedicke, S. Diele, H. Utschick, B. Hisgen, H. Ringsdorf, Study of the Microphase Separation in Liquid-Crystalline Polymers with Paired Mesogens. *Polymer Bulletin (Berlin, Germany)*, **1990**, 23, (4), 373-9, and references therein.
58. P. Collings, M. Hird, *Introduction to Liquid Crystals*, Taylor and Francis, New York, **1997**.
59. V. Tsvetkov, *Acta Physicochim (U.S.S.R)*, **1942**, 16, 132.
60. I. Dierking, *Textures of Liquid Crystals*, Wiley-VCH, Weinhiem, **2003**.

- 
61. W. L. McMillan, Simple Molecular Theory of the Smectic C Phase. *Physical Review A: Atomic, Molecular, and Optical Physics*, **1973**, 8, (4), 1921-9.
62. R. B. Meyer, W. L. McMillan, Simple Molecular Theory of the Smectic C, B, and H phases. *Physical Review A: Atomic, Molecular, and Optical Physics*, **1974**, 9(2), 899-906.
63. A. Wulf, Steric model for the smectic-C phase. *Physical Review A: Atomic, Molecular, and Optical Physics*, **1975**, 11(1), 365-75.
64. H. Kitzerow, D. Bahr, *Chirality in Liquid Crystals*, Springer-Verlag, New York, **2001**.
65. R. Eelkema, B. L. Feringa, Amplification of Chirality in Liquid Crystals, *Organic & Biomolecular Chemistry*, **2006**, 4, (20), 3729-3745.
66. D. B. Amabilino, J. Veciana, Supramolecular Chiral Functional Materials, *Topics in Current Chemistry*, **2006**, 265, 253-302.
67. R. P. Lemieux, Chirality Transfer in Ferroelectric Liquid Crystals, *Accounts of Chemical Research*, **2001**, 34,(11), 845-853.
68. R. P. Lemieux, Molecular recognition in chiral smectic liquid crystals: The effect of core-core interactions and chirality transfer on polar order. *Chemical Society Reviews*, **2007**, 36, (12), 2033-2045.
69. J. W. Goodby D. A. Dunmur and P. J. Collings, Lattice Melting at the Clearing Point in Frustrated Systems, *Liquid Crystals*, **1995**, 19, 703.
70. J. W. Goodby, Chirality in Liquid Crystals, *Journal of Materials Chemistry*, **1991**, 1, 307-318.
71. R. B. Meyer, L. Liebert, L. Strzelecki, P. Keller, Ferroelectric liquid crystals, *Journal Physical Letters*, **1975**, 36, L69.
72. N. A. Clark, S. T. Lagerwall, *Applied Physical Letters*, **1980**, 36, 899.
73. H.-S. Kitzerow, C. Bahr, *Chirality in Liquid Crystals*, Springer-Verlag, Berlin, **2001**.
74. J. A. Dean, *The Analytical Chemistry Handbook*. McGraw Hill Inc. New York, **1995**.
75. I. Dierking, *Textures of Liquid Crystals*, Wiley-VCH, Weinheim, **2003**.
76. L. Smart, E. Moore, *Solid State Chemistry*, Chapman & Hall. **1992**.

- 
77. D. Demus, J. W. Goodby, H.-W. Gray, V. Spiess, *Handbook of Liquid Crystals, Second Ed.*, Oxford University Press, New York, 1993.
78. T. Kato, Self-Assembly of Phase-Segregated Liquid Crystal Structures. *Science* (Washington, DC, United States), **2002**, 295, (5564), 2414-2418.
79. I. W. Hamley, Nanotechnology with Soft Materials. *Angewandte Chemie International ed. in English*, **2003**, 42, (15), 1692-712.
80. I. M. Saez, J. W. Goodby, Electro-optic Response in a Racemic Smectic C Liquid Crystal. *Advanced Materials* (Weinheim, Germany), **2005**, 17(8), 1077-1080.
81. T. Kato, N. Mizoshita, K. Kishimoto, Liquid-Crystal Composites Composed of Photopolymerized Self-Assembled Fibers and Aligned Smectic Molecules. *Advanced Functional Materials*, **2006**, 16(17), 2218-2224.
82. K. Ichimura, Photoalignment of Liquid-Crystal Systems. *Chemical Reviews* (Washington, D. C.), **2000**, 100(5), 1847-1873.
83. T. Ikeda, A. Kanazawa. *Molecular Switches* (Ed.: B. L. Feringa), Wiley-VCH, Weinheim, **2001**, pp. 363 – 397.
84. T. Ikeda, Holographic Image Storage in Polymer Azobenzene Liquid Crystals. *Molecular Crystals and Liquid Crystals*, **2003**, 401, 149-159.
85. M. Even, B. Heinrich, D. Guillon, D. M. Guldi, M. Prato, R. A. Deschenaux, A Mixed Fullerene-Ferrocene Thermotropic Liquid Crystal: Synthesis, Liquid-Crystalline Properties, Supramolecular Organization and Photoinduced Electron Transfer. *Chemistry - A European Journal*, **2001**, 7, (12), 2595-2604.
86. M. Sawamura, K. Kawai, Y. Matsuo, K. Kanie, T. Kato, E. Nakamura, Stacking of conical molecules with a fullerene apex into polar columns in crystals and liquid crystals. *Nature*, **2002**, 419, 702 – 705.
87. T. Chuard, R. Deschenaux, Design, Mesomorphic Properties, and Supramolecular Organization of [60]Fullerene-Containing Thermotropic Liquid Crystals. *Journal of Materials Chemistry*, **2002**, 12, (7), 1944-1951.
88. Y. Matsuo, A. Muramatsu, Y. Kamikawa, T. Kato, E. Nakamura, Synthesis and Structural, Electrochemical, and Stacking Properties of Conical Molecules Possessing Buckyferrocene on the Apex, *Journal of the American Chemical Society*. **2006**, 128, 9586 – 9587
89. M. Yamada, M. Kondo, R. Miyasato, Y. Naka, J.-I. Mamiya, M. Kinoshita, A. Shishido, Y. Yu, C. J. Barrett, T. Ikeda, Tomiki. Photomobile Polymer Materials-

- Various Three-Dimensional Movements. *Journal of Materials Chemistry*, **2009**, 19, (1), 60-62.
90. Y. Yu, M. Nakano, A. Shishido, T. Shiono and T. Ikeda, Effect of Cross-Linking Density on Photoinduced Bending Behavior of Oriented Liquid-Crystalline Network Films Containing Azobenzene, *Chemistry of Materials* **2004**, 16, 1637–1643
91. M. Kondo, Y. Yu and T. Ikeda, How Does the Initial Alignment of Mesogens Affect the Photoinduced Bending Behavior of the Azobenzene Liquid-Crystalline Elastomers? *Angewandte Chemie International ed. in English*, **2006**, 45, 1378–1382
92. Y. Yu, T. Maeda, J. Mamiya and T. Ikeda, Macro- and Micro- Soft Actuators Based on Liquid-Crystalline Elastomers, *Angewandte Chemie International ed. in English*, **2007**, 46, 881–883
93. J. Mamiya, A. Yoshitake, M. Kondo, Y. Yu and T. Ikeda, Is Chemical Crosslinking Necessary for the Photoinduced Bending of Polymer Films? *Journal of Materials Chemistry*, **2008**, 18, 63–65.
94. M. Kidowaki, T. Nakajima, J. Araki, A. Inomata, H. Ishibashi, I. Hitoshi, K. Ito, Novel Liquid Crystalline Polyrotaxane with Movable Mesogenic Side Chains. *Macromolecules (Washington, DC, United States)*, **2007**, 40, (19), 6859-6862.
95. E. D. Baranoff, J. Voignier, T. Yasuda, V. Heitz, J.-P. Sauvage, T. Kato, A Liquid-Crystalline [2]Catenane and its Copper(I) Complex. *Angewandte Chemie, International Edition*, **2007**, 46, (25), 4680-4683.
96. I. Aprahamian, T. Yasuda, T. Ikeda, S. Saha, W. R. Dichtel, K. Isoda, T. Kato, J. F. Stoddart, A Liquid-Crystalline Bistable [2]Rotaxane. *Angewandte Chemie, International Edition*, **2007**, 46, (25), 4675-4679.
97. H. W. Gibson, *Large Ring Molecules*; Semlyen, J. A., Ed.; John Wiley and Sons: New York, **1996**; Chapter 6, pp 191-262.
98. F. M. Raymo, J. F. Stoddart, Interlocked Molecules, *Chemical Reviews*. **1999**, 99, 1643-1664.
99. C. Gong, H. W. Gibson, *Molecular Catenanes, Rotaxanes and Knots*, Sauvage, J.-P., Dietrich-Buchecker, C. O., Eds.; Wiley-VCH, Weinheim, **1999**; Chapter 11, pp 277-321.
100. T. Shimomura, T. Akai, T. Abe, K. Ito, Atomic force microscopy observation of insulated molecular wire formed by conducting polymer and molecular nanotube *Journal of Chemical Physics*. **2002**, 116, 1753-1756.

101. P. N. Taylor, M. J. O'Connell, L. A. McNeill, M. J. Hall, R. T. Aplin, H. Anderson, Insulated molecular wires: synthesis of conjugated polyrotaxanes by Suzuki coupling in water *Angewandte Chemie, International Edition*, **2000**, *39*, 3456-3460.
102. T. Ooya, K. Arizono, N. Yui, Synthesis and characterization of an oligopeptide-terminated polyrotaxane as a drug carrier *Polymers for Advanced Technologies*. **2000**, *11*, 642-651.
103. T. Ooya, N. Yui, Molecular mobility of interlocked structures exploiting new functions of advanced biomaterials, *Chemistry - A European Journal*, **2006**, *12*, 6730-6737.
104. K. Kishimoto, M. Yoshio, T. Mukai, M. Yoshizawa, H. Ohno, T. Kato Nanostructured Anisotropic Ion-Conductive Films, *Journal of the American Chemical Society*, **2003**, *125*, 3196 – 3197.
105. M. Even, B. Heinrich, D. Guillon, D. M. Guldi, M. Prato, R. Deschenaux, A mixed fullerene-ferrocene thermotropic liquid crystal: synthesis, liquid-crystalline properties, supramolecular organization and photoinduced electron transfer *Chemistry - A European Journal*, **2001**, *7*, 2595-2604.
106. S. Campidelli, E. Vázquez, D. Milic, J. Lenoble, C. A. Castellanos, G. Sarova, D. M. Guldi, R. Deschenaux, M. Prato, Liquid-Crystalline Bisadducts of [60]Fullerene *Journal of Organic Chemistry*, **2006**, *71*, 7603-7610.
107. D. Fazio, C. Mongin, B. Donnio, Y. Galerne, D. Guillon, D. W. Bruce, Bending and shaping: cubics, calamitics and columnars. *Journal of Materials Chemistry*, **2001**.
108. S. H. Eichhorn, A. Paraskos, K. Kishikawa, T. M. Swager, The Interplay of Bent-Shape, Lateral Dipole and Chirality in Thiophene Based Di-, Tri-, and Tetracatenar Liquid Crystals *Journal of the American Chemical Society*, **2002**, *124*, 12742-51.
109. L. Vyklicky, S. H. Eichhorn, and T. J. Katz, Helical Discotic Liquid Crystals *Chemistry Of Materials*. **2003**, *15*, 3594-3601.
110. X. B. Zeng, G. Ungar, Y. S. Liu, V. Percec, S. E. Dulcey, J. K. Hobbs, Supramolecular dendritic liquid quasicrystals *Nature* **2004**, *428*, 157-160.
111. B. Chen, X. B. Zeng, U. Baumeister, G. Ungar, C. Tschierske, Liquid Crystalline Networks Composed of Pentagonal, Square, and Triangular Cylinders *Science* **2005**, *307*, 96-99.
112. B. L. Allwood, N. Spencer, H. Shahriari-Zavareh, J. F. Stoddart, D. J. Williams, Complexation of Paraquat by a Bisparaphenylene-34-crown-10 Derivative. *Journal of the Chemical Society, Chemical Communications* **1987**, (14), 1064-6.



113. S. J. Loeb, J. A. Wisner, A New Motif for the Self-Assembly of [2]Pseudorotaxanes; 1,2-bis(pyridinium)ethane Axles and [24]crown-8 Ether Wheels. *Angewandte Chemie, International Edition* **1998**, 37, (20), 2838-2840.
114. S. J. Loeb, J. Tiburcio, S. J. Vella, J. A. Wisner, A Versatile Template for the Formation of [2]Pseudorotaxanes. 1,2-Bis(pyridinium)ethane axles and 24-crown-8 ether wheels. *Organic & Biomolecular Chemistry* **2006**, 4, (4), 667-680.
115. Tiburcio, J.; Davidson, G. J. E.; Loeb, S. J., Pseudo-polyrotaxanes based on a protonated version of the 1,2-bis(4,4'-bipyridinium)ethane-24-crown-8 ether motif. *Chemical Communications (Cambridge, United Kingdom)* **2002**, (12), 1282-1283.
116. Loeb, S. J.; Wisner, J. A., 1,2-Bis(4,4'-dipyridinium)ethane: a versatile dication for the formation of [2]rotaxanes with dibenzo-24-crown-8 ether. *Chemical Communications (Cambridge)* **1998**, (24), 2757-2758.
117. Davidson, G. J. E.; Loeb, S. J.; Parekh, N. A.; Wisner, J. A., Zwitterionic [2]rotaxanes utilising anionic transition metal stoppers. *Journal of the Chemical Society, Dalton Transactions* **2001**, (21), 3135-3136.
118. Davidson, G. J. E.; Loeb, S. J., Iron(II) complexes utilising terpyridine containing [2]rotaxanes as ligands. *Dalton Transactions* **2003**, (22), 4319-4323.
119. Davidson, G. J. E.; Loeb, S. J.; Passaniti, P.; Silvi, S.; Credi, A., Wire-type ruthenium(II) complexes with terpyridine-containing [2]rotaxanes as ligands: synthesis, characterization, and photophysical properties. *Chemistry--A European Journal* **2006**, 12, (12), 3233-3242.
120. Loeb, S. J.; Wisner, J. A., [3]Rotaxanes employing multiple 1,2-bis(pyridinium)ethane binding sites and dibenzo-24-crown-8 ethers. *Chemical Communications (Cambridge)* **2000**, (10), 845-846.
121. Hubbard, A. L.; Davidson, G. J. E.; Patel, R. H.; Wisner, J. A.; Loeb, S. J., Hostguest interactions template: the synthesis of a [3]catenane. *Chemical Communications (Cambridge, United Kingdom)* **2004**, (2), 138-139.
122. Loeb, S. J.; Wisner, J. A., [2]Rotaxane molecular shuttles employing 1,2-bis(pyridinium)ethane binding sites and dibenzo-24-crown-8 ethers. *Chemical Communications (Cambridge)* **2000**, (19), 1939-1940.
123. S. J. Vella, J. Tiburcio, S. J. Loeb, Optically Sensed, Molecular Shuttles Driven by Acid-Base Chemistry. *Chemical Communications (Cambridge)*, 2007, 7, (45), 4752-4.
124. D. A. Tramontozzi, N. D. Suhan, S. H. Eichhorn, S. J. Loeb, The Effect of Incorporating Fréchet Dendrons into Rotaxanes and Molecular Shuttles Containing the

---

1,2-bis(dipyridinium)ethane $\subset$ 24-crown-8 Templating Motif, *Chemistry - A European Journal*, submitted Aug. **2009**.

125. Loeb, S. J.; Tramontozzi, D. A., Branched [n]rotaxanes (n = 2-4) from multiple dibenzo-24-crown-8 ether wheels and 1,2-bis(4,4'-dipyridinium)ethane axles. *Organic & Biomolecular Chemistry* **2005**, 3, (8), 1393-1401.
126. Tramontozzi, D. A. Dendrimeric and Polymeric Rotaxanes Incorporating the Loeb Recognition Motif. Windsor, Windsor, **2005**.
127. Loeb, S. J., Metal-organic rotaxane frameworks; MORFs. *Chemical Communications (Cambridge, United Kingdom)* **2005**, (12), 1511-1518.
128. Loeb, S. J.; Tiburcio, J.; Vella, S. J., A mechanical "flip-switch". Interconversion between co-conformations of a [2]rotaxane with a single recognition site. *Chemical Communications (Cambridge, United Kingdom)* **2006**, (15), 1598-1600.
129. F. M. Menger, J. S. Keiper, Gemini Surfactants *Angewandte Chemie International Edition* **2000**, 39, (1), 1907-1920.
130. D. Fazio, D. W. Bruce, Bending and Shaping: Cubics, Calamitics and Columnars. *Journal of Materials Chemistry* **2001**, 11, (11), 2852-2863.
131. J. W. Leon, M. Kawa, J. M. J. Fréchet, Isophthalate Ester-Terminated Dendrimers: Versatile Nanoscopic Building blocks with Readily Modifiable Surface Functionalities. *Journal of the American Chemical Society* **1996**, 118, (37), 8847-8859. (section 2.2.1)
132. P. Krasik, Synthesis of Sterically Hindered Esters via Titanium Catalyzed Transesterification. *Tetrahedron Letters* **1998**, 39, (24), 4223-4226. (section 2.2.1)
133. C. A. Hunter, J. K. M. Saunders, The nature of  $\pi$ - $\pi$  interactions. *Journal of the American Chemical Society* **1990**, 112, (14) 5525-34. (section 2.2.3)
134. C. A. Hunter, K. R. Lawson, J. Perkins, C. J. Urch, Aromatic Interactions. *Journal of the Chemical Society, Perkin Transactions 2* **2001**, (14), 651-669. (section 2.2.3)
135. A. I. Kitaigorodsky, Molecular Crystals and Molecules, Academic Press, New York and London, **1973**, 18-21.
136. A. R. Ubbelohde, Melting and Crystal Structure, Clarendon Press, Oxford, **1965**, 9-11.
137. G. M. Sheldrick, SHELXTL 5.03 Program Library, Brüker Analytical Instrument Division, Madison, Wisconsin, USA. (section 2.5.15)

138. DIAMOND 3.1 - Visual Crystal Structure Information System CRYSTAL IMPACT, Postfach 1251, D-53002 Bonn, **2006**. (section 2.5.15)
139. G. M. Whitesides, J. P. Mathias, C. T. Seto, Molecular self-assembly and nanochemistry: a chemical strategy for the synthesis of nanostructures *Science*, **1991**, 254, 1312.
140. P. J. Collings, *Liquid Crystals: Nature's Delicate Phase of Matter*, Princeton University Press: Princeton, New Jersey, 1990.
141. Y. Peng, G. Song, X. Qian, *Synthetic Communications* Imidation of Cyclic Carboxylic Anhydrides Under Microwave Irradiation **2001**, 31, (12), 1927-1931.
142. H. Zhu, X. Wang, Y. Li, Z. Wang, F. Yang, X. Yang, Xiurong. Microwave synthesis of fluorescent carbon nanoparticles with electrochemiluminescence properties. *Chemical Communications (Cambridge, United Kingdom)*, **2009**, (34), 5118-5120.
142. S. Tsurulnikov, M. Nikulnikov, V. Kysil, A. Ivachtchenko, M. Krasavin, Mikhail. Streamlined access to 2,3-dihydropyrazino[1,2-a]indole-1,4-diones via Ugi reaction followed by microwave -assisted cyclization. *Tetrahedron Letters*, **2009**, 50,(39), 5529-5531.
143. N. D. Pingale, S. R. Shukla, S. R. Microwave -assisted aminolytic depolymerization of PET waste. *European Polymer Journal* **2009**, 45,(9), 2695-2700.
144. H. A. Abdel-Aziz, S. M. Gomha, A new aspect of the pfitzinger reaction: microwave -assisted synthesis of the new heterocyclic ring system 6-arylbenzo[4,5]imidazolo[2,1-b]quino[4,3-e]-1,3-thiazin-14-one. *Zeitschrift fuer Naturforschung, B: A Journal of Chemical Sciences*, **2009**, 64,(7), 826-830.
145. L. Perez-Picaso, J. Escalante, H. F. Olivo, M. Y. Rios, Efficient microwave assisted syntheses of 2,5-diketopiperazines in aqueous media. *Molecules* **2009**, 14,(8), 2836-2849.
146. J. A. Farrington, A. Ledwith, M. F. Stam, Cation-Radicals: Oxidation of Methoxide Ion with 1,1'-Dimethyl-4,4'-bipyridinium Dichloride (Paraquat Dichloride), *Chemical Communications* **1969**, 55, 259-260.
147. A. D. Baker, A. Casadevall, A Clock Reaction with Paraquat, *Journal of Chemical Education* **1980**, 57, (7) 515-516.
148. A. L. Rieger, J. O. Edwards, Hydrogen Exchange between Methyl Viologen Cation and Basic Deuterium Oxide, *Journal of Organic Chemistry* **1985**, 50, (25), 5102-5104.

149. A. L. Rieger, J. O. Edwards, Methyl Viologen Reactions. Rates and Mechanism of Cation-Radical Formation in Aqueous Base, *Journal of Organic Chemistry* **1988**, 53, (7), 1481-1485.
150. D. A. Leigh, E. M. Perez, Shuttling Through Reversible Covalent Chemistry. *Chemical Communications (Cambridge)* **2004**, (20), 2262-2263.
151. C. M. Keaveney, D. A. Leigh, Shuttling Through Anion Recognition. *Angewandte Chemie, International Edition* **2004**, 43, (10), 1222-1224.
152. S. P. Perkins, D. E. Shoosmith, H. J. Coles, Novel Room Temperature Fluorinated Ferroelectric Organosiloxane Liquid Crystal Mixtures. *Molecular Crystals and Liquid Crystals Science and Technology, Section A: Molecular Crystals and Liquid Crystals* **2001**, 364, 943-950.
153. T. Ganicz, W. A. Stanczyk, E. Bialecks-Florjanczyk, I. Sledzinska, Liquid Crystal Dimers with Organosilicon Spacers as Models for Side Chain LC Polymers. *Polymer*, **1999**, 40, (17), 4733-4739.
154. H. J. Coles, R. Simon, Investigations of Smectic Polysiloxanes. 3. Ultrahigh Contrast Smectic Polymer Storage Effect. *Molecular Crystals and Liquid Crystals, Letters*, **1985**, 1, (3), 75-81.
155. R. Simon, H. J. Coles, Investigations of Smectic Polysiloxanes. 1 - Electric Field Induced Turbulence. *Molecular Crystals and Liquid Crystals*, **1984**, 102, (2), 43-8.
156. G. W. Gray, Side Chain Liquid Crystal Polymers, ed. C. B. McArdle, Blackie, Glasgow and London, **1989**.
157. T. Ganicz, T. Pakula, W. A. Stanczyk, Novel Liquid Crystalline Resins Based on MQ Siloxanes, *Journal of Organometallic Chemistry*, **2006**, 691, 5052-5055.
158. K. Nakazono, S. Kuwata, T. Takata, Crown Ether-tert-Ammonium Salt Complex Fixed as Rotaxane and Its Derivation to Neutral Rotaxane, *Tetrahedron Letters* **2008**, 49, 2397 - 2401.
159. N. Kihara, N. Nakakoji, T. Takata, Tributylphosphine-Catalyzed Acylation of Alcohol by Active Ester Directed Toward Effective End-Capping of Pseudorotaxane Consisting of Ammonium Group and Crown Ether *Chemical Letters* **2002**, (9) 924 - 925.
160. J.-T. Zhang, C.-J. Pan, T. Keller, R. Bhat, M. Gottschaldt, U. S. Schubert, K. D. Jandt, Monodisperse, Temperature-Sensitive Microgels Crosslinked by Si-O-Si Bonds. *Macromolecular Materials and Engineering*, **2009**, 294, (6-7), 396-404.
161. J. J. Li, Z. Mu, C. He, Q. Hu, L. D. Li, J. Cheng, Z. Hao, S. Z. Qiao, Promoted and Controllable Self-Assembly of Hydrolyzed Siloxane and Triblock Copolymer

- under Organic Polyhydroxy Acids. *Industrial & Engineering Chemistry Research*, **2009**, 48, (13), 6308-6314.
162. L. Guertin, S. J. Loeb, An Undergraduate Thesis. *University Of Windsor* **2008**, 1-37.
163. F. Kazemi, H. Sharghi, M. A. Naseri, A Cheap, Simple and Efficient Method for the Preparation of Symmetrical Carboxylic Acid Anhydrides *Synthesis* **2004**, 2, 205-207.
164. M. Ibn-Elhaj, A. Skoulios, D. Guillon, J. Newton, P. Hodge, H. J. Coles, Structural Characterization of New Ferroelectric Liquid-Crystalline Siloxanes. *Journal of Physics II*, 1996, 6, (2), 271-9.
165. R. Mueller, M. Huerzeler, C. Boss, Synthesis of Plasmepsin II Inhibitors - Potential Antimalarial Agents. *Molecules* **2003**, 8, (7), 556-564.
166. G. Durand, Ph. Martinot-Lagarde, Physical Properties of Ferroelectric Liquid Crystals, *Ferroelectrics*, **1980**, 24, 89-97.
167. J. W. Goodby, R. Blinc, N. A. Clark, S. T. Lagerwall, M. A. Osipov, S. A. Pikin, T. Sakurai, K. Yoshino, B. Zeks, *Ferroelectric Liquid Crystals, Principles, Properties and Applications*, Gordon & Breach, Philadelphia, 1991.
168. S. T. Lagerwall, *Ferroelectric and Antiferroelectric Liquid Crystals*, Wiley-VCH, Weinheim, **1999**.
169. I. Musevic, R. Blinc, B. Zeks, *The Physics of Ferroelectric and Antiferroelectric Liquid Crystals*, World Scientific, Singapore, **2000**.
170. A. Sandanayaka, H. Sasabe, Y. Araki, Y. Furusho, O. Ito, T. Takata, Photoinduced Electron-Transfer Processes Between [C60]Fullerene and Triphenylamine Moieties Tethered by Rotaxane Structures. Through-Space Electron Transfer via Excited Triplet States of [60]Fullerene. *Journal of Physical Chemistry A*, **2004**, 108, (24), 5145-5155.
171. Y. Liu, Y. Chen, S.-Z. Kang, L. Li, C.-H. Diao, H.-Y. Zhang, Synthesis of Novel Benzo-15-Crown-5-Tethered - Cyclodextrins and Their Enhanced Molecular Binding Abilities by Alkali Metal Cation Coordination. *Journal of Inclusion Phenomena and Macrocyclic Chemistry*, **2003**, 47, (1-2), 91-95.
172. Y. Liu, S.-Z. Kang, C.-H. Diao, Synthesis of Crown Ether-Tethered - Cyclodextrin and Fabrication of its Self-Assembled Monolayer on Gold Surface. *Chinese Chemical Letters*, **2001**, 12, (10), 891-892.
173. E. Luboch, A. Cygan, J. F. Biernat, The Synthesis of Some Aromatic Crown Ether Derivatives and Their Non-Selective Electrode Properties. *Tetrahedron*, **1990**, 46, (7), 2461-72.

174. J.-P. Sauvage, Transition Metal-Complexed Catenanes and Rotaxanes as Molecular Machine Prototypes. *Chemical Communications (Cambridge, United Kingdom)* **2005**, (12), 1507-1510.
175. A. G. Johnston, D. A. Leigh, L. Nezhat, J. P. Smart, M. D. Deegan, Structurally Diverse and Dynamically Versatile Benzylic Amide [2]Catenanes Assembled Directly from Commercially Available Precursors. *Angewandte Chemie, International Edition in English*, **1995**, 34, (11), 1212-16.
176. M. Fujita, Self-Assembly of [2]Catenanes Containing Metals in Their Backbones, *Accounts of Chemical Research*, **1999**, 32, (1), 53-61.
177. T. Hoshino, M. Miyauchi, Y. Kawaguchi, H. Yamaguchi, A. Harada, Daisy Chain Necklace: Tri[2]rotaxane Containing Cyclodextrins, *Journal of the American Chemical Society*, **2000**, 122, (40), 9876-9877.
178. M. J. Gunter, N. Bampos, K. D. Johnstone, J. K. M. Sanders, Thermodynamically Self-Assembling Porphyrin-Stoppered Rotaxanes. *New Journal of Chemistry*, **2001**, 25, (1), 166-173.
179. J. A. Wisner, P. D. Beer, M. G. B. Drew, M. R. Sambrook, Anion-Templated Rotaxane Formation, *Journal of the American Chemical Society*, **2002**, 124, (42), 12469-76.
180. K. Kim, Mechanically Interlocked Molecules Incorporating Cucurbituril and their Supramolecular Assemblies. *Chemical Society Reviews*, **2002**, 31, (2), 96-107.
181. K. Euan, D. A. Leigh, Z. Francesco Synthetic Molecular Motors and Mechanical Machines. *Angewandte Chemie, International ed. in English*, **2007**, 46, (1-2), 72-191.
182. S. Shinkai, T. Nakaji, T. Ogawa, K. Shigematsu, O. Manabe, Photoresponsive Crown Ethers. 2. Photocontrol of Ion Extraction and Ion Transport by a bis(Crown Ether) with a Butterfly-Like Motion. *Journal of the American Chemical Society*, **1981**, 103, (1), 111-15.
183. T. Kelly, D. Ross, D. Harshani, R. A. Silva, Unidirectional Rotary Motion in a Molecular System. *Nature (London)*, **1999**, 401, (6749), 150-152.
184. F. Luigi; F. Francesco, P. Stefano, P. Piersandro, T. Angelo, A Sleeping Host Awoken by its Guest: Recognition and Sensing of Imidazole-Containing Molecules Based on Double Cu<sup>2+</sup> Translocation Inside a Polyaza Macrocyclic. *Angewandte Chemie International ed. in English*, **2004**, 43, (38), 5073-7.
185. D. L. Ross, J. Blanc, *Photochromism by Cis-trans Isomerization*, Brown, G. H. Ed. Wiley-Interscience: New York, **1971**, Vol. III, 471-556.

- 
186. H. Adams, C. A. Hunter, K. R. Lawson, J. Perkins, S. E. Spey, C. J. Urch, J. M. Sanderson, A Supramolecular System for Quantifying Aromatic Stacking Interactions. *Chemistry - A European Journal*, **2001**, 7, (22), 4863-4877.

---

**VITA AUCTORIS**

**Name:** Natalie Suhan

**Date of Birth:** May, 1979

**Place of Birth:** Windsor, Ontario, Canada

**Citizenship:** Canadian

**Education:**

Ph. D. Chemistry (2009)  
University of Windsor,  
Windsor, Ontario

B. Sc. Honours Biochemistry (2003)  
University of Windsor,  
Windsor, Ontario

**Professional Work History:**

Research Assistant  
University of Windsor, Windsor, Ontario, Canada  
September 2003-April 2009

Graduate Assistant  
University of Windsor, Windsor, Ontario, Canada  
September 2003-August 2009

**Scholarships and Awards:**

Award	Amount	Type of Award	Year Held
Tuition Scholarship	6300	Institutional	Sep. 2005-Aug. 2006
Tuition Scholarship	6300	Institutional	Sep. 2006-Aug. 2007
Travel Award	500	Institutional	May 2006
Tuition Scholarship	6300	Institutional	Sep. 2007-Aug. 2008
Travel Award	500	Institutional	May 2007
Travel Award	500	Institutional	Aug. 2007
Tuition Scholarship	6300	Institutional	Sep. 2008-Aug. 2009



---

**Publications:**

D. A. Tramontozzi, N. D. Suhan, S. H. Eichhorn, S. J. Loeb. The Effect of Incorporating Fréchet Dendrons into Rotaxanes and Molecular Shuttles Containing the 1,2-bis(dipyridinium)ethane $\subset$ 24-crown-8 Templating Motif, *Chemistry - A European Journal*, submitted Aug. **2009**.

**Conference Presentations:**

N. D. Suhan, S. J. Loeb. Liquid Crystalline [2]Rotaxanes. *8<sup>th</sup> Chemistry Biochemistry Graduate Research Conference*. Concordia, University, Montréal, Quebec, Canada, **2005**. (Ph.D. Work- poster presentation)

N. D. Suhan, S. J. Loeb, & S. H. Eichhorn. Design, Synthesis & Liquid Crystal Studies of [2]Rotaxanes. *89<sup>th</sup> Canadian Chemistry Conference*, Halifax, Nova Scotia, Canada, **2006**. (Ph.D. Work- poster presentation)

N. D. Suhan, S. J. Loeb, and S. H. Eichhorn. Self-Organizing [2]Rotaxanes. *90<sup>th</sup> Canadian Chemistry Conference*, Winnipeg, Manitoba, Canada, **2007**. (Ph.D. Work- oral presentation)

N. D. Suhan, S. J. Loeb, & S. H. Eichhorn. Self-Organizing [2]Rotaxanes. *GRC: Liquid Crystals*, New London, New Hampshire, United States of America, **2007**. (Ph.D. Work- poster presentation)

N. D. Suhan, S. J. Loeb, & S. H. Eichhorn. Probing Mesomorphic Properties of Various Substituted [2]Rotaxanes. *22nd International Liquid Crystal Conferences*, JeJu, South Korea, **2008**. (Ph.D. Work- poster presentation)

N. D. Suhan, S. J. Loeb, and S. H. Eichhorn. Improving Phase Stability in Multiple Liquid Crystalline [2]Rotaxanes. *92<sup>th</sup> Canadian Chemistry Conference*, Hamilton, Ontario, Canada, **2009**. (Ph.D. Work- oral presentation)

N. D. Suhan, S. J. Loeb, & S. H. Eichhorn. Improving Phase Behaviour in Liquid Crystal [2]Rotaxanes. *GRC: Liquid Crystals*, New London, New Hampshire, United States of America, **2009**. (Ph.D. Work- poster presentation)

**Invited Presentations:**

N. D. Suhan, S. J. Loeb, & S. H. Eichhorn. Various Self-Organizing [2]Rotaxanes. *GRC: Liquid Crystals*, New London, New Hampshire, United States of America, **2007**. (Ph.D. Work- oral presentation)